GEOCHEMISTRY AND PGE MINERALIZATION OF THE KITTO INTRUSION: A PRODUCT OF MESOPROTEROZOIC PLUME MAGMATISM THROUGH FAULT BOUNDED ARCHEAN CRUST, EAST NIPIGON EMBAYMENT, NORTHERN ONTARIO

Jordan Elliot Laarman

Submitted in partial fulfillment of the requirements of a Master of Science Degree in Geology, Lakehead University

May 2007

ABSTRACT

The Kitto intrusion is a Mesoproterozoic 1117.7 ±1.8 Ma peridotitic to gabbroic intrusion, that formed as a result of plume magmatism and was emplaced along Mesoproterozoic and Archean faults in the East Nipigon Embayment of northern Ontario. The plume signature for the Kitto intrusion is suggested by five samples with OIB (ocean island basalt)-like primitive mantle normalized multielement patterns in the lherzolite-olivine websterites.

In the southern part of the intrusion, the sequence of lithologies from top to bottom is lherzolite, olivine websterite, vari-textured pyroxenite, pyroxenite and melanogabbro. The basement is banded iron formation and mafic metavolcanic rocks. Lithologies on surface are dominantly lherzolite, with olivine websterite present in the area of the Phoenix mineralized occurrence. The Kitto intrusion is dominated by lherzolite that exhibits cumulate to pyroxene-poikilitic textures dominated by olivine with lesser clinopyroxene and poikilitic orthopyroxene. The lithologies crop out as a 15 to 30 cm thick layer cake bed dipping from 0 to 30° to the SE and SW. The olivine websterite displays similar cumulate to pyroxene-poikilitic textures, but contains more abundant clinopyroxene. The pyroxenite exhibits orthocumulate textures consisting of cumulate clinopyroxene and intergranular plagioclase. The melanogabbro comprises poikilitic plagioclase and minor cumulate clinopyroxene. In the central part of the intrusion, lithologies from east to west are lherzolite, olivine websterite, pyroxene-porphyritic melanogabbro and granophyric gabbro. Lherzolite and olivine websterites in the central part of the intrusion are more fractionated than at the southern part of the intrusion, and are characterized by the presence of secondary pyroxene and minor plagioclase. The pyroxene-porphyritic melanogabbro also contains secondary pyroxene and, along with cumulate clinopyroxene, there is enrichment in intercumulus plagioclase component.

The lithologies of the Kitto intrusion have geochemical signatures consistent with crustal contamination of a primitive magma. The lherzolite-olivine websterites are characterized by primitive mantle normalized multielement patterns with negative Nb and Ti anomalies, consistent with assimilation of Archean continental crust. All the lithologies have ε_{Nd} contents of -5.54 to -6.53 consistent with contamination by an older crustal source. Trace element modeling of assimilation-fractional crystallization suggests the lithologies probably assimilated metasedimentary rock of the QST (Quetico Sedimentary Terrane) and mafic metavolcanic rock of the BGB (Beardmore-Geraldton Greenstone Belt) at depth. Emplacement at shallower depths was accompanied by assimilation of mafic metavolcanic rock and banded iron formation. In the central part of the intrusion, pyroxene-porphyritic melanogabbros have more pronounced negative Nb anomalies indicative of greater assimilation of continental crust.

Emplacement of the Kitto intrusion occurred with an initial pulse of pyroxenite-melanogabbro followed by a pulse of lherzolite-olivine websterite magma in the southern part of the intrusion. The initial pyroxenite-melanogabbro pulse is suggested by a trend of increasing forsterite and enstatite contents, and decreasing ferrosilite in olivine and pyroxene minerals from the melanogabbro to the higher pyroxenite. A second pulse is suggested by a trend of replenishment to higher forsterite, enstatite, and ferrosilite contents, but lower wollastonite content in olivine and pyroxene minerals in the lherzolite-olivine websterite. Towards the top of the intrusion trends of decreasing forsterite, enstatite and ferrosilite contents, but increasing wollastonite content, in olivine and pyroxene are consistent with fractionation of the magma.

The Kitto intrusion was probably emplaced along north-south Proterozoic and east-west Archean faults in the East Nipigon Embayment. Possible north-south orientated faults include the Nipigon River and Pijitawabik Faults. As the magmas came in contact with the east-west orientated Blackwater, Empire, Princess Lake, Standingstone and Sandy Creek Faults of the BGB, they were displaced east or west along the faults, creating the ring-shaped form of the intrusion.

Mineralization of the Kitto intrusion is represented by interstitial Ni-Cu-PGE sulphides in one zone at the bottom of the lherzolite-olivine websterite, two zones in the underlying pyroxenite, and one zone at the contact of the melanogabbro and the basement iron formation. On the surface outcrops, high Ni contents in the lherzolites and trends of increasing Ni with MgO in all the lithologies, show that Ni partitioned into olivine as the magma evolved. On the surface outcrops in the central part of the intrusion, lower Ni contents are associated with higher Cu contents in the pyroxene-porphyritic melanogabbros, suggesting the lithologies did not contain sufficient olivine that would partition the Ni. Generally, anomalous PGE contents occur with anomalous Ni and Cu contents in the lithologies. Se and S data suggest that externally derived sulphur resulted in sulphur saturation and the precipitation of Ni-Cu-PGE sulphides. High Se contents are detected in the main mineralized zone at the bottom of the lherzolite-olivine websterite, and in the zones of the underlying pyroxenite. High Se contents have also been detected in basement iron formation and SVU (Southern Volcanic Unit) mafic metavolcanic rocks consistent with these lithologies being sulphur sources for contamination and mineralization.

ACKNOWLEDGEMENTS

I first thank Bob Middleton of East West Resource Corporation and Maple Minerals Corporation for access and funding of the geological mapping and surface rock sampling and analysis performed for this thesis. I thank Dr. Pete Hollings of Lakehead University for his continual support, supervision and funding of analyses throughout this thesis. I thank Chris Lane for helping me collect and map the rocks in the field. I thank Anne Hammond for rock preparation. I finally thank my family; my parents, brothers and sisters for continual moral support through my working of this thesis and my time at Lakehead University in general. Thanks again.

TABLE OF CONTENTS

List of Figures

List of Tables

CHAPTER 1

INTRODUCTION

1.1 Magmatic Ni-Cu-PGE Deposits

Magmatic Ni-Cu-PGE deposits are important sources for PGE (Platinum Group Elements) in a variety of deposits worldwide. Magmatic Ni-Cu-PGE deposits have been subdivided into sulphide-rich Ni-Cu-Co-(PGE) deposits and sulphide-poor PGE-(Cu)-(Ni) deposits (Lesher, 2005). Examples of sulphide-rich Ni-Cu-Co-(PGE) deposits are the stratiform massive/net-textured/disseminated Ni-Cu-(PGE) deposits of Noril'sk, Kambalda, Pechenga, Raglan, Sudbury and Thompson (Lesher, 2005). On the other hand sulphide-poor PGE-(Cu)-(Ni) deposits include stratiform "reef style" low-sulphide PGE-(Cu)-(Ni) deposits of Bushveld, Stillwater and the Great Dyke (Lesher, 2005). Sulphide-rich "Noril'sk-type" deposits formed as magmas became saturated with sulphur early in their crystallization histories to precipitate sulphides that settled to basal zones of the complexes (Lesher, 2005). Usually these intrusions or volcanic rocks were contaminated either by continental or S-rich crust that caused them to be saturated with sulphur and precipitate Ni-Cu-PGE minerals that may concentrate as deposits. Contamination by continental crust could cause Si and Al-enrichment or fractionation in the intrusions or volcanics resulting in sulphur partitioning out of the magnesian magma into sulphide phases. Contamination by sulphur-rich crust could cause metals to partition into external sulphides when introduced to the magmatic systems. On the other hand, sulphide-poor "Bushveld-type" deposits formed as magmas became saturated with sulphur due to magma mixing and have not been contaminated with crustal material, but rather were saturated with

magmatic sulphur to precipitate out sulphides (Lesher, 2005). Recently, exploration programs have focused on Ni-Cu-PGE deposits of the Mesoproterozoic Nipigon Embayment of the Southern Geological Province as it contains gabbroic to peridotitic intrusions that are similar to Noril'sk type intrusions. The Midcontinent Rift System and Nipigon Embayment have been described as a Noril'sk-type setting as there is a major rift structure, extensive chalcophile depleted flood basalts, and extensive Proterozoic sediments containing abundant sources of sulphur (Schulz et al., 1996). Two intrusions undergoing exploration in the Nipigon Embayment are the Seagull Intrusion and the Kitto intrusion (http://www.eastwestres.com). The Kitto intrusion has been described as a Noril'sk-type setting because:

a) it is among a group of picrites that intruded along large faults such as the Black Sturgeon Fault similar to the Noril'sk-Kharaelakhsky Fault in Siberia,

b) it intruded through sulphur-rich continental crust that includes large mineralized banded iron formations which are potential sources of sulphur,

c) it contains differentiated peridotites and pyroxenites that show textures similar to those of a dynamic magmatic system and

d) it contains up to 0.28% Ni, 0.13% Cu and 563 ppb Pt+Pd in a 1.22 m interval of sulphidized olivine websterite.

1.2 Thesis Objective

The purpose of this thesis is to investigate the petrogenetic processes involved in forming the Kitto intrusion and investigate magmatic activity along older fault structures within the Nipigon Embayment and Beardmore-Geraldton Greenstone Belt of the Superior Subprovince. Investigation of processes for contamination of an ultramafic magma in order to saturate it with respect to sulphur and precipitate sulphides associated with PGE minerals is undertaken. Objectives are to investigate the intrusion including a) mapping of the various lithologies on surface and logging them in drill core; b) petrographic analysis to distinguish textures and

mineralogy of the various units; c) plotting of geochemical trends of the units to investigate origin and c) comparing the geochemistry and mineralogy with the metal contents of the units to investigate mineralization with intrusion. This thesis includes: a) a petrographic analysis of various lithotypes to understand crystallization processes; b) a bulk rock and trace element geochemical analysis to understand fractionation histories of the intrusion; c)a REE (rare earth element) and trace element geochemical analysis to investigate the origin and contamination histories of the lithologic units; d) a radiogenic Sm-Nd analysis to determine magmatic origin of the units; e) an analysis of metal variation in the units; f) a Se and S analysis to examine contamination by external sulphur sources and g) mineral compositional data of zonation and variation within the intrusion.

1.3 Location and Geomorphology

The Kitto intrusion is located approximately 190 km northeast of Thunder Bay near Beardmore, Ontario on the eastern shore of Lake Nipigon (Fig 1.1). It is a 6 km diameter semicircular peridotitic-gabbroic ring complex that cross-cuts mafic metavolcanic and metasedimentary rocks of the Beardmore Geraldton Greenstone Belt and Quetico Subprovince, and is in turn cut by Nipigon diabase intrusions (Fig. 1.2; Oliver, 2001; Hart et al., 2002). The intrusion is surrounded by large diabase ridges that have steep cliffs on the western side and talus slopes on the eastern side.

1.4 Previous Work

Previous work on the Kitto intrusion includes work from reconnaissance mapping and exploration. Mapping by Mackasey (1969) in Eva and Summers townships outlined the character of the metavolcanic and metasedimentary rocks in the townships and a westward-dipping intrusive diabase sheet in the eastern part of the townships. The Geological Survey of

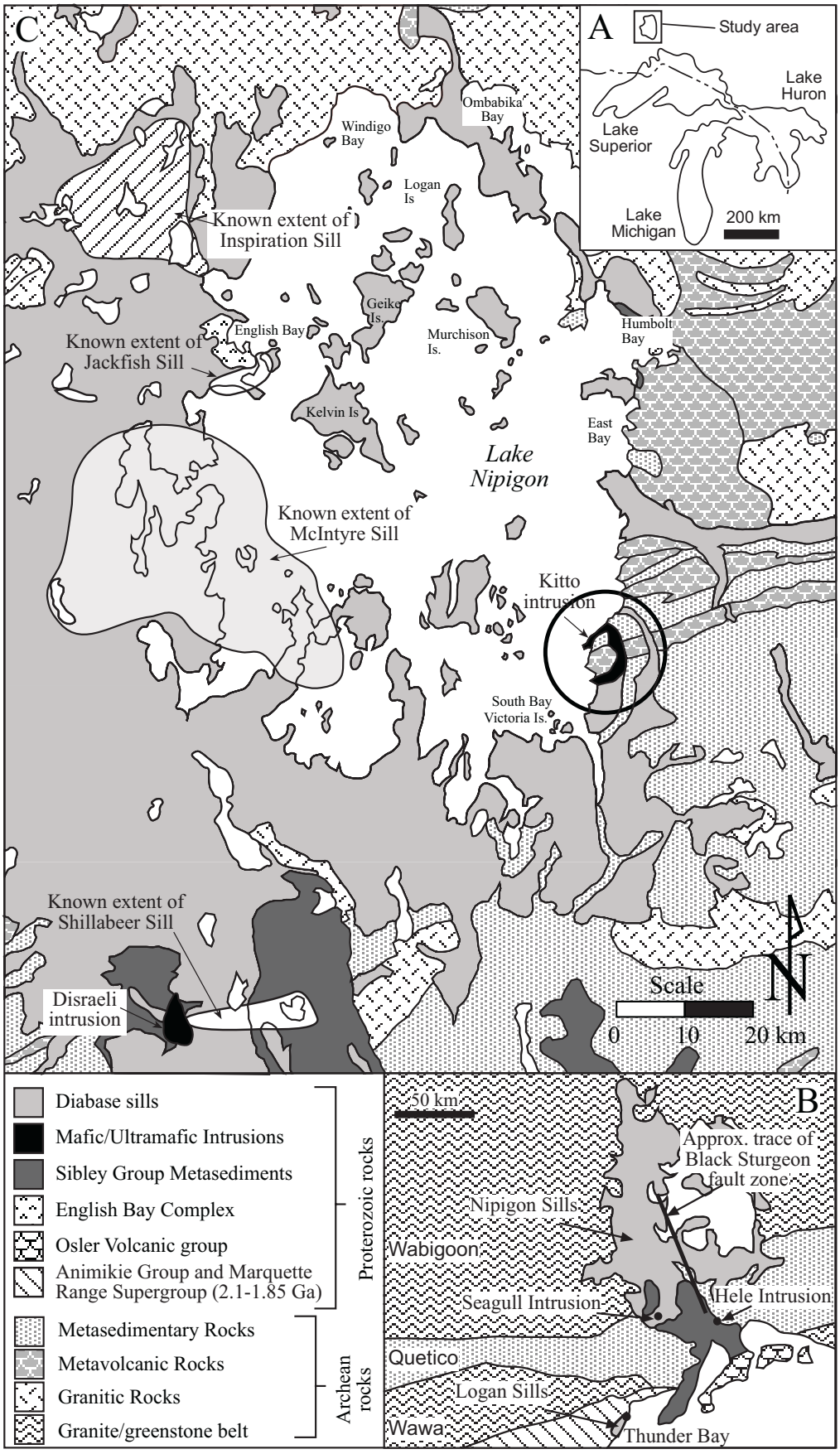

Figure 1.1: A) Location of the study area in relation to the Great Lakes. B) Simplified regional geological map showing location of members of the Logan Igneous Suite. C) Simplified geological map of the Nipigon region showing the extent of the main Proterozoic intrusions recognized here. Unless otherwise indicated the diabase sills indicated on the map are part of the Nipigon sills. The Kitto intrusion is circled in black. Modified after Sutcliffe (1986) and Hart and MacDonald (2007).

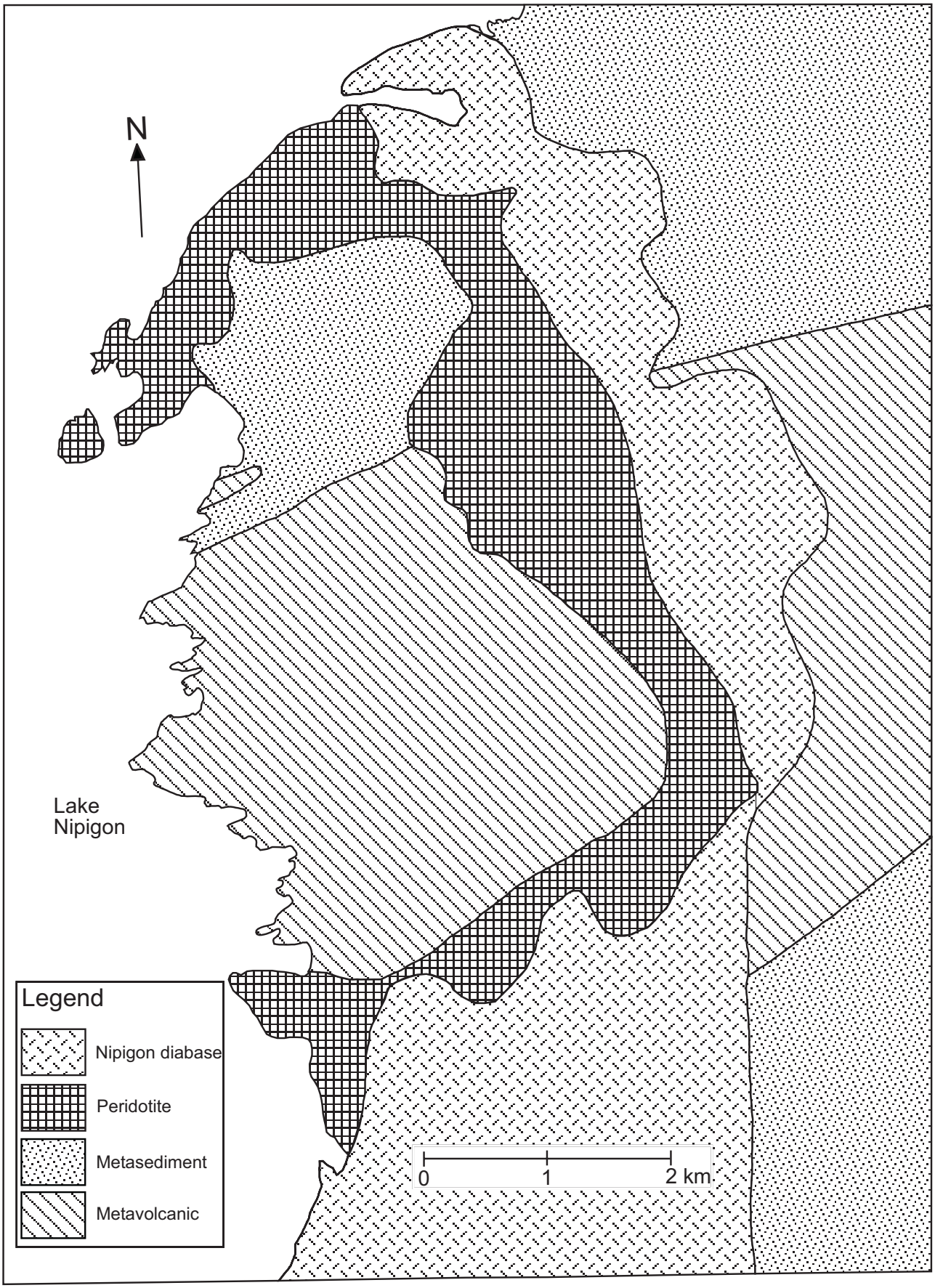

Figure 1.2: Simplified geological map of the Kitto intrusion. The Kitto intrusion is a semi-circular shaped peridotitic-gabbroic ring complex that cross-cuts mafic metavolcanic and metasedimentary rock of the Beardmore Geraldton Greenstone Belt and Quetico Subprovince and is surrounded by Nipigon diabase intrusions. Modified after Hart et al. (2002).

Canada (GSC, 1974) performed an airborne EM survey over the eastern part of Kitto intrusion outlining EM conductors related to iron formations.

Sutcliffe (1986) in 1981 mapped the Nipigon Plate and first delineated the Eva-Kitto Township intrusion. In 1986, R.H Sutcliffe wrote a Ph.D. thesis on the tectonics and petrology of mafic igneous rocks in the Lake Nipigon area. Sutcliffe (1986) undertook geochemical analysis of the picritic rocks of the Nipigon Embayment. Picritic rocks were first delineated on the east shore of Lake Nipigon in Eva and Kitto Townships (Sutcliffe, 1986). Rock types ranged from lherzolite and wehrlite to olivine gabbronorite that outcropped in a circular ring structure interpreted to be a ring dike, surrounding Archean metavolcanic and metasedimentary rocks. Inside the ultramafic ring dike, a small intrusion of olivine gabbro was identified. The rocks investigated by standard petrographic methods contained 40 to 70 modal % olivine, 15 to 40 modal % clinopyroxene, 0 to 15 modal % orthopyroxene, 0 to 10 modal % plagioclase, with minor chromite, ilmenite, amphibole and biotite (Sutcliffe, 1986). Olivine melagabbro units were texturally similar to ultramafic rocks, except for the presence of 10 to 35 modal % plagioclase. Mineral compositions were determined to be $Fo_{80\ to\ 69}$ for olivine, $En_{44\text{-}54}Fs_{7\text{-}14}Wo_{38\text{-}46}$ for clinopyroxene, and $En_{76\text{-}80}Fs_{17\text{-}21}Wo_{2\text{-}4}$ for orthopyroxene (Sutcliffe, 1986). The picritic rocks were interpreted to outcrop in areas of magmatic centres for feeders of the diabase sills. However, variation in Al_2O_3 vs SiO_2 and MgO vs SiO_2 have shown that picrites and diabase units have different fractionation histories, and that the picrites are not parental to diabase (Sutcliffe, 1986). The picrite units were interpreted as feeder conduits for more-evolved cone sheets of diabase. The diabases surrounding the Eva and Kitto Townships picrite were interpreted to be emplaced as an inward westward dipping cone sheet structure into Archean plutonic and metamorphic rocks (Sutcliffe, 1986). Whole rock geochemical analyses of the

picritic chill samples showed high TiO_2, K_2O and P_2O_5 similar to transitional Fe-Ti basalts like the Osler Group volcanic rocks (Sutcliffe, 1986). The high abundances showed that the parent magma of the picrites was enriched in incompatible elements relative to diabase and that it had assimilated crustal material.

Kenting Earth Sciences (GSC, 1988) performed an airborne EM survey for the Geological Survey of Canada over the Beardmore-Geraldton Belt outlining conductors bordering the intrusion. Questor Surveys Limited (Salib, 1989) performed an airborne TDEM survey for Glen Auden Resources Ltd., in exploration for gold and base metal deposits, and detected anomalies associated with the iron formations. The Geological Survey of Canada in 1990 noted anomalous nickel, copper and chromium contents in lake sediments over the Eva-Kitto intrusion. Shanks (1993) mapped the intrusion in Eva Township and delineated websterite and peridotite units in the field. Petrographic studies defined the units as peridotite and olivine melagabbronorite.

The Ontario Geological Survey in 2001 mapped the intrusion, after a forest fire in 1999, and revealed a showing with weak copper, nickel and PGE mineralization in a creek (the Phoenix occurrence). Hart et al. (2002) in an open file report on the Precambrian geology of Eva and Kitto townships studied the intrusion in detail. Based on field mapping by the Ontario Geological Survey the previous year, the intrusion was subdivided into an inner zone of olivine gabbro, a central zone of massive peridotite, and an outer zone of pyroxene porphyritic peridotite. Petrographic analyses performed by Duggan (2002) subdivided the intrusion into a lherzolitic outer zone, a wehrlite core and a granophyric gabbro inner zone. Geochemical whole rock analyses were undertaken to delineate geochemical trends in the intrusion. On a La/Sm vs. Gd/Yb plot, peridotite samples showed no variation and the magma was interpreted to exhibit

very little contamination. Primitive mantle normalized plots were interpreted as an OIB (ocean island basalt) or plume-like signature of the peridotite and granophyric olivine gabbro units. Similar geochemical trends between olivine gabbro and peridotite, and lack of variation in REE within the peridotite led to the interpretation that the intrusion was formed by a single pulse of magma with a base at the outer eastern edge of the intrusion that underwent fractional crystallization resulting in the formation of olivine gabbro towards the top.

Hunter Dickinson Incorporated (Oliver, 2001) undertook prospecting and sampling in the area of the intrusion returning assays for ppb Pt and Pd. Based on prospecting performed by the OGS the previous year, Kennecott Canada Exploration Inc (Fugro Airborne Surveys, 2002) supervised an airborne MegaTEM and magnetics survey done by Fugro Airborne Surveys Corp. EM and magnetic anomalies were prospected with some assays running at 901 and 1065 ppb Pt+Pd at the Phoenix Occurrence. Kennecott Canada Exploration Inc (Coombes and Rossell, 2003) drilled four DDH (diamond drill holes). Hole EK-2 intersected disseminated po-cpy (pyrrhotite-chalcopyrite) mineralization and was the only drill hole to intersect the magnetite-rich metapelites of the Archean basement. Assays were up to 0.28% Ni, 0.13% Cu and 563 ppb Pt+Pd in a 1.22 m interval.

1.5 Methods

In order for samples to be collected for analysis of the intrusion, the four drill holes drilled by Kennecott Canada Exploration Inc. termed EK-01, EK-02, EK-03 and EK-04, from the southern part of the Kitto intrusion, were logged by the author. In addition, another drill hole EK-05-01 was logged that was drilled in concurrence with other work performed as a result of this thesis. On the basis of logging the different lithologies in the drill holes, samples were selected for geochemical analysis. Two weeks of surface mapping and sampling of surface

exposures also took place resulting in a geological map delineating the different lithologies of the intrusion.

1.5.1 XRF (X-Ray Fluorescence spectrometry) and ICP-MS (Inductively Coupled Plasma-Mass Spectrometry)

42 samples were chosen for whole rock and Se analysis from the four Kennecott drill holes investigated. The 42 samples were chosen to be representative of each lithological type, with the majority of samples chosen from each lithology in the mineralized core from DDH EK-02. The samples were slabbed and polished thin sections were made for study using a petrographic microscope and SEM-EDS (Scanning Electron Microscope-Energy Dispersion Spectrometry) analysis. 64 surface samples were collected in the field as part of an exploration project funded by East West Resource Corp. and Maple Minerals Corp. These samples were taken principally from the southern and central parts, and with a few from the northern part of the Kitto intrusion. 37 of the 64 surface samples were chosen to be slabbed and made into thin sections. The surface samples were chosen to document lithologic variation throughout the surface exposure of the intrusion. Preliminary examination of the thin sections for texture and mineralogy was carried out using both transmitted and reflected light microscopy.

Primary crushing of the 42 samples was done using a carbide tungsten mallet and metal plate, breaking them down to 3 to 4 mm fragments. Milling was done using an agate rotary mill reducing the samples to 200 μm. The samples were wrapped in paper on the metal plate, and the metal plate and agate mill cup were cleaned with methanol between each sample to avoid contamination. The powders were analysed by XRF (X-Ray Fluorescence spectrometry) and ICP-MS (Inductively Coupled Plasma-Mass Spectrometry) at the Geoscience Laboratories (Geo Labs) of the Ministry of Northern Development and Mines in Sudbury, Ontario. Together with the drill core samples, 37 of the 64 surface samples were crushed into powders and sent to Geo

Labs for REE (rare earth elements) using ICP-MS. Samples were analyzed for major elements by XRF and for trace and REE by ICP-MS. XRF was performed on fused discs of the samples. Totals for major element oxide data were generally 100 wt. %±2% and have been recalculated to a 100 wt. % volatile-free basis. Detection limits for major elements are 0.01 wt. % and relative standard deviations of duplicate analyses are within ±5 %. Trace elements and REE were analysed using a Perkin-Elmer Elan 9000 ICP–MS following a variation on the protocol described by Burnham and Schweyer (2004) and Tomlinson et al. (1998). Twenty four trace elements were determined using a 200 mg aliquot of powder digested by a two stage procedure involving an initial decomposition in a closed beaker by a mixture of HF with lesser HCl and $HClO_4$ followed second mixture of dilute HCl and $HClO_4$ as described by Burnham et al. (2002). Detection limits for some critical elements, defined as 3σ of the procedural blank, are as follows: Th (0.032 ppm), Nb (0.044 ppm), Hf (0.085 ppm), Zr (3.2 ppm), La (0.048 ppm) and Ce (0.08 ppm) (Burnham and Schweyer 2004).

The 64 surface samples were crushed into powders and analysed by ICP-MS and XRF at ALS Chemex. Sample preparation included the splitting off of 250 g per rock and the pulverizing to better than 85% and passing 75 μm. In preparation for ICP-MS analysis on PGE metals, samples were reduced by fire assay fusion of 30 g of sample. For fire assay fusion, samples were first dissolved into a two-phase melt of barren borosilicate slag and molten lead using an aggregate fusion mixture of litharge (lead oxide) and fluxes such as sodium carbonate, borax, silica, potassium nitrate and household flour. The two-phase melt was poured into an iron mold to cool and solidify a lead button. The lead button, that contains the PGE metals, was placed on a magnesia cupel in a furnace at 960 to 1000ºC to melt and oxidize the lead leaving a small bead of PGE metal behind for analysis by ICP-MS. In preparation for ICP-MS analysis of

base metals and trace elements, the 64 samples were reduced by aqua regia digestion, which involves the treating of the samples with a 3:1 mixture of hydrochloric and nitric acids followed by drying to dissolve out the elements for analysis. The elements were then analysed by ICP-MS for 50 elements with detection limits in the level of ppm. In preparation for XRF whole rock geochemical analysis, the 64 samples were reduced by lithium borate fusion. Fusions were carried out in an automated Claisse-type fluxer. Fusion melts were then poured into disks and were analysed by XRF.

1.5.2 SEM-EDS (Scanning Electron Microscope-Energy Dispersion Spectrometry)

SEM-EDS analysis was performed on 17 of the 42 drill core samples and 10 of the 37 surface samples at Lakehead University using a JEOL 5900 LV SEM equipped with an Oxford EDS detector, and using LINK ISIS SEMQUANT computer software. Thin sections were carbon coated to prevent charging during analysis. Samples were analysed with an accelerating voltage of 20 kV, a beam current of 0.475 nÅ on a Ni standard, with raw EDS spectra acquired for 30 seconds live time. The standard used for analysis of olivine was the gl-olivine standard for Mg, Fe, and Si elements and the pyroxene DJ35 standard for analysis of Mg, Fe, Ca and Si in pyroxene. The DJ35 standard was also used for plagioclase analyses.

1.5.3 TIMS (Thermal Ionization Mass Spectrometry)

TIMS analysis was performed on 10 of the 42 drill core samples at Carleton University for Sm and radiogenic Nd. Powders were prepared at Lakehead University by crushing rock sections using a tungsten carbide mallet and metal plate, and secondly reducing them to powders in the agate rotary mill. At Carleton University, the powders were first spiked with a mixed ^{149}Sm-^{148}Nd spike and dissolved in Savillex Teflon beakers. Samples were first dissolved with 1.5 to 2 ml 2.5N HCl in screw-cap vials for four minutes. For Sm separation, samples were

added to borosilicate glass columns containing AG50-X8 cation resin using a 0.5 ml pipette. The sides of the column were then washed with 1 ml 2.5 N HCl. The 21 ml of 2.5 N HCl were added, let pass through the columns and discarded. The 3 ml of 6 N HCl were then added and let pass through. The screw cap vials were then rinsed out with ultrapure H_2O and placed under the column for collecting REE. The 9 ml of 6 N HCl was then added to the columns and collected in the vial. When collected, the vial was put on a hot plate to dry into a residue. The 0.26 N HCl was then added to the REE residue in the vial and left to dissolve for 30 minutes. For Nd separation, samples were pipetted in 0.26 N HCl into columns and let drain. Columns were then washed with 1 ml 0.26 N HCl and let drain. Columns were filled with 0.26 N HCl, and acids were left to drip for a prescribed Nd wash time. After 20 minutes, columns were topped off with 0.26 N HCl. At the end of the wash period, Nd was collected in clean snap-cap beakers for 25 to 30 minutes until beakers were full. At the end of collection, the beakers were placed on the hotplate to dry into a residue. Columns were then washed with 0.5 N HCl and let drain for a prescribed Sm wash time. After 20 minutes, columns were topped off with 0.5 N HCl. At the end of the wash period, Sm was collected in clean snap-cap beakers for 20 minutes until beakers were full. At the end of collection, the beakers were placed on the hotplate to dry into a residue. For TIMS analysis, samples were loaded with HNO_3 on rhenium double filaments and run in a Thermo Finnigan Triton Isotope Ratio Mass Spectrometer with a 4.5 A current for 30 minutes until the HNO_3 was evaporated. Nd isotopic ratios could then be measured using a La Jolla standard of $^{143}Nd/^{144}Nd = 0.511850$. Initial ε_{Nd} values were calculated using a U-Pb zircon age of 1117 Ma.

CHAPTER 2

GEOLOGICAL SETTING

2.1 Geological setting of the Kitto intrusion

The geological setting of the Kitto intrusion involves the tectonic history of the East Nipigon Embayment, which involves both an Archean basement and a Proterozoic component. The Archean basement includes the Beardmore-Geraldton Greenstone Belt and Quetico Sedimentary Terrane that surround the intrusion. Regionally, these terranes are part of the Superior Province, a large Archean craton with an area of 1,572,000 km^2 (Fig. 2.1; Thurston, 1991). Paleoproterozoic magmatism is recorded by the ca. 2100 to 2076 Ma Marathon and Fort Frances dike swarms, and intrusion of the Pickle Crow diabase dikes at ca. 1880 Ma (Fig. 2.2; Buchan et al., 1996; Ernst, 2005). Mesoproterozoic tectonism of the Nipigon Embayment involves: intrusion of the English Bay Complex ca. 1537 Ma; the Sibley Group sandstone, mudstone and dolostone sedimentation; a series of peridotitic-gabbroic intrusions along north to northwest orientated faults, and intrusion of the Nipigon diabase sills (Davis and Sutcliffe, 1985). The Kitto peridotitic intrusion intruded the East Nipigon Embayment along east-west faults of the surrounding Beardmore-Geraldton Greenstone Belt (Fig. 2.3; Sutcliffe, 1986)

2.2 Archean geological setting of the Beardmore-Geraldton Greenstone Belt and the Quetico Sedimentary Terrane

The Beardmore-Geraldton Greenstone Belt (BGB) and Quetico Sedimentary Terrane (QST) have a tectonic history from ca. 2800 to 2700 Ma (Tomlinson et al., 1996). In the vicinity of the Kitto intrusion, the SVU (Southern Volcanic Unit) of the BGB consists of metabasalts, magnetite-chert iron formations and plagioclase-megacrystic flow units. The QST

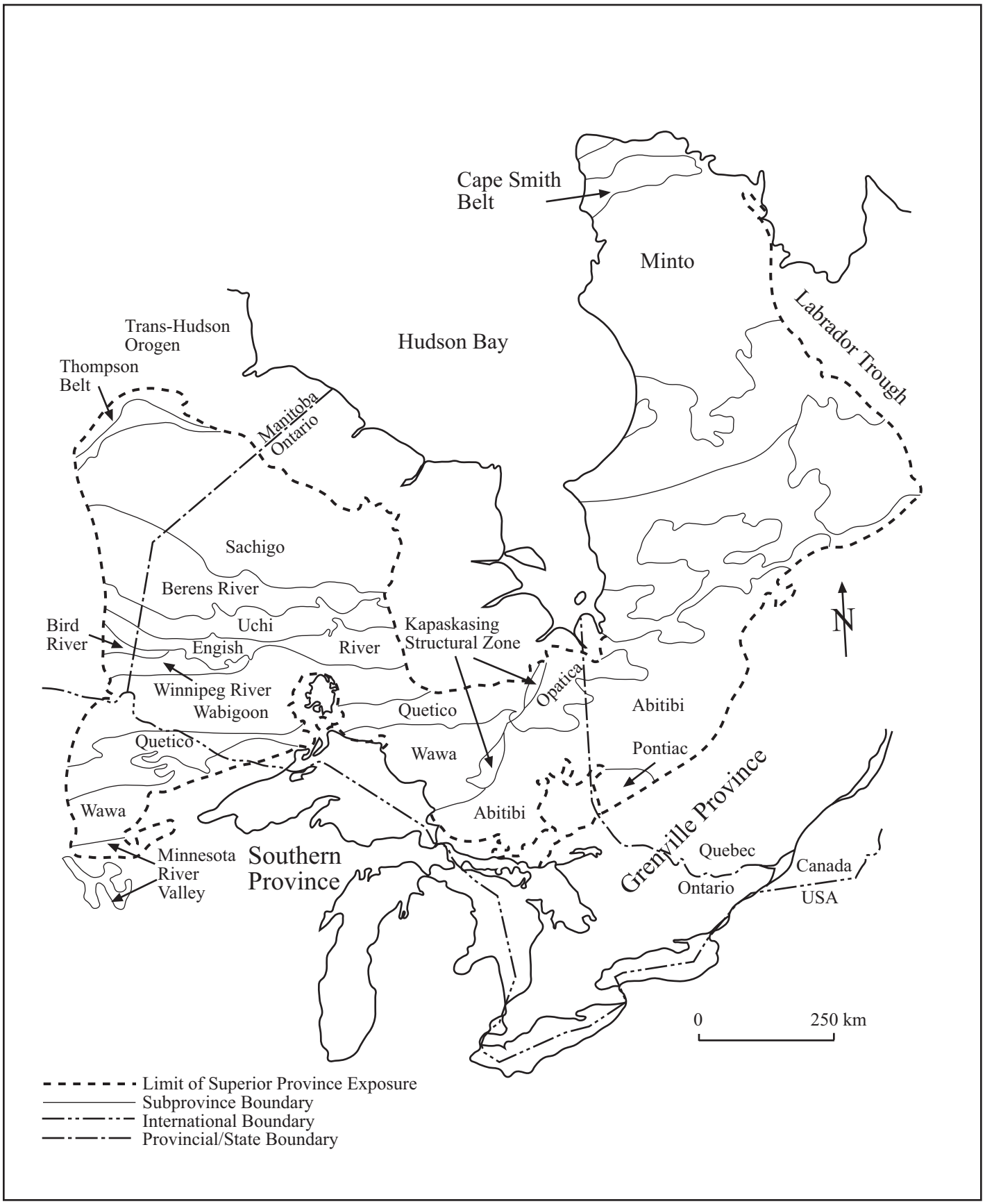

Figure 2.1: Simplified geological map of the Superior Geological Province, showing general east-west striking greenstone, plutonic high grade gneiss and metasedimentary subprovinces. The Beardmore-Geraldton Greenstone Belt is located on the south margin of the Wabigoon Subprovince east of Lake Nipigon. Modified after Card & Ciesielski (1986).

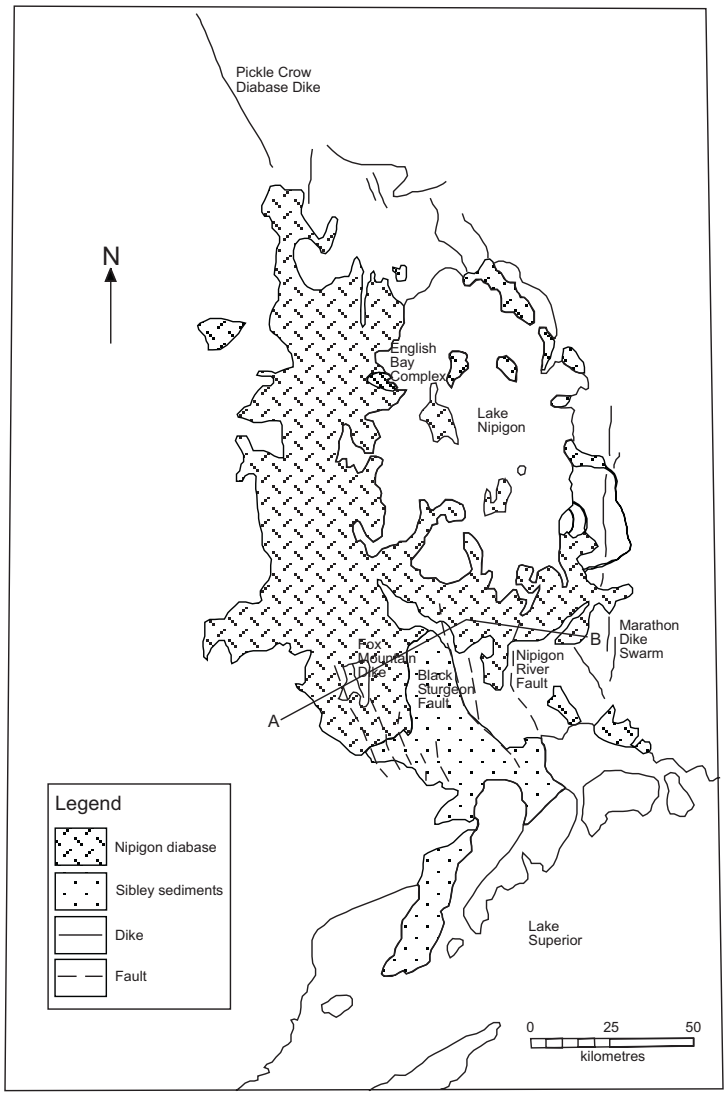

Figure 2.2: The N-S trending diabase dikes of the Marathon dike swarm, and the northwest trending Pickle Crow diabase dike were Paleoproterozoic structures on Archean basement before successive intrusions preceeding the Keewanawan Midcontinent Rift event ca. 1.08 Ma. The northwest trending Clearwater and Black Sturgeon Faults developed in the West Nipigon Embayment whereas the Nipigon River Fault and Pijitawabik Canyon formed in the East Nipigon Embayment. A cross-section of the Nipigon Embayment is located along line A-B (Figure 2.8). Modified after Sutcliffe (1986).

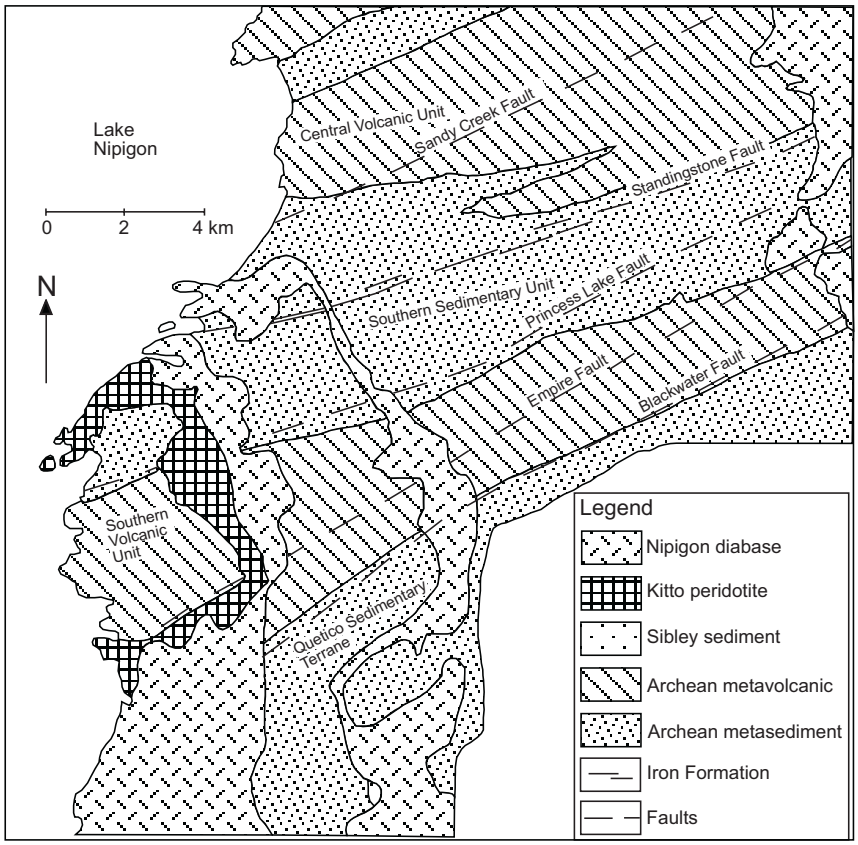

Figure 2.3: East-west faults bound the Beardmore-Geraldton Greenstone Belt. The Kitto intrusion occurs along the Empire and Blackwater Faults to the south and the Sandy Creek and Standingstone Faults to the north. Modified after Hart et al. (2002).

occurs south of the Kitto intrusion and consists of feldspathic metawacke, lithic metawacke siltstone and polymictic metaconglomerate units. In the BGB, formation of a micro-arc system occurred with the subduction of mid-oceanic ridge basalts (MORB) of the Southern Volcanic Unit (SVU) beneath a calc-alkaline andesitic island arc of the Central Volcanic Unit (CVU) (Fig. 2.4; Tomlinson et al., 1996). Basalts and andesites of the Northern Volcanic Unit are divided into the island arc andesites of the Poplar Point Assemblage and the MORB basalts of the Bish Bay Assemblage. After volcanism and accretion of BGB assemblages to the northern Onaman-Tashota Terrane (OTT) of the Wabigoon Subprovince, there was erosion of the OTT to form the accretionary sediments of the Southern Sedimentary Unit (SSU), Central Sedimentary Unit (CSU), Northern Sedimentary Unit (NSU) and the QST south of the BGB (Fig. 2.5; Williams, 1989). With northward accretion of the Wawa Arc to the QST-BGB-OTT, underthrusting and regional metamorphism occurred in all the units (Fig. 2.4; Tomlinson et al., 1996).

The Southern Volcanic Unit greenstone sequence consists of mid-oceanic ridge volcanism ca. 2.7 Ga and associated precipitation of magnetite-chert iron formation, followed by tuffaceous volcanism as the volcanic units subducted beneath the Central Volcanic Unit magmatic arc to the north (Fig. 2.4; Tomlinson et al., 1996; Hart et al., 2002). Plagioclase-megacrystic flows form marker horizons at the bottom of the lower mafic volcanic sequence (Hart et al., 2002). These units erupted as ponded magma chambers formed, allowing olivine and pyroxene fractionation to occur, followed by ascent of the less dense melts to lower pressure magma chambers (Blackburn et al., 1991). Higher in the sequence, massive basalt flows erupted with the partial melting of an undepleted to slightly depleted upper mantle (Tomlinson et al., 1996). The basalts have light rare earth element (LREE) depleted patterns similar to N MORB (normal MORB) tholeiites (Hart et al., 2002). After massive volcanism, pillowed and amygdular

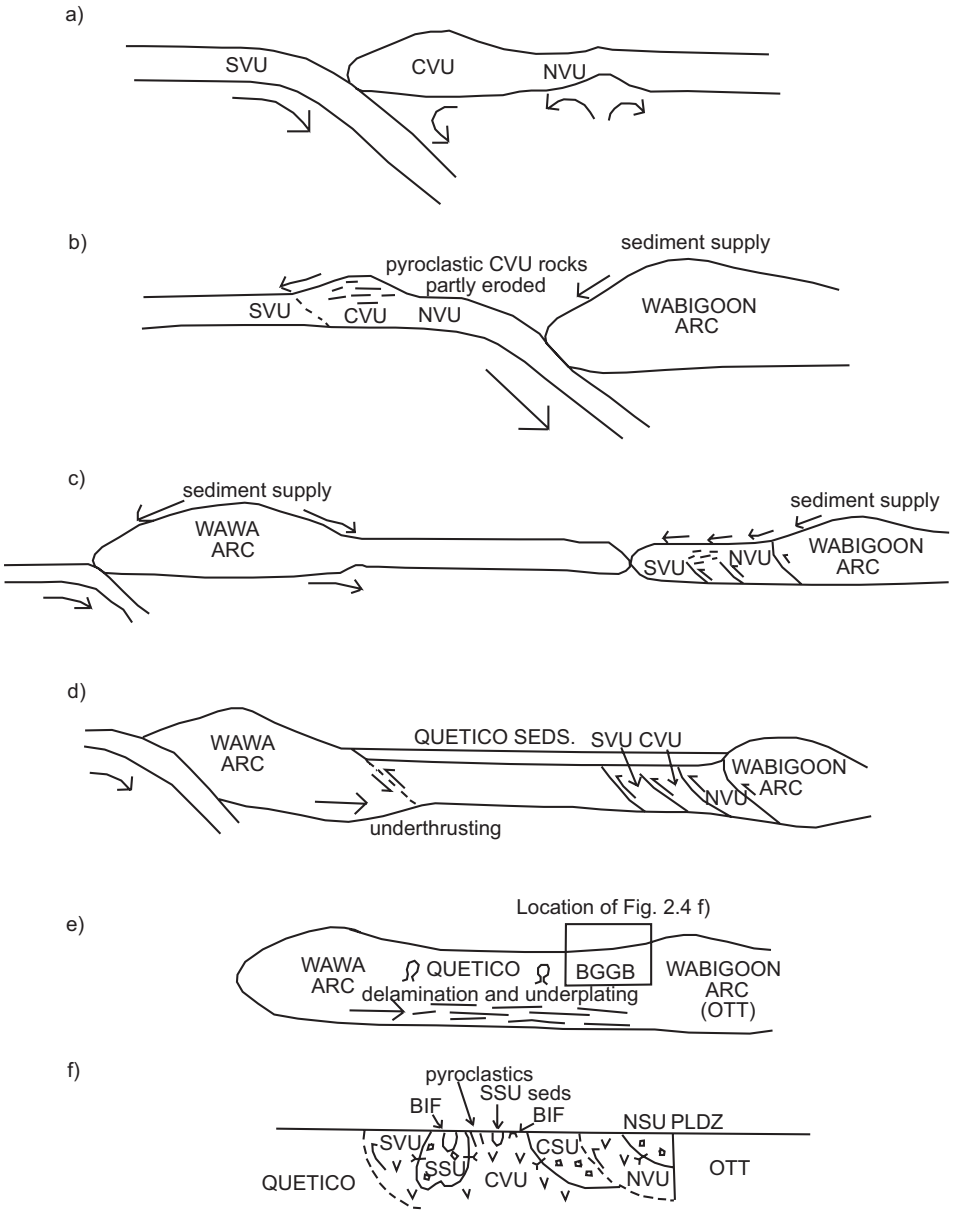

Figure 2.4: Tectonism of the Beardmore-Geraldton Greenstone Belt. (a) Formation of a micro-arc system occurred with the subduction of MORB basalts of the Southern Volcanic Unit (SVU) beneath a calc-alkaline andesitic island arc of the Central Volcanic Unit (CVU). (b) Local erosion and alluvial fan sedimentation of the CVU andesites occurred to form the Southern Sedimentary Unit between the SVU and the CVU. (c) After collision and the closing of the ocean between the Beardmore-Geraldton Belt and the Onaman-Tashota Terrane, there was large-scale erosion of OTT volcanic and plutonic rocks southward onto the BGB to form the Southern Sedimentary Unit and Quetico Sedimentary Terrane. (d) With the approach of the northward subducting Wawa Arc from the south towards the accreted Quetico Sedimentary Terrane-Beardmore-Geraldton Belt-Onaman-Tashota Terrane to the north, underthrusting of the Southern Volcanic and Southern Sedimentary Units occurred causing development of major east-west faults between the units. (e) Metamorphism occurred in the Quetico Sedimentary Terrane. (f) Present configuration of the Beardmore-Geraldton Greenstone Belt. Modified after Tomlinson et al. (1996).

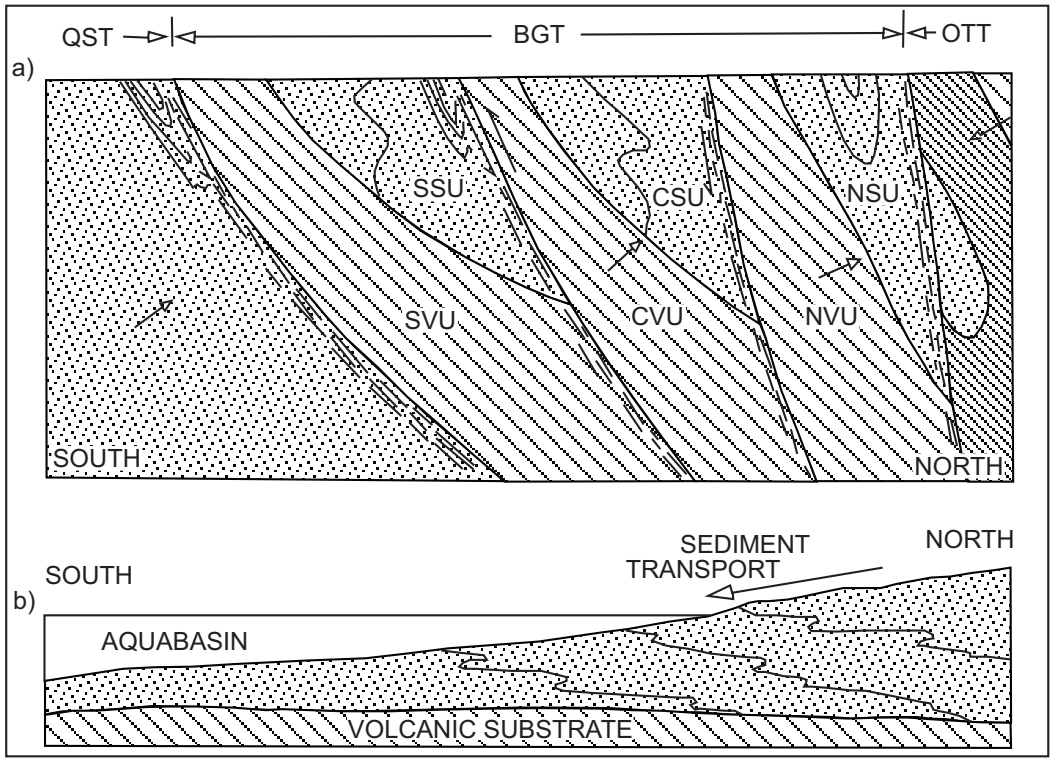

Figure 2.5: Schematic cross-section of the Beardmore-Geraldton Greenstone Belt.
a) Underthrusting of the Southern Volcanic and Southern Sedimentary Units occurred causing development of major east-west faults between the units.
b) After collision of terranes of the Beardmore-Geraldton microarc system, there was large-scale erosion of OTT volcanics and plutonics southward onto the BGB to form the Southern Sedimentary Unit and Quetico Sedimentary Terrane. Modified after Williams (1990).

flows erupted outward from the central vent fissures (Hart et al., 2002; Shanks, 1993). Successive cycles of massive volcanism continued along with eruption of pillow basalts. Synvolcanic gabbros mark these fissures as feeder intrusions to the surrounding basalts (Hart et al., 2002). These units are coarser grained but geochemically the same as the MORB basalts (Hart et al., 2002). In addition to volcanism, there was discharge of hydrothermal fluids from the vent fissures into the ocean causing the precipitation of Algoman magnetite-chert iron formations (Hart et al., 2002). These units are discontinuous horizons interlayered with the volcanic units, indicative of their local sites of origin. Iron formations are outlined by positive linear magnetic anomalies that follow the stratigraphy and geological foliations of the SVU in the Beardmore-Geraldton Belt (Fig. 2.6). In the Archean, as the central fissures of the SVU ocean floor basalts approached the calc-alkaline magmatic-erupting volcanoes of the CVU, volcanic units became more tuffaceous in character reflecting ejecta thrown outward from the island arc volcanoes of the CVU onto the massive and pillowed flows of the SVU (Hart et al., 2002).

The SVU ocean floor basalts continued to subduct beneath the CVU magmatic arc until the SVU accreted to the arc with the closing of an ocean between the two assemblages (Fig. 2.4; Tomlinson et al., 1996). Local erosion and alluvial fan sedimentation of the CVU andesites occurred to form the Southern Sedimentary Unit between the SVU and the CVU (Shanks, 1993). At this time, the BGB micro-arc system migrated north until it collided with the OTT (Fig. 2.4; Tomlinson et al., 1996).

After closing of the ocean between the Beardmore-Geraldton Belt and the Onaman-Tashota Terrane, there was large-scale erosion of OTT volcanics and plutonics southward onto the BGB to form the Southern Sedimentary Unit and the northern part of the Quetico Sedimentary Terrane (Fig. 2.5; Tomlinson et al., 1996). Large-scale alluvial fan sedimentation

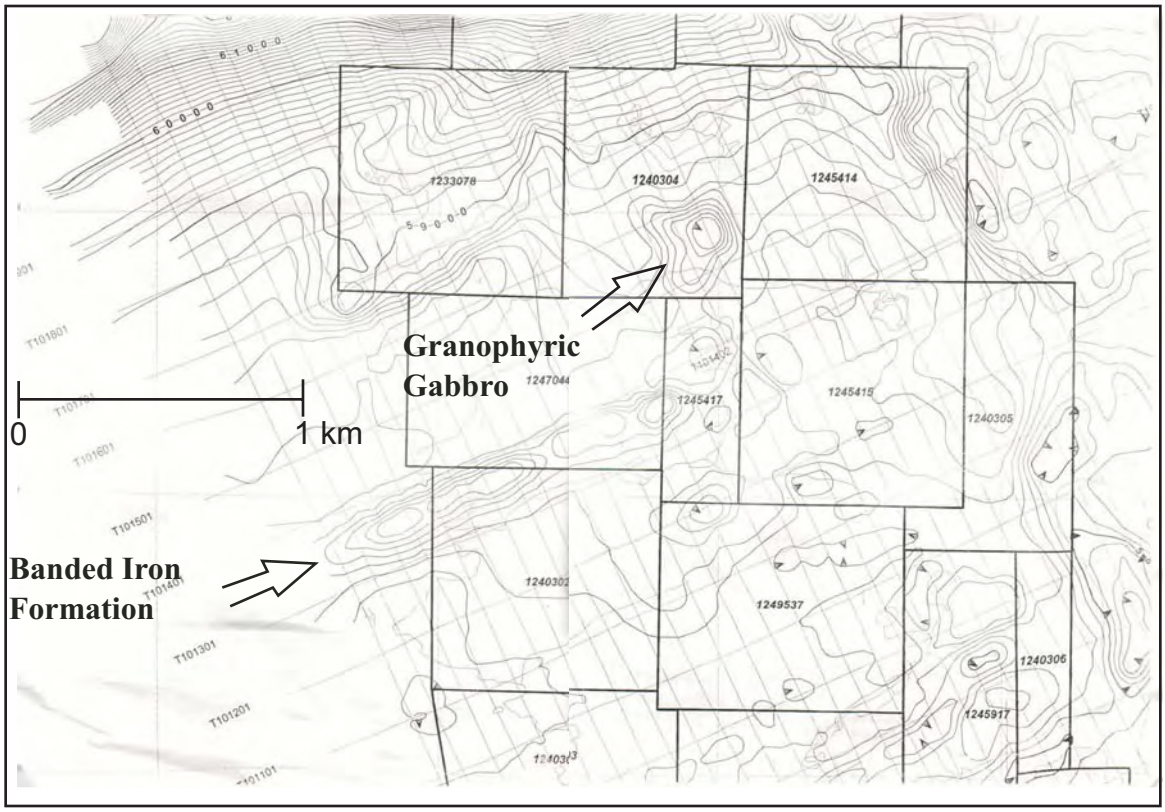

Figure 2.6: Airborne total magnetic map shows a linear array of positive magnetic conductors striking toward the centre of the Kitto intrusion. The bullseye negative magnetic anomaly to the north of the iron formation represents the granophyric gabbro in the centre of the zoned Kitto ring complex. Modified from Fugro Airborne Surveys (2002).

occurred to form the SSU turbidites north of the SVU basalts (Shanks, 1993). These sediments consist of feldspathic wackes, siltstones and argillites that have graded beds, rip-up clasts of sand, and flame sedimentary structures that show younging directions to the north (Hart et al., 2002). Coarsening upward sequences from south to north of argillite to siltstone to wacke cycles indicate environments of deposition for the SSU metasedimentary rocks ranging from delta front to distal submarine fan (Barrett and Fralick, 1989). Between the siltstone to wacke cycles are large, continuous, tens of km long and up to 25 m wide clastic-magnetite-argillite iron formations (Hart et al., 2002). The continuous nature and thickness of these units outlines them as distinct shoreline horizons that formed at the switch of anoxic eugeoclinal to oxidative miogeoclinal sedimentary environments of deposition with the progradation of delta lobe fronts outwards into the oceanic basins (Barrett and Fralick, 1985).

The northern part of the Quetico Sedimentary Terrane formed as part of the submarine fan turbiditic sedimentation from the Onaman-Tashota Terrane to the north of the Beardmore-Geraldton Belt (Devaney and Williams, 1989). Lithofacies in the QST include AB to ABC turbidites of northward-younging feldspathic wacke, lithic wacke, siltstone units that exhibit normal grading and rarer coarsening upward successions (Hart et al., 2002; Fralick et al., 1992; Devaney and Williams, 1988). The development of ABC turbidites in contrast to just A turbidites of the SSU shows that the depositional environment was more distal into the basin than that of the SSU (Fralick et al., 1992). The rare coarsening upward successions developed with depositional lobing of sediment on the distal fan.

With the approach of the northward subducting Wawa Arc from the south towards the accreted Quetico Sedimentary Terrane-Beardmore-Geraldton Belt-Onaman-Tashota Terrane in the north, underthrusting of the Southern Volcanic and Southern Sedimentary Units occurred

causing development of major east-west faults between the units (Figs. 2.4, 2.5; Tomlinson et al., 1996). The faults mainly associated with the boundaries of the SVU and SSU include the Blackwater River Fault at the lower boundary of the SVU with the QST; the Empire and Princess Lake Faults at the boundaries of the SVU and SSU; the Standingstone Fault associated with the banded iron formations in the SSU; and the Sandy Creek Fault at the north boundary of the SSU and the CVU (Fig. 2.3, Hart et al., 2002).

Along with the development of major thrust faults, the SVU volcanics and SSU sedimentary rocks underwent regional lower to middle greenschist facies metamorphism during three deformation events, while upper greenschist facies metamorphism occurred in the QST. In the BGB, the units were first imbricated from ca. 2696 to 2691Ma during D1 thrusting and accretion. S1 fabrics are shown by refolded folds in the banded iron formations of the SSU (Hart et al., 2002). D2 folding then occurred leading to the development of east-west oriented isoclinal folds within the SSU feldspathic wackes and iron formations (Kehlenbeck, 1986). S2 fabrics are shown by the dominant 245º to 275º slaty to phyllitic foliations in rocks of the SSU and SVU, isoclinal folds in the banded iron formations of the SSU, and the change from N-younging to S-younging sedimentary rocks in the SSU (Hart et al., 2002). The units finally underwent a D3 dextral shearing event to develop tight isoclinal folds and crenulation cleavages in banded iron formations (Lafrance et al., 2004). Along with development of foliation fabrics, mineralogical changes include the replacement of primary plagioclase-biotite-hornblende-pyroxene minerals in basalts of the SVU with albite-chlorite-actinolite and biotite minerals (Hart et al., 2002). In the SSU, quartz-feldspar-muscovite of feldspathic wackes are replaced by quartz-sausseritized albite-sericite and epidote minerals (Hart et al., 2002). In the QST, abundant medium to coarse grained biotite with albite and muscovite replace primary mineralogy of feldspathic wackes.

Associated with D3 shearing was the fluidization of Au-bearing hydrothermal fluids through fault boundaries between and within the SVU and SSU and along iron formation horizons of the SVU (Lafrance et al., 2004). Gold is hosted by crack-seal textured quartz-carbonate and sulphide-bearing quartz veins containing pyrite, arsenopyrite, chalcopyrite and tetrahedrite in carbonatized brittle-ductile dilatant shear zones at the Leitch and Sand River mines in the SSU (Smyk et al., 2005). Gold is also hosted by *en echelon* quartz veins containing pyrite, arsenopyrite, pyrrhotite and chalcopyrite in carbonatized metavolcanic rocks and iron formations such as at the Northern Empire mine in the SVU (Smyk et al., 2005).

2.3 Proterozoic geology of the Nipigon Embayment

Proterozoic magmatism in the northwest Superior Province, after the 2450 Ma Kenoran Orogeny, began with plume-related magmatism of the Marathon and Fort Frances diabase dike swarms from 2100 to 2076+5/-4 Ma (Fig. 2.7; Buchan et al., 1996). These swarms are interpreted to be the result of a mantle plume located to the south of the Superior Province (Buchan et al., 1996). Subsequently, at the time of development of the Animikian Basin to the south, there was ca. 1880 Ma intrusion of the 250 km long Pickle Crow diabase dike northwest of Lake Nipigon (Fig. 2.2; Ernst, 2005).

Tectonism of the West Nipigon Embayment began at 1599±1 Ma with intrusion of the Badwater Creek gabbro and the 1590.1±0.8 Ma intrusion of the Badwater Creek syenite (Heaman and Easton, 2006). Later volcanism associated with the Pillar Lake mafic volcanics occurred some time between 1514 and 1120 Ma in the Northwest Nipigon Embayment (Heaman and Easton, 2006). At ca. 1537+10/-2.3 Ma, anorogenic plutonism formed the English Bay granite-rhyolite Complex (Davis and Sutcliffe, 1985) as a result of plume activity at depth, and later intrusion along north-to-northwesterly trending faults within the Nipigon Embayment

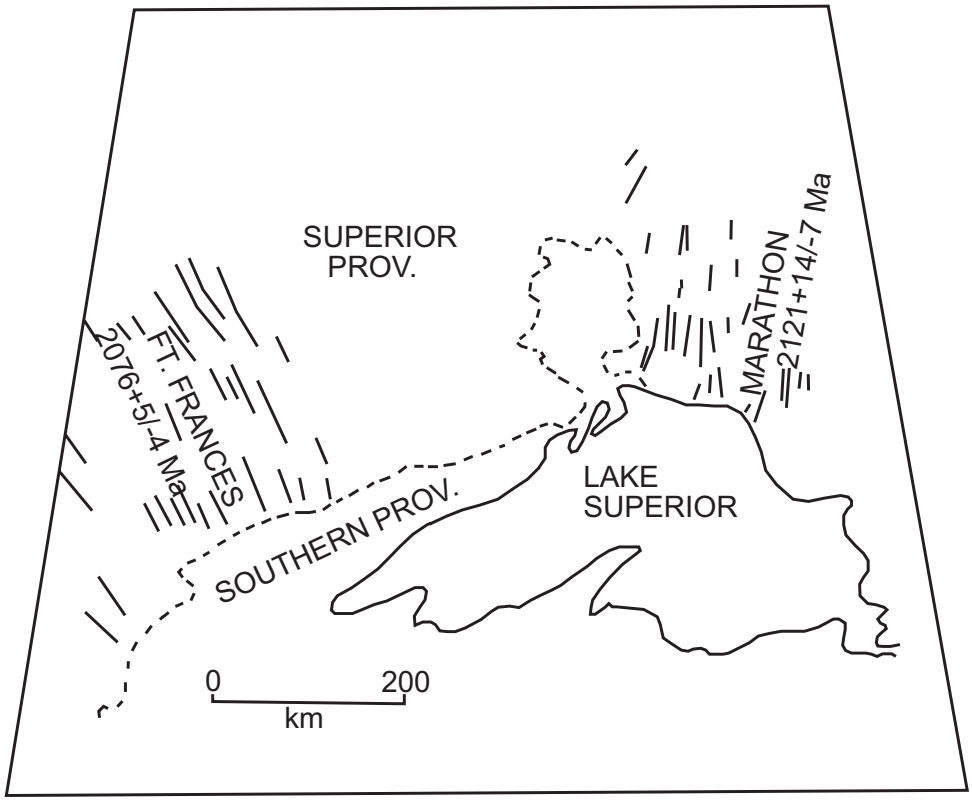

Figure 2.7: The Marathon and Fort Frances dike swarms intruded from ca. 2121 to 2076 Ma through Archean crust as a result of a mantle plume to the south. Modified from Buchan et al. (1996).

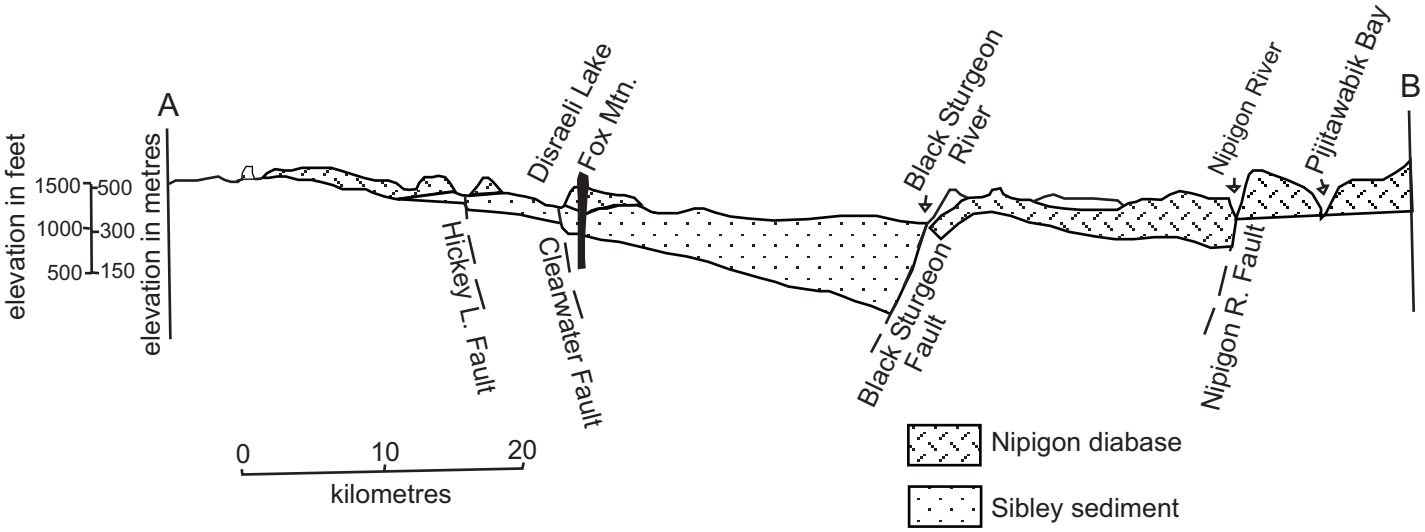

Figure 2.8: Cross-section of the Nipigon Embayment along line A-B on Figure 2.2. The Nipigon Embayment developed as a result of a series of intrusions along north to northwest trending faults. The Clearwater and Black Sturgeon Fault developed in the West Nipigon Embayment while the Nipigon River Fault and Pijitawabik Canyon developed in the East Nipigon Embayment. Between the Clearwater and Black Sturgeon Faults, a subsiding half-graben developed from reduction of asthenospheric upwelling below the crust after cessation of plume magmatism of the English Bay Complex. Block faulting and subsidence occurred along the Black Sturgeon Fault with loading of Sibley sediments between the faults. Modified from Sutcliffe (1986).

(Hollings et al., 2004; Hart and Magyarosi, 2004; Sutcliffe, 1986). The lithologies of the English Bay Complex consist of granite which has an equigranular phaneritic texture, and contains perthitic feldspars and polycrystalline clusters of quartz. The rhyolitic rocks are true porphyries with phenocrysts of alkali feldspar, quartz and hornblende in an aphanitic matrix of the same minerals (Hollings et al., 2004). Geochemically, the English Bay complex is composed of A-type granites and rhyolites, which have high K, high $K_2O + Na_2O$ and enrichment in Zr, Nb, Y and REE (Hollings et al., 2004).

In the East Nipigon Embayment, peneplanation of Sibley sediments occurred as the initial Proterozoic activity (between ca. 1537 and 1350 Ma) following the Marathon diabase dike swarm event (Rogala et al., 2005). The Sibley Group comprises a red bed molasse sedimentation sequence that was deposited with northward erosion of Penokean granitoids from the south (Franklin, 1970). Block faulting began in the Nipigon Embayment with broad subsidence from reduction of asthenospheric upwelling below the crust after cessation of plume magmatism of the English Bay Complex (Hollings et al., 2004). With continued loading of sediment, block faulting continued in the West Nipigon Embayment with subsidence between the Clearwater, Black Sturgeon and Nipigon River Faults (Fig. 2.8; Sutcliffe, 1986). The subsiding faults developed a half graben that controlled the remaining deposition of Sibley sediments (Fig. 2.8; Sutcliffe, 1986). In the East Nipigon Embayment, only a small amount of Sibley sedimentation is preserved that was partially-controlled by the Nipigon River Fault (Sutcliffe, 1986). Sibley Group sedimentation in the East Nipigon Embayment constituted a short history of cyclic mudstone to arenaceous dolomite sedimentation within a playa lake environment (Rogala et al., 2005).

In the West Nipigon Embayment, ultramafic and gabbroic plume magmatism occurred from ca. 1116 to 1106 Ma along north to northwest trending faults (Hart and Magyarosi, 2004). The faults are delineated by N-S aeromagnetic and topographic lineaments (Figs. 2.9 and 2.10; Hart, 2005).The Seagull ultramafic-to-gabbroic layered intrusion intruded along the Clearwater Fault ca. 1116.2±1.2 Ma (Fig. 2.11; Hart and Magyarosi, 2004; Sutcliffe, 1986; Heaman and Easton, 2006). In drill core, the intrusion deepens to 750 m at the Leckie Stock along the Clearwater Fault (Heggie, 2005; Hart, 2005). In the field, the Seagull intrusion consists of peridotite, olivine melagabbro, olivine gabbro and monzogabbro. The peridotite is medium to coarse grained, massive, commonly ophitic textured and composed predominantly of olivine and clinopyroxene. Whole rocks have up to 38.04 wt. % MgO and follow an olivine and clinopyroxene fractionation trend. The olivine melagabbro and olivine gabbro are fine-to-medium grained, medium-to-dark green, massive, and composed of pyroxene, up to 30 modal % plagioclase and up to 40 modal % olivine. The olivine melagabbro contains 11 and 17 wt. % MgO and follows a trend that changes from olivine and clinopyroxene control to clinopyroxene and plagioclase controlled fractionation. The olivine gabbro has <11 wt. % MgO and follows a plagioclase and clinopyroxene fractionation trend (Hart, 2005).

The Seagull intrusion has been studied in detail by Heggie (2005) and the following is a summary of that work. The intrusion consists of cumulate-textured dunite, lherzolite, olivine-amphibole pyroxenite, olivine websterite, websterite, plagioclase-bearing pyroxenite, olivine gabbro and hornblende gabbro units that have olivine compositions between 80 and 89 wt. % forsterite (Heggie, 2005). The intrusion has been subdivided in drill core on the basis of REE geochemistry into a basal unit characterized by LREE enrichment and HREE depletion and $(La/Sm)_n$ ratios of 1.4 to 3.0. The basal unit is overlain by a sub-main unit with lower LREE and

Figure 2.9: A topographic relief map of the West Nipigon Embayment displays many northwest to north-south orientated topographic lineaments indicative of faults and the north to northwest orientated nature of intrusion of diabase dikes and sills. Trends of lineaments are indicated by lines. Modified from OGS (2004).

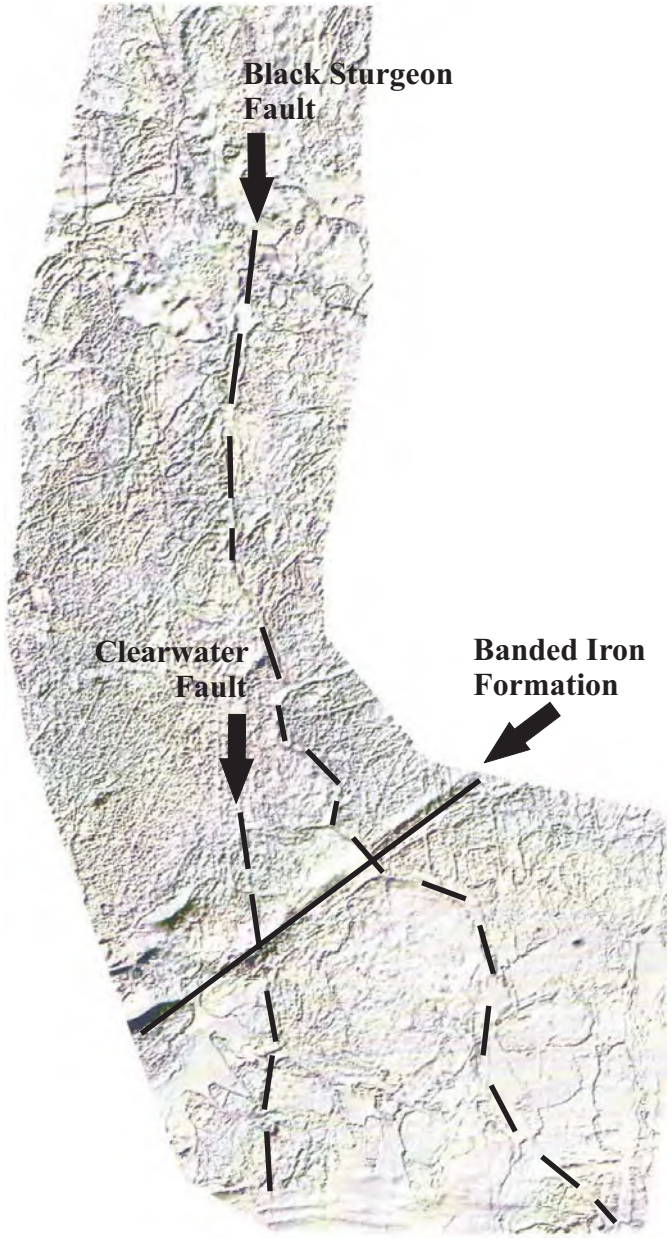

Figure 2.10: A total magnetic relief map of the West Nipigon Embayment displays northwest to north-south orientated lineaments of negative magnetic conductors indicative of faults. Modified from OGS (2004).

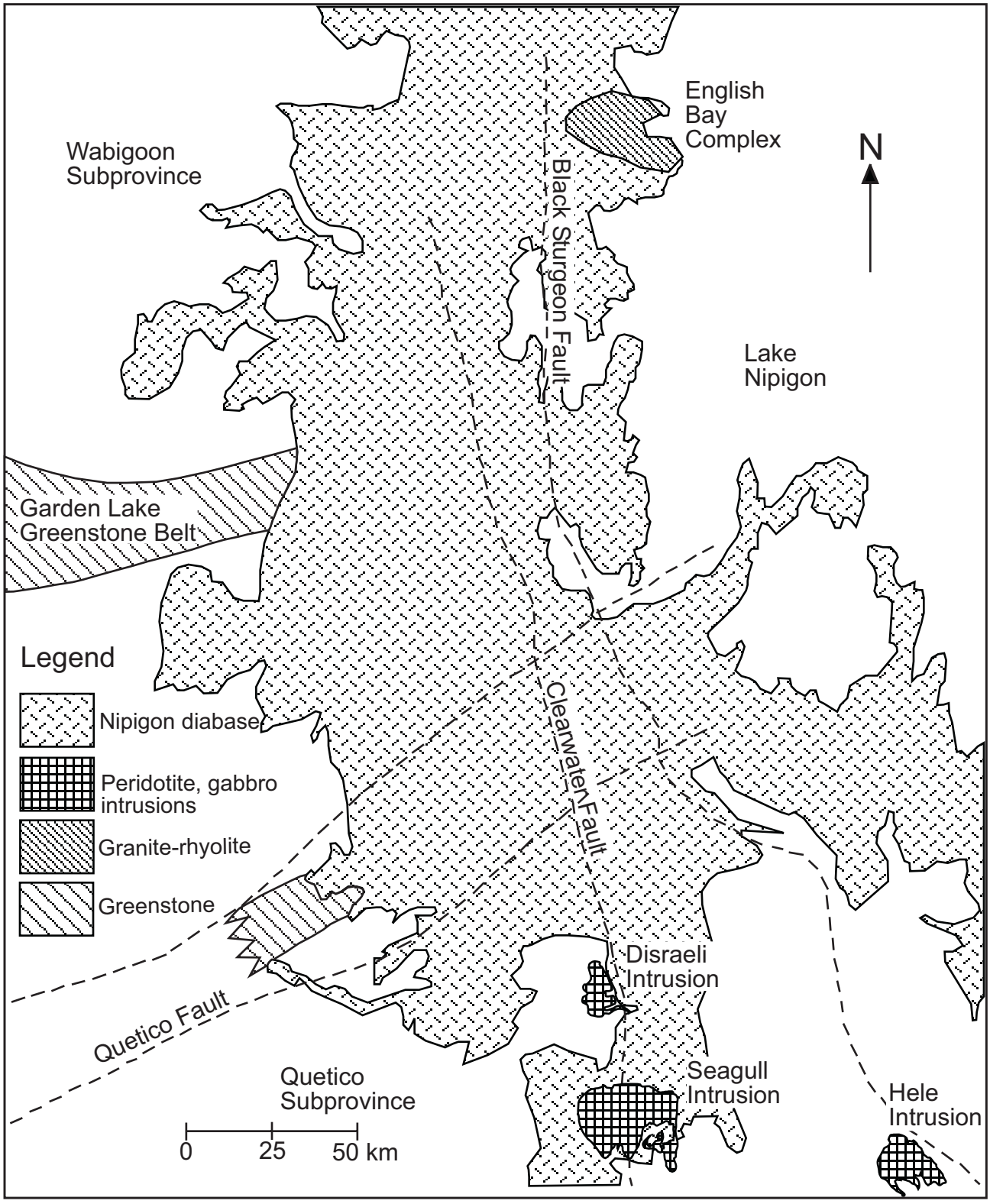

Figure 2.11: The West Nipigon Embayment contains north to northwest trending faults such as the Clearwater and Black Sturgeon Faults. The Seagull and Disraeli intrusions intruded along the Clearwater Fault, while the Hele intrusion intruded along the Black Sturgeon Fault. Modified from Hart (2005) and McNaughton (2002).

higher HREE and a main unit with $(La/Sm)_n$ ratios of 0.9 to 1.9 (Heggie, 2005). Overall, REE and HFSE ratios are comparable to ocean island basalts (Heggie, 2005). Ni-Cu-PGE mineralization is present in all three units, but most significant in the basal and sub-main units. Mineralization in the basal unit is at the contact with basement Quetico metasedimentary rocks and was caused by sulphur saturation of the magma during initial stages of emplacement. Mineralization in the sub-main unit of the intrusion occurs as horizons at 580 m in the RGB Zone. These horizons formed from episodic sulphide saturation events with continual input of magma and accumulation of olivine in the magma chamber with crystallization of the intrusion (Heggie, 2005). Variations toward unevolved forsterite contents in olivine from the bottom to top of the intrusion in four distinct zones give evidence of multiple replenishment events of magma within the crystallization history of the intrusion. In terms of isotope geochemistry, the Seagull intrusion has ε_{Nd} values of -0.2, reflecting an enriched plume mantle source, to -4.0 and $^{87}Sr/^{86}Sr$ ratios of 0.70 to 0.72 reflecting crustal assimilation by basement Quetico metasedimentary rocks and Sibley sedimentary rocks (Heggie, 2005).

The Disraeli intrusion intruded along the Clearwater Fault to the north of the Seagull intrusion ca. 1111.6±1.9 Ma (Fig. 2.11; Hart and Magyarosi, 2004; Sutcliffe, 1986; Heaman and Easton, 2006). The intrusion consists of lower pyroxene peridotite, olivine gabbro and monzogabbro units. The pyroxene peridotite is medium-to-coarse grained, massive, dark green to greenish black and composed predominantly of olivine and pyroxene. The peridotite has high MgO content and crystallized under olivine and pyroxene controlled fractionation (Hart and Magyarosi, 2004). The olivine gabbro is fine to medium grained, massive, and composed of pyroxene, plagioclase and up to 20 modal % olivine. The olivine gabbro crystallized under clinopyroxene and plagioclase controlled fractionation. In terms of REE geochemistry, both the

peridotite and olivine gabbro have REE and high field strength elements (HFSE) comparable to ocean island basalts which is probably indicative of a plume source (Hart and Magyarosi, 2004). The olivine gabbro has a high K_2O content interpreted as the result of crustal assimilation of basement Sibley sedimentary rocks (Hart and Magyarosi, 2004).

The 1106.6±1.5 Ma Hele gabbroic intrusion possibly intruded along the Black Sturgeon Fault (Fig. 2.11; Hart, 2005; Heaman and Easton, 2006). The intrusion consists of peridotite, olivine melagabbro and olivine gabbro. The peridotite is dark green, medium to coarse grained, massive and variable ophitic-textured. The peridotite has up to 29 wt. % MgO and follows an olivine and clinopyroxene fractionation trend. The olivine melagabbro-olivine gabbro is fine to medium grained, medium to dark green, massive and composed of pyroxene, up to 30% modal plagioclase and up to 40 modal % olivine. The olivine melagabbro has between 11 and 17 wt. % MgO and displays a change from olivine and clinopyroxene control to a clinopyroxene and plagioclase fractionation trend. The olivine gabbro has <11 wt. % MgO and follows a plagioclase and clinopyroxene fractionation trend. The monzogabbro is medium to coarse grained, massive, with variable amphibole content, and with pink feldspar in irregular pods. On a primitive mantle normalized multielement plot, the intrusion has weak negative TiO_2 and Zr anomalies and a wider range of Gd/Yb values reflecting increased fractionation compared to the Seagull and Disraeli intrusion. High K_2O contents in a monzogabbro may reflect assimilation of Sibley sedimentary rocks in the intrusion (Hart, 2005) as assimilation of Sibley would cause enrichment in alkali elements.

Contemporaneously with emplacement of peridotite and gabbro, there was intrusion of five suites of Nipigon sills in the West Nipigon Embayment from ca. 1119 to 1106 Ma (Richardson et al., 2005; Heaman and Easton, 2006). The sills intruded as flat-lying hypabyssal,

medium grained subophitic to ophitic olivine gabbronorite. The diabase intrusions resemble plume-related basalts comparable to modern oceanic island basalts with the majority characterized by negative Nb anomalies and elevated Th contents (Richardson et al., 2005). These are consistent with contamination of the intrusions by older LREE-enriched sources comparable to Archean granites (Richardson et al., 2005). The main Nipigon suite intruded as the predominant suite of diabase sills throughout the Nipigon Embayment. These diabase intrusions first emplaced as feeder dikes along north-to-northwest faults such as the Fox Mountain diabase dike along the Clearwater Fault (Fig. 2.2, 2.8; Sutcliffe, 1986). After intrusion of dikes, there was successive emplacement of diabase sills from the faults that ramped upward along the pre-existing fault structures and formed broad saucer-shaped bodies (Hart, 2005). The Nipigon suite diabase intrusions have sill thicknesses of 120 to 150 m to an excess of 250 m. The diabases are composed of 50 to 60 modal % plagioclase which occur as randomly orientated laths; 40 to 50 modal % pyroxene which form equant oikocrysts; up to 1 modal % olivine and <1 modal % hornblende and biotite (Richardson et al., 2005). Geochemically, the Nipigon suite has MgO values of 2.3 to 11.4 wt. %, Mg# of 21 to 63, low TiO_2 values from 0.7 to 2.7 wt. % and $(La/Yb)_{cn}$ ratios from 1.3 to 6.5 (Richardson et al., 2005). For REE geochemistry, the Nipigon suite units have the shallowest REE slopes with $(La/Yb)_{cn}$ from 2 to 5, and have negative Nb, Ti and V anomalies. The Inspiration suite diabase sills intruded ca. 1119.6±2.4 Ma. in the northwest Nipigon Embayment (Heaman and Easton, 2006). Geochemically, the Inspiration sills have high Zr/TiO_2, La/Sm, Nb/Y and La/Yb compared to the main Nipigon suite of sills (MacDonald et al., 2005). The Jackfish Island suite olivine gabbro to peridotitic sills intruded the English Bay Complex in the northwest Nipigon Embayment ca. 1112.4±2.8 Ma (MacDonald et al., 2005; Heaman and Easton, 2006). The McIntyre suite diabase sills intruded ca. 1106.2±2.1

Ma (Heaman and Easton, 2006). Geochemically, the McIntyre suite has higher TiO_2 from 2.7 to 3.1 wt. % and higher $(La/Yb)_{cn}$ ratios from 6.4 to 7.2 compared to the main Nipigon suite (Richardson et al., 2005). In terms of REE geochemistry, the Jackfish Island suite and McIntyre suite have near identical REE plots suggesting the two are related with the Jackfish Island suite as the more primitive and less contaminated end member. The Shillabeer suite intruded as 5km wide shallow inward-dipping sills between the Black Sturgeon and Clearwater Faults (Hart, 2005). The Shillabeer suite has elevated TiO_2 from 2.6 to 2.8 wt. % and the highest $(La/Yb)_{cn}$ ratios of 12.3 to 14.9 compared to the other Nipigon sill suites (Richardson et al., 2005). In terms of isotope geochemistry, all the diabase sill suites have negative εNd values ranging from -0.5 in the Jackfish suite to -6.5 in the Inspiration suite, which is consistent with magmas being contaminated by older crustal sources.

In the East Nipigon Embayment, initial Mesoproterozoic Keewanawan magmatism began with intrusion of the Kitto peridotitic ring complex at 1117.7±1.8 Ma (Heaman and Easton, 2006). The intrusion is identified as a ring dike or complex because it is observed to intrude as a dike or plug through Archean crust in a horseshoe or ring-like form. It is referred to as a complex because of the various peridotitic to gabbroic to granophyric gabbro lithologies that have been recognized. The Kitto intrusion was emplaced as a partially fault-controlled intrusion into predominantly Archean crust during initial asthenospheric upwelling of a mantle plume into the upper lithosphere (Sutcliffe, 1986). On a topographic relief map, the intrusion is located along a topographic lineament that extends north of the Pijitawabik Canyon in the East Nipigon Embayment (Fig. 2.12). Geochemically, the main Kitto peridotite has high Ti/Zr, Zr/Y and $(La/Yb)_n$ ratios that reflect a plume mantle source. MgO ranges from 18 to 33 wt. % and Mg# from 0.71 to 0.80 indicative of the primitive nature of the main peridotite unit (Hart et al., 2002).

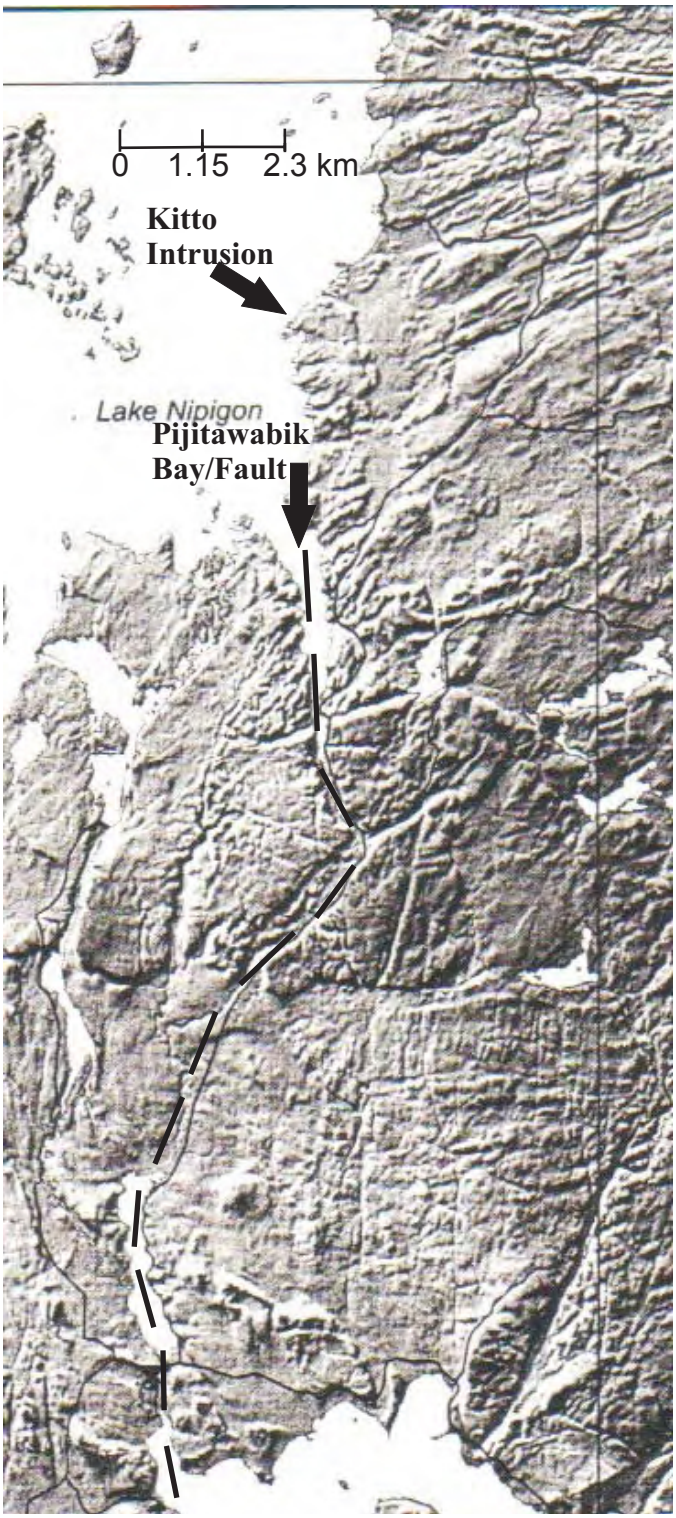

Figure 2.12: The Pijitawik Canyon and Bay are long and narrow topographic lineaments outlined on the topographic relief map. The Kitto intrusion emplaced along a topographic lineament that extends north of the Pijitawabik Canyon in the East Nipigon Embayment. Modified from Barnett (2005).

To the south, the intrusion cuts across mafic metavolcanic rock and iron formations of the Southern Volcanic Unit of the Beardmore-Geraldton Greenstone Belt. To the north it cut across metasedimentary feldspathic wackes of the Southern Sedimentary Unit of the BGB (Fig. 2.3).

Nipigon diabase magmatism occurred as sill emplacement in the East Nipigon Embayment 1110.8±4.3 Ma (Heaman and Easton, 2006). The Nipigon diabase intrusions are tholeiitic magmas that were emplaced as fractionated basalt underplated sills as part of the Midcontinent event (Sutcliffe, 1986). The Nipigon diabase of the East Nipigon Embayment is represented by the main Nipigon suite of sills with MgO of 2.3 to 11.4 wt. %, Mg# of 21 to 63 and La/Yb ratios of 1.3 to 6.5 (Hart et al., 2002). Emplacement mechanisms of the diabase intrusions include primary ponding upward of diabase through faults as dikes and sills, and upon reaching the surface, the shallowing outward as capping sheets (Sutcliffe, 1986; Pye, 1965). Intrusion of diabase dikes along northwest lineaments is evidenced by large straight northwest aeromagnetic lineaments (Fig. 2.13). These lineaments are dextrally displaced to the northeast when in contact with older Archean structures as evidenced by earlier mapping of diabase intrusions along such structures and the presence of aeromagnetic anomalies along these faults (Fig. 2.14; GSC, 1934). As the various diabase intrusions came in contact with the major east-west faults of the BGB, the magmas ponded westward along the faults (Hart and MacDonald, 2007). Evidence for westward intrusion of magmas through the faults include left-lateral displacement of *en echelon* N-S faults in a northern diabase intrusion in Dorothea Township (Mackasey, 1975). With continued intrusion of diabase magmas along the faults, the magmas either ballooned out as plugs, such as in the vicinity of the Kitto intrusion; or they surfaced outward from the central fault fissures as capping sheets and sills, such as the large diabase sheets to the south and west of the Kitto intrusion (Pye, 1965). Evidence for the plugging of

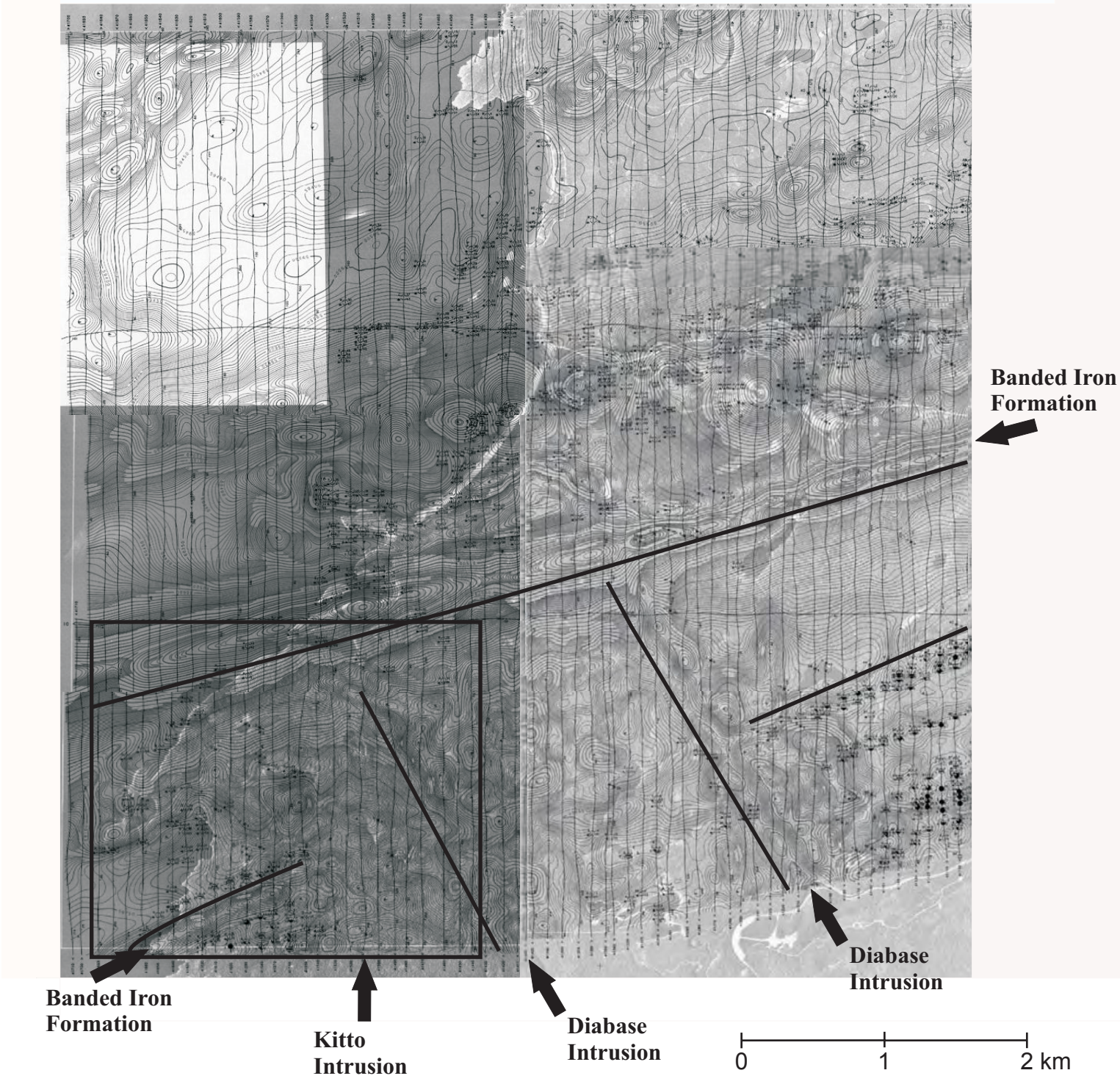

Figure 2.13: An aeromagnetic map shows two sets of northwest striking diabase intrusions surrounding the Kitto intrusion. Also highlighted are banded iron formation units located to the north that strike east-west and through the centre of the Kitto intrusion. Trends of the intrusions and iron formations are indicated by the black lines. Modified from Aerodat (1989).

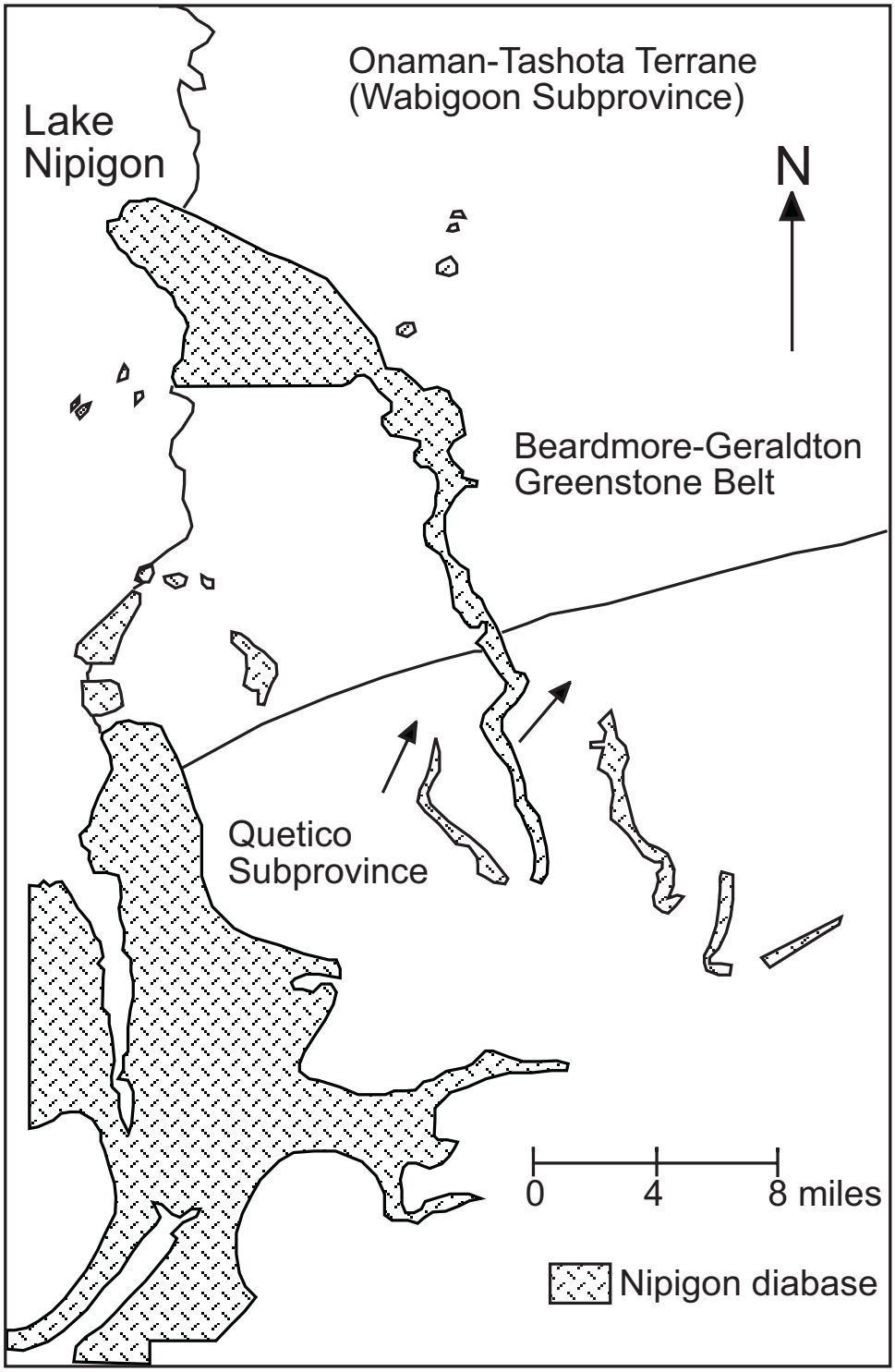

Figure 2.14: The 1934 GSC map of the Sturgeon River Area shows north to northwest striking diabase intrusions that intrude through Archean crust. In the Quetico Subprovince, some of the intrusions are dextrally displaced i.e. turn to the northeast and follow the trends of east-west orientated Archean faults and boundaries. Areas of dextral displacement are indicated by arrows. Modified from GSC (1934).

diabase dikes are shallow west and east-dipping bedding joint structures on both sides of a diabase intrusion in Summers Township, indicative of shallowing out of sills to the east or west of the faults (Hart et al., 2002). Around the Kitto intrusion, the diabase magmas ponded out as flat-lying, shallow westward dipping sheets (Sutcliffe, 1986). The magmas intruded the Archean Southern Volcanic Unit metavolcanic rocks and iron formations and Southern Sedimentary Unit metasedimentary rocks. To the south of the Kitto intrusion, the diabase magmas emplaced along the Blackwater Fault, and to the North they emplaced along the Sandy Creek Fault and Standingstone Fault. In the centre of the Kitto intrusion, a granophyric gabbro geochemically the same as the diabase sills intruded along the Princess Lake Fault (Hart et al., 2002).

CHAPTER 3

FIELD MAPPING & PETROGRAPHY

3.1 Introduction

The petrography of the Kitto intrusion varies with both depth and the north-south and east-west extents of the lithologic units (Fig 3.1). In the southern part of the intrusion, data were obtained from field and drill core samples (see Fig. 3.2a for plan view of drill holes). In drill core, the intrusion is represented by hole EK-02 which has the most petrographic variation. Lithologies from the top to the bottom of the hole include lherzolite, olivine websterite, sulphidized olivine websterite, vari-textured pyroxenite, pyroxenite and melanogabbro (Figs. 3.2b and 3.3; Appendix 1). Classification of the plutonic ultramafic rocks was based on the classification scheme by Streckeisen (1973). The nature of the contacts is gradational between all the lithologies except for sharp contacts between pyroxenite and olivine websterite which is represented by the heterolithic vari-textured pyroxenite unit. Xenoliths of Sibley sandstone occur in the lherzolite as displayed in DDH EK-02 (Appendix 1). Basement beneath the intrusion in EK-02 are Archean magnetite-chert banded iron formation and mafic metavolcanic rocks. Basement beneath holes EK-01, EK-03, and EK-04 consist of Sibley sandstone (Appendix 1). The basement lithologies are in turn cut by Nipigon diabase sills (Fig. 3.2b). Surface outcrops in the southern part of the intrusion are lherzolitic except at the border zone with the diabase sills and dikes at the Phoenix occurrence, where there are mineralized olivine websterites (Fig. 3.1; Appendix 2). In the central part of the intrusion, lithologies from east to west consist of lherzolite, olivine websterite, pyroxene-porphyritic melanogabbro and granophyric gabbro toward contact with basement mafic metavolcanics and banded iron formation (Fig. 3.1). In the northern part of the intrusion, pyroxene-porphyritic melanogabbros

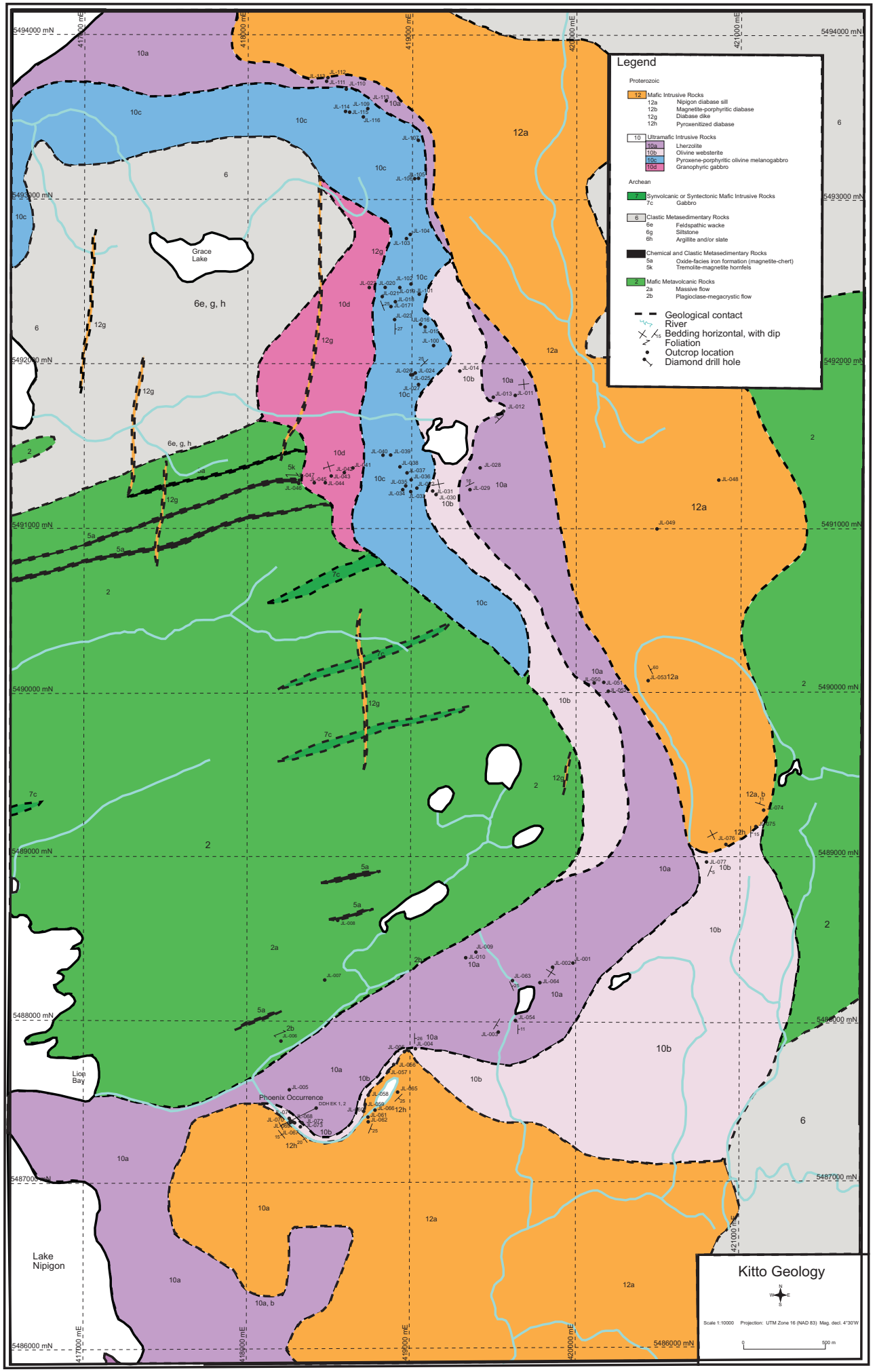
Legend
Proterozoic
12 Mafic Intrusive Rocks
12a Nipigon diabase sill
12b Magnetite-porphyritic diabase
12g Diabase dike
12h Pyroxenitized diabase
10 Ultramafic Intrusive Rocks
10a Lherzolite
10b Olivine websterite
10c Pyroxene-porphyritic olivine melanogabbro
10d Granophyric gabbro
Archean
7 Synvolcanic or Syntectonic Mafic Intrusive Rocks
7c Gabbro
6 Clastic Metasedimentary Rocks
6e Feldspathic wacke
6g Siltstone
6h Argillite and/or slate
Chemical and Clastic Metasedimentary Rocks
5a Oxide-facies iron formation (magnetite-chert)
5k Tremolite-magnetite hornfels
2 Mafic Metavolcanic Rocks
2a Massive flow
2b Plagioclase-megacrystic flow
Geological contact
River
Bedding horizontal, with dip
Foliation
Outcrop location
Diamond drill hole
Kitto Geology
Grace Lake
Lion Bay
Phoenix Occurrence
Lake Nipigon
Scale 1:10000 Projection: UTM Zone 16 (NAD 83) Mag. decl. 4°30'W
0 500 m
5494000 mN
5493000 mN
5492000 mN
5491000 mN
5490000 mN
5489000 mN
5488000 mN
5487000 mN
5486000 mN
417000 mE
418000 mE
419000 mE
420000 mE
421000 mE

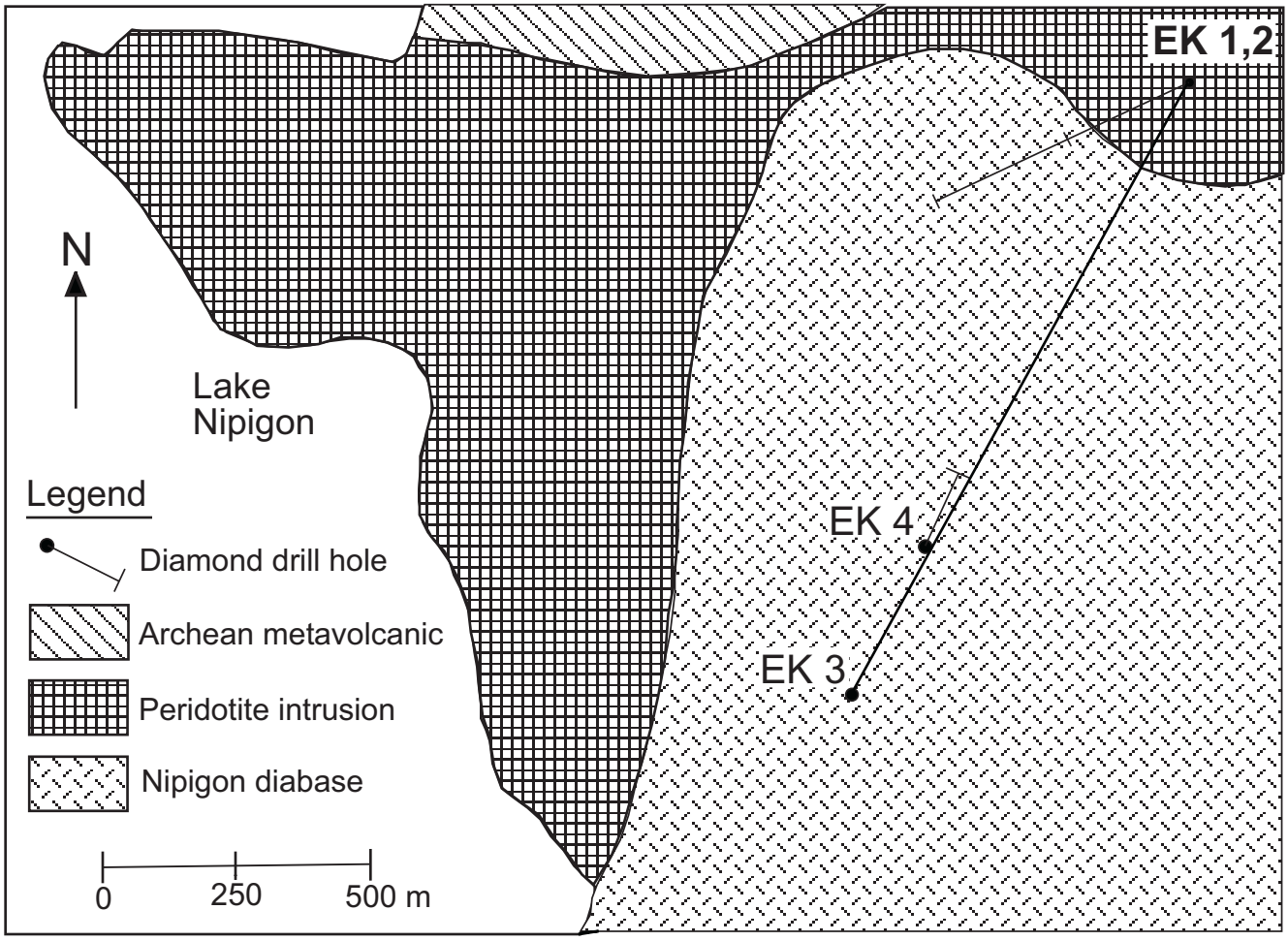

Figure 3.2a: Plan view of DDH holes with line of cross-section for Figure 3.2b in the southwestern part of the Kitto intrusion. DDH EK-01 and EK-03 are vertical holes. Modified from Hart et al. (2002).

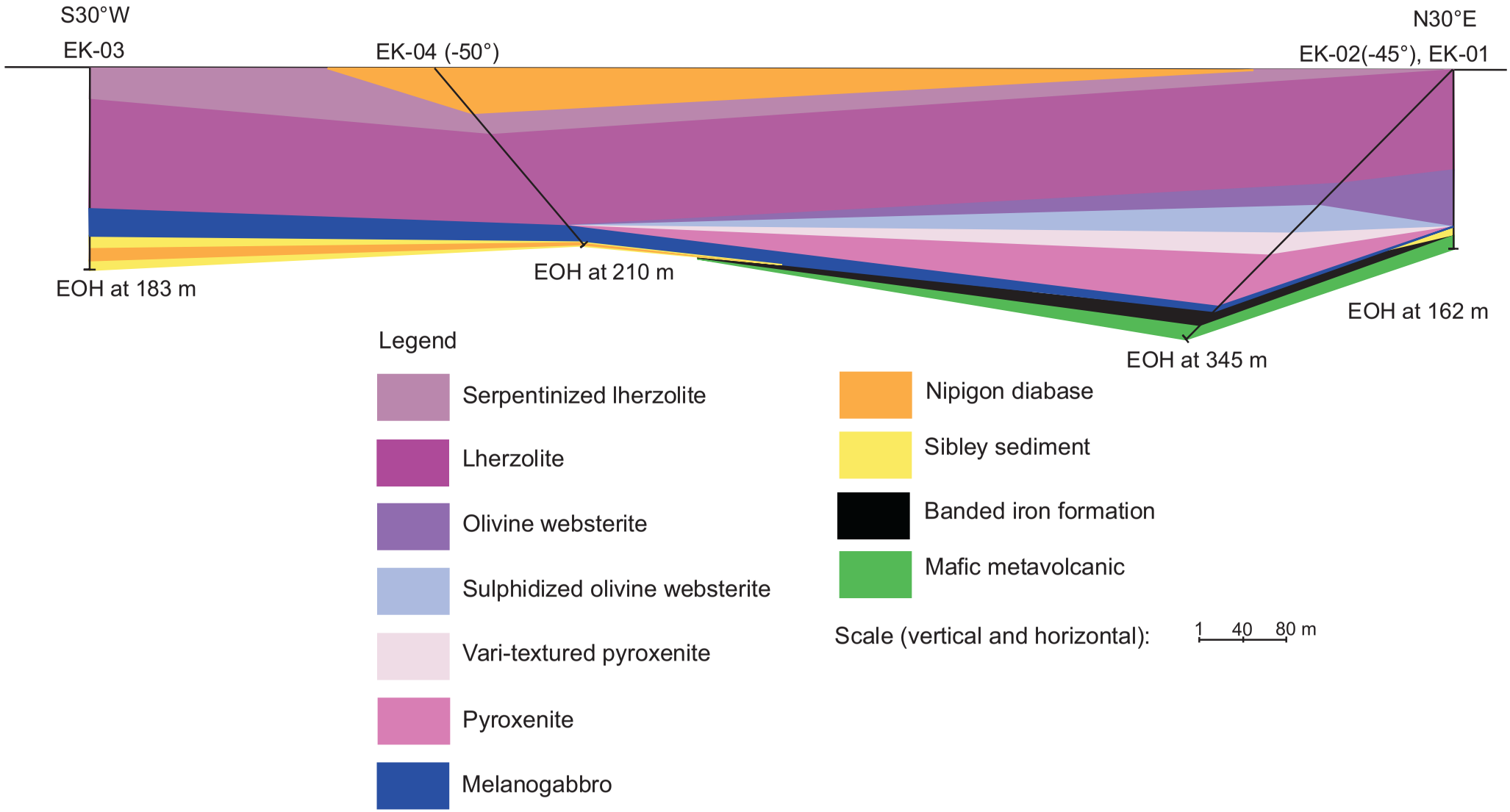

Figure 3.2b: Cross section of the Kitto intrusion through DDH holes EK-03, EK-04, EK-02 and EK-01.

From (m)	To (m)	Cu %	Ni %	Pt (ppm)	Pd (ppm)	Au (ppm)
169.50	172.50	0.010	0.093	0.016	0.008	<0.001
172.50	179.78	0.020	0.120	0.028	0.037	<0.002
179.78	208.00	0.040	0.170	0.093	0.145	0.007
208.00	212.50	0.020	0.110	0.021	0.024	0.002
268.50	270.00	0.008	0.040	0.017	0.006	0.003
270.00	276.00	0.070	0.080	0.076	0.125	0.015
276.00	277.50	0.011	0.047	0.011	0.007	<0.001
302.00	307.05	0.015	0.048	0.014	0.007	0.002

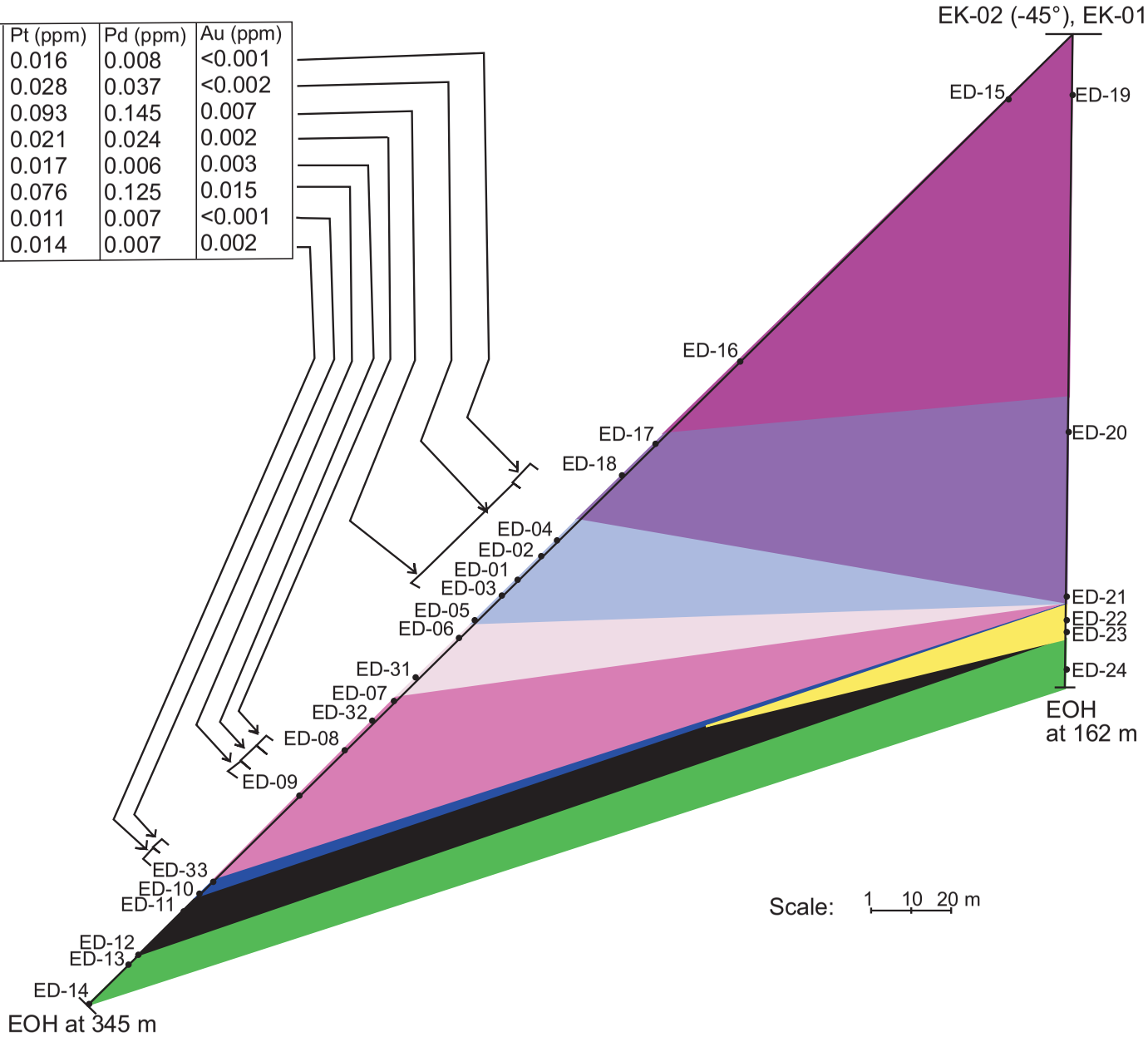

Figure 3.3: Cross section of the Kitto intrusion at the Phoenix occurrence through DDH holes EK-02 and EK-01. Sample locations are numbered down the holes and mineralized zones are identified. For legend of rock units down the holes, see Figure 3.1. Assay data are from Coombes and Rossell (2003).

continue along a north-south orientated fault and are ringed by minor lherzolites, except at the northern part of the intrusion at Lake Nipigon where there is lherzolite peridotite (Fig. 3.1).

3.2 Intrusive lithologies

3.2.1 Lherzolite

Lherzolite is a massive cumulate textured to pyroxene-poikilitic rock and represents the dominant peridotite lithology of the Kitto intrusion (Fig. 3.4). Surface exposures of lherzolite occur in southern and central parts of the intrusion with one occurrence in the northern part of the intrusion (Fig. 3.1). On surface outcrop, lherzolite occurs as 15 to 30 cm thick layer cake beds that are generally horizontal to dipping up to 15º to the east in the south part of the intrusion (Fig. 3.5 and Fig. 3.1). In the central part of the intrusion, the layers dip horizontal to 16º west toward a central trough where lherzolite thickens to 245 m in DDH EK-05-01. Closer to the contact with the plagioclase-porphyritic melanogabbro, the layer joints dip steeper at an angle of 25º. At the contacts with the surrounding diabase sills, the layers dip toward the diabase, as the peridotites are closer to feeder conduits of the diabase surrounding the peridotites. In the south part of the intrusion, at the creek bed of the Phoenix occurrence, local pyroxenitic peridotites dip up to 15º to the southeast or southwest toward the contact with diabase (Fig. 3.1). These peridotites possibly intruded along the same feeder conduits as the diabase since both occur and deepen along the Blackwater Fault. This is shown by the thickening of the ultramafic rocks outward toward the diabase in hole EK-02 (Figs. 3.2b, 3.3 and 3.1). In hand sample, the rock contains small 1 mm or less equant, rounded translucent light green olivine crystals enclosed by large up to 1 cm black to dark green pyroxenes (Fig 3.4). Individual olivine crystals show conchoidal fracturing and diffuse pale green reaction rims between the crystals. Pyroxenes are massive, randomly orientated equant crystals, with some occurring as small 1-2 mm spotted crystals to up to 1cm oikocrysts. Plagioclase is a very minor component at <5 modal % composition. In the vertical DDH EK-03 and the 50º dipping EK-04 drill holes, lherzolite is

Figure 3.4: Lherzolite in hand sample at 48 m depth in DDH EK-02 is a massive cumulate textured to pyroxene-poikilitic rock. The 1 cm wide silvery white mineral circled in black is a poikilitic pyroxene. In the groundmass, the fine grained light green ovoidal minerals are olivine while the darker minerals are pyroxene and biotite.

Figure 3.5: Lherzolite in the field occurs as 15 to 30 cm thick layer cake beds that are generally horizontal to dipping up to 15° to the east in the south part of the intrusion. Serpentine veins in the cracks between the beds give the intrusion a blocky texture (Sutcliffe, 1986). This photo was taken on the shore of Lake Nipigon. 15 cm wide tree roots and 30 cm tall plant for scale. Total vertical outcrop extent is 12 m.

serpentinized in the upper portions of the lithology (Fig. 3.2b). On fresh surfaces, it is dark red to green to purplish, serpentinized and hematized (Fig 3.6). At depth, the lherzolites are highly altered and overprinted by green chert and/or serpentine veins spaced 10 to 20 cm apart. These veins decrease in abundance in the central parts of the lithologies down hole up to the mineralized contact areas with underlying basement. Lherzolites are orange, weathered on surface exposures and are biotitiferous compared to other lithologies (Fig. 3.7). This is due to alteration of olivine crystals to biotite or serpentine. Calcite veinlets occur in some areas.

In thin section, lherzolite displays a mesocumulate texture with dominant 30 to 40 modal % cumulate olivine crystals that are rounded, ovoidal, irregularly fractured and with parallel extinction (Fig. 3.8). Some crystals, as in sample ED-20, are hexagonally shaped and have higher relief than cumulate pyroxenes (Fig. 3.9). Crystals are 0.5 to 1 mm in size. Olivine crystals are often serpentinized along fractures within the crystals occurring near serpentine veins, as in sample ED-19 (Fig. 3.10). Cumulate clinopyroxene comprise 30 to 40 modal % of the lithologies, are generally larger than olivine from 1 to 2 mm, and show a parting cleavage. Poikilitic orthopyroxene forms large, up to 5 to 6 mm, crystals that enclose all other cumulate minerals and constitute 20 modal % of the lithology (Fig. 3.11). Sample JL-052, located between the south and central parts of the intrusion, contains minor growth of twinned secondary pyroxene crystals that have serrated crystal boundaries and surround primary cumulate crystals (Fig. 3.12). Intercumulus plagioclase is a minor component of the lithologies (<5 modal %) with 3 to 4 mm crystals with local skeletal sericitization overprinted preferentially on twin lamellae of the crystals. Biotite is abundant comprising up to 5 modal % occurring as crystals surrounding or in association with <5 modal % opaque magnetite crystals (Fig. 3.8). Hornblende is a minor component at <5 modal %. Biotite and hornblende together with magnetite and oxidation products, represent late deuteric material overprinting primary cumulate textures.

Figure 3.6: In the vertical EK-03 and 50° dipping EK-04 drill holes, lherzolite is largely serpentinized in the upper portions of the unit. On fresh surface, the lithologies are dark red to green to purplish serpentinized and hematized. Sample is from 15 m depth in DDH EK-03.

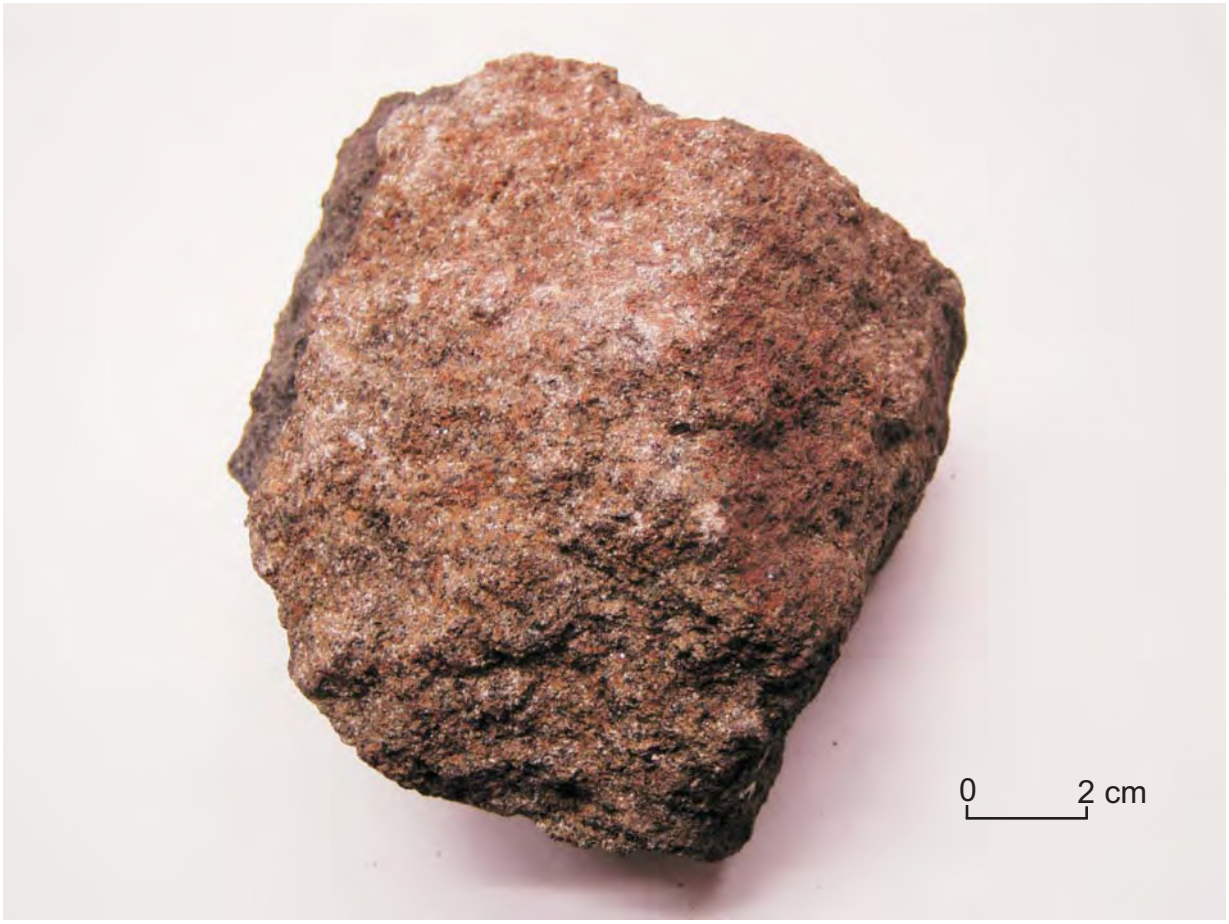

Figure 3.7: Lherzolites on the surface are orange weathered due to Fe oxidation. In the photo, the ovoidal orange minerals are olivine while the black minerals are pyroxene.

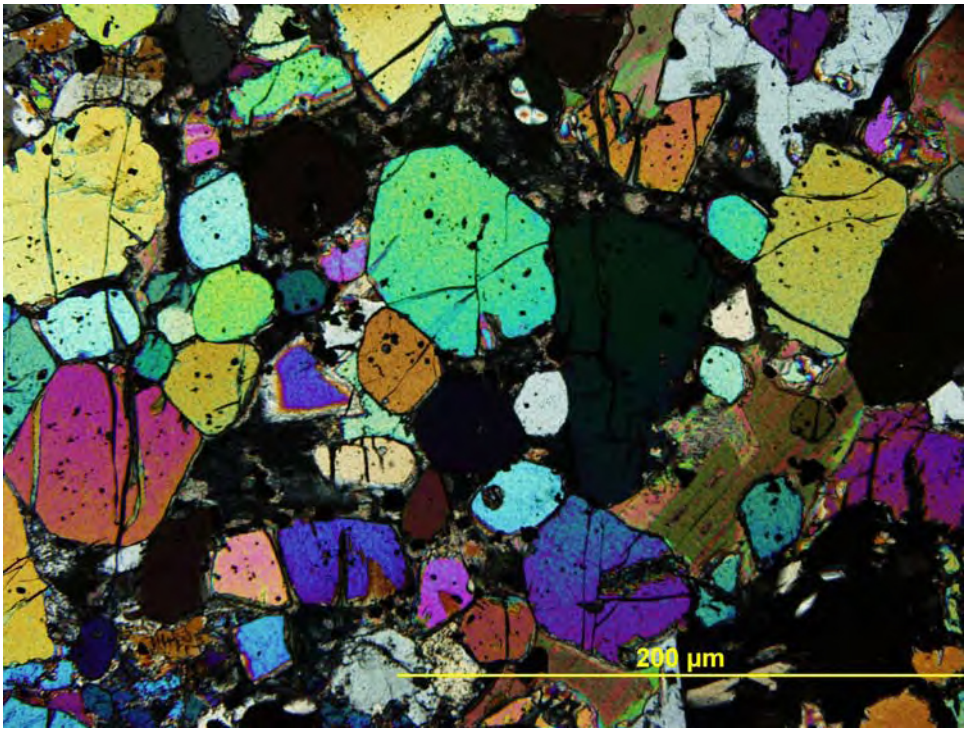

Figure 3.8: Lherzolite in sample ED-16 displays a mesocumulate texture of dominant round cumulate olivine crystals. Biotite is 5 modal % composition and occurs as crystals in association with oxide minerals.

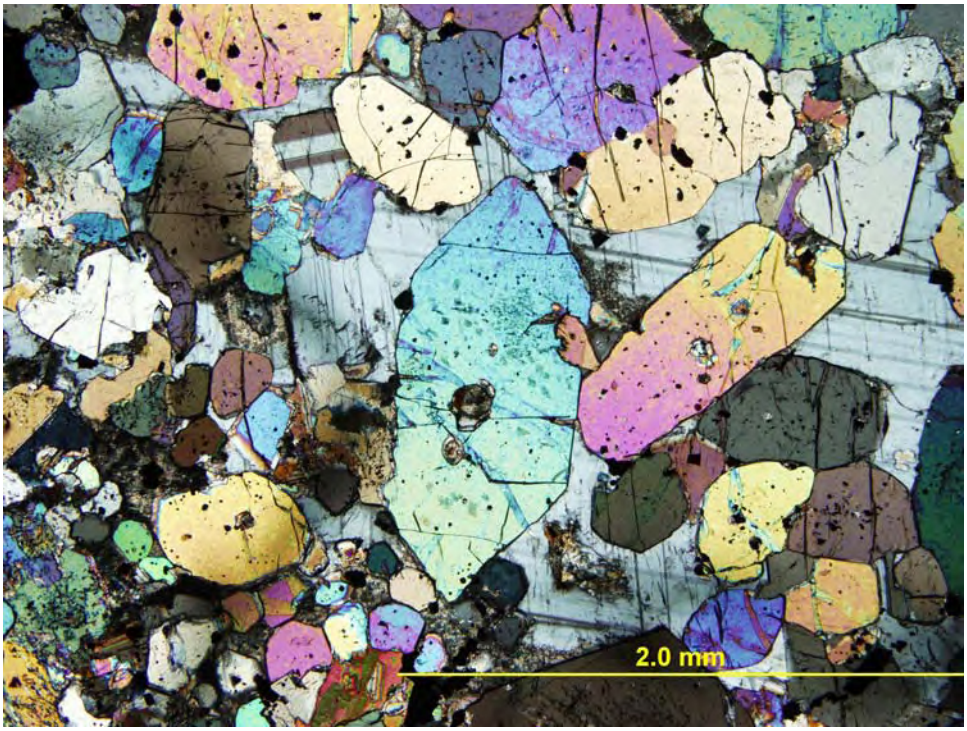

Figure 3.9: Olivine crystals, in lherzolite sample ED-20, are sometimes hexagonally shaped crystals and have higher relief than cumulate pyroxenes.

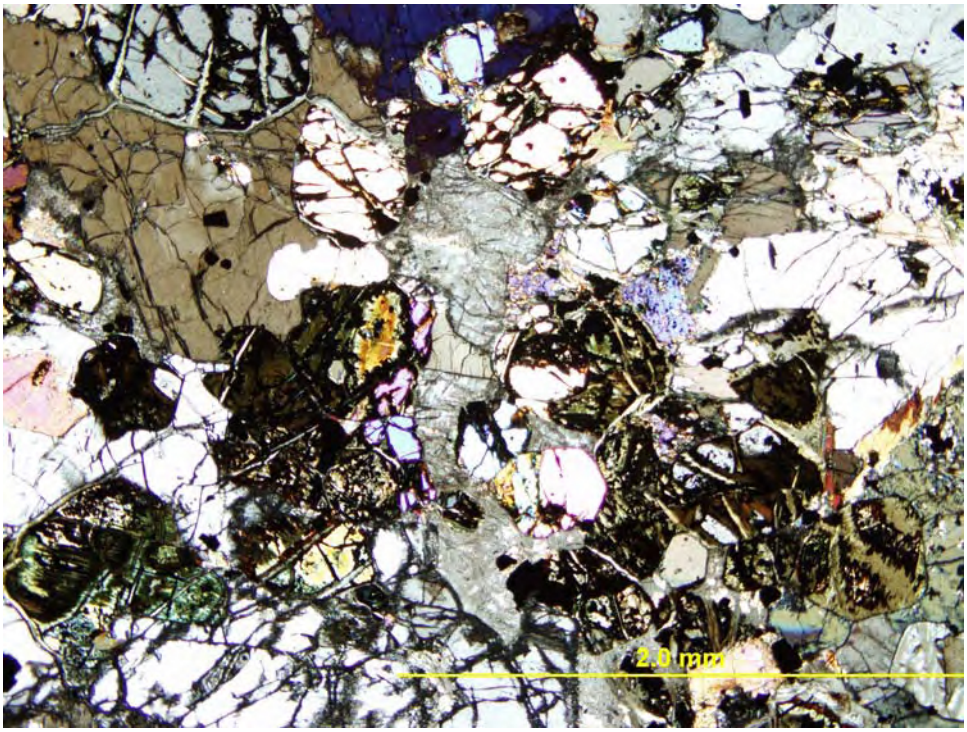

Figure 3.10: Olivine crystals in lherzolite are often serpentinized along fractures within the crystals, as in sample ED-19.

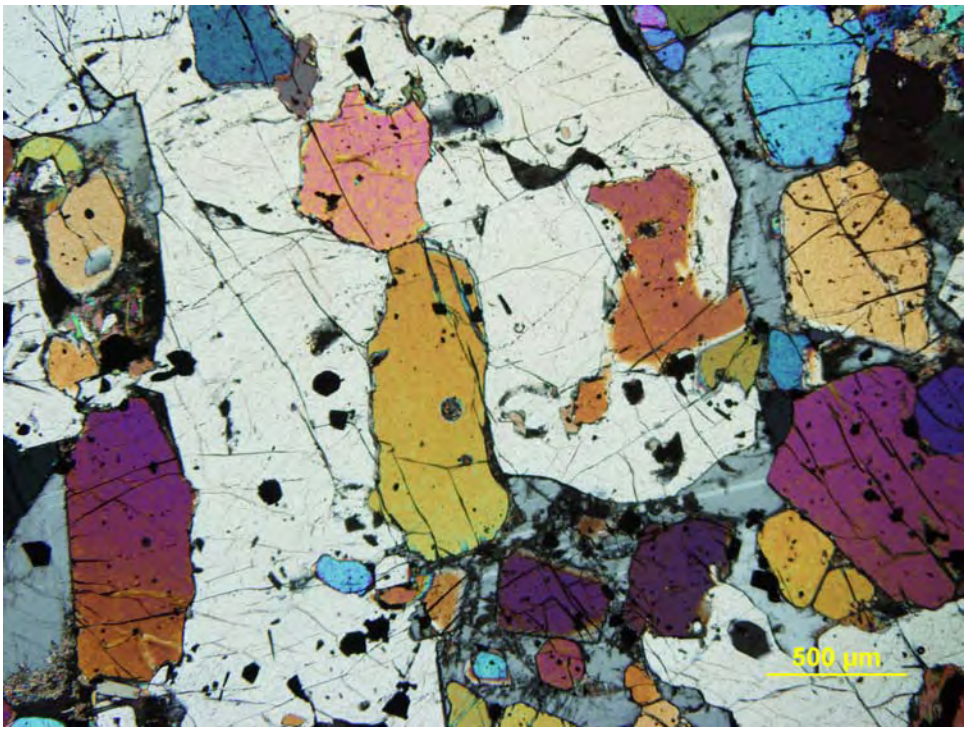

Figure 3.11: Large up to 6 mm poikilitic orthopyroxenes host smaller cumulate olivines and clinopyroxenes in lherzolite.

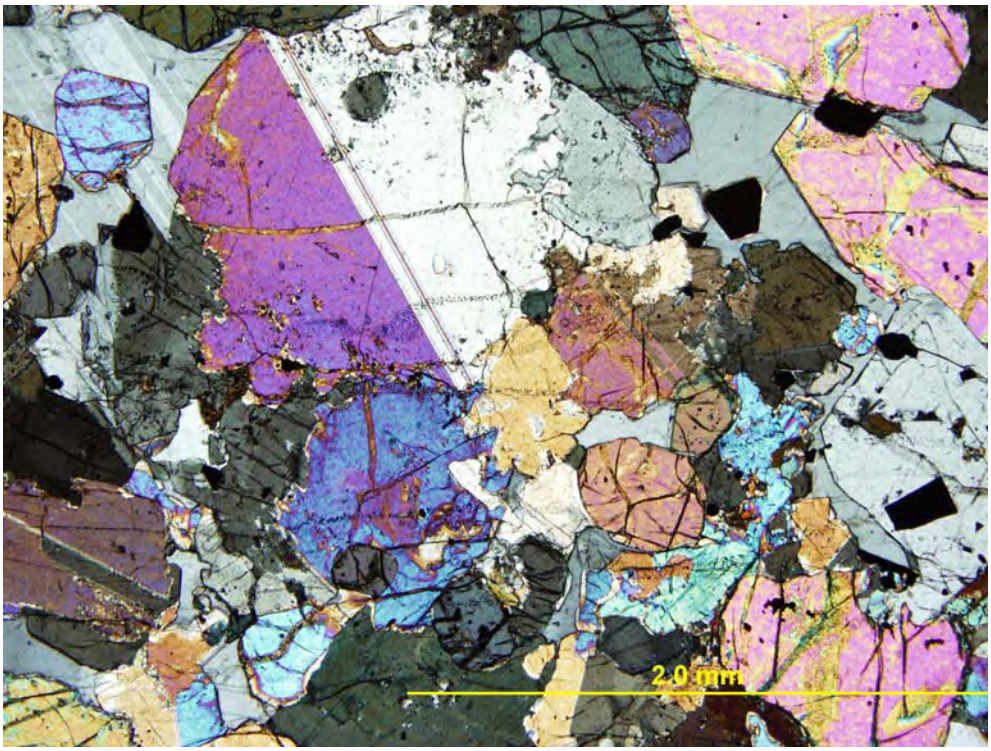

Figure 3.12: Between the south and central parts of the intrusion in sample JL-052, lherzolites contain minor growth of twinned secondary pyroxene crystals that have serrated crystal boundaries and surround primary cumulate crystals.

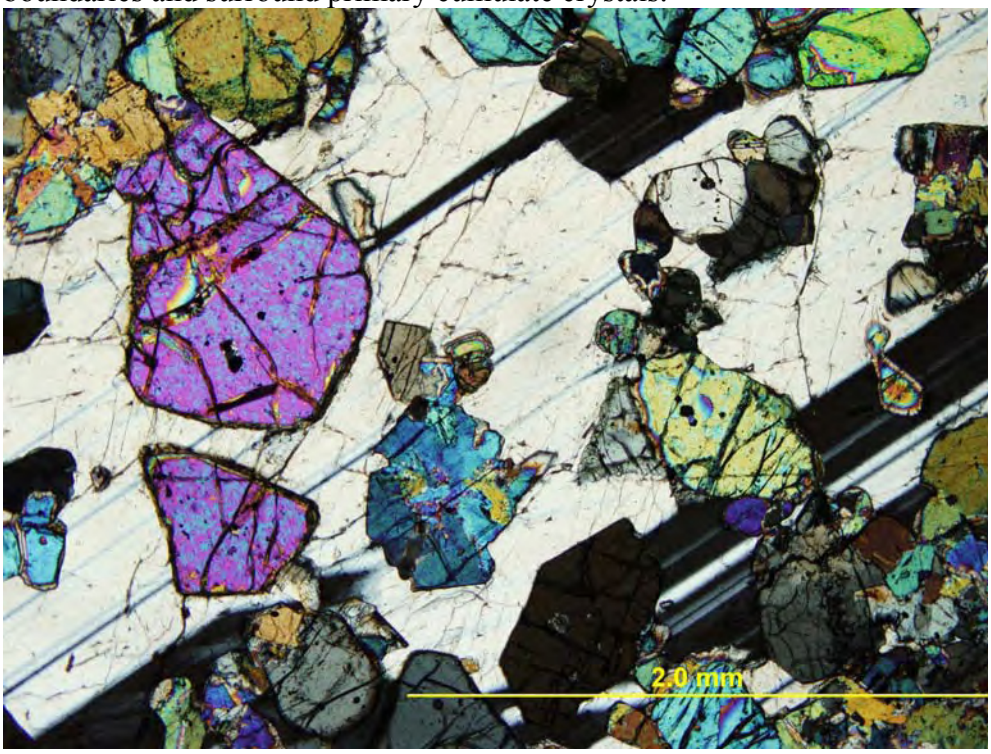

Figure 3.13: Sample JL-027 represents a more fractionated olivine websterite with up to 40 modal % intercumulus plagioclase surrounding primary cumulate clinopyroxene crystals.

3.2.2 Olivine websterite

The olivine websterite exhibits a cumulate to pyroxene-poikilitic texture similar to the lherzolite, only it is more pyroxenitic in composition. In drill core, olivine websterite is found below the lherzolite (Fig. 3.3). In hand sample, olivine websterite is a darker grey than the lherzolite with a fine grained pyroxene dominated composition. The lithology shows a patchy to spotted pyroxenitic texture in contrast to cumulate olivine and pyroxene in the lherzolite. The lithology is still biotite-rich like the lherzolite. Cumulate pyroxene crystals are up to 3 mm in length. The mineralized part of olivine websterite is from 172 to 209 m in hole EK-02 (Fig. 3.3). Deep brassy yellow chalcopyrite crystals coexist with bronzy pyrrhotite. At the Phoenix occurrence, olivine websterite is only found at the contact of the diabase with the peridotite (Fig. 3.1). Olivine websterites are biotite-rich with green chert and/or serpentine patches. JL-070 has a groundmass composed of 1 mm rounded pyroxene crystals separated by green serpentine and chert. At the central part of the intrusion, the olivine websterite is a pyroxene-poikilitic, cumulate pyroxene and olivine bearing rock, similar in texture to lherzolite, only with coarsening of cumulate pyroxenes relative to olivine. Westward, toward the pyroxene-porphyritic melanogabbro, the lithology becomes more plagioclase-rich bordering the contact with the pyroxene-porphyritic melanogabbro as seen in sample JL-027 (Fig. 3.13).

In thin section, olivine websterite from drill core at the southern part of the intrusion show a variable cumulate texture from very little to some 20-30 modal % cumulate olivine crystals. Sample ED-01 contains large 3 to 4 mm oikocrysts of orthopyroxene that are pervasively biotitized along cleavage planes. These crystals surround cumulate clinopyroxene, but not olivine (Fig. 3.14). Some orthopyroxenes show undulose extinction possibly indicative of growth textures for hydrothermal pyroxenitization of large poikiloblasts. In the groundmass, haphazardly orientated actinolite crystals replace the poikiloblasts. The orthopyroxene oikocrysts are pervasively sericitized and chloritized along fractures to yield a granular mass of

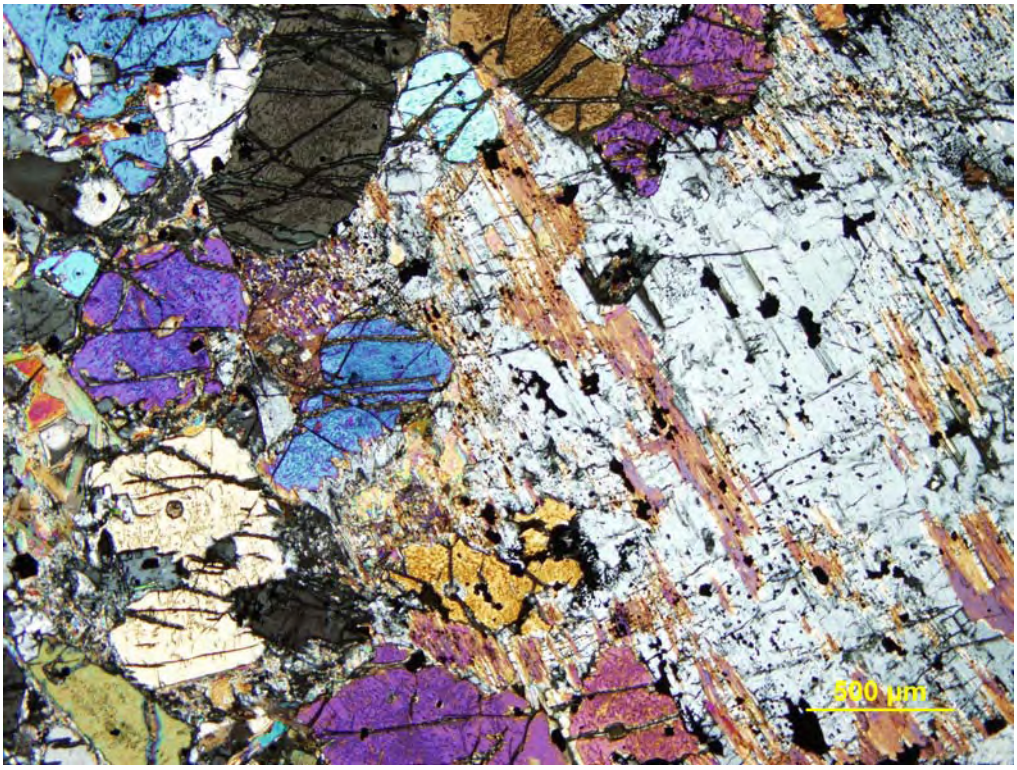

Figure 3.14: Olivine websterite in sample ED-01 displays a poikilitic texture where large oikocrysts of orthopyroxene enclose smaller cumulate clinopyroxene and minor olivine crystals. Orthopyroxene is pervasively biotitized along cleavage planes.

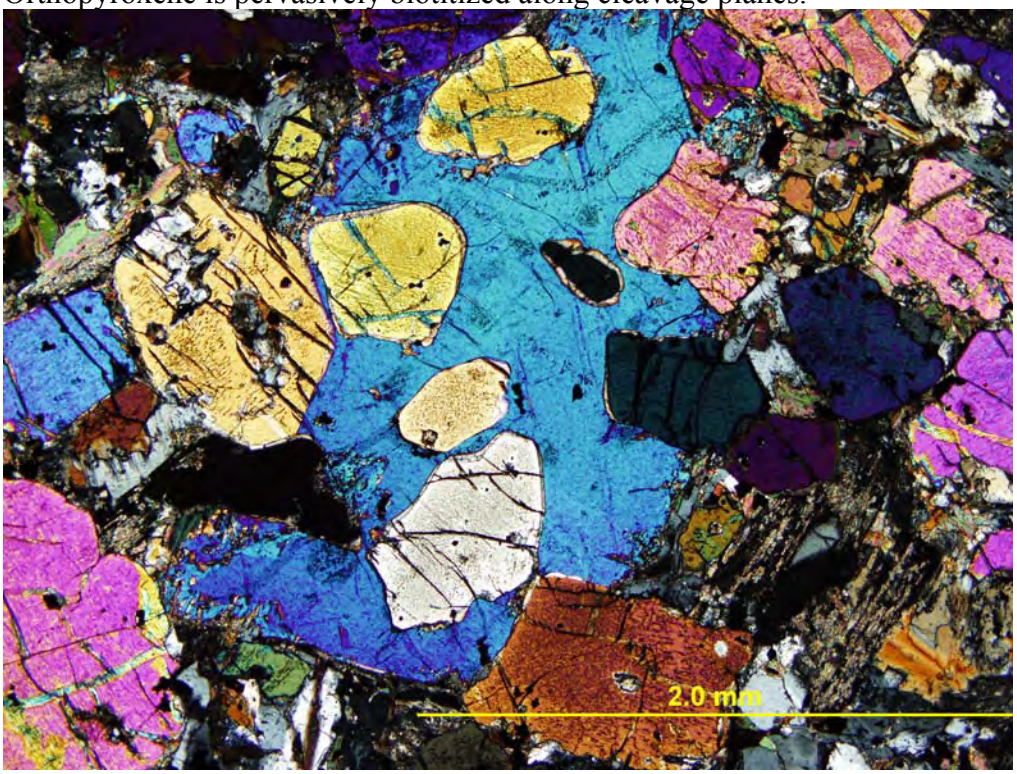

Figure 3.15: Olivine websterite in sample ED-02 contains some large poikilitic cumulate olivine crystals that enclose dominant cumulate clinopyroxene crystals.

crystals within the groundmass. In sample ED-02, some large cumulate olivine crystals poikilitically enclose dominant cumulate clinopyroxene crystals (Fig. 3.15). In sample ED-04, large oikocrysts of clinopyroxene contain concentric zoning diagnostic of augite clinopyroxene (Fig. 3.16). Large-scale biotitization is indicated by up to 10 modal % intercumulus biotite crystals largely found in association with up to 10 modal % sulphides and oxides (Fig. 3.17). Interstitial disseminated pyrrhotite-pentlandite-chalcopyrite immiscible textured sulphides are found in 1-2 mm patches (Figure 3.18). Plagioclase is a very minor component and is often sericitized.

In thin section, olivine websterites from the surface at the central part of the intrusion are more feldspathic than those of the drill core and contain secondary pyroxene growth textures. Cumulate grain sizes are progressively smaller than in the lherzolite found to the east. In sample JL-031 large, up to 6 mm, oikocrysts of orthopyroxene house smaller cumulate olivines and pyroxenes (Fig. 3.19). There is 40 modal % clinopyroxene but only 20 modal % olivine. In sample JL-014, secondary growth crystals of twinned clinopyroxene are lower relief crystals with serrated crystal boundaries that surround primary cumulate olivines and pyroxenes (Fig. 3.20). Biotite is a minor component at 3 modal % and is found in association with oxides and sulphides. JL-027 represents a more fractionated olivine websterite east of the contact with the pyroxene-porphyritic melanogabbro. Primary cumulate clinopyroxene and olivine crystals are variably sized from 1 to 4 mm and constitute 40 modal % of the lithology, with the other 20 modal % constituting secondary pyroxene and biotite. These crystals are surrounded by up to 40 modal % intercumulus plagioclase crystals (Fig. 3.13). There are some local patches of <0.5 mm secondary pyroxene that exist as lower relief, intergrown phases.

3.2.3 Vari-textured pyroxenite

Below the olivine websterite, at depth from 209 to 236 m in DDH EK-02, a vari-textured to spotted pyroxenite represents a transitional lithology from olivine websterite to pyroxenite

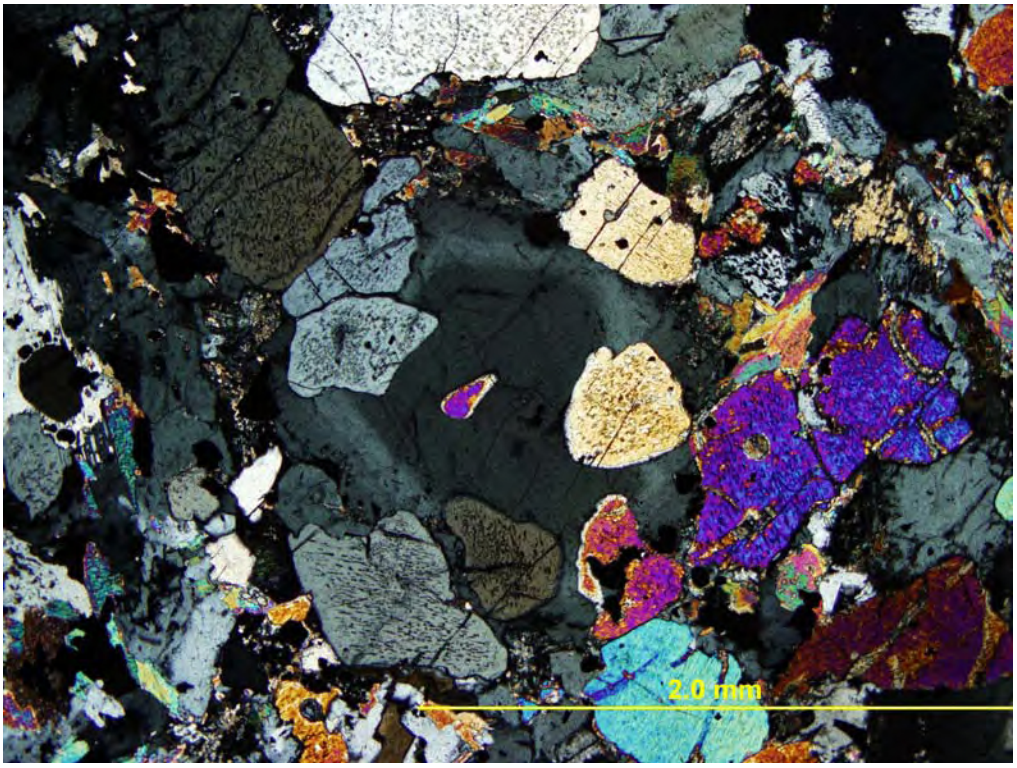

Figure 3.16: In olivine websterite sample ED-04, large oikocrysts of clinopyroxene contain concentric zoning diagnostic of augite clinopyroxene.

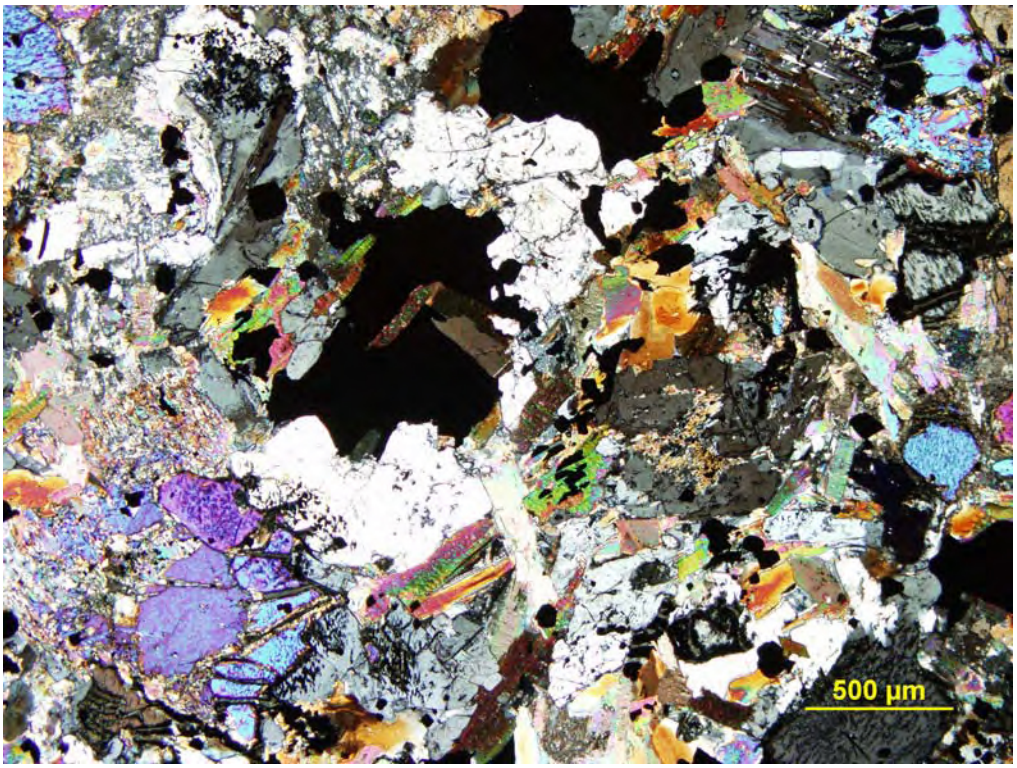

Figure 3.17: Olivine websterite in sample ED-04 contains 10 modal % coarse grained biotite around oxide and sulphide crystals.

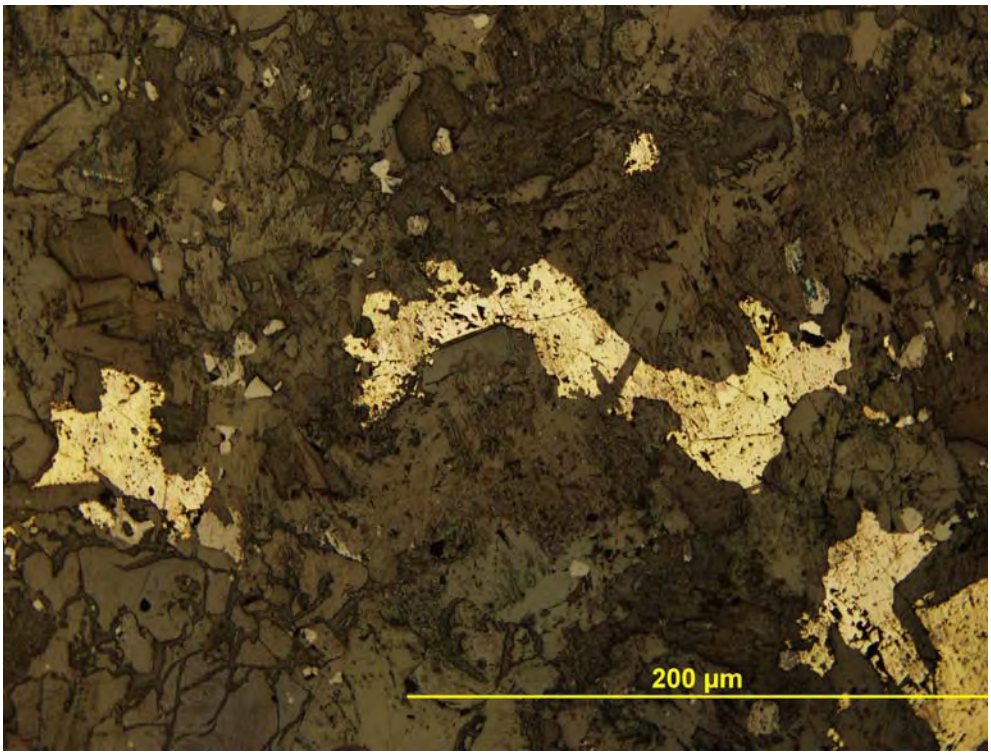

Figure 3.18: Interstitial disseminated pyrrhotite-pentlandite-chalcopyrite immiscible textured sulphides characterize mineralization found in sulphidized olivine websterite sample ED-04.

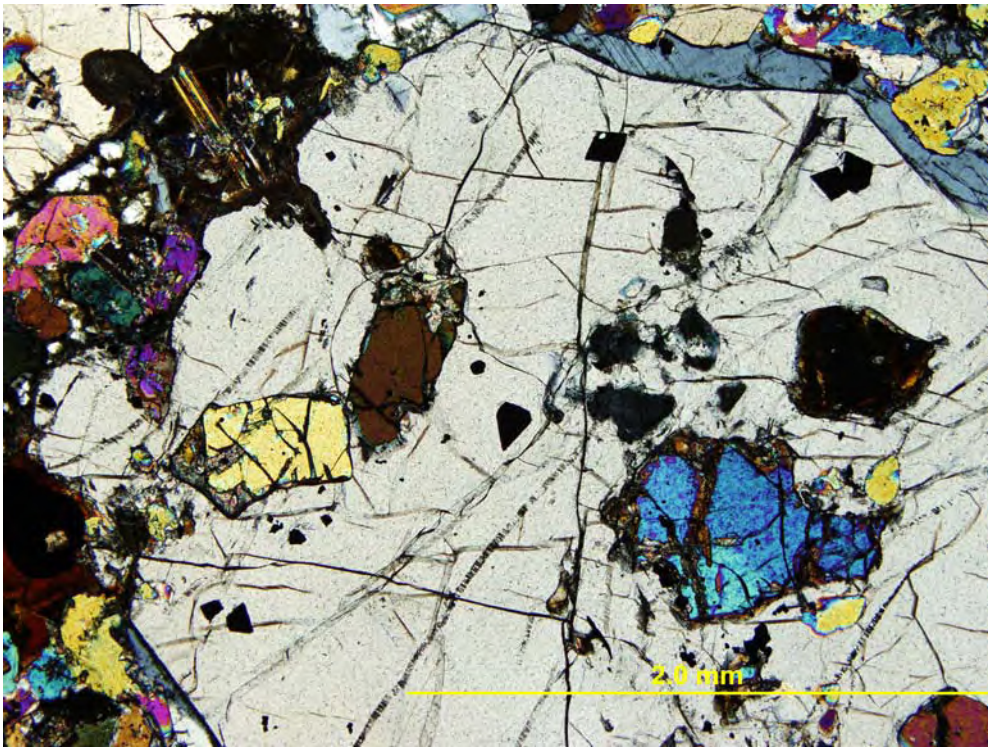

Figure 3.19: Olivine websterite surface exposure sample JL-031 contains large up to 6 mm oikocrysts of orthopyroxene that house smaller cumulate olivines and pyroxenes.

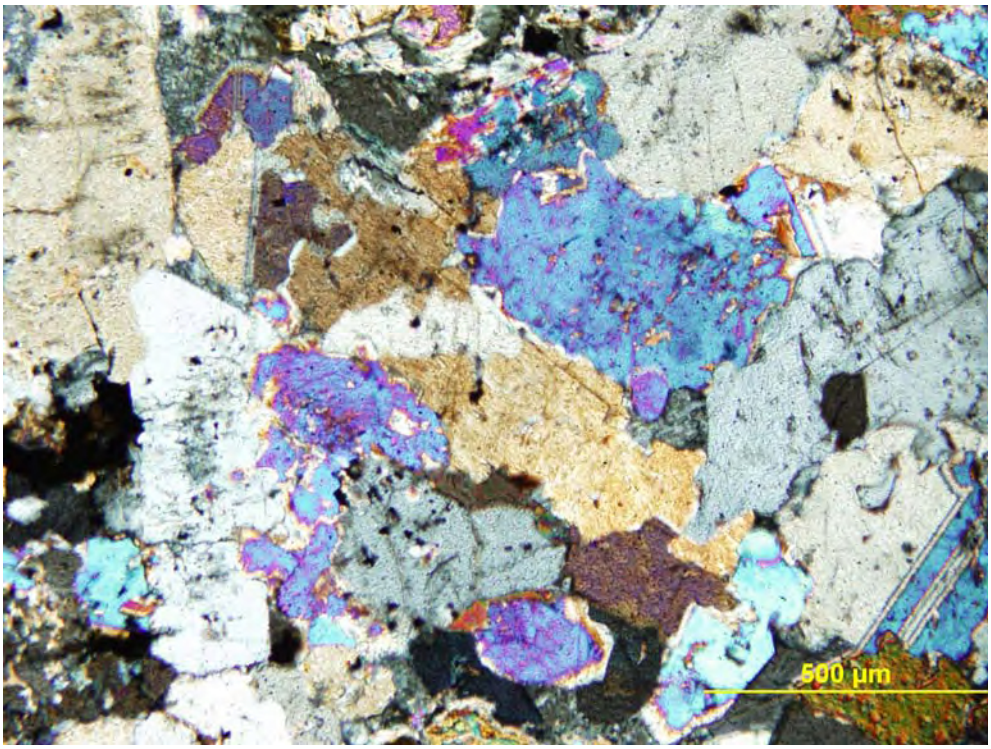

Figure 3.20: Olivine websterite in sample JL-014 from surface exposure displays secondary clinopyroxene growth textures. Secondary pyroxenes are twinned anhedral crystals with serrated boundaries that surround primary cumulate pyroxenes.

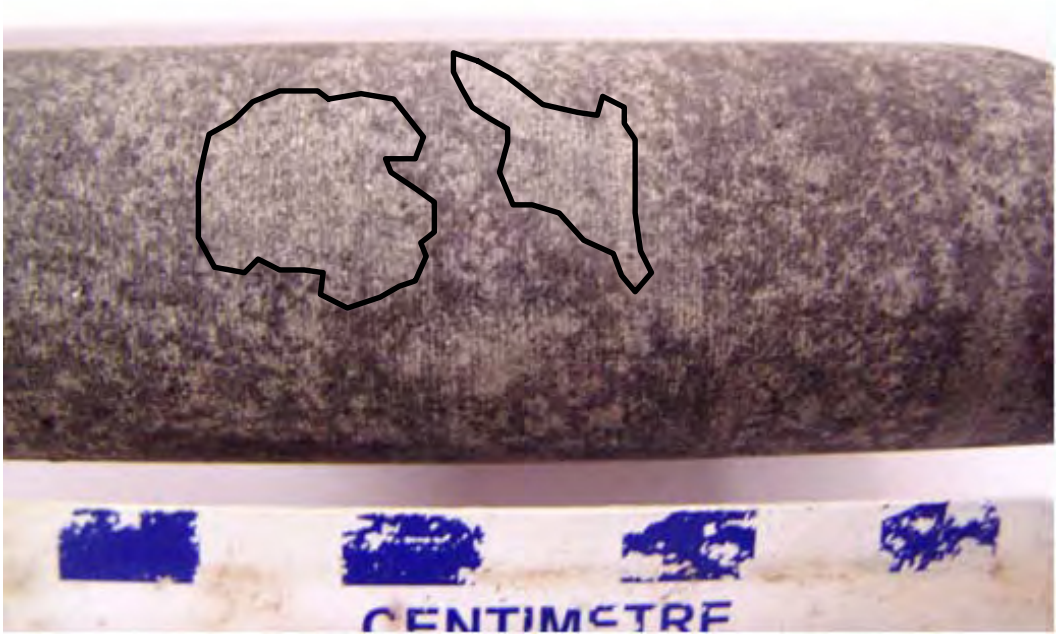
Figure 3.21: In hand sample, vari-textured pyroxenite contains light green leucocratic patches of olivine websterite up to 2 to 3 cm long irregularly enclosed in a groundmass of cumulate pyroxenite. Two patches are outlined in black. Sample is from 221 m in DDH EK-02.

(Fig. 3.3). In hand sample, patches of olivine websterite up to 2 to 3 cm long are irregularly enclosed in a groundmass of cumulate pyroxenite. Olivine websterite is represented by irregular light green leucocratic patches surrounded by darker cumulate clinopyroxenes (Fig. 3.21). Patches range from 3 mm spots at 209 m depth to large 2 to 3 cm patches from 220 to 230 m depth until there is a dominant groundmass of patchy continuous pyroxenite (Fig. 3.21). In thin section, in sample ED-06, the leucocratic patches contain unaltered secondary recrystallized clinopyroxenes <1 mm in size that occur as large clusters between altered cumulate pyroxene crystals (Fig. 3.22). Secondary pyroxenes, which are 30 modal % of the lithology, exhibit simple twinning in most crystals, small cleavage fractures, and crystalloblastic associations (i.e., development of 120º triple junctions between crystals). The 5mm clusters are secondary pyroxenes since they crystallized around primary cumulate crystals and do not occur in cross-cutting decussate association within the clusters. Also, as in sample ED-08, some pseudomorphed outlines of primary cumulate crystals are composed of recrystallized clusters of secondary pyroxenes (Fig. 3.23). The minerals overprint primary intergranular acicular plagioclase crystals since plagioclase laths occur in the interior of pyroxene crystals and are cross-cut by them. In hand sample, patches of olivine websterite up to 2 to 3 cm long are irregularly enclosed in a groundmass of cumulate pyroxenite. Olivine websterite is represented by irregular light green leucocratic patches surrounded by darker cumulate clinopyroxenes (Fig. 3.21). Patches range from 3 mm spots at 209 m depth to large 2 to 3 cm patches from 220 to 230 m until there is a dominant groundmass of patchy continuous pyroxenite (Fig. 3.21). In thin section, in sample ED-06, the leucocratic patches contain unaltered secondary recrystallized clinopyroxenes <1 mm in size that occur as large clusters between altered cumulate pyroxene crystals (Fig. 3.22). Secondary pyroxenes, which are 30 modal % of the lithology, exhibit simple twinning in most crystals, small cleavage fractures, and crystalloblastic associations i.e. development of 120º triple junctions between crystals. The 5mm clusters are secondary

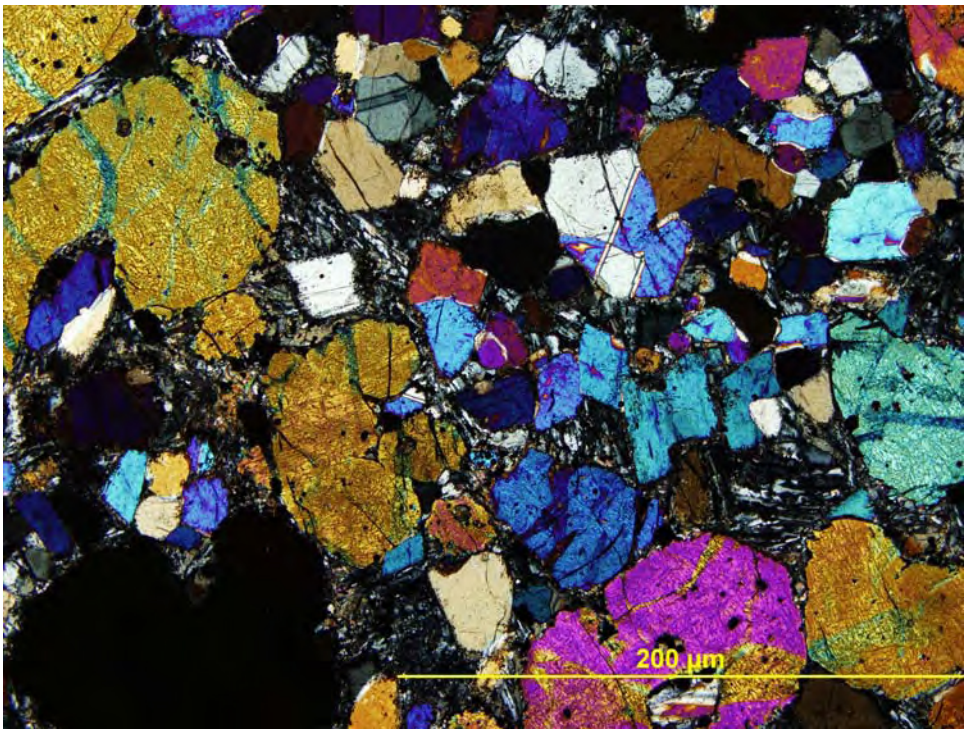

Figure 3.22: A vari-textured pyroxenite occurs between olivine websterite and pyroxenite lithologies in drill core. Sample ED-06 shows leucocratic patches of smaller cumulate secondary pyroxene crystals occurring as large clusters between larger altered primary clinopyroxene cumulates. Secondary pyroxenes exhibit simple twinning and crystalloblastic associations.

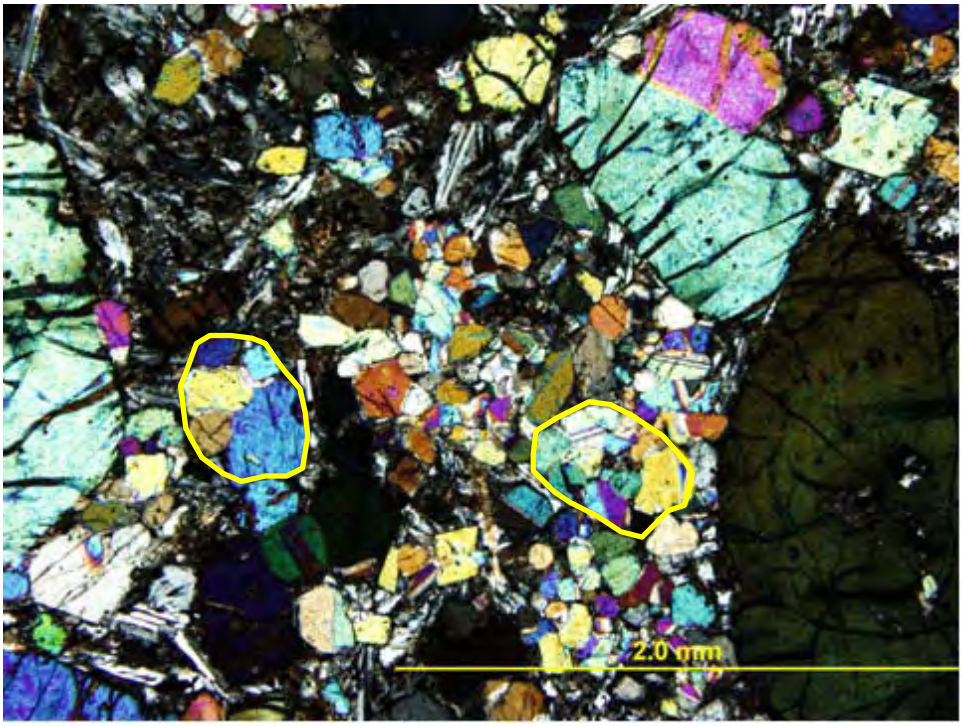

Figure 3.23: In sample ED-08, some pseudomorphed outlines of primary cumulate crystals are composed of recrystallized clusters of secondary pyroxene. Two crystal outlines are in yellow.

pyroxenes since they crystallize around primary cumulate crystals and do not occur in cross-cutting decussate association within the clusters. Also, as in sample ED-08, some pseudomorphed outlines of primary cumulate crystals are composed of recrystallized clusters of secondary pyroxenes (Fig. 3.23). The minerals overprint primary intergranular acicular plagioclase crystals since plagioclase laths occur in the interior of pyroxene crystals and are cross-cut by them. Primary cumulate pyroxenes, which are 50 modal % of the lithology, are round, up to 3mm, anhedral crystals that are fractured and frosted on the surface, and are incipiently broken up and replaced by secondary pyroxenes in some areas. Surrounding the cumulate pyroxenes are subophitic plagioclase laths in intergranular association with pyroxenes. These crystals have growth orientation of long axes of crystals surrounding the pyroxene cumulates as evidence of later crystallization of plagioclase. Late stage fracturing cuts through all primary and secondary crystals associated with hydrothermal serpentine and coarse biotite vein alteration.

3.2.4 Pyroxenite

Pyroxenite occurs below the vari-textured pyroxenite in drill core (Fig. 3.3) and displays an orthocumulate texture of clinopyroxene and plagioclase. In hand sample, pyroxenite shows a patchy to spotted association of cumulate pyroxene with secondary pyroxene and plagioclase (Fig. 3.24). Pyroxene crystals are equant, 1 to 2 mm dark minerals, while secondary pyroxenes appear as 1 to <1 mm leucocratic phases. Pyroxene crystals are in interlocking association with each other. In thin section, samples ED-07 and ED-32 are pyroxenites dominantly composed of cumulate clinopyroxene crystals, identified by etched surfaces of cleavage developments that make the crystals appear darker than secondary crystals. Intergranular texture is displayed by 50 to 60 modal % cumulate pyroxene crystals enclosed by a groundmass of 30 to 40 modal % lathy to acicular plagioclase crystals in sample ED-07 (Fig. 3.25). Sample ED-32 shows secondary pyroxene at 30 to 40 modal % compared to 40 to 50 modal % cumulate pyroxene and 20 to 30

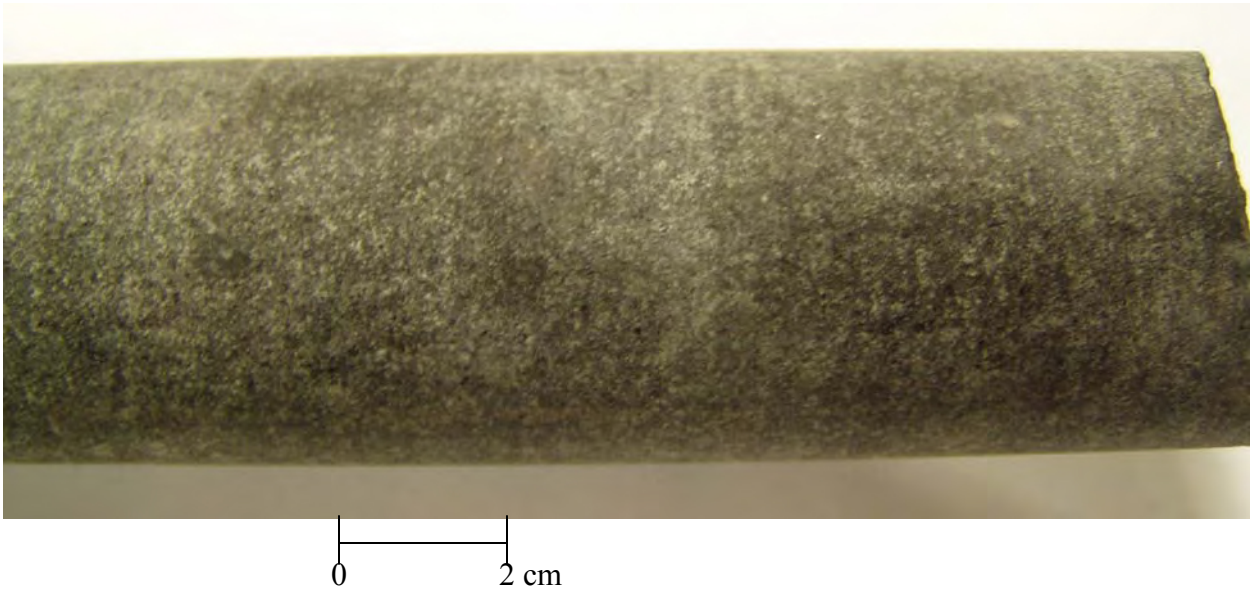

Figure 3.24: In hand sample, pyroxenite shows a patchy to spotted association of cumulate pyroxene with plagioclase and minor secondary pyroxene. Sample is from 249 m depth in DDH EK-02.

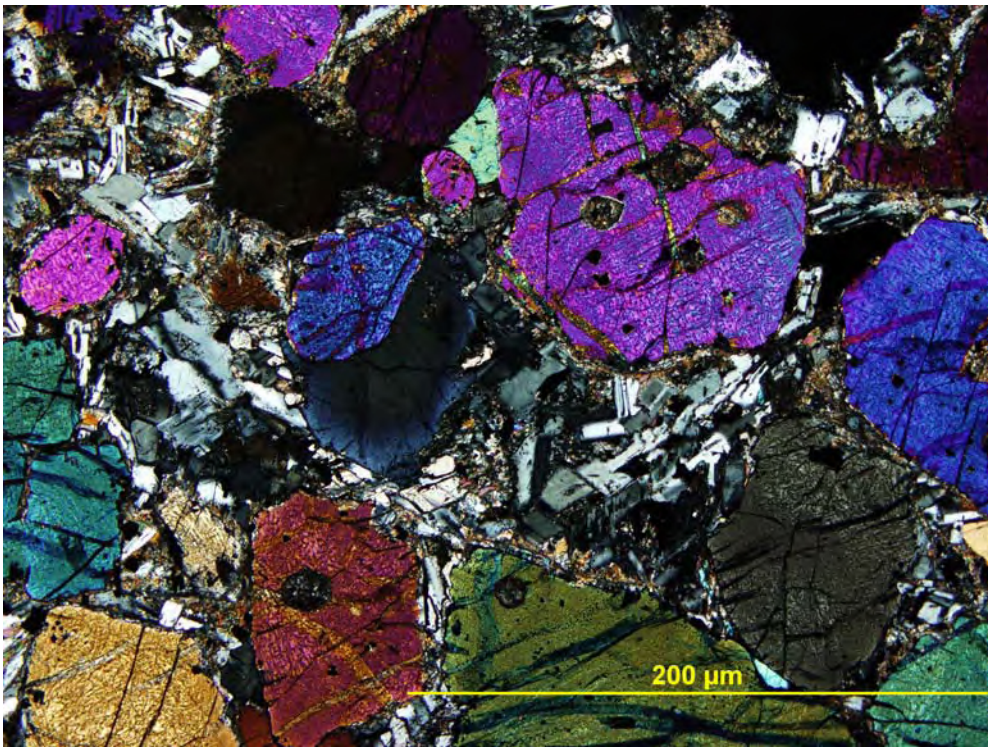

Figure 3.25: Pyroxenite in sample ED-32 displays an orthocumulate texture of clinopyroxene minerals enclosed by and in intergranular association with a groundmass of laths of scapular to acicular plagioclase crystals.

modal % intergranular plagioclase. Sericitization occurs within lathy plagioclase and parting cleavage planes of clinopyroxenes. Olivine is a minor cumulate phase at <10 modal %. Biotitization is very minor within the lithology.

3.2.5 Pyroxene-porphyritic melanogabbro

Pyroxene-porphyritic melanogabbro is a common lithology observed in the central to northern parts of the Kitto intrusion. The pyroxene-porphyritic melanogabbro outcrops as round knobby exposures of up to 30 cm thick layers. In the central part of the intrusion, along the Princess Lake Fault, the pyroxene-porphyritic melanogabbros are horizontal or dip slightly to the north (Fig. 3.1). At sample JL-024 surface exposure dips 25º to the northwest while further to the west at samples JL-021 and JL-023, surface exposures dip 25 to 27º to the northeast or east. Sample JL-026 contained anomalous Pt and Pd contents of 242 and 37 ppb respectively. The opposing dips of the lithologies and mineralization found in surface exposure between them may be the result of a central north-south trough, north of the Princess Lake Fault, within or below the pyroxene-porphyritic melanogabbro that represents a centre of plutonism of the intrusion (Fig. 3.1). In hand sample, pyroxene-porphyritic melanogabbro is a feldspathic, biotite-rich lithology with up to 2 cm porphyritic pyroxenes occurring in a groundmass of equigranular plagioclase-pyroxene and olivine (Fig. 3.26). On weathered surfaces, plagioclase occurs as a weathered out component surrounding large pyroxene crystals. Half centimeter wide feldspathic veinlets run through the lithology at JL-036 and JL-038.

In thin section, pyroxene-porphyritic melanogabbro has a mesocumulate to orthocumulate texture of dominantly clinopyroxenitic composition. Cumulate clinopyroxene are 1 to 2 mm crystals that along with minor olivine, represent 50 to 60 modal % of the composition. Large, up to 6 mm, oikocrysts of orthopyroxene comprise 20 to 30 modal % of sample JL-017 (Fig. 3.27). In sample JL-019, large laths of up to 2 mm secondary clinopyroxene crystals occur

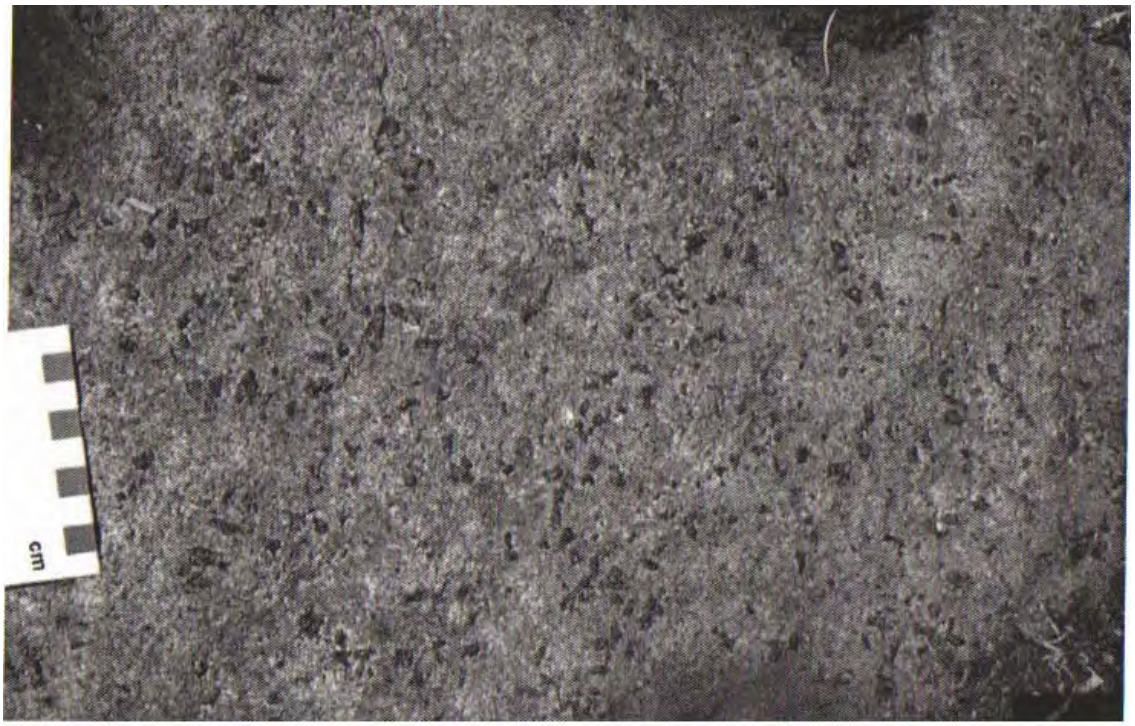

Figure 3.26: In hand sample, pyroxene-porphyritic melanogabbro is a feldspathic, biotite-rich lithology with up to 2 cm porphyritic pyroxenes occurring in a groundmass of equigranular plagioclase-pyroxene and olivine. On weathered surface, plagioclase occurs as a weathered out component surrounding large pyroxene crystals. Photo is from Hart et al. (2002).

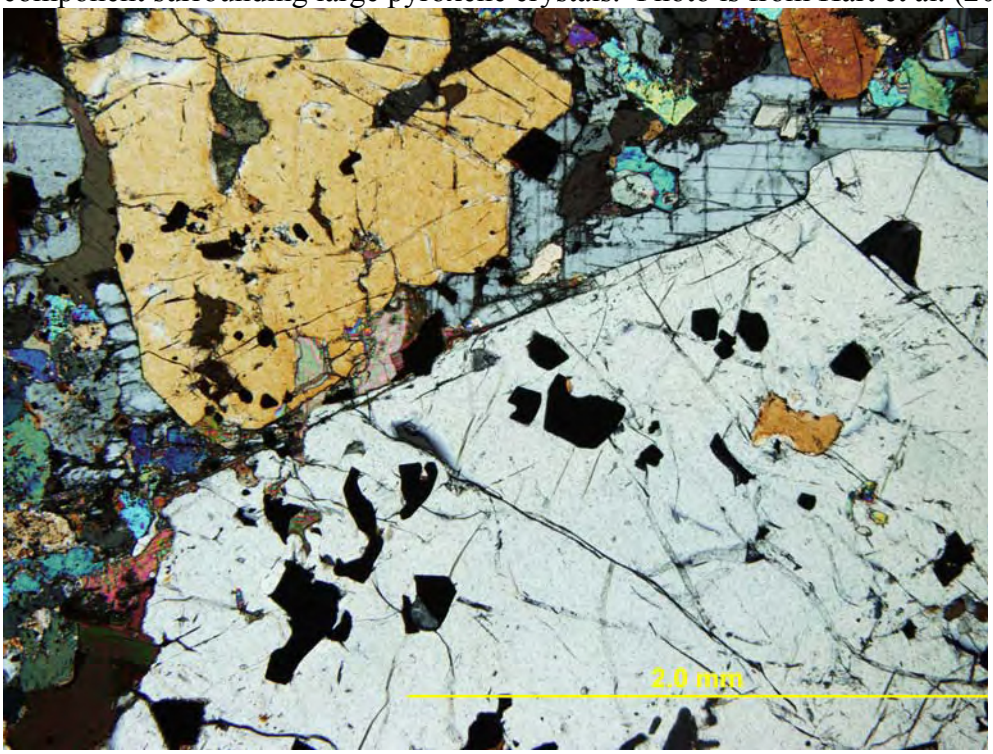

Figure 3.27: Large, up to 6 mm, oikocrysts of orthopyroxene comprise up to 30 modal % of the pyroxene-porphyritic melanogabbro in sample JL-017.

in clumps and are surrounded by large up to 7 mm long coarse intercumulus plagioclase (Fig. 3.28). In sample JL-020, intercumulus plagioclase crystals surround chains of cumulate clinopyroxene crystals (Fig. 3.29). Plagioclase is 30 modal % of the composition. Secondary pyroxene crystals are etched twinned cumulate crystals that are sericitized at the edges. Biotite crystals are coarse grained, up to 4 mm long in sample JL-017 (Fig. 3.30). Biotite is a late phase intercumulus mineral that surrounds magnetite crystals. As pyroxene-porphyritic melanogabbros become more fractionated and richer in plagioclase to the west of the central part of the intrusion, there is a decrease in size of all primary and secondary cumulate clinopyroxene and olivine crystals to between 0.5 to 1 mm.

3.2.6 Melanogabbro

Melanogabbro is the most evolved lithology in drill core and is found at the lower contacts of the lherzolite or pyroxenite with basement lithologies (Figs. 3.2b and 3.3). In hand sample, melanogabbro has an ophitic texture with a dominant association of interlocking up to 0.8 mm elongate plagioclase laths with dark equant 1 to 2 mm pyroxenes (Fig. 3.31). Intercumulus aphanitic olivine is dispersed in the groundmass as a minor phase. In feldspathic melanogabbros, up to 1 cm pitted, round vugs are present that represent chemical dissolution of plagioclase. In hole EK-04, the feldspathic peridotite or melanogabbro is a patchy weathered lithology that displays a mottled texture of round irregular 1 to 2 cm dark weathered serpentinized olivine patches with a dominant groundmass of oikocrystic pyroxene and ovoidal olivine in 20 modal % intercumulus plagioclase. Modal composition of melanogabbro is 50 to 60 modal % pyroxene, 20 to 30 modal % plagioclase and 10 modal % olivine. Mineralization in hole EK-02 at 303 m is represented by minor blebs of pyrrhotite towards the contact with Archean iron formation. In hole EK-3, melanogabbro is pervasively hematized at the contact with bordering Sibley sandstone. The lithology becomes progressively finer grained and hornfelsed towards the margin of basement sandstones in holes EK-03 and EK-04.

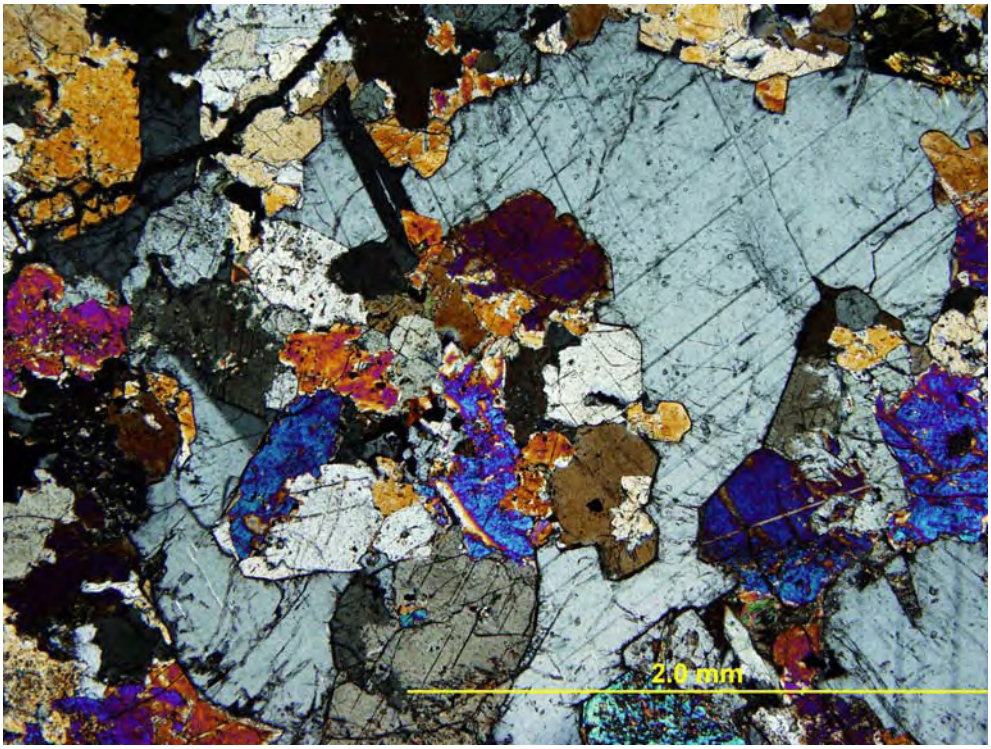

Figure 3.28: In sample JL-019, pyroxene-porphyritic melanogabbro contains large laths of up to 2 mm secondary clinopyroxene crystals that occur in clumps and are surrounded by large up to 7 mm long coarse intercumulus plagioclase.

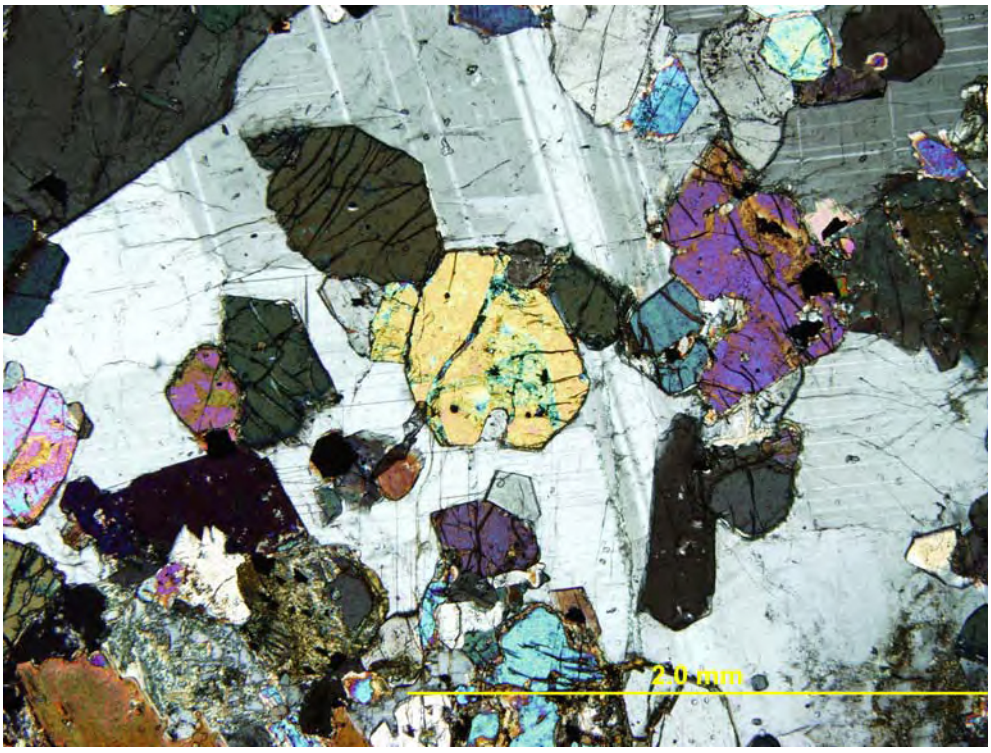

Figure 3.29: Pyroxene-porphyritic melanogabbro in sample JL-020 shows 30 modal % intercumulus plagioclase surrounding chains or clusters of cumulate clinopyroxene crystals.

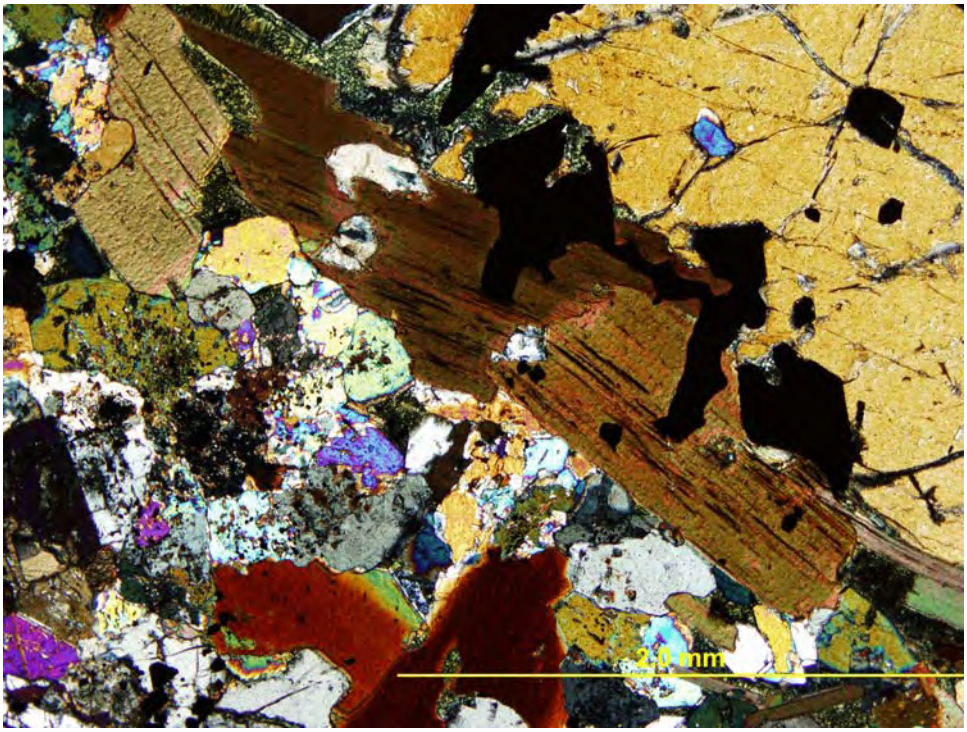

Figure 3.30: Biotite crystals are coarse grained up to 4 mm long in sample JL-017. Biotite is a late phase intercumulus mineral that surrounds magnetite crystals.

Figure 3.31: In hand sample, melanogabbro has an ophitic texture with a dominant association of interlocking <0.5 to 0.8 mm elongate plagioclase laths with dark equant 1 to 2 mm pyroxenes. Sample is from 301 m depth in DDH EK-02.

In thin section, melanogabbro displays an intergranular texture. In sample ED-33, large laths of plagioclase up to 3.5 mm occur in intergranular association with round anhedral crystals of cumulate pyroxene up to 0.8 mm long (Fig. 3.32). Many of the pyroxenes are replaced by chlorite and skeletal sericite. Melanogabbro is composed of up to 45 modal % plagioclase, 15 modal % sericite and 30 modal % pyroxene. Minor up to 1 modal % biotite, 2 modal % oxide and 1 modal % sulphide are accessory phases. In sample ED-10, contact mineralization with basement iron formation is characterized by up to 2.5 mm blebby immiscible pyrrhotite-chalcopyrite sulphides between cumulate crystals (Fig. 3.33). PGE grades are 14 ppb Pt and 7 ppb Pd over 5 m from 302 to 307 m (Coombes and Rossell, 2003).

3.2.7 Granophyric gabbro

Granophyric gabbro represents a separate intrusive phase from the other Kitto intrusive lithologies. It is located just west of the pyroxene-porphyritic melanogabbro at the core of the Kitto ring complex (Fig. 3.1). In hand sample granophyric gabbro displays a massive coarse grained leucocratic texture. Large, up to 1.5 cm, laths of potassium and plagioclase feldspar to rounded 1 to 2 mm feldspar crystals surround elongate up to 2 cm acicular crystals of pyroxene (Fig. 3.34). On the surface, the lithology is light pink due to the potassium-rich nature of the alkali feldspar component. In thin section, large feldspar laths up to 4 mm in size constitute 60 modal % of the rock. In some areas, the potassium and plagioclase feldspars display cuneiform granophyric to myrmekitic textures (Fig. 3.35). Otherwise, most feldspars display simple Carlsbad to albite twinning. Cumulate pyroxene crystals are <0.5 mm crystals that occur in chains or clusters as 20 modal % of the lithology. Hornblende makes up 3 modal % of the rock as up to 0.5 mm crystals and occurs in association with magnetite oxides. Minor muscovite and biotite minerals exist as accessory alteration phases. The lithology contains up to 15 modal % magnetite oxide. Large scale Fe oxidation occurs as alteration on cumulate pyroxene crystals.

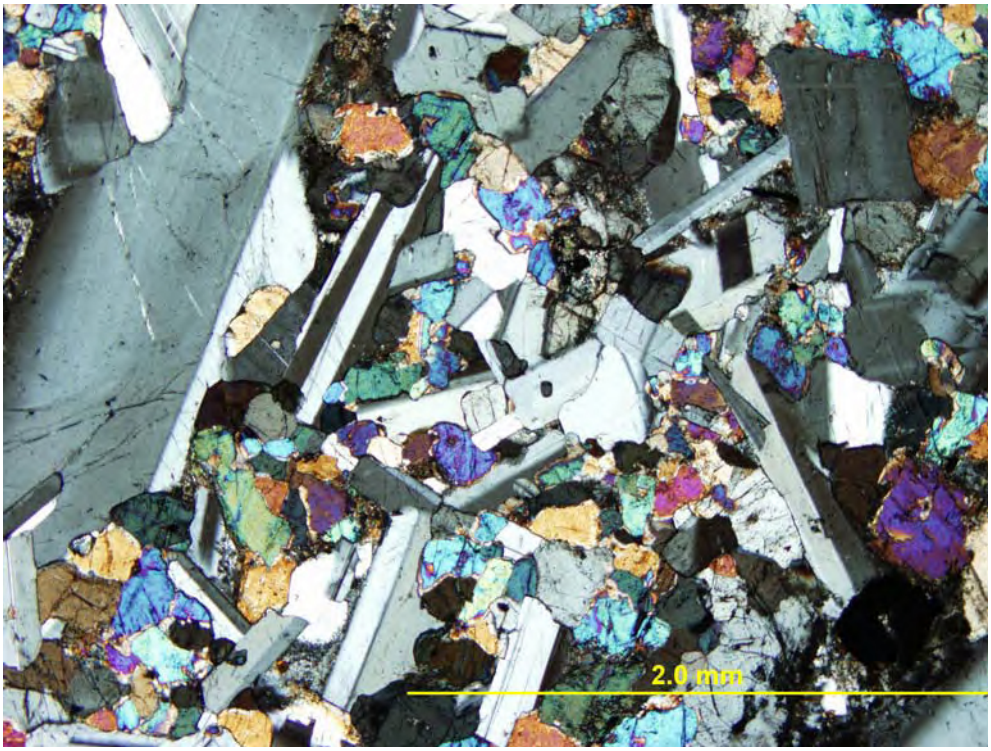

Figure 3.32: Melanogabbro in drill core sample ED-33 shows an intergranular texture. Large laths of plagioclase up to 3.5 mm in size occur in intergranular association with round anhedral crystals of cumulate pyroxene up to 0.8 mm in size.

Figure 3.33: Contact mineralization of melanogabbro with basement iron formation is shown in sample ED-10, where up to 2.5 mm blebby immiscible pyrrhotite-chalcopyrite sulphides occur between cumulate crystals.

Figure 3.34: In hand sample granophyric gabbro displays a massive coarse grained leucocratic texture. Large, up to 1.5 cm, laths of feldspar to rounded 1 to 2 mm crystals surround elongate up to 2 cm acicular crystals of pyroxene.

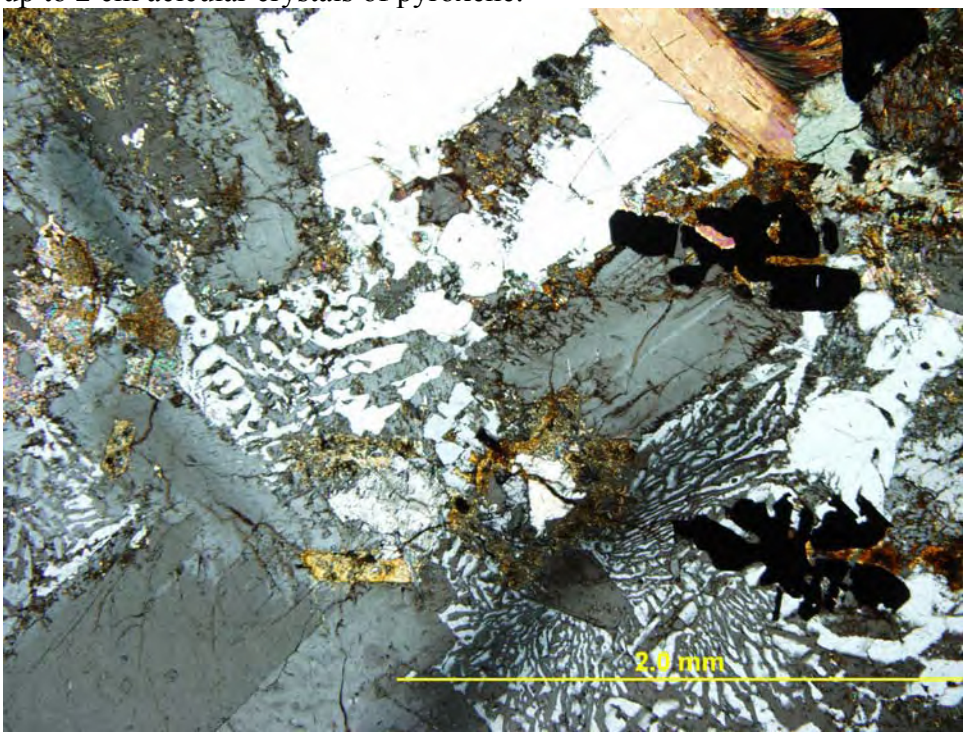

Figure 3.35: Granophyric gabbro in sample JL-043 displays a cuneiform granophyric to myrmekitic texture of alkali feldspar and plagioclase intercumulus crystals surrounding altered clinopyroxene and oxide crystals.

Cumulate pyroxenes are also broken down or sericitized at the margins of the crystals as a result of subsequent alteration.

3.2.8 Nipigon diabase

Nipigon diabase occurs as dikes and sills surrounding the Kitto intrusion. Hand sample JL-055b is a pyroxenitized diabase at the contact with the intrusion that displays primary diabasic textures. In hand sample, Nipigon diabase is massively textured and contains very fine to fine grained ophitic associations of plagioclase and pyroxene (Fig. 3.36). Oxide minerals are fine to medium grained anhedral phases. Locally, there is coarser equant crystalline development of pyroxenes around carbonate-chlorite serpentine veins indicative of a hydrothermal fabric. In drill core, diabase occurs from 2 to 50 m as a sill at the top of hole EK-04. The diabase is chilled from 49 to 50 m at the contact with the lherzolite, confirming the younger U-Pb age of the lithology. A separate sill is found interstratified with Sibley sandstone at the bottom of holes EK-03 and EK-04. In thin section, Nipigon diabase contains an ophitic association of 40 modal % plagioclase with 50 modal % cumulate pyroxene. Plagioclase laths are elongate crystals up to 2mm long that are intergrown with <0.5mm to up to 3mm cumulate pyroxene crystals (Fig. 3.37). Oxides are 5 modal % of the composition.

3.3 Basement lithologies

3.3.1 Mafic metavolcanic rock

Mafic metavolcanic rocks are the dominant basement lithology of the Kitto intrusion south of the Princess Lake Fault (Fig. 2.4, Fig. 3.1). In drill core, the metavolcanic rocks are metabasalts that are massive lithologies that occur from 328 to 345 m at the end of drill hole EK-02 (Fig. 3.3). Down to 333 m, the metavolcanic rocks are altered with sulphidized calcite veins running irregularly throughout, along with associated blebby pyrite sulphides. The alteration of the lithology at the contact with the iron formation is probably indicative of the hydrothermal epigenetic deposition of the iron formation. Below 333 m, mafic metavolcanic rock is darker

Figure 3.36: In hand sample, Nipigon diabase is massively textured and contains very fine to fine grained ophitic associations of plagioclase and pyroxene. Oxide minerals are fine to medium grained anhedral phases.

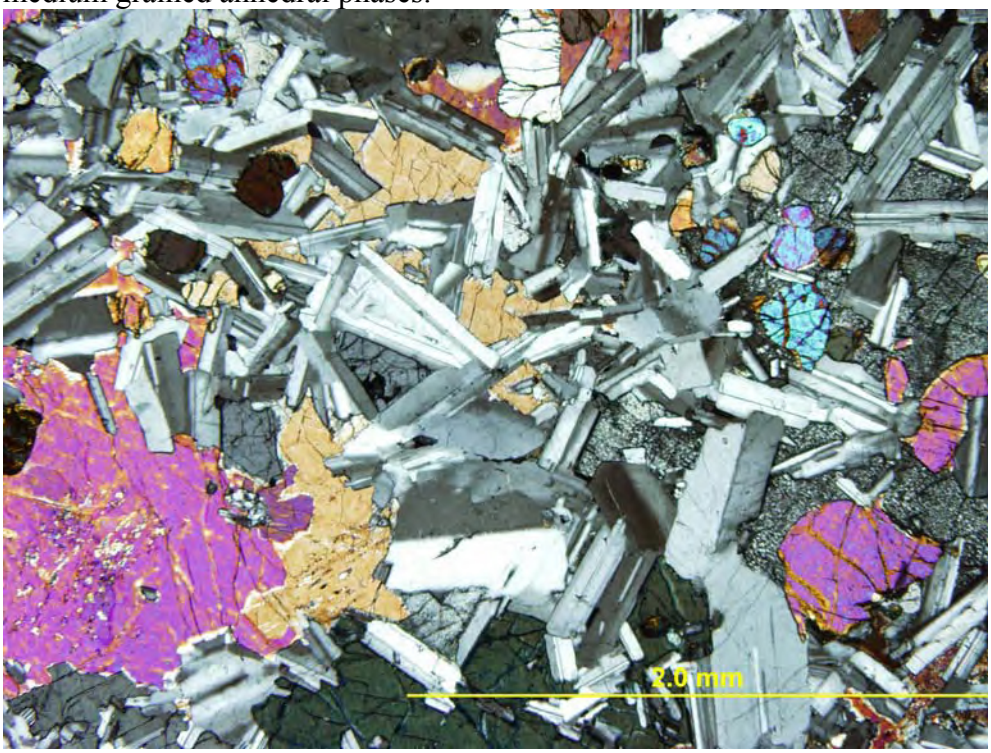

Figure 3.37: Nipigon diabase in sample JL-055b displays an ophitic texture of 40 modal % elongate, up to 2 mm, plagioclase crystals in association with 50 modal % <0.5 mm to up to 3 mm cumulate pyroxene crystals.

green and chloritized with irregular calcite veining and pyrite mineralization. At 338 m, pyrite occurs in botryoidal form as round concentric layered minerals with rims of calcite. Within the large calcite altered zones are thinner irregularly orientated serpentine veinlets. In thin section, sample ED-24 is a dominantly chloritized metabasalt with <0.5 mm pyroxenes crystals dispersed throughout the groundmass (Fig. 3.38). Some pyroxene crystals are up to 3 mm in size and are altered in cracks and edges of the laths. The lithology contains 70 to 80 modal % chlorite and up to 5 modal % Fe oxide component. Field sample JL-007 is also a pervasively chloritized lithology. Iron oxidation occurs in fractures along foliation planes of the rock.

3.3.2 Banded iron formation

Magnetite-chert banded iron formations are intercalated with mafic metavolcanic rocks north of the Empire Fault and south of the Princess Lake Fault within the Southern Volcanic Unit (Fig. 2.4, Fig. 3.1). North of the Empire Fault, the banded iron formation occurs from 307 to 328 m in drill hole EK-02 beneath the pyroxenite to melanogabbro lithologies of the intrusion (Fig. 3.3). The banded iron formation is a strongly magnetic oxide-rich banded iron formation with up to 2 cm wide sulphidized calcite veins cross-cutting the lithology throughout. Massive pyrite occurs in association with calcite veins. Veins are sometimes vuggy with dissolution of calcite. In hand sample, surface exposure JL-008 is a tremolitized to orange carbonatized iron formation lithology that is strongly magnetic (Fig. 3.1). Magnetite crystals are <1 mm in size and are dispersed throughout the lithology in between up to 2 cm long acicular crystals of tremolite. The lithology is sulphide stained on the surface. Dense up to 1 cm wide magnetite layers are separated by zones of tremolite and magnetite. Carbonate occurs as an alteration vein that breaks up the primary layer band textures of the lithology. South of the Princess Lake Fault, in the vicinity of the central part of the intrusion, banded iron formation occurs as an altered magnetite-chert lithology with pyrite sulphides (Fig. 3.1). Bands of magnetite 1 to 2 cm thick are spaced 5 cm apart in a cherty groundmass. In hand sample JL-046, up to 2 cm long sheafy textured

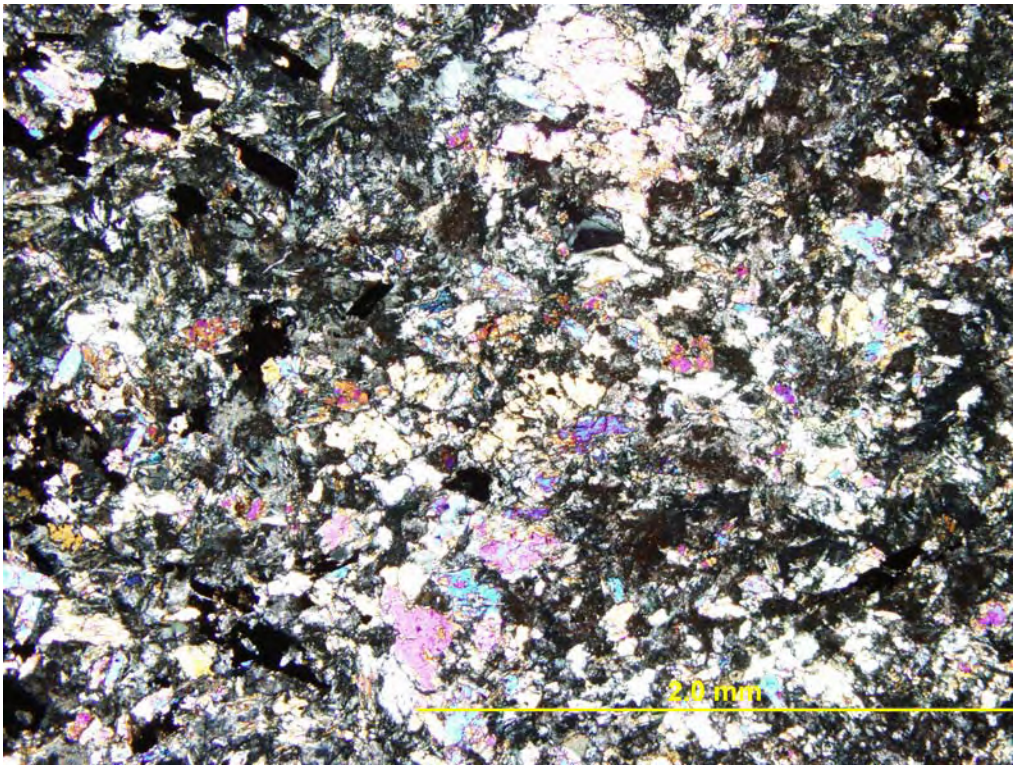

Figure 3.38: Sample ED-24 is a basement chloritized metabasalt. Less than 0.5 mm crystals of clinopyroxene are dispersed throughout a chloritized groundmass.

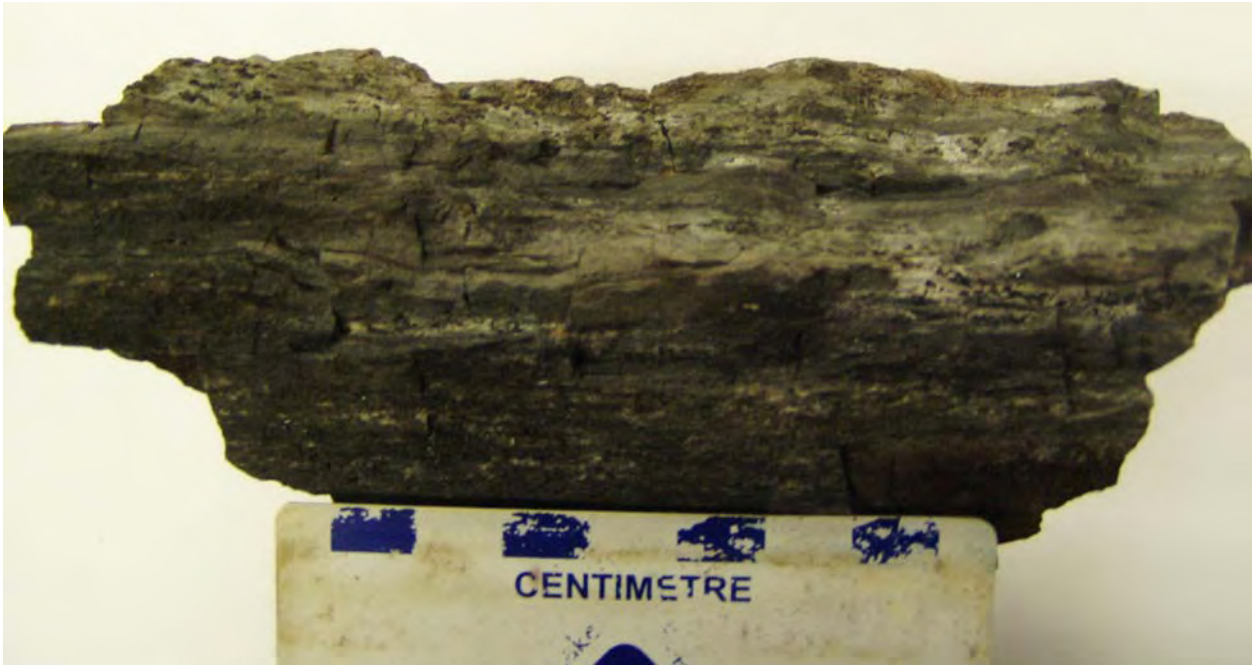

Figure 3.39: In banded iron formation hand sample JL-046, up to 2 cm long sheafy textured elongate silvery white pyroxenes are orientated along the foliation and separate the magnetite bands.

elongate silvery white pyroxenes are orientated along the foliation and separate the magnetite bands (Figure 3.39).

In thin section, drill core sample ED-11 is an iron formation that consists of 70 modal % oxide component (Fig. 3.40). Up to 0.5 mm clusters of quartz crystals make up 5 to 10 modal % of the groundmass. The groundmass is largely sericitized. Sample JL-008 is a largely tremolitized iron formation with 70 modal % up to 5 mm long acicular to radiating spindle fibre crystals of tremolite randomly orientated throughout the rock (Fig. 3.41). The banded iron formation contains 15 to 20 modal % Fe oxide crystals, of which some are leucoxenized. The groundmass consists of 10 to 20 modal % very fine grained <0.5 mm cherty quartz. In the vicinity of the central part of the intrusion, sample JL-046 is a foliated to finely magnetite banded iron formation. Bands of up to 3 mm crystals of pyroxene surround oxide minerals. Large poikiloblasts of sheafy pyroxene are overprinted by 70 to 80 modal % sericite. Magnetite occurs as up to 3 mm elongate crystals orientated along the foliation planes of the rock.

3.3.3 Sibley quartz sandstone

Sibley quartz sandstone from the Rossport Formation occurs as a thin basement lithology beneath lherzolite to melanogabbro lithologies in drill holes EK-03, EK-04, and EK-01 (Figs. 3.2b and 3.3). Sibley sandstone is from the Rossport Formation since it consists of calcareous mudstones and dolostones found in the Rossport Formation (Hart et al., 2002). Also, the lithology is mapped as Rossport Formation on the southeastern shore of Lake Nipigon (Rogala et al., 2005). In hole EK-03 from 150 to 163 m, the calcareous sandstone is white, friable, chalky, well-sorted with interlayering of up to 4 cm thick bands of chocolate brown argillite and thinner light green clay minerals. From 150 to 153 m in EK-03, the rock is a lighter green massive sandstone due to serpentine/chlorite alteration from the overlying lherzolite-melanogabbro lithologies. From 161 to 163 m, the sandstone contains orange-greenish alteration due to ankeritization as a result of intrusion of bordering diabase sills. In thin section, sample ED-023

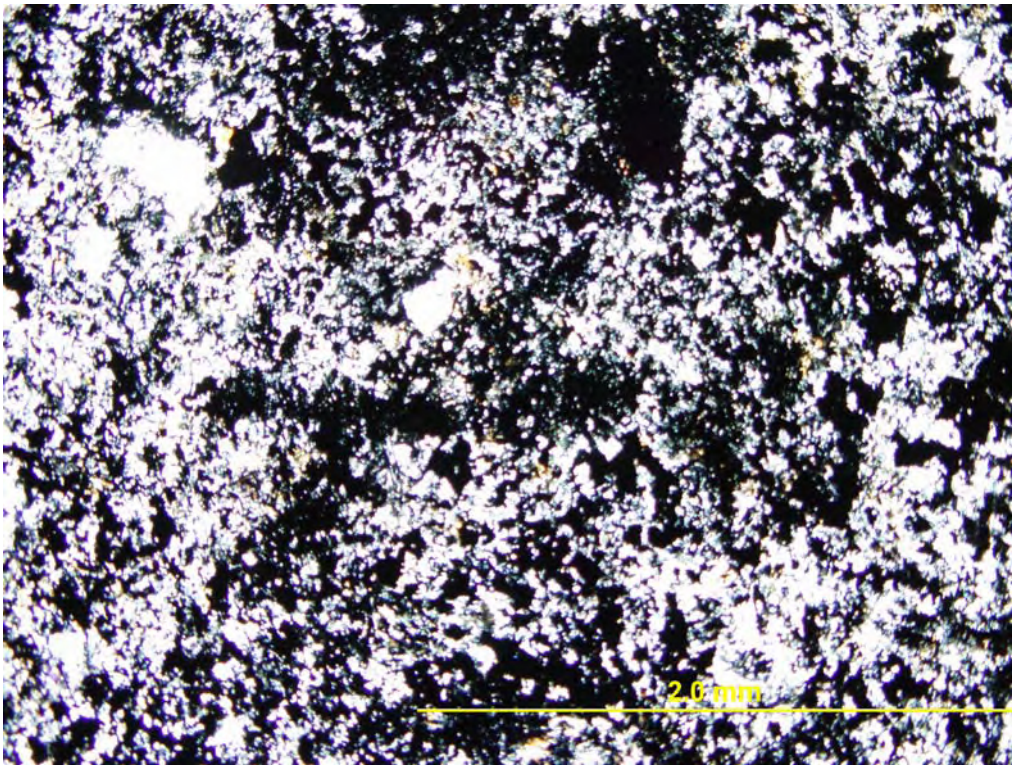

Figure 3.40: Basement iron formation sample ED-11 consists of 70 modal % iron oxide component in a sericitized groundmass.

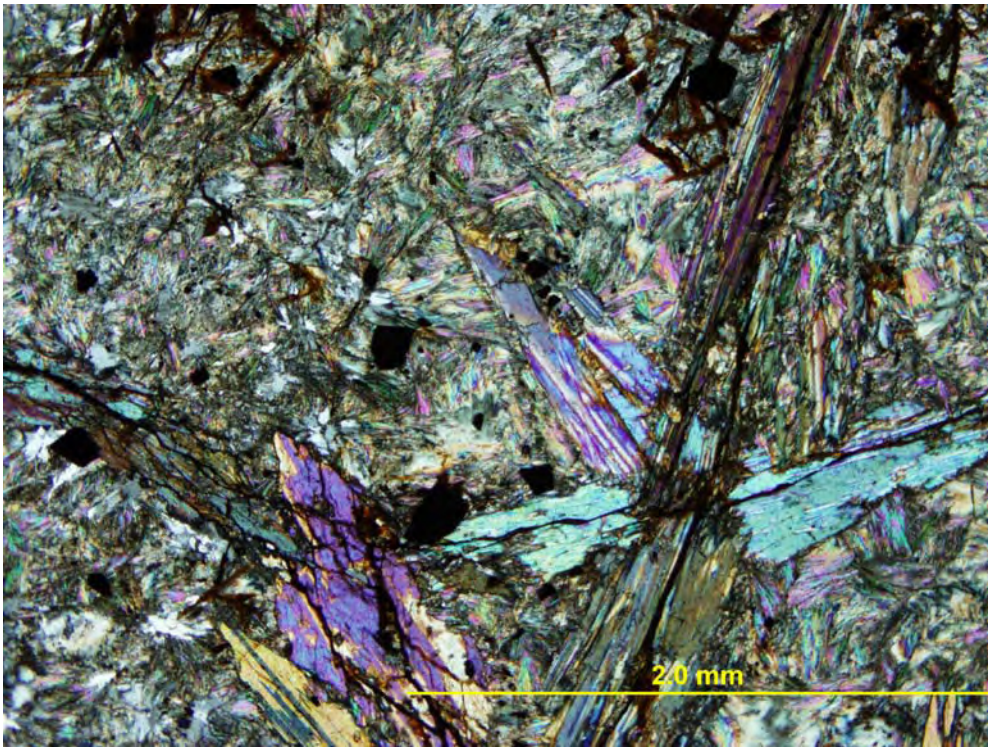

Figure 3.41: Field sample JL-008 represents a tremolitized iron formation north of the Empire Fault. 70 modal % up to 5 mm long acicular to radiating spindle fibre crystals of tremolite are haphazardly orientated throughout the rock and surround oxide crystals.

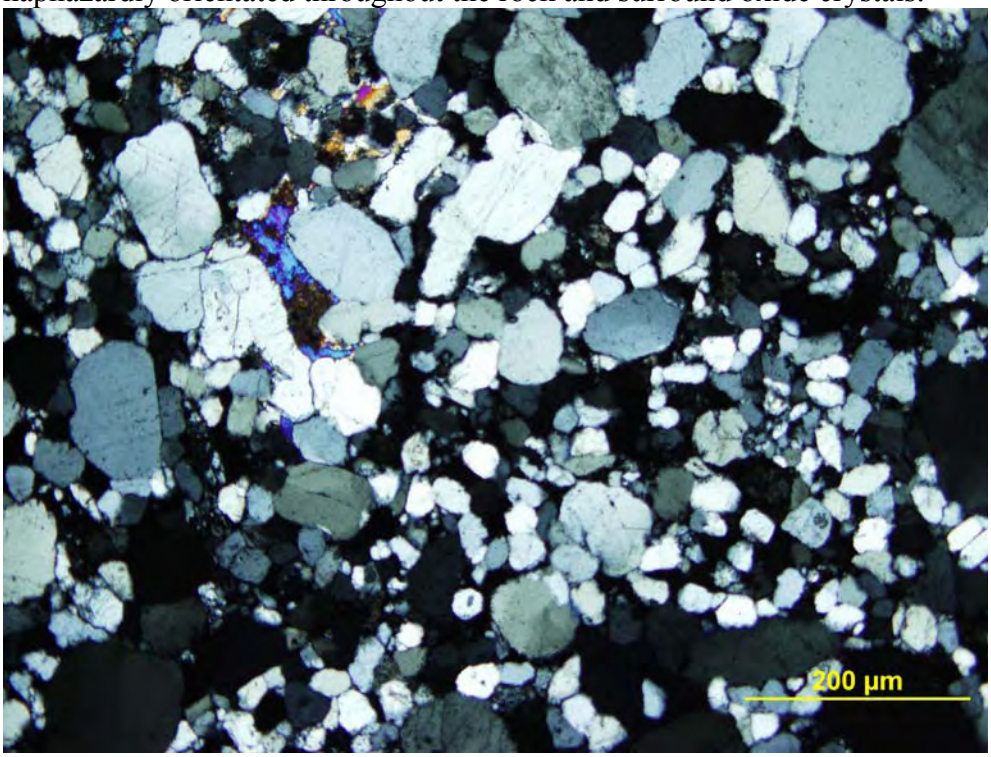

Figure 3.42: Sibley quartz sandstone is represented by sample ED-23. The sandstone consists of 80 to 90 modal % rounded crystals of quartz with very minor specks of mafic crystals occurring in the groundmass.

contains 80 to 90 modal % round crystals of quartz with very minor specks of mafic crystals occurring in the groundmass (Fig. 3.42). The quartz crystals exhibit undulose extinction and range from 0.1 to 0.75 mm in size.

3.4 Summary

Lithologies in the vicinity of the Kitto intrusion consist of intrusive lithologies and surrounding basement lithologies. Lherzolite is the dominant peridotite lithology of the Kitto intrusion. It contains massive cumulate to pyroxene-poikilitic textures of cumulate olivine, clinopyroxene and poikilitic orthopyroxene minerals. Field outcrops of horizontal to 16° dipping 15 to 30 cm layer cake beds of the lithology show that it is relatively flat-lying but dips at the contacts with diabase and to the west in the central part of the intrusion where the lithology thickens in a trough-like structure. Some lherzolites are more fractionated in locally restricted areas as evidenced by the crystallization of secondary pyroxene minerals. Olivine websterite is a cumulate to poikilitic textured lithology similar to the lherzolite and occurs adjacent to lherzolite in areas of contact mineralization with surrounding diabase at the Phoenix occurrence and to the west of the lherzolite in more fractionated portions of the central part of the intrusion. In drill core, since olivine websterite is located below the lherzolite and contains Ni-Cu-PGE mineralization, it is probably a cumulate lithology related to the upper lherzolite due to the settling of basal cumulate and interstitial sulphide minerals. In the field, olivine websterite shows progressive fractionation from lherzolite with more feldspar and secondary pyroxene growth textures. Below the olivine websterite, in drill core, is a patchy vari-textured pyroxenite lithology which represents the transition to lower pyroxenite. Vari-textured pyroxenite contains patches of recrystallized secondary pyroxene minerals that are surrounded by primary cumulate clinopyroxene and intergranular plagioclase. Pyroxenite, located below the vari-textured pyroxenite in drill core, displays cumulate to intergranular textures of dominant cumulate clinopyroxene and lathy plagioclase. Pyroxene-porphyritic melanogabbro, located to the west of

olivine websterite on the surface, consists of layered beds that dip into a trough-like structure in the central part of the intrusion. The pyroxene-porphyritic melanogabbro contains a cumulate texture of dominant clinopyroxene composition, but displays the development of secondary pyroxene and intercumulus plagioclase, suggesting the lithologies are fractionates of the lherzolite and olivine websterite. Melanogabbro occurs below pyroxenite in drill core at the contact with basement lithologies. It is the most evolved lithology and contains an intergranular texture of dominant plagioclase and pyroxene. Granophyric gabbro occurs to the west of pyroxene-porphyritic melanogabbro on surface and intruded as a late stage partial melt from the Kitto intrusion. Typically more alkalic intrusive phases occur and crystallize last in sequence in the upper portions of layered intrusions such as the granophyres in the upper portions of the Skaergaard Intrusion in Greenland. Such late stage melts of granophyric to monzogabbro have been observed to form in other intrusions of the Nipigon Embayment such as the monzogabbros of the Seagull and Disraeli Intrusions and the upper pegmatitic zones of the Nipigon diabase sills (Hart, 2005; Hart and Magyarosi, 2004; Sutcliffe, 1986). The granophyric gabbro contains unique granophyric to myrmekitic leucocratic textures not found in the other lithologies. Nipigon diabase, of geochemical affinity to the Nipigon sills on the west side of Lake Nipigon, occurs as dikes and sills that cross-cut and surround the intrusion. The diabase displays an ophitic texture of plagioclase and pyroxene.

Basement lithologies to the Kitto intrusion consist of Archean mafic metavolcanic rock, magnetite-chert banded iron formation and Sibley quartz sandstone. Mafic metavolcanic rocks are massively textured and chloritized lithologies that occur below iron formation in drill core and on surface along the inward contacts of the southern part of the intrusion. Iron formation occurs as a magnetite oxide banded lithology, a tremolitized spindle fibre-textured lithology, and fine grain magnetite and sheafy pyroxene banded lithology below the melanogabbro in drill core, and is interlayered with mafic metavolcanic rock on surface. Sibley quartz sandstone, which

occurs as basement in holes EK-01, EK-03 and EK-04; contains 80 to 90 modal % rounded quartz crystals with very minor mafic minerals in the groundmass.

CHAPTER 4

GEOCHEMISTRY

4.1 Whole rock geochemistry

Whole rock geochemical analysis was carried out on 64 surface samples and 42 samples from drill core. Drill core previously sampled by Kennecott Canada Exploration Ltd. from the mineralized horizons of DDH EK-02 was also interpreted along with the 42 samples chosen for this thesis. Full results are presented in Appendix 3. Discussion of geochemical trends is presented below and is divided into analysis of major oxide variations displayed in surface samples and drill core samples.

4.1.1 Surface sample major oxide variation

Lithologies in the Kitto intrusion were subdivided based on major oxides. In the central part of the intrusion, ultramafics of the pyroxene-porphyritic melanogabbro, olivine websterite and lherzolite display gradational lateral chemical variations from one lithology to the next. Major oxide variations of the lithologies are displayed in Table 4.1. From the lherzolite to pyroxene-porphyritic melanogabbro, there is an increase in SiO_2, Al_2O_3, TiO_2 and CaO, and a decrease in MgO. The increase in SiO_2 is due to increased evolution to more felsic lithologies from east to west. With increased evolution of the rocks, there is increased Al_2O_3 which is due to increased plagioclase crystallization. The decrease in MgO is due to less olivine crystallization in more felsic lithologies and crystallization of plagioclase. From the lherzolite to olivine websterite and pyroxene-porphyritic melanogabbro, the increase in CaO is due to predominance of pyroxene crystallization relative to olivine in the latter lithologies.

Table 4.1: Major oxide wt. % in lithologies on surface.

Central part of the Intrusion	**SiO_2 wt. %**	**TiO_2 wt. %**	**Al_2O_3 wt. %**	**CaO wt. %**	**MgO wt. %**
Lherzolite	42 to 44	0.6 to 0.7	3.1 to 3.5	5 to 7.8	25 to 28
Olivine websterite	43 to 47	0.7 to 0.9	3.5 to 4.3	8.8 to 12	20 to 25
Pyroxene-porphyritic melanogabbro	45 to 48	0.8 to 1.3	4.5 to 8.2	8 to 14	14 to 20
Granophyric gabbro	49 to 60	1.6 to 3.6	9.6 to 14	6.4 to 8.4	2 to 9
Southern part of the intrusion					
Lherzolite	40 to 42	0.5 to 0.7	2.7 to 3.7	2.6 to 6.7	28 to 33
Olivine websterite	38 to 41	0.4 to 0.8	2.4 to 3.8	2.6 to 8.2	29 to 32

Granophyric gabbros have very different chemical compositions than the ultramafics with higher SiO_2, Al_2O_3, Na_2O and K_2O contents reflecting dominance of plagioclase and potassium feldspar. TiO_2 contents are higher in this lithology than the other lithologies possibly due to precipitation of ilmenite oxide in the gabbro. This would be consistent with about 15 modal % magnetite with exsolved phases of ilmenite examined in thin section. CaO and MgO contents are lower than the peridotite lithologies due to lack of crystallization and accumulation of magnesian minerals.

In the southern part of the intrusion, lherzolite and olivine websterite display different major oxide variation trends than that of the central part of the intrusion. Lherzolites are less evolved and more ultramafic in the southern part than in the central part of the intrusion. SiO_2 contents are lower, while MgO contents are the highest in the intrusion indicative of the more primitive and ultramafic chemistry of the lithologies, and Al_2O_3 is lower indicative of less crystallization of plagioclase. Olivine websterites are similar to lherzolite in the southern part of

the intrusion, with high MgO contents indicative of primitive chemistry and lower Al_2O_3 indicative of lack of plagioclase crystallization. The olivine websterites have slightly higher CaO contents due to more cumulate pyroxene mineralogy. Compared to olivine websterites in the central part of the intrusion, these lithologies have more primitive olivine and pyroxene cumulate, and less feldspathic compositions (Chapter 3.2.2).

4.1.2 Downhole major oxide variation

Drillhole EK-02 displays variation in major oxides of SiO_2, Al_2O_3, TiO_2, MgO, Fe_2O_3, CaO and MgO with depth of the lithologies down the hole (Figs. 4.1 to 4.6). From the top to the bottom of the hole, the Kitto intrusive units have general trends of increasing SiO_2, Al_2O_3, TiO_2, CaO and decreasing MgO. At the top of the hole at 22 m, lherzolites have high MgO, low SiO_2, Al_2O_3, TiO_2, and CaO indicating primary olivine lherzolitic composition of the main intrusion. An increase in TiO_2 from 22 to 116 m can be seen possibly due to an accumulation of Ti-bearing minerals toward the bottom of the lherzolite. At 145 m an increase is displayed in SiO_2 and Al_2O_3 and a decrease in MgO due to evolution to olivine websterite. An increase is also displayed in CaO because there is accumulation of pyroxene minerals in the olivine websterite (Chapter 3, section 3.2.2). A maximum in SiO_2, Al_2O_3 and TiO_2 and depletion in MgO is displayed at 157 m in sample ED-18 possibly due to a nearby quartz vein that contains pyrrhotite-chalcopyrite mineralization. From 169 to 177 m, the K-series data (Kennecott data) display a large drop in MgO while there is a maximum in SiO_2 and CaO (Figs. 4.1, 4.2 and 4.6). The high SiO_2 and low MgO is due to the presence of a sandstone xenolith in drillcore, within a serpentinized alteration zone, that has a felsic composition, and high CaO due to the carbonate content of the sandstone. From 157 to 185 m, SiO_2, Al_2O_3 and TiO_2 decrease while MgO increases since these samples are at the bottom of the intrusion where there is an accumulation of

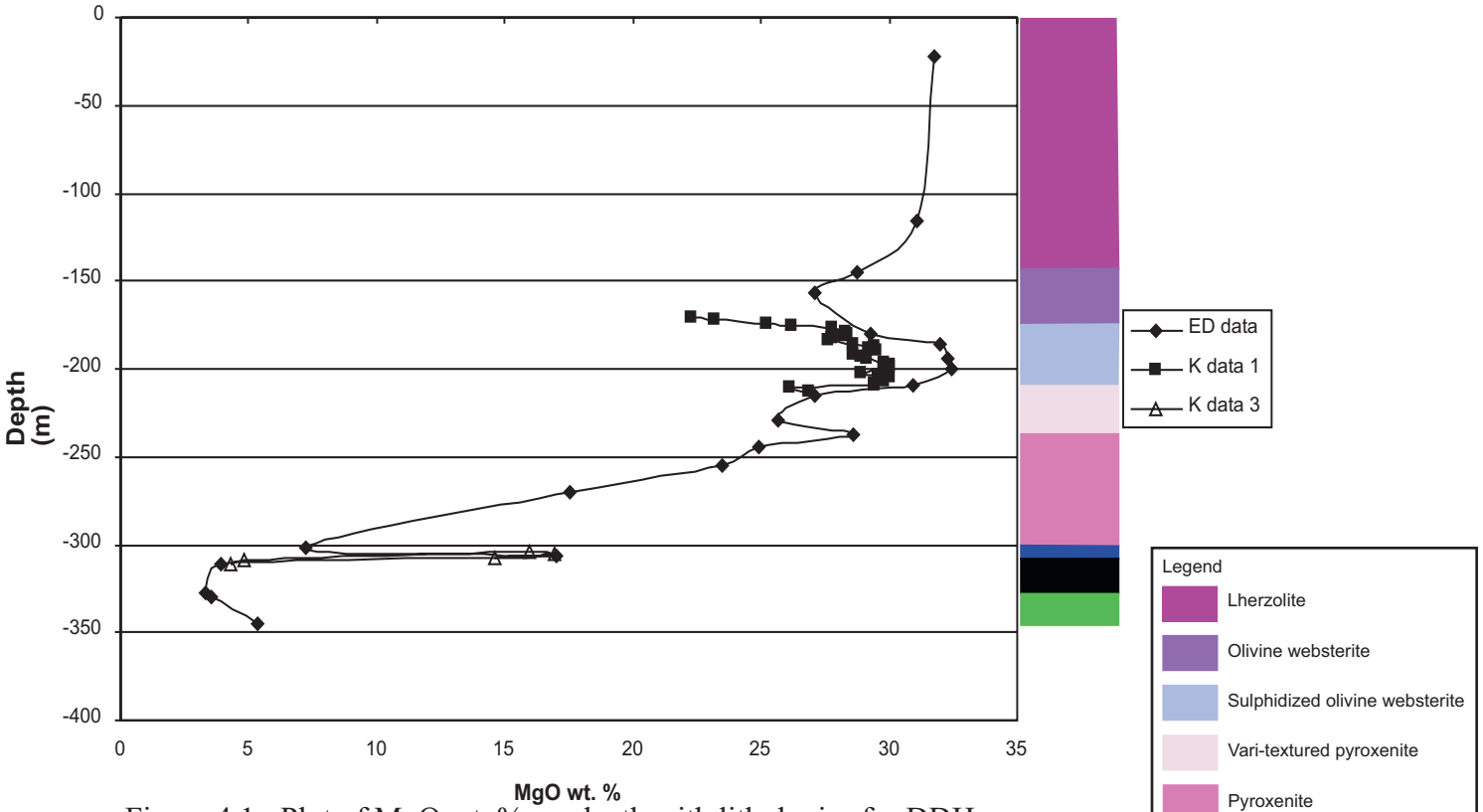

Figure 4.1: Plot of MgO wt. % vs. depth with lithologies for DDH EK-02. ED data is Eva Kitto drill hole data series from this study while K data is Kennecott data series (Coombes and Rossell, 2003).

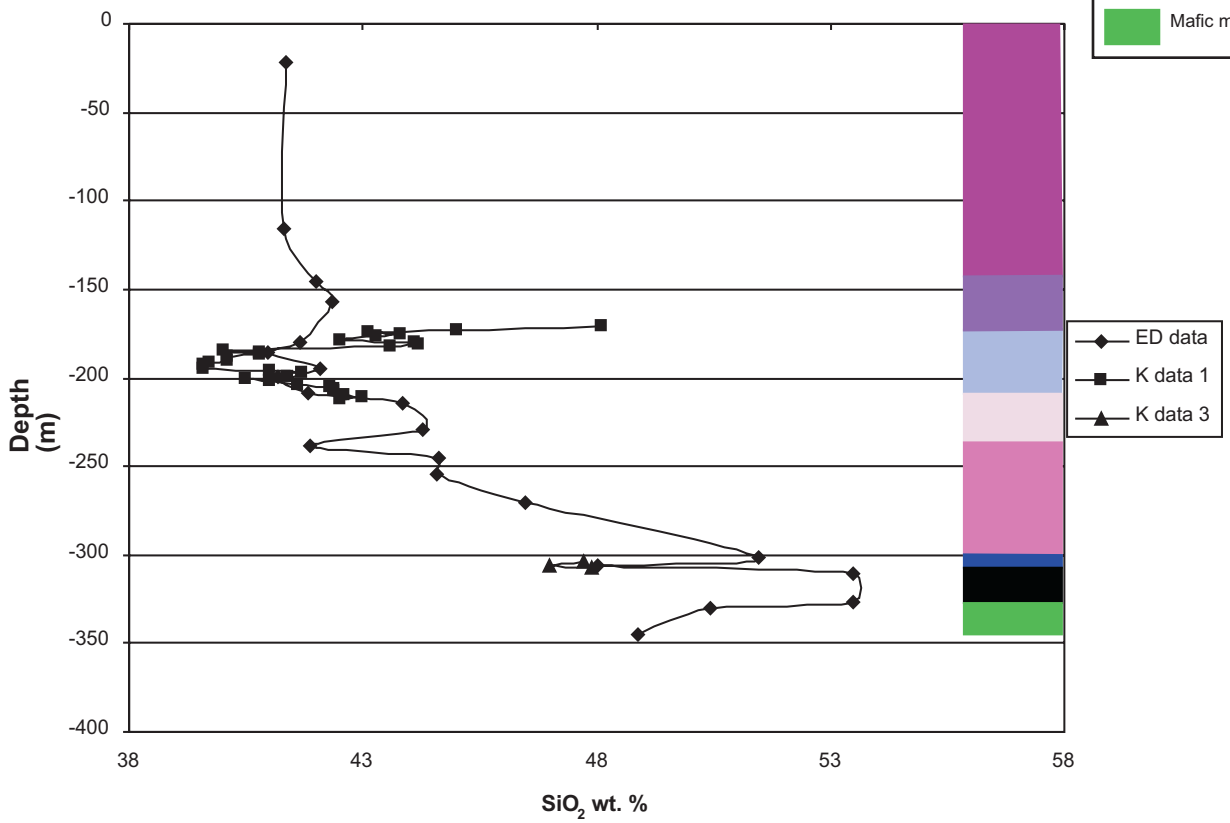

Figure 4.2: Plot of SiO_2 wt. % vs. depth with lithologies for DDH EK-02. ED data is Eva Kitto drill hole data series from this study while K data is Kennecott data series (Coombes and Rossell, 2003).

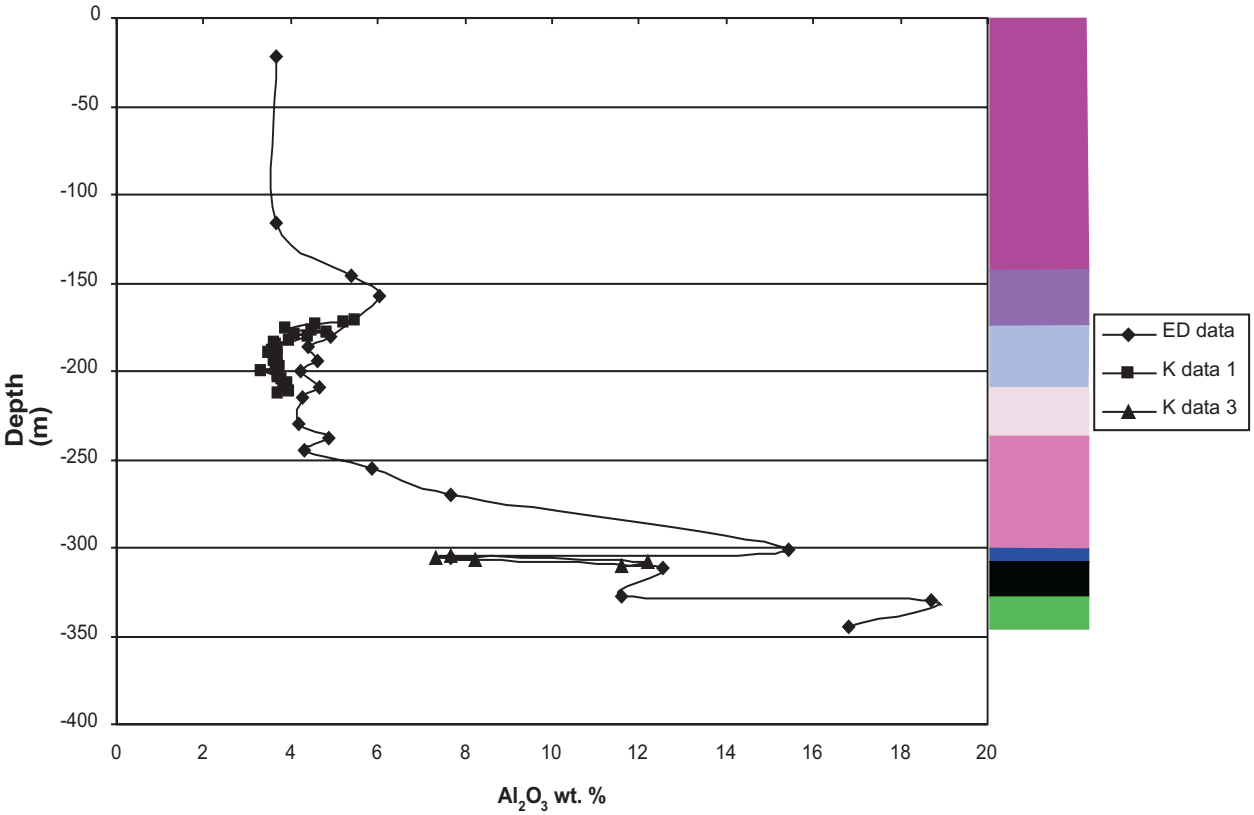

Figure 4.3: Plot of Al_2O_3 wt. % vs. depth with lithologies for DDH EK-02. ED data is Eva Kitto drill hole data series from this study while K data is Kennecott data series (Coombes and Rossell, 2003). For legend of lithologies, see Figure 4.1.

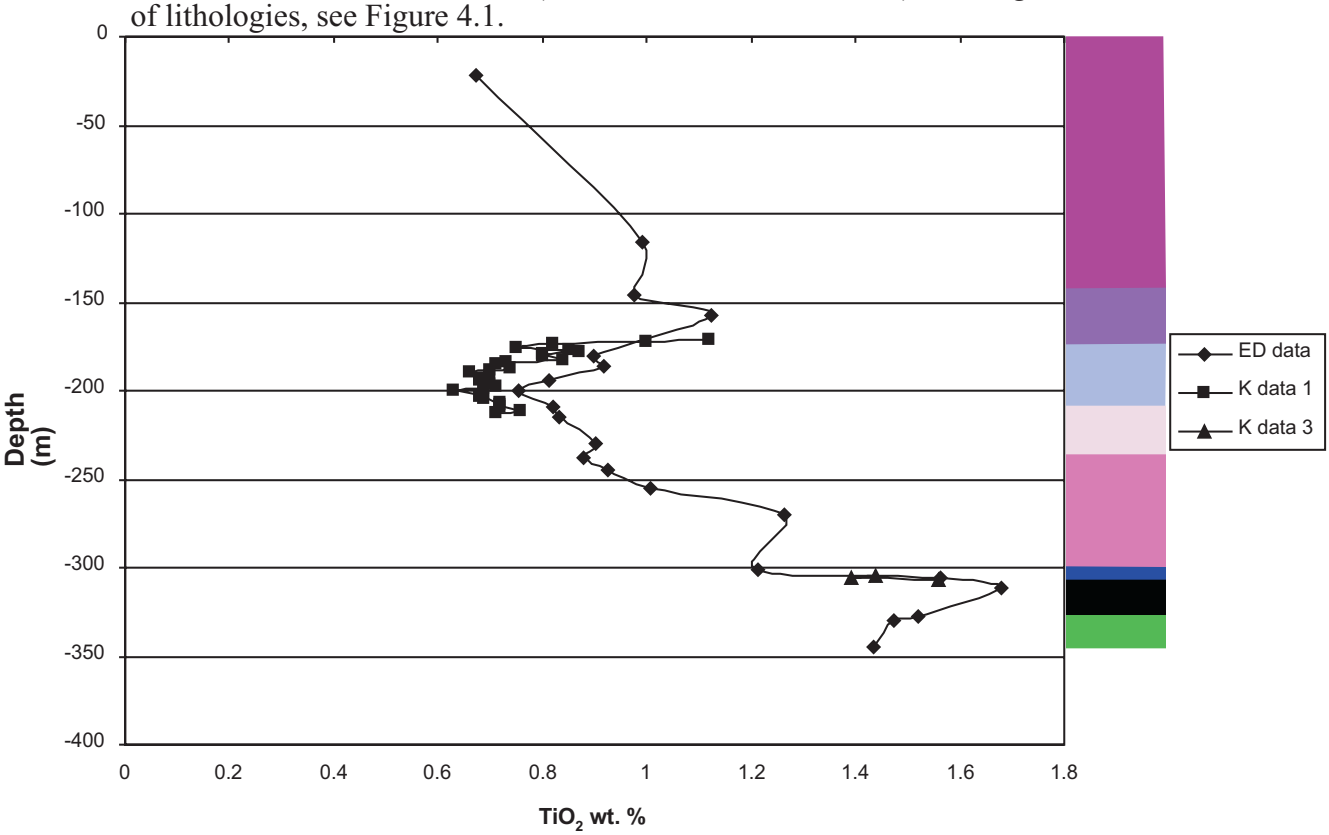

Figure 4.4: Plot of TiO_2 wt. % vs. depth with lithologies for DDH EK-02. ED data is Eva Kitto drill hole data series from this study while K data is Kennecott data series (Coombes and Rossell, 2003). For legend of lithologies, see Figure 4.1.

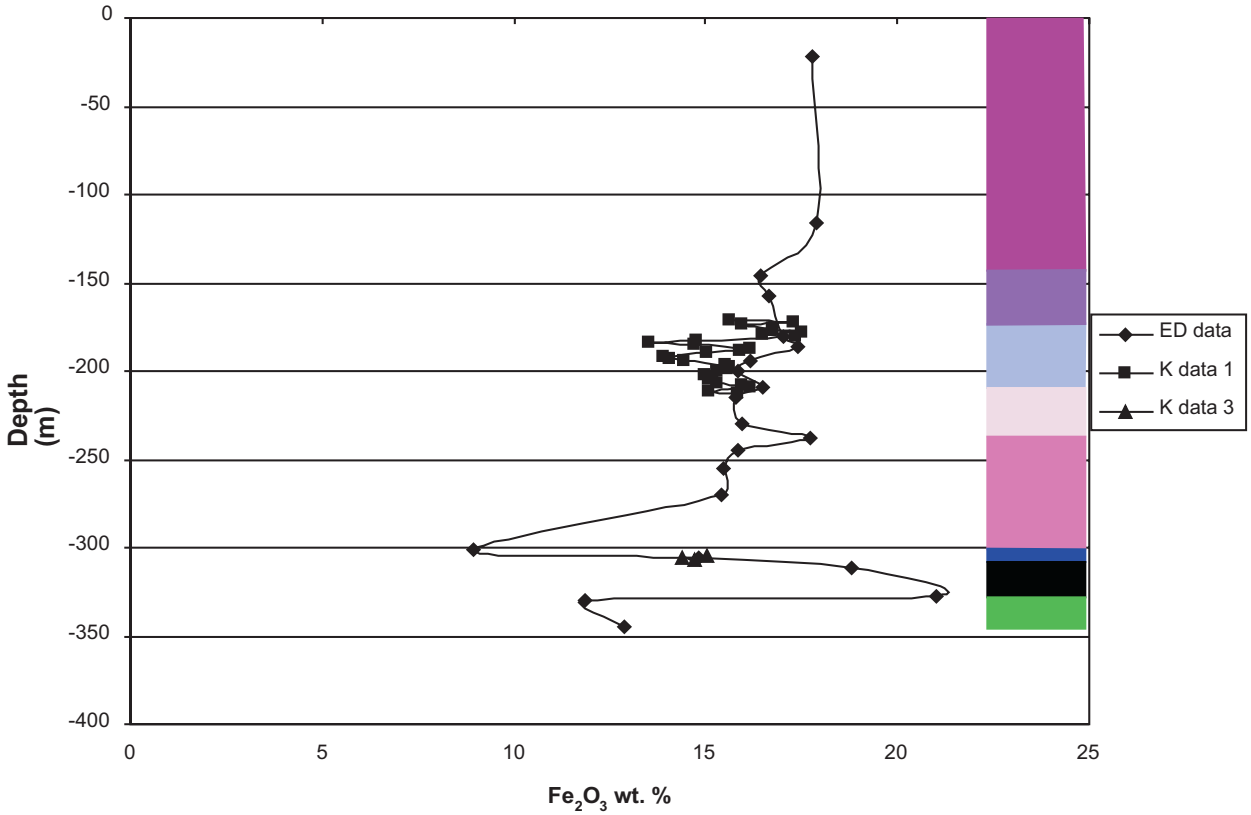

Figure 4.5: Plot of Fe_2O_3 wt. % vs. depth with lithologies for DDH EK-02. ED data is Eva Kitto drill hole data series from this study while K data is Kennecott data series (Coombes and Rossell, 2003). For legend of lithologies, see Figure 4.1.

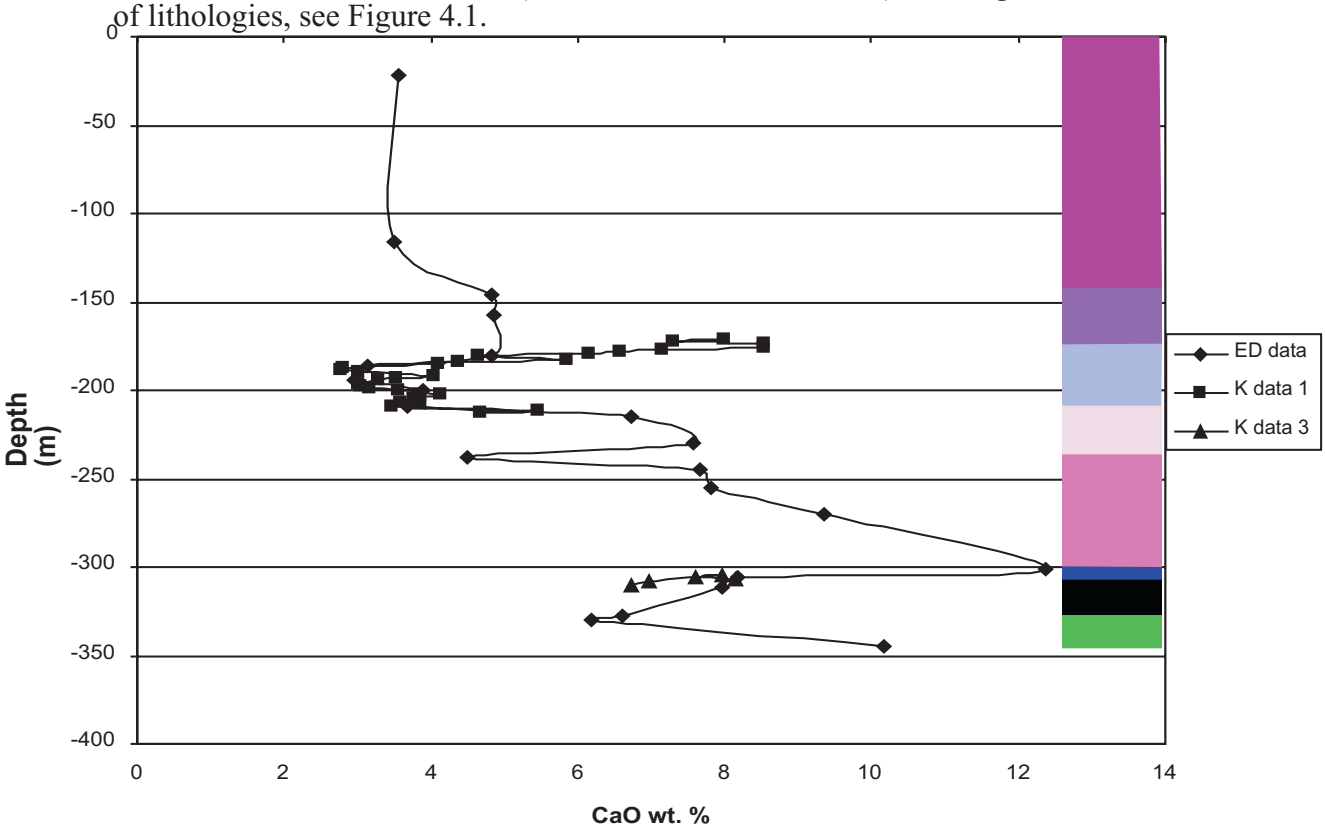

Figure 4.6: Plot of CaO wt. % vs. depth with lithologies for DDH EK-02. ED data is Eva Kitto drill hole data series from this study while K data is Kennecott data series (Coombes and Rossell, 2003). For legend of lithologies, see Figure 4.1.

olivine and pyroxene cumulate minerals at the basal mineralized olivine websterite (Figs. 4.1, 4.2, 4.3 and 4.4). At 199 m, a depletion occurs in TiO_2 and a maximum in MgO since sample ED-03 occurs at the bottom of the mineralized olivine websterite (Figs. 4.1 and 4.4). From 199 to 270 m a steady increase in TiO_2 and a sharp increase in CaO occurs with accumulation of pyroxene in the vari-textured pyroxenite to pyroxenites (Figs. 4.4 and 4.6). An MgO maximum and SiO_2 and CaO depletions occur at 237 m in sample ED-07 where there are large leucocratic patches of secondary pyroxene of lherzolitic composition (Figs. 4.1, 4.2 and 4.6). From 270 to 301 m, a sharp increase occurs in SiO_2, Al_2O_3, TiO_2 and CaO and a decrease in MgO with crystallization of plagioclase in the bottom melanogabbros near the contact with the basement iron formation (Figs. 4.1, 4.2, 4.3, 4.4 and 4.6). A large increase in MgO and decrease in SiO_2, Al_2O_3, and TiO_2 occurs at 305 m in sample ED-10 where there are cumulate olivine and pyroxene minerals that contain blebby interstitial pyrrhotite mineralization (Figs. 4.1, 4.2, 4.3 and 4.4). Basement lithologies are represented by the last four samples to the end of the hole. A maximum occurs in SiO_2, a small increase in Al_2O_3, a maximum in TiO_2 and depletions in MgO and CaO occur in samples ED-12 and ED-13 of the basement iron formation where there is fractionation of cherty quartz and dominant magnetite oxide (Figs. 4.1, 4.2, 4.3, 4.4 and 4.6). Notably there is a sharp increase in Fe_2O_3 with appearance of magnetite oxide in the iron formation (Fig. 4.5). From 327 m to 344 m at the end of hole, a slight increase occurs in MgO, and a decrease in the other oxides as a change occurs to a more mafic composition as that of the bordering metabasalt (Figs. 4.1 to 4.6).

4.1.3 Al_2O_3 vs. MgO variation

Al_2O_3 vs. MgO wt. % for surface samples from lherzolite-olivine websterite through pyroxene-porphyritic melanogabbro to granophyric gabbro shows an increase in Al_2O_3 with

decreasing MgO (Fig. 4.7). This is due to evolution from the mafic lherzolite through to the granophyric gabbros. Nipigon diabase sills all plot within a high Al_2O_3 and low MgO range. The large increase in Al_2O_3 vs. MgO in the diabases shows that the diabase follows a plagioclase controlled crystallization trend in contrast to the olivine-pyroxene to pyroxene-plagioclase controlled crystallization trends of the lherzolite-olivine websterite and pyroxene-porphyritic melanogabbros. A large scattering of data points occurs in the pyroxene-porphyritic melanogabbros. The cluster is probably due to different local crystallization histories and timings of plagioclase crystallization in various locations within those lithologies. At around 30 wt. % MgO, a maximum in Al_2O_3 at that MgO composition is found in samples JL-051, JL-052 and JL-050 between the southern and central parts of the intrusion (Fig. 4.7). These lherzolites occur together in outcrop and possibly underwent plagioclase crystallization at a very early stage in their crystallization histories to account for higher Al_2O_3 at higher MgO compared to the lherzolites of the southern and central parts of the intrusion. At 34 wt. % MgO, a low in Al_2O_3 at that MgO composition is found in samples in the southern part of the intrusion and in the vicinity of the Phoenix occurrence mineralization (Fig. 4.7). These lherzolites are largely pyroxene cumulate lithologies and of a primitive composition with little plagioclase crystallization.

Al_2O_3 vs. MgO wt. % for drill core samples has a general trend of evolution with increasing Al_2O_3 and decreasing MgO, from lherzolite to pyroxenite to melanogabbro lithologies (Fig. 4.8). Nipigon sill samples have the highest Al_2O_3 and lowest MgO due to a dominant plagioclase-controlled crystallization trend. From 25 to 27 wt. % MgO, the vari-textured pyroxenite follows a trend from no increase in Al_2O_3 with decreasing MgO to a final increase in Al_2O_3 with decreasing MgO (Fig. 4.8). The lack of increase in Al_2O_3 is attributed to lack of plagioclase crystallization from lherzolite to pyroxenites.

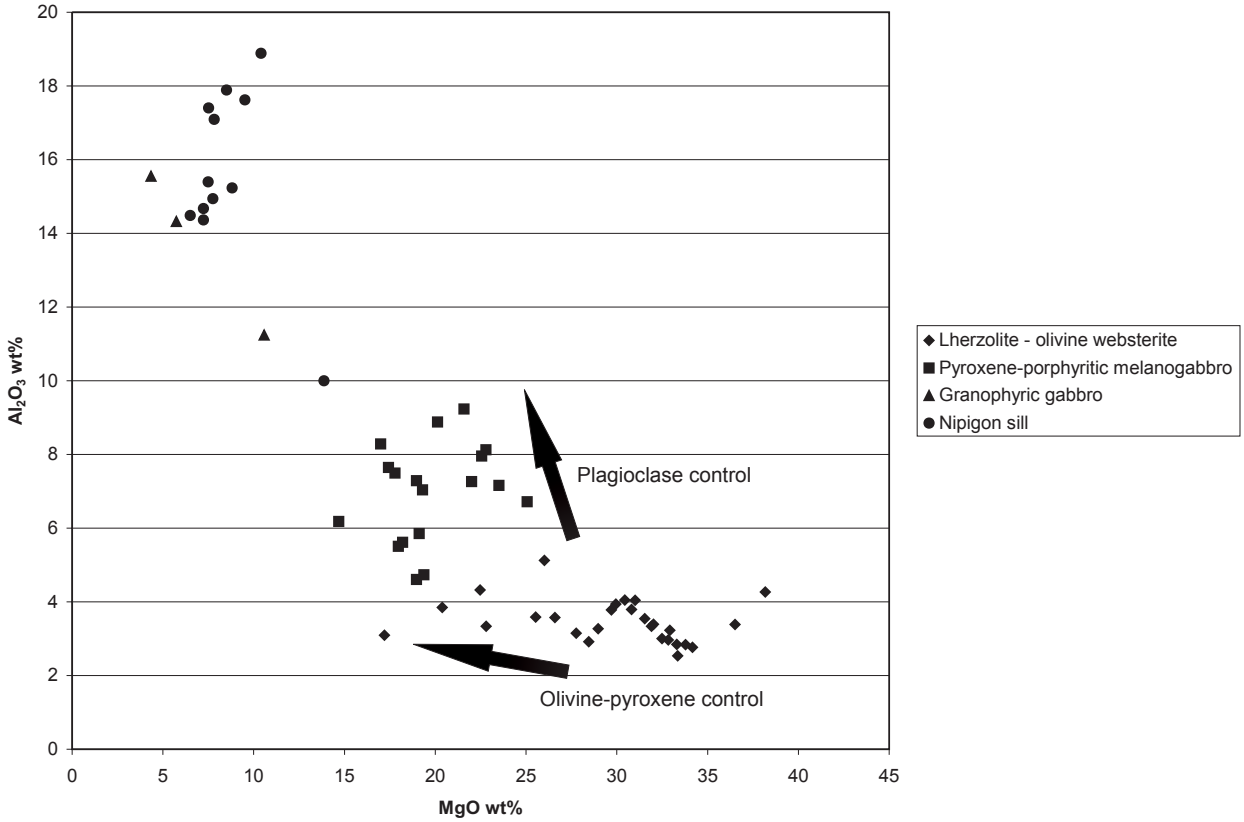

Figure 4.7: Plot of Al_2O_3 vs. MgO wt. % for surface samples. Arrows indicate mineral control lines after Sutcliffe (1987). Olivine-pyroxene control lines are based on mineral compositions of Forsterite 70-80, Wollastonite 40, and Enstatite 45 for picrites in the Nipigon Embayment.

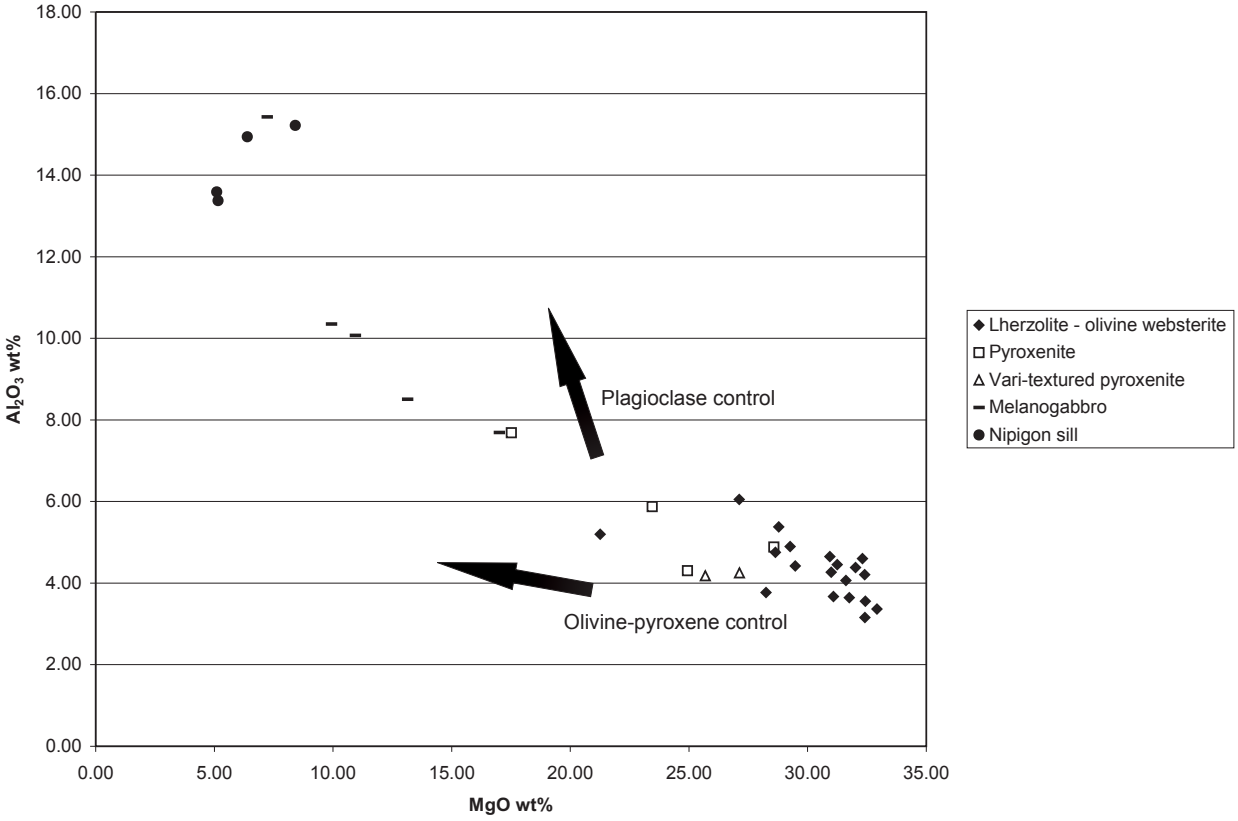

Figure 4.8: Plot of Al_2O_3 vs. MgO wt. % for DDH samples. Arrows indicate mineral control lines after Sutcliffe (1987). Olivine-pyroxene control lines are based on mineral compositions of Forsterite 70-80, Wollastonite 40, and Enstatite 45 for picrites in the Nipigon Embayment.

4.1.4 TiO_2 vs. MgO variation

TiO_2 vs. MgO wt. % diagrams for surface and drill core samples show general trends of evolution with increasing TiO_2 and decreasing MgO from lherzolite-olivine websterite to pyroxene-porphyritic melanogabbro to granophyric gabbro in the surface samples. Lherzolite-olivine websterites have the lowest concentration of TiO_2. The pyroxenite to melanogabbro display increases in TiO_2 due to felsification and assimilation of crust towards the wallrock lithologies in the drill core samples (Figs. 4.9 and 4.10). In the surface samples, there is a very large increase in TiO_2 wt. % in the granophyric gabbro samples. This indicates a distinctly different crystallization history for the granophyric gabbro compared to the lherzolite-olivine websterite to pyroxene-porphyritic melanogabbros.

4.1.5 CaO vs. MgO variation

CaO vs. MgO wt. % for surface samples show olivine-pyroxene, pyroxene and pyroxene-plagioclase controlled crystallization trends (Fig. 4.11). From 25 to 39 wt. % MgO, a general trend of increasing CaO with decreasing MgO occurs that represents a trend of olivine-pyroxene controlled crystallization within the lherzolite to pyroxene-porphyritic melanogabbros. Variable olivine vs. pyroxene crystallization is shown by higher CaO contents in certain samples off the main trend (e.g., 4.6 wt. % CaO at 38.1 wt. % MgO, 6.6 wt. % CaO at 36.5 wt. % MgO), however, all lherzolitic samples generally follow the olivine-pyroxene control line. The clusters at 30 wt. % MgO and 10 wt. % CaO represent the samples JL-052, JL-050 and JL-051 between the central and southern parts of the intrusion which show more pyroxene control vs. olivine in their crystallization trends (Fig. 4.11). This shows there was evolution of the lithologies from the southern to central parts of the intrusion. In thin section, this is shown by crystallization of secondary pyroxene in the lithologies. The cluster between 31 and 35 wt. % MgO and 2 and 5

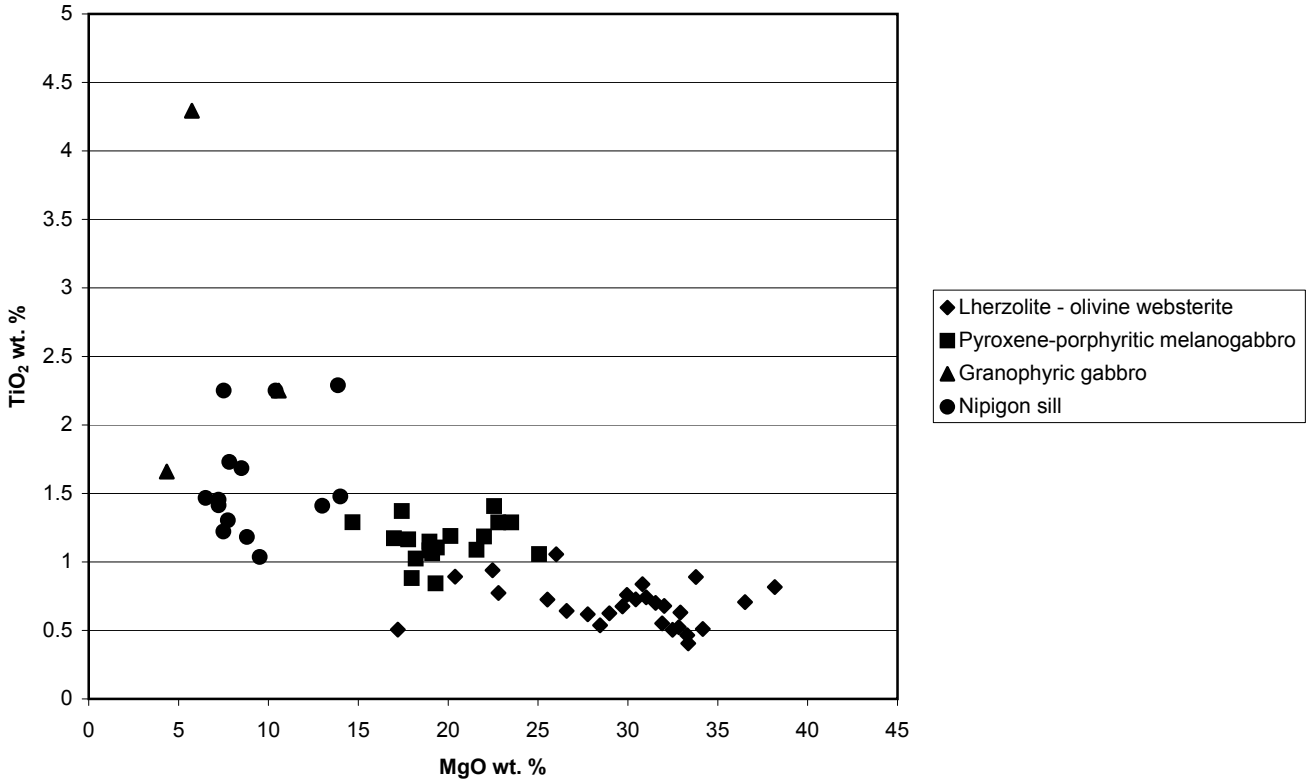

Figure 4.9: Plot of TiO_2 vs. MgO wt. % for surface samples.

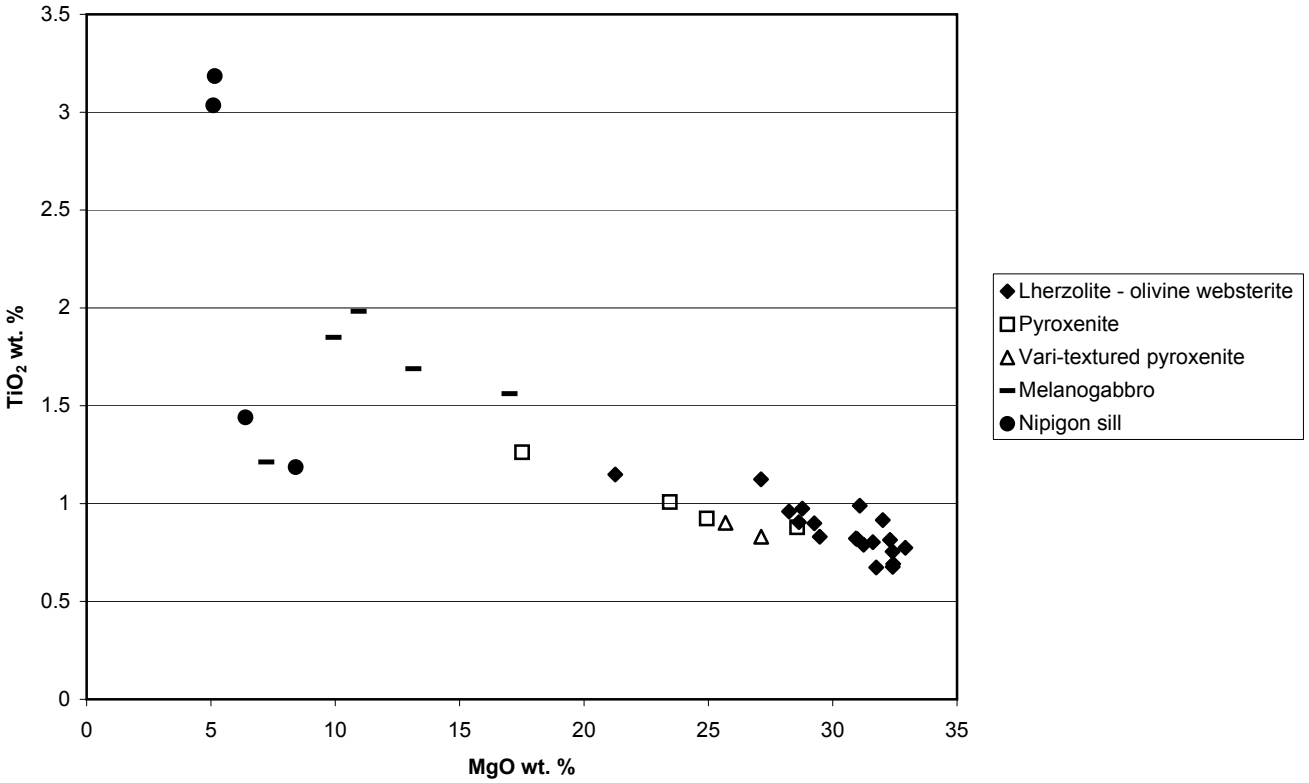

Figure 4.10: Plot of TiO_2 vs. MgO wt. % for DDH samples.

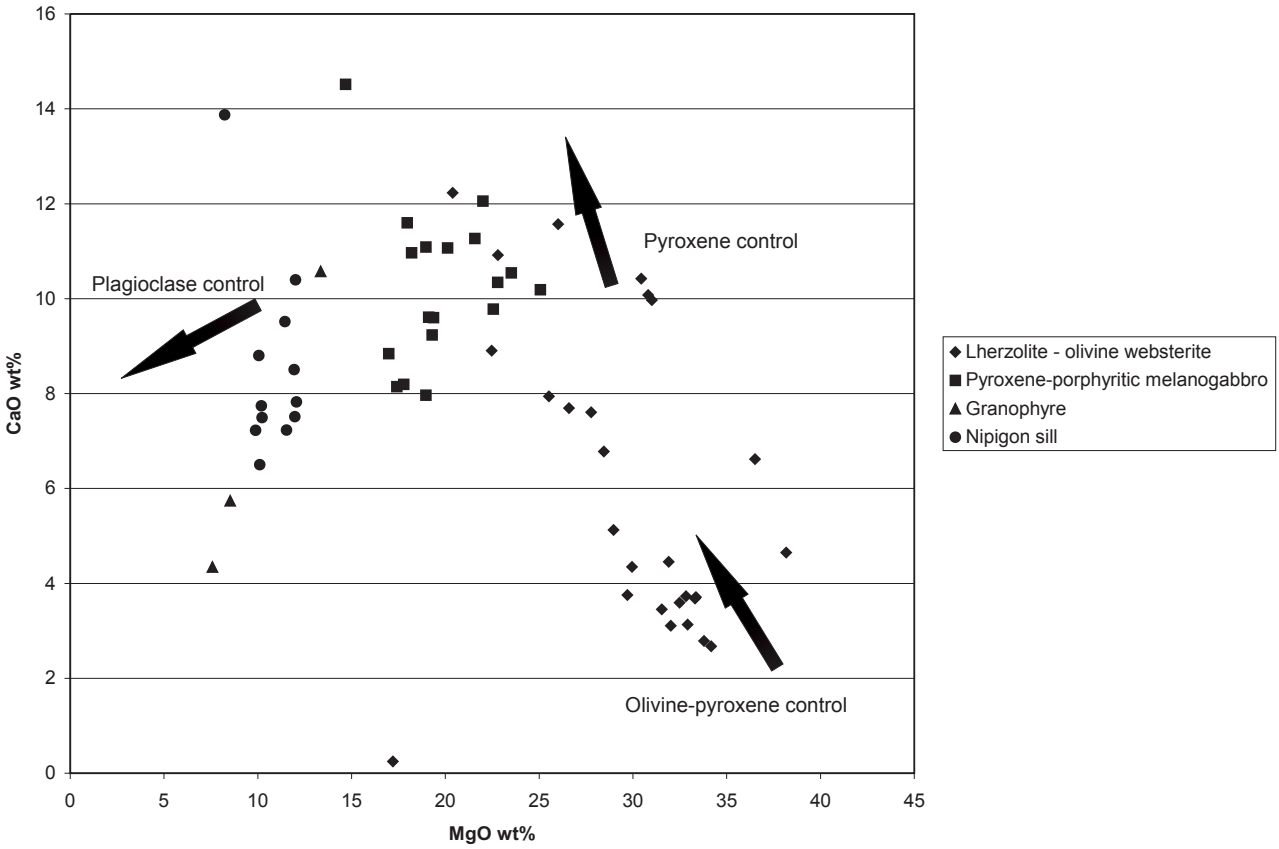

Figure 4.11: Plot of CaO vs. MgO wt. % for surface samples. Arrows indicate mineral control lines after Sutcliffe (1987). Olivine-pyroxene control lines are based on mineral compositions of Forsterite 70-80, Wollastonite 40, and Enstatite 45 for picrites in the Nipigon Embayment.

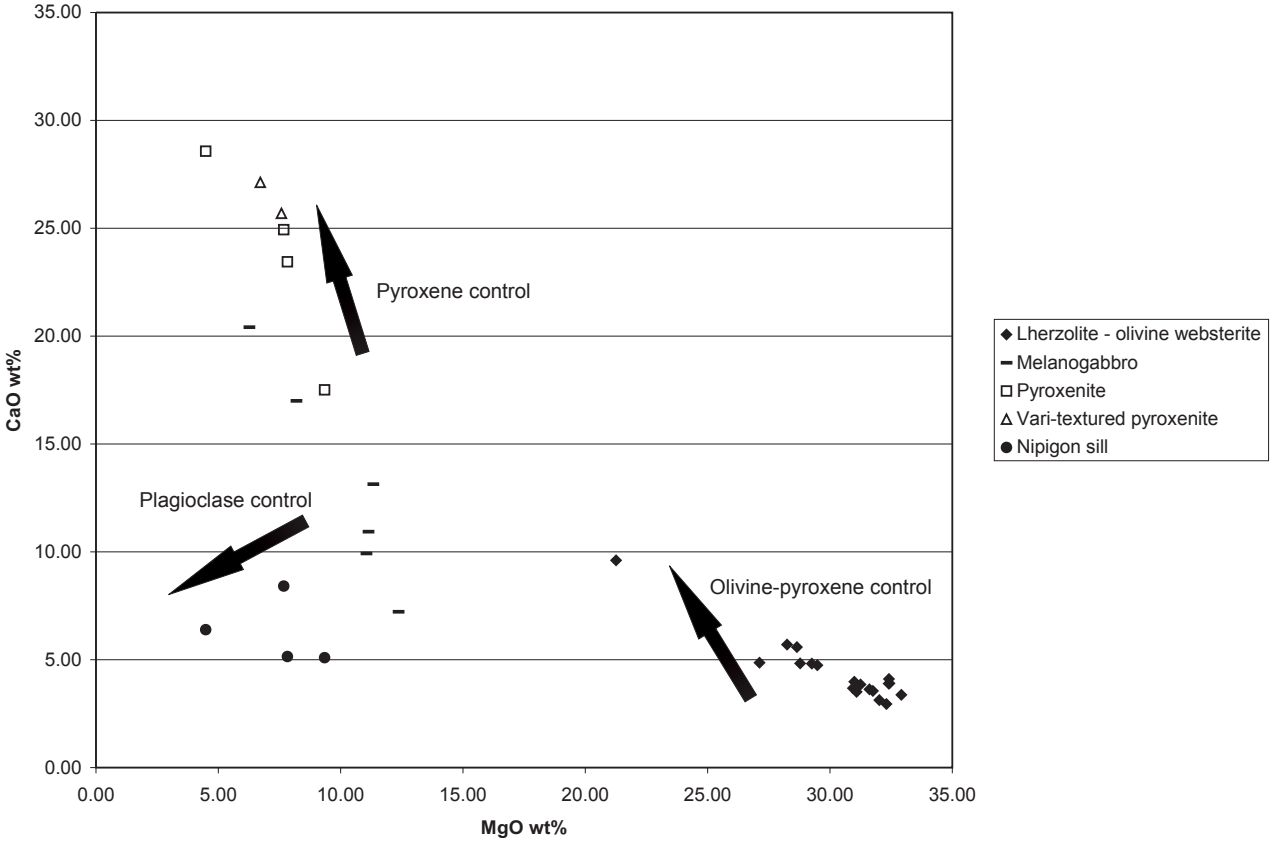

Figure 4.12: Plot of CaO vs. MgO wt. % for surface samples. Arrows indicate mineral control lines after Sutcliffe (1987). Olivine-pyroxene control lines are based on mineral compositions of Forsterite 70-80, Wollastonite 40, and Enstatite 45 for picrites in the Nipigon Embayment.

wt. % MgO represents lherzolite-olivine websterite samples in the southern part of the Kitto intrusion and in the vicinity of the Phoenix occurrence. These lithologies have the most MgO-rich chemical compositions and olivine-pyroxene mineralogical compositions within the intrusion since there is large accumulation of magnesian minerals within this mineralized lithology. Between 16 and 26 wt. % MgO, pyroxene-porphyritic melanogabbros generally show a maximum of high CaO compositions, which is indicative of dominant pyroxene control in the evolution of these lithologies (Fig. 4.11). From 7 to 14 wt. % MgO, trends of decreasing CaO with decreasing MgO occur in the granophyric gabbro and Nipigon sills which represent dominant pyroxene-plagioclase control on the evolution of these lithologies (Fig. 4.11).

CaO vs. MgO wt. % for drill core samples shows olivine-pyroxene, pyroxene-plagioclase and pronounced pyroxene crystallization trends (Fig. 4.12). From 21 to 33 wt. % MgO, lherzolites display an olivine-pyroxene controlled crystallization trend of increasing CaO with decreasing MgO. From 4 to 13 wt. % MgO, pyroxenite to melanogabbros display a steeper increase in CaO with decreasing MgO separate from the trend displayed by the lherzolites (Fig. 4.12). This trend is due to dominant pyroxene controlled accumulation rather than olivine crystallization in the lithologies (Chapter 3, section 3.2.4). The same trend displayed by the pyroxenite and melanogabbros shows that they have the same crystallization and accumulation history, separate from the lherzolites. Vari-textured pyroxenite plots at the top of the pyroxene crystallization trend, which shows that this lithology primarily follows the evolutionary history of the pyroxenite. From 4 to 10 wt. % MgO, the Nipigon sill follows a pyroxene-plagioclase crystallization trend separate from the peridotites (Fig. 4.12).

4.2 Rare earth and trace element geochemistry

Rare earth element and trace element analyses were performed on 42 samples from Kitto drill holes EK-02, EK-03, EK-04, EK-01, and on 37 surface samples. Results of REE and trace element analyses are displayed in Appendix 1.

4.2.1 Primitive mantle normalized multielement plots

Lherzolite to olivine websterites in drill core show a rare earth element (REE) fractionation pattern of decreasing REE abundance from light rare earth elements (LREE) to heavy rare earth elements (HREE) (Fig. 4.13). The lithologies in general display LREE enrichment over middle rare earth element (MREE) with $(La/Sm)_{cn}$ ratios of 1.60 to 3.13, MREE enrichment over HREE with $(Gd/Yb)_{cn}$ ratios of 2.64 to 3.06, and $(Eu/Eu^*)_{cn}$ ratios of 0.75 to 1.20 (Table 4.2). Two geochemical trends are distinguished in the drill core lherzolite-olivine websterites. One trend contains samples with lower La/Nb, Th/Nb, less pronounced Nb anomalies, positive Ti anomalies and negative Eu anomalies (Fig. 4.13). Examples of lithologies with low La/Nb are samples ED-34, ED-25 and ED-19. These lithologies have La/Nb ratios of 0.80, 0.96, and 0.94 respectively. Samples ED-35 and ED-29 are lherzolites with smaller Th/Nb ratios of 0.89 and 1.06, and ED-41 has a positive Ti anomaly. In contrast, the majority of samples show higher Th/Nb, La/Nb, and negative Nb and Ti anomalies (Fig. 4.14). Samples ED-17, ED-18 and ED-20 have either high La/Nb of 1.72 in ED-17 or high Th/Nb ratios of 1.36 and 1.17 in ED-18 and ED-20 respectively. Samples ED-01, ED-02, ED-03, ED-04 and ED-05 are mineralized olivine websterites that have high La/Nb ratios ranging from 1.12 to 1.74 and negative Nb. Sample ED-15 has a higher La/Nb ratio of 2.30.

Lherzolite-olivine websterites from outcrop have REE and trace element fractionation patterns of lithologies in areas of both the Phoenix occurrence and northward to the central parts

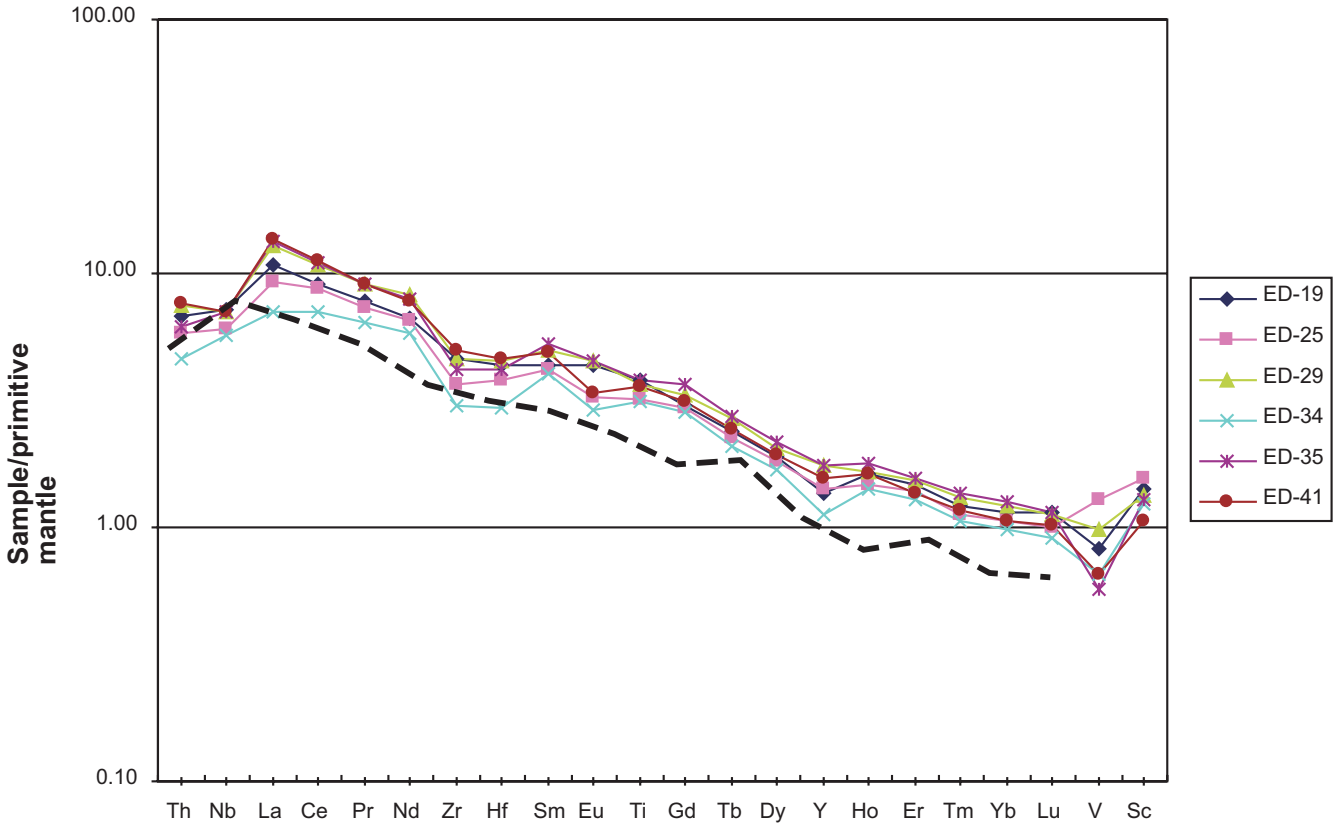

Figure 4.13: Primitive mantle multielement plot of the first group of lherzolite-olivine websterite in DDH samples. An example of an OIB unaltered volcanic rock from Jenner (1996) is the black dashed line. Primitive mantle normalizing values of McDonough and Sun (1995).

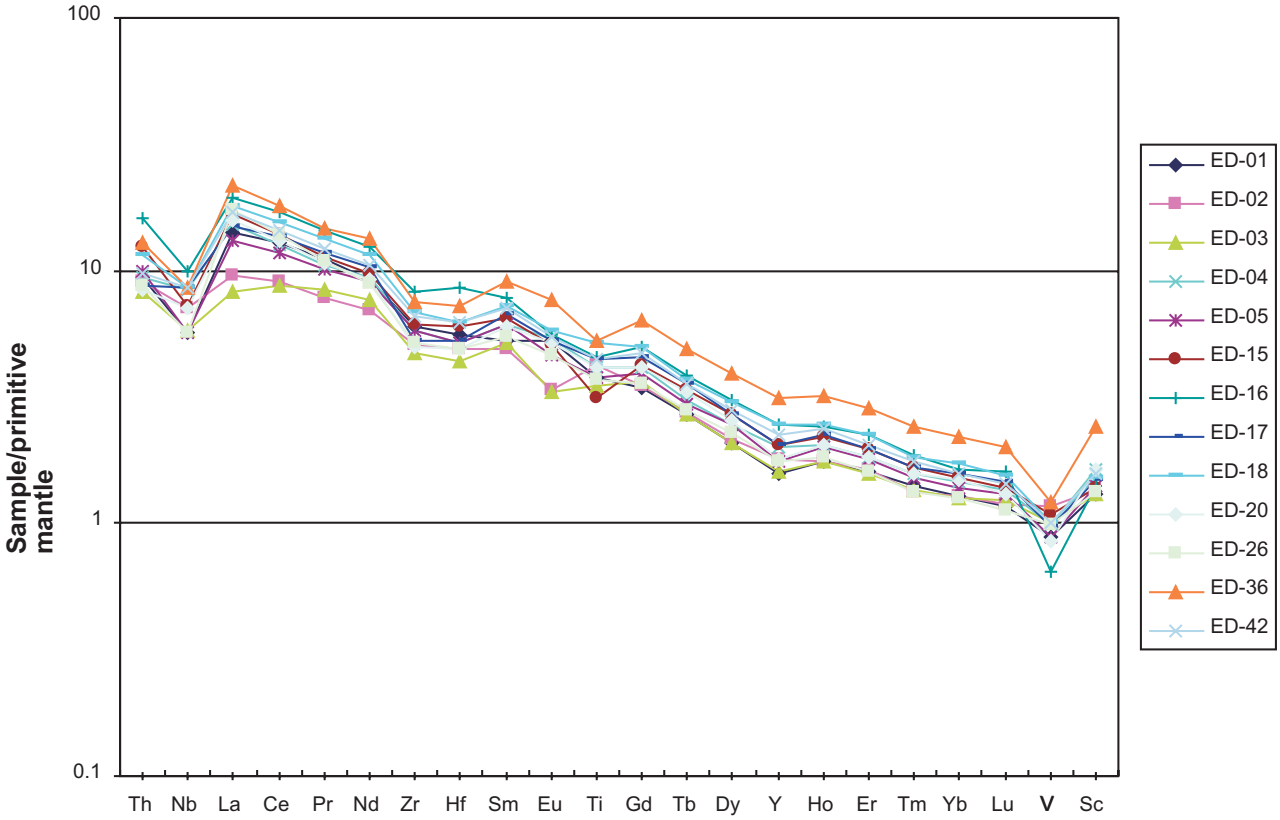

Figure 4.14: Primitive mantle multielement plot of the second group of lherzolite-olivine websterite in DDH samples. Primitive mantle normalizing values of McDonough and Sun (1995).

of the Kitto intrusion next to pyroxene-porphyritic melanogabbros (Fig. 4.15; Fig. 3.1). The lithologies display LREE enrichment over MREE with $(La/Sm)_{cn}$ ratios of 1.74 to 2.76, MREE enrichment over HREE with $(Gd/Yb)_{cn}$ ratios of 2.60 to 2.99, and $(Eu/Eu^*)_{cn}$ ratios of 0.71 to 1.10 (Table 4.2). The REE and trace element fractionation trends of the surface samples display patterns of increasing negative Nb and Ti anomalies and increasing La/Nb ratios. Surface sample JL-073, at the Phoenix occurrence, has sharp negative Nb and Ti anomalies and a higher La/Nb ratio of 1.93. Sample JL-077 is an olivine websterite bordering a diabase intrusion in the southeast part of the Kitto intrusion (Fig. 3.1) that has pronounced negative Nb and Ti

Table 4.2: REE ratios in the lithologies.

Lithologies	**$(La/Sm)_{cn}$**	**$(Gd/Yb)_{cn}$**	**$(Eu/Eu^*)_{cn}$**
Lherzolite-olivine websterite (drill core)	1.60 to 3.13	2.64 to 3.06	0.75 to 1.20
Lherzolite-olivine websterite (surface)	1.74 to 2.76	2.60 to 2.99	0.71 to 1.10
Vari-textured pyroxenite (drill core)	2.00 to 2.05	2.67 to 2.83	0.92 to 0.95
Pyroxenite (drill core)	2.00 to 2.67	2.64 to 2.85	0.95 to 1.05
Pyroxene-porphyritic melanogabbro (surface)	1.66 to 2.79	2.51 to 2.89	0.92 to 1.07
Melanogabbro (drill core)	1.81 to 2.70	2.80 to 2.95	0.84 to 1.06
Granophyric gabbro (surface)	2.22 to 2.35	1.57 to 2.94	0.97
Nipigon sill (drill core)	1.80 to 2.02	1.40 to 2.60	0.93 to 1.00

anomalies and a high La/Nb ratio of 2.34. Northward, between the southern and central parts of the Kitto intrusion, sample JL-052 displays sharp negative Nb and Ti. JL-052 has a high La/Nb ratio of 2.63. Surface samples JL-011 and JL-012 are lherzolite-olivine websterites that display sharp negative Nb and Ti anomalies. La/Nb ratios for these lithologies are 2.99 and 2.03 respectively. In contrast, many lherzolite-olivine websterites have shallower Nb and Ti anomalies and lower La/Nb ratios. Samples JL-004, JL-056, JL-001, JL-063 are lherzolites in

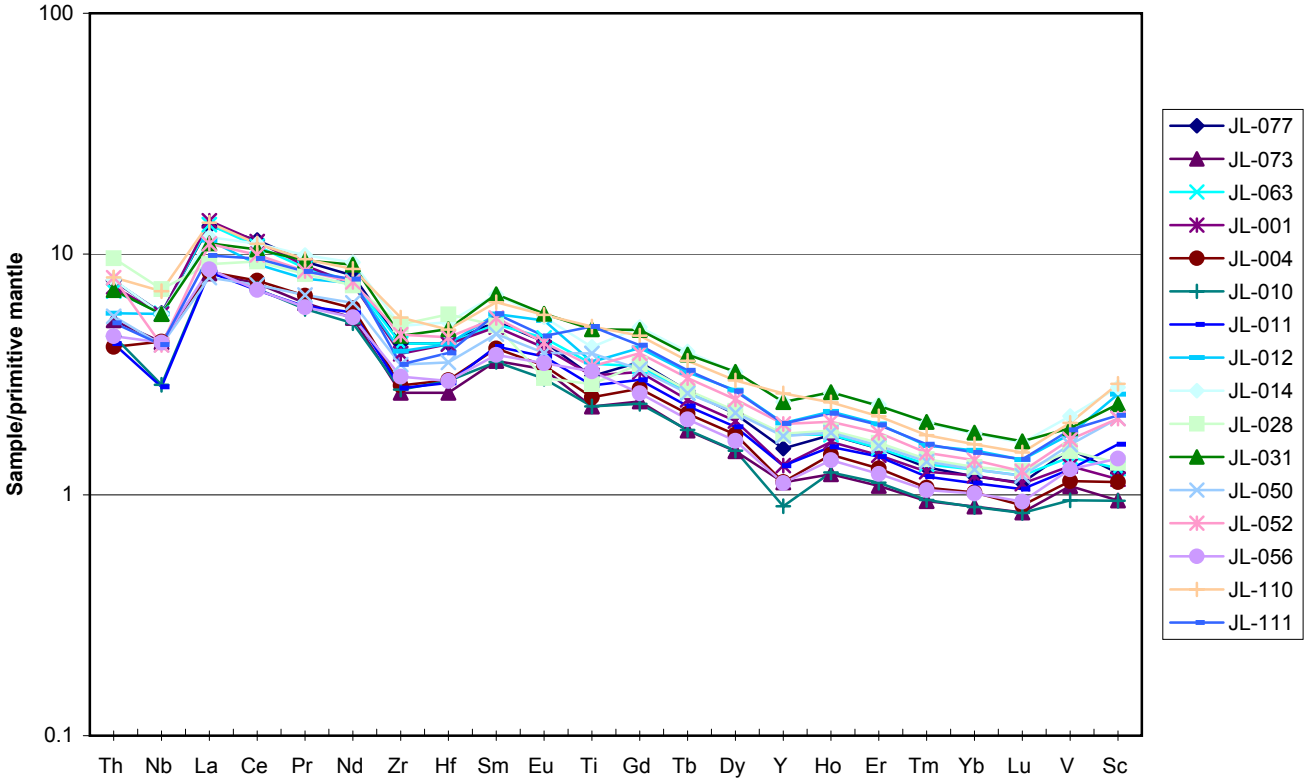

Figure 4.15: Primitive mantle multielement plot of lherzolite-olivine websterite in surface samples. Primitive mantle normalizing values of McDonough and Sun (1995).

the southern part of the intrusion that either have shallow negative Nb and/or Ti anomalies. Samples JL-004 and JL-056 have shallow Nb anomalies with La/Nb ratios of 1.95 and 2.02 and shallow Ti anomalies, while samples JL-001 and JL-063 display shallow Ti anomalies. Surface sample JL-111 has a positive Ti anomaly.

Vari-textured pyroxenites are located between the lherzolite-olivine websterite and pyroxenites in DDH EK-02 (Fig. 3.3). The lithology displays LREE enrichment over MREE with $(La/Sm)_{cn}$ ratios of 2.00 to 2.05, MREE enrichment over HREE with ratios $(Gd/Yb)_{cn}$ ratios of 2.67 to 2.83, and $(Eu/Eu^*)_{cn}$ ratios of 0.92 to 0.95 (Fig. 4.16). All these ratios fall within the range of the lherzolites. Nb and Ti anomalies are similar to those of lherzolite-olivine websterite with La/Nb ratios of 1.68 to 1.90.

Pyroxenites are located below the lherzolite-olivine websterites in DDH EK-02 and display a similar REE pattern to lherzolite, only with more pronounced negative Nb and Ti anomalies in the lithologies (Fig. 4.17). Two melanogabbros (samples ED-10 and ED-33) are also displayed with pyroxenite that have greater abundance of REE overall than the pyroxenite, but similar REE patterns as the pyroxenite. Both lithologies displays LREE enrichment over MREE with $(La/Sm)_{cn}$ ratios of 2.00 to 2.67, MREE enrichment over HREE with $(Gd/Yb)_{cn}$ ratios of 2.64 to 2.85, and $(Eu/Eu^*)_{cn}$ ratios of 0.95 to 1.05. All these ratios fall within the range of the lherzolites. The pyroxenites show more pronounced negative Nb anomalies and Ti anomalies than the lherzolites with La/Nb ratios of 1.97 to 2.28.

Pyroxene-porphyritic melanogabbros are found to the west of the lherzolite-olivine websterites in the central part of the Kitto intrusion (Fig. 3.1). The pyroxene-porphyritic melanogabbro displays a greater range of LREE than the lherzolites with $(La/Sm)_{cn}$ ratios of 1.66 to 2.79 (Fig. 4.18). The lithology displays MREE enrichment over HREE with $(Gd/Yb)_{cn}$ ratios

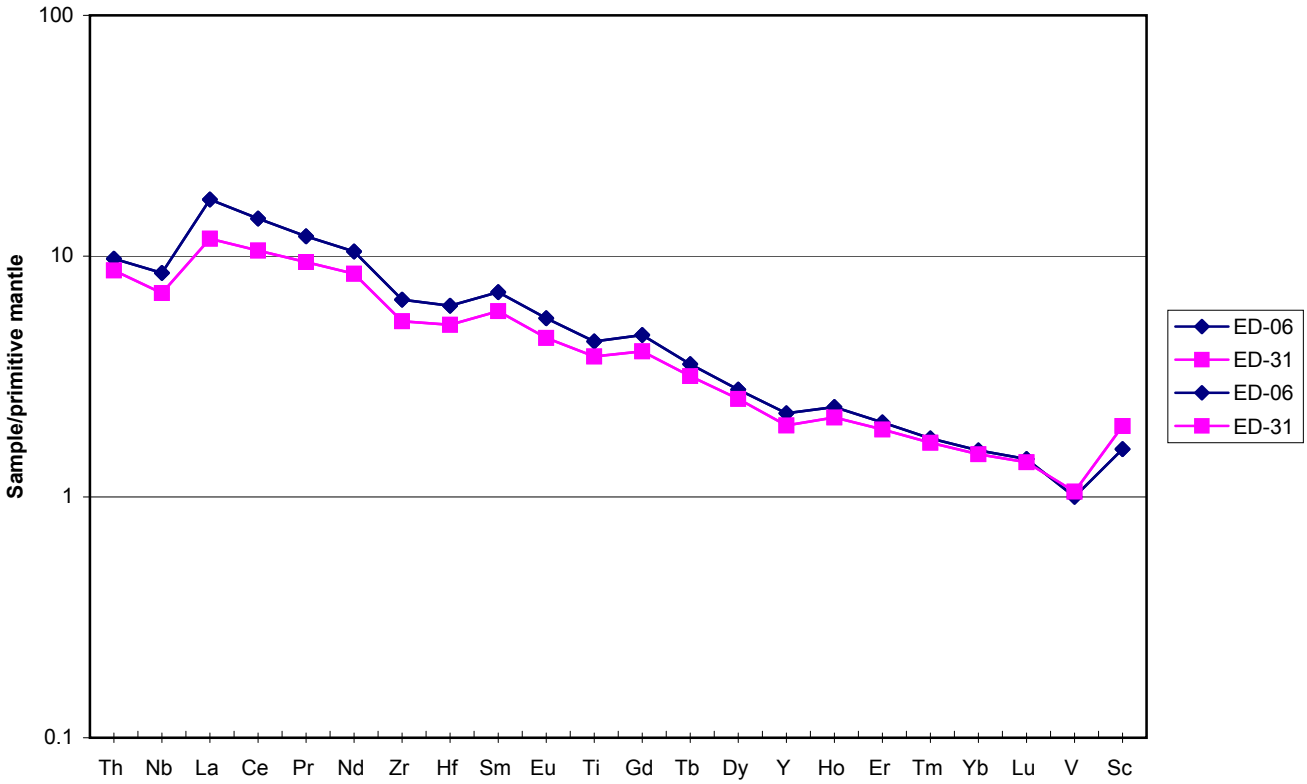

Figure 4.16: Primitive mantle multielement plot of vari-textured pyroxenite in DDH samples. Primitive mantle normalizing values of McDonough and Sun (1995).

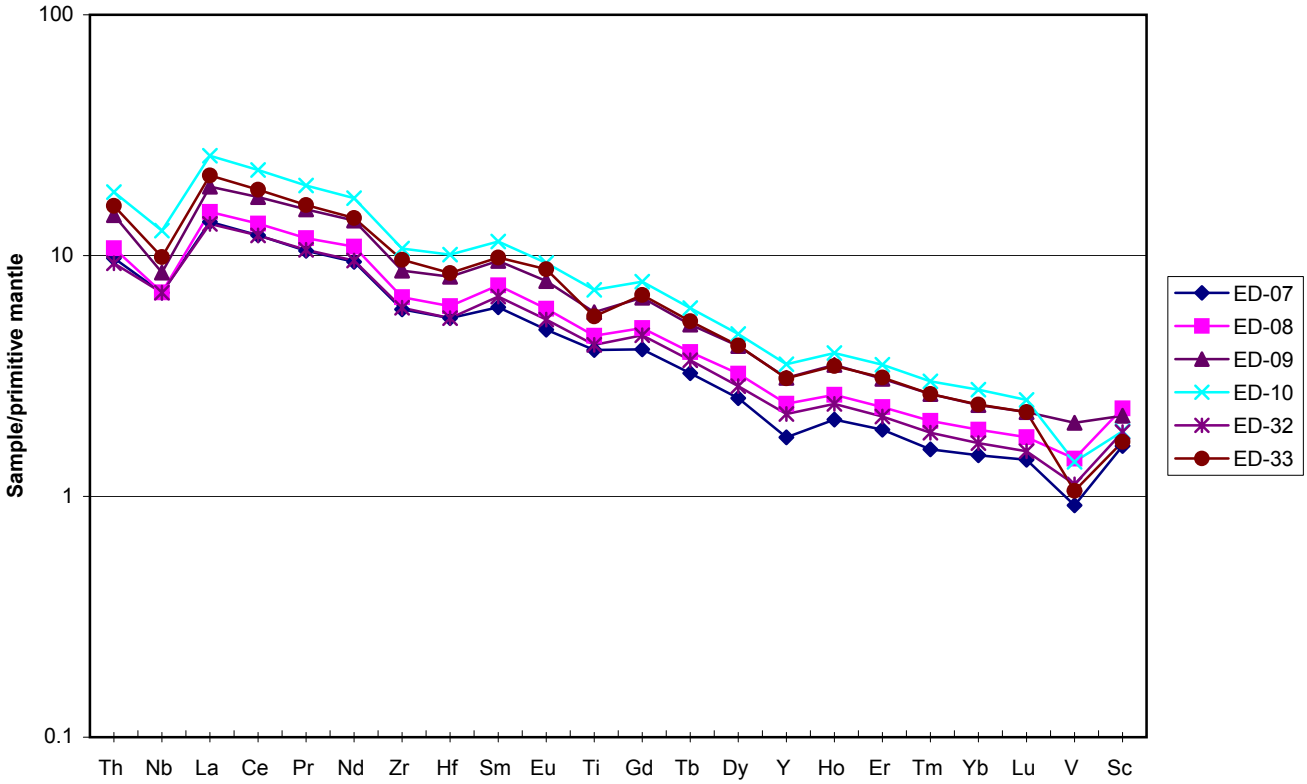

Figure 4.17: Primitive mantle multielement plot of pyroxenite in DDH samples. Primitive mantle normalizing values of McDonough and Sun (1995).

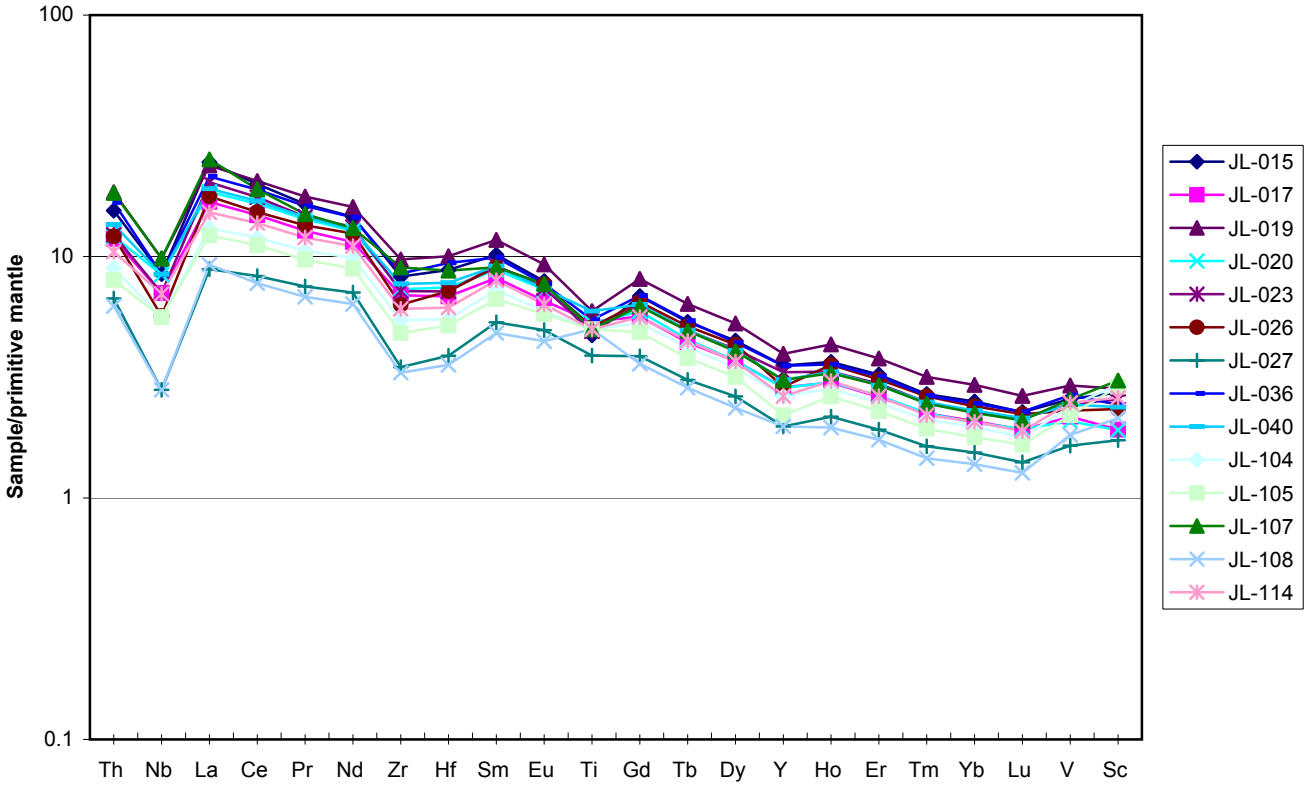

Figure 4.18: Primitive mantle multielement plot of pyroxene-porphyritic melanogabbro in surface samples. Primitive mantle normalizing values of McDonough and Sun (1995).

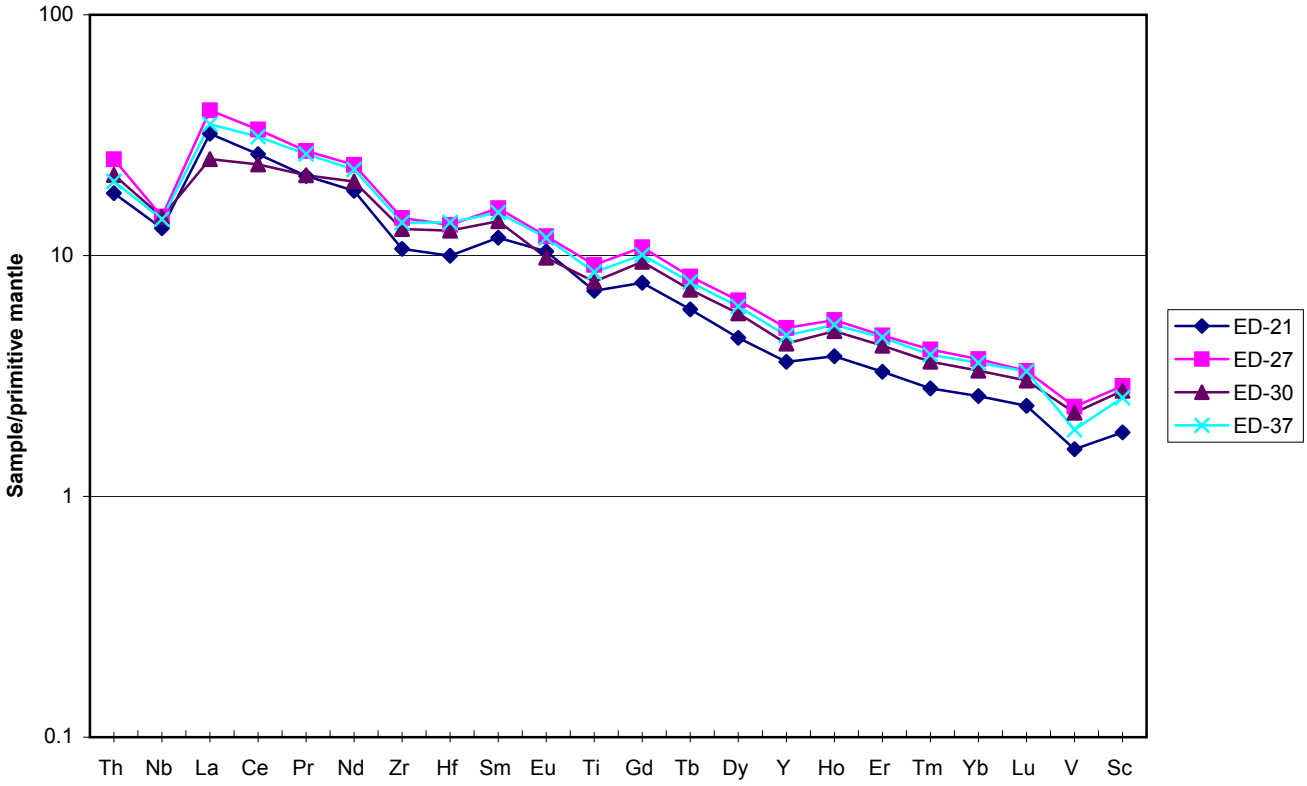

Figure 4.19: Primitive mantle multielement plot of melanogabbro in DDH samples. Primitive mantle normalizing values of McDonough and Sun (1995).

of 2.51 to 2.89 and $(Eu/Eu^*)_{cn}$ ratios of 0.92 to 1.07. The primitive mantle plots display sharper negative Nb and Ti anomalies, the presence of negative Zr and Hf anomalies and higher La/Nb ratios than lherzolites, with La/Nb ratios between 2.17 and 3.16.

Melanogabbros in drill core, which are located below lherzolite in holes EK-03, EK-04 and EK-01, have fractionation patterns with greater abundance of REE overall and with steeper Nb anomalies than lherzolites (Fig. 4.19). Lithologies display LREE enrichment over MREE with $(La/Sm)_{cn}$ ratios of 1.81 to 2.70, MREE enrichment over HREE with $(Gd/Yb)_{cn}$ ratios of 2.80 to 2.95, and $(Eu/Eu^*)_{cn}$ ratios of 0.84 to 1.06. These ratios fall within the range of the lherzolites. Negative Nb anomalies are generally more pronounced than both lherzolite and pyroxenite with La/Nb ratios of 2.47, 2.76 and 2.48 for samples ED-21, ED-27 and ED-37. Negative Ti anomalies are also characteristic of the melanogabbros. Small positive Eu anomalies are also displayed in the lithologies.

Granophyric gabbros are located to west of pyroxene-porphyritic melanogabbros in the central part of the Kitto intrusion (Fig. 3.1). Granophyric gabbro is represented by surface sample JL-043 and a more plagioclase fractionated granophyric gabbro to the north represented by sample JL-022. The two samples display LREE enrichment over MREE with $(La/Sm)_{cn}$ ratios of 2.22 to 2.35, MREE enrichment over HREE with $(Gd/Yb)_{cn}$ ratios of 1.57 to 2.94, and a $(Eu/Eu^*)_{cn}$ ratio of 0.97 (Fig. 4.20). Sample JL-022 has a very low $(Gd/Yb)_{cn}$ ratio of 1.57 compared to the other peridotites. The granophyric gabbro as represented by sample JL-043 has a similar pattern as the pyroxene-porphyritic melanogabbro and lherzolite-olivine websterite. The REE and trace element abundance is greater in the granophyric gabbro than the other peridotites. Both samples JL-043 and JL-022 display negative Nb anomalies with varying La/Nb slopes from 2.46 in sample JL-043 to 1.60 in sample JL-022, and positive Ti anomalies.

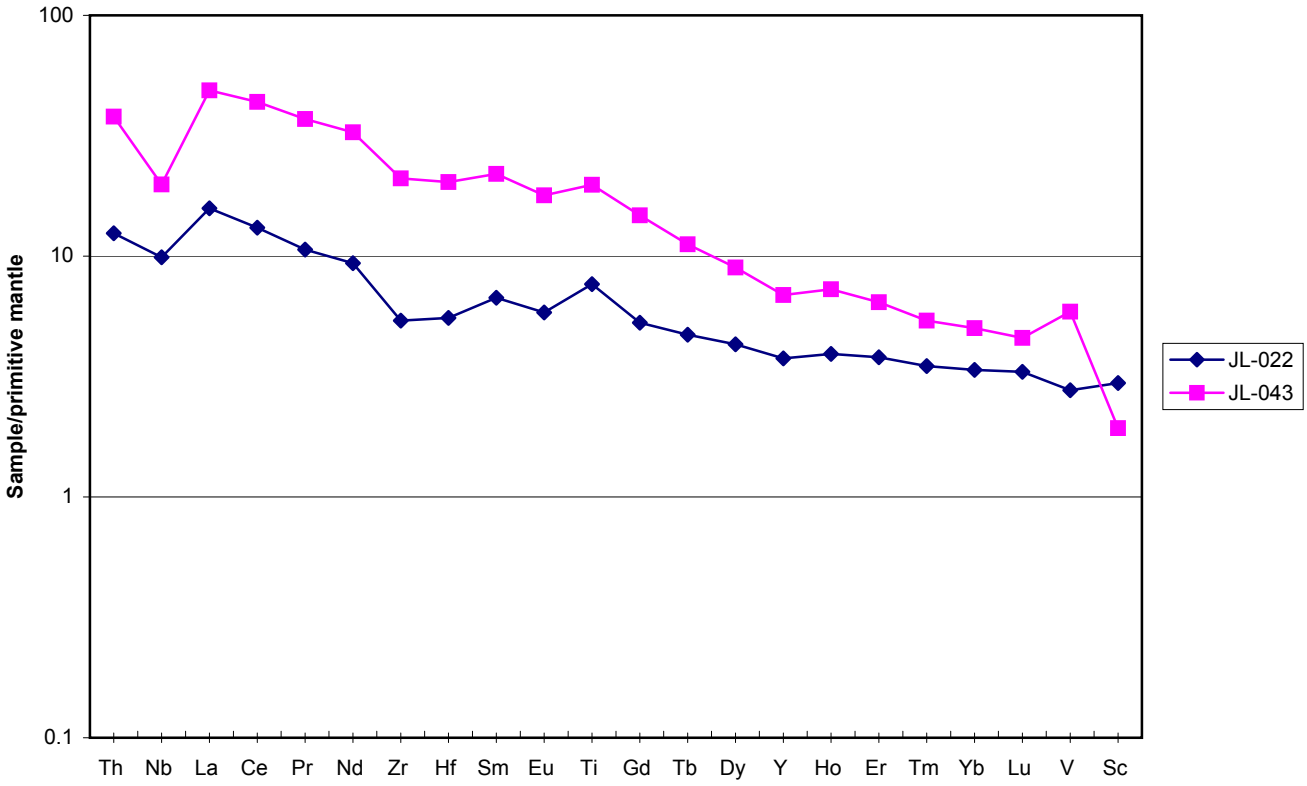

Figure 4.20: Primitive mantle multielement plot of granophyric gabbro in surface samples. Primitive mantle normalizing values of McDonough and Sun (1995).

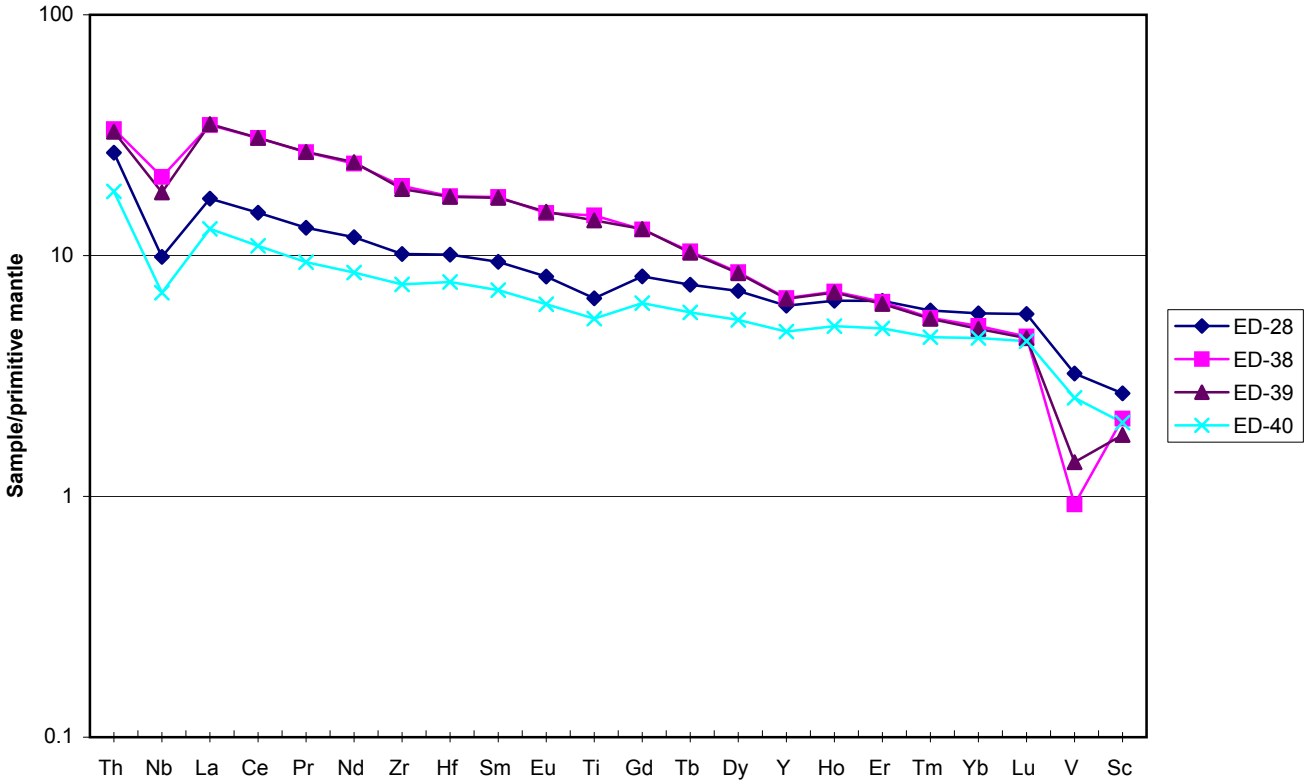

Figure 4.21: Primitive mantle multielement plot of Nipigon sill in DDH samples. Primitive mantle normalizing values of McDonough and Sun (1995).

Nipigon diabase sills are found within Sibley sedimentary rock below the Kitto intrusion in DDH EK-03 and also above the intrusion in DDH EK-04 (Fig. 3.1). The lithologies display LREE enrichment over MREE with $(La/Sm)_{cn}$ ratios of 1.80 to 2.02, MREE enrichment over HREE with $(Gd/Yb)_{cn}$ ratios of 1.40 to 2.60 and $(Eu/Eu^*)_{cn}$ ratios of 0.93 to 1.00 (Fig. 4.21). The diabases show different REE fractionation patterns than the peridotitic to granophyric gabbros of the Kitto intrusion. Difference in REE include higher Th, lower La, less pronounced negative Nb anomalies, lack of negative Zr and Hf anomalies, lower LREE enrichment to MREE and lower MREE enrichment to HREE. Th/Nb ratios are higher with ratios increasing from 1.58 to 2.71.

4.3 Radiogenic isotope geochemistry

ε_{Nd} is a measure of the radiogenic decay of Nd from radiogenic Sm. As the mantle-derived magma is assumed to evolve from an original uniform reservoir, a measure of the fractionation of Nd termed ε_{Nd} is calculated relative to that uniform reservoir, which is assumed to be CHUR (i.e., the chondritic meteorite uniform reservoir). With increased fractionation of Nd from that reservoir, there is an increase in ε_{Nd} from a content of zero in CHUR. The higher the ε_{Nd}, the more fractionated and depleted the magma is of original Sm in the melt from that of CHUR.

The 10 samples taken from DDH EK-02 were analysed for Nd and were shown to have negative ε_{Nd} contents within the range from -5.54 to -6.53 at an age of 1117Ma. The exception is a basement metabasalt sample that has an ε_{Nd} content of 3.43 (Table 4.3). Variation of ε_{Nd} contents within the intrusive lithologies is from the most negative ε_{Nd} contents in pyroxenite to increasing contents in the melanogabbro to lherzolites.

Table 4.3: Results of Sm-Nd isotope analysis

Sample	Lithology	Nd (ppm)	Sm (ppm)	$^{143}Nd/^{144}Nd$ (±2σ)	εNd (±0.5)	$^{147}Sm/^{144}Nd$
ED-15	lherzolite	15.46	3.37	0.511856(8)	-5.98	0.1317
ED-16	lherzolite	12.47	2.70	0.511846(4)	-6.09	0.1311
ED-18	olivine websterite	15.13	3.19	0.511849(8)	-5.54	0.1277
ED-09	pyroxenite	20.73	4.90	0.511909(6)	-6.53	0.1428
ED-10	melanogabbro	23.62	5.31	0.511878(7)	-6.14	0.1359
ED-14	mafic metavolcanic	8.22	2.50	0.512722(4)	3.43	0.1842
ED-29	lherzolite	11.58	2.52	0.511843(8)	-6.22	0.1316
ED-30	melanogabbro	31.14	6.84	0.511853(5)	-6.18	0.1327
ED-35	lherzolite	11.54	2.57	0.511885(5)	-5.86	0.1349
ED-37	melanogabbro	30.77	6.69	0.511835(5)	-6.36	0.1315

4.4 Base and precious metal geochemistry

Base and precious metal geochemical analysis was carried out on 21 samples from Kitto DDH EK-02. Drill core samples from the mineralized horizons of DDH EK-02 drilled and sampled by Kennecott Canada Exploration Inc. were also interpreted along with the 21 samples chosen for this thesis. Analysis was also carried out on the 64 surface samples used for the whole rock geochemical analysis. Results of base and precious metal analysis are given in Appendix 3. Analysis of geochemical trends was carried out for surface sample metal variation and variation of metals down DDH EK-02.

4.4.1 Surface sample metal variation

Surface rocks were sampled for metals throughout the southern and central parts of the Kitto intrusion. In the central part of the intrusion, anomalous metal contents have been detected at the contact of pyroxene-porphyritic melanogabbro with olivine websterites, and within the pyroxene-porphyritic melanogabbro (Fig. 3.1). The highest anomalous PGE contents are detected in the pyroxene-porphyritic melanogabbros (Fig. 4.22). Samples JL-015 and JL-026

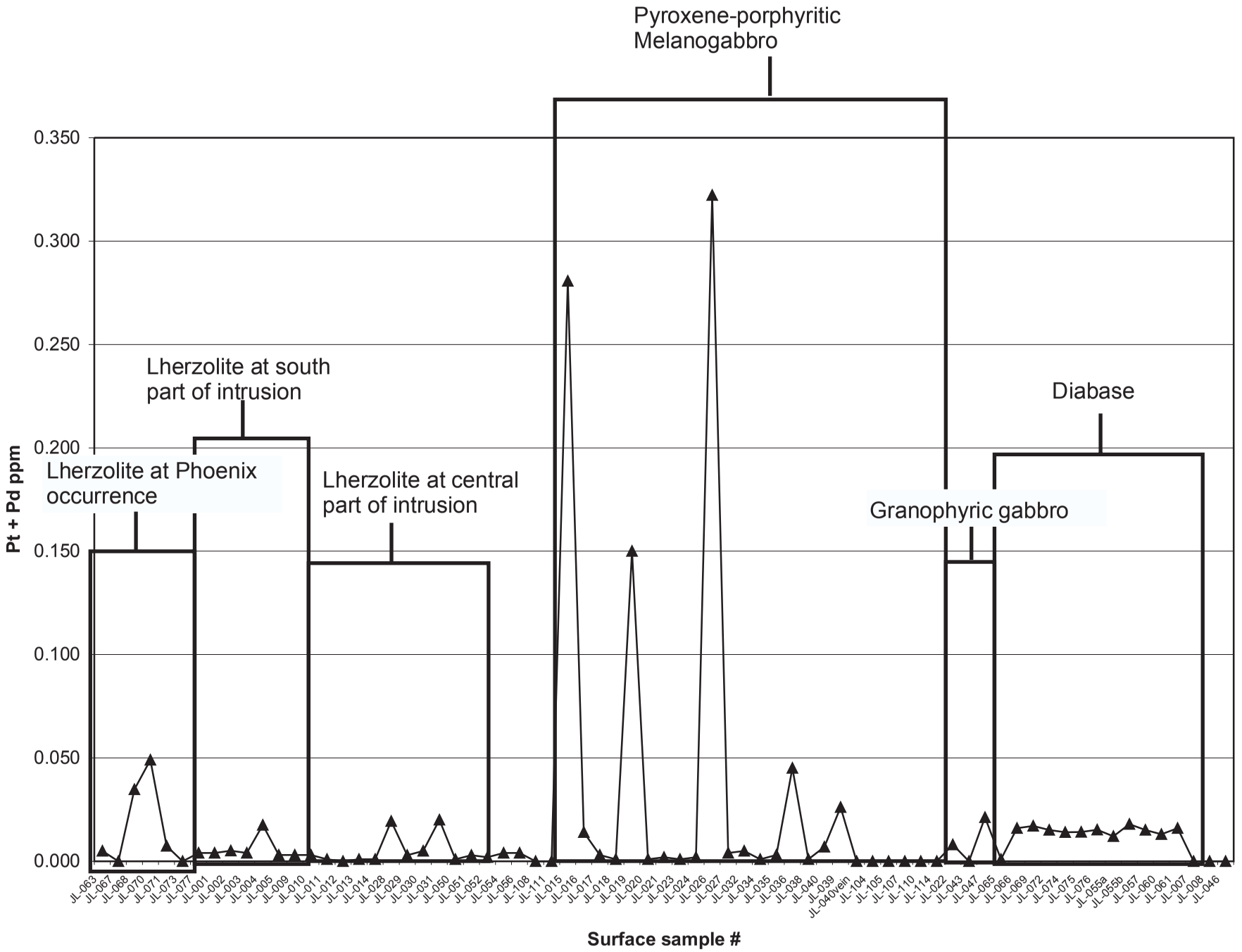

Figure 4.22: Surface sample combined Pt + Pd variation from the southern, central and northern parts of the Kitto Intrusion.

taken from near the contact with the olivine websterite have Pt, Pd contents of 242, 37 ppb and 139, 180 ppb respectively. Ni, Cu contents of JL-015 and JL-026 are 320, 77.4 ppm and 393, 163.5 ppm respectively. JL-019 from within the pyroxene-porphyritic melanogabbro has Pt, Pd of 100, 50 ppb and Ni, Cu of 181.5, 276 ppm. Other anomalous contents at the contact include the pyroxene-porphyritic melanogabbro sample JL-036 with Pt, Pd of 25, 20 ppb and the olivine websterite sample JL-031 with Pt, Pd of 14, 6 ppb. JL-039 from within the pyroxene-porphyritic melanogabbro has Pt, Pd of 18, 8 ppb respectively. Generally, the pyroxene-porphyritic melanogabbros have been found to contain lower Ni with contents between 292 to 590 ppm compared to lherzolites at the central and southern parts of the intrusion (Fig. 4.23). Lherzolite to olivine websterites in the central area have Ni contents of 516 to 1124 ppm which are greater than in the pyroxene-porphyritic melanogabbros. Where Ni is anomalous with respect to background contents of about 600 to 650 ppm in the lherzolites, there is PGE and Cu mineralization. Cu contents, on the other hand, are generally higher in the pyroxene-porphyritic melanogabbro of the central part of the intrusion compared to the southern part of the intrusion with anomalous maximum contents in samples JL-016, JL-019, and JL-039 (Fig. 4.24). Generally, where Cu contents are high, there is higher PGE content. In contrast to the peridotites, the diabases all have high Cu contents but no anomalous Cu contents. PGE contents in the diabase are also consistent to about 15 ppb Pt+Pd (Fig. 4.22).

Surface samples from the southern part of the intrusion generally have anomalous metal contents (compared to background contents in the lherzolite in general) in the vicinity of the Phoenix occurrence where DDH EK-02 was drilled, a zone to the east of the occurrence and in the far eastern part of the intrusion (Fig. 3.1). In the lherzolites of the southern part of the intrusion, background Ni contents are higher than those lithologies of the central part (Fig. 4.23).

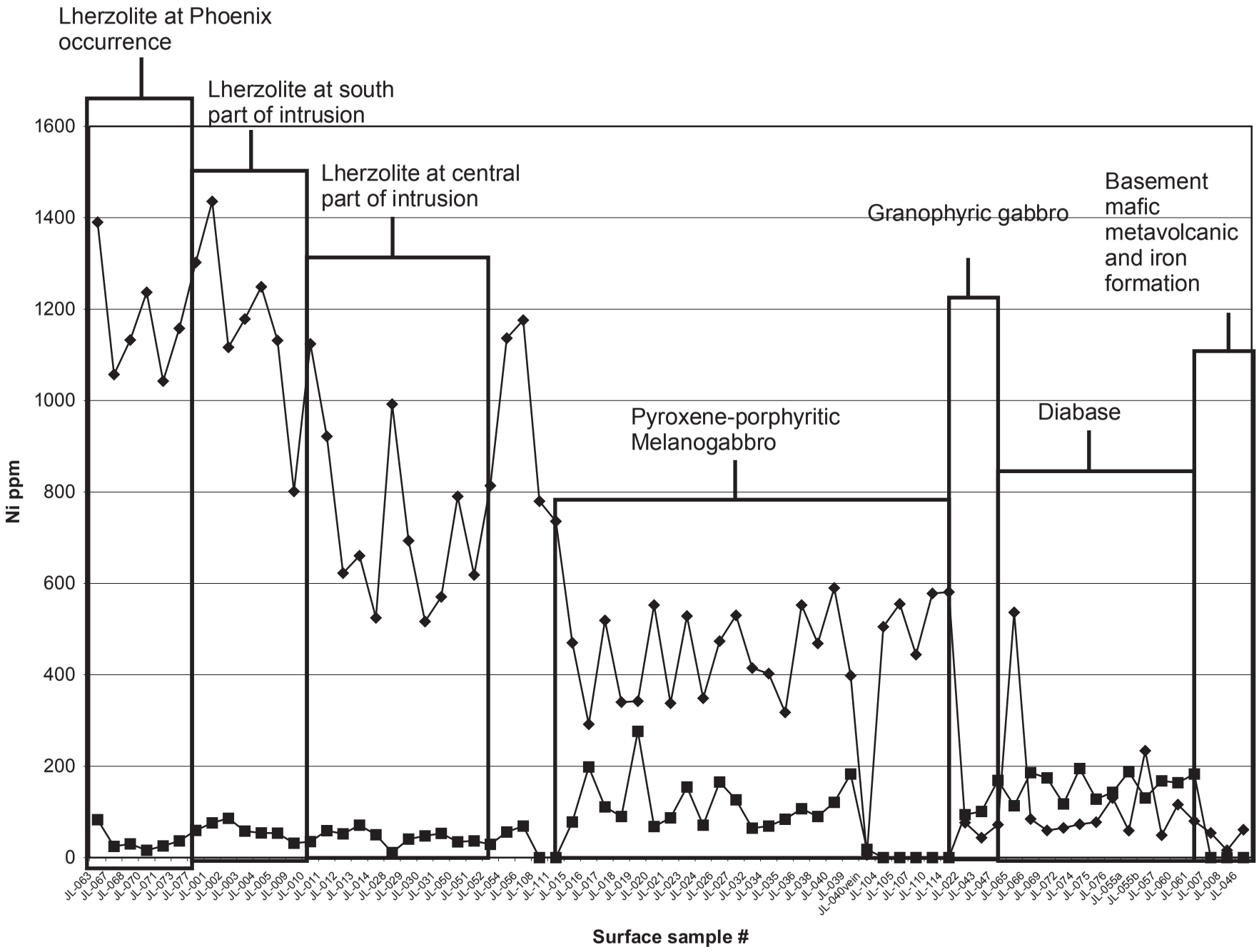

Figure 4.23: Surface sample Ni and Cu (lower numbers) variation from the southern, central and northern parts of the Kitto Intrusion.

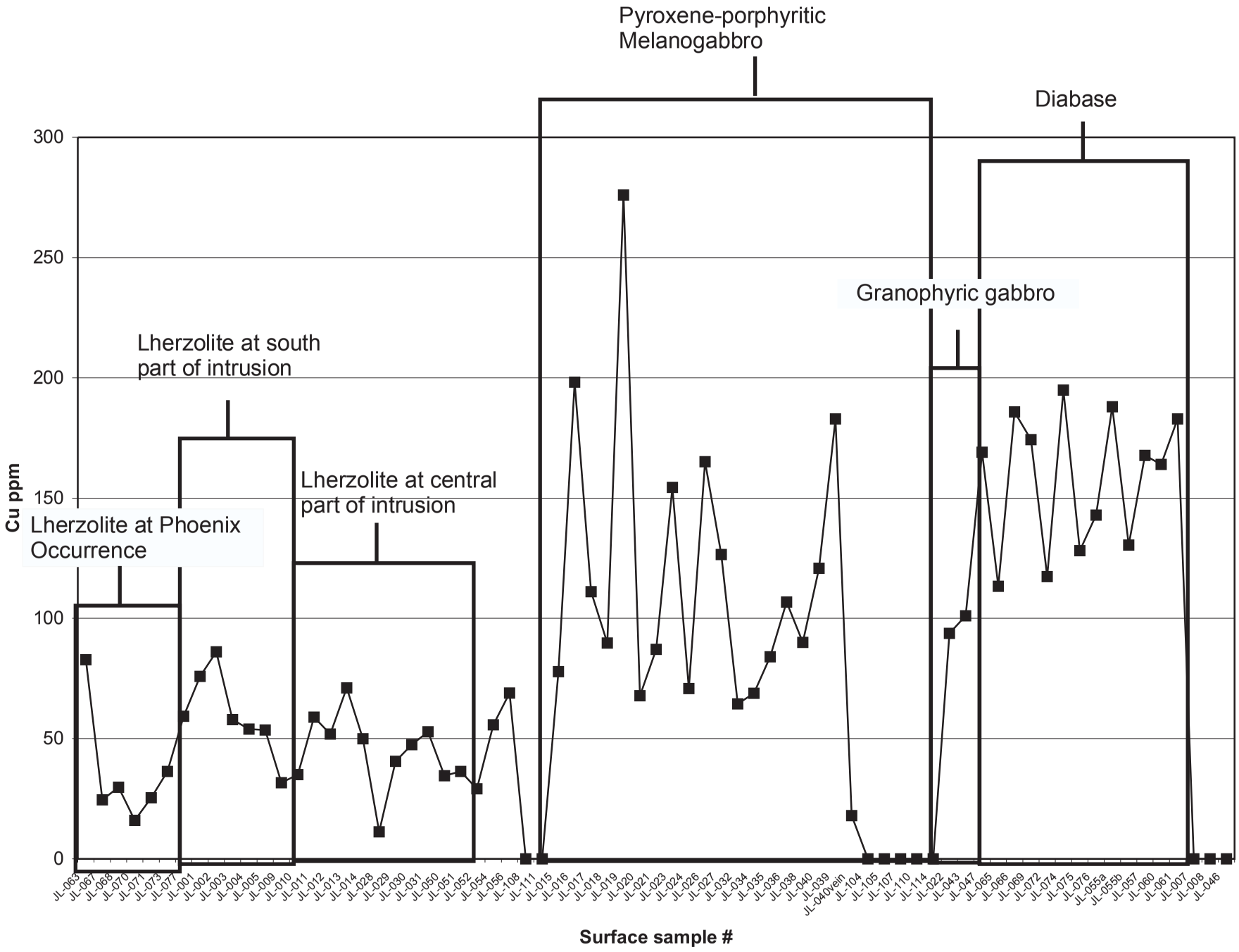

Figure 4.24: Surface sample Cu variation from the southern, central and northern parts of the Kitto Intrusion.

Background Ni contents in these lithologies range from 1043 to 1170 ppm in the lherzolites. Lithologies hosting mineralization in the southern part of the intrusion are the olivine websterite and bordering Nipigon diabases. Samples JL-067, JL-068, JL-069, JL-070, and JL-072 taken from the contact of the olivine websterite with Nipigon diabase at the Phoenix occurrence area all have anomalous contents; JL-070 and JL-068 having Pt, Pd contents of <5, 49 ppb and 12, 21 ppb respectively (Fig. 4.22). JL-070 has a Ni content of 1125 ppm. Samples JL-004, JL-055, JL-057, JL-060, JL-061 are also taken from the contact zone to the east of the Phoenix occurrence. Diabases throughout the intrusion have high Cu contents and have potential to host PGE, however the lithologies also have low Ni contents thereby making them an unlikely source for magmatic mineralization (Figs. 4.23 and 4.24). JL-055b is a pyroxenitized Nipigon diabase with Pt, Pd contents of 6, 12 ppb and a Cu content of 130.5 ppm that has visible pyrrhotite and chalcopyrite in hand sample. JL-004 is a lherzolite bordering the contact zone to the north with Pt, Pd of 12, 5 ppb and a Ni content of 1015 ppm. Another area of contact zone mineralization is at the Nipigon diabase to the far east of the intrusion. JL-074, JL-075, and JL-076 are Nipigon diabases with anomalous Pt, Pd contents of <5, 15 ppb each and Cu contents of 194, 127, and 141 ppm respectively. JL-077 is an olivine websterite with visible blebby pyrrhotite and an anomalous Ni content of 1025 ppm.

4.4.2 Downhole metal variation

Drillhole EK-02 displays variation in Pt, Pd, Ni, Cu and Cr metals in proportion to the depth down the hole. Pt, Pd, Ni, Cu and Cr were first analysed by Kennecott Canada Exploration Inc. at 1.5 m intervals in mineralized parts of the drillhole. These are from 169.5 to 212.5 m within the sulphidized olivine websterite, 268.5 to 277.5 m within pyroxenite, and 302.55 to 310.9 m within melanogabbro at the contact with basement banded iron formation.

Additional whole rock sampling was carried out for Ni, Cu and Cr down the hole as part of this thesis.

Platinum and palladium metals display very similar metal abundance patterns within the mineralized zones of the intrusion down the hole with Pd being slightly greater in concentration (Figs. 4.25 and 4.26). PGE mineralization occurs within the olivine websterite, pyroxenite and contact melanogabbro with maximum contents in the olivine websterite (Figs. 4.25 and 4.26). The maximum PGE contents within the sulphidized olivine websterite are displayed in Table 4.4. The Pt and Pd metals display similar metal abundance patterns to each other. Similar patterns are also displayed between PGE and Ni and Cu patterns (Fig. 4.27).

Table 4.4: Maximum Pt and Pd contents in DDH EK-02.

From (m):	To (m):	Pt (ppb):	Pd (ppb):
179.78	181	206	357
185.5	187	135	210
193	194.5	118	158
199	200.5	127	198

Copper contents down the hole display maximum mineralization contents within the sulphidized olivine websterite, two zones in the pyroxenite, and anomalous Cu in the basement banded iron formation (Fig. 4.27). Maximum Kennecott data contents within the sulphidized olivine websterite range from 1390 ppm at 179.78 to 181 m, to 550 ppm at 187 to 188.5 m, and to 640 ppm at 197.5 to 199 m. Within the pyroxenite, two zones are displayed from the ED data series. The second zone has the second largest maximum Cu content down the hole with a content of 750 ppm at 270 to 271.5 m. Again, the general association of increased PGE with increased Cu is displayed (Fig. 4.27). Anomalous Cu contents of 263 ppb have been detected in the basement iron formation.

Nickel contents display both dominant background mantle Ni and maximum mineralization contents down the hole corresponding to the largest Ni-Cu-PGE mineralized zone

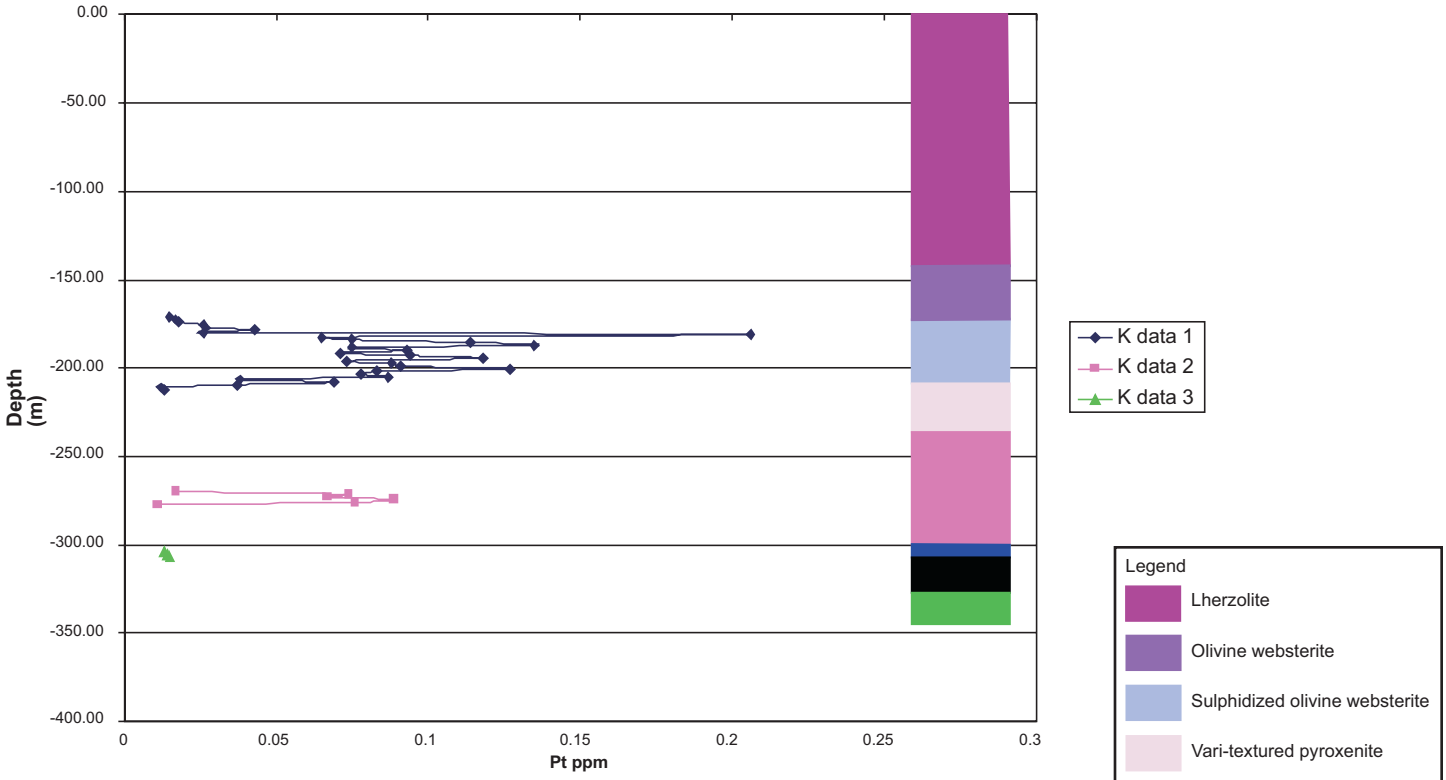

Figure 4.25: Plot of Pt ppm vs. depth with lithologies for DDH EK-02. K data is Kennecott data series (Coombes and Rossell, 2003).

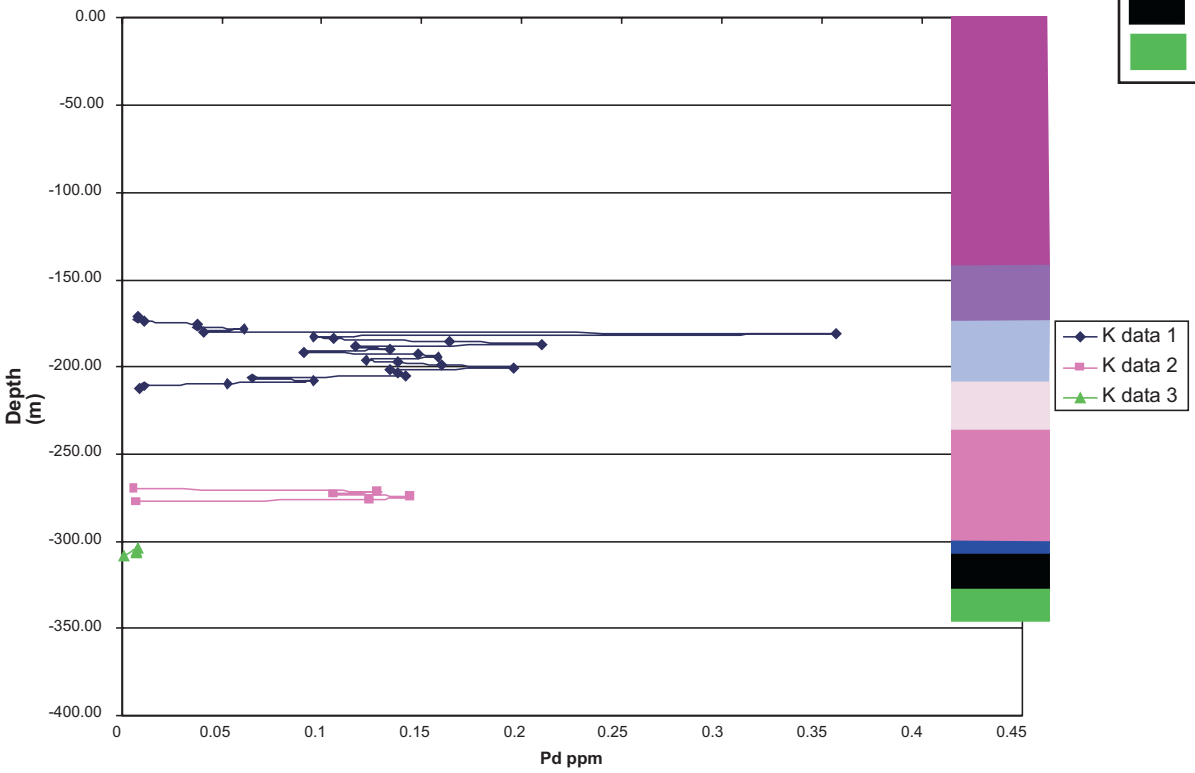

Figure 4.26: Plot of Pd ppm vs. depth with lithologies for DDH EK-02. K data is Kennecott data series (Coombes and Rossell, 2003).

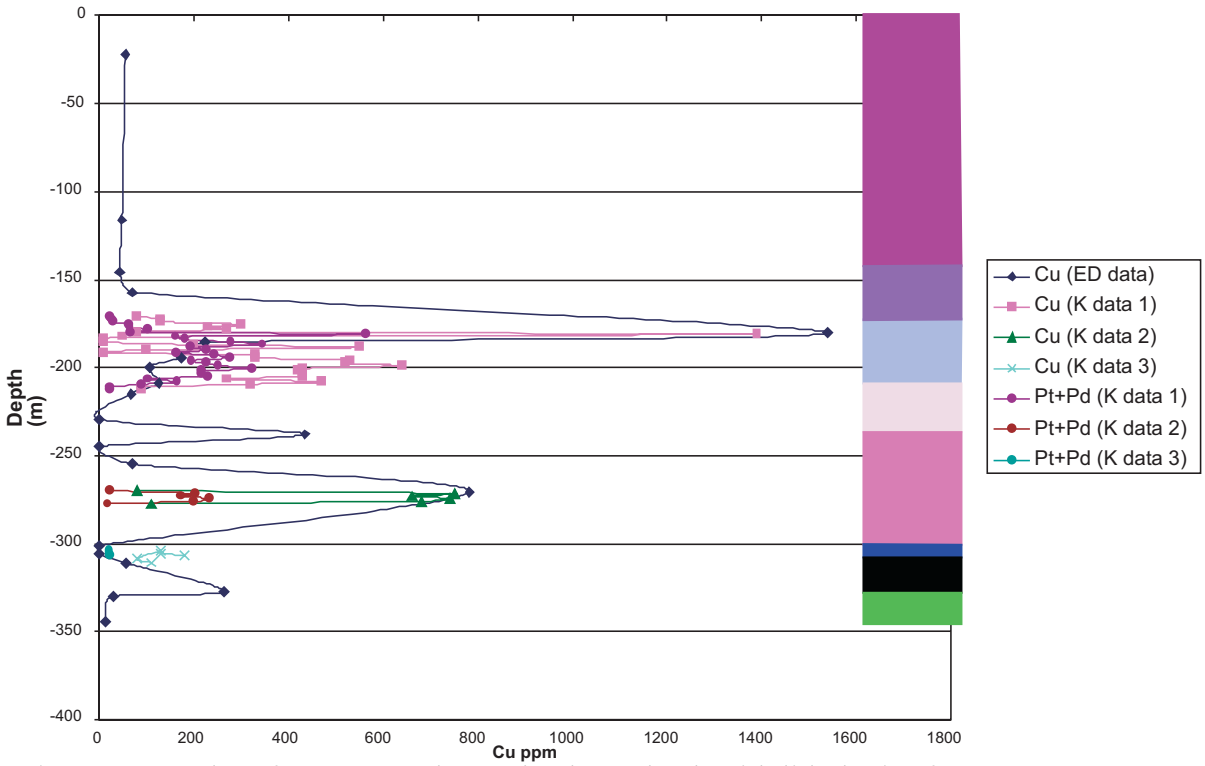

Figure 4.27: Plot of Cu ppm and Pt+Pd ppb vs. depth with lithologies for DDH EK-02. ED data is Eva Kitto drill hole data series from this thesis while K data is Kennecott data series (Coombes and Rossell, 2003). For legend of lithologies, see Figure 4.25.

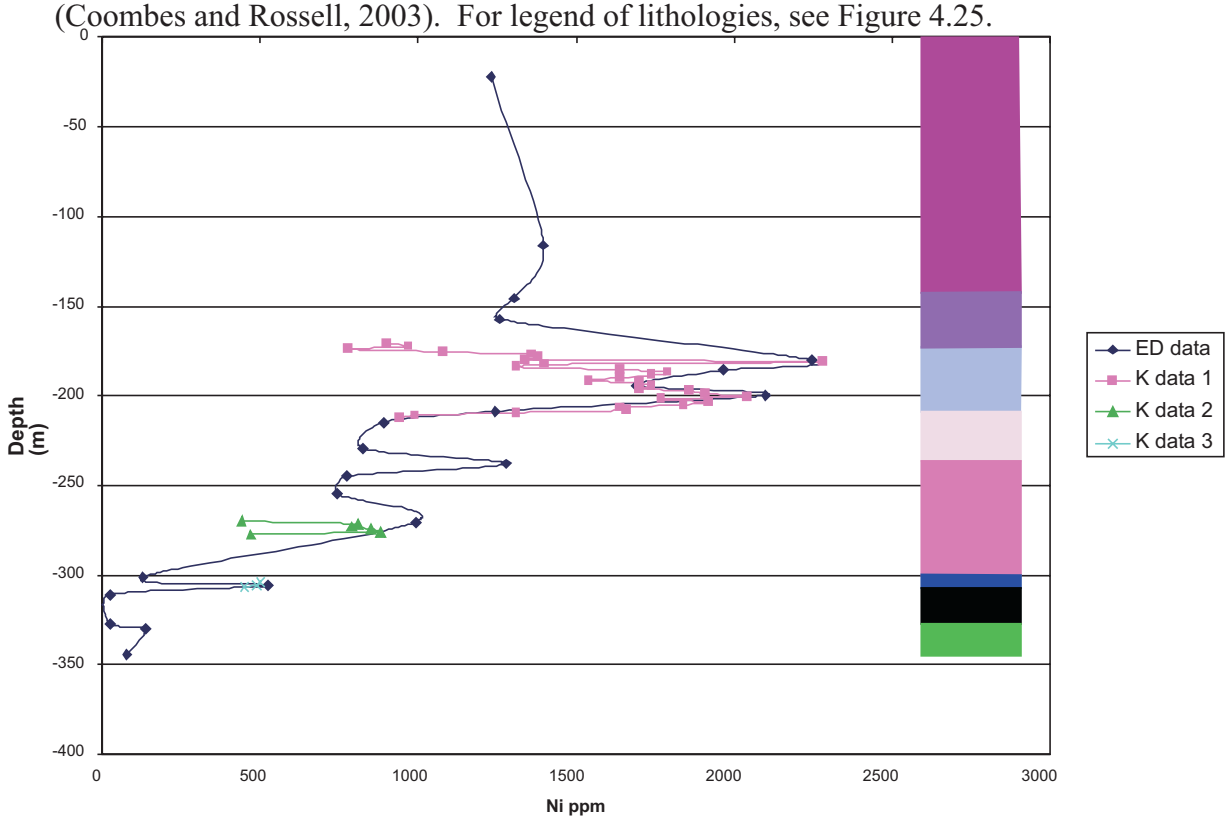

Figure 4.28: Plot of Ni ppm vs. depth with lithologies for DDH EK-02. ED data is Eva Kitto drill hole data series from this thesis while K data is Kennecott data series (Coombes and Rossell, 2003).

in the sulphidized olivine websterite, two mineralized zones in the pyroxenite and one in the contact melanogabbro (Fig. 4.28). Background Ni contents occur with concentrations of 1230 ppm and 1396 ppm displayed in samples ED-15 and ED-16 at 22 and 116 m respectively within the lherzolite. Within the sulphidized olivine websterite, maximum K-series data Ni contents range from 2280 ppm at 179.78 to 181 m, to 1790 ppm at 185.5 to 187 m, and to 2040 ppm at 199 to 200.5 m. Further down the hole, the overall Ni content decreases in the more evolved vari-textured pyroxenite, pyroxenite and melanogabbros. Samples of anomalous Ni contents taken within the pyroxenite (ED data series) show that there are at least two mineralized horizons in the pyroxenite. Generally, with increased Ni abundance, there is increased PGE abundances.

Chromium contents down the hole display a similar pattern as the Ni contents with background Cr contents and maximum mineralization contents (Fig. 4.29). In samples ED-15 and ED-16 at 22 and 116 m respectively, background Cr contents of 2992 ppm and 3904 ppm reflect abundant chromium oxide precipitation within the lherzolite. In the olivine websterite, a sharp decrease in Cr content occurs before mineralization maxima with a large content of 7694 ppm at 185.75 m in the ED data series. The decrease is due to the occurrence of sandstone xenolith in the drill hole. General maximum anomalous Cr contents are displayed in the K-series data within the sulphidized olivine websterite in occurrence with the Ni-Cu-PGE mineralization. Further down the hole, the overall Cr content decrease with lack of precipitation of Cr oxide minerals in the pyroxenite to melanogabbros.

4.5 Mineral Chemistry

Mineral compositions were determined out on 17 drill core samples from DDH EK-02 in the southern part of the intrusion and 10 surface samples from the central part of the intrusion. Results of the analyses are given in Appendix 4 and are discussed below for each mineral.

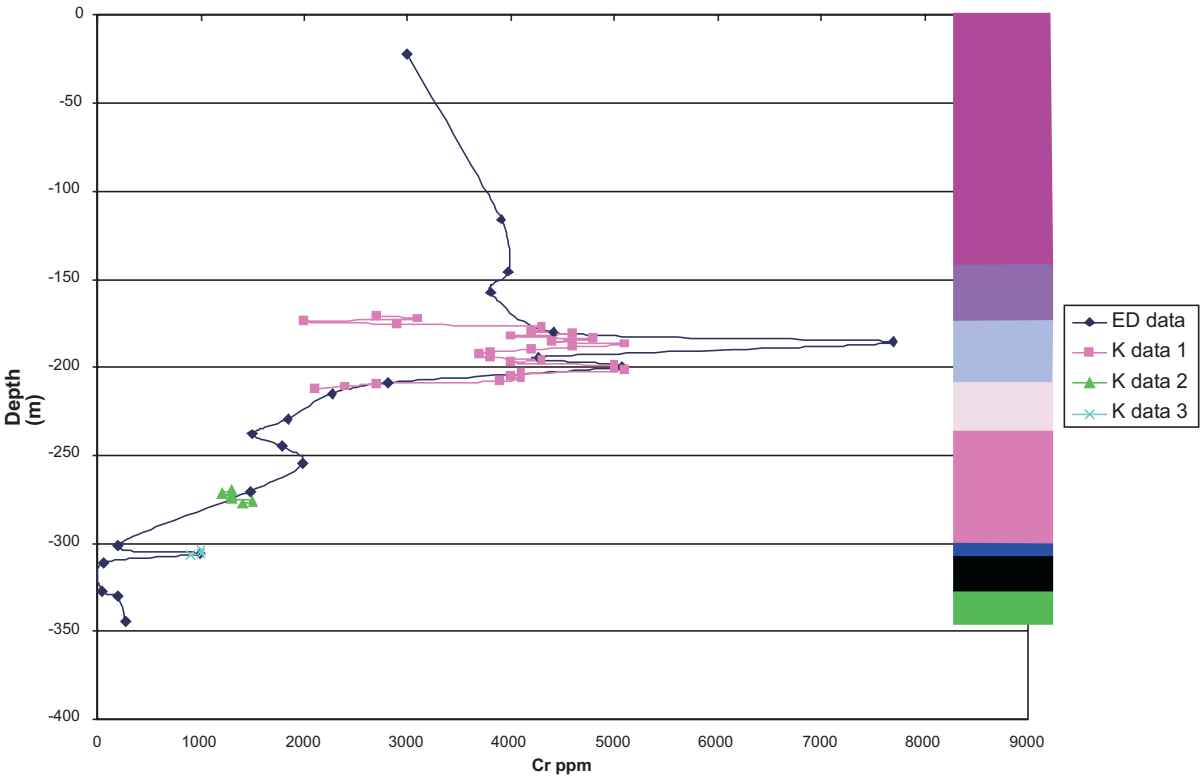

Figure 4.29: Plot of Cr ppm vs. depth with lithologies for DDH EK-02. ED data is Eva Kitto drill hole data series from this thesis while K data is Kennecott data series (Coombes and Rossell, 2003).

4.5.1 Olivine

Olivine compositions show evolutionary trends in average Forsterite % (Fo %) from lherzolite to pyroxene-porphyritic melanogabbros in surface samples from the central part of the intrusion. The more primitive lherzolites are represented by samples JL-28 and JL-11 with Fo % contents of 78.4 for JL-28 and 79.3 for JL-11 (Fig. 3.1). In the olivine websterites, olivine shows progressive evolution with lower contents of 73.9 for JL-31 and 75.1 for JL-14. Pyroxene-porphyritic melanogabbros have the lowest Fo % contents as they are the most evolved lithologies. South of the lake to the west of sample JL-31 on Figure 3.1, sample JL-36 has a Fo % content of 71.8, while further to the west, sample JL-40 has a Fo % content of 73.2. Sample JL-40 is located lower down in the eastward dipping side of the pyroxene-porphyritic melanogabbro since it has a higher Fo % content than JL-36. Therefore since JL-36 has the lowest Fo % contents, it is located in the upper most evolved part of the pyroxene-porphyritic melanogabbro. The most evolved lithologies are located close to the centre of the intrusion where it deepens the most south of the lake in the central part of the intrusion (Fig. 3.1). North of the lake and to the west of sample JL-14 (Fig. 3.1), sample JL-26 from the pyroxene-porphyritic melanogabbro has a more evolved Fo % content of 72.3 compared to the more primitive higher forsterite composition of 75.1 in sample JL-14. To the northwest of JL-14 (Fig. 3.1), sample JL-15 from the pyroxene-porphyritic melanogabbro also displays progressive trend in the central and upper parts of the intrusion with a minimum Fo % content of 69.2. Further to the west, samples JL-23 and JL-20 have Fo % contents of 71.9 and 71.9 since they are located in lower parts of an eastward dipping pyroxene-porphyritic melanogabbro (Fig. 3.1) i.e. the lithologies become enriched in MgO again in the lower parts of the lithology. In general, increased evolution occurs from the lherzolite to olivine websterite to pyroxene-porphyritic

melanogabbro from east to west in the central part of the intrusion as shown by trends of decreasing Fo % through the lithologies. As the intrusion reaches the surface to the west, higher Fo % contents occur in lower parts of the pyroxene-porphyritic melanogabbro.

Olivine compositions are plotted as average Fo % from 3 to 4 mineral analyses per sample down DDH EK-02 in the southern part of the Kitto intrusion (Fig. 4.30). Forsterite variation is described from the bottom to the top of the hole from the melanogabbro through to pyroxenite, vari-textured pyroxenite, sulphidized olivine websterite, olivine websterite and to lherzolites. At the bottom of the hole at 305 m, melanogabbro displays a minimum average Fo % of 74.3. Above the melanogabbro, pyroxenite displays a general increase in Fo % from 73.3 at 270 m to 78.1 at 254 m. At 237 and 229 m, larger Fo % contents of 80.3 and 80.1 are displayed in the vari-textured pyroxenite. From 229 to 22 m, the sulphidized olivine websterite to upper lherzolites follow trends of increasing Fo % and later decreasing Fo % through the upper parts of the intrusion. From 229 to 199 m, Fo % contents increase from 80.1 to 83.4. Maximum Fo % contents of 83.4 occur in the sulphidized olivine websterite. From 199 to 22 m, Fo % contents generally decrease to 79.2 in the upper part of the lherzolite-olivine websterite.

4.5.2 Clinopyroxene

Clinopyroxene compositions show evolutionary trends in average enstatite % (En %), ferrosilite % (Fs %), and wollastonite % (Wo %) from lherzolite to pyroxene-porphyritic melanogabbros in surface samples from the central part of the intrusion. In terms of composition, all clinopyroxenes plot within the augite field of the pyroxene quadrilateral (Fig. 4.31). Evolution is shown by decrease in En % and increase in Fs %. The more primitive lherzolite to olivine websterites have highest En % while lowest Fs %. Lherzolite samples JL-28 and JL-11 have En %, Fs % and Wo % contents of 48.3 En %, 9.8 Fs % and 41.9 Wo % and 48.1

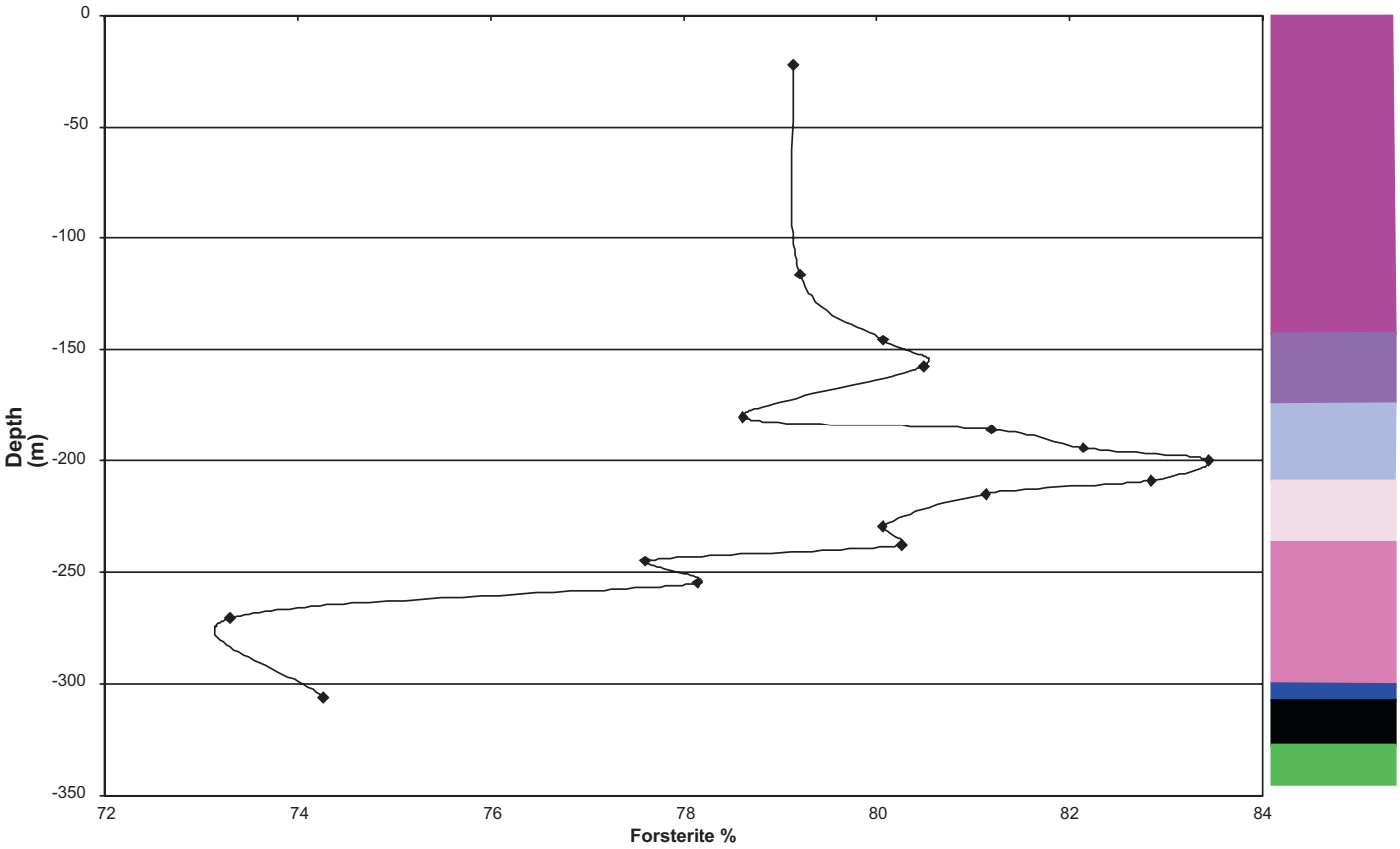

Figure 4.30: Plot of average Forsterite % in olivine vs. depth (m) with lithologies for DDH EK-02. For legend of lithologies see Figure 4.25.

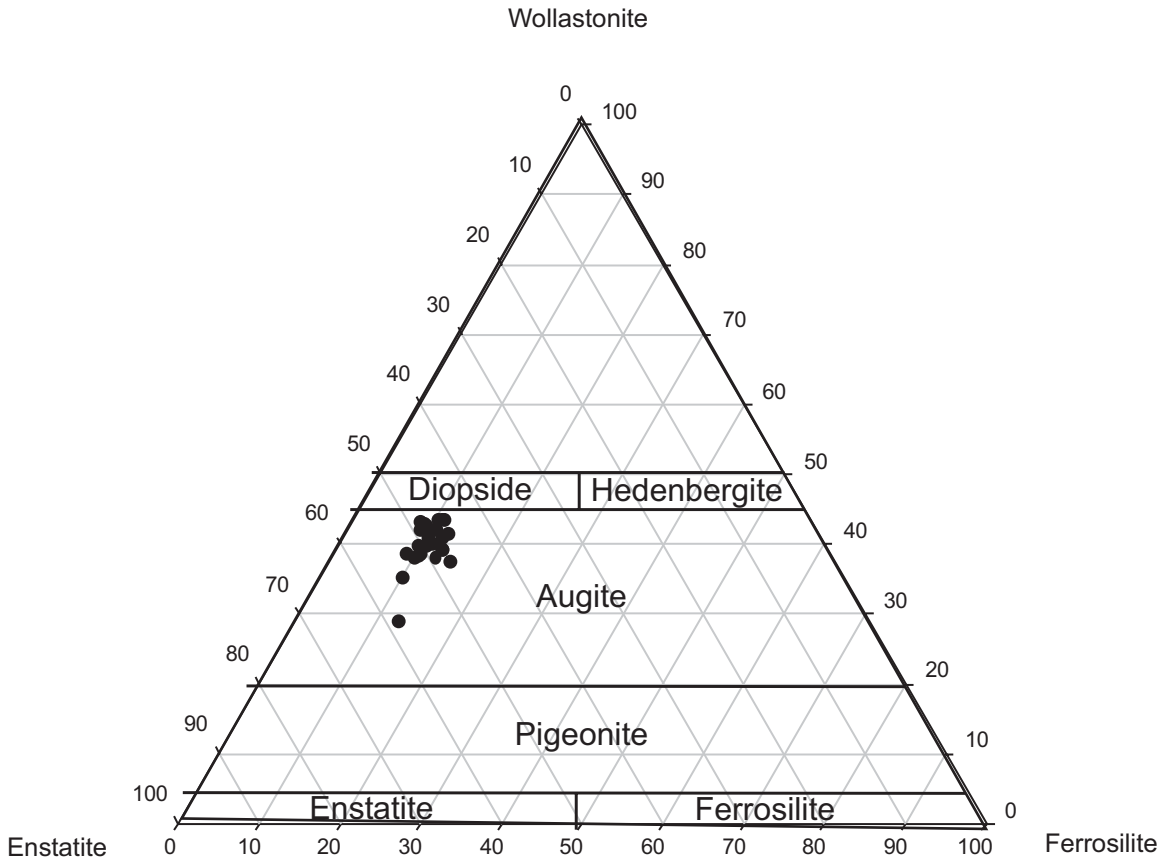

Figure 4.31: Ternary plot of clinopyroxene compositions. Clinopyroxene plots in the augite field. Source of fields from Deer et al. (1978).

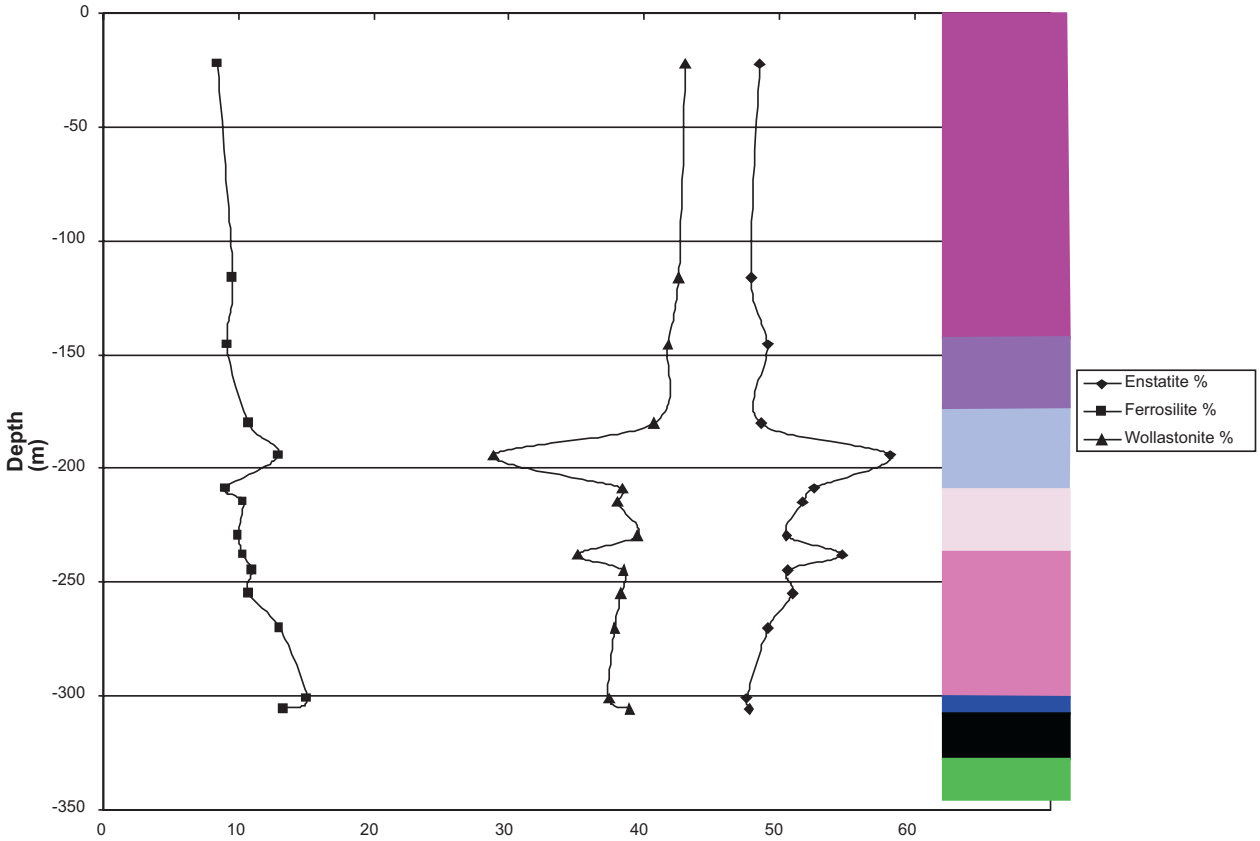

Figure 4.32: Plot of Enstatite %, Ferrosilite % and Wollastonite % vs. depth (m) for clinopyroxene with lithologies in DDH EK-02. For legend of lithologies, see Figure 4.25.

En %, 9.2 Fs % and 42.7 Wo % respectively. Olivine websterite sample JL-031 shows decrease in En % to 47.1 while increase in Fs % to 11.0. Sample JL-14 has anomalous En% of 49.4 and Fs % of 11.0 due to the lower Wo % at 39.6 Wo % in this sample. The trend of decreasing En % and increasing Fs % continues with the more fractionated pyroxene-porphyritic melanogabbro. Samples JL-036 and JL-15 have minimum and maximum of En % and Fs % with contents of 45.5 En %, 11.1 Fs % and 45.8 En %, 12.8 Fs % respectively. Further to the west in the lower eastward-dipping parts of the pyroxene-porphyritic melanogabbro, there is a general increase in En % and sometimes decrease in Fs %, with the exception of sample JL-20, which has higher Wo %. Sample JL-40 east of JL-036 has higher En % of 46.95, but a higher Fs % content of 12.4 due to the lower Wo % content of 40.7 in this sample. Sample JL-26 west of JL-15 has higher En % and lower Fs % with contents of 46.2 En %, 10.5 Fs % and 43.3 Wo %. Sample JL-23 also west of JL-15 has higher En % of 48.6, but higher Fs % of 11.5 due to the lower amount of Wo % at 40.0 Wo %.

Clinopyroxene compositions down DDH EK-02 show variation from the bottom to the top of the hole through the melanogabbro to the pyroxenite, vari-textured pyroxenite, olivine websterite, and lherzolites similar to the olivine trends (Fig. 4.32). At the bottom of DDH EK-02, melanogabbro has the lowest En % and highest Fs % with contents of 47.6 En %, 15.1 Fs %, 37.4 Wo % at 301 m in sample ED-33. From 301 to 237 m, pyroxenite shows trends of increasing En %, decreasing Fs %, and slightly increasing Wo % of contents up to 54.6 En %, 10.3 Fs %, and 35.1 Wo %. At 237 m in sample ED-07, contents are anomalous with a high En % content of 54.6, and a low Wo % content of 35.1. From vari-textured pyroxenite at 229 m to sulphidized olivine websterite, there is an increase in En %, slight increase in Fs % and depletion in Wo % to maximum contents of 58.2 En %, 12.9 Fs %, and 28.9 Wo % in sample ED-01 at

194m. From 194 m to 22 m at sample ED-15, there is a general decrease in En %, decrease in Fs % and increase in Wo % to contents of 48.5 En %, 8.4 Fs %, and 43.1 Wo % at ED-15.

4.5.3 Orthopyroxene

Orthopyroxene compositions were measured in three surface samples from the olivine websterite and pyroxene-porphyritic melanogabbros from the central part of the intrusion. In terms of composition, all orthopyroxenes are within the enstatite field of the pyroxene quadrilateral (Fig. 4.33) The olivine websterite displays the least evolved composition of highest En % and lowest Fs % and Wo % contents of 76.3 En %, 21.0 Fs % and 2.8 Wo % in sample JL-31. North of the lake, sample JL-15 displays evolution from sample JL-31 to lower En % and higher Fs % and Wo % with contents of 73.8 En %, 23.3 Fs % and 2.9 Wo %. Further to the west in the lower parts of an east-dipping pyroxene-porphyritic melanogabbro, sample JL-26 displays an increase in En % and decrease in Fs % and Wo % with contents of 74.2 En %, 23.2 Fs % and 2.6 Wo %.

Orthopyroxene variation in DDH EK-02 shows a trend to higher En % and lower Fs % from the bottom melanogabbro to pyroxenite, olivine websterite and upper lherzolites (Fig. 4.34). The bottom evolved melanogabbro at 305 m in sample ED-10 has the lowest En % and highest Fs % with contents of 70.1 En %, 25.7 Fs %, and 4.2 Wo %. A lower sulphidized pyroxenite at 270 m in sample ED-09 also has low En % and high Fs % with contents of 69.5 En %, 28.8 Fs % and 1.7 Wo %. From 270 m to 244 m, there is an increase in En % and decrease in Fs % to contents of 76.0 En %, 22.2 Fs %, and 1.8 Wo % in sample ED-32. A trend occurs to high En % and low Fs % in the upper lherzolite-olivine websterites with contents ranging from 78.4 En %, 18.0 Fs %, 3.5 Wo % at 185 m in sample ED-02 to 78.5 En %, 19.0 Fs %, 2.5 Wo % at 116 m in sample ED-16 to 78.2 En %, 17.9 Fs %, 3.9 Wo % at 22 m in sample ED-15.

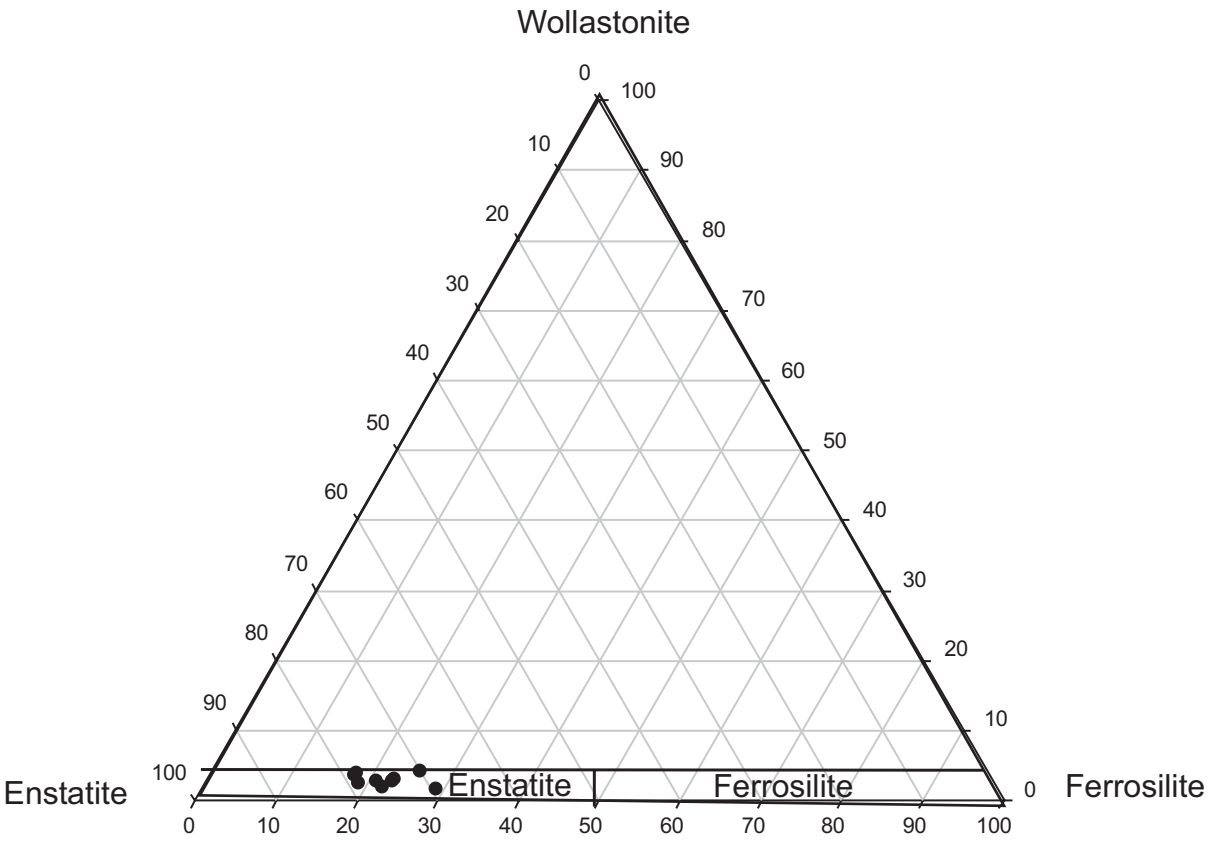

Figure 4.33: Ternary plot of orthopyroxene compositions. Orthopyroxene plots in the enstatite field. Source of fields is Deer et al. (1978).

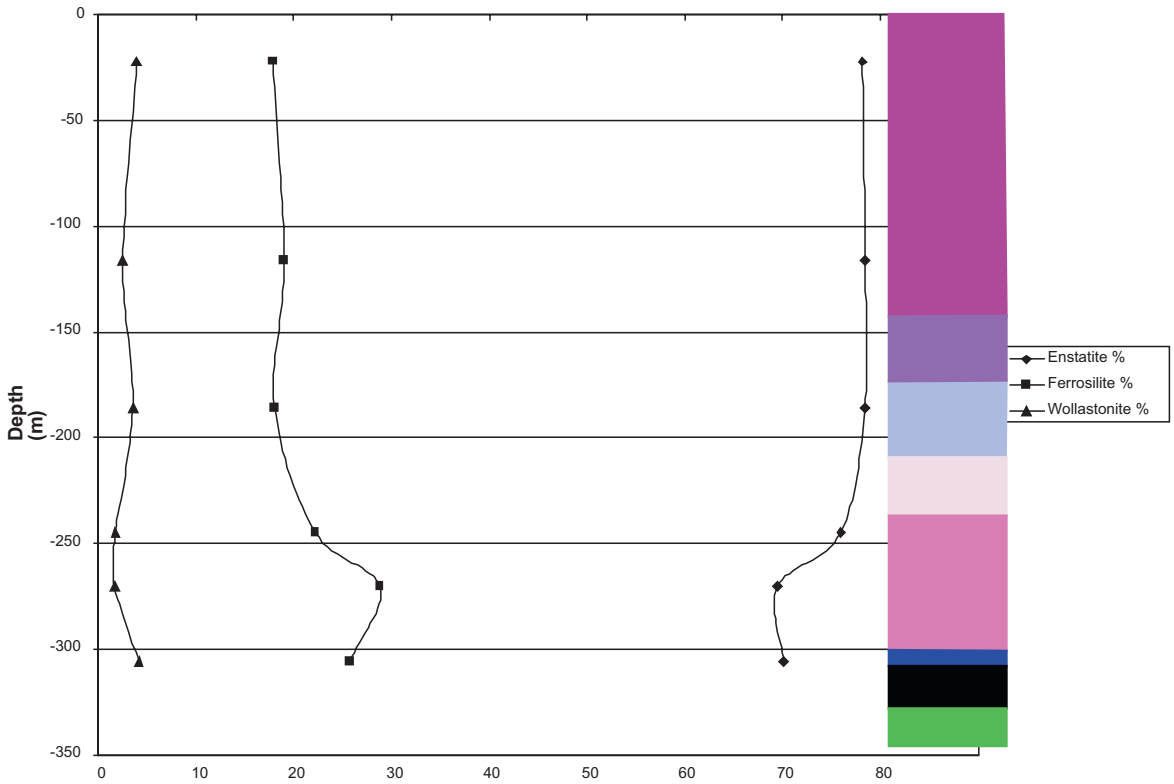

Figure 4.34: Plot of Enstatite %, Ferrosilite % and Wollastonite % vs. depth (m) for orthopyroxene with lithologies in DDH EK-02. For legend of lithologies, see Figure 4.25.

4.5.4 Plagioclase

Plagioclase compositions in the Kitto intrusion are located in the lower melanogabbros of DDH EK-02 in the southern part of the intrusion and in the olivine websterite and pyroxene-porphyritic melanogabbros of the central part of the intrusion. In terms of composition, plagioclases plot in the labradorite and andesine fields of the orthoclase-albite-anorthite plot (Fig. 4.35). Plagioclase within the melanogabbros have a labradorite to andesine composition with contents ranging from 43.3 Ab %, 55.2 An % and 1.5 Or % in sample ED-33 to 57.1 Ab %, 40.1 An % and 2.9 Or % in sample ED-10. In the central part of the intrusion, plagioclase is labradorite in composition with contents ranging from 48.4 Ab %, 50.1 An % and 1.4 Or % in olivine websterite sample JL-14 to 45.8 Ab %, 52.7 An % and 1.5 Or % in pyroxene-porphyritic melanogabbro sample JL-36 to 48.4 Ab %, 49.5 An % and 2.0 Or % in pyroxene-porphyritic melanogabbro sample JL-23.

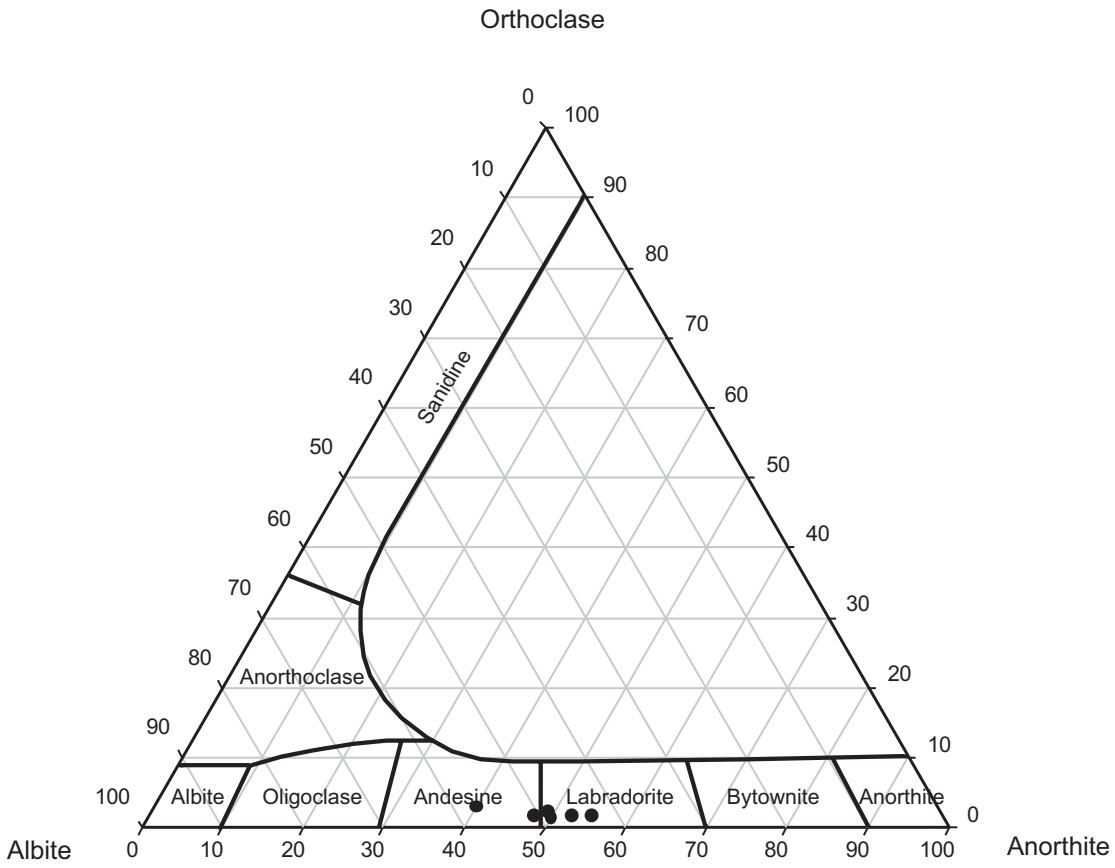

Figure 4.35: Ternary plot of plagioclase compositions. Plagioclases plot in the labradorite and andesine fields. Source of fields from Deer et al. (1963).

CHAPTER 5

DISCUSSION

5.1 Origin of the Kitto magma

The Kitto intrusion is one of a group of picritic intrusions in the Nipigon Embayment outlined by Sutcliffe (1986). Picrites of the Nipigon Embayment were considered to be Keweenawan in age (i.e. related to the Midcontinental Rift Event) since they post-dated the Sibley Group sedimentary rocks (Sutcliffe, 1986). Geochronology has since been undertaken on the ultramafic rocks of the Nipigon Embayment dating the rocks to 1117 Ma for the Kitto intrusion, consistent with them being Keweenawan in age (Heaman and Easton, 2006). The Keweenawan plutonic and later continental rift volcanic rocks have been postulated to be the result of primary plume impingement on the crust (Nicholson and Shirey, 1990). Generally, superplumes at depth are considered to cause continental rift systems as supercontinents insulate the mantle to cause the rising of a mantle plume where there are geoid highs, while recycling of crust by way of subduction occurs at geoid lows (Anderson, 1994). The Midcontinental Rift (MCR) has a geophysical expression of large gravity and magnetic highs in the crust which is consistent with it being derived from a superplume with depth (Hinze et al., 1982). Gravity highs as geophysical expressions of feeder zone magmas to Keweenawan intrusions have also been interpreted for a large gravity high underlying the Kopka cone sheet diabase intrusions in the northwest Nipigon Embayment (Fig. 5.1; Sutcliffe, 1986). A gravity high also occurs offset from the Kitto intrusion to the northwest that could represent the feeder zone plume for the intrusion (Fig. 5.1). The Nipigon Embayment occurs as a gravity and magnetic high in contrast

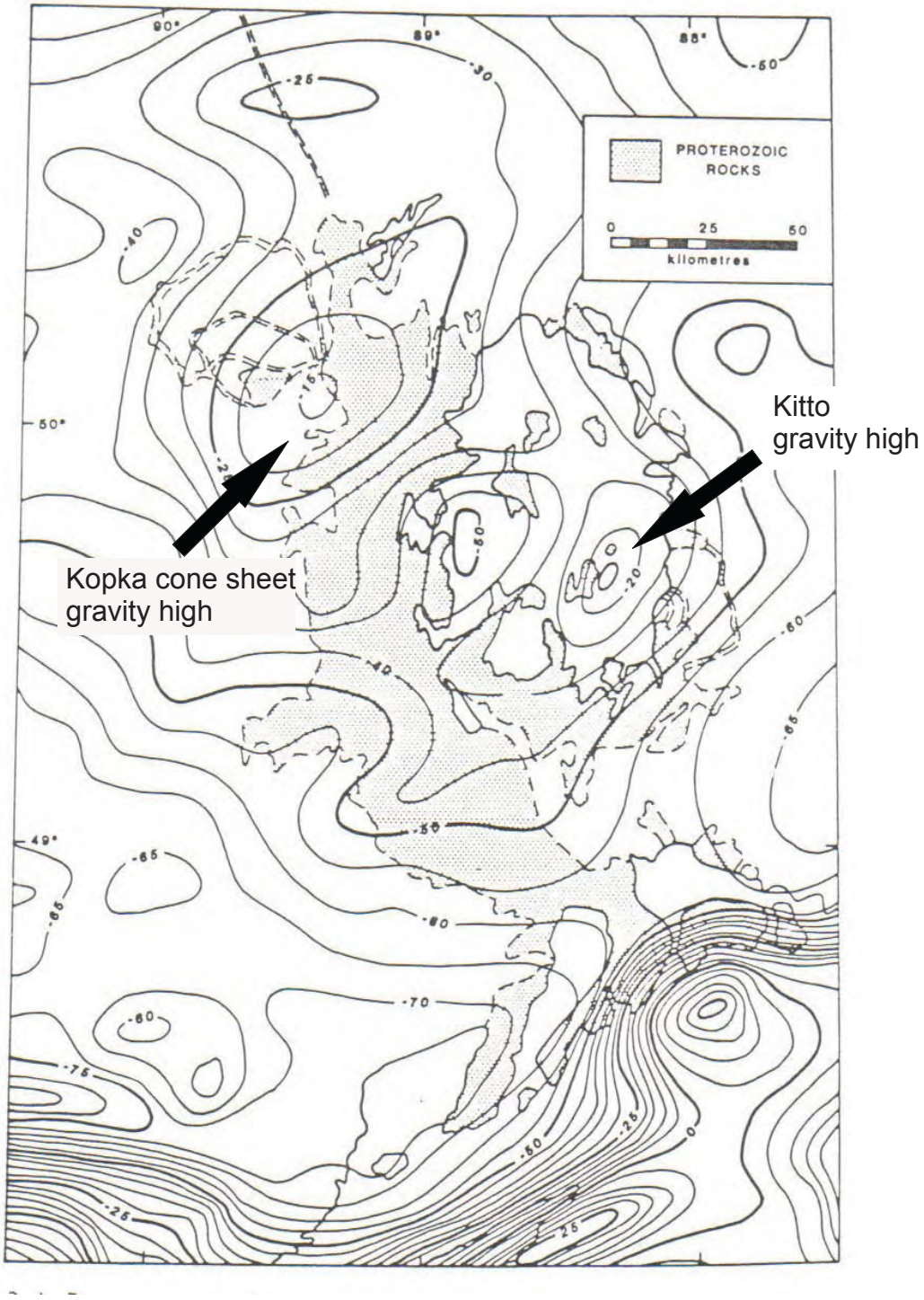

Figure 5.1: A gravity map of the Nipigon Embayment. Two gravity highs may represent two plume feeder zone magmas to the Kopka Cone Sheet in the northwest Nipigon Embayment and the Kitto intrusion in the East Nipigon Embayment. Modified after Sutcliffe (1986).

to surrounding Archean crust and is an extension of the MCR (Hinze et al., 1982; Gupta, 1991). Evidence for plume activity can be seen in geochemical signatures of plutonic and volcanic rocks of the MCR. The Mamainse Point Formation is a supergroup of Keweenawan mafic volcanic rocks that occur on the northeastern shore of Lake Superior. Group 2 and 8 lavas of the ca. 1100 Ma Mamainse Point Formation have been shown to contain plume signatures of ε_{Nd} contents of zero and Group 1 lavas of the same formation have more negative ε_{Nd} contents with low Ta/La ratios interpreted to be the result of plume impingement on the sub-continental lithospheric mantle (Shirey et al., 1994). Groups 1 and 2 lavas, in light of lower Th/La ratios, have also been interpreted to be of a MORB or OIB source consistent with continental rift or plume-related rocks. Group 8 lavas of the same formation have enrichment in LREE similar to OIB (Ocean Island Basalt) rocks and along with having ε_{Nd} contents of zero, are interpreted to be of OIB or plume origin (Shirey et al., 1994). Other volcanic rocks located south of Lake Superior of plume origin with ε_{Nd} contents near or equal to zero include the Lower Siemens Creek and Kallander Creek volcanic rocks of the Powder Mill Group, and the Portage Lake volcanic rocks of the Bergland Group (Nicholson et al., 1997; Nicholson and Shirey, 1990). Intrusions formed as a result of earlier plume impingement on the crust include the picritic intrusions such as the Seagull intrusion, Kitto intrusion, Nipigon sills in the Nipigon Embayment. The Nipigon Suite of Nipigon sills has ε_{Nd} contents as low as -0.8 and the Jackfish Suite of the sills have ε_{Nd} contents from -0.5 to -1.1 reflecting a primitive plume origin of the lithologies (Hollings et al., 2007b). The low ε_{Nd} contents in the Jackfish Suite sills has led Richardson et al. (2006) to suggest that the ultramafic intrusions and sills of the Nipigon Embayment were derived at greater depths and were transported rapidly through the crust with little assimilation of crustal material,

probably along crustal-scale faults. The Seagull intrusion has ε_{Nd} contents as low as -0.2 reflecting a plume origin for the lithologies (Heggie, 2005).

The Kitto and Seagull intrusions represent the earliest phase of plume magmatism yet recognized in the MCR, with an age of 1117 Ma for the Kitto intrusion (Heaman and Easton, 2006). A plume origin for the Kitto intrusion can be seen in a few OIB-like primitive mantle normalized trace element patterns of the lherzolite-olivine websterites (Fig. 4.13). An example of an OIB composition from Jenner (1996) is plotted along with the lherzolite-olivine websterites (Fig. 4.13). Lherzolite and other lithologies of the Kitto intrusion show primitive mantle plot patterns of decreasing REE abundance from LREE to HREE which are comparable to OIB or plume signatures before crustal contamination (Fig. 4.13). Patterns of LREE enrichment also occur in lithologies from island arc geologic settings and negative Nb anomalies would suggest the conservation of Nb with the subduction of a slab of crust (Jenner, 1996). However, some of the primitive mantle plot patterns of the Kitto intrusive units do not have negative Nb anomalies which would suggest they are of primary OIB composition (e.g., samples ED-35, ED-34 and ED-25; Fig. 4.13). Also the Kitto intrusive units emplaced as part of Mesoproterozoic magmatism associated with the Midcontinent Rift system, which is interpreted by Nicholson and Shirey (1990) to consist of magmatic rocks of a mantle-plume origin that subsequently initiated the formation of a continental rift.

5.2 Petrography and lithogeochemistry of the intrusive units

The dominant lithology of the Kitto intrusion is lherzolite peridotite. The lherzolites of the southern part of the intrusion contain the most MgO-rich rocks with cumulate-textured to pyroxene-poikilitic olivine and pyroxene compositions. On surface, MgO contents range from 28 to 33 wt. % in the lithologies. On MgO vs. CaO and Al_2O_3 variation diagrams, these

lithologies display olivine and clinopyroxene-controlled fractionation lines with lower CaO and Al_2O_3 at higher MgO (Figs. 4.8 and 4.12). On surface, lherzolites have the greatest Ni ppm contents of between 535 and 1170 ppm in the southern part of the intrusion due to the predominance of olivine minerals in these lithologies. The high-MgO primitive compositions, high Ni in olivine contents, OIB source compositions, and lowest ε_{Nd} contents of -5.54, suggest lherzolite as the most primitive magma source in the southern part of the intrusion. Similar least contaminated REE patterns, and lowest ε_{Nd} contents have led Heggie (2005) to interpret peridotite to dunite as being the primitive magma source composition of the Seagull intrusion.

In DDH EK-02, olivine websterite occurs below lherzolite and represents a cumulate olivine and pyroxene-rich lithology that probably formed from the accumulation of these minerals from the main lherzolite magma. Evidence for original cumulate formation of the olivine websterite from a lherzolite magma is the predominance of cumulate pyroxene and olivine, poikilitic pyroxene similar to lherzolite, and high MgO contents similar to lherzolite and similar primitive mantle multielement patterns. Also a slight increase in MgO from lherzolite to the bottom olivine websterite occurs with accumulation of these magnesian minerals (Fig. 4.1).

Below the lherzolite-olivine websterites in DDH EK-02 at the southern part of the intrusion is pyroxenite. The pyroxenite formed from the accumulation of dominant pyroxene minerals. Textural evidence for accumulation of the lithology is the predominance of cumulate clinopyroxene minerals that are separated by intergranular plagioclase (Fig. 3.25). Increase in plagioclase minerals as intercumulus phases shows that the magma was more evolved than the upper lherzolite-olivine websterite. In terms of geochemistry, the lithologies show a steady decrease in MgO, while increase in SiO_2, Al_2O_3, TiO_2 and CaO as a result of increased evolution in the lithologies relative to lherzolite-olivine websterite with accumulation of lower amounts of

magnesian minerals (Figs. 4.1 to 4.6). On a CaO vs. MgO plot, the lithologies fall on trend with steady increase in CaO with lower MgO indicative of pyroxene as the dominant mineral crystallized (Fig. 4.12).

Melanogabbros occur at the bottom of the Kitto intrusion bordering the basement lithologies in the southern part of the intrusion. Melanogabbro displays an ophitic to intergranular texture with dominant plagioclase minerals interlocking with pyroxene (Fig. 3.32). In terms of geochemistry, it has the most evolved composition with highest SiO_2, Al_2O_3, TiO_2 and CaO with decreasing MgO due to contamination of pyroxenitic magma at the border with basement lithologies (Figs. 4.1 to 4.6). On an Al_2O_3 vs. MgO variation plot, the lithologies have highest increase in Al_2O_3 with decreasing MgO indicative of dominant plagioclase-controlled crystallization (Fig. 4.8).

In the central part of the intrusion, the lithologies from east to west show progressive evolution from lherzolite to olivine websterite to pyroxene-porphyritic melanogabbro lithologies, and a late stage final melt intrusion of granophyric gabbro. Moving northward from the southern toward the central part of the intrusion, lherzolite contains more secondary textures such as secondary pyroxene in addition to cumulate olivine and pyroxene, which probably formed with evolution from more primitive compositions (Fig. 3.12). The secondary pyroxene minerals probably represent crystallization of partial melt left behind between cumulate olivine and pyroxene minerals in a more evolved magmatic system. Lherzolite is geochemically more evolved in the central part of the intrusion than in the southern part with MgO contents between 25 and 28 wt. %. Low Al_2O_3, CaO, TiO_2 contents with increasing MgO show lherzolite crystallized under olivine and pyroxene control (Figs. 4.1 to 4.6). From lherzolite to olivine

websterite, there is increased evolution of magmas as evidenced by increase in SiO_2, Al_2O_3, CaO while decrease in MgO with contents from 20 to 25wt. % MgO.

From east to west in the central part of the intrusion, pyroxene-porphyritic melanogabbros are more evolved than the lherzolite-olivine websterites. Pyroxene-porphyritic melanogabbro contains cumulate textures of dominant clinopyroxene with up to 30% intercumulus plagioclase (Fig. 3.29). Along with increase in the amount of plagioclase, the increase in occurrence of secondary pyroxene show the lithology evolved with increased fractionation (Fig. 3.28). The lithologies in general show a more fractionated geochemistry with increases in SiO_2, Al_2O_3, and CaO with decreasing MgO to contents from 14 to 20 wt. % MgO.

Granophyric gabbro is the most evolved lithology of the Kitto intrusion and is located in the centre of intrusion to the west of pyroxene-porphyritic melanogabbro. Petrographically, this contains unique igneous textures and major element compositions different to the other lithologies. In hand sample, the lithologies display a massive coarse grained leucocratic texture, in contrast to the melanocratic textures of the other lithologies (Fig. 3.34). In thin section, feldspar constitutes 60% of the rock and sometimes displays cuneiform granophyric to myrmekitic textures (Fig. 3.35). Geochemically, granophyric gabbro contains the most felsic composition with highest SiO_2, TiO_2, Al_2O_3 and lowest MgO from 2 to 9 wt. %. On an Al_2O_3 vs. MgO plot, the lithologies show the highest Al_2O_3 at lowest MgO indicative of dominant plagioclase crystallization in the lithologies (Fig. 4.7). On a CaO vs. MgO plot, the lithologies have decreasing CaO at lowest MgO, indicative of plagioclase-controlled crystallization of the lithologies (Fig. 4.11).

5.3 Modification of the Kitto magma

5.3.1 Primitive mantle normalized multielement plots

Negative Nb and Ti anomalies and LREE enrichment exhibited on primitive mantle plots of the Kitto intrusive units indicate that the magmas have been modified by crustal contamination within the intrusion. Generally, continental crust is enriched in highly incompatible elements such as Ce, U, Th, Nb, Ta and LREE such as La. However, the upper crust is less enriched in Ta and Nb relative to Th, and less enriched in Ti relative to MREE, which is attributed to retention of these elements in oxide phases in eclogite during crustal recycling (Lesher, 2001). As a consequence, magmas contaminated by continental crust should be enriched in highly incompatible lithophile elements, with pronounced negative Ta and Nb anomalies, and should be moderately enriched in moderately incompatible lithophile elements, with slightly negative Ti anomalies (Lesher, 2001). Crustal contamination signatures such as negative Nb and Ti anomalies, and LREE enrichment occur in komatiitic to ferropicritic rocks in general such as those from the Kambalda komatiites and peridotites of the Cape Smith Belt (Lesher et al., 2001; Lesher, 2005). In the Nipigon Embayment, the Seagull intrusion is interpreted to be crustally contaminated in the Basal Unit, Basal Main Unit and weakly in the Main Unit, as seen by negative Nb anomalies which correlate with negative ε_{Nd} contents also interpreted to be a result of contamination (Heggie, 2005).

In the Kitto intrusion, two geochemical trends are distinguished within the lherzolites in drill core that represent either primitive lithologies or lithologies that have undergone higher degrees of contamination (Figs. 4.13 and 4.14). The lithologies with lower La/Nb, Th/Nb and less pronounced Nb anomalies represent the most primitive compositional lithologies that have undergone little to no crustal assimilation than lithologies with more pronounced Nb anomalies

(Fig. 4.13). These lithologies also have positive Ti anomalies and negative Eu anomalies indicative of no assimilation of crust and non-fractionation of plagioclase respectively. Samples ED-34, ED-25 and ED-19 are the most primitive compositional lherzolites found at the top of DDH EK-03 and EK-01. Samples ED-35 and ED-29 are primitive lherzolites with smaller Th/Nb ratios of 0.89 and 1.06 indicative of primitive nature of the lithologies. Sample ED-41 has a positive Ti anomaly, which is either indicative of primitive nature of the lithology or the occurrence of magnetite (Fig. 4.13). In contrast, the larger amount of samples showing larger Th/Nb, La/Nb, and negative Nb and Ti anomalies underwent some degree of assimilation of crust before accumulation of cumulate minerals and mineralization (Fig. 4.14). The samples ED-17, ED-18 and ED-20 that have either high La/Nb of 1.72 in ED-17 or high Th/Nb ratios of 1.36 and 1.17 in ED-18 and ED-20 respectively, are representative of crustally contaminated cumulate accumulated olivine websterites at the bottom of the lherzolite-olivine websterites. The samples ED-01, ED-02, ED-03, ED-04 and ED-05 that have high La/Nb ratios ranging from 1.12 to 1.74 and negative Nb anomalies are mineralized olivine websterites that underwent assimilation of crust with mineralization. Sample ED-15 has a higher La/Nb ratio of 2.30 due to alteration with serpentinization (Fig. 4.14).

In the lherzolite-olivine websterites from the surface, primitive mantle plots show evolution to increased evolution with assimilation of crust in areas of both the Phoenix occurrence and moving northward to the central parts of the Kitto intrusion next to pyroxene-porphyritic melanogabbros (Fig. 4.15; Fig. 3.1). The sharp Nb and Ti anomalies and a higher La/Nb ratio of 1.93 in surface sample JL-073 are possibly indicative of increased crustal contamination with evolution to olivine websterite and mineralization within the lithologies at the Phoenix occurrence. This is consistent with the more evolved lithologies of the Kitto

intrusion such as seen in the later pyroxenite and pyroxene-porphyritic melanogabbros. Since sample JL-077 is an olivine websterite bordering a diabase intrusion in the southeast part of the Kitto intrusion, the sharp negative Nb and Ti anomalies and a high La/Nb ratio of 2.34 are possibly reflective of evolution and crustal contamination of the lithology at the border of basement wallrock metabasalt (Fig. 3.1). Moving north, the sharp negative Nb and Ti anomalies of sample JL-052 reflect increasing crustal assimilation in the lherzolite-olivine websterites toward the central part of the intrusion relative to the primitive lherzolites at the southern part of the intrusion in drill core. The more contaminated sample JL-052 with sharp negative Nb and Ti anomalies is consistent with the lherzolites generally being more evolved and contaminated toward the central part of the intrusion with lower MgO contents and the occurrence of secondary pyroxene being precipitated in the crystallization histories of the lithologies. In the central part of the intrusion, the sharp negative Nb and Ti anomalies displayed in lherzolite-olivine websterite surface samples JL-011 and JL-012 are reflective of crustal assimilation and evolution to olivine websterite westward toward the pyroxene-porphyritic melanogabbros. In contrast, the many lherzolite-olivine websterites having shallower Nb and Ti anomalies and lower La/Nb ratios are reflective of little evolution and non-assimilation of crust in the crystallization histories of the lithologies. These lithologies are probably of primitive lherzolite composition like most lherzolites in the southern part of the intrusion. In surface sample JL-111, the positive Ti anomaly is possibly reflective of non-assimilation of crust.

In the vari-textured pyroxenites, all the ratios fall within the range of the lherzolites with the same REE and trace element abundance indicative of the primary lherzolitic compositions of the lithologies (Fig. 4.16). The Nb and Ti anomalies, that are similar to those of lherzolite-olivine websterite with La/Nb ratios of 1.68 to 1.90, are also indicative of primary lherzolitic

compositions in these lithologies. This is consistent with the lithologies having secondary pyroxene textures suggestive of upper lherzolite compositional lithologies. The lherzolites would then churn up lower pyroxenites to cause the patchy secondary pyroxene textures between cumulate primocrysts of clinopyroxene.

In the pyroxenites, the similar primitive mantle plots to lherzolite, only with more pronounced Nb and Ti anomalies in the lithologies, are indicative of increased assimilation of crust in the lithologies than that of upper lherzolite (Fig. 4.17). Evidence for increased degrees of assimilation of crust in the more evolved pyroxenites are also seen in the steeper trends of $(La/Sm)_{cn}$ vs. Nb/Nb* in the lithologies. All the REE and trace element ratios falling within the range of the lherzolites indicate the cumulate pyroxenites are of the same primary magma source as the lherzolite. Since the lithologies have more pronounced negative Nb anomalies, they probably crystallized from a lower pulse of magma that was more crustally contaminated than the higher lherzolite-olivine websterites. Evidence for greater crustal contamination in the lithologies is also seen in the more negative ε_{Nd} content of -6.53 compared to the lherzolite-olivine websterites (Table 4.3) with contents of down to -5.54. Assimilation of crust probably first occurred with the pulsing of a pyroxenitic magma in the magma chamber. A successive pulse of lherzolite to olivine websterite would then be a new input of primitive magma into the magma chamber that either assimilated crust or retained its primitive OIB composition. In the lherzolite-olivine websterite unit, the lithologies were either crustally contaminated with first intrusion into the magma chamber and assimilation of wall rocks or represent replenishment of new magma that had little interaction with the basement crust.

On surface in the central part of the intrusion, pyroxene-porphyritic melanogabbros have a greater range in LREE which is attributed to greater variation of the lithologies with

assimilation of crust and evolution to more felsic compositions in the central part of the intrusion (Fig. 4.18). Pyroxene-porphyritic melanogabbros show the greatest degree of crustal contamination with the most pronounced negative Nb anomalies and negative Ti anomalies on primitive mantle normalized multielement plots. Increases in Nb and Ti anomalies and La/Nb ratios is attributed to greater degree of crustal assimilation with evolution of the lithologies than the lherzolites to the east in the central part of the intrusion and the lherzolites in the southern part of the intrusion. The presence of negative Zr and Hf anomalies alludes to a different source of contaminant in the lithologies than those of the southern part of the intrusion.

Melanogabbros in drill core have REE and trace element ratios that fall within the range of the lherzolites indicative of the same magma source of the lithologies (Fig. 4.19). The steeper Nb anomalies are indicative of assimilation of crust in the lithologies with felsification of lherzolite-olivine websterite and pyroxenites at the border with basement wallrock metavolcanic and iron formation lithologies. Pronounced negative Nb anomalies in the lithologies show they were crustally contaminated with evolution compared to OIB primitive mantle plot patterns of the more primitive samples ED-34 and ED-25. Negative Ti anomalies are indicative of assimilation of crust from the basement wallrocks. Small positive Eu anomalies are indicative of plagioclase crystallization in these lithologies. The general increase in abundance of all REE and trace elements in the melanogabbros is also reflective of increased evolution to more felsic compositions to form the lithologies, relative to that of the lherzolite-olivine websterites.

Granophyric gabbro in the central part of the intrusion, as represented by sample JL-043, has a similar pattern to the pyroxene-porphyritic melanogabbro and lherzolite-olivine websterite reflective of the same magma source of the lithologies (Fig. 4.20). The greater abundance in REE and trace elements in the granophyric gabbro than the peridotites is due to a greater degree

of crystallization of alkalic minerals in the unit. The negative Nb anomalies are due to crustal assimilation in the lithologies, with varying degrees as represented by varying La/Nb slopes from 2.46 in sample JL-043 to 1.60 in sample JL-022. Therefore, the lithologies also underwent crustal contamination in their crystallization histories to cause negative Nb anomalies. Field mapping by Hart et al. (2002) outlined the presence of angular fragments of country rock xenoliths in the granophyric gabbros indicating the lithologies probably assimilated the metagreywackes of the bordering Southern Sedimentary Unit in their contamination histories. Positive Ti anomalies are due to fractionation of ilmenite oxides in the lithologies. This is consistent with the lithologies containing up to 15% magnetite oxides that have exsolved ilmenite.

In the Nipigon diabase sills, differences occur in the overall primitive mantle plot patterns compared to the Kitto intrusive units due to the different source of magmatism in the lithologies (Fig. 4.21). Primitive mantle plot patterns are similar to those of the Nipigon Suite of sills from Richardson et al. (2005). The lack of negative Zr and Hf anomalies and lower La/Nb ratios from 1.64 to 1.92 show the lithologies evolved from a different source and underwent less assimilation of crust than the peridotites. The higher Th/Nb ratios with ratios increasing from 1.58 to 2.71 are reflective of assimilation of Th-rich crustal material or increased evolution in the lithologies. This is consistent with Hart et al. (2002) interpreting the diabase as assimilating Th-rich material.

5.3.2 Trace element modeling

Trace element modeling of the Kitto intrusion was undertaken in order to investigate the various primitive mantle normalized multi-element plots produced by possible scenarios of fractionation and incorporation of contaminants within the evolutionary histories of the lithologies. A primitive starting composition can be identified from MgO-rich and least crustally

contaminated samples in the lherzolite-olivine websterites. Along with highest MgO and least contamination, the primitive lithologies would have high Ni in olivine contents (provided S-saturation is not attained and Ni removed as sulphide), OIB source compositions, and lowest ε_{Nd} contents of -5.54. One primary composition is sample ED-34 which is a lherzolite higher up in DDH EK-03 that has a primitive mantle plot pattern similar to OIB with LREE enrichment over HREE and lack of negative Nb anomalies. Another primary composition is sample ED-25 which is also a lherzolite higher up in DDH EK-03. Both of these lithologies texturally represent unaltered lherzolites with both cumulate olivine and pyroxene mineralogy and poikilitic orthopyroxene consistent with lherzolites higher up in the drill holes. Since more Th-enrichment was necessary to generate primitive mantle plots similar to the lherzolite-olivine websterites with fractionation or the addition of a contaminant, sample ED-25 was chosen as the starting composition as it has more Th. However, ED-34 is used as the starting composition for fractionation with addition of Quetico contaminant because Quetico metasedimentary rock is inferred to have caused Th-enrichment to a more primitive OIB-like source. Mineralogy of sample ED-25 is that of lherzolite with 45% olivine, 5% plagioclase, 30% clinopyroxene and 20% orthopyroxene. Modeling of the lithologies was performed with the parent composition of ED-25 of the above percent mineralogy. Modeling of the compositions of the lherzolite-olivine websterites was done with 25% fractionation which is comparable to modeling results produced in the Seagull intrusion at 20% fractionation (Heggie, 2005). Also up to 20% crustal contaminant was input for AFC (assimilation fractional crystallization) processes similar to 15% contaminant used for modeling in the Seagull intrusion (Heggie, 2005). 20% crustal contamination was also used since it is inferred that the magma first intruded mafic metavolcanic rocks at depth possibly at 5% crustal contamination, and successively intruded mafic

metavolcanic and iron formation at 15% crustal contamination at shallower depths to cause the LREE enriched contamination patterns seen in the primitive mantle plots of the lithologies.

In the southern part of the intrusion, with 25% simple fractionation from a parent composition of ED-25, the final composition produced by modeling has only slightly negative Nb anomalies, a lower La composition in proportion to adjacent elements, and very slight Th enrichment (Fig. 5.2). The negative Nb anomalies are not pronounced enough, compared to the primitive mantle plots of the lherzolite-olivine websterite, and require the addition of continental crust. The La composition is low compared to that of the lherzolite-olivine websterite patterns from DDH EK-02. Also the finishing composition of ED-18 plots exactly within the compositions produced by fractionation at 45%. 45% fractionation in the Kitto intrusion is not realistic given the limited change in SiO_2 in the rocks to only mafic compositions, therefore the higher trace elements observed in ED-18 must have been produced by crustal contamination.

In order to determine the contamination history of the intrusion, distinction must be made between whether the intrusion was contaminated by a single event (i.e., undergo simple mixing) or whether it was continuously contaminated with fractionation (i.e., undergo assimilation fractional crystallization). With simple mixing of 90% primary composition ED-34 with 10% Quetico metasedimentary rock contaminant, the primitive mantle plot produced displays low La and low abundance of all the other trace elements, while Th is higher than the primitive mantle plots of the lithologies (Fig. 5.3). Since Th is too high compared to that seen in the intrusive units, the Quetico contaminant was probably not added by just simple mixing and was probably added through AFC. Also plotted are iron formation and mafic metavolcanic that have similar La and trace element abundance patterns, except for Th, as the Quetico contaminated crust (Fig. 5.3).

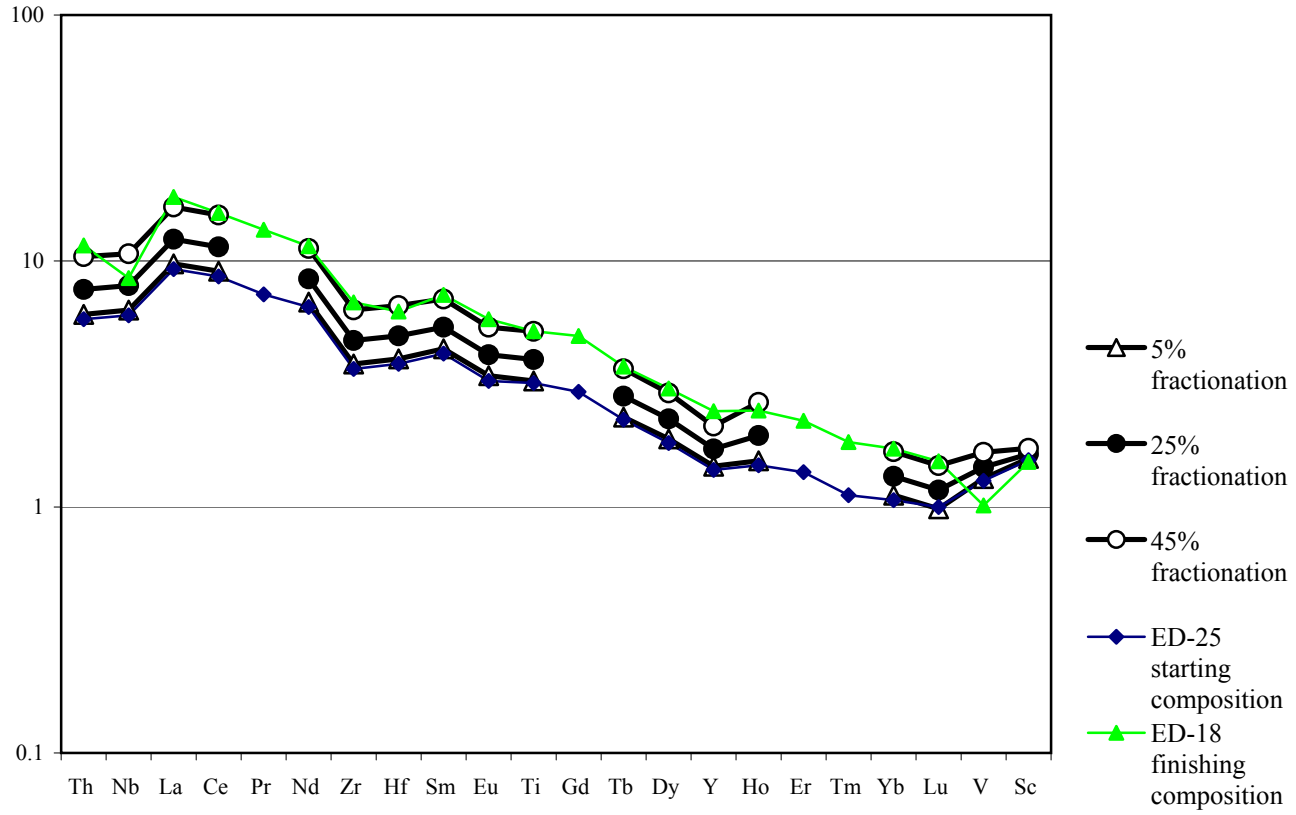

Figure 5.2: Trace element modeling of lherzolite from fractional crystallization with percentage of fractionation on the side. Primitive mantle normalizing values of McDonough and Sun (1995).

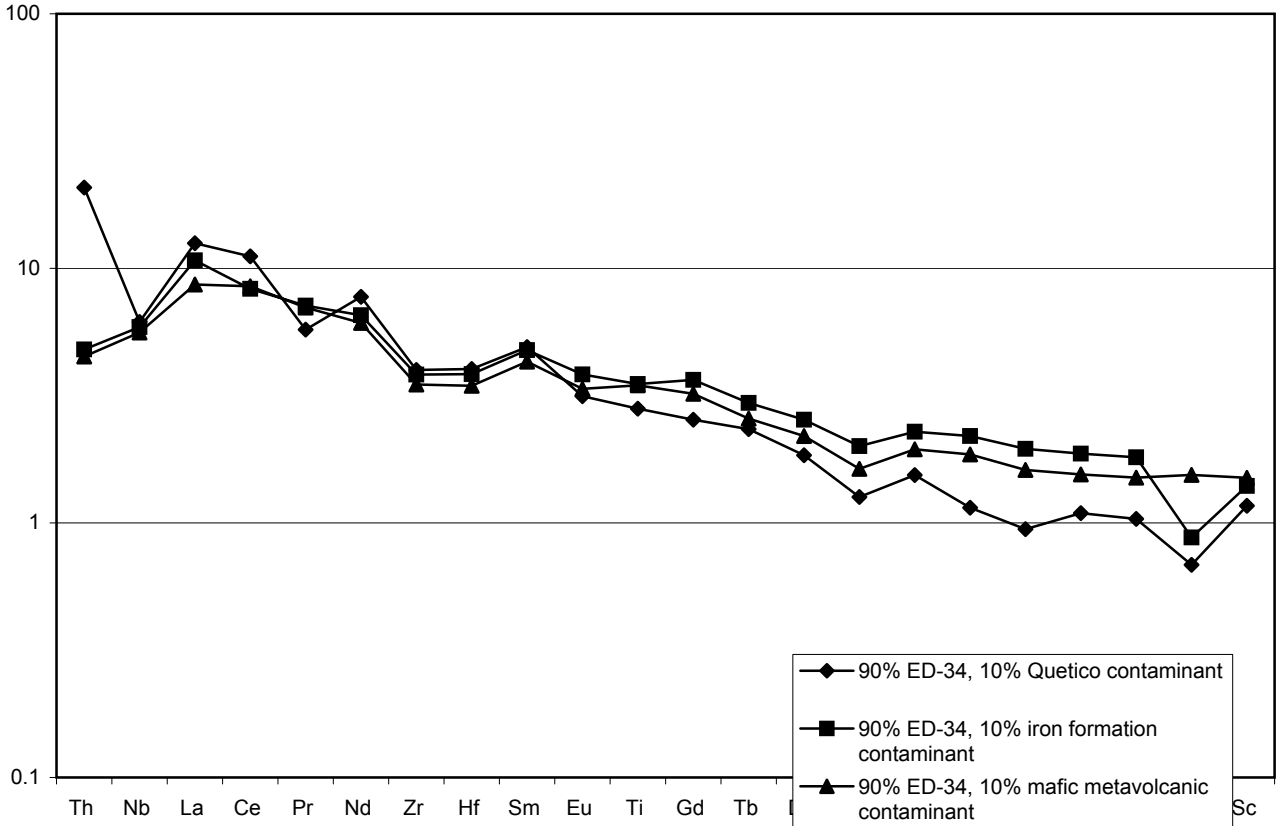

Figure 5.3: Trace element modeling of lherzolite from simple mixing of Quetico, iron formation and mafic metavolcanic contaminants. Primitive mantle normalizing values of McDonough and Sun (1995).

For AFC processes, Quetico metasedimentary rock is a possible contaminant since the Kitto intrusion, in the southern part of the intrusion, intrudes along the Blackwater River Fault which is bounded to the south by Quetico metasedimentary rock. With addition of 20% Quetico continental crust contaminant from the more primitive ED-34 and AFC fractionation at 25%, the final composition produced has very large Th/Nb and a high La composition (Fig. 5.4). The Th composition is too high compared to that of the lherzolite-olivine websterite patterns, but the La composition is similar. In addition, the remaining trace elements plotted at 25% fractionation are below that produced by sample ED-18. Therefore, more contamination by a different contaminant and less than 20% contamination of Quetico metasedimentary rock is needed in order to produce patterns similar to the lherzolite-olivine websterites. With addition of 5% Quetico contaminant at 25% fractionation, primitive mantle plot patterns produced are only similar to the lherzolite-olivine websterite with the amount of Th content that is almost equal to the La content (Fig. 5.5). However, more La enrichment and enrichment of all the other trace elements is needed to produce patterns as sample ED-18. Southern Volcanic Unit (SVU) mafic metavolcanic rock and banded iron formation are also both possible contaminants since these lithologies are basement rock to the intrusion. With addition of 20% mafic metavolcanic contaminant at 25% fractionation from a parent composition of ED-25, the final composition produced has La enrichment similar to the lherzolite-olivine websterite patterns, but only slight Th enrichment (Fig. 5.6) and the other trace element abundances plotting just below sample ED-18. Up to 20% contamination of mafic metavolcanic and iron formation is used since it is inferred that the intrusion was contaminated primarily by Quetico and SVU mafic metavolcanic at depth, and then successively contaminated by mafic metavolcanic and iron formation where the intrusion is mineralized at the Phoenix occurrence. Also enough contamination by these two

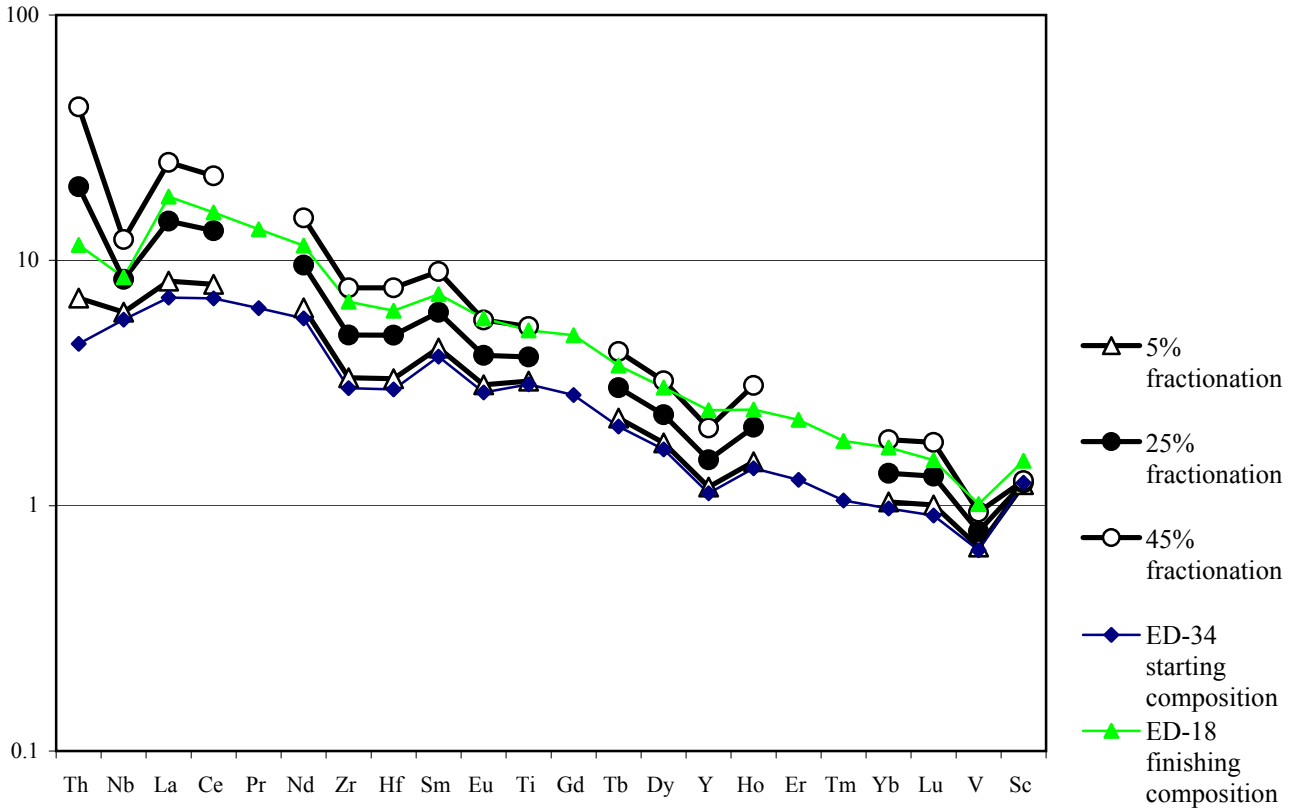

Figure 5.4: Trace element modeling of lherzolite from 20% contamination of Quetico metasedimentary rock with percentage of fractionation on the side. Primitive mantle normalizing values of McDonough and Sun (1995).

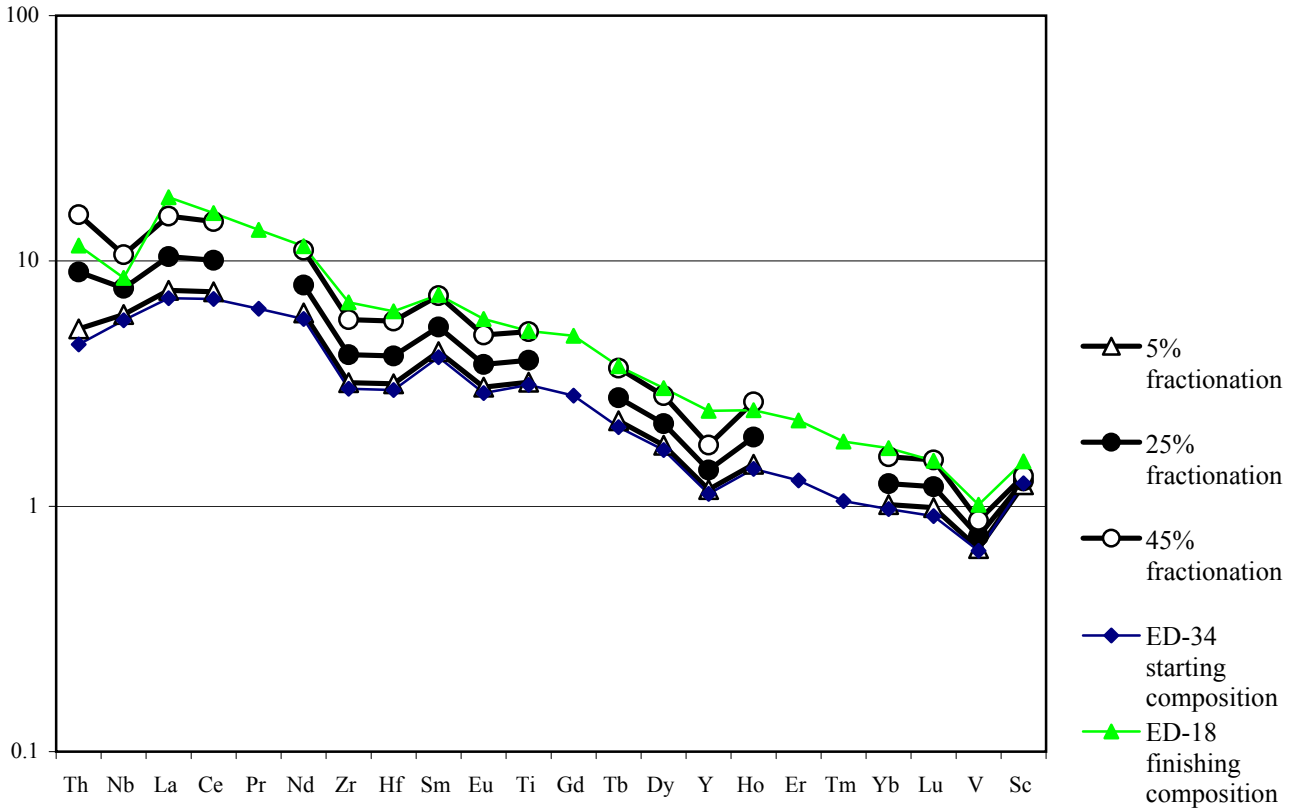

Figure 5.5: Trace element modeling of lherzolite from 5% contamination of Quetico metasedimentary rock with percentage of fractionation on the side. Primitive mantle normalizing values of McDonough and Sun (1995).

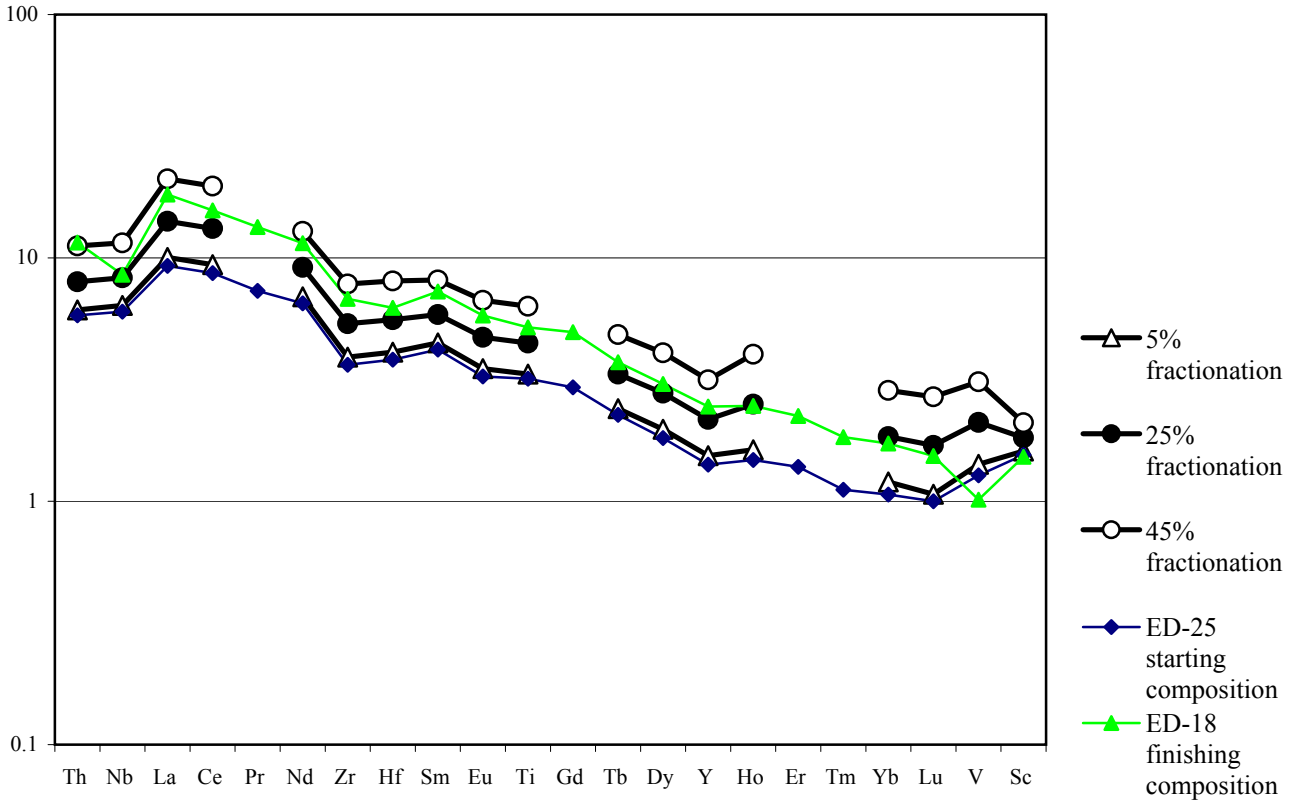

Figure 5.6: Trace element modeling of lherzolite from 20% contamination of SVU mafic metavolcanic rock with percentage of fractionation on the side. Primitive mantle normalizing values of McDonough and Sun (1995).

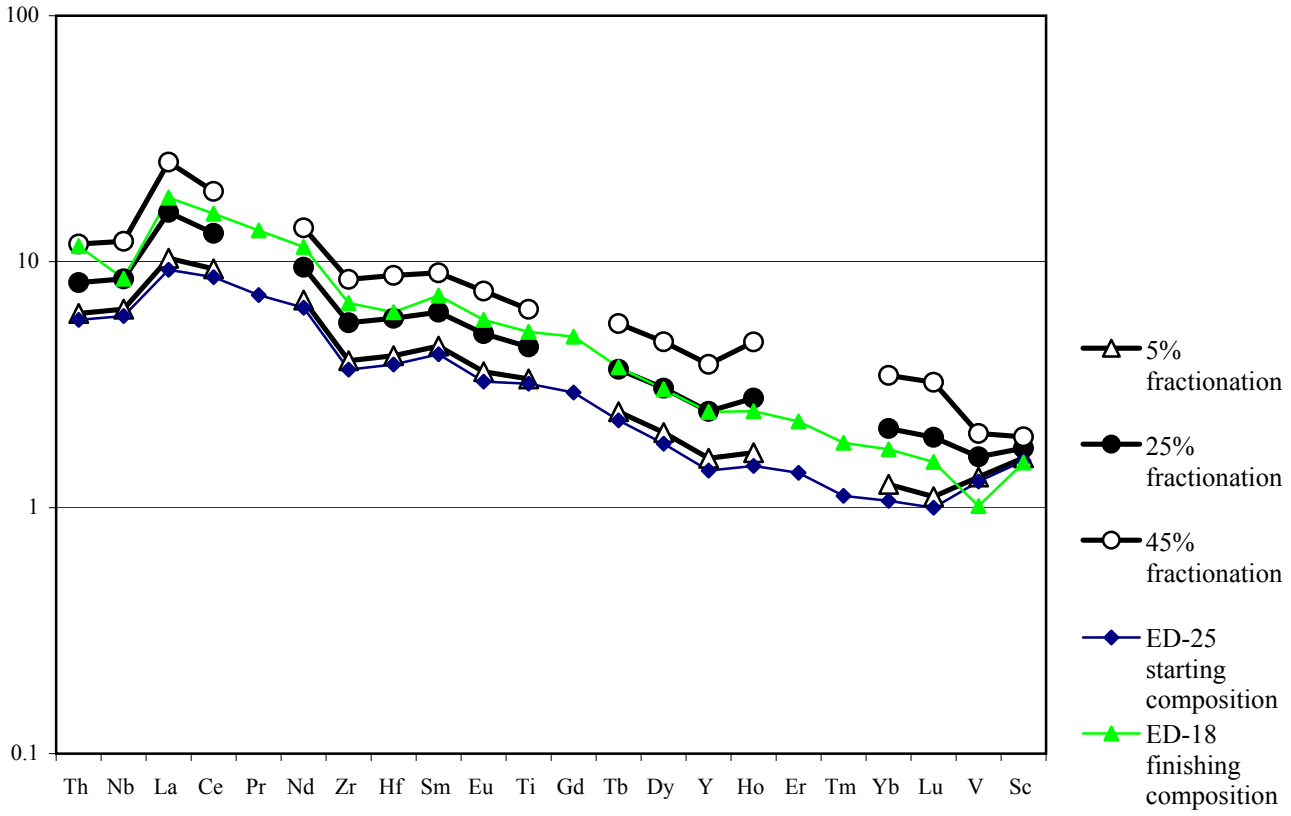

Figure 5.7: Trace element modeling of lherzolite from 20% contamination of banded iron formation with percentage of fractionation on the side. Primitive mantle normalizing values of McDonough and Sun (1995).

components is needed to cause the La enrichment while lower Th ratios seen in the lherzolite-olivine websterite primitive mantle plots. With addition of 20% iron formation contaminant at 25% fractionation from ED-25, the final composition produced has even higher La enrichment, the same amount of the rest of the trace elements to ED-18, but only slight Th enrichment (Fig. 5.7). La is more enriched compared to adjacent Ce and Pr elements. With continued fractionation and addition of mafic metavolcanic and iron formation contaminants, negative Zr and Hf anomalies become less pronounced in contrast with them being consistently anomalous with addition of Quetico assimilant. From the lherzolite-olivine websterites to more fractionated pyroxenites and melanogabbros, Zr and Hf anomalies become less pronounced (Figs. 4.14 and 4.17). There is similar character among Nb, Zr and Hf anomalies between the modeled and actual lherzolite-olivine websterites with addition of mafic metavolcanic and iron formation contaminants, however, there is only slight enrichment in Th in the modeled compositions. The negative Nb anomalies, less pronounced Zr and Hf, enriched La, and greater abundance in the other trace elements probably indicate these basement lithologies were added as continental crust components to the intrusive units in their fractionation histories.

Since Th enrichment is necessary to produce primitive mantle plot patterns similar to the lherzolite-olivine websterites, it is suggested that the intrusive units first underwent contamination by 5% basement Quetico metasedimentary rock and mafic metavolcanic and then assimilated basement mafic metavolcanic and iron formation at higher crustal levels to produce La enrichment in the primitive mantle plot patterns. Isotopic modeling performed by Hollings et al. (2007b) of 5% contamination of Quetico metasedimentary rock on the Jackfish Sills in the West Nipigon Embayment produced results with ε_{Nd} contents of -5, since the Quetico metasedimentary rocks have highly negative ε_{Nd} contents or -16 to -23. The lithologies would

have been contaminated by Quetico metasedimentary rock and mafic metavolcanic rocks at deeper levels of the crust (Hollings et al., 2007b) and then by mafic metavolcanic and iron formation lithologies higher up in stratigraphy to become sulphur-saturated and precipitate Ni-Cu-PGE sulphides. Evidence for the lithologies being contaminated by mafic metavolcanic and iron formation lithologies higher up in stratigraphy can be seen in trace element modeling of iron formation contaminant on source composition ED-03. Sample ED-03 represents a lherzolite-olivine websterite that has Th enrichment probably attained by assimilation of Quetico metasedimentary rock with depth, but the La enrichment seen in lherzolite-olivine websterites such as ED-18 is absent. Modeling of 20% contamination of iron formation with fractionation at 25% on sample ED-03 produces an end composition with the Th enrichment, La enrichment and Nb depletion seen in sample ED-18 (Fig. 5.8). This confirms the mafic metavolcanic and iron formation lithologies as being later contaminants on the lherzolite-olivine websterites since there is lack of La enrichment with contamination by only a Quetico contaminant.

Sibley Group quartz sandstone is a possible contaminant for the intrusion since it occurs as basement rock in DDH EK-03, EK-04 and EK-01 and also as xenoliths and skarnified lithologies within the intrusive units in DDH EK-02 and EK-05-01 (Fig. 3.2b, 3.3 and Appendix 1). Up to 20% contamination by Sibley Group sandstone is needed to produce primitive mantle plot patterns similar to the lherzolite-olivine websterites at 25% fractionation. Although in actuality, since the Sibley Group sandstone is a thin lithology at higher crustal levels, there was probably a lower amount of contamination by this component. With addition of 20% Sibley Group sandstone continental crust contaminant at 25% fractionation from ED-25, the final composition produced has slightly negative Nb anomalies, a lower La composition in proportion to adjacent elements similar to that produced from only simple fractionation, and slight Th

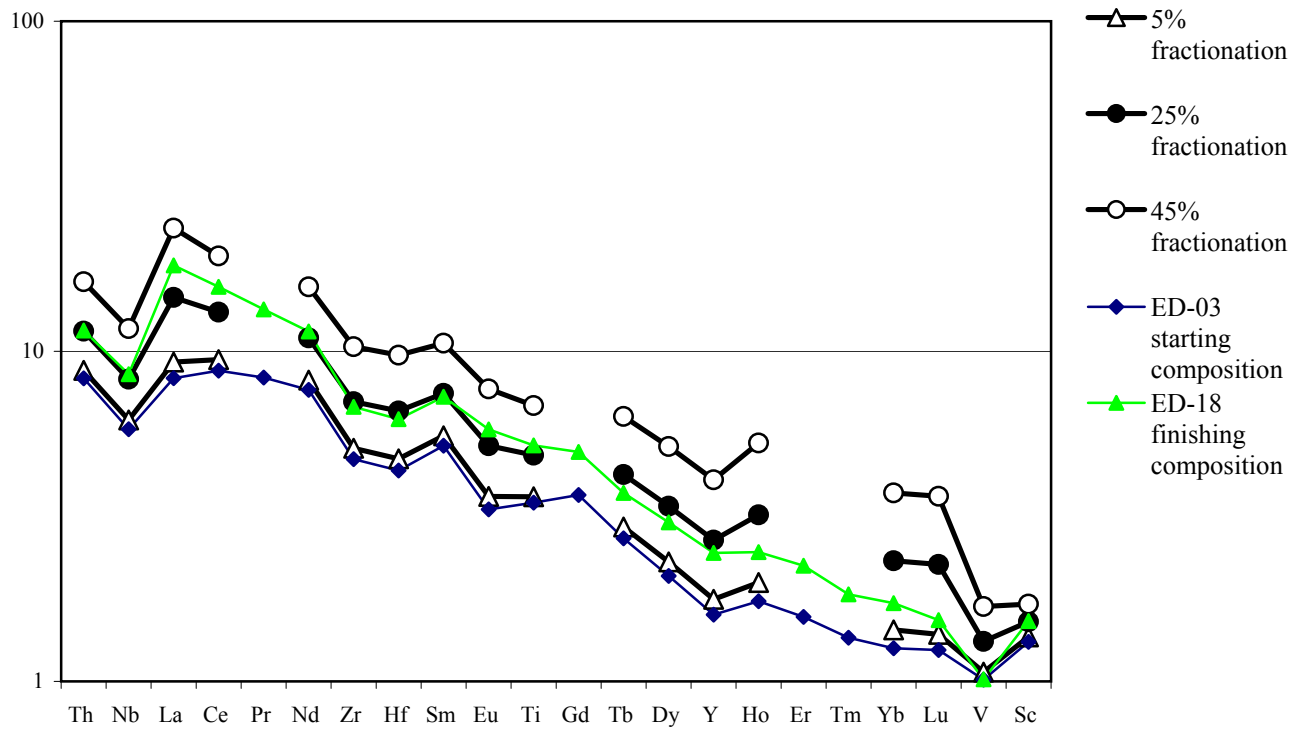

Figure 5.8: Trace element modeling of lherzolite from 20% contamination of banded iron formation from starting composition sample ED-03 with percentage of fractionation on the side. Primitive mantle normalizing values of McDonough and Sun (1995).

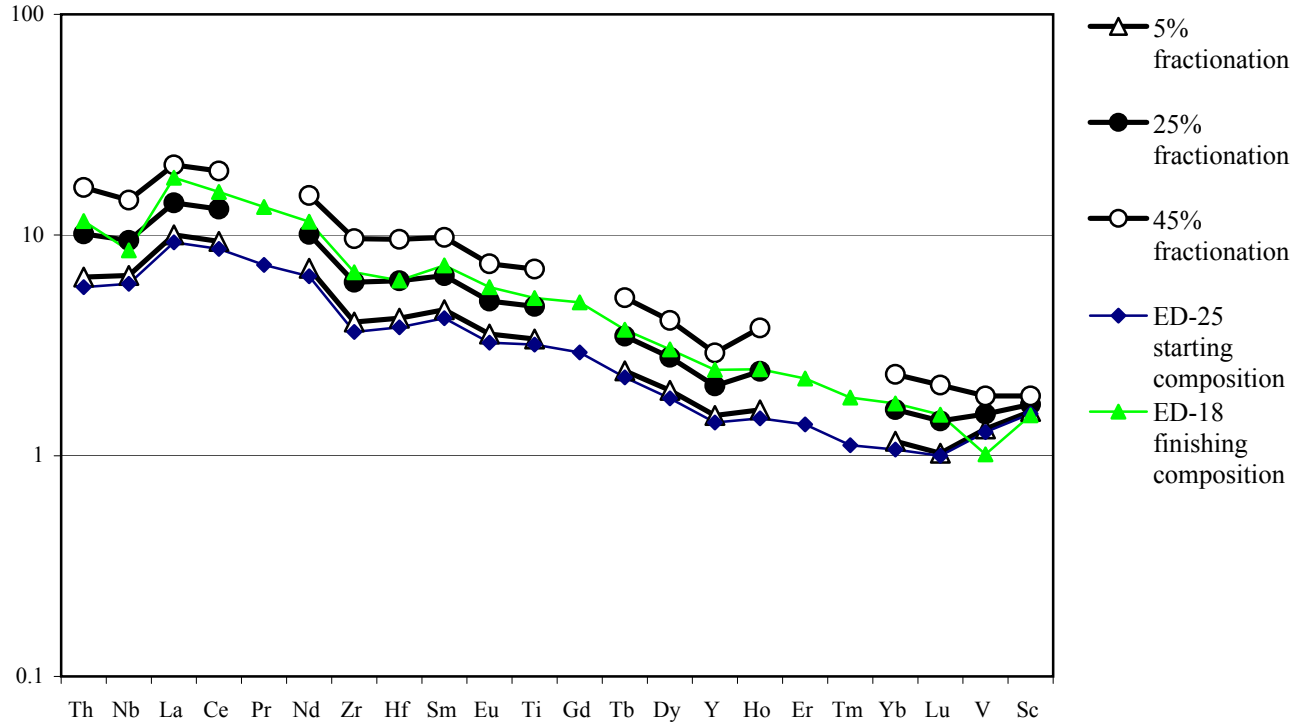

Figure 5.9: Trace element modeling of lherzolite from 20% contamination of Sibley quartz sandstone with percentage of fractionation on the side. Primitive mantle normalizing values of McDonough and Sun (1995).

enrichment (Fig. 5.9). Sibley Group sandstone contaminant produces lower La and adjacent element compositions in comparison to the actual lherzolite-olivine websterites. Although there is Th enrichment, it is low in comparison to that produced with Quetico contaminant, and is low in comparison to the primitive mantle plots of the lithologies. Therefore, since there is only low Th enrichment with the addition of Sibley Group sandstone, lack of La enrichment, less pronounced negative Nb anomalies, and the fact that a smaller amount of the lithology was probably assimilated, the Sibley Group sandstone was also probably not a strong crustal contaminant to the lherzolite-olivine websterites. The Sibley Group sandstones only occur at shallow depths which preclude them from being contaminants for the Kitto intrusive units with depth such as that of the Quetico contaminant or basement mafic metavolcanic and iron formation. Evidence for the lithologies being contaminated with depth would be the lack of variation of ε_{Nd} contents of between -5 and -6 for all the lithologies in drill core. Also the high ε_{Nd} contents of up to -6.53 in pyroxenite give support for the lithologies being contaminated by contaminants with lower ε_{Nd} contents such as the Quetico metasedimentary rocks and basement SVU mafic metavolcanic and iron formation lithologies. However, the Sibley Group sandstone was still assimilated as seen by xenoliths and rafts of the lithology in drill core.

In the central part of the intrusion, pyroxene-porphyritic melanogabbros have strongly negative Nb anomalies indicative of crustal assimilation, but also strongly negative Zr and Hf anomalies that are produced unlike the lithologies in drillcore. Since Quetico metasedimentary rock assimilant produces negative Zr and Hf anomalies when added to the fractionation histories of the lithologies, it would seem to be a possible contaminant. However, there are no Quetico basement rocks at the central part of the intrusion. A possible crustal assimilant would be the metagreywacke rock of the Southern Sedimentary Unit, since the intrusive units intrude along

the Princess Lake Fault which is bounded by the SSU to the north. With addition of a 20% SSU metagreywacke sample (taken by Hart et al. (2002)) at 25% fractionation from a parent composition of ED-25, results produced higher Th ratios than with iron formation, mafic metavolcanic rocks and Sibley Group sandstone; and there is La enrichment; more pronounced negative Nb anomalies and negative Zr and Hf anomalies (Fig. 5.10). The higher Th ratios, La enrichment and pronounced negative Nb anomalies probably indicate the SSU metagreywacke was a contaminant in the fractionation histories of the pyroxene-porphyritic melanogabbro and lherzolite-olivine websterites. Iron formation from the central part of the intrusion (sample JL-046), when added as 20% crustal contaminant at 25% fractionation from ED-25, produced similar primitive mantle plot patterns with even greater La enrichment, and negative Zr and Hf anomalies seen in the pyroxene-porphyritic melanogabbros that were not modeled with iron formation and mafic metavolcanic lithologies from the DDH samples. However, there is only slight Th enrichment, therefore causing the Nb anomalies to be less pronounced (Fig. 5.11). Since there is La enrichment and negative Zr and Hf anomalies with the addition of iron formation and probable mafic metavolcanic contaminants, these were probable contaminants to the lithologies. Another possible contaminant to pyroxene-porphyritic melanogabbro would be Sibley Group sandstone since it was found as a large raft or xenolith in DDH EK-05-01 within the lherzolite (Fig. 5.12). Sibley Group sandstone, when added as a contaminant, also produces Th enrichment, but not La enrichment and only slight negative Nb anomalies (Fig. 5.9). The Th enrichment with addition of Sibley Group sandstone is lower than the Th enrichment produced with metagreywacke contaminant. So this, along with low La enrichment, precludes the Sibley Group sandstone as a strong contaminant in the lherzolite and pyroxene-porphyritic melanogabbros from the central part of the intrusion. Also, the Sibley Group sandstones were

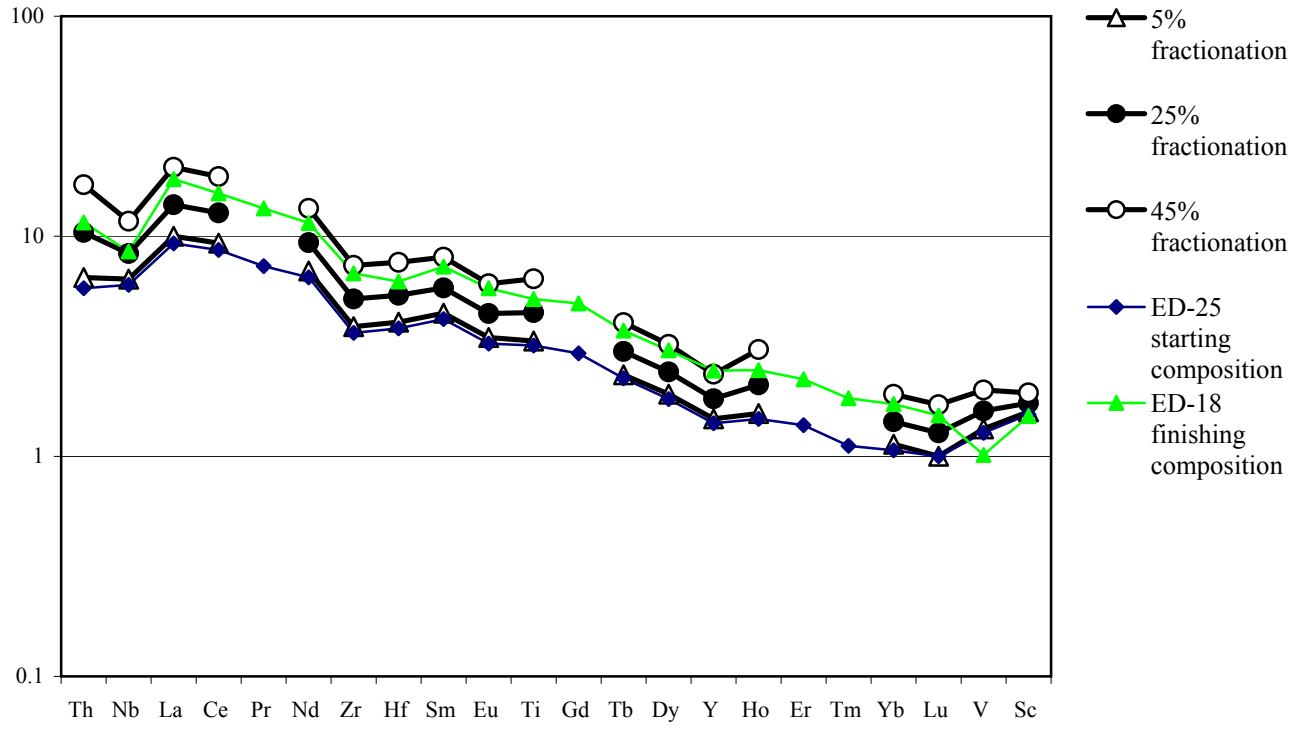

Figure 5.10: Trace element modeling of lherzolite from 20% contamination of SSU metagreywacke with percentage of fractionation on the side. Primitive mantle normalizing values of McDonough and Sun (1995).

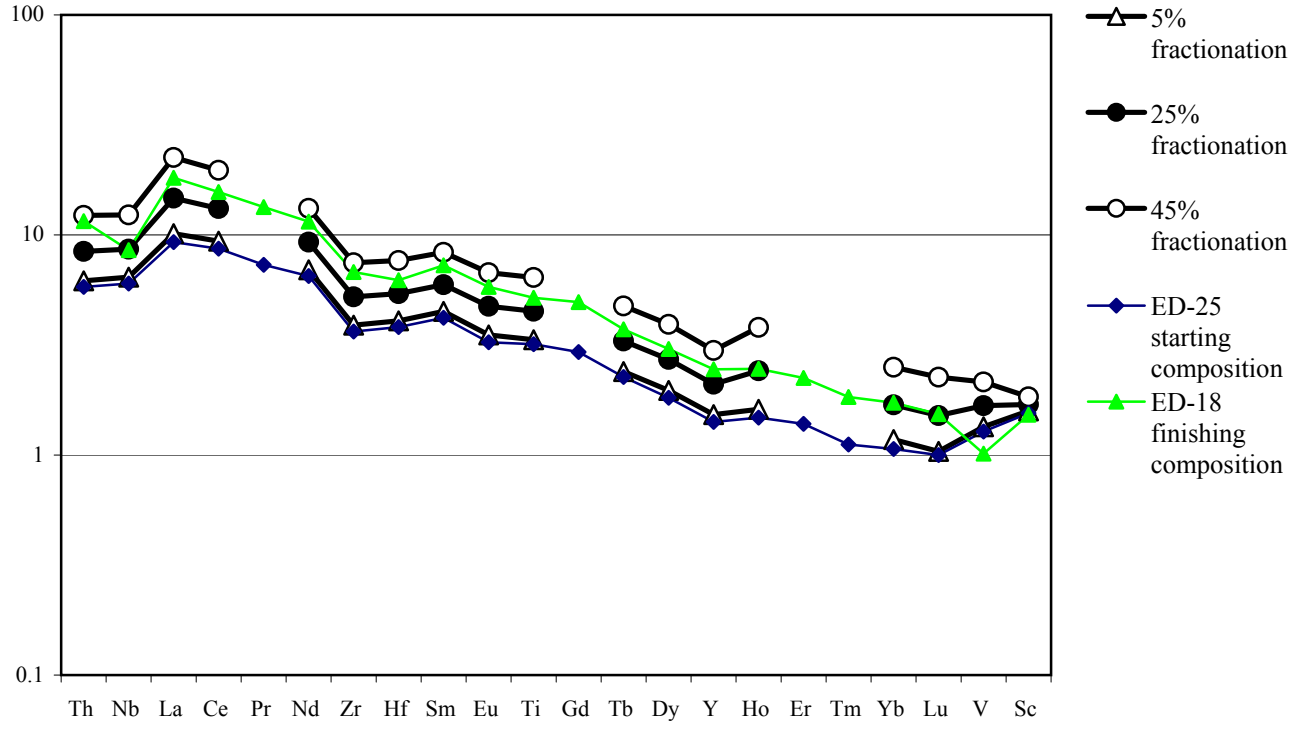

Figure 5.11: Trace element modeling of lherzolite from 20% contamination of iron formation sample JL-046 with percentage of fractionation on the side. Primitive mantle normalizing values of McDonough and Sun (1995).

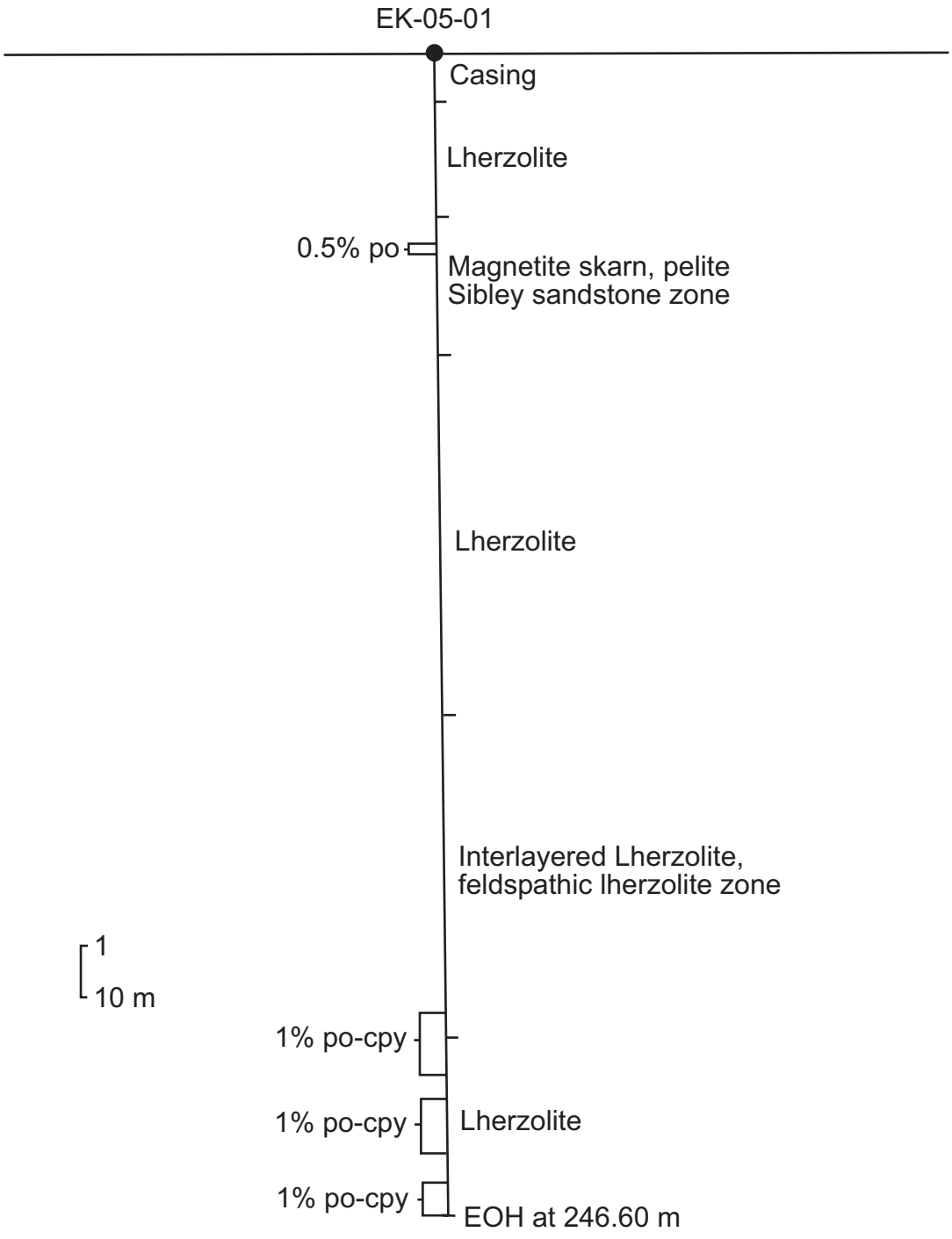

Figure 5.12: Drill hole section of DDH EK-05-01. In the lower MgO-rich units, there is disseminated pyrrhotite-chalcopyrite mineralization from 180 m to the end of hole.

not strong contaminants due to the Sibley units having lower ε_{Nd} contents of -5 compared to contents of up to -6.53 observed in the drill core lithologies (Hollings et al., 2007b; Table 4.3). Therefore, crustal contamination in the central part of the intrusion probably occurred with a mixture of SSU metagreywacke and mafic metavolcanic and iron formation contaminants in the evolutionary histories of the lithologies. However, the Sibley unit was still assimilated as it is present as a large raft in drill core.

5.3.3 $(La/Sm)_{cn}$ vs. Nb/Nb ratios*

$(La/Sm)_{cn}$ vs. Nb/Nb* diagrams show interpreted trends of crustal contamination in the drill core samples and in surface samples. In these samples, the degree of LREE fractionation is measured by $(La/Sm)_{cn}$, which is the degree of LREE enrichment over MREE normalized to chondrite. La/Sm ratios have been used to measure crustal contamination in other magmatic systems such as the Raglan komatiites and sills of the Cape Smith Belt and the Talnakh intrusions of Noril'sk (Lesher, 2005). The degree of Nb fractionation is measured by Nb/Nb*, which is the Nb abundance relative to adjacent elements on a primitive mantle normalized multielement plot. Generally with increased LREE fractionation, there is decreased amount of Nb due to crustal assimilation to conserve the amount of Nb in the rocks.

In the drill core samples, two geochemical trends of decreasing Nb/Nb* with increasing $(La/Sm)_{cn}$ are distinguished and identified as two contamination trends or histories in the rocks (Fig. 5.13). The first contamination trend is a straight line that has a steeper slope and contains melanogabbro, vari-textured pyroxenite, pyroxenite to lherzolite-olivine websterites. The steeper decrease in Nb with increasing LREE fractionation, and also lower amounts of Nb indicate that Nb was conserved in the fractionation histories of these lithologies, and they were more contaminated. Basement metabasalts are plotted on this linear trend, which is supportive of the

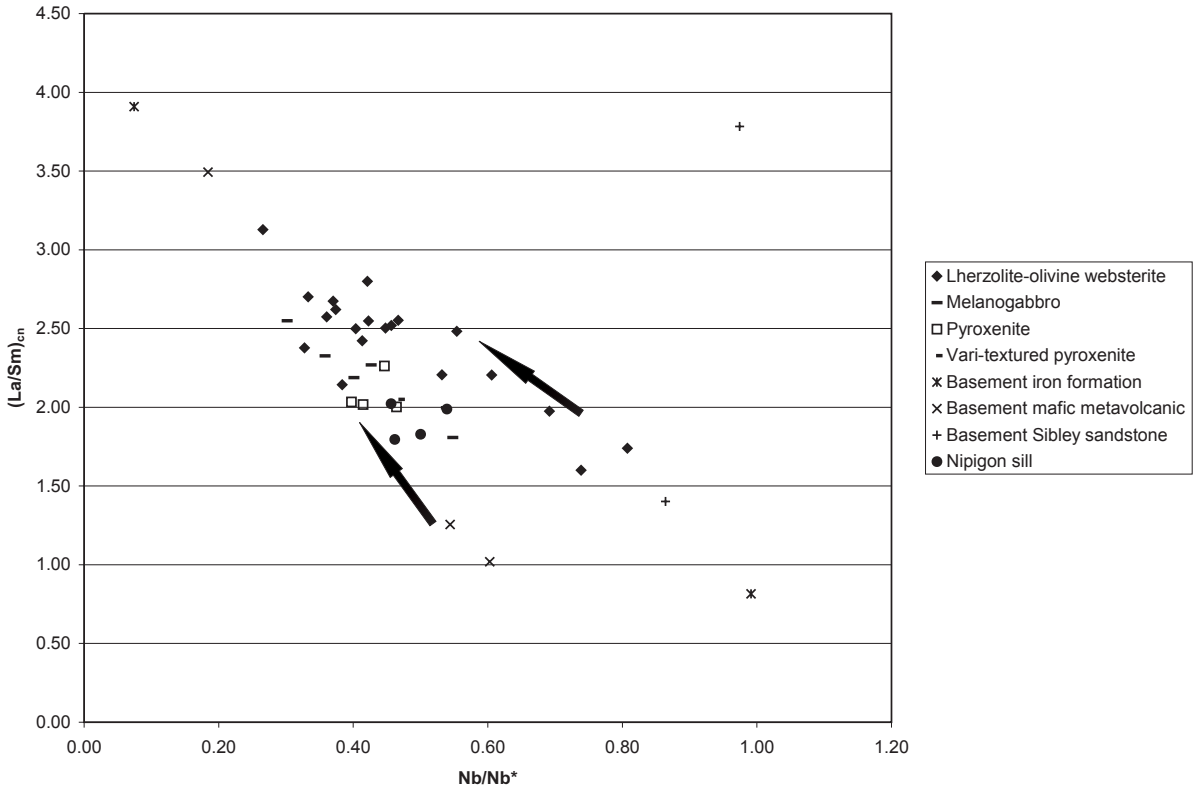

Figure 5.13: Plot of $(La/Sm)_{cn}$ vs. Nb/Nb* for DDH samples. Arrows indicate two trends of increasing $(La/Sm)_{cn}$ with decreasing Nb/Nb*.

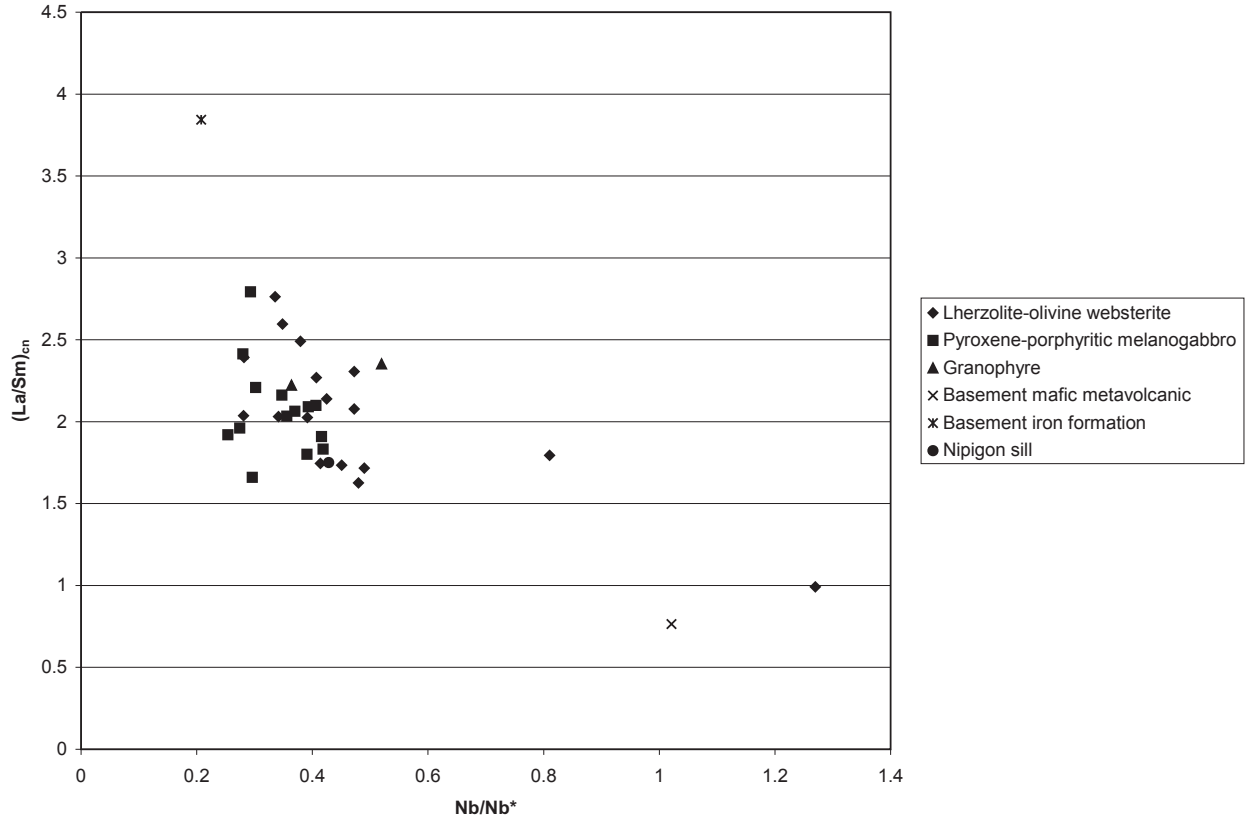

Figure 5.14: Plot of $(La/Sm)_{cn}$ vs. Nb/Nb* for surface samples.

lithologies being contaminants in the contamination histories of the intrusive units. However, the basement lithologies plotted at both ends of the trend is suggestive that the basement lithologies with only high $(La/Sm)_{cn}$ and low Nb/Nb* were used as contaminants to the intrusive units to cause the increase in $(La/Sm)_{cn}$ and decrease in Nb/Nb* in the lithologies. The melanogabbros follow the same contamination trend of decreasing Nb/Nb* with increasing $(La/Sm)_{cn}$ as the pyroxenites. This probably indicates that the fractionation histories of the lithologies are related (Fig. 5.13). The lithologies would have related fractionation histories since both pyroxenite and melanogabbro would be contaminated by mafic metavolcanic to produce the same enrichment in LREE and depletion in Nb as it is conserved in the rocks.

The second contamination trend is a straight line that has a shallower slope and contains lherzolite-olivine websterites (Fig. 5.13). These lithologies have a shallower decrease in Nb with increased LREE fractionation and generally have higher amounts of Nb, indicating more Nb was fractionated and they were less contaminated than the lithologies following the first trend. Iron formation lithologies lie on this trend, giving support to the primary lherzolite-olivine websterites being contaminated by the iron formation lithologies within their fractionation histories. Though, again, the basement lithologies plotted at both ends of the trend is suggestive that only the basement lithologies with high $(La/Sm)_{cn}$ vs. low Nb/Nb* were used as contaminants to the intrusive units. One Sibley Group sandstone plots on the iron formation trend while another plots off the trend indicating that basement Sibley Group sandstone was another contaminant in the contamination histories of the intrusive units.

In the surface samples, the lithologies generally have decreased amounts of Nb with increased LREE fractionation as displayed by a large cluster of the lithologies with low Nb/Nb* ratios from 0.25 to 0.49 at high $(La/Sm)_{cn}$ ratios from 1.62 to 2.79 (Fig. 5.14). Within the large

cluster, the pyroxene-porphyritic melanogabbros plot at higher slopes of decreased Nb with LREE fractionation, indicating they were more contaminated than the other lithologies. The lherzolite-olivine websterite are also largely contaminated as they plot within the cluster, but at lower amounts than the pyroxene-porphyritic melanogabbro as shown by higher Nb at lower LREE fractionation. Plots of basement iron formation and metabasalt plotted on the geochemical trends shows that both lithologies were involved in the contamination histories of the intrusive units.

5.3.4 Rb/La and Ba/Th variation

Variation of Rb/La and Ba/Th ratios can show that there was crustal contamination in an intrusive suite since Rb and Ba elements are derived from continental crustal components, and are incompatible with cumulus phase minerals (Zhong et al., 2004). Generally, in the Kitto intrusives, the higher Rb/La or Ba/Th displayed, the more the samples are contaminated or show contamination by a Rb or Ba-rich component. This is similar to the Xinjie Intrusion from Zhong et al (2004) where maximum Rb/La ratios at the bottom of the marginal unit in the Xinjie Intrusion are also interpreted to be due to crustal contamination from bordering wallrocks with the pulsing of that unit. As shown by the geochemistry of the surface samples, continental crust contamination occurs in the lherzolite-olivine websterite and pyroxene-porphyritic melanogabbros from the southern and central parts of the intrusion. The largest Rb/La ratios are in the lherzolite-olivine websterites at the Phoenix occurrence with maximum Rb/La ratios of 14.02 at JL-071 and 5.19 at JL-073 (Fig. 5.15). Lherzolite in the central part of the intrusion also has a maximum ratio of 5.40 ppm Rb/La at JL-029. Within the pyroxene-porphyritic melanogabbro, maximum Rb/La ratios range from 3 to 4 ppm.

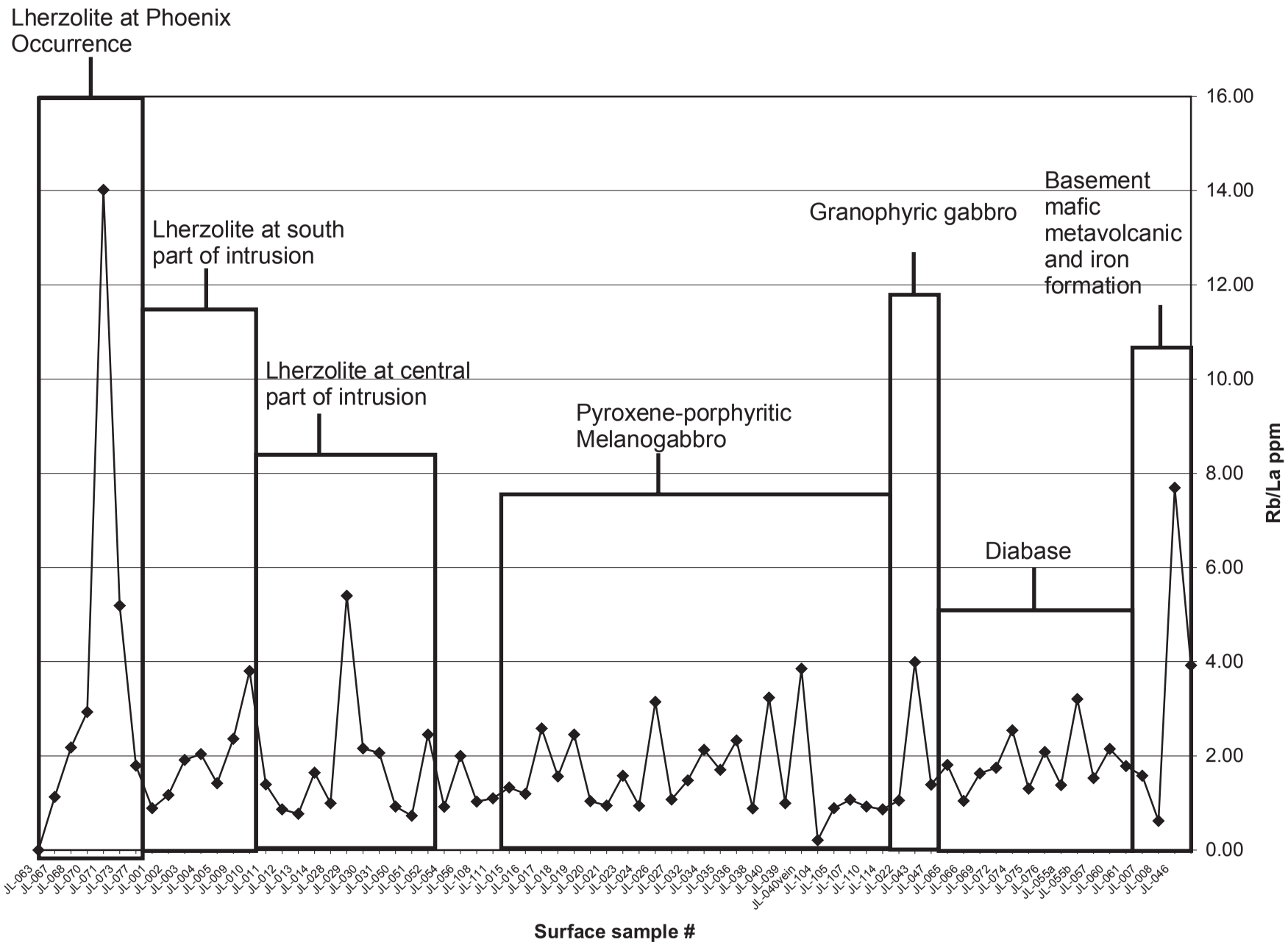

Figure 5.15: Surface sample Rb/La variation from the southern, central and northern parts of the Kitto Intrusion.

In DDH EK-02, Rb/La shows a general contamination of continental crust in the lherzolite from 0 to 180 m (Fig. 5.16). Rb/La then maximizes at 185 m and has the largest maximum ratio of 5.63 ppm at 199 m within the sulphidized olivine websterite unit. From 208 to 305 m, Rb/La ratios remain at background ratios of close to 1 Rb/La in the pyroxenite to melanogabbro. At the basement iron formation from 311 to 327 m, the Rb/La ratios are really low until they have their largest maximum ratios of 8.21 ppm and 5.98 ppm in the basement mafic metavolcanic rock from 330 to 344 m. The large maximum Rb/La ratios in the sulphidized olivine websterite and general increase in Rb/La ratios throughout the lherzolite-olivine websterites compared to the lower pyroxenite to melanogabbro lithologies show that these lithologies preferentially assimilated continental crust material compared to the lower pyroxenite. The maximum Rb/La ratio at 199 m shows there was a second pulse of magma that intruded and was contaminated with continental crust to cause the magma to be saturated with sulphur and precipitate sulphides at that zone. The maximum Rb/La ratios in the basement mafic metavolcanic provide Rb/La ratios necessary for that continental crust component. An alternate lithology that could supply Rb is Quetico metasedimentary rock with a ratio of 2.39 ppm for average Quetico crust. Evidence for mineralization with this second pulse of magma is the basal mineralization located at the bottom of the lherzolite-olivine websterite at that level. Correlation of maximum Rb/La ratios with the basal mineralization that occurred with a new pulse of magma is similar to the elevated Rb/La ratios in the pyroxenite unit of the Xinje Intrusion that were the result of a new pulse of contaminated magma that mixed with the magma of the lower peridotites and precipitated PGE metals at that horizon (Zhong et al., 2004).

Ba/Th ratios also show continental crust contamination in the lithologies down DDH EK-02 (Fig. 5.17). From 22 to 116 m, lherzolite has background Ba/Th ratios of 196 and 152 ppm.

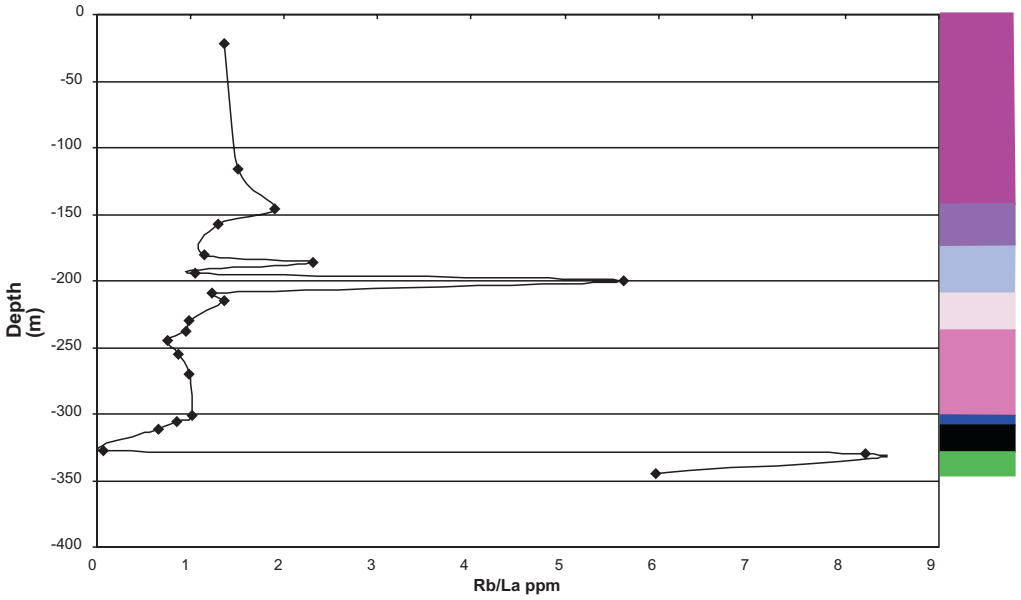

Figure 5.16: Plot of Rb/La ppm vs. depth (m) for DDH EK-02.

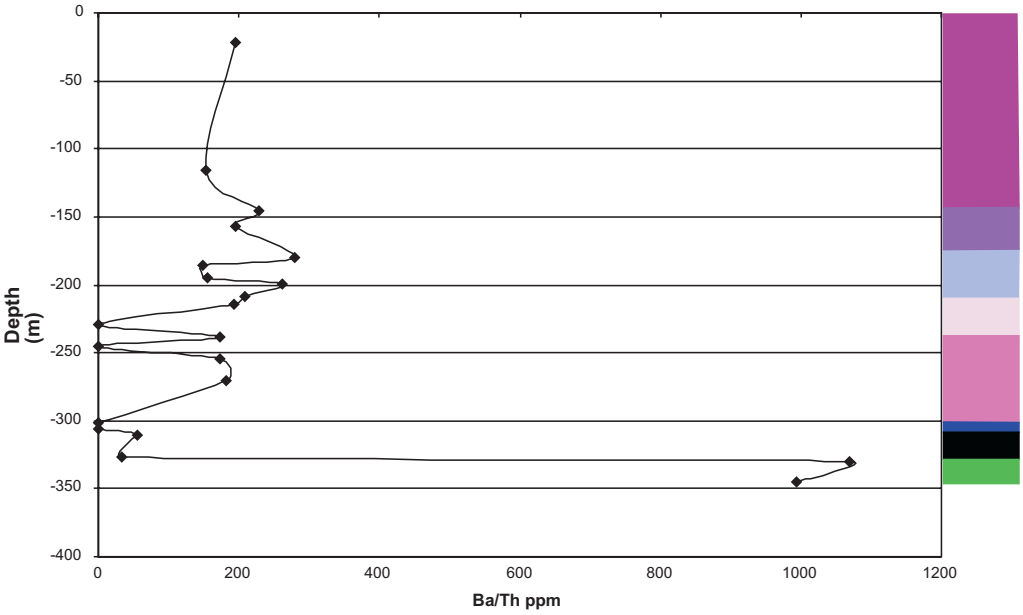

Figure 5.17: Plot of Ba/Th ppm vs. depth for DDH EK-02.

An increase in Ba/Th to 228 ppm occurs in the olivine websterite indicative of crustal contamination. Maximum ratios of Ba/Th occur within the sulphidized olivine websterite unit, with 279 ppm at 180 m and 262 ppm at 199 m. A geochemical break then occurs at 208 m at contact with lower pyroxenite to melanogabbro lithologies. From 208 to 270 m, background Ba/Th ratios range from 207 to 173 ppm. Basement iron formation has low Ba/Th ratios of 55 and 32 ppm while basement mafic metavolcanic lithologies have maximum Ba/Th ratios of 1068 and 994 ppm. The lack of large maximum Ba/Th ratios in the intrusive units show that the units did not preferentially incorporate Ba from continental crust, compared to the high Rb ratios. However, the general increase of Ba/Th in the olivine websterite compared to the lower pyroxenite shows that a second pulse of magma of olivine websterite occurred that was more crustally contaminated with Ba than the lower pyroxenite to melanogabbro lithologies. The maximum Ba/Th ratios in the basement mafic metavolcanic provide Ba/Th ratios necessary for that continental crust component.

5.3.5 Radiogenic isotope geochemistry

Plume or enriched mantle rocks have ε_{Nd} contents at or close to zero in general, compared to positive ε_{Nd} contents of depleted rocks or negative ε_{Nd} contents for continental crust or rocks that were contaminated by continental crust. Plume rocks with ε_{Nd} contents of zero have been detected in such MCR rocks as the Portage Lake Volcanic rocks on the south shore of Lake Superior (Nicholson and Shirey, 1990). In the Kitto intrusive units, 10 samples from DDH EK-02 display a restricted range of ε_{Nd} contents from -5.54 to -6.53 (Table 4.3). The small range of negative ε_{Nd} contents within the lherzolite-olivine websterite to pyroxenite to melanogabbro lithologies shows that all these lithologies have been crustally contaminated to account for the highly negative contents. The magmas involved in the intrusion probably originally had primary

source compositions enriched in Sm/Nd relative to CHUR and close zero ε_{Nd} contents like that of continental or plume basalts, but were then crustally contaminated to be driven to the highly negative contents. Assuming the lherzolites as having the closest to primary compositions and that crustal contamination drives the lithologies to more negative ε_{Nd} contents, the pyroxenite followed by melanogabbro appear to be the most contaminated lithologies from the most primitive compositions closest to CHUR. The contaminants on the magmatic histories of these lithologies must have ε_{Nd} contents more negative than -6. Two possible contaminants are Quetico metasediments with ε_{Nd} contents between -16 and -23 and Wabigoon mafic metavolcanic rocks with ε_{Nd} contents between -14 and 7 (Heggie, 2005; Tomlinson et al., 2003). Contaminants with more negative ε_{Nd} contents, such as the Quetico metasediments, have been modeled at 5% contaminant to yield ε_{Nd} contents of about -5 in the Jackfish Sills of the West Nipigon Embayment; and the Shillabeer, Inspiration and two samples of Nipigon Sills have also been postulated to undergo contamination by these more negative ε_{Nd} components (Hollings et al., 2007b). This is consistent with the Kitto intrusive units being contaminated by about 5% Quetico contaminant with depth to display Th enrichment on primitive mantle multielement plots as seen by the trace element modeling. This is in contrast to the intrusive units being contaminated by Sibley sedimentary rock, which only have ε_{Nd} contents of -5 and are not negative enough, with as much as the unrealistic content of 90% contaminant, to produce the negative ε_{Nd} contents of between -5.54 and -6.53 in the intrusive units (Hollings et al, 2007b).

5.4 Magmatic evolution of the Kitto intrusion

5.4.1 Mineral chemistry

Olivine compositions in the central part of the Kitto intrusion show evolutionary trends of decreasing Fo % from lherzolite to olivine websterite to pyroxene-porphyritic melanogabbro.

The consistent trends of decrease in Fo % westward to the overlying pyroxene-porphyritic melanogabbros are consistant with the lherzolite to pyroxene-porphyritic melanogabbro lithologies representing a single pulse of lherzolitic magma that fractionated to upper roof pyroxene-porphyritic melanogabbro. Evidence for the lherzolite to pyroxene-porphyritic melanogabbro lithologies as being a part of the same magmatic system is the similar but decreasing MgO and increasing Al_2O_3, SiO_2, CaO and TiO_2 from the lherzolite to olivine websterite to pyroxene-porphyritic melanogabbro. Also DDH EK-05-01 shows little textural variation in the main lherzolite from top to the bottom of the hole although MgO has been observed to decrease from 26 at the top to 31 wt. % to the bottom of the hole.

In DDH EK-02, at the southern part of the intrusion, forsterite shows trends of increasing Fo % from melanogabbro through pyroxenite to olivine websterite, followed by decreasing Fo % to upper lherzolite (Fig. 4.30). At the bottom of the hole at 305 m, melanogabbro displays a minimum average Fo % of 74.3 due to the fractionated chemistry of the unit. The large increase in Fo % in the pyroxenite is due to a replenishment of a pulse of pyroxenitic magma in the lower parts of the Kitto intrusion. Replenishment of magma is shown by increase in Fo % to more Fo-rich magmatic compositions. Replenishment with increasing Fo % has also been observed within the ultramafics in specific olivine zones of the Seagull intrusion by Heggie (2005), who interpreted the zones to be due to episodic pulses of replenishing primitive magma. At 237 and 229 m, higher Fo % contents of 80.3 and 80.1 are displayed in the vari-textured pyroxenite as it represents a transition to the second pulse of olivine websterite to lherzolite magma in the higher parts of the intrusion. From 229 to 22 m, the sulphidized olivine websterite to upper lherzolite follow trends of increasing Fo % due to a replenishment of primitive magma and decreasing Fo % due to evolution of the lherzolite through the upper parts of the intrusion. From 229 to 199 m,

Fo % contents increase from 80.1 to 83.4 with a replenishment of primitive lherzolite to olivine websteritic magma. Maximum Fo % contents of 83.4 occur in the sulphidized olivine websterite as accumulation of primitive olivine minerals occurs in the lower parts of the unit. From 199 to 22 m, Fo % contents generally decrease to 79.2 as evolution to higher parts of a magma chamber occurs in the upper part of the lherzolite-olivine websterite unit.

In DDH EK-02, clinopyroxene displays variation with increase in En %, decrease in Fs % followed by increase in En %, Fs % and decrease in Wo % to maximum contents, followed by a final decrease in En %, Fs % and increase in Wo % in the upper lithologies (Fig. 4.32). The increase in En % and decrease Fs % in the lower melanogabbro to pyroxenite is due to a first pulse of replenishing pyroxenitic magma. At 237 m in sample ED-07, contents are anomalous with a high En % content of 54.6, and a low Wo % content of 35.1 in the vari-textured pyroxenite possibly due to a mixture with more primitive lherzolite-olivine websterite magma. From 237 to 199 m, there is an increase in En %, Fs% and decrease in Wo % to maximum contents. The increase in En % and Fs % and decrease in Wo % is due to replenishment of a second upper pulse of lherzolite-olivine websterite magma. This correlates with an increase to maximum contents of Fo % in olivine at these levels. From 199 m to the top of the hole, there is a general trend of decreasing En %, Fs % and increasing Wo % in the olivine websterite to lherzolite. This trend is due to evolution and smaller amount of clinopyroxene fractionation in the upper lherzolite unit.

Orthopyroxene variation in DDH EK-02 shows progressive replenishment to higher En % and lower Fs % from the bottom melanogabbro to pyroxenite, olivine websterite and upper lherzolite lithologies (Fig. 4.34). From 270 m to 244 m, replenishment of a pyroxenitic magma is displayed by increase in En % and decrease in Fs % to contents of 76.0 En %, 22.2 Fs %, and

1.8 Wo % in sample ED-32. A final new pulse of primitive magma is displayed by high En % and low Fs % in the upper lherzolite-olivine websterites with contents ranging from 78.4 En %, 18.0 Fs %, 3.5 Wo % at 185 m in sample ED-02 to 78.4 En %, 19.0 Fs %, 2.5Wo % at 116 m in sample ED-16 to 78.2 En %, 17.9 Fs %, 3.9 Wo % at 22 m in sample ED-15.

5.4.2 Emplacement of the intrusive units

Lherzolite-olivine websterites in the southern part of the intrusion represent a main pulse of magma of the Kitto intrusion that overlies pyroxenite to melanogabbro lithologies. On the surface, lherzolite outcrops as up to horizontal to shallow dipping 30 cm thick layer cake beds which occur probably due to shallow sill-like emplacement of the lithologies. Hart et al. (2002) observed the shallow dipping joints within the intrusion and interpreted them to be an indication of the originally shallow-dipping orientation of an ultramafic sill. However, deeper troughs of dominant lherzolite lithology are located where the intrusions emplaced along east-west faults such as the Blackwater Fault. An example would be the Phoenix occurrence where the lithologies along with lower pyroxenite to melanogabbro deepen to 220 m. These deeper troughs along the east-west orientated Blackwater Fault could point to an isolated feeder conduit to the intrusion at the intersection of the north-south to northwest orientated Nipigon River or Pijitawabik Fault and the Blackwater Fault (Hart and MacDonald, 2007).

Olivine websterite represents an accumulation of magnesian minerals from one main pulse of lherzolite-olivine websterite magma in the magma chamber. Evidence for the olivine websterite being of the same magmatic pulse as lherzolite are the continual forsterite, enstatite and ferrosilite depletion trends of olivine and pyroxene minerals from the bottom olivine websterite to top lherzolite (Figs. 4.30 and 4.32). This trend is due to progressive evolution from lower olivine websterite to lherzolite at the top of the magma chamber. Similar evolutionary

trends are observed in other intrusions such as from the basal dunite to higher gabbro in the east subchamber of the Jinchuan Intrusion (Chai and Naldrett, 1992). With the pulsing of the lherzolite-olivine websterite magma above the lower pyroxenite, there was crustal contamination in the lherzolite-olivine websterite with assimilation of Rb from basement mafic metavolcanic rocks, as evidenced by a maximum increase in Rb/La ratio at the bottom of the lithology (Fig. 5.16). Another possible source of Rb is Quetico metasedimentary rock with an average Rb/La ratio of 2.39 ppm. Evidence for a second pulse of lherzolite-olivine websterite over lower pyroxenite is the contamination with maximum Rb/La ratios in lherzolite-olivine websterite compared to lower Rb/La ratios in pyroxenite that would be the result of a new pulse of magma, and also the patchy textures of the vari-textured pyroxenite between the lower pyroxenite and higher lherzolite-olivine websterite which gives textural evidence of a dynamic magma churning up the lower pyroxenite. Similar patterns of maximum Rb/La ratios at the bottom of the marginal unit in the Xinjie Intrusion are also interpreted to be due to crustal contamination from bordering wallrocks with the pulsing of that unit (Zhong et al., 2004). Lherzolite and olivine websterite also follow the same contamination trend of increasing $(La/Sm)_{cn}$ with decreasing Nb/Nb* probably indicative of the lithologies following the same crustal contamination history with crystallization (Fig. 5.13). The lithologies were probably contaminated along the Blackwater Fault by Quetico metasedimentary and SVU mafic metavolcanic rocks with depth, and with intrusion of the SVU metabasalts and iron formation at higher crustal levels, became crustally contaminated by those lithologies to be sulphur-saturated and precipitate Ni-Cu-PGE sulphides.

Pyroxenite to melanogabbro lithologies, located below lherzolite-olivine websterite, formed from a first pulse of magma before the second main pulse of upper lherzolite-olivine

websterite. On a primitive mantle normalized multielement plot, all the pyroxenites fall within the range of REE and trace elements of lherzolite-olivine websterite, only all the lithologies have pronounced negative Nb anomalies (Fig. 4.17). The similary of primitive mantle plot patterns probably indicate the pyroxenite formed from an earlier pulse of the same magma as the lherzolite-olivine websterite. The lithology formed from a replenishing i.e. injection of more primitive MgO-rich magma as evidenced by the increasing Fo %, En % and decreasing Fs % and Wo % trends from the bottom toward the upper lherzolite-olivine websterites (Figs. 4.30 and 4.32). Trends of replenishment with increasing Fo % and En % and decreasing Fs % and Wo % in olivine and pyroxene are also seen in such zones as olivine zone 2 in the Seagull intrusion where olivine minerals become more Fo-rich with influx of primitive, relatively uncontaminated magma (Heggie, 2005). However, there was an influx of contaminated magma in the Kitto intrusion, as evidenced by pronounced Nb anomalies on primitive mantle plots of the lithologies. From pyroxenite to lower melanogabbro, there was evolution of the lithologies toward wallrock basement iron formation. On a primitive mantle normalized multielement plot, evolution to melanogabbro is shown by an increase in all the REE and trace elements relative to the lherzolite-olivine websterites (Fig. 4.19).

Moving north to the central part of the intrusion, lherzolites are more evolved than those in the southern part of the intrusion. Lherzolite in the central part of intrusion outcrops as 16° dipping beds that dip westward toward a central trough which is overlain by pyroxene-porphyritic melanogabbro to the west (Fig. 3.1). There is a trend of decreasing Fo %, En % while increase in Fs % in olivine and pyroxene minerals from lherzolite to olivine websterite, which is reflective of evolution from lherzolite to olivine websterite.

From east to west in the central part of the intrusion, there is evolution from the more MgO-rich lherzolite-olivine websterite to the more SiO_2-rich and crustally contaminated pyroxene-porphyritic melanogabbro. These pyroxene-porphyritic melanogabbros probably formed higher up in a magma chamber with a magma that was originally lherzolitic in composition. Evidence for the lithologies as being more evolved from primary lherzolite higher up in a magma chamber are in decreasing Fo %, En % while increasing Fs % trends in olivine and pyroxene minerals moving westward toward the centre of the intrusion. A magma chamber that shows evolution from lherzolite to olivine websterite to pyroxene-porphyritic melanogabbro higher up in sequence is similar to the east subchamber of the Jinchuan Intrusion which contains lower dunite and more evolved gabbro lithologies higher up in sequence that formed the roof of the magma chamber (Chai and Naldrett, 1992b). The pyroxene-porphyritic melanogabbros probably formed the fractionated roof members in the magma chamber where the intrusion deepens in a trough that eventually shallows out to the west. Evidence for the pyroxene-porphyritic lithologies as being roof fractionated in a deep trough are the opposing dips of outcrops from dipping to the west in sample JL-024 to dipping to the east in samples JL-021 and JL-023 (Fig. 3.1). The opposing dips allude to pyroxene-porphyritic melanogabbros as located in the centre of a bowl-shaped system that contains bottom lherzolites. The lower contacts of lherzolite with olivine websterite are located to the west of the pyroxene-porphyritic melanogabbro and dip to the west toward pyroxene-porphyritic melanogabbro in the centre of the intrusion. Also the pyroxene-porphyritic melanogabbros show the most decrease in Fo % and En %, while increase in Fs % in the centre of the intrusion before there is increase in Fo % and En %, while decrease in Fs % in olivine and pyroxene minerals in pyroxene-porphyritic melanogabbros as the intrusion shallows out to the west again. The decrease in Fo % and En %

while increase in Fs% from lherzolite to pyroxene-porphyritic melanogabbro occurs with evolution of magmas from the bottom to evolved tops of a magma chamber. The pyroxene-porphyritic melanogabbros also probably evolved from a parent lherzolite primitive magma in a magma chamber as evidenced by less MgO-rich compositions than lherzolite-olivine websterite and deepening of lithologies in the central part of the intrusion.

Granophyric gabbros formed as late stage final melts of the Kitto intrusive units and are situated to the west of the pyroxene-porphyritic melanogabbros. Primitive mantle normalized multielement plots of granophyric gabbro show primitive mantle plot patterns similar to the lherzolites, indicating the lithologies formed from the same magma source as lherzolite. However, the lithologies have higher overall abundance of REE and trace elements indicative of the lithologies being more evolved than the lherzolite-olivine websterite to pyroxene-porphyritic melanogabbros (Fig. 4.20).

5.4.3 Comparison with the Jinchuan, Munni Munni and Seagull Intrusions

Magmatic evolutionary mechanisms for the Kitto intrusion can be deduced by comparison with other world-class Ni-Cu-PGE bearing intrusions such as the Jinchuan Intrusion in China. The Jinchuan Intrusion is an ultramafic dyke-like body that has three subchambers: a west, west-central, and east subchamber (Fig. 5.18). The west subchamber is laterally zoned from a dunite core through lherzolite to olivine pyroxenite toward the margins. The east subchamber, in contrast, shows vertical stratification from dunite at the base upward to lherzolite and plagioclase lherzolite, and then back to lherzolite at the top (Chai and Naldrett, 1992b). In the west subchamber, changes in grain size from coarse grained dunites in the core to fine grained pyroxenite at the margins were interpreted to be due to different cooling rates from slower crystallization of magma of constant composition in the core to rapid crystallization of

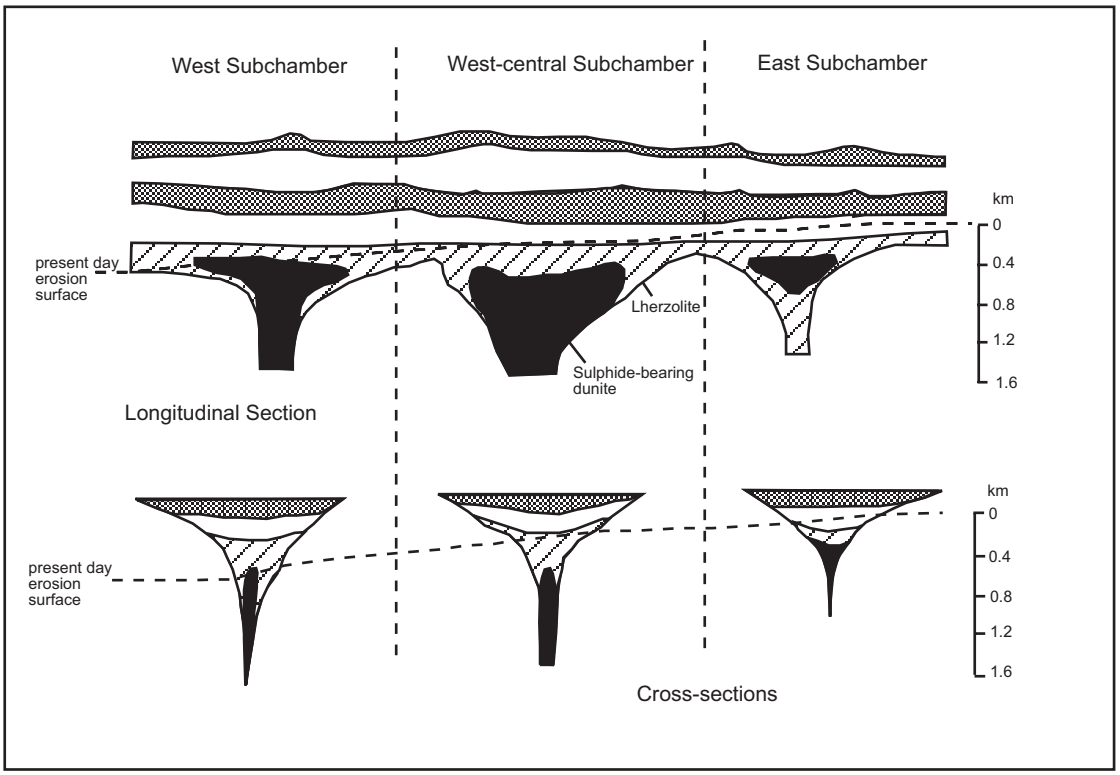

Figure 5.18: A cross-section of the Jinchuan Intrusion in China shows three subchambers: the West Subchamber, the West-central Subchamber and the East Subchamber. The Kitto intrusion formed from processes similar to those in the West and East subchambers. Modified after Chai and Naldrett (1992b).

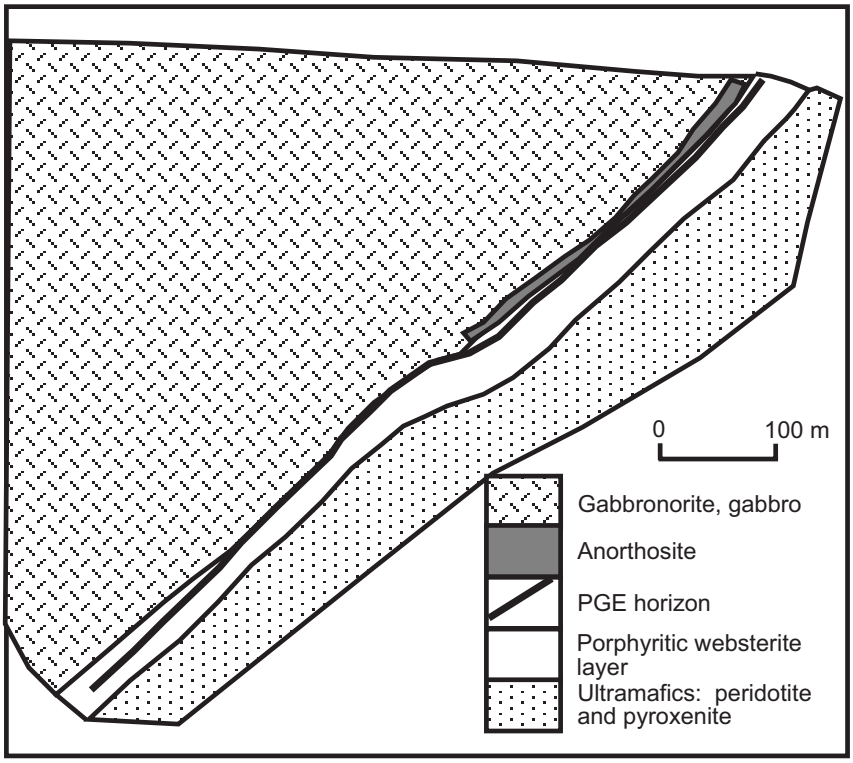

Figure 5.19: A cross-section of the Munni Munni Complex in Australia shows a basal ultramafic unit that is overlain by the porphyritic websterite and gabbro units. The Kitto intrusion formed similarly to processes in the porphyritic websterite and gabbro units. Modified after Hoatson and Sun (2002).

nearly chilled magma at the margins (Chai and Naldrett, 1992b). The constant large cumulate grain sizes in the core of the western subchamber has been attributed to continuous magma flow replenishment resulting in overgrowth of olivine cumulate minerals with constant composition. The changes in the amount of cumulus olivine to being more concentrated in the core suggested the transverse movement of olivine minerals toward the central axis with emplacement of magma by flowage differentiation (Chai and Naldrett, 1992b). Along with cumulate concentration at the core, there was concentration of sulphide droplets. In the east subchamber, the cumulus textures, gross phase layering and widening of the magma chamber suggested it formed by gravitational differentiation. In the ultramafics, olivine started to accumulate as layers, and the liquid composition higher up in the lithologies gradually evolved away from olivine (Chai and Naldrett, 1992b). Repeated additions of new magma in higher layers also gave rise to repetitive formation of olivine-bearing layers. At higher levels of the magma chamber, a thick layered gabbro sequence formed from more evolved magma.

The southern part of the Kitto intrusion probably formed by mechanisms similar to the Jinchuan Intrusion in both the west and east subchambers of that intrusion. In the lower pyroxenite to melanogabbro lithologies in DDH EK-02, there is enrichment in the amount of cumulate pyroxene minerals from the melanogabbro to the pyroxenite lithologies, and there is fractionation of melanogabbro at the contact with basement iron formation. The concentration of cumulate pyroxene vs. intercumulus plagioclase in the pyroxenite is probably due to the concentrating of minerals with flow differentiation to a central core, like the west subchamber of the Jinchuan Intrusion. Textural evidence for flow differentiation is displayed by enrichment of poikilitic plagioclase and pyroxene in ED-09 toward dominant secondary pyroxene, intergranular plagioclase and cumulate pyroxene mineralogy in samples ED-32 and ED-08 to dominant

cumulate pyroxene and intergranular plagioclase in sample ED-07 higher up in section (Fig. 3.3). The prevalence of cumulate pyroxene in sample ED-07 occurs with flow differentiation from ED-09 to the upper lithologies. Evidence for an enrichment of cumulate MgO-rich lithology can also be deduced from progressive replenishment to higher Fo % and En % in olivine and pyroxene minerals from the contact melanogabbros to the central pyroxenite. In contrast, the upper lherzolite-olivine websterites probably formed dominantly by gravitational differentiation like the east subchamber of the Jinchuan Intrusion. In the lower olivine websterite unit, there is an accumulation of olivine and pyroxene cumulates and interstitial Ni-Cu-PGE sulphides similar to the basal dunite of the east chamber of the Jinchuan Intrusion. The accumulation of cumulate minerals is evidenced by the increase in MgO contents in the bottom olivine websterites and a replenishment to maximum Fo %, En % and Fs % contents in olivine and clinopyroxene minerals. A new pulse of magma in the higher lherzolite-olivine websterite can also be deduced by the more MgO-rich compositions in the lherzolite-olivine websterite compared to the lower pyroxenite-melanogabbros, and also the dominant trend of decreasing Fo %, En % and Fs % in olivine and clinopyroxene minerals, compared to constant trend of Fo % and En % replenishment in the lower pyroxenite-melanogabbros.

Magma evolution of the southern part of the Kitto intrusion can also be deduced by comparison with the Munni Munni Complex. The Munni Munni Complex in the Western Australian Pilbara Craton consists of three lithologic zones: a lower Ultramafic Zone, a Porphyritic Websterite Layer and a higher Gabbroic Zone, of which the latter two can be related to the Kitto intrusion (Fig. 5.19; Barnes and Hoatson, 1994). The Ultramafic Zone contains about 20 cyclic lithologies of olivine and clinopyroxene cumulus minerals with periodic reversals of Fo % to more primitive cumulus mineral compositions followed by periodic

depletions indicative of rhythmic layering through to the upper parts of the unit. As the Ultramafic Zone grades into the Porphyritic Websterite Layer at the top, there is a sharp depletion in Fo % toward more fractionated compositions found in the higher Gabbroic Zone. The base of the higher Porphyritic Websterite Layer is defined by the disappearance of cumulus olivine minerals. The Porphyritic Websterite Layer, which marks the contact zone between the Ultramafic and Gabbroic Zone, consists of alternating discontinuous layers of porphyritic olivine-augite-bronzite cumulate minerals (Barnes and Hoatson, 1994). In the top of this layer, bronzite disappears and plagioclase is the dominant intercumulus mineral. Disseminated sulphides and PGE are hosted within this unit. Pyroxenes in the Porphyritic Websterite Unit become much more Fe-rich toward the top of the unit. The abrupt changes to lower Fo % and decrease in Cr content from the Ultramafic to the Porphyritic Websterite Layer preclude it from being formed by a continuous process of fractional crystallization, and rather a model of magma mixing of a Cr-poor and Fe-rich tholeiitic magma into primitive magma of the Ultramafic Zone (Barnes and Hoatson, 1994). Within the Porphyritic Websterite Layer and in the lower portion of the Gabbroic Zone, there is a complex assemblage of xenolithic blocks of bronzitite and olivine bronzitite composition; and banded norite and pigeonite gabbronorite. The Gabbroic Zone is marked by the first appearance of cumulus plagioclase and the dominant appearance of pigeonite cumulate minerals. Most of the zone is massive and unlayered. The Gabbroic Zone shows a steady increase in iron content of pyroxene, albite content of plagioclase and steady decrease in Fo % of olivine indicating closed system fractionation in a magma chamber that underwent little if any replenishment (Barnes and Hoatson, 1994).

In the Kitto intrusion, there is no lithology like the Ultramafic Zone of the Munni Munni Complex where there is cyclical rhythmic layering throughout the unit shown by episodes of

replenishment and fractionation through to the top of the unit. However, the vari-textured pyroxenite between the pyroxenite and overlying olivine websterites of DDH EK-02 is similar to the Porphyritic Websterite Layer, because it is followed by the first appearance of different cumulate minerals such as olivine and secondary pyroxene similar to pigeonite and plagioclase minerals in the Gabbroic Zone of the Munni Munni Complex; and the vari-textured pyroxenite shows a change in magmatic composition to primarily lherzolite. The vari-textured pyroxenite is comparable to the xenolithic unit just above the Porphyritic Websterite Layer in the Munni Munni Complex where in the vari-textured pyroxenite, many small nucleations of secondary pyroxene surround primocrysts of altered clinopyroxene similar to the many small nucleations of bronzite surrounding primocrysts of olivine in the Porphyritic Websterite Layer. Therefore, the vari-textured pyroxenite probably formed by magma mixing or churning up of a pulse of lherzolitic magma into pyroxenite like that of the gabbro into the ultramafic magma in the Porphyritic Websterite Layer. Textures of primocrysts of clinopyroxene surrounded by patches of secondary pyroxene give evidence of the dynamic churning up of lherzolite into lower pyroxenite. The top lherzolite in DDH EK-02 is similar to the overlying Gabbroic Zone in the Munni Munni Complex because it has continued depletion of Fo % due to closed system fractionation similar to the depleting Fo % in the Gabbroic Zone.

The southern part of the Kitto intrusion formed similarly to the Seagull intrusion in the Nipigon Embayment, only it did not have a protracted crystallization history like the Seagull intrusion. The Seagull intrusion has a more protracted crystallization history than the Kitto intrusion because it is a larger and deeper lopolith-shaped intrusion that was interpreted to form as a result of several episodic pulses of magma in at least four zones, outlined by variations toward primitive forsterite contents in olivine minerals through the intrusion (Heggie, 2005).

Along with the pulsing of the zones, there was episodic sulphur saturation of the magma to precipitate sulphides from a main basal zone to upper zones such as the RGB mineralized zone (Heggie, 2005). The pulsing of magmas upward in the intrusion has also been detected by different primitive mantle normalized multi-element plots of three units: a basal unit, a sub-main unit and a main unit (Heggie, 2005). In the Kitto intrusion, at least two magmatic pulses are delineated by a replenishment of magma to higher forsterite contents of olivine in the lower melanogabbro-pyroxenite unit, followed by replenishment to higher forsterite of the main olivine websterite to lherzolite lithologies and depletion of forsterite with fractionation and accumulation of the lherzolite-olivine websterites in a closed system. The two pulses can be seen in petrographic analysis of the vari-textured pyroxenite unit, which has a patchy texture of cumulate pyroxene minerals and growth clusters of secondary pyroxene which probably formed as a primary lherzolitic magma churned up and underwent magma mixing with the lower pyroxenite cumulate minerals, which formed earlier from a first pulse of magma. Evidence of this second pulse is also seen in maximum Rb/La variation at the bottom of the lherzolite-olivine websterite over low Rb/La contents of the bottom pyroxenite unit. The maximum Rb/La contents can be attributed to assimilation of crust with the primary pulsing of the lherzolitic magma. This is similar to the Xinjie Intrusion from Zhong et al (2004) where maximum Rb/La ratios at the bottom of the marginal unit in the Xinjie Intrusion are also interpreted to be due to crustal contamination from bordering wallrocks with the pulsing of that unit. Although there appears to be a second pulse of lherzolitic magma, the primitive mantle normalized multi-element plots of lherzolite appear similar to the more fractionated patterns of the lower pyroxenite to melanogabbro lithologies in contrast to the different primitive mantle plot patterns between the lithologies of the Seagull intrusion (Figs. 4.13 and 4.17). The similarity of the patterns alludes to

a uniform source magma of the Kitto intrusive units. This contrasts with the different magma primitive mantle plot patterns of the different lithologies of the Seagull intrusion. A possible explanation for similarity of primitive mantle plot patterns for two pulses of magma would be that the pyroxenite magma first became trapped and settled out cumulate minerals in a footwall embayment structure within a magma chamber to form the pyroxenite to melanogabbro lithologies (Fig. 5.20; Lesher, 2005). After crystallization of pyroxenite, there would be successive influx of lherzolite-olivine websterite from the same magma conduit that churned up the lower pyroxenite to form the vari-textured pyroxenite between the lithologies (Lesher, 2005). Footwall embayment structures form from transgression or erosion of footwall rocks to trap the magma and are common for many extrusive Ni-Cu-PGE complexes such as Raglan and Kambalda (Fig. 5.20; Lesher, 2005). However, turbulence of magma with intrusion through footwall rocks along magma conduits such as faults could possibly explain how erosion occurred at the bottom of a magma chamber to settle out the cumulate pyroxenite-melanogabbros, followed by lherzolite-olivine websterite. The pyroxenite-melanogabbros are found to occur only at the intersection of the Blackwater and either the Nipigon River or Pijitawabik Faults. These major structures could provide openings for such erosional or transgressional processes to occur to trap and settle out the pyroxenite-melanogabbros.

5.4.4 Soret fractionation model for the pyroxenite-melanogabbro lithologies

Another model suggestive of the formation of the lower pyroxenite-melanogabbro lithologies in the southern part of the Kitto intrusion, either than flow differentiation and felsification of magmas by contamination of bordering wallrocks, is Soret fractionation of a marginal compositional reversal. Soret fractionation is a type of diffusion crystallization process that occurs between a liquid boundary layer and the magma chamber wall due to the contrasting

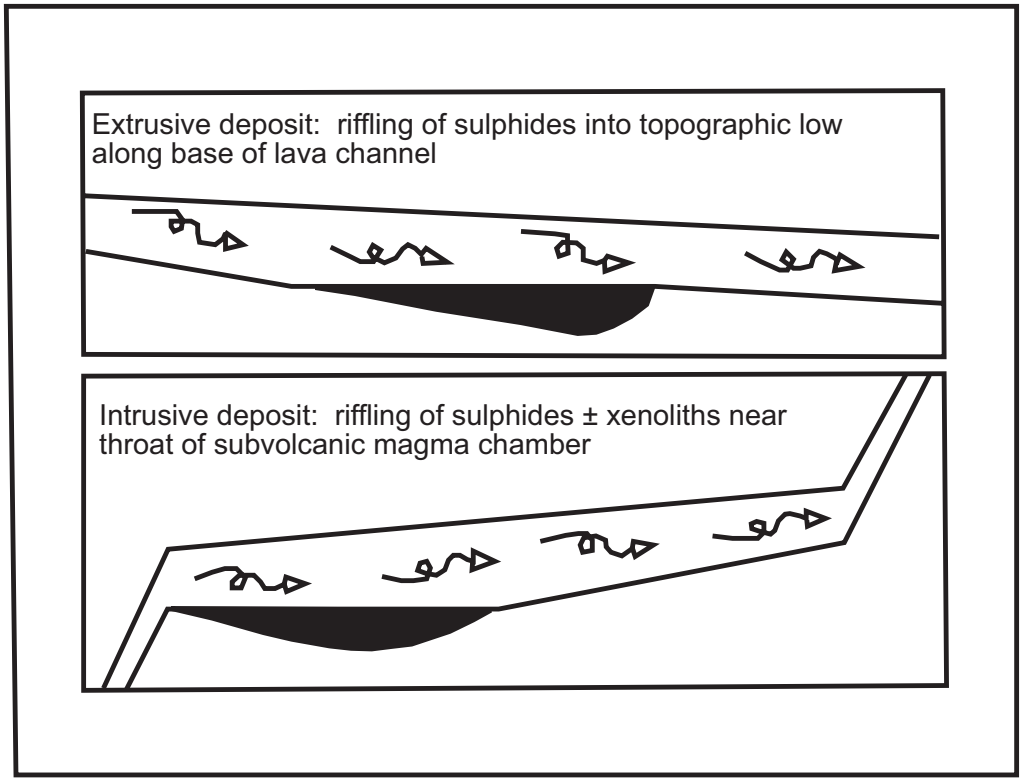

Figure 5.20: Footwall embayment structures occur in both extrusive and intrusive Ni-Cu-PGE complexes. The pyroxenite unit of the Kitto intrusion probably formed by a dynamic pulse of magma that transgressed the bottom footwall to settle out dominant cumulate pyroxene minerals. Modified after Lesher (2005).

heat fluxes between the wall rocks and magma in the main chamber (Latypov, 2003). With Soret fractionation, there is development of a basal marginal reversal zone separate from the main convecting magma in the upper layered series of layered intrusions and sills. In Soret fractionation, a liquid boundary layer is first formed by diffusion of olivine, pyroxene and plagioclase components toward the main chamber to form a liquid boundary layer in a non-equilibrium state (Latypov, 2003). The liquid boundary layer moves progressively inward toward the magma chamber while there is continual convection of magma in the main magma chamber. With inward movement of the liquid boundary layer, a marginal reversal forms when the magma composition between the liquid boundary layer and the chamber wall moves up the liquidus and crystallizes from the least mafic to most mafic toward a crossover maximum, at which point successive "normal" fractional crystallization begins to occur in the magma chamber (Latypov, 2003). Marginal reversals occur in basic-ultramafic sills such as the basal zone of the Monchegorsk intrusion in the Kola Peninsula and the bottom olivine-bearing and taxitic gabbrodolerites of the Noril'sk intrusions that are located below typical gravitational accumulated layered series rocks (Latypov, 2003). In comparison to the main layered series of intrusions, marginal reversals are characterized by lack of mass balances of major oxides between the lower part of the reversals and the bulk composition of the intrusion; and contain phase crystallization sequences and mineral compositional trends that are the inverse of the upper layered series rocks. In the Kitto intrusion, the lower pyroxenite-melanogabbro appears to be a marginal reversal since there is a lack of mass balance of major oxides as shown by more forsterite depletion in olivines and lower MgO contents in the lower pyroxenite-melanogabbros compared to the upper parts of the main lherzolite-olivine websterite (Figs. 4.30 and 4.1). Also the crystallization sequences of plagioclase and pyroxene to cumulate pyroxene and olivine is the

reverse of Bowen's reaction series compared to the sequence of more to less primitive olivine and pyroxene minerals upwards through the lherzolite-olivine websterite. The general forsterite-, enstatite- and MgO-enrichment trends in the pyroxenite-melanogabbro are also the inverse of the forsterite- and enstatite-depleting trends in the lherzolite-olivine websterite (Figs. 4.30, 4.32 and 4.1).

However, the melanogabbro to pyroxenite lithologies probably do not constitute a marginal reversal since the lithologies do not have "mirror images" of the crystallization of minerals as the upper lherzolite-olivine websterites like those of the Monchegorsk and Noril'sk intrusions, otherwise they would have the same rock names. Also, the pyroxenite-melanogabbros were only found to occur at the bottom of DDH EK-02 and not in the surrounding DDH EK-01, -03, and -04 drill holes, therefore limiting the extent of the lithologies to a probable footwall embayment structure and not along the base of the whole intrusion. Soret fractionation also does not explain the sorting of cumulate pyroxene minerals toward the upper pyroxenite compared to the melanogabbro to lower pyroxenite as could be explained by flow differentiation. Also, the lack of mass balance of MgO wt % and forsterite % between the basal pyroxenite-melanogabbro and upper lherzolite-olivine websterite can be explained by felsification of the pyroxenite-melanogabbro magma by contamination of bordering wallrocks to cause the depletions in MgO and forsterite content. Therefore, a mechanism for formation of the lower pyroxenite-melanogabbro is better explained by flow differentiation in a localized footwall embayment structure along with felsification of melanogabbro by contamination of bordering wallrocks rather than by Soret fractionation of a marginal compositional reversal.

5.4.5 Fault emplacement of the Kitto intrusion

The Kitto intrusion is a semi-circular ring complex that probably formed from a mantle plume at depth that intruded along a large north-south orientated fault. Primitive mantle multielement plots of lithologies of the intrusion point to a plume source of the intrusion that was crustally contaminated (Figs. 4.13 to 4.20). Other intrusions found in the Nipigon Embayment that emplaced along faults include the plume-derived English Bay Complex, Seagull intrusion, Disraeli intrusion, Hele intrusion, and the Nipigon diabase sills (Hollings et al., 2004; Hart and MacDonald, 2007). Sutcliffe (1986) first suggested that north-south to northwest trending faults provided magma conduits for the mafic to ultramafic intrusions, the Nipigon diabase sills, and controlled the geomorphology of the diabase sills intruding the Archean rocks on the peripheries of the Embayment. Hart and MacDonald (2007) interpreted these north-south to northwest trending faults to represent deep crustal structures that have had a protracted history of movement with periods of activation and reactivation occurring since the Mid-Archean. Hart and MacDonald (2007) concluded that during periods of re-activation, the faults provided the conduits for several intrusive and extrusive magmatic events. These faults in turn controlled the formation of the Nipigon Embayment (Hart, 2005). One large fault in which the Kitto intrusion could have been emplaced from is the Nipigon River Fault (Fig. 5.21). Hart and MacDonald (2007) interpreted that the Kitto intrusion occurs and was emplaced along the Nipigon River Fault. Another large fault that can be delineated in the East Nipigon Embayment is the Pijitawabik Fault (Fig. 5.21). The Nipigon River Fault may be the locus for emplacement of the Kitto intrusion since it trends toward the intrusion in the Lake Nipigon area. However, the Pijitawabik Fault appears to serve as a conduit for Nipigon diabase intrusions in the same area, since the diabase intrusions occur along northeast splays off of the Pijitawabik Fault that turn to a

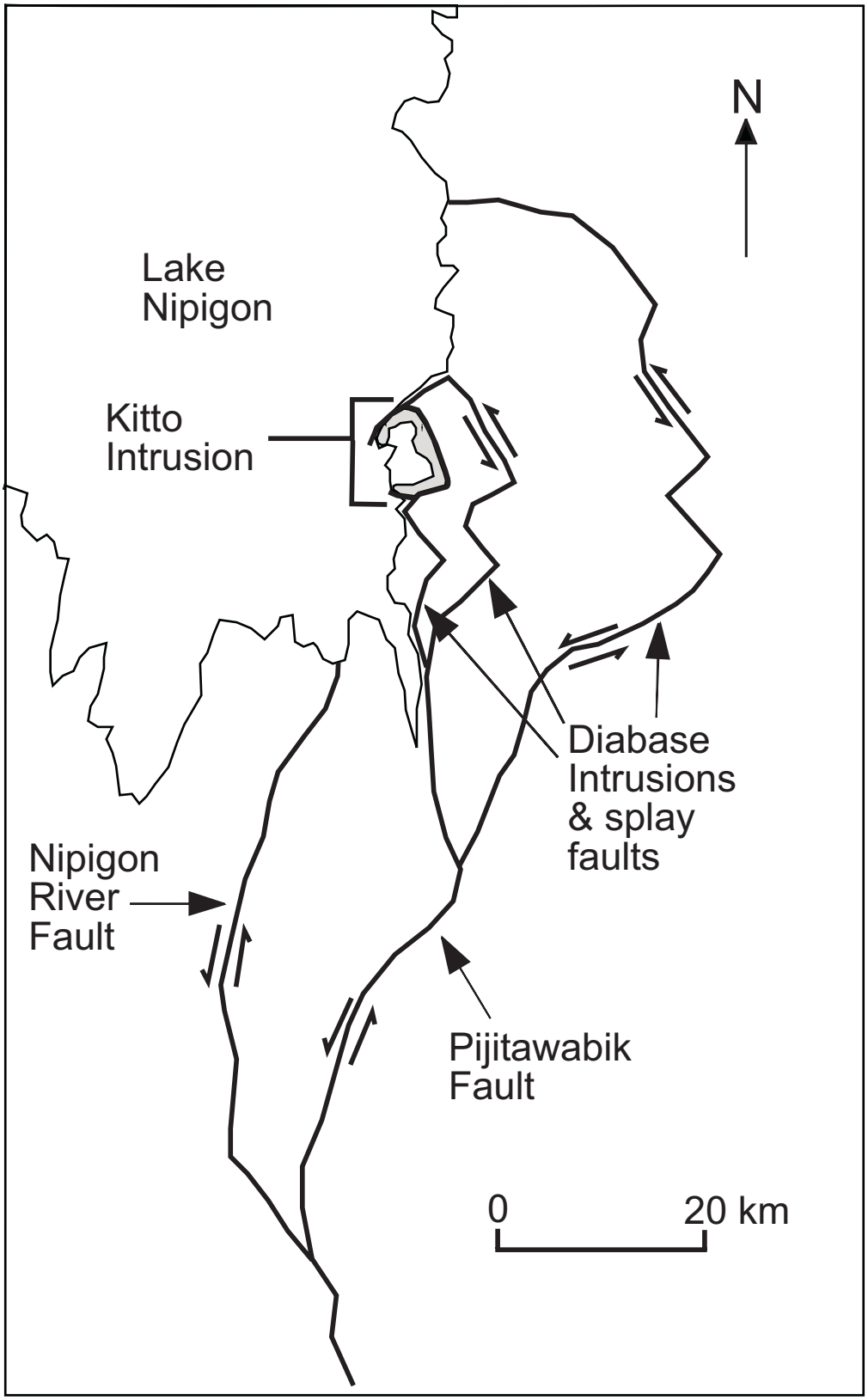

Figure 5.21: The Kitto intrusion possibly emplaced along the north-south orientated Nipigon River Fault or Pijitawabik Fault along with three sets of diabase intrusions. Modified after Gupta (1991).

northwest orientation parallel the Kitto intrusion (Fig. 5.21). On a topographical relief map, the Pijitawabik Fault is indicated by the indentation of Pijitawabik Bay and Canyon on the southeast shore of Lake Nipigon (Fig. 2.12). Generally, this fault runs parallel to other north-south orientated faults to the west such as the Nipigon River and Black Sturgeon Faults. North of Pijitawabik Bay, the fault (as determined by topographic relief, aeromagnetic anomalies, and outcropping of Nipigon diabase sills) splits off to the northeast and then follows a northwesterly trend parallel to the diabase dike intrusions and intersects the Kitto intrusion in Kitto Township (Fig. 5.21). Three sets of diabase intrusions intrude northwesterly faults that are parallel the Pijitawabik Fault. The fault also runs parallel with the Marathon dike swarm and the Pickle Crow diabase dike west and north of Lake Nipigon respectively (Figs. 2.2, 5.21). Since Hart and MacDonald (2007) interpreted the faults to be reactivated since the Archean, a possible origin for the Pijitawabik Fault, the Nipigon River Fault and the other major faults of the West Nipigon Embayment is the reopening of pre-existing structures such as the Pickle Crow diabase dike and the Marathon dike swarm structures that emplaced during plume induced activity ca. 1880 Ma and 2100 Ma respectively, before any Keewanawan-induced fault activity (Ernst, 2005; Buchan et al., 1996). Other evidence of pre-Keewanawan fault activity would be the intrusion of the 1537Ma English Bay Complex at the north end of the Black Sturgeon Fault and the fault-controlled sedimentation of the Sibley Group basin sequence (Davis and Sutcliffe, 1985; Hollings et al., 2004; Hart, 2005). Hart and MacDonald (2007) proposed that isolated feeder conduits to the Disraeli intrusion, Kitto intrusion and diabase intrusions occur at the intersection of the Archean east-west faults with the north-south to northwest trending faults, although evidence for feeder conduits of the intrusion has not been found. In the West Nipigon Embayment, the Disraeli intrusion is localized near the intersection of the Quetico Fault and the

Clearwater Fault (Fig. 2.11; Hart and MacDonald, 2007). In the East Nipigon Embayment, the Kitto intrusion is localized at the intersection of the Blackwater Fault and either the Nipigon River Fault or a splay off of the Pijitawabik Fault (Hart and MacDonald, 2007). Locally the intrusions along the northwest-orientated faults have changed direction to emplace along east-west orientated faults of the Archean basement in the Quetico Subprovince and the Beardmore-Geraldton Greenstone Belt (BGB; Fig. 2.14). In the BGB, the Kitto intrusion intruded to the west along the Blackwater Fault, Empire Fault, Princess Lake Fault and extensions of the Standingstone and Sandy Creek Faults to cause the ring shaped form of the intrusion (Fig. 2.3). Evidence for intrusion along these faults is the outcropping of peridotites along them and the deepening of the intrusion in DDH EK-02 along the Blackwater Fault (Fig. 3.2b). Notably, the three sets of northwest orientated diabase intrusions also intruded westward along such east-west faults in the BGB.

5.5 Mineralization: Base and precious metal geochemistry, Se and S and comparisons

5.5.1 Surface sample metal variation

Surface rocks sampled for metals throughout the southern and central parts of the Kitto intrusion generally show dominant magmatic Ni-Cu-PGE mineralization within peridotites and possibly only minor hydrothermal remobilization mineralization in contact Nipigon diabases. Evidence for hydrothermal remobilization in diabases would be the presence of coarse grained patchy to spotty pyroxenitized diabases such as in samples JL-055, JL-057, JL-065, JL-066, JL-075, and JL-076 (Appendix 2; Fig. 3.1). Also Hart et al. (2002) detected sulphidized diabases immediately adjacent to peridotite with anomalous PGE contents, trace to 1 modal % sulphide mineralization, and anomalous nickel that probably remobilized sulphides and PGE from basement peridotite. Generally, the pyroxene-porphyritic melanogabbros have been found to

contain lower Ni contents with contents comparable to lherzolites at the central and southern parts of the intrusion, since there were decreased amounts of olivine fractionated to partition the Ni (Fig. 4.23). Lherzolite to olivine websterite lithologies in the central lithologies have Ni contents of 516 to 1124 ppm indicative of greater olivine fractionation than the melanogabbros. Cu contents, on the other hand, are generally higher in the pyroxene-porphyritic melanogabbro of the central part of the intrusion compared to the southern part of the intrusion with anomalous maximum contents in samples JL-016, JL-019, and JL-039 (Fig. 4.24) due to the progressive evolution in the lithologies. Generally, more evolved lithologies become more sulphur saturated than the primitive ultramafics. With progressive evolution and crustal contamination, the solubility of copper in the magma is less resulting in more copper precipitated (Lightfoot et al., 1997). Anomalous Cu contents in the pyroxene-porphyritic melanogabbro show that the lithology was saturated enough to precipitate sulphides. The pyroxene-porphyritic melanogabbros contain higher Cu contents since the lithologies are more evolved and more able to be sulphur saturated to cause higher Cu contents in general and were more crustally contaminated to cause anomalous Cu contents to maximize above background more so than the lherzolites. Associated with these anomalous Cu contents are maxima of PGE contents (Fig. 4.22). In contrast to the peridotites, the diabases all have high Cu contents but no anomalous Cu contents, indicating the lithologies were already sulphur saturated and could not precipitate magmatic sulphides with addition of external sulphur. In the lherzolites of the southern part of the intrusion, background Ni contents are higher than those lithologies of the central part, reflecting the more primitive nature of these lithologies (Fig. 4.23).

5.5.2 Downhole metal variation

Mineralized zones with anomalous metal contents occur at the basal zone horizon in the lherzolite-olivine websterite unit, and three zones of mineralization in the pyroxenite-melanogabbros in DDH EK-02. The similar metal abundance patterns of the Pt and Pd in the mineralized zones are due to both metals being precipitated with sulphides in a magmatic intrusion that has become saturated with sulphur (Figs. 4.25 and 4.26; Kissin et al., 2006). Kissin et al. (2006) have shown sulphur saturation to take place with PGE maxima being above a line of 0.4 in sulphur contents. The similar patterns of PGE with Ni and Cu patterns show that the intrusion underwent dominant magmatic Ni-Cu-PGE mineralization, rather than hydrothermal mineralization or remobilization processes.

Cu displays maximum contents in the basal zone of the lherzolite-olivine websterite and in the lower zones. Again, the general association of increased PGE with increased Cu is displayed as the PGE partition into chalcopyrite sulphides with magmatic mineralization (Fig. 4.27). Anomalous Cu contents of 263 ppb in the basement iron formation provide an external source for contamination of the ultramafic magma and saturating it with respect to sulphur for precipitation of Ni-Cu-PGE metals.

Background Ni contents reflect the partitioning of Ni into olivine with concentrations of 1230 ppm and 1396 ppm displayed in samples ED-15 and ED-16 at 22 and 116 m respectively within the lherzolite (Fig. 4.28). Further down the DDH EK-02, the overall Ni content of the magma decreases as less olivine is precipitated in the more fractionated vari-textured pyroxenite, pyroxenite and melanogabbro lithologies. The increase in PGE with the sulphides is probably due to the pentlandite sulphides being precipitated, with successive precipitation of chalcopyrite from a mono-sulphide solid solution, and PGE partitioning into the sulphides. Evidence for the

precipitation of these metals is seen in the immiscible sulphide textures in the sulphidized olivine websterite unit.

5.5.3 Ni vs. MgO variation

Ni ppm vs. MgO wt. % plots for surface samples are used to investigate if Ni partitioned into sulphide phases with evolution of the peridotites. If the Ni concentrations follow the main igneous trend, Ni contents probably remained within olivine minerals with fractionation of the peridotites. However, if there are higher nickel contents than the regular trend, this would indicate that Ni precipitated as sulphide with evolution of the peridotites. Ni vs. MgO variation has been used to differentiate sulphide-bearing from non-sulphide bearing magmatic intrusions and extrusive deposits such as the Talnakh intrusions of Noril'sk and the ore-bearing Kambalda komatiites and Perseverance sills (Lesher, 2005; Lesher, 2001). Generally, sulphide accumulation occurs with Ni contents higher than the main increasing Ni with MgO trend (Lesher, 2001). Olivine accumulation occurs with a slight increase in Ni with increasing MgO from an original magmatic composition and olivine AFC (Assimilation fractional crystallization) fractionation occurs with decreasing Ni and MgO from an original magmatic composition (Lesher, 2001). In the surface samples, granophyre to pyroxene-porphyritic melanogabbro to lherzolite lithologies display the main evolutionary trend of increasing ppm Ni with increasing wt. % MgO (Fig. 5.22). Since the trend is linear with increasing Ni with MgO, it probably represents the olivine AFC trend from more primitive lherzolite-olivine websterite to pyroxene-porphyritic melanogabbro to granophyric gabbro lithologies. From 14 to 26 wt. % MgO, pyroxene-porphyritic melanogabbros do not show anomalous Ni contents, however clusters are depicted where anomalous Pt,Pd contents have been found in the surface samples. From 17 to 20 wt. % MgO and from 469 to 552 ppm Ni, a cluster is shown with higher Ni contents per wt.

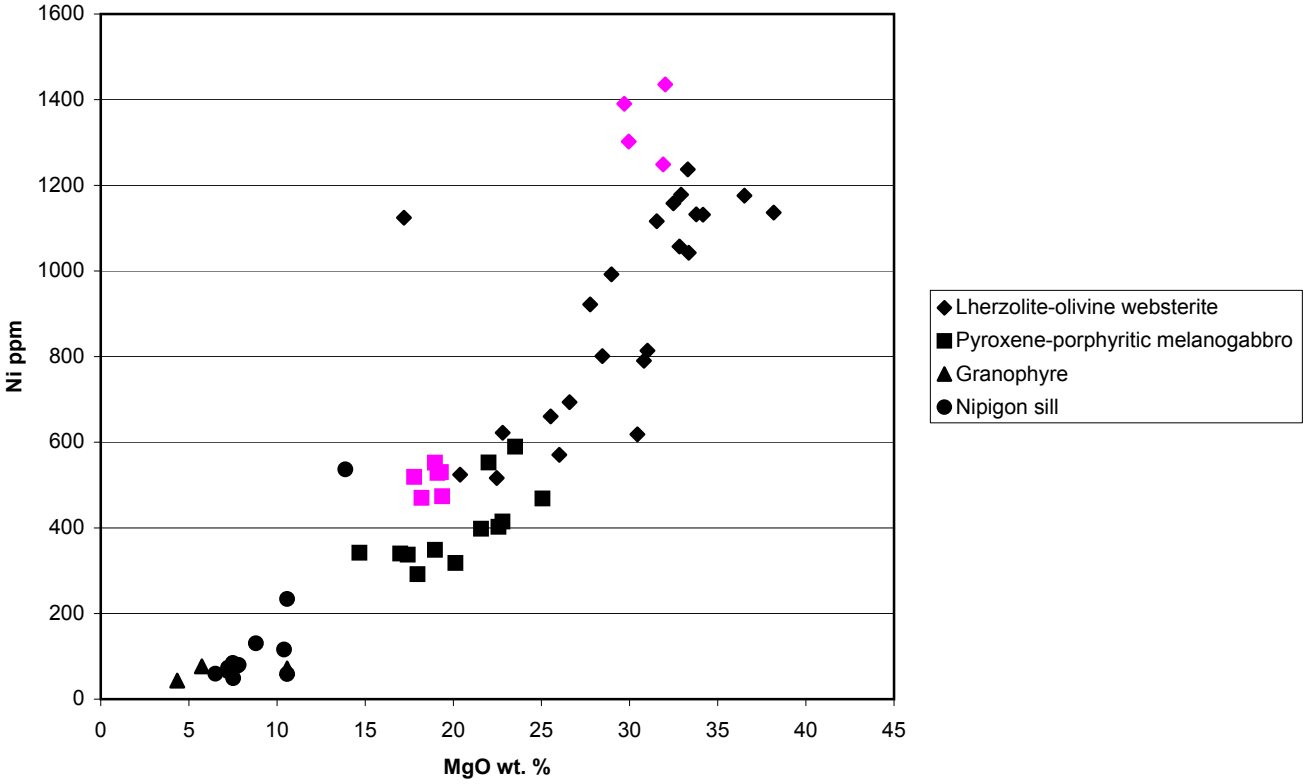

Figure 5.22: Plot of Ni ppm vs. MgO wt. % for surface samples. Anomalous Ni contents are in pink.

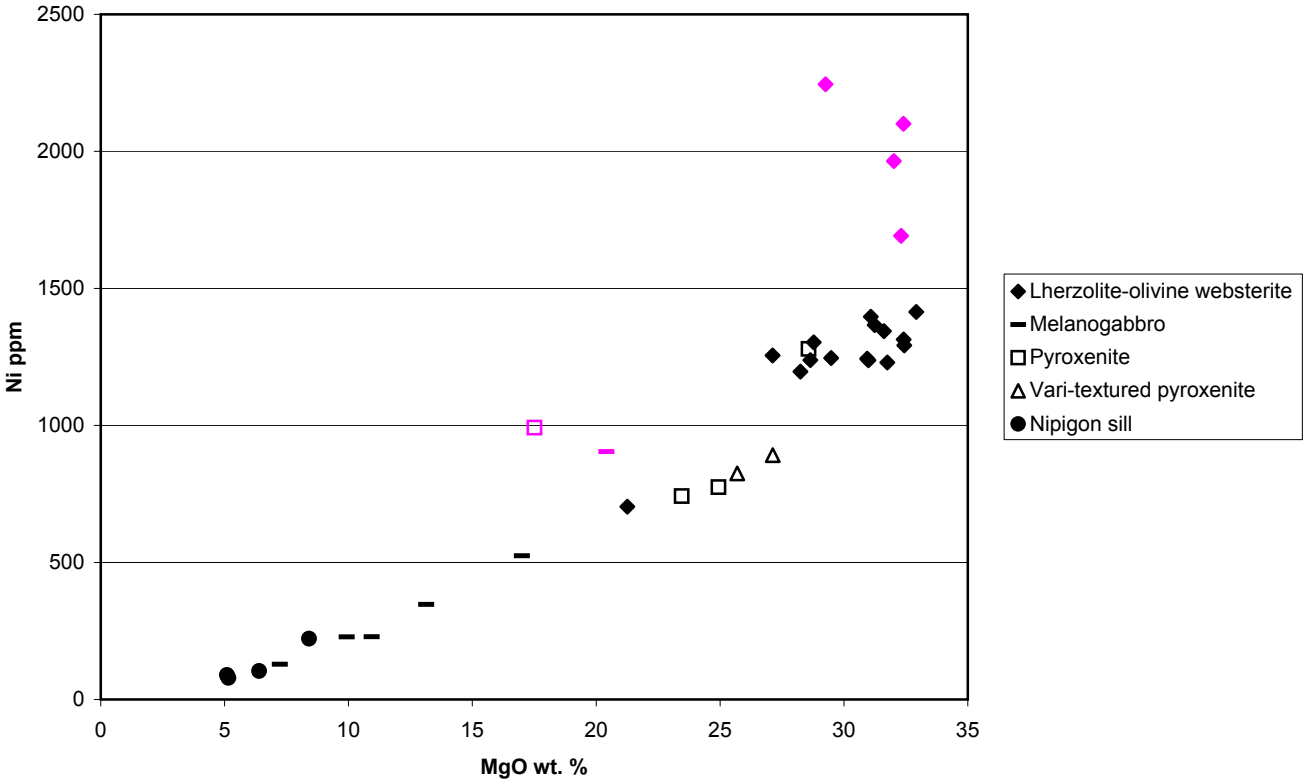

Figure 5.23: Plot of Ni ppm vs. MgO wt. % for DDH samples. Anomalous Ni contents are in pink.

% MgO for surface samples JL-017, JL-020, JL-027, JL-023, JL-015 and JL-026 which are north of the lake in the central part of the intrusion. Sample JL-026 has been found to contain Pt, Pd contents of 139, 180 ppb and sample JL-015 contains Pt, Pd contents of 242, 37 ppb. From 20 to 39 wt. % MgO, most of the lherzolites follow the dominant evolutionary trend while some samples at higher MgO contents contain anomalous Ni contents above the trend. Anomalous contents are found between 29 and 34 wt. % MgO in samples JL-001, JL-063, JL-077 and JL-004 at contents of 1435, 1390, 1302 and 1248 ppm Ni respectively. These samples are at different locations within the southern part of the Kitto intrusion where lherzolites in mineralized zones had Ni partition into sulphide phases more so than lherzolites in other areas of the intrusion. Notably, samples JL-063, JL-077, and JL-004 are lherzolites located at contact areas with diabase where Ni-Cu-PGE mineralization has been found, for example, at the Phoenix occurrence. From 4 to 11 wt. % MgO, granophyric gabbros have low Ni at low MgO. These lithologies have too little Ni in their systems to account for any Ni sulphide mineralization.

Ni ppm vs. MgO wt. % for drill core samples also shows a general evolutionary trend of increasing Ni with increasing MgO, with some anomalous Ni maxima at certain MgO contents in the pyroxenite, melanogabbro and lherzolite-olivine websterites (Fig. 5.23). The anomalous Ni contents within these lithologies indicate they are Ni mineralized. Sample ED-09 contains an anomalous maximum of 992 ppm Ni at 17.51 wt. % MgO and is found at 270 m in DDH EK-02 within a mineralized zone in the middle of the pyroxenite unit. Sample ED-21 contains an anomalous maximum of 904 ppm Ni at 20.41 wt. % MgO, and is found at 139 m in DDH EK-01 within the melanogabbro at the contact with basement Sibley Group sandstone and metavolcanic lithologies. Four anomalous Ni samples are found in the Phoenix mineralized zone of the lherzolite-olivine websterite unit. Samples ED-04, ED-03, ED-02, and ED-01 are olivine

websterites found between 179 and 200 m of DDH EK-02 that contain anomalous Ni contents of 2245, 2100, 1965 and 1692 ppm respectively at respective MgO contents of 29.26, 32.41, 32.02 and 32.31 wt. %.

5.5.4 Se and S analysis

Se and S contents are used to identify specific sulphur sources that contaminate a magma in order to saturate it with sulphur to precipitate Ni-Cu-PGE sulphides. In the Kitto intrusive samples, Se was measured in the 42 samples from drill core with geochemical trends analysed in detail for 21 samples from DDH EK-02. S was measured from drill core samples sampled from the mineralized horizons of DDH EK-02 by Kennecott Canada Exploration Inc. Both Se and S were measured in 64 surface samples from the central and southern parts of the intrusion.

Generally, with precipitation of sulphides in the intrusion, there is increase in both S and Se as they partition into sulphide phases (Franklin, 2001). However, extra Se measured beyond that measured from the sulphide can show that external sulphur was added to the magma along with mantle sulphur in order to precipitate the sulphides in the intrusion. Plots of S vs. Pt + Pd ppm and S vs. Ni and Cu ppm from the Kennecott data show that with increased mineralization of the metals, there is increased S content associated with the sulphides (Figs. 5.24 and 5.25). A plot of Se vs. Ni + Cu ppm from the ED data also shows that with increased mineralization, there is increased Se content (Fig. 5.26). However, it also shows that within low metal areas, there is large increase in Se content (Fig. 5.26). This shows there was external sulphur added to the system to account for large increases in Se beyond sulphide mineralization. For surface samples, with increased Ni and Cu mineralization there is an increase in S content associated with sulphide precipitation (Fig. 5.27). However, for Se vs. Ni + Cu ppm, increases in Se content also occur in non-mineralized areas of the intrusion (Fig. 5.28). The lack of correlation between Se

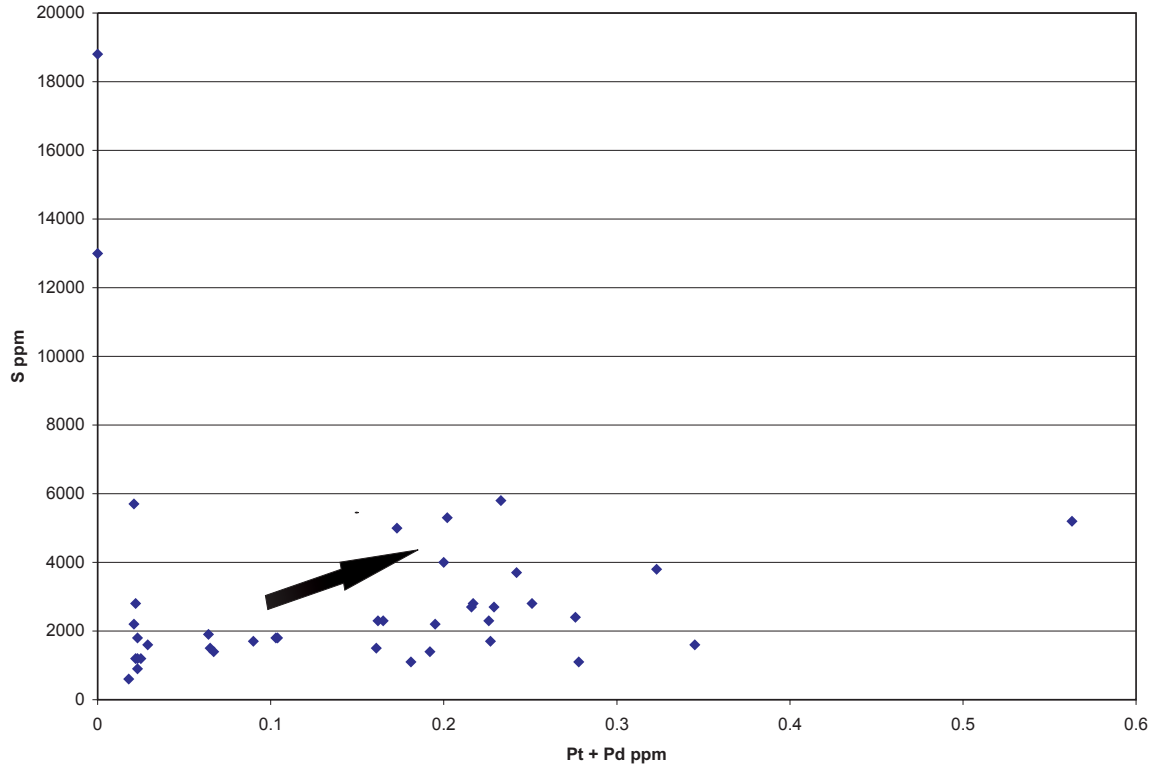

Figure 5.24: Plot of S ppm vs. Pt+Pd ppm for DDH EK-02. Arrow indicates trend of increasing Pt + Pd with increasing S.

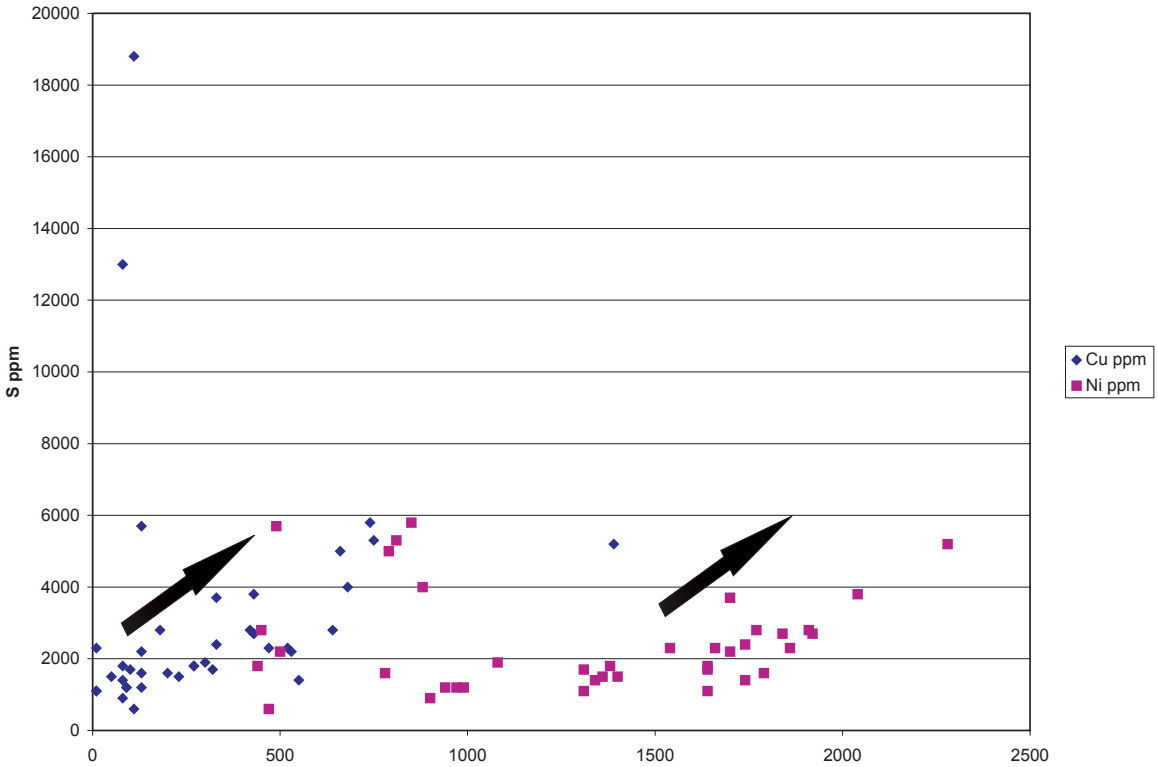

Figure 5.25: Plot of S ppm vs. Ni and Cu ppm for DDH EK-02. Arrows indicate trends of increasing Ni and Cu with increasing S.

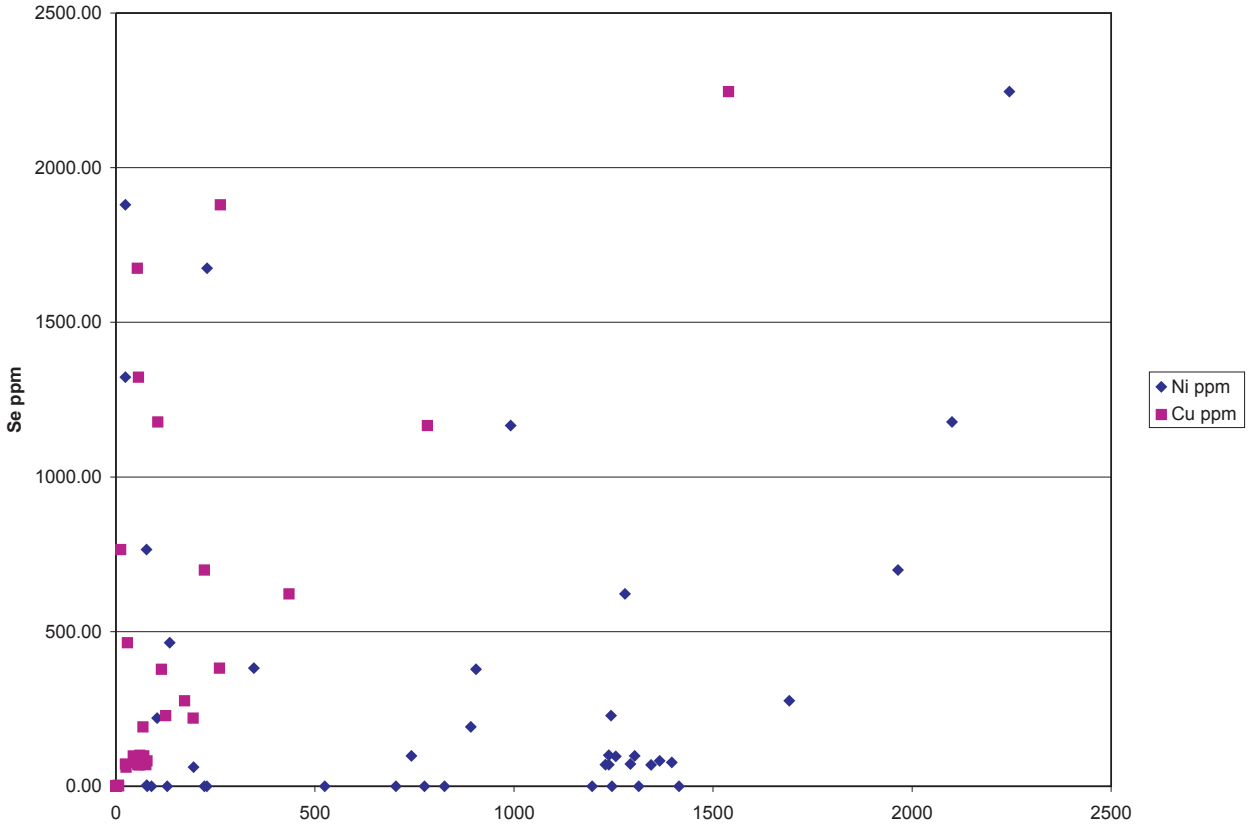

Figure 5.26: Plot of Se ppm vs. Ni and Cu ppm for DDH EK-02.

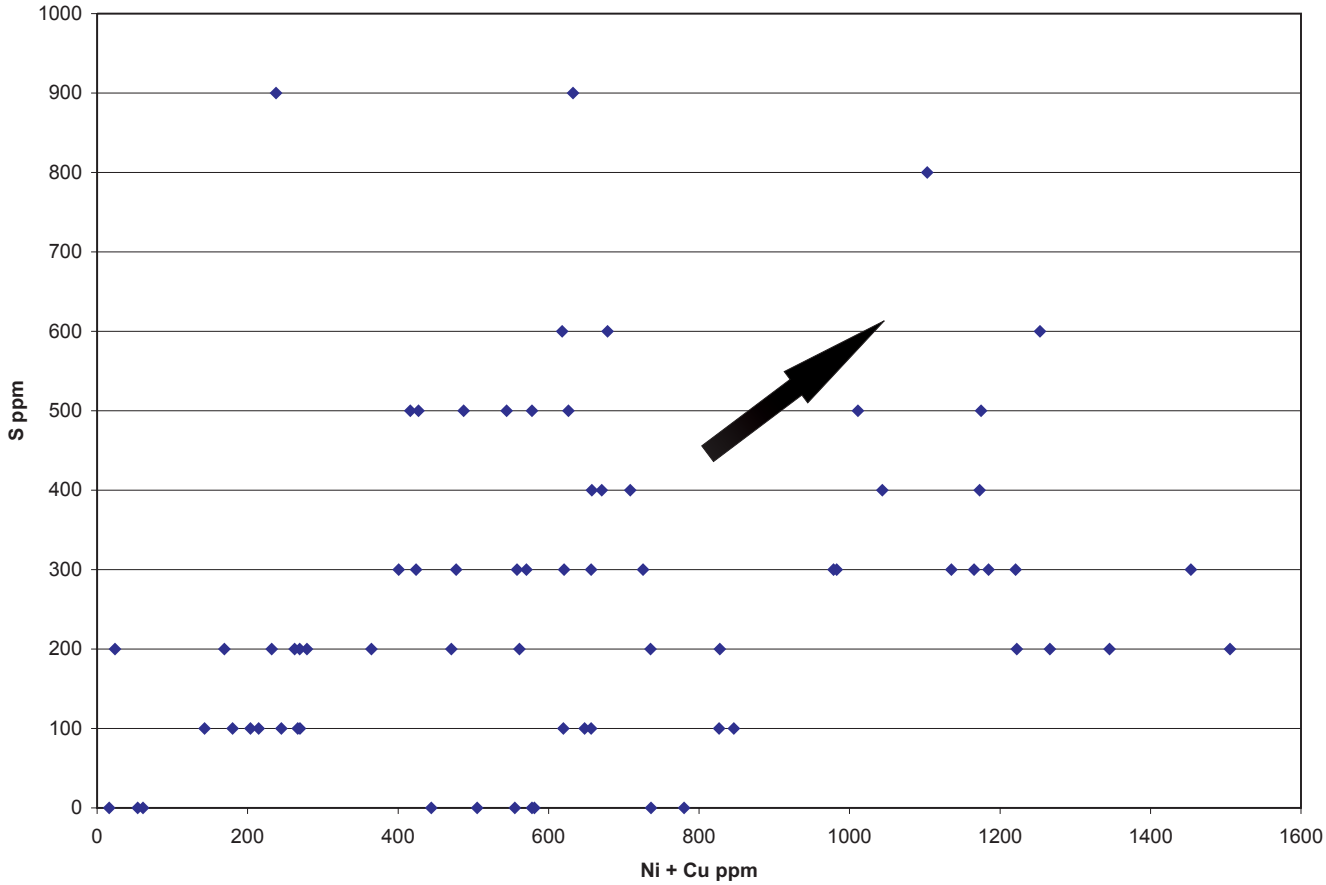

Figure 5.27: Plot of S ppm vs. combined Ni + Cu ppm for surface samples. Arrow indicates trend of increasing S with increasing Ni + Cu.

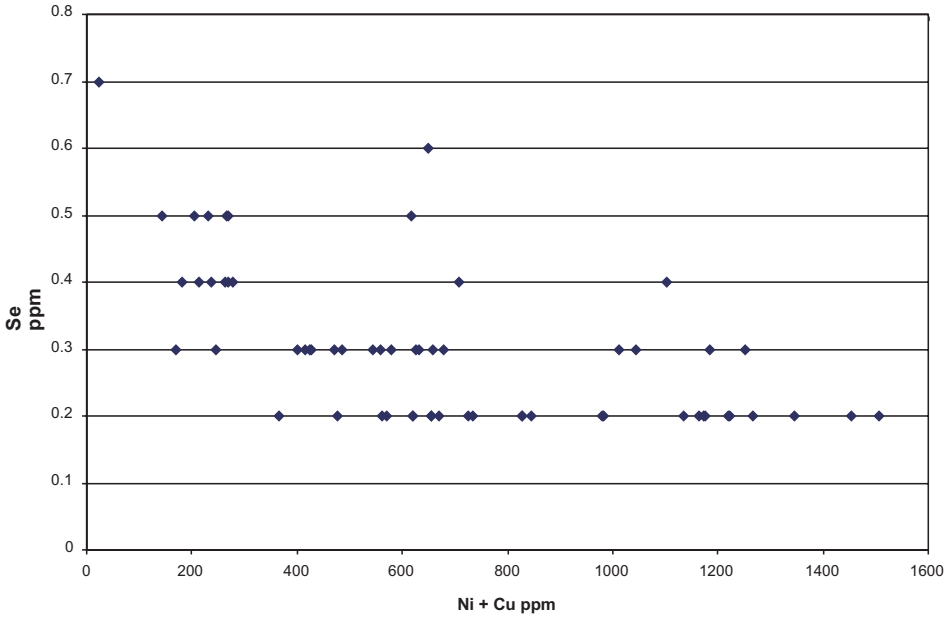

Figure 5.28: Plot of Se ppm vs. Ni + Cu ppm for surface samples.

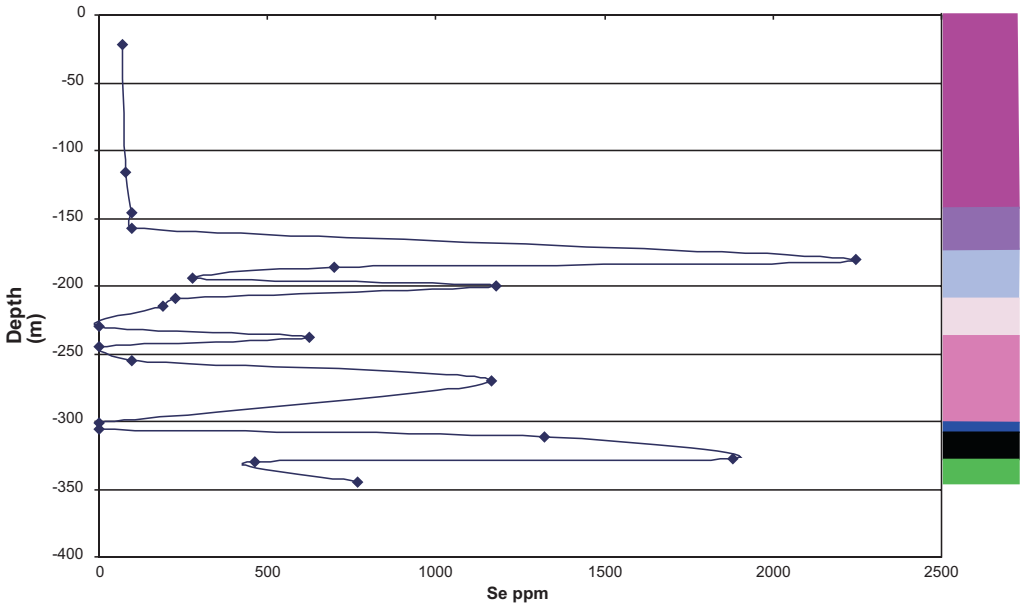

Figure 5.29: Plot of Se ppm vs. depth for DDH EK-02.

and Ni + Cu shows there was an extraneous external source of sulphur contributed by contamination in the intrusion.

Se/S ratios show the source of sulphur in the Kitto magmatic system, whether it is sulphur from the mantle, or that added from an external source. For surface samples, Se/S ratios are all higher than that of mantle contents with $Se/S*10^6$ contents between 300 and 6000, while mantle contents all plot in the range of 200 to 400 (Eckstrand et al., 1989). Samples from drill core display $Se/S*10^6$ contents from 992 to 16045 in the mineralized zones. The higher than mantle Se contents show there was contamination of the magma by a Se-rich external sulphur source to saturate the magma and precipitate Ni-Cu-PGE sulphides. This is in contrast to some magmatic systems being diluted by basement sedimentary sulphides to produce $Se/S*10^6$ contents lower than mantle such as those from the Thompson Nickel Belt ores and the PGE-depleted norites of the Dunka Road deposit in the Duluth Complex (Eckstrand et al., 1989; Thériault et al., 1997).

Selenium contents in DDH EK-02 generally show maximum contents associated with the mineralized zones through the lithologies (Fig. 5.29). Within the lherzolite unit, background Se contents are from 69 to 97 ppm Se from 22 to 157 m. Within the sulphidized olivine websterite unit, there is a large maximum of 2246 ppm Se at 180 m associated with the main mineralized zone and another maximum of 1178 at 199 m also associated with that zone. Within the pyroxenite unit, maxima are associated with the two zones of mineralization within that unit. At 237 m, there is 621 ppm Se and at 270 m, there is a large maximum content of 1166 ppm Se. In the basement banded iron formation bordering the intrusion, there is a large increase in Se to contents of 1322 ppm at 311 m and 1880 ppm at 327 m. The high Se contents in this lithology show that it is a good source of external sulphur for Ni-Cu-PGE mineralization in the intrusion.

Below the banded iron formation, there is basement mafic metavolcanic that has maximum Se contents of 464 ppm at 330 m and 765 ppm at 344 m. The high Se contents in the basement metavolcanic also make it a good source of external sulphur for mineralization in the intrusion.

Maximum contents of Se content are also found in DDH EK-03 and EK-04 at the bottom of the intrusive units in contact with basement Sibley sediments. In EK-03, an altered bottom melanogabbro in contact with Sibley sediments has a Se content of 1674.56ppm at 139 m. In EK-04, a bottom melanogabbro in contact with Sibley sediments has a Se content of 381.81 ppm at 193 m. The large Se contents show that the Sibley sediments also contributed as a sulphur source to the intrusion. However, the lack of Ni-Cu-PGE mineralization within these holes show that the sediments did not contribute as good a source of sulphur as the iron formation and mafic metavolcanic lithologies to contaminate the magma necessary for sulphide mineralization.

5.5.5 Mineralization model

Mineralization in the Kitto intrusion occurs in the lherzolite-olivine websterites in the bottom olivine websterite as the main basal zone mineralization between 169.5 and 212.5m in DDH EK-02. Potential mineralization in the Kitto intrusion was first studied by Hart et al., 2002 who examined the intrusion in detail as part of an Ontario Geological Survey of the region. In his work, he plotted up metal mantle-normalized element diagrams of the peridotite and olivine gabbro lithologies, which he found to show patterns similar to komatiites and high-MgO basalts of Barnes et al. (1987; Fig. 5.30 a and b). This shows that PGE contents were relatively unfractionated from mantle contents and were mineralized in a magmatic system. On a Pd/Ir vs. Ni/Cu diagram, peridotites plotted in the layered intrusion field trending toward komatiite (Fig. 5.31a). On a Cu/Pd vs. Pd diagram, the lithologies plotted with Cu/Pd ratios less than mantle contents and palladium contents slightly greater than mantle contents, indicating the parental

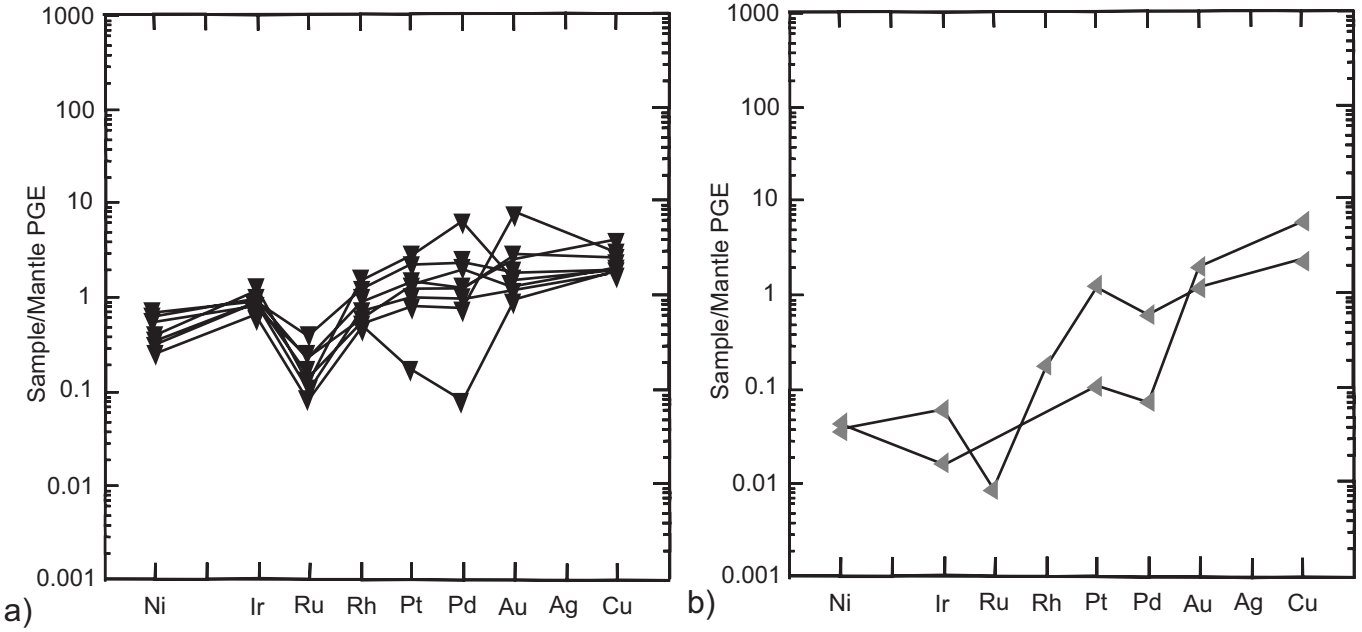

Figure 5.30: Metal mantle-normalized element diagrams of the a)peridotite and b)olivine or granophyric gabbro units of the Kitto Intrusion. The units show patterns similar to komatiites and high-MgO basalts of Barnes et al. (1987). Modified after Hart et al. (2002).

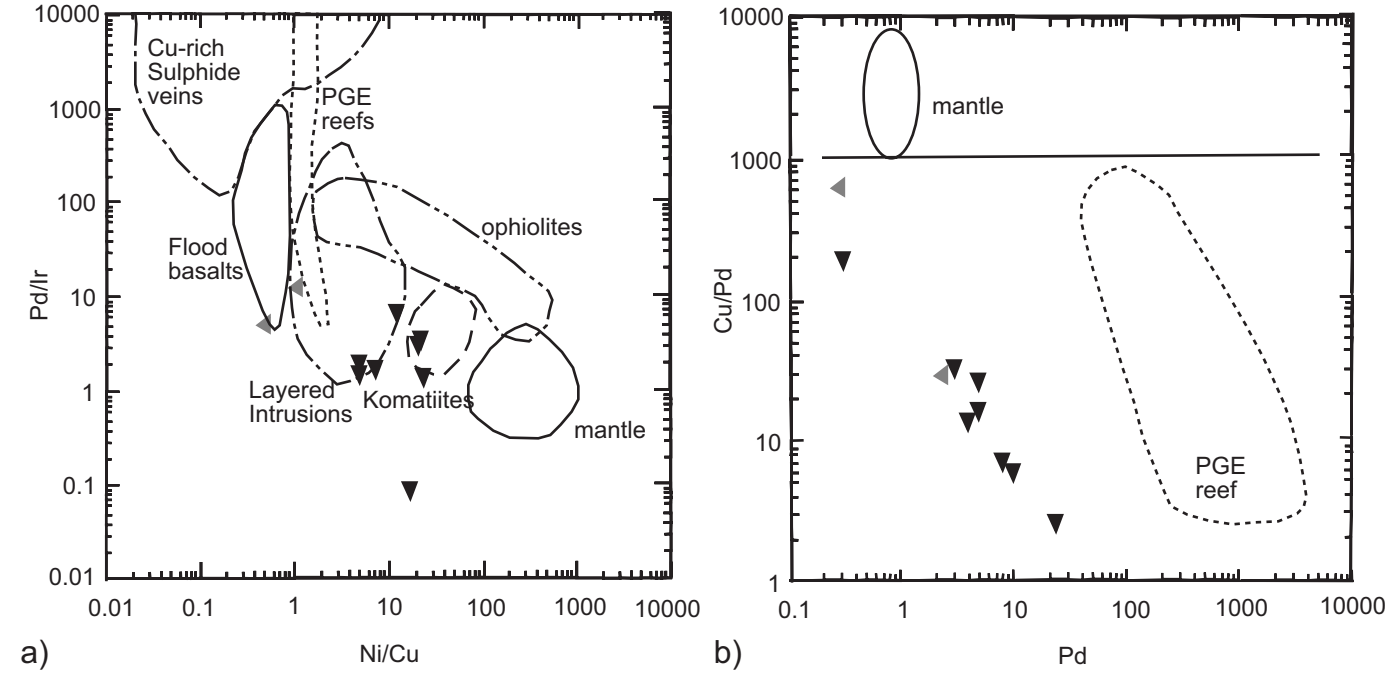

Figure 5.31: On a Pd/Ir vs. Ni/Cu diagram (a), Kitto peridotites (black triangles) and granophyric gabbros (grey triangles) plot in the layered intrusions field trending towards komatiite. On a Cu/Pd vs. Pd diagram (b), the units plot with Cu/Pd ratios less that mantle contents and palladium contents slightly greater than mantle contents. Modified after Hart et al. (2002).

magma was not depleted in PGE, but had the potential to host PGE mineralization if a sulphur source was available (Fig. 5.31b; Hart et al., 2002). Basal mineralization has since been detected with the drilling of DDH EK-02 into sulphidized olivine websterites, and the hole was also drilled into basement iron formation and mafic metavolcanic lithologies, of which would probably provide sulphur sources for mineralization (Fig. 3.3). Maximum increases in Se contents in DDH EK-02 observed as part of this thesis within the olivine websterite were probably due to addition of external sulphur from these basement lithologies to cause the lherzolite-olivine websterite magma to be saturated with S and precipitate the Ni-Cu-PGE bearing minerals. The large increases in Se in basement iron formation and mafic metavolcanic rocks appear to provide a sulphur source for mineralization. The mineralized zone probably formed from the settling of immiscible droplets of sulphur to the bottom of the lherzolite-olivine websterite magma chamber that precipitated as pyrrhotite-pentlandite-chalcopyrite sulphides upon contamination and sulphur saturation of the lithologies. These sulphides are seen in the petrography of the sulphidized olivine websterites (Samples ED-01, -02, -03, -04 and -05; Fig. 3.18). This basal zone mineralization is comparable to that of basal mineralization in other intrusions such as the basal zone mineralization in the olivine amphibole pyroxenite in the Seagull intrusion in the Nipigon Embayment and taxitic gabbro of the Talnakh intrusions of the Noril'sk area, Siberia (Heggie, 2005; Naldrett et al., 2002). Along with precipitation of sulphides, there was the partitioning of PGE into sulphides to maximum contents of up to 563 ppb Pt+Pd detected over a 1.5 m sampled interval. On surface, anomalous metal contents of 54 ppb Pt+Pd and 1125 ppm Ni have been detected in olivine websterite at the Phoenix occurrence in the vicinity of DDH EK-2. Boulders of the lithology at the occurrence have been sampled with assays running at 901 and 1065 ppb Pt and Pd (Coombes and Rossell, 2003). Ni and Cu

metals also concentrate within two zones of the pyroxenite unit, and textural evidence of pyrrhotite-pentlandite-chalcopyrite sulphides in sample ED-09 shows that mineralization occurred interstitial to cumulate minerals during crystallization of the lithologies. Also, a maximum increase in Ni and Cu with PGE in the bottom melanogabbro indicates there was also contact-style mineralization with fractionation of the melanogabbro. In thin section, mineralization occurs in the form of blebby pyrrhotite sulphides (Fig. 3.33). Mineralization within the melanogabbro is minor in comparison to the basal zone of the lherzolite-olivine websterite. However, in conjunction with high Se contents in the pyroxenite zones, it shows that the bordering iron formation wallrocks of the pyroxenite and melanogabbro lithologies provided a contaminant and sulphur source to cause mineralization of sulphides (Fig. 5.29). The high Se contents in bordering iron formation and mafic metavolcanic rocks is good evidence for contamination of the intrusion at shallower crustal levels.

Mineralization occurs in the pyroxene-porphyritic melanogabbro as anomalous PGE contents of 242, 37 ppb Pt, Pd have been detected in sample JL-026 and Pt, Pd contents of 139, 180 ppb in JL-015 in the central pyroxene-porphyritic melanogabbros close to the contact with olivine websterite (Fig. 4.22). DDH EK-05-01, that was drilled based on the anomalous PGE contents and on trend with electromagnetic conductors of iron formations, intersected 245 m of the lherzolite and ended from 180 to 245 m with basal 1% pyrrhotite-chalcopyrite sulphides, although anomalous PGE numbers were not detected (Fig. 5.12). The thickness of the lherzolite shows that it is probably thickest in the centre of the intrusion proximal to pyroxene-porphyritic melanogabbros. Along with deepening of the intrusion, it becomes more magnesian with depth from 26 to 31 wt. % increase in MgO. The gradual change to more MgO-rich compositions and the basal zone of sulphides probably indicates that the lherzolite to pyroxene-porphyritic

melanogabbro lithologies originated from one main pulse of lherzolite magma that fractionated to roof melanogabbro. In the magma chamber, the more MgO-rich lithologies would be at the bottom with more evolved lithologies towards the top. From logging of core from DDH EK-05-01, differentiated lithologies and layering were not observed throughout the section, and so probably shows that there was only one magmatic pulse (Appendix 1: EK-05-01 core log; Fig. 5.12). Along with the influx of magma, there was sulphur saturation to precipitate sulphides in a basal zone in the pyroxene-porphyritic melanogabbro to lherzolite lithologies. Surface metal contents in the pyroxene-porphyritic melanogabbro show lower Ni contents than lherzolite, but higher Cu contents with some anomalous Ni and Cu contents (Figs. 4.23 and 4.24). The lower Ni is due to less olivine crystallized, but higher Cu contents probably due to progressive evolution in the lithologies. Anomalous Ni and Cu contents probably indicate that the lithology was saturated in sulphur to precipitate sulphides like the lherzolites.

5.5.6 Comparison of the Kitto intrusion with Noril'sk

Primitive mantle normalized multi-element plots of lithologies in the southern part of the Kitto intrusion give evidence of crustal contamination of the magma for the formation of Ni-Cu-PGE sulphides in at least four zones of mineralization, analogous to crustal contamination and mineralization of the Noril'sk intrusions in Siberia (Naldrett et al., 1992). Crustal contamination signatures in the lherzolite-olivine websterite and pyroxenite-melanogabbro include pronounced negative Nb anomalies, La and LREE enrichment and negative Ti anomalies. The pulsing of magma in the lower pyroxenite-melanogabbro and upper lherzolite-olivine websterite in the Kitto intrusion with lesser contamination and more replenishment of magma in the lherzolite-olivine websterites in a closed magma chamber compared to the lower pyroxenite-melanogabbros is similar to the replenishing pulse of massive ore-bearing Talnakh-type Noril'sk

intrusions in a higher magma chamber at the Noril'sk deposit in Siberia (Naldrett et al., 1992). Similarities exist between lherzolite-olivine websterites of the Kitto intrusion and the Talnakh-type intrusions since both units carry Ni in olivine signatures, as evidenced by increasing Ni ppm with MgO in the lherzolite-olivine websterites compared to less contaminated Talnakh intrusions carrying Ni and Cu signatures to a higher magma chamber; and both underwent mineralization when contaminated with sulphur-rich wallrocks as evidenced by high Se contents in a main zone in the lherzolite-olivine websterite and high Se in wallrock iron formation and mafic metavolcanic rock compared to high Se contents in the Noril'sk intrusions in general (Arndt et al, 2003; Thériault, 1997). At Noril'sk, the Lower Talnakh-type intrusions first intruded along the Noril'sk-Kharayelakh Fault in association with contaminated Nadezhdinsky to Morongovsky flood basalts (Fig. 5.32; Naldrett et al., 1992). These intrusions have similar REE patterns as the Nadezhdinsky flood basalts with LREE enrichment and more pronounced negative Nb and Ti anomalies than the upper Mokulaevsky flood basalts (Naldrett et al., 1992). Along with intrusion, there was precipitation of disseminated Ni- and Cu-poor sulphides. These intrusions have the highest degree of contamination, yet low grade accumulation of sulphides since they were interpreted, in light of Os evidence of higher γOs contents, to have contaminated earlier and deposited sulphides in a lower magma chamber before moving upward through a feeder conduit and precipitating disseminated sulphides in a higher magma chamber (Fig. 5.32; Arndt et al., 2003). After intrusion of the Lower Talnakh-type intrusions, there was intrusion of the Talnakh-type intrusions in association with Mokulaevsky flood basalts (Fig. 5.32; Naldrett et al., 1992). These intrusions have REE patterns similar to the Mokulaevsky flood basalts with flatter LREE to HREE patterns, yet still have negative Nb anomalies (Naldrett et al., 1992). The Talnakh-type intrusions from bottom to top consist of taxitic gabbro-dolerite, picritic gabbro-dolerite, rare

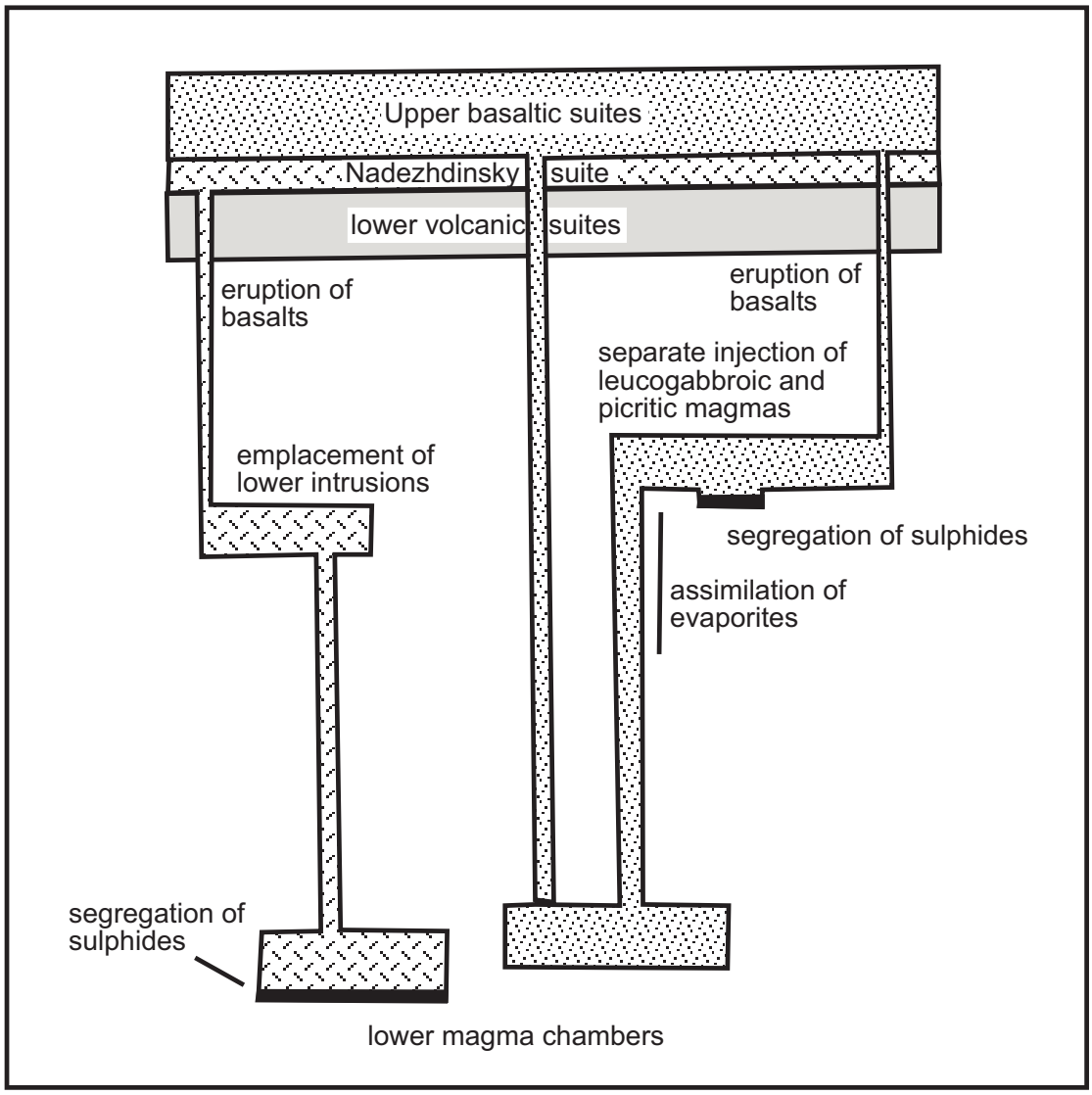

Figure 5.32: The Talnakh and Lower Talnakh Intrusions of the Noril'sk Ni-Cu-PGE deposits became crustally contaminated at different times to segregate sulphides in different chambers. The Lower Talnakh intrusions,associated with Nadezhdinsky flood basalts, became crustally contaminated and segregated sulphide in a deep magma chamber. The ore-bearing Talnakh Intrusions, associated with upper basaltic unit however assimilated evaporite sedimentary rock en route to a shallower magma chamber to segregate sulphides. The lherzolite-olivine websterite and pyroxenite-melanogabbro lithologies of the Kitto intrusion probably became crustally contaminated to segregate sulphides in a higher magma chamber similar to the Talnakh intrusions. After Arndt et al. (2003).

troctolite, rare plagioclase-peridotite and olivine-biotite gabbro-dolerite (Naldrett et al., 1992). Along with intrusion of the Talnakh-type intrusions, there was basal mineralization of massive Ni-, Cu- and PGE-rich ores in the taxitic gabbro-dolerite unit (Naldrett et al., 1992). Since these lithologies have lower LREE than the Lower-Talnakh intrusions, they were interpreted to carry Ni- and Cu-rich magmatic signatures to the surface with intrusion until they came in contact with sulphate-rich Devonian evaporates of the Siberian platform, became crustally contaminated and rained out massive sulphides in a basal zone (Fig. 5.32; Arndt et al., 2003). The Talnakh-type intrusions deposited in higher magma chambers as seen by lower γOs contents than the Lower Talnakh-type intrusions with higher γOs contents (Fig. 5.32; Arndt et al., 2003).

The Kitto intrusive units likely formed in a similar way to the Noril'sk intrusions, only they probably all formed in a higher magma chamber, where they were in contact with basement continental crust causing them to be crustally contaminated and precipitate sulphides. Evidence for the Kitto intrusive units as forming from the same source magma that emplaced in one magma chamber are similarity of primitive mantle plot patterns between the lherzolite-olivine websterite and lower pyroxenite-melanogabbro, similar negative ε_{Nd} contents between the lithologies, and primitive to crustally contaminated REE signatures in the lherzolite-olivine websterite. Evidence for mineralization in a higher magma chamber can be seen in the primitive chemistry and high Ni vs. MgO contents of some of the lherzolite-olivine websterites as being due to the lithologies carrying magmatic signatures of high Ni and Cu before settling out sulphides in a higher magma chamber. This is in contrast to the Lower Talnakh-type deposits that were already crustally contaminated from interaction with crust in a lower magma chamber before mineralizing only disseminated sulphides in a higher magma chamber. The pyroxenite-melanogabbro also formed similarly to the higher ore-bearing Talnakh-type intrusions, since it

did not previously segregate sulphide in a deep stage chamber before reaching a higher magma chamber. Evidence for pyroxenite-melanogabbros as also forming in one magma chamber are the similar primitive mantle plot, ε_{Nd} patterns as lherzolite-olivine websterite and retention of primary Ni vs. MgO contents in the lithologies. In the pyroxenite-melanogabbro, there was earlier crustal contamination in an earlier pulse of magma that assimilated crust and precipitated disseminated sulphides along with accumulation of pyroxene minerals. After the pyroxenite-melanogabbros, there was a replenishing pulse of lherzolite-olivine websterite that churned up the lower pyroxenite, as evidenced by the formation of the patchy vari-textured pyroxenite unit; assimilated crust and precipitated sulphides. The lherzolite-olivine websterite is similar to the Talnakh-type intrusions of the Noril'sk region where primitive magma that carried Ni- and Cu-rich signatures came in contact with S-bearing continental crust to be contaminated and precipitate sulphides in a basal zone. The vari-textured pyroxenite below the mineralized zone in the olivine websterite is similar to the fractionated taxitic gabbro unit of the Talnakh-type intrusions since there was assimilation of xenoliths of crust in the taxitic gabbro and fractionation with the new pulse of magma. Both the taxitic gabbro and vari-textured pyroxenite are evidence of dynamic magmatic conditions at the bottom of a staging magma chamber.

5.5.7 Intrusion in a Noril'sk-type setting

The Kitto intrusive units have been described to occur in a Noril'sk-type setting mainly due to similar continental rift setting of the Midcontinental Rift system in North America to the Siberian Platform-West Siberian Plate-Taimyr fold belt continental rift setting in Siberia (Naldrett, 1992; Simonov et al., 1994). The Kitto intrusion is related to the series of Keweenawan intrusive events in the Mid-Continental Rift system as the first series of ultramafic intrusions before contemporaneous to later intrusion of Nipigon diabase intrusions and extrusion

of Osler Volcanic Group basalts at 1108±1 Ma in the Nipigon Embayment (Davis and Green, 1997). Similarities have been drawn between the Midcontinental Rift and the Siberian Platform that include: 1) evolution related to a mantle plume that gave rise to voluminous basaltic magmatism; 2) magma emplacement along major faults; 3) crustal contamination of some magmas; and 4) chalcophile element depletion in some volcanic/intrusive sections indicating sulfide fractionation at depth (Schulz et al., 1996). Contemporaneous intrusion of Ni-Cu-PGE intrusions with chalcophile-depleted flood basalt volcanism would show that the flood basalts would have interacted with sulphide from the intrusion to cause metal depletion (Naldrett, 1992). The Osler Group Volcanic rocks have been shown to be chalcophile-depleted by Naldrett (1992) and therefore there would be potential of there being interaction with sulphides in contemporaneous Ni-Cu-PGE intrusions. However, the timing of flood basalt volcanism has been dated as later than ultramafic intrusions in the Nipigon Embayment (Kissin et al., 2006), with dates of 1108 Ma for the Osler volcanic rocks being younger than that of such intrusions as the Seagull intrusion at ca. 1124 to 1112 Ma and the Kitto intrusion at ca. 1117 Ma (Heaman and Easton, 2006). Therefore the Noril'sk model for the Nipigon Embayment has been concluded to be non-tenable (Kissin et al., 2006). However, a case can be made for chalcophile-depleted Nipigon sills that are relatively the same age as the intrusions.

The ultramafic intrusions of the Nipigon Embayment can be shown to be Noril'sk-type in that they assimilated continental crust, and assimilated S with interaction with S-bearing wallrocks to become mineralized. The geologic setting of continental plume magmatism in a continent rift environment is also similar to the continental rift setting of the Noril'sk area in Siberia, along with intrusion along large crustal faults such as the Black Sturgeon Fault. For the Seagull intrusion, it emplaced along the Clearwater Fault in the West Nipigon Embayment and

assimilated S-bearing Quetico metasedimentary rock to precipitate sulphides in a basal zone (Fig. 2.11; Hart, 2005; Heggie, 2005). For the Kitto intrusion, the intrusion emplaced along the Nipigon River or Pijitawabik Fault, first became crustally contaminated with assimilation of Quetico Metasedimentary rock and SVU mafic metavolcanic rock, and then became crustally contaminated with assimilation of S-bearing basement iron formation and metabasalt in its crystallization history to mineralize sulphides with crustal contamination. Crustal contamination for mineralization of sulphides in the lherzolite-olivine websterite and lower pyroxenite-melanogabbros of the Kitto intrusion is also shown to be comparable to the Talnakh Intrusions in the assimilation of crust for mineralization of sulphides in a higher magma chamber. High Se contents in the intrusive units are comparable to the high Se contents found in the Noril'sk intrusions (Thériault et al., 1997) as evidence of S assimilation with contamination to precipitate sulphides. Also, turbulent magma flow along crustal faults to precipitate and flow differentiate lower pyroxenite-melanogabbros, and the formation of patchy vari-textured pyroxenite lithologies with churning up of lower pyroxenite-melanogabbro magmas by higher lherzolite-olivine websterite similar to taxitic gabbro of the Talnakh intrusion can be attributed to dynamic magmatic systems similar to Noril'sk-type Ni-Cu-PGE-bearing intrusions.

5.6 Summary

A model for formation of the Kitto intrusion can be deduced largely from the geological, petrographic and geochemistry data attained with this thesis:

The Kitto intrusion intruded from a northwest Mesoproterozoic fault until it hit older Archean faults of the BGB and intruded westward along such structures (Fig. 5.21). Evidence for intrusion along a fault can be deduced by the outcropping of the lithologies along the Nipigon River or Pijitawabik Fault and the east-west faults of the BGB, the deepening of the lithologies

along the faults as seen in DDH EK-02, aeromagnetic anomalies of faults in the vicinity of the intrusion, and comparison with other intrusions such as the Seagull intrusion along the Clearwater Fault. In the southern part at the Phoenix occurrence, there was first intrusion of pyroxenite to melanogabbro lithologies. Fractionation occurred in the contact melanogabbros possibly by flow differentiation from a central pyroxenitic magma (Fig. 5.33). These lithologies crystallized under plagioclase to pyroxene-controlled fractionation trends. These lithologies first became crustally contaminated at depth by Quetico metasedimentary rock and SVU mafic metavolcanic rock as they intruded along the east-west orientated Blackwater Fault of the BGB. At higher crustal levels, the lithologies then intruded the SVU mafic metavolcanic rock and iron formation of the BGB, assimilated continental crust and were saturated with sulphur to precipitate sulphides in three zones of mineralization. After the pyroxenite to melanogabbro pulse of intrusion, there was a replenishing dynamic pulse of lherzolitic magma that accumulated olivine and clinopyroxene in lower olivine websterite (Fig. 5.33). The lherzolite-olivine websterite was a dynamic pulse since it caused the churning up of lower pyroxenitic rocks to form the patchy textures of the lower vari-textured pyroxenites. The lherzolite-olivine websterite magma was crustally contaminated by Quetico metasedimentary rock with depth, and then assimilated continental crust from the basement iron formation and mafic metavolcanic rock to become saturated with sulphur and precipitate sulphides in a basal horizon. With pulsing of the lherzolite-olivine websterite magma into the magma chamber, there was also gravitational accumulation of olivine and pyroxene minerals with fractionation to less MgO-rich and less Fo-, En- and Fs-rich upper lithologies (Fig. 5.33).

In the central part of the intrusion, lherzolite magma intruded through basement mafic metavolcanic rocks and iron formation along a north-south Mesoproterozoic fault and intruded

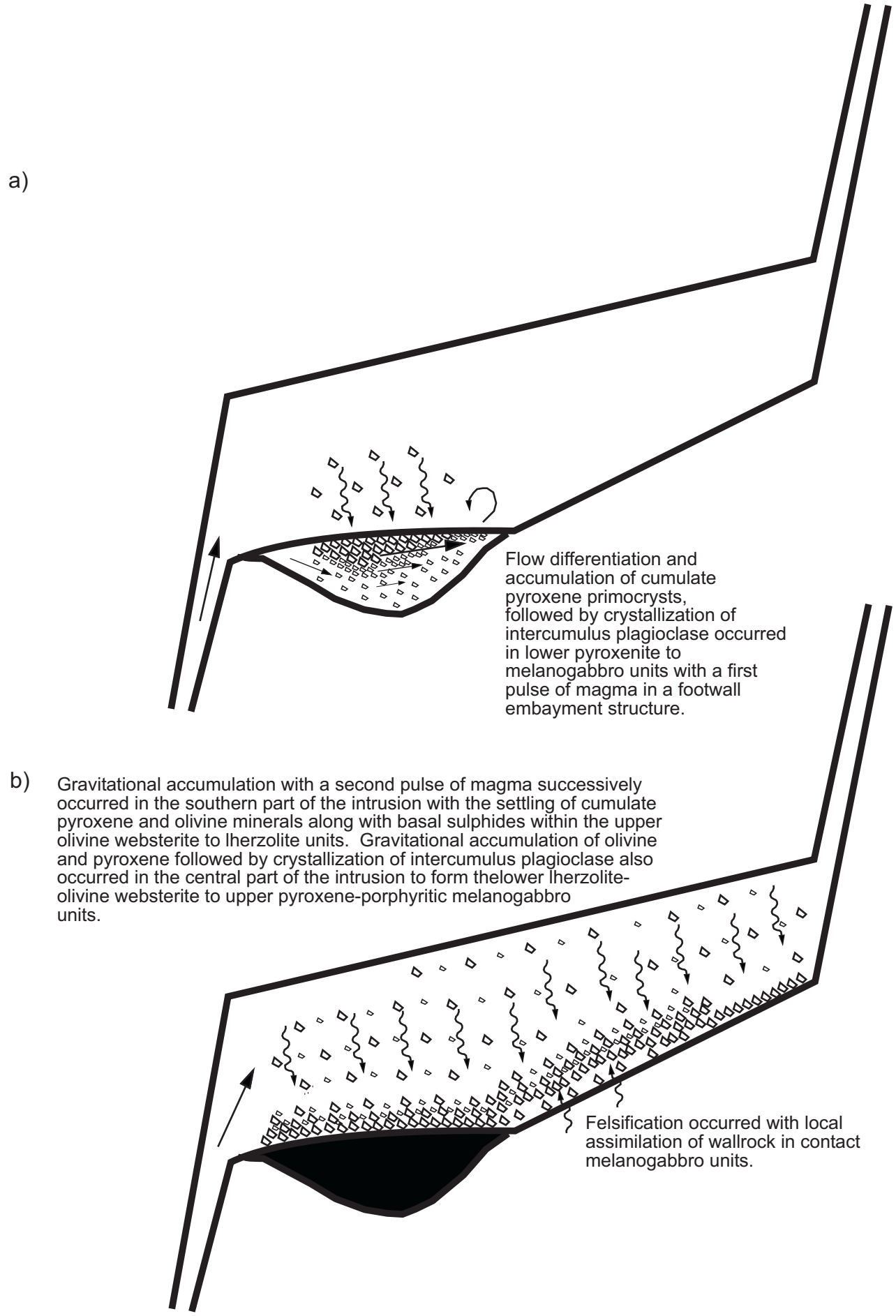

Figure 5.33 a) and b): Schematic diagrams summarizing the magma chamber processes involved in the formation of the Kitto intrusion.

westward along the Princess Lake Fault (Figs. 5.21 and 2.3). With intrusion of the magmas, there was progressive fractionation to olivine websterite and pyroxene-porphyritic melanogabbro lithologies at the roof of the magma chamber (Fig. 5.33). The large amount of pyroxene-porphyritic melanogabbro on surface probably indicates there is a deeper system of lower and more MgO-rich primitive lherzolite with depth. The intrusion assimilated continental crust from mafic metavolcanic rock, iron formation and SSU metagreywacke, and saturated the magma with sulphur to precipitate out sulphides with depth in the lower lherzolites. Evidence for sulphides with depth are in the recently drilled DDH EK-05-01 drill hole which shows dominant lherzolitic lithologies that become more MgO-rich with depth from 26 to 31 wt. %. In the lower MgO-rich lithologies, there is disseminated pyrrhotite-chalcopyrite mineralization from 180 m to the end of hole at 245 m, although no anomalous PGE numbers were detected (Fig. 5.12; Appendix 3: EK-05-01 core log). After peridotitic intrusion, there was intrusion of roof granophyric gabbro as late stage final melts to the west along the Princess Lake Fault.

CHAPTER 6

CONCLUSIONS

From the study of the Kitto intrusion, a number of conclusions can be drawn. One is that the Kitto intrusion is probably a fault-bounded intrusion that formed from a mantle plume at depth, intruded along a Mesoproterozoic north- to northwest-orientated fault and along older Archean faults of the Beardmore-Geraldton Greenstone Belt. There is no evidence of a plume signature, with the exception of one or two samples, since all the rocks have geochemical signatures that are attributed to crustal contamination. However, a probable enriched plume source or parent magma composition has been used to model similar primitive mantle normalized multielement plots in the lithologies of the intrusion, and so can be used as a starting composition of the intrusion. Evidence for the intrusion being intruded along a fault are the parallelism of the Kitto intrusion and surrounding diabase intrusions along northwest-orientated lineaments as observed by outcropping of the intrusions and aeromagnetic anomalies, and also the deepening and occurrence of the intrusion along east-west faults of the Beardmore-Geraldton Greenstone Belt.

Another conclusion is that from petrography, Rb/La, $(La/Sm)_{cn}$ vs. Nb/Nb* diagrams, mineral geochemistry, mineralized zones and comparison with other Ni-Cu-PGE intrusions, the Kitto intrusion is shown to consist of two magmatic pulses in the southern part of the intrusion and a large dominant peridotitic to pyroxene-porphyritic melanogabbroic pulse in the central to northern parts of the intrusion. Petrographic analysis for two pulses in the southern part of the intrusion are the contrasting mineral composition of lherzolite-olivine websterites to lower pyroxenites; and the vari-textured pyroxenite shows patchy textures of secondary pyroxene in

original cumulate pyroxene attributed to the churning up of the lower pyroxenite with a new pulse of lherzolite-olivine websterite. Rb/La ratios show maximum contents at the bottom of the lherzolite-olivine websterite unit attributed to a second pulse of contaminated magma. $(La/Sm)_{cn}$ vs. Nb/Nb* ratios show two distinct contamination trends of pyroxenite-melanogabbro vs. the lherzolite-olivine websterite contamination trend. Mineral geochemistry shows a replenishing pulse in lower pyroxenite-melanogabbro in contrast to replenishment followed by fractionation in the upper lherzolite-olivine websterite unit. Also mineral geochemical trends of decreasing Fo %, En % and increasing Fs % in olivine and pyroxene minerals in the lherzolite to olivine websterite to pyroxene-porphyritic melanogabbro lithologies in the central part of the intrusion show the latter two lithologies evolved from fractionation from a primary lherzolitic magma. Mineralization of pyrrhotite-chalcopyrite minerals trapped between cumulate minerals in two zones in the pyroxenite, a contact-style zone in the lower melanogabbro and a basal horizon at the bottom of the lherzolite-olivine websterite unit give supporting evidence for these two pulses.

Thirdly, fractionation from lherzolite in the southern part of the intrusion to lherzolite, olivine websterite and pyroxene-porphyritic melanogabbro lithologies in the central part of the intrusion is shown, in petrographic analysis, by the fractionation of secondary pyroxene and plagioclase minerals.

Another conclusion is that from primitive mantle normalized multielement plots of negative Nb, Zr, Hf, and Ti anomalies; trace element modeling of primitive mantle plots; $(La/Sm)_{cn}$ vs. Nb/Nb* ratios of two contamination trends of decreasing Nb/Nb* with increasing $(La/Sm)_{cn}$; negative ε_{Nd} contents; and increases in Rb/La and Ba/Th show that all the lithologies of the Kitto intrusion underwent crustal contamination. By comparison with other crustally contaminated Ni-Cu-PGE intrusions, crustal contamination in the lithologies of the Kitto

intrusion is also shown to cause sulphur saturation of the magmas for mineralization of sulphides. This mineralization is found in at least four zones in the lherzolite to pyroxenite and melanogabbro lithologies.

Finally, with crustal contamination of the intrusive units, there was also assimilation of external sulphur from the basement lithologies to cause sulphur saturation in the intrusive units for attending mineralization. External sulphur in the magmatic systems is shown by maximum increases in Se contents within the lithologies and the abundance in Se added in addition to S to cause the lithologies to be sulphur saturated.

REFERENCES

Aerodat Ltd. 1989. M81336. Geophysical/geochemical series, Tashota-Geraldton-Longlac area, airborne electromagnetic survey, total intensity magnetic survey, District of Thunder Bay.

Aerodat Ltd. 1989. M81337. Geophysical/geochemical series, Tashota-Geraldton-Longlac area, airborne electromagnetic survey, total intensity magnetic survey, District of Thunder Bay.

Anderson, D.L. January 1994. Superplumes or supercontinents? Geology, 22, p. 39-42.

Anglin, C.D. and Franklin, J.M. 1985. Gold mineralization in the Beardmore-Geraldton area of northwestern Ontario: structural considerations and the role of iron formation; in Current Research, Part A, Geological Survey of Canada, Paper 85-1A, p. 193-201.

Arndt, N.T., Czamanske, G.K., Walker, R.J., Chauvel, C., and Fedorenko, V.A. 2003. Geochemistry and Origin of the Intrusive Hosts of the Noril'sk-Talnakh Cu-Ni-PGE Sulfide Deposits. Economic Geology, 98, p. 495-515.

Barnes, S.-J., 1990. The use of metal ratios in prospecting for platinum-group element deposits in mafic and ultramafic intrusions. *In:* C.E. Dunn, G.C. Curtin and G.E.M. Hall *Editors,* Geochemistry of Platinum-Group Elements. Journal of Geochemical Exploration, 36, p. 91-99.

Barnes, S.J., Boyd, R., Korneliussen, A., Nilsson, L-P., Often, M., Pedersen, R.B. and Robins, B. 1987. The use of mantle normalization and metal ratios in discriminating between the effects of partial melting, crystal fractionation and sulphide segregation on platinum group elements, gold, nickel and copper: examples from Norway. *In:* Geo-Platinum '87, Elsevier, Barking, United Kingdom, p. 113-143.

Barnes, S.J. and Hoatson, D.M. 1994. The Munni Munni Complex, Western Australia: stratigraphy, structure and petrogenesis. Journal of Petrology, 35, part 3, p. 715-751.

Barnett, P.J. 2005. Fieldtrip 2 – Quaternary geology of the Beardmore-Nipigon area. *In:* Hollings, P. *Editor*. May 24-28, 2005. Institute on Lake Superior Geology: Part 2 – Field Trip Guidebook, 51st Annual Meeting, Nipigon, Ontario, 104 pages.

Barrett, T.J. and Fralick, P.W. 1985. Sediment redeposition in Archean iron formation: examples from the Beardmore-Geraldton Greenstone Belt. Journal of Sedimentary Petrology, 55, no. 2, p. 205-212.

Barrett, T.J. and Fralick, P.W. 1989. Turbidites and iron formations, Beardmore-Geraldton, Ontario: application of a combined ramp/fan model to Archaean clastic and chemical sedimentation. Sedimentology, 36, p. 221-234.

Blackburn, C.E., Johns, G.W., Ayer, J.A., and Davis, D.W. 1991. Wabigoon Subprovince. *In:* Thurston, P.C., Williams, H.R., Sutcliffe, R.H., and Stott, G.M. *Editors.* Geology of Ontario. Ontario Geological Survey Special Volume 4, Part 1. Ministry of Northern Development and Mines, 711 pages.

Buchan, K.L., Halls, H.C. and Mortensen, J.K. 1996. Paleomagnetism, U-Pb geochronology, and geochemistry of Marathon dykes, Superior Province, and comparison with the Fort Frances swarm. Canadian Journal of Earth Science, 33, p. 1583-1595.

Burnham, O.M., and Schweyer, J. 2004. Trace Element Analysis of Geological Samples by ICP-MS at the Geoscience Laboratories: Revised Capabilities Due to Improvements to Instrumentation. *In* Summary of Field Work and Other Activities 2004. Ontario Geological Survey Open File Report 6145: 54-1 to 54-20.

Burnham, O.M., Hechler, J.H., Semenyna, L., and Schweyer, J. 2002. Mineralogical controls on the determination of trace elements following mixed acid dissolution. *In* Summary of Field Work and Other Activities 2002. Ontario Geological Survey Open File Report 6100: 36-1 to 36-12.

Card, K.D. and Ciesielski, A. 1986. DNAG#1, Subdivisions of the Superior Province of the Canadian Shield. Geoscience Canada 13, p. 5-13.

Chai, G. and Naldrett, A.J. 1992a. Characteristics of Ni-Cu-PGE Mineralization and Genesis of the Jinchuan Deposit, Northwest China. Economic Geology, 87, p. 1475-1495.

Chai, G. and Naldrett, A.J. 1992b. The Jinchuan Ultramafic Intrusion: Cumulate of a High-Mg Basaltic Magma. Journal of Petrology, 33, part 2, p. 277-303.

Coates, M.E. 1972. Geology of the Black Sturgeon River area, District of Thunder Bay. Ontario Department of Mines and Northern Affairs, Geological Report 98, 41 pages. Accompanied by Maps 2233, 2234, 2235, 2236, scale 1 inch to 1 mile.

Coombes, S. and Rossell, D. 2003. June 2003 Report on Diamond Core Drilling on the Eva Kitto Property. NTS: 052H-09, Thunder Bay Mining Division, Ontario. Kennecott Canada Exploration Inc. June 19, 2003.

Davis, D.W. and Sutcliffe, R.H. 1985. U-Pb ages from the Nipigon plate and northern Lake Superior. Geological Society of America Bulletin, v. 96, p. 1572-1579.

Davis, D.W. and Green, J.C. 1997. Geochronology of the North American Midcontinent rift in western Lake Superior and implications for its geodynamic evolution. Canadian Journal of Earth Sciences, 34, p. 476-488.

Deer, W.A., Howie, R.A., and Zussman, J. 1963. Rock-forming minerals: framework silicates, Volume 4. Longmans, Green and Co. Ltd.

Deer, W.A., Howie, R.A., and Zussman, J. 1964. Rock-forming minerals: ortho- and ring silicates, Volume 1. Longmans, Green and Co. Ltd.

Deer, W.A., Howie, R.A., and Zussman, J. 1978. Rock-forming minerals: single-chain silicates, Volume 2A, 2nd Ed. John Wiley & Sons Inc.

Devaney, J.R. and Williams, H.R. 1989. Evolution of an Archean subprovince boundary: a sedimentological and structural study of part of the Wabigoon-Quetico boundary in northern Ontario. Canadian Journal of Earth Sciences, 26, p. 1013-1026.

Duggan, B.M. 2002. The geology and potential mineralization of the Kitto Township Proterozoic layered ultramafic intrusion in Beardmore, Ontario; unpublished BSc thesis, Queen's University, Kingston, Ontario, 65 pages.

Duzhikov, O.A. and Distler, V.V. 1992. Geology and metallogeny of sulfide deposits Noril'sk Region U.S.S.R. Society of Economic Geologists Special Publication Number 1, 242 pages.

Eckstrand, O.R., Grinenko, L.N., Krouse, H.R., Paktunc, A.P., Schwann, P.L. and Scoates, R.F. 1989. Preliminary data on sulphur isotopes and Se/S ratios and the source of sulphur in magmatic sulphides from the Fox River sill, Molson dykes, and Thompson nickel deposits, northern Manitoba. Current Research, Part C, Geological Survey of Canada, Paper 89-1C, p. 235-242.

Ernst, R.E. 2005. May Large Igneous Province of the Month: Ca. 1880 Ma Circum-Superior LIP. Geological Survey of Canada. http://www.largeigneousprovinces.org/May.html.

Evans-Lamswood, D. 1998. Physical and geometric controls on the distribution of magmatic and sulphide bearing phases within the Voisey's Bay nickel-copper-cobalt deposit, Voisey's Bay, Labrador. *Unpublished* MSc. Thesis, Memorial University of Newfoundland, 308 pages.

Fralick, P.W., Davis, D.W. and Kissin, S.A. 2002. The age of the Gunflint Formation, Ontario, Canada: single zircon U-Pb age determinations from reworked volcanic ash. Canadian Journal of Earth Science, 39, p. 1085-1091.

Fralick, P.W. and Kronberg, B.I. 1997. Geochemical discrimination of clastic sedimentary rock sources. Sedimentary Geology, 113, p. 111-124.

Fralick, P.W., Wu, J. and Williams, H.R. 1992. Trench and slope basin deposits in an Archean metasedimentary belt, Superior Province, Canadian Shield. Canadian Journal of Earth Science, 29, p. 2551-2557.

Franklin, J.M. 2001. Review of Sulfur isotope, S/Se ratio and PGE contents of Sulfide Separates Wolf Mountain, Central Nipigon Plate Thunder Bay Districts, Ontario For East-West Resource Corp. Franklin Geosciences Ltd.

Franklin, J.M. 1970. Metallogeny of the Proterozoic rocks of Thunder Bay District Ontario. *Unpublished* PhD. Thesis, The University of Western Ontario, London, Canada.

Franklin, J.M., McIlwaine, W.H., Poulsen, K.H. and Wanless, R.K. 1980. Stratigraphy and depositional setting of the Sibley Group, Thunder Bay district, Ontario, Canada. Canadian Journal of Earth Science, 17, p. 633-651.

Fugro Airborne Surveys. 2002. Logistics and Processing Report; Airborne Magnetic and Megatem II Electromagnetic Multicoil Survey of the Eva Kitto Area, Lake Nipigon, Ontario on behalf of Kennecott Canada Exploration Inc. Job 781, June 2002, Ottawa, Ontario.

Geological Survey of Canada.1934. Map 312A. Sturgeon River Area, Thunder Bay District, Ontario.

Geological Survey of Canada.1974. Map 20,115 G 52 H/9a Ontario. Resource Geophysics and Geochemistry Division.

Geological Survey of Canada. 1988. Aeromagnetic Vertical Gradient Map C41471G, Shakespeare Island, Ontario. Ministry of Northern Development and Mines.

Gupta, V.K. 1991. Map 2585: Shaded image of total magnetic field of Ontario, West-central sheet. Ministry of Northern Development and Mines, Ontario.

Hart, T.R. 2005. Precambrian geology of the southern Black Sturgeon River and Seagull Lake area, Nipigon Embayment, northwestern Ontario; Ontario Geological Survey, Open File Report 6165, 63 pages.

Hart, T.R. and Magyarosi, Z. 2004. Precambrian geology of the northern Black Sturgeon River and Disraeli Lake area, Nipigon Embayment, northwestern Ontario; Ontario Geological Survey, Open File Report 6138, 56 pages.

Hart, T.R. and MacDonald, C.A. 2007. Proterozoic and Archean Geology of the Nipigon Embayment: Implications for Emplacement of the Nipigon Diabase Sills and PGE-enriched mafic to ultramafic intrusions. Canadian Journal of Earth Sciences, in press.

Hart, T.R., terMeer, M. and Jolette, C. 2002. Precambrian geology of Kitto, Eva, Summers, Dorothea and Sandra townships, northwestern Ontario: Phoenix Bedrock Mapping Project; Ontario Geological Survey, Open File Report 6095, 206p.

Heaman, L.M. and Easton, R.M. 2006. Preliminary U/Pb Geochronology Results: Lake Nipigon Region Geoscience Initiative. Ontario Geological Survey Miscellaneous Release Data 191, 78 pages.

Heggie, G. 2005. Whole rock geochemistry, mineral chemistry, petrology and Pt, Pd mineralization of the Seagull Intrusion, Northwestern Ontario. *Unpublished* M.Sc. Thesis, Lakehead University, Thunder Bay, Canada, 160 pages.

Heggie, G.J., and Hollings, P. 2003. Lake Nipigon Region Geoscience Initiative. Petrology and Mineral Chemistry of the Seagull Intrusion. Summary of Field Work and Other Activities, Ontario Geological Survey Open File Report 6120, p. 48-1 to 48-5.

Hinze, W.J., Wold, R.J. and O'Hara, N.W. 1982. Gravity and magnetic anomaly studies of Lake Superior. *In:* Wold, R.J. and Hinze, W.J. *Editors.* Geology and Tectonics of the Lake Superior Basin. The Geological Society of America, Inc. Memoir 156.

Hoatson, D.M. and Sun, S-S. 2002. Archean Layered Mafic-Ultramafic Intrusions in the West Pilbara Craton, Western Australia: A Synthesis of Some of the Oldest Orthomagmatic Mineralizing Systems in the World. Economic Geology, 97, p. 847-872.

Hollings, P., Fralick, P., and Kissin, S. 2004. Geochemistry and geodynamic implications of the Mesoproterozoic English Bay granite-rhyolite complex, northwestern Ontario. Canadian Journal of Earth Sciences, 41, p. 1329-1338.

Hollings, P., Hart, T., Richardson, A. and MacDonald, C.A. 2007a. Geochemistry of the Midproterozoic intrusive rocks of the Nipigon Embayment, Northwestern Ontario. Canadian Journal of Earth Sciences, in press.

Hollings, P., Richardson, A., Creaser, R.A. and Franklin, J. 2007b. Radiogenic isotope characteristics of the Mesoproterozoic Intrusive Rocks of the Nipigon Embayment, Northwestern Ontario. Canadian Journal of Earth Sciences, in press.

Jenner, G.A. 1996. Trace element geochemistry of igneous rocks: geochemical nomenclature and analytical geochemistry. *In:* Wyman, D.A. *Editor.* Trace Element Geochemistry of Volcanic Rocks: Applications For Massive Sulphide Exploration. Geological Association of Canada, Short Course Notes, 12, p. 51-77.

Keays, R.R. 1995. The role of komatiitic and picritic magmatism and S-saturation in the formation of ore deposits. Lithos, 34, p. 1-18.

Kehlenbeck, M.M. 1986. Folds and folding in the Beardmore-Geraldton fold belt. Canadian Journal of Earth Science, 23, p. 158-171.

Kimura, G., Ludden, J.N., Desrochers, J-P. and Hori, R. 1993. A model of ocean-crust accretion for the Superior province, Canada. Lithos, 30, p. 337-355.

Kissin, S.A., Heggie, G.J. and Somarin, A.K. 2006. Sulphide saturation mechanisms in gabbroic intrusions in the Nipigon Embayment: Lake Nipigon Region Geoscience Initiative. Ontario Geological Survey, Open File Report 6176, 17 pages.

Lafrance, B., DeWolfe, J.C. and Stott, G.M. 2004. A structural reappraisal of the Beardmore-Geraldton Belt at the southern boundary of the Wabigoon subprovince, Ontario, and implications for gold mineralization. Canadian Journal of Earth Science, 41, p. 217-235.

Latypov, R.M. 2003. The origin of marginal compositional reversals in basic-ultrabasic sills and layered intrusions by Soret fractionation. Journal of Petrology, 44, p. 1579-1618.

Lesher, C.M. 2005. February 10-11, 2005 Mineral Deposit Short Courses: Magmatic Ni-Cu-PGE Sulfide Deposits, University of Ottawa Department of Earth Sciences.

Lesher, C.M., Burnham, O.M., Keays, R.R., Barnes, S.J., Hulbert, L. 2001. Trace-element geochemistry and petrogenesis of barren and ore-associated komatiites. The Canadian Mineralogist, 39, p. 673-696.

Lightfoot, P.C., Hawkesworth, C.J., Olshefsky, K., Green, T., Doherty, W. and Keays, R.R. 1997. Geochemistry of Tertiary tholeiites and picrites from Qeqertarssuaq (Disko Island) and Nuussuaq, West Greenland with implications for the mineral potential of comagmatic intrusions. Contributions to Mineralogy and Petrology, 128, p. 139-163.

Lightfoot, P.C. and Lavigne, Jr., M.J. 1995. Nickel, copper and platinum group element mineralization in Keweenawan intrusive rocks: new targets in the Keweenawan of the Thunder Bay region, northwestern Ontario; Ontario Geological Survey, Open File Report 5928, 32 pages.

Lightfoot, P.C. and Naldrett, A.J. *Editors*. 1994. Proceedings of the Sudbury-Noril'sk Symposium, Special Volume 5. Ontario Ministry of Northern Development and Mines, 423 pages.

Lightfoot, P.C., Hawkesworth, C.J., Hergt, J., Naldrett, A.J., Gorbachev, N.S., Fedorenko, V.A., and Doherty, W. 1993. Remobilisation of the continental lithosphere by a mantle plume: major-, trace-element, and Sr-, Nd-, and Pb-isotope evidence from picritic and tholeiitic lavas of the Noril'sk District, Siberian Trap, Russia. Contributions to Mineralogy and Petrology, 114, p. 171-188.

MacDonald, C.A., Tremblay, E. and Easton, R.M. 2005. Precambrian geology of the west-central map area, Nipigon Embayment, northwestern Ontario, Lake Nipigon Region Geoscience Initiative; Ontario Geological Survey, Open File Report 6164, 49 pages.

Mackasey, W.O. 1975. Geology of Dorothea, Sandra, and Irwin Townships District of Thunder Bay. Ontario Division of Mines, Geological Report 122, 83 pages. Accompanied by Map 2294, scale 1 inch to ½ mile.

Mackasey, W.O. 1969. Eva and Summers Townships District of Thunder Bay, p. 25-28 *In:* Pye, E.G. *Editor.* Summary of field work, 1969 by the Geological Branch. Ontario Department of Mines Miscellaneous Paper 32.

MacTavish, A.D. 1992. The geology, petrology, geochemistry, sulphide and platinum-group element mineralization of the Quetico Intrusions, Northwestern Ontario. *Unpublished* M.Sc. Thesis. Lakehead University, Thunder Bay, Canada.

Maier, W.D., Barnes, S.-J. deWaal, S.A. 1998. Exploration for magmatic Ni-Cu-PGE sulphide deposits: a review of recent advances in the use of geochemical tools, and their application to some South African ores. South African Journal of Geology, 101(3), p. 237-253.

Manson, M.L. and Halls, H.C. 1997. Proterozoic reactivation of the southern Superior Province and its role in the evolution of the Midcontinent rift. Canadian Journal of Earth Science, 34, p. 562-575.

McNaughton, K.C. 2002. August 2002 Nickel sulphide exploration of the Nipigon Plate Thunder Bay, Ontario Summary of Activities. Canplats Resources Corporation, 71 pages.

Middleton, R.S., Borradaile, G.J., Baker, D. and Lucas, K. 2004. Proterozoic diabase sills of northern Ontario: magnetic properties and history. Journal of Geophysical Research, 109, p. 1-12.

Nabil, H., Clark, T., Barnes, S-J. 2004. A Ni-Co-PGE massive sulfide prospect in a gabbronorite dike at Lac Volant, eastern Grenville Province, Quebec. Memoir – Geological Society of America, 197, p. 145-161.

Naldrett, A.J., Asif, M., Krstic, S. 2000. The Composition of Mineralization at the Voisey's Bay Ni-Cu Sulfide Deposit, with Special Reference to Platinum-Group Elements. Economic Geology, 95, p. 845-865.

Naldrett, A.J., Lightfoot, P.C., Fedorenko, V.A., Doherty, W. and Gorbachev, N.S. 1992. Geology and Geochemistry of Intrusions and Flood Basalts of the Noril'sk Region, USSR, with Implications for the Origin of the Ni-Cu Ores. Economic Geology, 87, p. 975-1004.

Nicholson, S.W., Cannon, W.F. and Schulz, K.J. 1992. Metallogeny of the Midcontinent rift system of North America. Precambrian Research, 58, p. 355-386.

Nicholson, S.W., and Shirey, S.B. 1990. Midcontinent Rift volcanism in the Lake Superior Region: Sr, Nd and Pb isotopic evidence for a mantle plume origin. Journal of Geophysical Research, 95: 10 851-10 868.

Nicholson, S.W., Shirey, S.B., Schulz, K.J. and Green, J.C. 1997. Rift-wide correlation of 1.1 Ga Midcontinent rift system basalts: implications for multiple mantle sources during rift development. Canadian Journal of Earth Sciences, 34, p. 504-520.

Oliver, J. 2001. Eva Kitto Ring Complex Lithogeochemistry. Hunter Dickinson Inc. October 26, 2001.

Ontario Geological Survey. 2004. GDS 1047B Ontario Airborne Geophysical Surveys, Magnetic and Gamma-Ray Spectrometric Data, Grid Data (Geosoft ® Format) and Vector Data, Lake Nipigon Embayment Area.

Percival, J. 1989. A regional perspective of the Quetico metasedimentary belt, Superior Province, Canada. Canadian Journal of Earth Science, 26, p. 677-693.

Pye, E.G. 1965. Georgia Lake Area. Ontario Department of Mines, Geological Report 31, 113 pages. Accompanied by Map 2056, scale 1 inch to 1 mile.

Reichov, M.K., Saunders, A.D., White, R.V., Al'Mukhamedov, A.I. and Medvedev, A.Ya. 2005. Geochemistry and petrogenesis of basalts from the West Siberian Basin: an extension of the Permo-Triassic Siberian Traps, Russia. Lithos, 79, issues 3-4, p. 425-452.

Richardson, A.J., Hollings, P. and Franklin, J.M. 2005. Geochemistry and radiogenic isotope characteristics of the sills of the Nipigon Embayment: Lake Nipigon Region Geoscience Initiative; Ontario Geological Survey, Open File Report 6175, 86 pages.

Ripley, E.M. 1990. Se/S ratios of the Virginia Formation and Cu-Ni sulfide mineralization in the Babbit Area, Duluth Complex, Minnesota. Economic Geology, 85, p. 1935-1940.

Ripley, E.M., Al-Jassar, T.J. 1987. Sulfur and Oxygen Isotope Studies of Melt-Country Rock Interaction, Babbitt Cu-Ni Deposit, Duluth Complex, Minnesota. Economic Geology, 82, p. 87-107.

Rogala, B., Fralick, P.W. and Metsaranta, R. 2005. Stratigraphy and sedimentology of the Mesoproterozoic Sibley Group and related igneous intrusions, northwestern Ontario: Lake Nipigon Region Geoscience Initiative; Ontario Geological Survey, Open File Report 6174, 128 pages.

Rossell, D. 2003. November 2003 Report on Diamond Core Drilling on the Eva Kitto Property. NTS: 052H-09, Thunder Bay Mining Division, Ontario. Kennecott Canada Exploration Inc. November 14, 2003.

Salib, P. 1989. Interpretation Report Input Mark VI Electromagnetic/Magnetic Survey; Glen Auden Resources Ltd., Lake Nipigon, Ontario Project #88022. Questor Surveys Limited.

Schulz, K.J., Cannon, W.F., Nicholson, S.W., Woodruff, L.G., Foose, M.P. 1996. Potential for magmatic Ni-Cu deposits in the Midcontinent Rift; a new look based on Voisey's Bay and Noril'sk. Geological Society of America Abstracts with Programs, 28, no. 7, page 92.

Shanks, W.S. 1993. Geology of Eva and Summers Townships, District of Thunder Bay. Ontario Geological Survey, Open File Report 5821, 93 pages.

Shenghao, Y., Zhaochong, Z., Denghong, W., Bailin, C., Lixin, H., Gang, Z. 2003. Kalatongke magmatic copper-nickel sulfide deposit. International Association on the Genesis of Ore Deposits Guidebook Series, 10, p. 131-151.

Shirey, S.B., Klewin, K.W., Berg, J.H. and Carlson, R.W. 1994. Temporal changes in the sources of flood basalts: Isotopic and trace element evidence from the 1100Ma old Keweenawan Mamainse Point Formation, Ontario, Canada. Geochimica et Cosmochimica, 58, no. 20, p. 4475-4490.

Simonov, O.N., Lul'ko, V.A., Amosov, Yu.N., Salov, V.M. 1994. Geological Structure of the Noril'sk Region. *In:* Lightfoot, P.C. and Naldrett, A.J. *Editors*. Proceedings of the Sudbury-Noril'sk Symposium, Special Volume 5. Ontario Ministry of Northern Development and Mines, 423 pages.

Sutcliffe, R.H. 1987. Petrology of Middle Proterozoic diabases and picrites from Lake Nipigon, Canada. Contributions to Mineralogy and Petrology, 96, p. 201-211.

Sutcliffe, R.H. 1986. The petrology, mineral chemistry and tectonics of Proterozoic rift-related igneous rocks at Lake Nipigon, Ontario. *Unpublished* PhD. Thesis, The University of Western Ontario, London, Ontario.

Smyk, M., Fralick, P. and Hart, T.R. 2005. Fieldtrip 1 – Geology and gold mineralization of the Beardmore-Geraldton greenstone belt. *In:* Hollings, P. *Editor*. May 24-28, 2005. Institute on Lake Superior Geology: Part 2 – Field Trip Guidebook, 51st Annual Meeting, Nipigon, Ontario, 104 pages.

Southwick, D.L. and Day, W.C. 1983. Geology and petrology of Proterozoic mafic dikes, north-central Minnesota and western Ontario. Canadian Journal of Earth Sciences, 20, p. 622-638.

Streckeisen, A.L. 1973. Plutonic rocks – Classification and nomenclature recommended by the IUGA Subcommission on Systematics of Igneous Rocks. Geotimes, 18, p. 26-30.

Thériault, R.D., Barnes, S-J. and Severson, M.J. 1997. The influence of country-rock assimilation and silicate to sulfide ratios (R factor) on the genesis of the Dunka Road Cu-Ni-platinum-group element deposit, Duluth Complex, Minnesota. Canadian Journal of Earth Sciences, 34, p. 375-389.

Thurston, P.C. 1991. Archean Geology of Ontario: Introduction *In:* Thurston, P.C., Williams, H.R., Sutcliffe, R.H. and Stott, G.M. *Editors.* Geology of Ontario. Ontario Geological Survey, Special Volume 4, Part 1, Ministry of Northern Development and Mines, 711 pages.

Tomlinson, K.Y., Bowins, R., and Heshler, J. 1998. Refinement of Hafnium (Hf) and Zirconium (Zr) analysis by improvement in the sample digestion procedure. Ontario Geological Survey, Miscellaneous Paper 169: 189–192.

Tomlinson, K.Y., Hall, R.P., Hughes, D.J., Thurston, P.C. 1996. Geochemistry and assemblage accretion of metavolcanic rocks in the Beardmore-Geraldton greenstone belt, Superior Province. Canadian Journal of Earth Sciences, 33, p. 1520-1533.

Williams, H.R. 1991. Quetico Subprovince. *In:* Thurston, P.C., Williams, H.R., Sutcliffe, R.H., and Stott, G.M. *Editors.* Geology of Ontario. Ontario Geological Survey Special Volume 4, Part 1. Ministry of Northern Development and Mines, 711 pages.

Williams, H.R. 1990. Subprovince accretion tectonics in the south-central Superior Province. Canadian Journal of Earth Science, 27, p. 570-581.

Wold, R.J. and Hinze, W.J. *Editors.* 1982. Geology and Tectonics of the Lake Superior Basin. The Geological Society of America, Inc. Memoir 156.

Yakubchuk, A., Nikishin, A. 2004. Noril'sk-Talnakh Cu-Ni-PGE deposits: a revised tectonic model. Mineralium Deposita, 39, p. 125-142.

Zhong, H., Yao, Y., Prevec, S.A., Wilson, A.H., Viljoen, M.J., Viljoen, R.P., Bing-Guang, L., and Yao-Nan, L. 2004. Trace-element and Sr-Nd isotopic geochemistry of the PGE-bearing Xinjie layered intrusion in SW China. Chemical Geology, 203, issue 3-4, p. 237-252.

Zhou, M-F., Zhao, T-P., Malpas, J., Sun, M. 2000. Crustal-contaminated komatiitic basalts in Southern China: products of a Proterozoic mantle plume beneath the Yangtze Block. Precambrian Research, 103, p. 175-189.

APPENDIX 1

Core logs for DDH EK-01, -02, -03, -04 and EK-05-01

Eva Kitto 03-EK-01 Collar Location: 418447E 5487240N NAD 27 Dip vertical Az. N/A

From (m):	To (m):	Rock Type:	Description:
0	6	Overburden	
6	140.54	Lherzolite	Lherzolite: Massively textured fine-grained ultramafic consists of large poikilitic black to dark green? Pyroxenes enclosing anhedral to rounded 1mm-sized pale green olivine crystals. Biotites are 1-2mm irregular bronzy crystals dispersed as minor 3 to 5% phases in groundmass. Some pyroxenes are broken up to phases ~1mm in size. Large oikocrysts have serrated boundaries.
6	22.7		Vein serpentine - carbonate altered zone in lherzolite with 10 to 20cm spaced 3 to 5mm wide green serpentine or white calcite veins running 55 to 70º to CA to near vertical in orientation
	at 21.85		8mm wide long serpentine-talc-calcite vein with 18 to 20º orientation contains tr pyrite
	at 35.15		up to 1cm wide dominantly calcite to serpentine vein that pinches and swells along fracture interior is filled with sugary creamy-coloured vuggy calcite; green 1mm membrane of serpentine alteration haloe surrounding vein is black pockety with respect to main lherzolite unit. Pockets consist of aphanitic weathered out pits of gritty serpentinized olivine? finer grained chill margins; haloes are 0.5 to 2mm in size
49.25	50.2		light olive-green altered zone in lherzolite with irregular and thin serpentine-filled fractures some vuggy white calcite in centres of veins; larger proportion of bitotite mineralogy within zone of serpentine fractures ~10%
	at 49.25		serpentine calcite vein oriented 42º to CA
55.25	56.9		olive green darker largely wholesale serpentinized zone - olivines within oikocrystic pyroxenes are serpentinized
55.35	55.45		<1mm capillary veins of malachite run parallel and between lined serpentinized olivine grains some calcite selvages among malachite
56.36	56.5		thick 1.2cm wide vein of serpentine-calcite contains numerous 1 to 3mm cg biotite within alteration haloe; vein runs 18º to CA
56.62	56.87		olive green biotitized malachite altered and serpentinized zone - some calcite selvages
58.4	68.45		vein serpentinized zone in lherzolite with 10 to 30cm spaced ~0.7cm light green veins of calcite-serpentine - some associated malachite in some veins
71.75	72.35		long vein of calcite-serpentine running along CA is also largely biotitized with 1mm dispersed biotite grains

	72.75	72.87		aphanitic mafic dike intruding lherzolite 80º to CA on ;upper contact to 30º to CA on lower contact ~ massive aphanitic textured and non-magnetic
	88.93	89.12		vein of 1cm serpentine-calcite with cg biotite growth within haloe
		at 90		lherzolite testurally becomes spotted and has a more sheafy association of pyroxenes rather than large oikocrysts; however, pyroxenes still have poikilitic intergrowths of olivine and the rock is biotitiferous like that of the main lherzolite
		at 114.60		0.3cm thick potassic altered felsic veinlet runs irregularly trough peridotite 20 to 30º to CA - irregular contacts veinlets also found at 106.5 and 109.3 (also contains vein calcite - vuggy)
		at 121.25		possible fg chalcopyrite along fracture serpentine vein that runs 55º to CA
	122	123		gradational increase in feldspar content of peridotite
	132.82	140.54		development of thin thread-like to coarser 0.8cm white calcite - distinct with some associated serpentine in the thicker veinlets - selvage appears to be a haphazardly non-structurally controlled veinlet infilling cement
		at 140.54		serpentine calcite veins are in contact with Sibley sediments
	140.54	145.2		contact of spotted lherzolite with hornfels; contact zone contains up to 145.2: banded zone of aphanitic green to orange-altered hematized hornfels with porphyritic 1mm crystals of biotite and some fg spotted mod magnetic grey peridotite
		at 140.6		0.5cm veinlets of serpentine calcite run 80º to CA at edge of contact hornfels zone
145.2	149.7		Sandstone	Sibley sandstone

Eva Kitto 03-EK-02 Collar Location: 418447E 5487240N NAD 27 Dip -45º Az. 245º

From (m):	To (m):	Rock Type:	Description:
0	7	Overburden	
7	209	Lherzolite	Lherzolite: Small ~1mm or less equigranular rounded translucent light green olivine crystals are enclosed by large up to 1cm black to dark green clinopyroxenes. Individual olivine crystals show conchoidal fracturing and show diffuse pale green reaction rims between grains; plagioclase is a very minor component. Texture is massive with randomly oriented spady pyroxene oikocrysts. Some pyroxenes are small ~ 1 to 2mm spotty to chewed up grains. No visible sulphide. Modal %: 40-50% olivine, 40-50% pyroxene, 1-5% plagioclase
17	37.8		Zone of carbonate-serpentine vein alteration within lherzolite; veins are 0.5 to 1cm thick and X-cut unit at 40º to CA veins become progressively more carbonate-rich toward centre with light to dark serpentine/chlorite at edges metallic magnetite oxides occur on rims
27.75	27.8		Carbonate-rich 5cm wide zone with crystals of calcite that are tabular, up to 3cm long fill in myarolitic cavities. Clasts of peridotite occur in fluidal carbonate groundmass
43.65	43.73		Large alteration haloe around serpentine vein oriented 32º to CA with growth of cg biotite Cg biotite within alteration haloes of serpentine veins oriented ~30º to CA also found from 45.4 to 45.45, 46.87 to 47, and 56.78 to 57
75.8	76.1		Calcitized, zeolitiferous vuggy alteration zone with cg platy biotite - pegmatoid?
76.95	89.85		Zone of 1cm wide serpentine veins cut across at variable degree angles within fractured lherzolite zone. They mostly cut at 40º to CA and are spaced 10 to 20cm apart. Veins contain outer serpentine with sometimes inner cavity-filled crystalline calcite that is also sometimes sugary textured.
93.95	94		Serpentinization with associated malachite ~1mm or less calcite-filled cracks

	94	94.95	(mafic dike)	X-cutting 3cm wide aphanitic mafic dike at 57º to CA
	94.82	95.4	(mafic dike)	Aphanitic mafic dike cuts across 57º to CA at lower contact; contact at top is broken up / granulated From 94.82 to 95, mafic is largely filled with calcite in fractured ~ continues to lower degree through rest of unit
	99.55	99.75		Calcitized, vuggy pegmatoid? with cg biotite, Cpx, plagioclase
	105	105.32		Regularly oriented serpentine veins run 40º to CA
	127.42	127.62		Calcitized with Na-plagioclase altered pegmatoid with diffuse non-gradational contacts at 25º to CA; granophyre - coarse crystalline
	138	142.39		Zone of more prolific serpentine-carbonate vein alteration with 10 to 30cm spaced veins cutting along core axis at 138.07 to 60º to CA at 141.50
	at 142.39		Olivine websterite	Olivine websterite unit - rock becomes gradationally darker grey with fine grained pyroxene dominated composition; rock is still biotitiferous, but shows an overall pockety/spotty pyroxenitic texture
	144.12	144.3		Sugary calcite ~ white radiating spindle fibres, zeolitiferous
	at 149.75			Chalcopyrite - 5mm bleb in websterite, associated malachite alteration
	at 157.17			0.8 to 1cm thick quartz vein X-cuts at 40º - po, cpy are <1mm to 1mm blebs
	166.15	166.47		Parallel oriented 0.5 to 1.5cm thick quartz veins spaced 7 to 10cm apart run 35º to 40º to CA; somewhat calcitized and pink-potassic altered in 1.5cm vein
172.45	209.2		Sulphidized olivine websterite	Sulphidized olivine websterite - similar to lherzolite only pyroxene crystals are smaller ~ 3mm in size; carbonate vein alteration occurs along brittle fractures; sulphides: chalcopyrite - deep brassy yellow phases coexist with bronzy pyrrhotite sulphides; dominant pyroxene composition, biotitiferous toward 209.2 - gradationally becomes broken up by websterite

	at 173.27			1cm thick quartz vein X-cuts at 60º to CA
	173.42	173.65	(metasand-stone)	Pod of silica-talc-carbonate - metasandstone (calcareous)
	174	174.6		Zone of irregular 0.5cm silica-carbonate veins X-cut unit - no alteration haloes; pyrrhotite sulphides occur as anhedral ~1mm blebs dispersed in intercumulus
	180.75	180.9		Vult of carbonate-quartz with cg biotite growth contain up to 1cm patches of chalcopyrite minerals intergrown with pyrrhotite - irregular anhedral minerals
	at 183			Large 2cm irregular patch of pyrrhotite with haloe of serpentine vein
	191.65	191.9		Green serpentine-chert vein runs across CA with round blebs of calcite along foliation
209.2	236.4		Xenolithic websterite	Xenolithic websterite - patches of pyroxenite up to 2-3cm long irregularly enclosed in groundmass of broken up olivine websterite; olivine minerals are 1 to 2mm ovoidal phases enclosed in intercumulus broken up by pyroxene oikocrysts; patches range from spots in websterite at 209.2 to large patches at 220.25, 221.15, 221.40-221.45, up to 230 until there's a dominant groundmass of patchy continuous pyroxenite
236.4			Websterite	Websterite - a cumulate textured rock shows a patchy to spotted association of pyroxene and olivine. Pyroxene crystals are spady 1-2mm darker minerals while olivines occur as 1mm or less ovoidal to prismatic phases that appear as more leucocratic portions on the surface. Pyroxene crystals are in interlocking association with each other while olivine crystals appear to be broken intercumulus phases Modal %: pyroxene 50-60%, olivine 40%, plagioclase <10%, calcite/serpentine 1% or less
	at 258			16cm wide siderite? in pyroxenite oriented 50º to CA - banded silica with aphanitic unit ~ 0.3-0.5cm thick bands of aphanitic unit
	270.37	277.3		Mineralized po-cpy zone in websterite - cpy often occurs intergrown with po as 1-2mm blebs irregularly shaped - dominant po sulphides occur along with pyroxene between olivine minerals

300.72	301.4		Melanogabbro	Melanogabbro - an ophitic textured rock show a dominant association of interlocking up to 0.8mm elongate plagioclase laths with dark spady 1-2mm pyroxenes between them. Intercumulus aphanitic olivines are dispersed in groundmass. Up to 1cm pitted, round vugs within unit probably broke with chemical dissolution of plagioclase. Modal%: pyroxene 50%, plagioclase 20%, olivine 30%
	at 303			Mineralization - minor pyrrhotite toward contact with Archean sediments
	307.12	328	Pyritic metasediment	Pyritic metasediment - a strongly magnetic aphanitic oxide-rich black shale with up to 2cm wide sulphidized calcite veins running throughout. Massive pyrite sulphides occur in association with veins. Veins are sometimes vuggy with dissolution of calcite. Contact of melanogabbro with pyritic metasediment is sharp.
	328		Maf. Volcanics	Mafic volcanics: Up to 333, mafics are altered massively textured to pillowy and non-sheared with sulphidized calcite veins running irregularly throughout unit with associated pyrite blebs. Past 333, the unit is darker green and chloritized, massively textured with largescale irregular calcite veining and pyrite mineralization. Zones of large pyrite-calcite are at 337, 339.60 to 348.08, 342.85 to 343. Pyrite occurs in botryoidal form at 338.29 ~ 4cm long round concentric-layered pyrite minerals with rims of calcite. Within large calcite-altered zones are thinner irregularly-oriented serpentine

Eva Kitto 03-EK-03 Collar Location: 417825E 5486169N NAD 27 Dip vertical Az. N/A

From (m):	To (m):	Rock Type:	Description:
0	10	Overburden	
10	22	Serpentinized lherzolite	Serpentinized lherzolite: Altered dark greenish-red rock with finer ovoidal grains ~1mm or less in size of serpentinized pseudomorphed olivines; minor biotite - porphyritic <1mm phases dispersed throughout groundmass; numerous stringy white calcite veins up to 1.5cm thick with outside green serpentine spaced 10 to 20cm apart. Red alteration - jasperoidal cherty component or hematite. Lighter pyroxenitic patches 1-3mm long with irregular contacts dispersed within darker aphanitic serpentinized groundmass.
22	39	Lherzolite	Lherzolite: A pervasively serpentine/calcite vein altered fine to medium grained lherzolite contains large cpx oikocrysts poikilitically enclosing 1mm ovoidal olivine minerals. Veins are 5 to 25cm apart that run 60 to 80º to CA
48.12	50.32		Pervasive thick 2cm calcite-serpentine-chalcedony chert vein alteration in lherzolite. Interiors of veins filled in by either white calcite or green chert-serpentine.
at 49.28			Light blue chert-carbonate? Mineral occurs in botryoidal form along vein fracture
56.42	57.9		From 56.42 to 56.57, brecciated clasts of green chalcedonic chert occur in a white calcitic groundmass - variably sized angular fragments 0.1 to 1.5 cm long. At 57.05, a 5cm wide green chert vein cuts across unit at 40º to CA and contains large alteration haloe of serpentinized rock - also at 57.85 and 57.90 (thinner vein).
62.43	62.61		Largely serpentinized zone with few irregular white selvage calcite veinlets; development of cg platy biotite minerals within alteration zone - up to 1cm long crystals
63.14	63.25		Serpentinized zone contains brecciated serpentine clasts with granulated felsite-pegmatoid interior the alteration haloe; also massive irregularly shaped radiating sugar white calcite growth found enclosing serpentine fragments at margins
64.21	64.31		Serpentinized haloe contains haphazardly oriented brown coarse grained up to 3mm biotite crystals preferentially grown along vein axis

64.85	65.01	Vein of broken up chalcedonic green chert fragments autobrecciated in a lighter green cherty groundmass. Chert clasts also found in more hematized/serpentinized groundmass - some minor selvages of white calcite seep through
66.2	66.74	Heterolithic brecciated clasts of dark green chert-serpentine or creamy up to 1.2cm angular calcite-silica clasts in matrix of lighter green to greenish-white-grey chalcedony-serpentine. Autobrecciated units are 5 to 10cm long and occur every 20cm within miner
72	72.2	Heterolithic cherty brecciated chert-serpentine unit with minor calcite squirts
81.25	81.4	Cherty brecciated unit with angular 0.3cm clasts of calcite-silica and smaller 1mm subrounded darker green serpentine within variable light to dark green cherty matrix with some inter-selvaging of calcite. Unit contains post-mineralized (secondary) 1mm b mineralization. Zones of
81.7	82.8	Largely serpentinized aureole of lherzolite with occasional squirty calcite infills
87.4	87.8	Vuggy serpentinized green cherty brecciated zone within lherzolite - angular fragments ~0.8cm of hematized re serpentinite to dark green chert-serpentine in matrix of light green to siliceous chert. Serpentinized alteration haloes surround brecciated units. Serpentine gradationally becomes more prolific toward feldspathic peridotite/melanogabbro.
103.48	110	Large scale serpentinization associated with light green cherty veins with local red hematized spots and selvages of hematite in interior of green cherty veins; variable orientations of veins ~25º to 40º to CA
107.62	107.96	From 107.62 to 107.71, and 107.85 to 107.96, carbonate (white) altered potassic feldspathic pegmatoids occur within serpentinized zone.
122	126	At 122, peridotite gradationally contains more patchy pyroxene and feldspar associations. Up to 126.6, feldspathic peridotite zone is largely vein-olive green cherty-serpentinized with veins variably spaced 5 to 20cm apart and at different orientations - 1cm thick veins. Preferential hematization around serpentinized/slightly carbonatized zone though not extensive.

126.6	136.2	Melanogabbro	Melanogabbro - fine to medium grained salt + pepper textured 1:1 ratio of feldspar to pyroxene; ophitic textured unit that contains gradationally more wholesale hematization of the unit. Serpentine vein alteration decreases to fewer areas with thicker veins from 129 to 130.35 - spaced 10 to 20cm apart and 1 to 2cm thick.
136.2	142.7		Altered melanogabbro - finer grained with more pervasive hematization of unit
142.7	150	Fault zone	Fault zone - poor core recovery; aphanitic chilled mafic contact with Sibley sediments; variable greenish to purple reflects hematite/serpentinite altered muds and stains.
150	163.2	Sandstone	Sibley calcareous sandstone - white friable, chalky well sorted interlayered with up to 4cm thick bands of chocalate-brown argillite and thinner light green clays; occasional areas like at 156.2 - scapolite? - contains zone of spotted chlorite. From 150 to 153, rock contains more light green massive sandstone due to serpentine/chloritic alteration of overlying peridotite. From 161.6 to 163.2, sandstone contains orange-greenish alteration ~ ankeritized due to bordering mafic sill.
163.2	172.93	Diabase	Diabase - very fine to fine grained massively textured compositionally mafic intrusion contains very fine to fine grain acicular amphiboles haphazardly oriented in very fine to aphanitic groundmass of plagioclase-pyroxene. Up to 167.1, rock is aphanitic textured on the surface with some chloritic veining incorporating mafic clasts to give a pillow-brecciated texture in some areas.
167.1	167.64	Sandstone	Fine grained chloritized clastic sandstone with chlorite-altered argillite and clay bands; some occasional ~0.6cm hematite spots
167.64	172.7	Diabase	Diabase is massively textured with very fine to fine grained ophitic associations of plagioclase-pyroxene. From 172.1 to 172.4, diabase becomes plagioclase-phyric towards contact with Sibley sediments with 1 to 2mm plagioclase phenocrysts in a fine grain mineralization. Zo
172.7	183	Sandstone	Sibley calcareous banded mottly sandstone

Eva Kitto 03-EK-04 Collar Location: 417975E 5486442N NAD 27 Dip -50º Az. 25º

From (m):	To (m):	Rock Type:	Description:
0	2	Overburden	
2	50.43	Diabase	Diabase - massively textured unit contains very fine to fine grained ophitic associations of plagioclase-pyroxene. Oxide minerals are fine to medium grained anhedral phases. Locally around carbonate-chlorite-serpentine veins, there is coarser spady development of pyroxene. At 14.4, there's a 20º fracture vein of chlorite-serpentine. From 49 to 50.43, a chilled contact zone of diabase contains fine to aphanitic grain sizes. Modal%: pyroxene 45%, plagioclase 45-50%, oxide 2%, biotite 1%
50.43	64.4	Serpentinized lherzolite	Serpentinized lherzolite: dark red-green purplish serpentinized and hematized units with white 1 to 5mm irregular calcite veins running throughout variably spaced 10 to 30cm apart; also more minor thin veins of serpentine. Rock contains a patchy texture of unaltered leucocratic cpx-olivine irregular 1 to 3mm patches in a serpentinized and hematized groundmass of very fine grained ovoidal olivine. Ratio of patches to groundmass is 1:4. At 63.4, a 1.5cm thick vein of green chert-serpentine x-cuts unit at 35º to CA. Locally around calcite veins, the unit is vuggy and more preferentially hematized.
64.4	76.9		Zone of hematization occurs preferentially around 0.5 to 1cm wide veins of calcite-serpentine within dominant lherzolite unit. Veins are oriented 45 to 55º to CA.
76.9	184.7	Lherzolite	Lherzolite: A non-sulphidized unit contains up to 1cm spady pyroxene oikocrysts variably dispersed and oriented which poikilitically enclose <1 to 1mm ovoidal olivine grains. Lighter olivine phases are found in association with darker 1mm broken pyroxene crystals. Biotite minerals are porphyritic 1 to 2mm crystals occasionally found in groundmass. Serpentine-calcite veins x-cut unit throughout and are spaced average 20 to 30cm apart - alteration haloes with darker coarse pyroxene growth.
88.2	88.3		1cm green chert-serpentine veins x-cut 50º to CA and contain 2 to 3cm alteration haloes.

	at 78.65, 83.5, 91.15		Felsic veins x-cut lherzolite that are 2 to 3cm wide at 30 to 50º to CA - carbonatized felsic veinlets
105.6	146.12		Green cherty serpentine veins increase throughout unit, are 0.5 to 1cm wide, spaced 5 to 10cm apart, oriented 40 to 65º to CA
127.4	128.07		Calcitized vuggy zone within green-cherty serpentine altered lherzolite. Vugs are 0.5 to 0.8cm in diameter.
	at 171		Lherzolite contains patchier texture of intercumulus plagioclase of 1 to 2mm crystals between pyroxene oikocrysts; preferential development of cg biotite along with pyroxene at alteration haloes of veins
184	204.2	Feldspathic peridotite / melanogabbro	Feldspathic peridotite: A patchy weathered unit with mottly texture of round irregular 1 to 2cm dark weathered serpentinized olivine patches within dominant groundmass of oikocrystic pyroxenes with ovoidal olivine minerals in cumulus - 10-20% plagioclase
201	204.2		Hornfelsed margin of less weathered feldspathic peridotite. Serpentinized olivine patches decrease in size to 1mm spots within a dominant oikocrystic pyroxene with olivine groundmass and minor intercumulus plagioclase crystals surrounding oikocrysts - 1mm tabular grains with variable orientations - ophitic association. At chilled contact of sediments, olivine crystals are weathered out as vugs.
204.2	210	Sandstone	Sandstone: From 204.2 to 207.74 and 208 to 210, calcareous banded clastic Sibley sandstone contains green to white to orange bands - progressive ankerite alteration to end of hole; banded chloritic muds with hematite (local) - chocolate brown argillite; orientation of bands throughout unit are 50 to 60º to CA.
207.74	208	Mafic sill	Aphanitic mafic sill is vuggy and contains minor chlorite selvages.

EK-05-01 Drill log

0.00 - 10.00m **CASING**

10.00 - 34.20m **LHERZOLITE**

Massive textured, fine grained unit consists of poikilitic up to 1.4cm tabular clinopyroxenes enclosing 1mm ovoidal cumulate olivines and pyroxenes. 1 to 3mm irregular patches of biotite are dispersed throughout groundmass. Unit consists of 40-45% olivine, 35-45% pyroxene, 3% biotite, <5% plagioclase. Ovoidal olivines are often serpentinized cumulate grains.

At 15.5m, coarser 3mm wide veinlet of dark chert with surrounding medium grained pyroxene
20.3-20.6m, unit is darker - more pyroxenitic - and contains more serpentinized olivine and chert with 1-3% <1mm irregular blebs of marcasite
25.53-26.35m, darker unit
At 28.3m, irregular up to 1cm wide magnetite-chert veining continuous throughout unit 10%

Alteration: <1 to 2mm wide irregular oriented dark green chlorite to blue grey chert to light green serpentine fracture veinlets spaced inconsistently 10 to 30cm apart

34.20 - 39.90m **CARBONATIZED LHERZOLITE**

Wholesale carbonate bleaching and serpentine vein alteration of olivine and Ca-pyroxenes within unit
35-38.3m, continuous 0.5 to 1cm splitting serpentine-calcite vein runs down axis of core. Vein is calcitized with <1 to 1mm blebs of marcasite scattered along vein 3%. Vein cuts through dominant leuco-carbonatized ultramafic.
At 38m, vein is green mafic chlorite 1 to 2mm wide with surrounding vein sugary calcite.
At 39.9m, long vertical contact along CA of carbonatized with underlying magnetized ultramafic.

39.90 - 42.00m **MAGNETITE-ALTERED LHERZOLITE**

Magnetite-veined, hydrothermal 'leopard-textured' fine to medium euhedral black pyroxene-spotted lherzolite. Magnetite veins up to 2mm thick are continuously dispersed irregularly throughout groundmass 30%; thin <1mm wide pyrite veinlet alteration.
At 41.5m, 1 to 2mm rounded pyrrhotite sulphides found within dark magnetite patches.

42.00 - 48.00 **LHERZOLITE**

Unit contains <5% irregular 2mm wide magnetite continuous veining generally horizontal to 15 °CA. Darker altered 1mm cumulate pyroxenes occur along altering veins; minor serpentine-chert-calcite in vein spots.

48.00 - 48.30m **MAFIC SILL**

Chilled leucocratic light brownish grey very fine grained plagioclase-rich groundmass contains <5% 1mm brown porphyritic biotite. Feldspars occur in 3mm weathering spots and constitute up to 5% intercumulus groundmass. From 48.00 to 48.05m, 3cm long mafic injection contains up to 4mm wide patchy coarse biotite altered crystal within surrounding alteration haloes.

48.05-48.15m, 10cm long aureole of very fine magnetite and 2mm dark pyroxene crystals.

48.30 - 48.65m **CARBONACEOUS PELITE**

Black very fine carbonaceous to 1mm spot-bedded turquoise serpentinized. Beds are 1mm wide foliations oriented 75 to 90 °CA. Unit has moderately magnetic groundmass to highly magnetic <1mm veinlets running through <1% of unit.

48.65 - 49.10m **MAGNETITE SKARN - SIBLEY SANDSTONE**

Largely biotitized interlayered magnetite skarn zone with 30% Sibley sandstone digestion. 10cm turquoise to blue Sibley intervals contain medium grain silvery sheafy porphyroblastic biotite minerals. Intervals are separated 3 to 7cm by fine jet blue-black magnetiferous layers at zones with patchy biotitization.

49.10 - 49.67m **MAGNETITE SKARN**

Magnetite skarn with patchy 5cm locally epidotized porphyritic Sibley digestions. Sibley units are wholesale turquoise/black zones with 30% medium grained biotite. Very fine grain pyrite sulphides occur along minor <1mm calcite veinlets.

49.60-49.67m, darker magnetite aureole with 3 to 5mm biotite growths throughout

49.67 - 49.95m **MAFIC SILL**

Chilled mud grey unit. Anhedral rounded carbonate crysts contain 5% 3mm wide amygdular clear/grey-blue to very light green chert filled vein to void fills. Unit contains up to 4mm poikilitic pyroxenes, very minor olivine-serpentine as <1mm ovoidal grains. Unit is <1% 3mm local porphyritic magnetized. At 49.79m, sill is broken up by very fine magnetite with coarse porphyritic biotite near vertical angle to CA - 3cm zone within sill.

49.95 - 50.10m **SIBLEY SANDSTONE**

Light green-turquoise matrix Sibley unit with 3mm patches of bronzy porphyritic biotite. Unit has sharp contacts at both ends of mafic sill.

50.10 - 50.50m **MAFIC SILL**

As above. Unit contains chert-filled amygdules and minor local 3mm magnetite patches. Few vugs with silica edges were dissolved chert amygdules. At 50.35m, aphanitic carbonaceous <1cm wide bands are oriented vertical to CA.

50.50 - 51.13m **CARBONACEOUS PELITE**
Aphanitic soft carbonaceous pelite.

50.80-51.13m, calcite fills up light green, broken up voidal amygdules. Epidotized mafic sill digestions contain black carbon and are largely <1mm irregular calcite veinletized.

51.13 - 51.85m **LHERZOLITE**
Unit is largely magnetite veined at beginning. From 51.65 to 51.85m, a progressive dominant fine grain 50% magnetized to magnetite-vein rich zone breaks up lherzolite. Coarse 3mm porphyritic bronzy biotites occur as local patches in magnetized part. Unit has a sharp contact with lower mafic sill oriented 60 to 70°CA - varies since a lithologic contact. Contact is very fine grain veinlet pyritized.

51.85 - 52.22m **MAFIC SILL**
Unit is chilled very finely at contact with lherzolite. Unit is phyllitic and very finely biotitized, with minor 3mm vugs to silica filled amygdules. At 52.05m is a 3cm wide carbon interlayer. Surrounding interlayer are 3mm wide carbon patches breaking up the sill unit.

52.22 - 52.75m **SIBLEY SANDSTONE**
52.22-52.45m, prominent 1 to 3mm wide silica-layered sandstone with algal silica to sand layering oriented 70°CA. Fine silvery biotite is scattered throughout chert interbands/aligned 1mm rounded crystal zones
52.45-52.75m, turquoise chert Sibley unit with grey voids of 50% 1mm grey chert; local silica parts

52.75 - 53.80m **MAGNETITE SKARN - SIBLEY SANDSTONE**
Magnetite-Sibley skarn interlayered zone.

53.50-53.67m, siliceous patch of Sibley with >60% silvery up to 6mm coarse sheafy biotite. Sharp contact of Sibley with lower mafic sill oriented 60°CA.

53.80 - 54.15m **MAFIC SILL**
Mafic sill with <5% chert to silica-filled amygdules; one up to 1.5cm wide. Unit has sharp contact oriented 60°CA with lower carbon pelite-Sibley interlayered unit. Few 1mm pyrite-pyrrhotite blebs and one 6mm bleb of pyrrhotite occur at contact in mafic sill.

54.15 - 54.37m **CARBONACEOUS PELITE - SIBLEY SANDSTONE**
Carbonaceous pelite with digested Sibley unit from 54.2 to 54.25m. Sibley unit is biotitized with calcite veinlets.

54.37 - 54.47m **MAFIC SILL**
Unit contains silica amygdules. Sulphides include 1mm blebs of pyrrhotite and veinlet pyrite sulphides at contact with underlying carbon unit.

54.47 - 54.84m **CARBONACEOUS PELITE**
At 54.67m, there's a broken up digestion of mafic sill.

54.84 - 56.12m **LHERZOLITE**
Up to 55m, unit is a wholesale carbonatized silicified cumulate with few magnetite veins along CA.

56.12 - 56.35m **MAFIC SILL**
Largely amygdular-chert filled unit. A 2mm wide serpentine-chert vein runs 25°CA.

56.35 - 58m **MAGNETITE SKARN - PELITE**
Magnetite skarn-pelite dominant zone with Sibley digestion from 56.47 to 56.60m. Sibley unit is turquoise, biotitized with 1mm wide blue magnetite layering and up to 5mm coarse porphyrite biotite. Silvery blades of <1mm biotite are dispersed 10-20% throughout very fine groundmass of magnetiferous pelite.

58 - 58.52m **MAFIC SILL**
1 to 3mm silica-chert amygdules occur <5% throughout unit. From 58.19 to 58.26m, there's magnetiferous pelite. Calcite veinlets run within sill. 1% 1 to 2mm porphyritic bronzy biotite grains are dispersed in sill.

58.52 - 60.10m **LHERZOLITE**
Unit has sharp contact oriented 65°CA with upper mafic sill. Unit contains few 1 to 2mm wide magnetite-pyroxene veins with calcite. Unit has diffuse broken contact with lower Sibley sandstone.

60.10 - 60.20m **SIBLEY SANDSTONE**
Crumbly unit with mafic 2mm round crysts; coarse biotite at contact with lherzolite.

60.20 - 60.65m **MAFIC SILL**
Brown-grey massive textured leucocratic unit contains poikilitic pyroxenes.

60.65 - 60.95m **CARBONACEOUS PELITE** with silvery biotite

60.95 - 61.28m **MAFIC SILL**
At 61.15m, there's a 3cm wide interlayer of carbonaceous pelite.

61.28 - 61.89m **MAGNETIFEROUS PELITE - SIBLEY SKARN ZONE, MAFIC SILL**

61.47-61.54m, turquoise patch of Sibley
61.61-61.67m, 61.81-61.89m, mafic sill

61.89 - 62.92m **MAGNETIFEROUS PELITE - SIBLEY SKARN ZONE**
Interlayered (diffusely) mt-pelite Sibley skarn zone with 1mm blades of biotite dispersed 10 to 20%. Layering is oriented 45°CA.

62.92 - 63.25m **SIBLEY SANDSTONE**
Light green crumbly epidotized unit.

63.25 - 63.35m **MAFIC SILL**
Unit contains 1 to 3mm wide chert amygdules. Contact with lower lherzolite is 45°CA.

63.35 - 140.00m **LHERZOLITE**
Massively textured fine grained olivine-pyroxene cumulate.

66.60-67.33m, up to 4mm wide continuous fracture vein of calcite along CA with dark pyroxene.
69.70-71.45m, calcite vein along CA with dark pyroxene, biotite as 0.5cm wide aureole. In wider area at 71.20m, vein contains dark green chert-serpentine. At 71.30m, vein contains vuggy calcite.
71.80-72.10m, two 1cm wide green chert-serpentine with altered pyroxene veins spaced 10cm apart run 20 to 25°CA.
73.00-74.65m, zone of calcite-chert fracture veinlets with haloes up to 2.5cm wide, interval spacing 5 to 10cm apart, run 40 to 45°CA.
75.55m, single 1cm wide to 2cm haloed calcite vein runs 35°CA.
76.30-76.90m, largely irregularly fractured, calcite vugged in spots, dark serpentinized with magnetite - moderately magnetic and slightly hematized zone with bronzy coarse grain biotite at 76.90m.
77.57m, dark green haloed 0.5cm wide serpentine vein runs 80°CA.
77.70-77.85m, large patched green serpentine veined with surrounding fine magnetized zone, minor hematite, white vuggy calcite with serpentine.
78.40-78.60m, irregular fracture veinlets of magnetite-pyroxene.
79.00-79.40m, large patched green serpentinized with surrounding magnetite, pyroxene vein altered zones.

79.10-89.10m, lherzolite contains 5 to 20cm interval spaced dominant veinlet calcite-magnetite-pyroxene fracture veinlets generally run 40°CA; 0.5 to 1cm wide serpentine with calcite in thicker veined spots from 80.33-80.65m, 82.17-82.60m.
89.10-89.90m, brecciated zone of leucocratic coarse grain biotitized clasts 1.5 to 10cm wide - digestions.
after 89.90m, continue zone of fracture magnetite-calcite veins.
90.85-91.15m, light green-white serpentine calcite brecciated veins with selvaging of magnetite - altered zone.

91.15-99.30m, lherzolite contains 1-2mm wide continuous irregular fracture magnetite-calcite veinleting. At 97.00m, veinlets are 35 to 45°CA and are spaced 30 to 40cm apart.
99.30-106.00m, continuous flat fracture veinlets.
106.00-111.00m, 15 to 20°CA orientation in fracture veinlets, spaced 5 to 20cm apart.
111.70-115.50m, unit is largely vein magnetite-pyroxenitized: 0.5cm wide green chlorite-serpentine veins with 1.5cm alteration haloes of magnetite-pyroxene surrounded by irregular 1 to 2mm wide pyroxene-magnetite veinlets; coarse grain up to 3mm wide blady silver-bronze biotite minerals border the serpentine-chlorite veins. Vein is vugged in spots that were calcite filled. The large vein is generally continuous along CA.
115.50-116.40m, 1 to 2mm wide magnetite-pyroxene veinlets spaced 5 to 10cm apart run 40 to 45°CA.
116.40-126.60m, veinlets spaced 30 to 40cm apart oriented 20 to 30°CA.
127.35-127.82m, veinlets spaced 10cm apart oriented 40°CA.
127.82-128.30m, 0.3cm wide light green clacite-serpentine vein with bordering 1 to 2mm wide blady coarse grain biotite minerals and surrounding pyroxene-magnetite alteration haloe runs 15°CA.

128.30-140m, lherzolite contains few vertical calcite-chert veins that are 2 to 3mm wide and spaced 50cm to 1m apart.
132.62-132.71m, a magnetite-calcite 2mm wide vein runs vertical to CA and is followed by a 0.7cm wide green chert-serpentine vein that runs 70°CA. Vein contain 1cm wide magnetite-pyroxene haloes.
139.30 toward 140m, general irregular en echelon fracturing angles up 15 to 20°CA.

140.00-151.00m **FELDSPATHIC LHERZOLITE**
Lherzolite contains more weathering out of plagioclase to 10% and is still dominant olivine-pyroxene cumulate; biotite is progressive to 15%. Olivine is more weathered out/serpentinized throughout groundmass.

140.00-144.30m, variable orientations - 25, 35, 60, 70°CA - of 0.5cm wide green-blue chert serpentine veins spaced 10 to 15cm apart in local spots. Veins contain 1cm wide dark pyroxene haloes. At 144.30m, there are discontinuous angle veins.
144.55-144.70m, 146-147m, blue-green 0.3 to 0.6cm wide chert-serpentine veins run along CA and contain up to 2cm wide pyroxene-serpentine haloes.

149.15-152.75m **LHERZOLITE -** contains shallow 5 to 10°CA lithologic contact with overlying feldspathic lherzolite.

152.75-155.38m **FELDSPATHIC LHERZOLITE -** contains sharp 45°CA contact with underlying lherzolite
154.10-154.34m, two 2 to 3mm wide chert-serpentine veins run 20°CA.

155.38-162.80m **LHERZOLITE -** contact with underlying feldspathic lherzolite along CA.
155.85-156.22m and 157.40-157.63m, 2 to 3mm wide serpentine veins run along CA.
159.90-160.45m, three 1 to 2mm wide serpentine veins run 10 to 20°CA.

162.80-164.35m **FELDSPATHIC LHERZOLITE** - contact with underlying lherzolite is 5°CA.

164.35-165.80m **LHERZOLITE**

165.80-166.60m **FELDSPATHIC LHERZOLITE**
166.33-166.84m, 0.5cm wide green serpentine vein with pyroxenitic alteration runs along CA.

166.60-169.35m **LHERZOLITE**

169.35-177.70m **FELDSPATHIC LHERZOLITE**
At 175.82 and 176.00m, two angle fracture veinlets oriented 35 and 48°CA.

177.70-183.00m **LHERZOLITE**
Shallow fingering of lherzolite with underlying feldspathic lherzolite - coagulation - melt contacts with feldspathic lherzolite as more fractionated member. Unit becomes pyrrhotite-chalcopyrite mineralized at 182.60m.
179.70-183.93m, thin 2mm wide angle fracture veinlets of blue chert, minor calcite are spaced 5 to 20cm apart and are generally 25 to 30°CA.
180.48-180.93m, fracture serpentine-chert veinlets run along CA discontinuously throughout
At 182.60m, unit contains a 1cm patch of fine interstitial pyrrhotite mineralization.

183.00-183.67m **FELDSPATHIC LHERZOLITE**
Unit contains melt xenocryst of lherzolite: an elongate 10cm long × 1.5cm wide rounded finger

183.67-184.58m **LHERZOLITE**

184.58-184.85m **FELDSPATHIC LHERZOLITE**

184.85-186.07m **LHERZOLITE**
At 185.70m, unit contains a 4cm patch of pyrrhotite and lesser chalcopyrite sulphides.
At 185.78m, vertical fracture veinlet.

186.07-186.45m **FELDSPATHIC LHERZOLITE**

186.45-192.75m **LHERZOLITE**
At 187.14, 188.30, 189.73, 189.86, and 190.22m, unit contains 80 to vertical CA fracture veinlets.
At 190.22m, a 3mm wide vein of serpentine-chert with a 0.3cm pyroxene haloe runs 75°CA.

191.48-197.47m, longer more continuous zone of pyroxenitic fracture veinlets due to shallower angles of 20°CA that taper off along CA.

192.75-193.09m **FELDSPATHIC LHERZOLITE**
193.09-198.55m **LHERZOLITE**
198.55-198.65m **FELDSPATHIC LHERZOLITE**
198.65-198.90m **LHERZOLITE**
198.90-199.40m **FELDSPATHIC LHERZOLITE**
199.40-199.60m **LHERZOLITE**
199.60-199.80m **FELDSPATHIC LHERZOLITE**
199.80-200.15m **LHERZOLITE**
200.15-200.45m **FELDSPATHIC LHERZOLITE**

200.45-218.00m **LHERZOLITE**
Unit is 1% patchy fine interstitial pyrrhotite-chalcopyrite mineralized from 202.60m to 215.85m.

At 205.70, 205.92m, two fracture veinlets of serpentine are oriented 65°CA.
206.37-210.50m, fracture veinlets are spaced 10 to 30cm apart and are oriented 15 to 30°CA.
At 217.30m, a 2mm wide blue chert vein runs 25°CA.

218.00-218.20m **FELDSPATHIC LHERZOLITE -** pinch out

218.20-246.60m **LHERZOLITE**

Unit is 1% patchy fine interstitial pyrrhotite-chalcopyrite mineralized from 220.80 to 232.40m and from 238.80 to 246.00m.

218.25-223.35m, fracture veinlets run 75 to 90°CA and are irregularly spaced 10 to 25cm apart.
223.35-223.70m, angle fracture veinlets 40 to 60°CA are spaced 20 to 30cm apart.
231.00-231.30m, a 2cm thick serpentine vein that forks wider is oriented 20°CA and contains a 3cm wide alteration haloe of dominant 1 to 2mm ovoidal cumulate pyroxene grains - orthocumulate with interstitial olivine. Few remelted 0.5cm wide bronzy biotite grains occur in haloe of vein.
231.30-236.40m, en echelon chlorite-chert fracture veinlets occur as a discontinuous series throughout unit and are oriented 20°CA. Veinlets flatten out to 10°CA past 233.00m

237.53-241, fracture veinleting of chlorite-chert-magnetite are discontinuous throughout unit and are oriented 10 to 20°CA.
238.90-241.20m, lherzolite is wholesale pyroxenitized with pyroxene-magnetite veinleting to >50%.

240.60-240.69m and 241.00-241.15m, unit is 70% haloe pyroxenitized with 1 to 2mm blebs of pyrrhotite sulphide. Magnetite veining runs 70 to 80°CA. A vein contains a 1.5cm squirt of serpentine-chert.
At 240.40 and 240.47m, two 2mm wide magnetite-pyroxene veins run 35°CA

241.30-242.20m, 2 to 3mm wide magnetite-coarse grain pyroxene vein runs along CA with minor 2cm wide blob of serpentine.

242.78-243.15m, 2mm thick magnetite veins with surrounding coarse grain pyroxenitization run irregularly throughout unit.
243.15-246.60m, variably oriented black chert veinlets run discontinuously throughout unit at 20 to 30°CA orientation and are spaced 15cm apart where veins become steeper 2mm wide green serpentine-chert angled at 80°CA.

246.60m **EOH**

APPENDIX 2

Geological field notes for surface samples

O/C #	Northing	Easting	Strike	Dip	Litho	Description	Mineralization	Samples	Assay #
JL-001	420002	5488360			Lherzolite	Olivines, pyroxenes, biotite; magnetic. On weathered surface, feldspar is visible, and rusty patches.	No	Yes	369901
JL-002					Lherzolite	Biotitiferous, weathered rusty surface, feldspars on surface	No	Yes	369902
JL-003					Lherzolite	Rusty, slightly pitted surface with feldspar visible. Small 3m exposure; magnetic. Unit strikes along small creek 75m to the east. Other small exposures to the NE.	No	Yes	369903
JL-004	419043	5487837		26E	Diabase	Pyroxenitic ophitic gabbro with pyroxene patches 1-2cm wide on surface. Biotite-rich, feldspathic, olivine. Unit is slightly calcitized.	No	Yes	369904
JL-005					Lherzolite	Peridotite contains biotite, pyroxene, olivine, feldspar; flat lying joints.	No	Yes	369905
JL-006					Variolitic gabbro	Metagabbro with varioles of sericitized albite up to 6cm; large quartz veins cutting foliation up to 10m wide	No	No	
JL-007					Basalt	Sheared basalt/andesite with epidote clasts, hematized; pyrite mineralization.	Yes	Yes	369906
JL-008					Mt-chert iron formation	Magnetic, oxidized unit with quartz veins; pyrite mineralization; serpentinized.	Yes	Yes	369907
JL-009	419409	5488423		22SW	Lherzolite	Massive unit rich in olivine and pyroxene, but little biotite; horizontal joints; equigranular on fresh surface; feldspars are visible on weathered surface.	No	Yes	369908
JL-010	419348	5488389			Lherzolite	Massive jointed unit on edge of cliff.	No	Yes	369909
Post	420492	5488225			Post Location	400W of #1 Post; Claim #3006073			
JL-011	419629	5491812			Lherzolite	Massive textured pyroxene-rich with groundmass olivine; unit is biotitiferous; weathered surface show weathering out of plagioclase - orange weathered; pyroxenes up to 5mm, olivine crystals are <1 to 1mm. Unit is layer-cake with 1 1/2 ft blocks horizontally layered; slightly magnetic in spots	No	Yes	369910
JL-012	419558	5491716	NE/SW	8NW	Lherzolite	Fine grain up to 1mm olivine crystals rounded and orange-weathered to amber coloured on weathered surface with surrounding interstitial plagioclase; cleaved pyroxene oikocrysts up to 1cm in size with replacement growth of olivine clusters interior the pyroxenes; slightly magnetic; layered beds 0.5m thick	No		369911
JL-013	419496	5491801			Olivine websterite	More pyroxenitic unit in proportion to olivine crystals; blue medium grained 0.75mm spady pyroxenes on fresh surface with weathering out of feldspars on fresh surface; weakly magnetic. On weathered surface, there's more abundant pyroxenes poking out. Outcrop is massive with no layering - possible surfacing of websterite.	No	Yes	369912

JL-014	419290	5491962			Lherzolite	Pyroxene-rich poikilitic peridotite; knobby pyroxenes jut out on surface; olivine is abundant; top exposure with no structure; slightly magnetic	No	Yes	369913
JL-015	419079	5492235			Olivine gabbro	Pyroxene-porphyritic, interstitial plagioclase-rich olivine gabbro; up to 2cm pyroxene crystals on weathered surface; massive, non-layered unit. Unit contains 25% feldspar, 60% pyroxene, 15% olivine	No	Yes	369914
JL-016	419052	5492249			Olivine gabbro	Olivine gabbro with porphyritic pyroxenes on weathered surface. Plagioclase is rich on fresh surface as weathered out component surrounding pyroxenes.	No	No	369915
JL-017	418871	5492357		49	Olivine gabbro	Olivine gabbro with finer interstial plagioclase surrounding olivine and pyroxene; equigranular pyroxene-plagioclase composition; some porphyritic pyroxenes on rusty weathered surface; biotite-rich composition; massive outcropping. Trend of ridge St 49.	No	No	369916
JL-018	418897	5492386			Olivine gabbro	Olivine gabbro top exposure - plag-pyroxene rich with minor olivine; spady pyroxenes; quite weathered out	No	No	369917
JL-019	418927	5492468			Olivine gabbro	Round knobby massive unit exposure; plag-pyroxene composition, minor olivine and biotite; porphyritic 1 to 1 1/2 cm pyroxenes	No	No	369918
JL-020	418837	5492468			Olivine gabbro	Round knobby exposure; plagioclase rich; pyroxene-porphyritic on surface	No	No	369919
JL-021	418817	5492418		70	25S Olivine gabbro		No	Yes	369920
						Large knobby spheroidal weathered ridge exposure; massive, thick unit; layered beds of massive gabbro 2ft thick.			
JL-022	418741	5492468			Granophyre	Gabbro granophyre - coarse felsic vein patches of albite-olivine, coarse up to 0.5cm pyroxenes; orthopyroxene-rich in groundmass plagioclase.	No	Yes	369921
JL-023	418894	5492279	N/S		27N Olivine gabbro	Plagioclase-rich medium-grained pyroxene-porphyritic; fine interstitial plagioclase; 30cm beds	No	No	369922
JL-024	419021	5491954	NE/SW		25NW Olivine gabbro	Cliff edge exposure; bedded layers 30cm thick	No	Yes	369923
JL-025	418996	5491943			Olivine gabbro	Cliff edge exposure; layered unit	No	No	
JL-026	419006	5491943			NW Lherzolite	Cliff edge exposure, bedded to massive	No	No	369924
JL-027	419042	5491884			Olivine gabbro	Pyroxene-porphyritic massive unit of olivine-biotite gabbro, plagioclase-rich unit; top of hill	No	Yes	369925
JL-028	419417	5491372			Lherzolite	Biotite-rich pyroxene-poikilitic lherzolite massive knob unit on hill, groundmass ovoidal olivine; rubbly-jutting pyroxenes on weathered surface, magnetic	No	Yes	369926
JL-029	419354	5491239			16NNW Lherzolite	Massive to layered unit with 30cm to 3/4m thick beds; primary pyroxene-poikilitic, olivine-rich	No	Yes	369927
JL-030	419152	5491215			Lherzolite		No	Yes	369928
						Massive unit - vertical edge with 1/2 metre thick vaguely layered showing flat to hummocky-style bedding; no direct flat dips; crack-vertical akerite joints run perpendicular to beds.			

JL-031	419132	5491236		Lherzolite	Massive peridotite; on weathered surface, there's acicular weathering out of plagioclase; more pyroxene than olivine in groundmass; poikilitic pyroxenes 0.5cm on weathered surface; massive flat unit - photo	No	Yes	369929
JL-032	419035	5491253		Olivine gabbro	Spheroidal weathered plagioclase and olivine-rich with poikilitic pyroxene; massive unit - photo: poikilitic texture; pyroxene phenocrysts really well seen on weathered surface have white feldspathic rims	No	Yes	369930
JL-033	418998	5491233		Olivine gabbro	Crumbly exposure	No	No	
JL-034	418949	5491244		Olivine gabbro	Crumbly unit; feldspar and olivine-rich; slightly magnetic.	No	Yes	369931
JL-035	418967	5491267		Olivine gabbro	Feldspathic to pyroxene-rich with some olivine; massive unit; poikilitic pyroxenes	No	Yes	369932
JL-036	419001	5491303		Olivine gabbro	Pyroxene-poikilitic and feldspar-rich, some olivine; 1/2cm feldspathic veinlets run through	No	Yes	369933
JL-037	418974	5491346		Olivine gabbro	Top exposure, rounded	No	No	
JL-038	418932	5491383		Olivine gabbro	Felsic veinlets cm-wide through massive olivine gabbro unit; pyroxene-poikilitic	No	Yes	369934
JL-039	418875	5491454		Olivine gabbro	Biotite-rich; large degree of feldspathic veinlets running through to develop coarser feldspars on weathered surface	No	Yes	369936
JL-040	418827	5491454		Olivine gabbro	Pyroxenitic with interstitial plagioclase, olivine abundant; massive unit	No	Yes	369935/369937
Post	418718 418722	5491404 5491179		Post Location	1200m North #3, Claim #1231912			
JL-041	418644	5491374		Granophyre	Coarse grained albite-pyroxene gabbro/norite granophyre; green pyroxenes up to 1cm long - Opx; pink potassic coarse interstitial phases	No	No	
JL-042	418593	5491346		Granophyre	Coarse grained leuco-phasic gabbro	No	No	
JL-043	418511	5491325		Granophyre	Coarse 0.5cm pyroxenes - prismatic to acicular in form interspersed in groundmass of albite/K-spar; minor olivine in finer areas; horizontal 20cm bedding	No	Yes	369938
JL-044	418477	5491285		Granophyre	Granophyric plagioclase-rich gabbro with scapular pyroxenes	No	No	
JL-045	418409	5491285		Granophyre	Medium grained plag-pyroxene-rich; massive textured; slightly oxidized.	No	No	
JL-046	418320	5491300	90	Hornfels iron formation	Tremolite hornfelsed magnetite-chert iron formation with pyrite sulphides; bands of magnetite are 1-2cm thick spaced 5cm apart in cherty groundmass	Yes	Yes	369939
JL-047	418315	5491282		Granophyre/Hornfels	Contact of granophyre fine chill zone to South and BIF to North; diabase texture plag-pyroxene in chill	No	Yes	369940
JL-048	420866	5491298		Diabase	Massive medium grained ophitic textured, no poikilitic pyroxene; weathered surface - orange weathering of Fe from pyroxene and weathering out of plagioclase.	No	No	
JL-049	420488	5491001		Diabase	Massive ophitic med-grained gabbro - summit of hill	No	No	

JL-050	420125	5490064				Lherzolite	Olivine-rich with up to 0.5cm poikilitic pyroxene in a fine grained olivine groundmass; massive unit; fine to medium grained	No	Yes	369941
JL-051	420183	5490068				Lherzolite	Olivine-rich fine to medium grained olivine-pyroxene; olivine is dominant, then pyroxene and feldspar is in low amounts	No	Yes	369942
JL-052	420213	5490012				Lherzolite	Olivine rich, massive lherzolite	No	Yes	369943
JL-053	420457	5490077		335	60ENE	Diabase	Ophitic pyroxene-rich med-grained gabbro with 20 to 30cm thick joint beds	No	No	
JL-054	419655	5488007	N/S		11	Lherzolite	Massively textured lherzolite with layer cake 15 to 30cm thick beds. Orange weathered biotite-rich uunit with 40% green olivine in groundmass. Plagioclase is weathered out on surface. Calcitic veinlets run through.	No	Yes	369944
JL-055	418976	5487819				Pyroxenitic diabase	JL-055a: Pyroxenitic, blotchy ophitic plag-pyroxene gabbro; massive textures, crumbly exposure. JL-055b: more weathered pyroxenitic gabbro with Fe oxidation and pyrrhotite-chalcopyrite mineralization	Yes	Yes	369945/369946
JL-056	418912	5487738				Olivine websterite	Po-cpy mineralized olivine websterite; massive fine to medium grained unit that appears blotchy pyroxenitic on the surface; biotitized with fine grained biotite	Yes	Yes	369947
JL-057	418878	5487693				Pyroxenitic diabase	Pyroxenitized gabbro - massive textured pyroxenite and plagioclase-rich, ophitic, no olivine; some Fe rust spots on fresh surface.	No	Yes	369948
JL-058	418757	5487547				Diabase	Massive textured, flat-lying, no sulphides	No	No	
JL-059	418740	5487491				Diabase	Massive exposure; biotite-rich, no blotch pyroxenes	No	No	
JL-060	418730	5487451				Olivine websterite	Spady pyroxenes in plagioclase interstitial groundmass; weathered surface is largely plagioclase-rich; photo: weathered surface	No	Yes	369949
JL-061	418756	5487417				Pyroxenitic diabase	Massive ophitic to spotty pyroxenitic, biotite-rich unit; bouldery, slope exposure S of creek	No	Yes	369950
JL-062	418759	5497388			20 to 30E	Diabase	Massive diabase - cliff side; crude joint layering of 30cm massive beds; ophitic, biotite-rich	No	No	
JL-063	419636	5488252			25ENE	Lherzolite	Massively textured, bedded plagioclase-weathered, orange unit; poikilitic pyroxene visible on weathered surface up to 0.5cm; 30cm thick beds; olivine-pyroxene groundmass, biotite-rich	No	Yes	369801
JL-064	419803	5488239				Lherzolite	Peridotite sill - massively textured, 15 to 20cm thick horizontal beds	No	No	
JL-065	418936	5487568			25SE	Pyroxenitic diabase	Massively textured pyroxene-spotted diabase exposure; weathered surface is orange white with around 1mm equant spots of pyroxene crystals; bedded joints; biotite-rich	No	Yes	369802
JL-066	418800	5487458				Pyroxenitic diabase	Fine to medium grained ophitic textured; white weathered; more pyroxenitic; massive texture; no biotite	No	Yes	369803

DDH	418440	5487470	Az.242		45	DDH EK-2			
JL-067	418310	5487379				Boulder olivine websterite	Boulder in creek sample #82981	No	Yes	369804
JL-068	418299	5487385				Boulder olivine websterite	Boulder of po-mineralized pyroxenite	Yes	Yes	369805
JL-069	418284	5487383		15 Az.232		Olivine websterite	Outcrop sample #82982, 15 to 20cm thick beds	No	Yes	369806
JL-070	418284	5487392				Boulder olivine websterite	Boulder. Biotite-rich, green chert patches in spots, gossan sulphidized; po-cpy mineralization; large up to 1cm poikilitic pyroxenes. Groundmass is very fine grained probably dominant pyroxene - rounded pyroxenes separated by green chert in groundmass	Yes	Yes	369807
JL-071	418274	5487406				Boulder olivine websterite	Boulder of plag-pyroxene rich diabasic textured; websterite sampled	No	Yes	369808
JL-072	418356	5487380		11SSW		Diabase chill	Chill margin - aphanitic, mafic composition; Fe oxidized on surface, bedding	No	Yes	369809
JL-073	418345	5487354		20 Az.235		Olivine websterite	Pyroxenite outcrop; bedding is massive 30cm thick; spherical cumulate pyroxene in very fine grained olivine-green cherty groundmass	No	Yes	369810
JL-074	421162	5489287		11Az.15-20		Diabase	Ophitic textured plag-pyroxene rich altered magnetite-rich massive jointed with 20 to 30cm thick beds; near bottom of ridge, layered flow	No	Yes	369811
JL-075	421112	5489187		15 Az.E		Pyroxenitic diabase	Cliff exposure, crumbly unit; pyroxene-rich with 30cm thick layered beds	No	Yes	369812
JL-076	420927	5489079				Pyroxenitic diabase	Fe-altered hematite; sulphidized pyroxenite; very coarse pyroxenite developing along fracture planes running irregularly throughout unit; photo; horizontal 30cm thick beds	Yes	Yes	369813
JL-077	420810	5488974		5SSE		Olivine websterite	Massive cumulate textureed pyroxene-rich with 1mm ovoidal cumulate Cpx dominating groundmass; unit is carbonate and green-chert serpentine altered, but only in veinlets; sample for assay; not as hematized; rich with biotite mica; 20 to 40cm thick beds; fine grained po sulphides; red lichen, hematized outcrop	Yes	Yes	369814

APPENDIX 3

Bulk, trace element and REE geochemistry data for:
ED-, JL- and K-data series rocks

Method	Sample Lithology	ED-01 Lherzolite-olivine websterite	ED-02 Lherzolite-olivine websterite	ED-03 Lherzolite-olivine websterite	ED-04 Lherzolite-olivine websterite	ED-05 Lherzolite-olivine websterite	ED-15 Lherzolite-olivine websterite	ED-16 Lherzolite-olivine websterite
XRF	SiO_2	40.33	39.39	38.76	40.78	40.72	39.28	40.06
XRF	TiO_2	0.78	0.88	0.71	0.88	0.8	0.64	0.96
XRF	Al_2O_3	4.41	4.21	3.96	4.79	4.53	3.46	3.56
XRF	Fe_2O_3	15.51	16.72	14.91	16.66	16.04	16.89	17.36
XRF	MnO	0.2	0.2	0.17	0.22	0.21	0.23	0.21
XRF	MgO	30.96	30.77	30.5	28.63	30.12	30.15	30.16
XRF	CaO	2.82	3.01	3.66	4.72	3.58	3.37	3.41
XRF	Na_2O	0.37	0.35	0.24	0.61	0.81	0.29	0.43
XRF	K_2O	0.37	0.49	1.12	0.47	0.45	0.58	0.72
XRF	P_2O_5	0.08	0.09	0.09	0.09	0.1	0.07	0.15
	LOI	1.72	1.53	3.31	0.69	0.85	2.92	1.15
	Sum	97.57	97.63	97.42	98.54	98.21	97.87	98.17
ICP-MS	Ti	4676	5276	4256	5276	4796	3837	5755
ICP-MS	P	349	393	393	393	436	305	655
ICP-MS	Cr	4192	7573	4896	4379	2788	2903	3858
ICP-MS	Co	135.218	152.758	170.36	165.293	148.155	156.54	143.943
ICP-MS	Ni	1662	1934	2029	2229	1233	1193	1380
ICP-MS	Rb	10	15	31	12	11	15	20
ICP-MS	Sr	134	77	33	147	160	103	95
ICP-MS	Cs	0.414	0.409	0.777	0.456	0.384	0.318	0.414
ICP-MS	Ba	122.82	112.38	178.57	223.48	172.19	202.13	207.19
ICP-MS	Sc	22	23	22	28	24	23	24
ICP-MS	V	73	97	82	83	74	88	53
ICP-MS	Ta	0.21	0.21	0.17	0.24	0.21	0.24	0.38
ICP-MS	Nb	4	5	4	6	4	5	7
ICP-MS	Zr	66	56	51	65	64	66	92
ICP-MS	Hf	1.7	1.5	1.3	1.6	1.6	1.8	2.6
ICP-MS	Th	0.79	0.76	0.68	0.8	0.83	1.03	1.36
ICP-MS	U	0.169	0.179	0.188	0.195	0.164	0.271	0.356
ICP-MS	Y	7	8	7	9	8	9	11
ICP-MS	La	9.52	6.51	5.5	10.49	8.99	11.08	13.25
ICP-MS	Ce	22.48	15.72	14.98	22.46	20.78	23.73	30.13
ICP-MS	Pr	2.986	2.131	2.221	2.896	2.76	3.056	3.946
ICP-MS	Nd	12.23	9.37	10	12.67	12.06	12.8	16.74
ICP-MS	Sm	2.3	2.13	2.22	2.69	2.71	2.78	3.42
ICP-MS	Eu	0.865	0.555	0.539	0.893	0.777	0.835	0.922
ICP-MS	Gd	2.029	2.047	2.113	2.43	2.328	2.46	2.923
ICP-MS	Tb	0.286	0.292	0.283	0.33	0.318	0.356	0.41
ICP-MS	Dy	1.509	1.564	1.485	1.816	1.8	1.939	2.229
ICP-MS	Ho	0.282	0.282	0.277	0.33	0.323	0.35	0.392
ICP-MS	Er	0.749	0.776	0.727	0.867	0.854	0.922	1.064
ICP-MS	Tm	0.102	0.097	0.097	0.116	0.112	0.12	0.135
ICP-MS	Yb	0.62	0.62	0.6	0.71	0.68	0.73	0.79
ICP-MS	Lu	0.085	0.087	0.089	0.1	0.095	0.1	0.117
ICP-MS	Cu	169.614	218.528	101.72	1527.845	123.9	53.31	46.79
ICP-MS	Zn	83.92	88.17	74.47	119.49	102.09	116.96	105.28
ICP-MS	Mo	0.5	0.51	0.27	0.47	0.3	0.54	0.51
ICP-MS	Cd	0.038		0.04	0.076	0.042	0.061	0.055
ICP-MS	Te	19.44	47.998	69.294	344.448	23.426	3.286	6.686
ICP-MS	Tl	0.14	0.1	0.2	0.11	0.09	0.13	0.14
ICP-MS	Pb	2.7	3.3	1.8	6.7	2.2	5.2	3
ICP-MS	Sn	0.68	0.4	0.59	0.75	0.59	0.68	0.72
ICP-MS	Sb		0.06	0.07				
ICP-MS	Ga	7.1	7.49	7.25	8.51	7.7	6.74	7.26
ICP-MS	Se	271.407	688.604	1138.054	2230.636	226.306	67.442	76.245
ICP-MS	W		0.06	0.07	0.12	0.06	0.1	0.08
ICP-MS	Li	8.52	11.13	14.86	11.26	13.77	8.23	8.52
ICP-MS	Be	0.4		0.32	0.58	0.59	0.52	0.57

Method	Sample	ED-17 Lherzolite-olivine websterite	ED-18 Lherzolite-olivine websterite	ED-19 Lherzolite-olivine websterite	ED-20 Lherzolite-olivine websterite	ED-21 Lherzolite-olivine websterite	ED-25 Lherzolite-olivine websterite	ED-26 Lherzolite-olivine websterite
XRF	SiO_2	40.09	40.67	39.11	40.93	43.51	37.33	39.96
XRF	TiO_2	0.93	1.08	0.78	0.87	1.48	0.63	0.78
XRF	Al_2O_3	5.13	5.81	4.07	4.57	7.48	3.24	3.95
XRF	Fe_2O_3	15.69	15.99	16.91	15.5	14.9	15.91	17.06
XRF	MnO	0.2	0.2	0.23	0.21	0.21	0.2	0.23
XRF	MgO	27.46	26.05	29.54	27.54	19.49	29.53	30.7
XRF	CaO	4.61	4.67	3.79	5.37	5.98	3.55	3.52
XRF	Na_2O	0.51	0.79	0.4	0.55	1.44	0.22	0.36
XRF	K_2O	0.67	0.67	0.44	0.52	0.82	0.37	0.47
XRF	P_2O_5	0.12	0.12	0.05	0.08	0.18	0.07	0.08
	LOI	2.42	1.28	2.52	1.21	2.77	6.59	0.89
	Sum	97.83	97.35	97.84	97.34	98.26	97.62	97.98
ICP-MS	Ti	5575	6475	4676	5216	8873	3777	4676
ICP-MS	P	524	524	218	349	786	305	349
ICP-MS	Cr	3878	3752	3033	3837	2677	3230	3768
ICP-MS	Co	132.212	127.128	150.419	139.89	91.78	144.531	154.296
ICP-MS	Ni	1271	1239	1206	1223	879	1205	1332
ICP-MS	Rb	19	16	12	12	18	10	13
ICP-MS	Sr	154	166	266	177	308	37	147
ICP-MS	Cs	0.454	0.487	0.241	0.372	1.173	0.354	0.342
ICP-MS	Ba	164.44	189.04	201.06	140.66	561.04	149.09	193.38
ICP-MS	Sc	25	26	24	28	31	25	23
ICP-MS	V	80	84	67	71	128	100	82
ICP-MS	Ta	0.26	0.33	0.2	0.28	0.51		0.23
ICP-MS	Nb	6	6	5	5	9	4	4
ICP-MS	Zr	58	75	50	55	116	38	57
ICP-MS	Hf	1.6	1.9	1.3	1.5	3	1.1	1.5
ICP-MS	Th	0.72	0.97	0.56	0.7	1.5	0.46	0.73
ICP-MS	U	0.178	0.242	0.176	0.19	0.431	0.133	0.194
ICP-MS	Y	9	11	6	8	16	6	8
ICP-MS	La	9.97	12.34	7.3	10.67	21.41	5.94	11.72
ICP-MS	Ce	23.63	27.47	15.83	22.84	45.48	14.33	24.48
ICP-MS	Pr	3.164	3.649	2.082	2.92	5.747	1.884	2.989
ICP-MS	Nd	13.58	15.35	8.82	12.42	24.45	8.21	11.83
ICP-MS	Sm	2.92	3.19	1.9	2.63	5.12	1.74	2.42
ICP-MS	Eu	0.87	0.962	0.715	0.857	1.699	0.51	0.777
ICP-MS	Gd	2.639	2.914	1.759	2.439	4.466	1.634	2.114
ICP-MS	Tb	0.376	0.397	0.251	0.353	0.628	0.228	0.302
ICP-MS	Dy	1.941	2.205	1.372	1.873	3.264	1.25	1.652
ICP-MS	Ho	0.358	0.399	0.258	0.333	0.609	0.226	0.299
ICP-MS	Er	0.928	1.061	0.688	0.869	1.536	0.62	0.76
ICP-MS	Tm	0.119	0.134	0.088	0.115	0.202	0.077	0.098
ICP-MS	Yb	0.76	0.84	0.55	0.72	1.25	0.49	0.62
ICP-MS	Lu	0.105	0.112	0.083	0.095	0.171	0.069	0.083
ICP-MS	Cu	42.32	68.66	73.02	58.92	111.17	21.93	58.56
ICP-MS	Zn	91.46	98.93	129.22	101.16	160.481	87.05	128.44
ICP-MS	Mo	0.34	0.44	0.48	0.5	1.52	0.38	0.49
ICP-MS	Cd	0.044	0.049	0.056	0.049	0.089	0.037	0.052
ICP-MS	Te	10.45	7.578	3.834	9.111	41.122	5.854	5.287
ICP-MS	Tl	0.13	0.12	0.11	0.14	0.22	0.09	0.12
ICP-MS	Pb	3.9	2.2	4.8	3.8	9.1	1.3	5.1
ICP-MS	Sn	0.66	0.69	0.54	0.59	1.04	0.4	0.52
ICP-MS	Sb				0.06	0.08		
ICP-MS	Ga	8.22	9.5	6.54	7.79	12.31	5.56	6.81
ICP-MS	Se	95.511	95.608	68.392	99.285	367.714	66.879	68.411
ICP-MS	W	0.1	0.06	0.26	0.06	0.37	0.04	0.13
ICP-MS	Li	10.64	10.49	8.4	11.34	13.74	16.93	9.44
ICP-MS	Be	0.37	0.64	0.3	0.36	0.79		0.4

Method	Sample	ED-29 Lherzolite-olivine websterite	ED-34 Lherzolite-olivine websterite	ED-35 Lherzolite-olivine websterite	ED-36 Lherzolite-olivine websterite	ED-41 Lherzolite-olivine websterite	ED-42 Lherzolite-olivine websterite	ED-06 Vari-textured pyroxenite
XRF	SiO_2	40.26	39.65	41.16	45.1	39.29	41.81	43.82
XRF	TiO_2	0.77	0.65	0.81	1.12	0.75	0.93	0.83
XRF	Al_2O_3	4.34	3.03	4.31	5.07	3.26	3.65	4.25
XRF	Fe_2O_3	16.64	16.43	16.58	14.38	17.28	16.15	15.79
XRF	MnO	0.22	0.2	0.21	0.21	0.21	0.22	0.21
XRF	MgO	30.45	31.11	28.76	20.73	31.9	27.36	27.11
XRF	CaO	3.75	3.94	4.63	9.37	3.27	5.52	6.71
XRF	Na_2O	0.59	0.42	0.66	0.85	0.37	0.58	0.73
XRF	K_2O	0.36	0.48	0.35	0.57	0.49	0.54	0.4
XRF	P_2O_5	0.08	0.07	0.08	0.12	0.08	0.11	0.09
	LOI	0.58	2.13	0.38	0.89	1.27	1.18	0.19
	Sum	98.02	98.11	97.93	98.41	98.16	98.05	100.14
ICP-MS	Ti	4616	3897	4856	6714	4496	5575	4976
ICP-MS	P	349	305	349	524	349	480	393
ICP-MS	Cr	3875	3209	3404	2276	3622	3384	2264
ICP-MS	Co	158.892						129.216
ICP-MS	Ni	1358	1285	1241	697	1396	1182	890
ICP-MS	Rb	8	14	9	13	13	13	11
ICP-MS	Sr	176	95	183	199	165	97	152
ICP-MS	Cs	0.226	0.365	0.232	0.49	0.274	0.345	0.466
ICP-MS	Ba	146.24						143.62
ICP-MS	Sc	23	21	22	41	18	27	34
ICP-MS	V	81	54	48	100	54	83	88
ICP-MS	Ta	0.21		0.21	0.34	0.23	0.3	0.2
ICP-MS	Nb	5	4	5	6	5	6	5
ICP-MS	Zr	51	33	47	83	55	73	60
ICP-MS	Hf	1.4	0.9	1.3	2.2	1.4	1.9	1.6
ICP-MS	Th	0.63	0.38	0.52	1.09	0.64	0.82	0.74
ICP-MS	U	0.161	0.118	0.128	0.25	0.191	0.225	0.152
ICP-MS	Y	8	5	8	14	7	10	9
ICP-MS	La	8.73	4.74	9.23	14.68	9.32	11.66	8.1
ICP-MS	Ce	19.08	12.16	19.31	31.53	19.62	25.12	18.7
ICP-MS	Pr	2.489	1.723	2.496	4.023	2.481	3.297	2.602
ICP-MS	Nd	10.99	7.68	10.78	17.83	10.3	13.98	11.42
ICP-MS	Sm	2.21	1.76	2.34	3.99	2.15	3.11	2.62
ICP-MS	Eu	0.759	0.476	0.754	1.279	0.558	0.917	0.767
ICP-MS	Gd	1.96	1.647	2.153	3.776	1.856	2.769	2.392
ICP-MS	Tb	0.287	0.222	0.293	0.529	0.259	0.38	0.342
ICP-MS	Dy	1.492	1.222	1.594	2.88	1.418	2.034	1.88
ICP-MS	Ho	0.269	0.228	0.294	0.522	0.261	0.383	0.35
ICP-MS	Er	0.727	0.599	0.748	1.347	0.65	0.968	0.914
ICP-MS	Tm	0.097	0.076	0.101	0.176	0.085	0.128	0.124
ICP-MS	Yb	0.6	0.47	0.62	1.08	0.52	0.76	0.74
ICP-MS	Lu	0.083	0.066	0.084	0.146	0.074	0.105	0.103
ICP-MS	Cu	77.6						67.9
ICP-MS	Zn	119.41						95.74
ICP-MS	Mo	0.56						0.44
ICP-MS	Cd	0.039						0.042
ICP-MS	Te	5.471						11.112
ICP-MS	Tl	0.07						0.1
ICP-MS	Pb	1.9	1	1.8	3.4	2.2	5.9	3.2
ICP-MS	Sn	0.48						0.57
ICP-MS	Sb							
ICP-MS	Ga	7.74						7.35
ICP-MS	Se	81.391						191.401
ICP-MS	W	0.11						0.06
ICP-MS	Li	7.35						7.13
ICP-MS	Be	0.39						0.38

Method	Sample	ED-31 Vari-textured pyroxenite	ED-07 Pyroxenite	ED-08 Pyroxenite	ED-09 Pyroxenite	ED-32 Pyroxenite	ED-10 Melano-gabbro	ED-27 Melano-gabbro
XRF	SiO_2	43.23	40.96	43.78	45.28	43.95	48.28	46.79
XRF	TiO_2	0.88	0.86	0.99	1.23	0.91	1.57	1.9
XRF	Al_2O_3	4.08	4.78	5.77	7.49	4.24	7.73	9.65
XRF	Fe_2O_3	15.57	17.34	15.19	15	15.63	14.87	12.82
XRF	MnO	0.22	0.21	0.2	0.2	0.2	0.24	0.14
XRF	MgO	25.08	27.95	23.03	17.06	24.57	17.09	10.48
XRF	CaO	7.4	4.39	7.68	9.1	7.56	8.23	10.67
XRF	Na_2O	0.69	0.85	1.06	1.36	1.03	1.6	2.37
XRF	K_2O	0.38	0.38	0.41	0.57	0.35	0.75	0.79
XRF	P_2O_5	0.09	0.1	0.1	0.13	0.09	0.16	0.21
	LOI	0.86		0.28	0.96		0.65	3.43
	Sum	98.47	97.74	98.5	98.38	98.41	101.17	99.25
ICP-MS	Ti	5276	5156	5935	7374	5455	9412	11391
ICP-MS	P	393	436	436	567	393	698	916
ICP-MS	Cr	1824	1497	1980	1461	1785	991	907
ICP-MS	Co		147.479	113.38	104.38			56.87
ICP-MS	Ni	818	1279	740	982	775	521	221
ICP-MS	Rb	9	9	9	13	7	15	17
ICP-MS	Sr	173	176	206	295	192	355	425
ICP-MS	Cs	0.463	0.34	0.195	0.561	0.197	0.639	1.165
ICP-MS	Ba		144.28	157.81	226.25			302.5
ICP-MS	Sc	30	28	40	37	32	32	48
ICP-MS	V	91	77	120	168	94	116	191
ICP-MS	Ta	0.21	0.23	0.26	0.32	0.22	0.47	0.65
ICP-MS	Nb	5	5	5	6	5	9	10
ICP-MS	Zr	65	67	75	96	68	119	155
ICP-MS	Hf	1.7	1.7	1.9	2.5	1.7	3.1	4
ICP-MS	Th	0.8	0.83	0.91	1.24	0.79	1.55	2.06
ICP-MS	U	0.155	0.169	0.184	0.239	0.16	0.303	0.5
ICP-MS	Y	9	8	11	14	10	16	22
ICP-MS	La	9.17	9.49	10.4	13.16	9.3	17.74	26.6
ICP-MS	Ce	21.13	21.56	24.05	30.76	21.54	39.98	57.22
ICP-MS	Pr	2.859	2.891	3.254	4.252	2.918	5.362	7.242
ICP-MS	Nd	12.85	12.76	14.71	18.75	12.91	23.3	31.1
ICP-MS	Sm	2.89	2.71	3.33	4.18	3	5.05	6.74
ICP-MS	Eu	0.881	0.827	1.008	1.305	0.911	1.556	1.953
ICP-MS	Gd	2.667	2.432	2.97	3.948	2.78	4.616	6.231
ICP-MS	Tb	0.375	0.351	0.428	0.553	0.397	0.65	0.853
ICP-MS	Dy	2.04	1.885	2.376	3.073	2.115	3.458	4.634
ICP-MS	Ho	0.369	0.342	0.432	0.571	0.397	0.642	0.855
ICP-MS	Er	0.977	0.909	1.124	1.464	1.03	1.679	2.16
ICP-MS	Tm	0.125	0.116	0.152	0.195	0.136	0.221	0.291
ICP-MS	Yb	0.78	0.73	0.93	1.17	0.82	1.36	1.77
ICP-MS	Lu	0.109	0.105	0.13	0.164	0.114	0.185	0.237
ICP-MS	Cu		435	69.55	774.763			52.05
ICP-MS	Zn		104.14	94.67	112.64			51.66
ICP-MS	Mo		0.45	0.53	0.53			0.61
ICP-MS	Cd		0.051	0.05	0.109			0.064
ICP-MS	Te		127.798	12.504	183.08			15.103
ICP-MS	Tl		0.08	0.05	0.12			0.09
ICP-MS	Pb	3.5	3.1	3.6	5.6	2.1	4.7	5.1
ICP-MS	Sn		0.62	0.67	0.94			1.19
ICP-MS	Sb							0.09
ICP-MS	Ga		7.46	9.33	12.16			16.7
ICP-MS	Se		621.753	97.727	1155.105			1616.689
ICP-MS	W		0.06	0.07	0.1			0.28
ICP-MS	Li		6.28	6.05	9.61			31.08
ICP-MS	Be		0.43	0.53	0.72			1.13

Method	Sample	ED-30 Melano-gabbro	ED-33 Melano-gabbro	ED-37 Melano-gabbro	ED-28 Diabase	ED-38 Diabase	ED-39 Diabase	ED-40 Diabase
XRF	SiO_2	48.85	51.79	49.83	49.22	49.07	50.23	48.81
XRF	TiO_2	1.65	1.22	1.84	1.44	3.14	3.08	1.2
XRF	Al_2O_3	8.31	15.52	10.3	14.94	13.19	13.79	15.4
XRF	Fe_2O_3	12.27	8.99	13.03	14.49	15.73	16.33	14.3
XRF	MnO	0.15	0.14	0.17	0.21	0.16	0.19	0.2
XRF	MgO	12.83	7.27	9.88	6.39	5.08	5.17	8.51
XRF	CaO	11.07	12.44	11	9.81	7.62	8.17	9.74
XRF	Na_2O	1.95	2.43	2.32	2.6	3.48	3.17	2.46
XRF	K_2O	0.41	0.68	0.94	0.74	0.85	1.07	0.47
XRF	P_2O_5	0.18	0.12	0.19	0.14	0.28	0.28	0.1
	LOI	3.13	0.52	1.05	0.62	0.94	0.31	0.05
	Sum	100.8	101.12	100.55	100.6	99.54	101.78	101.24
ICP-MS	Ti	9892	7314	11031	8633	18824	18465	7194
ICP-MS	P	786	524	829	611	1222	1222	436
ICP-MS	Cr	1203	196	765	138	39	36	107
ICP-MS	Co	64.24			54.23			
ICP-MS	Ni	336	128	226	103	78	89	222
ICP-MS	Rb	10	15	18	20	22	27	12
ICP-MS	Sr	346	633	450	193	409	432	174
ICP-MS	Cs	0.794	0.696	0.361	0.62	1.888	1.495	0.394
ICP-MS	Ba	252.03			226.04			
ICP-MS	Sc	46	29	44	46	36	31	35
ICP-MS	V	181	88	157	270	77	116	215
ICP-MS	Ta	0.56	0.37	0.61	0.45	0.85	0.82	0.28
ICP-MS	Nb	10	7	10	7	15	13	5
ICP-MS	Zr	140	107	152	113	216	211	85
ICP-MS	Hf	3.8	2.6	4.2	3.1	5.4	5.4	2.4
ICP-MS	Th	1.78	1.36	1.71	2.26	2.82	2.77	1.57
ICP-MS	U	0.374	0.288	0.456	0.711	0.643	0.612	0.449
ICP-MS	Y	19	14	21	28	30	30	22
ICP-MS	La	16.74	14.7	23.88	11.78	23.71	24.08	8.87
ICP-MS	Ce	41.16	33.18	54.74	26.59	54.17	54.57	19.48
ICP-MS	Pr	5.762	4.455	7.214	3.58	7.342	7.412	2.59
ICP-MS	Nd	26.65	19.3	30.5	16.04	32.35	32.98	11.51
ICP-MS	Sm	5.98	4.34	6.63	4.16	7.7	7.69	3.19
ICP-MS	Eu	1.596	1.468	1.97	1.366	2.501	2.548	1.055
ICP-MS	Gd	5.44	4.067	5.935	4.858	7.575	7.663	3.784
ICP-MS	Tb	0.756	0.574	0.83	0.813	1.114	1.106	0.627
ICP-MS	Dy	4.108	3.105	4.484	5.222	6.226	6.209	3.981
ICP-MS	Ho	0.772	0.568	0.837	1.058	1.151	1.148	0.835
ICP-MS	Er	1.965	1.488	2.169	3.093	3.057	3.017	2.39
ICP-MS	Tm	0.26	0.196	0.284	0.435	0.404	0.403	0.339
ICP-MS	Yb	1.59	1.18	1.75	2.82	2.49	2.44	2.24
ICP-MS	Lu	0.217	0.165	0.242	0.421	0.338	0.335	0.326
ICP-MS	Cu	251.839			192.919			
ICP-MS	Zn	82.84			112.8			
ICP-MS	Mo	1.2			0.76			
ICP-MS	Cd	0.086			0.093			
ICP-MS	Te	20.751			6.811			
ICP-MS	Tl	0.24			0.16			
ICP-MS	Pb	5.6	5.3	4.6	6.9	2.2	3.3	3
ICP-MS	Sn	0.92			1.11			
ICP-MS	Sb	0.07			0.07			
ICP-MS	Ga	14.38			20.6			
ICP-MS	Se	369.952			219.04			
ICP-MS	W	0.14			0.22			
ICP-MS	Li	22.17			18.77			
ICP-MS	Be	0.88			0.72			

Method	Sample	ED-22 Sibley quartz sandstone	ED-23 Sibley quartz sandstone	ED-11 Iron formation	ED-12 Iron formation	ED-13 Mafic meta-volcanic	ED-14 Mafic meta-volcanic	ED-24 Mafic meta-volcanic
XRF	SiO_2	49.65	90.74	52.3	52.12	48.97	48.35	46.35
XRF	TiO_2	2.15	0.17	1.64	1.48	1.43	1.42	1.37
XRF	Al_2O_3	11.68	5.29	12.25	11.28	18.14	16.64	15.54
XRF	Fe_2O_3	11.14	0.21	18.37	20.5	11.5	12.75	9.61
XRF	MnO	0.15	0.02	0.24	0.22	0.26	0.24	0.23
XRF	MgO	8.36	0.19	3.82	3.26	3.42	5.3	5.35
XRF	CaO	9.98	1.83	7.79	6.45	6	10.07	10.45
XRF	Na_2O	3.7	0.59	1.12	1.83	5.86	2.76	4.71
XRF	K_2O	0.94	0.06	0.07	0.15	1.38	1.33	1.58
XRF	P_2O_5	0.25		0.15	0.16	0.11	0.09	0.09
	LOI	2.02	0.89	2.62	2.48	2.28	1.48	4.3
	Sum	100.01	99.99	100.36	99.92	99.35	100.44	99.57
ICP-MS	Ti	12889	1019	9832	8873	8573	8513	8213
ICP-MS	P	1091	#VALUE!	655	698	480	393	393
ICP-MS	Cr	560	59	54	39	189	265	205
ICP-MS	Co	46.2	1.98	43.45	28.22	45.86	80.53	32.28
ICP-MS	Ni	191	7	23	23	132	76	74
ICP-MS	Rb	16	3	4	2	39	33	32
ICP-MS	Sr	588	10	176	181	193	321	433
ICP-MS	Cs	0.328	1.592	1.439	1.832	2.579	0.157	0.156
ICP-MS	Ba	356.48	6.14	28.26	18.7	363.17	298.32	396.24
ICP-MS	Sc	38		51	47	63	70	64
ICP-MS	V	165		250	232	417	382	763
ICP-MS	Ta	0.8		0.31	0.3	0.2	0.2	0.19
ICP-MS	Nb	13	3	6	5	4	4	3
ICP-MS	Zr	186	64	130	122	93	93	84
ICP-MS	Hf	4.7	1.9	3.6	3.5	2.6	2.6	2.3
ICP-MS	Th	2.46	0.53	0.51	0.57	0.34	0.3	0.32
ICP-MS	U	0.568	0.341	0.138	0.22	0.058	0.11	0.499
ICP-MS	Y	22	1	46	44	34	26	27
ICP-MS	La	14.3	2.05	6.11	29.47	4.75	5.52	15.09
ICP-MS	Ce	36.45	3.66	16.54	34.63	9.12	11.11	37.46
ICP-MS	Pr	5.579	0.399	2.735	3.755	1.337	1.797	3.357
ICP-MS	Nd	26.83	1.56	14.42	17.45	7.81	9.28	11.46
ICP-MS	Sm	6.59	0.35	4.84	4.87	3.01	2.84	2.79
ICP-MS	Eu	1.865	0.211	1.714	2.008	1.047	1.075	1.219
ICP-MS	Gd	6.336	0.495	6.558	6.414	4.654	3.658	3.842
ICP-MS	Tb	0.907	0.078	1.218	1.128	0.859	0.652	0.699
ICP-MS	Dy	4.958	0.42	8.036	7.313	5.893	4.394	4.717
ICP-MS	Ho	0.892	0.079	1.759	1.606	1.287	0.991	1.047
ICP-MS	Er	2.392	0.221	5.461	4.903	4.001	3.018	3.257
ICP-MS	Tm	0.316	0.032	0.817	0.728	0.594	0.451	0.474
ICP-MS	Yb	1.89	0.2	5.48	4.78	3.9	3.08	3.18
ICP-MS	Lu	0.266	0.034	0.825	0.714	0.603	0.505	0.486
ICP-MS	Cu	24.66	6.54	55.15	256.063	28.2	11.87	6.05
ICP-MS	Zn	31.28	4.67	67.6	44.45	48.14	50.59	26.31
ICP-MS	Mo	0.2	0.79	0.38	1.98	0.33	0.22	0.76
ICP-MS	Cd	0.049		0.064	0.058	0.032	0.038	
ICP-MS	Te	2.634	0.247	138.079	61.549	97.404	45.989	2.4
ICP-MS	Tl	0.09	0.01	0.05	0.11	0.4	0.36	0.12
ICP-MS	Pb	3	1.1	8.2	29.9	3.5	4.7	2.4
ICP-MS	Sn	0.82	0.17	1.43	1.18	0.96	0.78	0.78
ICP-MS	Sb	0.12	0.1	0.33	0.51	0.38	0.48	0.24
ICP-MS	Ga	20.21	4.72	20.89	22.24	22.14	21.82	22.08
ICP-MS	Se	60.765	1.626	1288.025	1833.489	453.375	753.908	3.323
ICP-MS	W	0.2	0.41	0.34	0.62	0.3	0.86	0.28
ICP-MS	Li	27.03	5.53	29.71	50.01	31.04	21.81	29.77
ICP-MS	Be	1.41		0.63	0.35	0.34	0.47	0.45

Method	Sample	JL-063 Lherzolite-olivine websterite	JL-067 Lherzolite-olivine websterite	JL-068 Lherzolite-olivine websterite	JL-070 Lherzolite-olivine websterite	JL-071 Lherzolite-olivine websterite	JL-073 Lherzolite-olivine websterite	JL-077 Lherzolite-olivine websterite
XRF	SiO_2	41.83	39.11	38.1	38.89	39.25	40.06	41.14
XRF	TiO_2	0.66	0.5	0.84	0.43	0.38	0.49	0.74
XRF	Al_2O_3	3.7	2.83	2.68	2.63	2.38	2.92	3.84
XRF	Fe_2O_3	17.19	16.97	16.8	14.55	15.91	17.32	16.95
XRF	MnO	0.25	0.25	0.22	0.16	0.22	0.24	0.25
XRF	MgO	29.05	31.34	31.88	30.77	31.29	31.56	29.19
XRF	CaO	3.67	3.56	2.63	3.4	3.48	3.49	4.24
XRF	Na_2O	0.95	0.54	0.36	0.34	0.35	0.62	0.56
XRF	K_2O	0.42	0.29	0.71	1.14	0.48	0.37	0.46
XRF	P_2O_5	0.09	0.07	0.14	0.08	0.06	0.09	0.1
XRF	Cr_2O_3	0.51	0.39	0.25	0.39	0.24	0.27	0.49
XRF	SrO	0.02	0.01	0.01			0.01	0.02
XRF	BaO	0.01	0.01	0.01	0.02			0.02
	LOI	1.31	3.47	5.04	6.77	5.29	2.42	1.17
	Sum	99.65	99.34	99.66	99.56	99.33	99.87	99.17
ICP-MS	Ti	980	730	1400	1350	690	680	1060
ICP-MS	P	330	240	570	270	230	300	350
ICP-MS	Cr	3930	294	284	2611	230	2212	3660
ICP-MS	Co	115	129	131.5	115	122	120	108
ICP-MS	Ni	1372	1020	1075	1237	987	1130	1287
ICP-MS	Rb	10	8.5	17.9	37	13.5	10	8
ICP-MS	Sr	171	82.6	30.4	12	28	127	190
ICP-MS	Cs	0.336	0.3	0.63	0.536	0.54	0.513	0.324
ICP-MS	Ba	100	120	130	130	150	100	140
ICP-MS	Sc	21	7.7	6.6	16	6.2	16	22
ICP-MS	V	128	16	35	81	21	89	119
ICP-MS	Ta	0.22						0.2
ICP-MS	Nb	4	0.17	0.2	3	0.14	3	4
ICP-MS	Zr	47	3.7	8.4	38	4.4	29	47
ICP-MS	Hf	1.3	0.07	0.15	1	0.07	0.8	1.3
ICP-MS	Th	0.65	0.3	0.5	0.6	0.3	0.44	0.59
ICP-MS	U	0.156	0.08	0.17	0.126	0.08	0.114	0.142
ICP-MS	Y	7	0.78	1.93	5	0.85	5	8
ICP-MS	La	8.87	3.9	6.1	2.64	2.6	5.57	9
ICP-MS	Ce	20.01	5.74	12.8	7.91	5.1	13.1	18.91
ICP-MS	Pr	2.533			1.308		1.686	2.388
ICP-MS	Nd	10.88			6.62		7.18	10.33
ICP-MS	Sm	2.3			1.72		1.56	2.24
ICP-MS	Eu	0.717			0.2		0.545	0.745
ICP-MS	Gd	2.095			1.57		1.422	2.018
ICP-MS	Tb	0.288			0.221		0.195	0.283
ICP-MS	Dy	1.574			1.232		1.092	1.612
ICP-MS	Ho	0.287			0.23		0.195	0.288
ICP-MS	Er	0.738			0.616		0.51	0.742
ICP-MS	Tm	0.095			0.081		0.068	0.098
ICP-MS	Yb	0.58			0.5		0.43	0.62
ICP-MS	Lu	0.082			0.073		0.061	0.088
ICP-MS	Cu	81.7	23.7	28.3	16	24	35.5	58.6
ICP-MS	Zn	73	76	68	37	70	81	71
ICP-MS	Mo	0.29	0.41	0.23	0.35	0.25	0.21	0.35
ICP-MS	Ag	0.04	0.02	0.01	0.02	0.02	0.03	0.04
ICP-MS	Cd	0.05	0.04	0.04	0.03	0.03	0.04	0.04
ICP-MS	Te	0.01	0.01	0.03	0.01	0.02	0.01	0.01
ICP-MS	Tl	0.05	0.1	0.06	0.06	0.02	0.05	0.06
ICP-MS	Pb	2.8	1.6	1.8	1.5	1.4	1.8	3.6
ICP-MS	Sn			0.2				
ICP-MS	Sb	0.06	0.31				0.36	
ICP-MS	Ga	2.26	2.04	3.12	2.82	2.58	1.96	2.47
ICP-MS	Ge	0.19	0.2	0.19	0.18	0.2	0.19	0.18
ICP-MS	As	0.6	0.8	0.8	0.5	0.4	0.3	0.3
ICP-MS	Se	0.2	0.3	0.4	0.3	0.3	0.2	0.2
ICP-MS	W		0.06					0.06
ICP-MS	Li	5.2	12.9	9.8	9.1	9.8	8.8	4.3
ICP-MS	Be	0.12	0.07	0.14	0.06	0.08	0.07	0.1
ICP-MS	S	300	400	800	600	500	300	200
ICP-MS	Bi	0.02	0.01	0.01	0.01	0.01	0.02	0.02
ICP-MS	Au	0.002						
ICP-MS	Pt			0.012				
ICP-MS	Pd	0.005		0.021	0.049	0.007		0.004

Method	Sample	JL-001 Lherzolite-olivine websterite	JL-002 Lherzolite-olivine websterite	JL-003 Lherzolite-olivine websterite	JL-004 Lherzolite-olivine websterite	JL-005 Lherzolite-olivine websterite	JL-009 Lherzolite-olivine websterite	JL-010 Lherzolite-olivine websterite
XRF	SiO_2	40.74	40.41	40.04	40.15	40.04	42.71	41.02
XRF	TiO_2	0.67	0.68	0.62	0.53	0.5	0.53	0.49
XRF	Al_2O_3	3.35	3.44	3.17	3.21	2.71	2.88	3
XRF	Fe_2O_3	17.86	17.12	17.66	16.16	17.56	16.69	16.67
XRF	MnO	0.26	0.25	0.26	0.25	0.24	0.24	0.24
XRF	MgO	31.61	30.61	32.35	30.66	33.49	28.07	30.91
XRF	CaO	3.07	3.35	3.08	4.28	2.62	6.69	3.81
XRF	Na_2O	0.63	0.67	0.56	0.46	0.34	0.55	0.44
XRF	K_2O	0.45	0.43	0.45	0.34	0.42	0.26	0.33
XRF	P_2O_5	0.09	0.09	0.09	0.06	0.1	0.04	0.07
XRF	Cr_2O_3	0.54	0.51	0.49	0.45	0.31	0.29	0.36
XRF	SrO	0.01	0.02	0.01	0.02	0.02	0.01	0.01
XRF	BaO	0.01	0.01		0.01		0.01	0.01
	LOI	0.39	1.44	1.13	2.78	0.99	0.63	2.05
	Sum	99.67	99.03	99.92	99.35	99.34	99.62	99.41
ICP-MS	Ti	1060	1030	1040	790	970	610	760
ICP-MS	P	330	380	340	280	390	210	250
ICP-MS	Cr	4064	348	350	3024	254	200	2437
ICP-MS	Co	120	113.5	123.5	120	135.5	110	125
ICP-MS	Ni	1430	1100	1165	1214	1120	796	1101
ICP-MS	Rb	11	10.7	11	8	11.1	7.6	8
ICP-MS	Sr	157	111.5	116	172	87.6	22.3	107
ICP-MS	Cs	0.264	0.49	0.3	0.247	0.23	0.35	0.303
ICP-MS	Ba	180	160	140	120	90	60	60
ICP-MS	Sc	20	4.2	4.7	19	5.4	5	16
ICP-MS	V	110	20	20	93	20	16	78
ICP-MS	Ta	0.2						
ICP-MS	Nb	4	0.18	0.15	3	0.11	0.15	2
ICP-MS	Zr	43	3.1	3.5	31	2.5	1.6	30
ICP-MS	Hf	1.3	0.06	0.08	0.9	0.05	0.03	0.9
ICP-MS	Th	0.62	0.5	0.4	0.34	0.3	0.2	0.38
ICP-MS	U	0.153	0.09	0.08	0.096	0.06		0.089
ICP-MS	Y	6	1.2	1.17	5	1.28	0.45	4
ICP-MS	La	9.41	5.6	5.4	5.63	4.7	2	5.74
ICP-MS	Ce	19.92	10.25	10.1	13.38	9.65	3.64	12.45
ICP-MS	Pr	2.461			1.803			1.599
ICP-MS	Nd	10.12			7.85			6.85
ICP-MS	Sm	2.2			1.75			1.55
ICP-MS	Eu	0.684			0.562			0.5
ICP-MS	Gd	1.923			1.601			1.394
ICP-MS	Tb	0.267			0.228			0.197
ICP-MS	Dy	1.488			1.276			1.101
ICP-MS	Ho	0.271			0.234			0.199
ICP-MS	Er	0.699			0.601			0.528
ICP-MS	Tm	0.092			0.077			0.069
ICP-MS	Yb	0.59			0.49			0.43
ICP-MS	Lu	0.082			0.065			0.061
ICP-MS	Cu	75.6	84.8	57.2	52.4	53	31.5	34.3
ICP-MS	Zn	96	72	81	73	79	66	69
ICP-MS	Mo	0.42	0.57	0.36	0.29	0.28	0.24	0.28
ICP-MS	Ag	0.04	0.04	0.04	0.03	0.04	0.03	0.02
ICP-MS	Cd	0.09	0.05	0.06	0.05	0.05	0.02	0.03
ICP-MS	Te	0.01	0.02	0.01	0.01	0.02	0.02	0.01
ICP-MS	Tl	0.09	0.07	0.05	0.05	0.05	0.02	0.03
ICP-MS	Pb	3.3	2.8	4.7	1.3	1.9	1	1.2
ICP-MS	Sn	0.2	0.2	0.2		0.2		
ICP-MS	Sb							
ICP-MS	Ga	2.24	2.32	2.4	2.5	2.53	1.78	2.42
ICP-MS	Ge	0.2	0.19	0.22	0.19	0.2	0.15	0.17
ICP-MS	As	0.3	0.4	0.3	0.3	0.7	0.4	0.3
ICP-MS	Se	0.2	0.3	0.2	0.2	0.2		
ICP-MS	W	0.07	0.09			0.05		
ICP-MS	Li	4.3	3.9	4	4.4	5.5	4.2	6.1
ICP-MS	Be	0.11	0.12	0.13	0.09	0.1		0.09
ICP-MS	S	200	300	200	200	400	200	300
ICP-MS	Bi	0.05	0.02	0.03	0.01	0.01	0.01	0.01
ICP-MS	Au							
ICP-MS	Pt				0.012			
ICP-MS	Pd	0.004	0.005	0.004	0.005	0.003	0.003	0.003

Method	Sample	JL-011 Lherzolite-olivine websterite	JL-012 Lherzolite-olivine websterite	JL-013 Lherzolite-olivine websterite	JL-014 Lherzolite-olivine websterite	JL-028 Lherzolite-olivine websterite	JL-029 Lherzolite-olivine websterite	JL-030 Lherzolite-olivine websterite
XRF	SiO_2	43.92	46.3	43.2	47.06	42.27	44.69	46.09
XRF	TiO_2	0.61	0.76	0.71	0.88	0.61	0.64	0.93
XRF	Al_2O_3	3.11	3.28	3.51	3.8	3.19	3.56	4.28
XRF	Fe_2O_3	14.96	13.55	16.4	13.43	16.5	15.25	15.02
XRF	MnO	0.23	0.26	0.25	0.22	0.22	0.23	0.22
XRF	MgO	27.41	22.41	24.97	20.12	28.27	26.48	22.25
XRF	CaO	7.51	10.73	7.77	12.07	5	7.66	8.82
XRF	Na_2O	0.6	0.58	0.63	0.71	0.4	0.79	0.94
XRF	K_2O	0.29	0.33	0.3	0.3	1.06	0.21	0.4
XRF	P_2O_5	0.07	0.08	0.08	0.09	0.06	0.06	0.09
XRF	Cr_2O_3	0.29	0.27	0.3	0.29	0.33	0.32	0.3
XRF	SrO	0.02	0.01	0.02	0.02	0.01	0.02	0.02
XRF	BaO		0.02	0.02	0.01	0.02	0.01	0.01
	LOI	0.18	0.52	0.78	0.65	2.02	-0.22	0.46
	Sum	99.19	99.11	98.94	99.65	99.96	99.7	99.83
ICP-MS	Ti	760	1020	910	1040	1490	730	1290
ICP-MS	P	240	300	270	330	270	240	370
ICP-MS	Cr	1969	2047	387	2264	2378	306	374
ICP-MS	Co	103	68.8	91.2	51.3	111.5	97.2	76
ICP-MS	Ni	920	619	655	521	972	695	514
ICP-MS	Rb	5	6	6.4	8	33	5.4	9.9
ICP-MS	Sr	152	150	96	132	32	12.6	15.5
ICP-MS	Cs	0.275	0.351	0.22	0.381	1.721	0.13	0.26
ICP-MS	Ba	70	230	130	90	140	50	80
ICP-MS	Sc	28	45	5.8	48	23	5.1	4.6
ICP-MS	V	107	149	28	177	125	22	39
ICP-MS	Ta				0.21	0.25		
ICP-MS	Nb	2	4	0.29	4	5	0.25	0.53
ICP-MS	Zr	31	44	2.6	56	56	2.2	3.7
ICP-MS	Hf	0.9	1.3	0.05	1.6	1.7	0.04	0.09
ICP-MS	Th	0.36	0.48	0.3	0.66	0.8	0.4	0.7
ICP-MS	U	0.078	0.097	0.06	0.127	0.301	0.06	0.1
ICP-MS	Y	6	9	0.59	11	8	0.55	0.85
ICP-MS	La	5.77	7.81	3.9	8.03	6.11	2.5	4.8
ICP-MS	Ce	12.54	16.01	5.75	19.48	16.22	4.38	8.43
ICP-MS	Pr	1.67	2.169		2.712	2.233		
ICP-MS	Nd	7.74	10.19		12.42	9.83		
ICP-MS	Sm	1.83	2.49		2.99	2.2		
ICP-MS	Eu	0.63	0.886		0.914	0.503		
ICP-MS	Gd	1.788	2.416		2.941	2.037		
ICP-MS	Tb	0.252	0.347		0.422	0.288		
ICP-MS	Dy	1.41	1.995		2.369	1.612		
ICP-MS	Ho	0.259	0.362		0.431	0.297		
ICP-MS	Er	0.691	0.941		1.13	0.773		
ICP-MS	Tm	0.088	0.118		0.146	0.102		
ICP-MS	Yb	0.55	0.75		0.88	0.63		
ICP-MS	Lu	0.078	0.103		0.121	0.091		
ICP-MS	Cu	58.8	51.6	70.5	49.6	11	40.6	47.3
ICP-MS	Zn	65	96	79	48	52	67	58
ICP-MS	Mo	0.34	0.22	0.34	0.25	0.26	0.18	0.35
ICP-MS	Ag	0.04	0.06	0.05	0.02	0.03	0.02	0.02
ICP-MS	Cd	0.04	0.11	0.07	0.04	0.02	0.03	0.03
ICP-MS	Te	0.02	0.01	0.02	0.01	0.01	0.02	0.01
ICP-MS	Tl	0.05	0.1	0.09	0.06	0.14		0.02
ICP-MS	Pb	2	6.7	4.9	6.2	0.9	0.9	0.9
ICP-MS	Sn					0.2		0.2
ICP-MS	Sb							
ICP-MS	Ga	1.72	1.81	2.07	1.81	3.3	1.21	2.26
ICP-MS	Ge	0.14	0.1	0.16	0.09	0.19	0.17	0.13
ICP-MS	As	0.3	0.3	0.8	0.4	1	0.1	0.3
ICP-MS	Se		0.2	0.2		0.2	0.2	0.2
ICP-MS	W			0.09				
ICP-MS	Li	3.6	2.3	2.7	3.7	9.6	2.5	2.4
ICP-MS	Be			0.07		0.07		0.06
ICP-MS	S	300	400	300	300	300	200	200
ICP-MS	Bi	0.01	0.04	0.04	0.01	0.02		
ICP-MS	Au			0.001				
ICP-MS	Pt					0.01		
ICP-MS	Pd	0.001		0.001	0.001	0.009	0.003	0.005

Method	Sample	JL-031 Lherzolite-olivine websterite	JL-050 Lherzolite-olivine websterite	JL-051 Lherzolite-olivine websterite	JL-052 Lherzolite-olivine websterite	JL-054 Lherzolite-olivine websterite	JL-056 Lherzolite-olivine websterite	JL-108 Lherzolite-olivine websterite
XRF	SiO_2	45.32	44.08	44.37	44.01	40.76	41.5	
XRF	TiO_2	0.88	0.7	0.61	0.62	0.66	0.57	
XRF	Al_2O_3	4.27	3.17	3.4	3.38	3.45	2.73	
XRF	Fe_2O_3	15.69	15.75	15.11	15.48	16.87	16.18	
XRF	MnO	0.23	0.24	0.24	0.24	0.25	0.25	
XRF	MgO	21.67	25.74	25.56	25.91	30.88	29.46	
XRF	CaO	9.64	8.42	8.75	8.33	3.76	5.34	
XRF	Na_2O	0.91	0.83	0.77	0.77	0.65	0.49	
XRF	K_2O	0.31	0.28	0.19	0.21	0.39	0.26	
XRF	P_2O_5	0.09	0.08	0.08	0.08	0.09	0.08	
XRF	Cr_2O_3	0.26	0.28	0.3	0.31	0.52	0.42	
XRF	SrO	0.02	0.01	0.01	0.01	0.02	0.01	
XRF	BaO	0.01	0.01		0.01		0.02	
	LOI	0.46	-0.23	-0.24	-0.37	1.44	1.92	
	Sum	99.74	99.37	99.15	98.99	99.74	99.23	
ICP-MS	Ti	1180	870	640	710	980	730	0
ICP-MS	P	370	290	250	280	330	260	
ICP-MS	Cr	2114	2166	223	2168	309	2982	2107
ICP-MS	Co	71.8	90.8	90.2	91.1	116.5	115.5	
ICP-MS	Ni	568	792	620	817	1120	1153	780
ICP-MS	Rb	7	4	5.4	7	10	6	7
ICP-MS	Sr	178	135	10	121	121.5	132	188
ICP-MS	Cs	0.298	0.145	0.15	0.185	0.35	0.254	0.295
ICP-MS	Ba	70	60	50	50	130	110	
ICP-MS	Sc	41	36	4.9	36	4.3	24	37
ICP-MS	V	158	136	17	143	18	105	153
ICP-MS	Ta	0.18			0.2			
ICP-MS	Nb	4	3	0.23	3	0.14	3	2
ICP-MS	Zr	51	39	2.2	52	2.8	34	37
ICP-MS	Hf	1.5	1.1	0.04	1.4	0.06	0.9	1.1
ICP-MS	Th	0.6	0.47	0.4	0.68	0.5	0.38	0.53
ICP-MS	U	0.122	0.094	0.05	0.132	0.08	0.099	0.11
ICP-MS	Y	11	8	0.49	9	1.04	5	9
ICP-MS	La	7.58	5.5	2.2	7.61	5	5.83	6.36
ICP-MS	Ce	18.48	13.24	3.9	17.68	8.09	12.36	13.76
ICP-MS	Pr	2.586	1.871		2.355		1.629	1.879
ICP-MS	Nd	12.18	8.51		10.42		7.26	8.61
ICP-MS	Sm	3.01	2.07		2.42		1.66	2.14
ICP-MS	Eu	0.945	0.654		0.724		0.58	0.749
ICP-MS	Gd	2.874	1.986		2.317		1.543	2.145
ICP-MS	Tb	0.411	0.286		0.331		0.218	0.309
ICP-MS	Dy	2.379	1.619		1.843		1.213	1.739
ICP-MS	Ho	0.436	0.298		0.331		0.224	0.321
ICP-MS	Er	1.118	0.77		0.872		0.575	0.837
ICP-MS	Tm	0.148	0.102		0.111		0.076	0.108
ICP-MS	Yb	0.89	0.63		0.69		0.49	0.68
ICP-MS	Lu	0.123	0.089		0.093		0.068	0.094
ICP-MS	Cu	52.6	34.6	36.4	29.2	54.9	67.6	
ICP-MS	Zn	61	66	79	67	79	84	
ICP-MS	Mo	0.23	0.22	0.23	0.19	0.45	0.35	
ICP-MS	Ag	0.03	0.02	0.02	0.02	0.03	0.04	
ICP-MS	Cd	0.03	0.04	0.05	0.04	0.06	0.07	
ICP-MS	Te	0.01	0.01	0.01	0.01			
ICP-MS	Tl	0.03	0.02			0.07	0.08	
ICP-MS	Pb	2.5	1.4	0.6	1.4	3.3	3.1	5.2
ICP-MS	Sn							
ICP-MS	Sb							
ICP-MS	Ga	2.09	1.32	1.02	1.14	2.19	1.85	
ICP-MS	Ge	0.13	0.16	0.17	0.17	0.19	0.18	
ICP-MS	As	0.2	0.2	0.2	0.2	0.6	0.5	
ICP-MS	Se	0.2	0.2			0.2		
ICP-MS	W					0.06		
ICP-MS	Li	3.3	2.3	2.1	2.3	5.3	5.9	
ICP-MS	Be					0.09	0.05	
ICP-MS	S	300	100	100		500	300	0
ICP-MS	Bi			0.01		0.02	0.02	
ICP-MS	Au			0.006	0.001	0.001	0.001	
ICP-MS	Pt	0.014						
ICP-MS	Pd	0.006	0.001	0.003	0.002	0.004	0.004	

Method	Sample	JL-111 Lherzolite-olivine websterite	JL-015 Pyroxene-porphyritic melano-gabbro	JL-016 Pyroxene-porphyritic melano-gabbro	JL-017 Pyroxene-porphyritic melano-gabbro	JL-018 Pyroxene-porphyritic melano-gabbro	JL-019 Pyroxene-porphyritic melano-gabbro	JL-020 Pyroxene-porphyritic melano-gabbro
XRF	SiO_2		46.7	46.74	46.23	47.02	48.5	47.11
XRF	TiO_2		1.01	0.87	1.15	1.16	1.27	1.14
XRF	Al_2O_3		5.54	5.44	7.4	8.2	6.09	7.24
XRF	Fe_2O_3		14.86	15	16	14.62	11.76	14.53
XRF	MnO		0.24	0.25	0.24	0.22	0.21	0.21
XRF	MgO		17.95	17.74	17.55	16.81	14.46	18.83
XRF	CaO		10.82	11.45	8.09	8.75	14.3	7.91
XRF	Na_2O		0.98	0.81	1.24	1.42	1.23	1.6
XRF	K_2O		0.46	0.33	0.7	0.62	0.57	0.57
XRF	P_2O_5		0.1	0.09	0.12	0.14	0.11	0.16
XRF	Cr_2O_3		0.21	0.2	0.17	0.16	0.22	0.19
XRF	SrO		0.02	0.02	0.03	0.04	0.03	0.03
XRF	BaO		0.02	0.02	0.01	0.03	0.02	0.02
	LOI		0.61	0.61	0.55	0.62	0.75	0.06
	Sum		99.53	99.57	99.47	99.82	99.51	99.6
ICP-MS	Ti	0	1610	1260	2210	2010	1350	1470
ICP-MS	P		380	270	520	530	410	630
ICP-MS	Cr	2149	1668	399	1218	437	1499	1414
ICP-MS	Co		55.2	48	54.9	50.1	27.6	62.4
ICP-MS	Ni	736	467	290	516	338	342	552
ICP-MS	Rb	9	20	8	18	15.7	17	12
ICP-MS	Sr	167	147	36	319	67.5	285	338
ICP-MS	Cs	0.317	0.419	0.29	0.52	0.38	0.455	0.397
ICP-MS	Ba		160	120	190	190	140	100
ICP-MS	Sc	37	47	3.2	33	2.9	49	33
ICP-MS	V	156	214	64	181	88	245	174
ICP-MS	Ta		0.36		0.28		0.47	0.3
ICP-MS	Nb	3	6	0.35	5	0.43	7	6
ICP-MS	Zr	39	92	2.7	77	5.9	109	82
ICP-MS	Hf	1.2	2.7	0.05	2.1	0.16	3.1	2.3
ICP-MS	Th	0.44	1.31	0.3	1	0.7	1.57	1.03
ICP-MS	U	0.09	0.27		0.231	0.08	0.315	0.205
ICP-MS	Y	9	16	0.6	13	1.63	18	13
ICP-MS	La	6.78	16.78	3.1	11.5	6.4	16.37	12.71
ICP-MS	Ce	17	35.2	5.11	26.21	13.35	36.5	29.33
ICP-MS	Pr	2.335	4.522		3.507		4.889	3.945
ICP-MS	Nd	10.65	19.65		15.46		21.73	17.31
ICP-MS	Sm	2.51	4.49		3.6		5.2	3.91
ICP-MS	Eu	0.768	1.321		1.096		1.558	1.227
ICP-MS	Gd	2.491	4.058		3.342		4.815	3.531
ICP-MS	Tb	0.355	0.575		0.473		0.687	0.49
ICP-MS	Dy	1.986	3.285		2.707		3.892	2.723
ICP-MS	Ho	0.358	0.596		0.49		0.71	0.494
ICP-MS	Er	0.937	1.547		1.253		1.817	1.274
ICP-MS	Tm	0.12	0.198		0.165		0.235	0.166
ICP-MS	Yb	0.74	1.23		1.02		1.45	1.01
ICP-MS	Lu	0.104	0.167		0.141		0.196	0.143
ICP-MS	Cu		77.4	197	110.5	89.2	276	67.8
ICP-MS	Zn		59	61	86	77	47	63
ICP-MS	Mo		0.25	0.21	0.45	0.38	0.28	0.24
ICP-MS	Ag		0.04	0.11	0.08	0.05	0.08	0.03
ICP-MS	Cd		0.06	0.07	0.08	0.06	0.08	0.04
ICP-MS	Te		0.01	0.03	0.02	0.01	0.05	0.01
ICP-MS	Tl		0.07	0.07	0.09	0.09	0.05	0.04
ICP-MS	Pb	1.7	6.3	5.5	4.9	1.7	10.2	2.8
ICP-MS	Sn		0.2	0.2	0.4	0.4	0.2	0.3
ICP-MS	Sb		0.1	0.09		0.39		
ICP-MS	Ga		3.07	2.72	4.69	4.75	3.29	2.8
ICP-MS	Ge		0.09	0.08	0.1	0.1	0.07	0.11
ICP-MS	As		0.5	0.5	0.6	0.4	0.4	0.2
ICP-MS	Se		0.3	0.3	0.3	0.3	0.5	0.2
ICP-MS	W		0.06		0.06		0.05	
ICP-MS	Li		3.4	2.6	3.7	3.9	2.8	3.4
ICP-MS	Be		0.06		0.14	0.13	0.06	0.11
ICP-MS	S	0	500	500	500	500	600	100
ICP-MS	Bi		0.04	0.03	0.04	0.02	0.04	0.01
ICP-MS	Au		0.001	0.006	0.002		0.044	
ICP-MS	Pt		0.242	0.005			0.1	
ICP-MS	Pd		0.037	0.009	0.003	0.001	0.05	0.001

Method	Sample	JL-021 Pyroxene-porphyritic melano-gabbro	JL-023 Pyroxene-porphyritic melano-gabbro	JL-024 Pyroxene-porphyritic melano-gabbro	JL-026 Pyroxene-porphyritic melano-gabbro	JL-027 Pyroxene-porphyritic melano-gabbro	JL-032 Pyroxene-porphyritic melano-gabbro	JL-034 Pyroxene-porphyritic melano-gabbro
XRF	SiO_2	47.77	46.33	46.72	46.46	46.26	46.01	46.95
XRF	TiO_2	1.36	1.05	1.07	1.09	0.84	1.08	1.19
XRF	Al_2O_3	7.59	5.78	4.55	4.67	7.01	6.81	6.73
XRF	Fe_2O_3	14.33	15.36	14.99	16.03	15.05	15.31	14.88
XRF	MnO	0.21	0.24	0.25	0.26	0.22	0.25	0.21
XRF	MgO	17.28	18.87	18.72	19.11	19.22	19.1	19.08
XRF	CaO	8.08	9.49	10.95	9.47	9.2	8.67	8.27
XRF	Na_2O	1.61	0.99	0.82	0.77	1.29	1.22	1.42
XRF	K_2O	0.8	0.53	0.57	0.69	0.42	0.53	0.56
XRF	P_2O_5	0.18	0.11	0.1	0.11	0.09	0.14	0.16
XRF	Cr_2O_3	0.17	0.17	0.22	0.17	0.21	0.2	0.19
XRF	SrO	0.03	0.03	0.02	0.02	0.03	0.03	0.03
XRF	BaO	0.03	0.02	0.02	0.02	0.03	0.01	0.03
	LOI	0.16	0.64	0.72	1	0.04	0.39	0.14
	Sum	99.61	99.61	99.71	99.88	99.91	99.75	99.83
ICP-MS	Ti	1750	1690	1730	2190	1300	1870	1590
ICP-MS	P	740	470	390	490	340	500	580
ICP-MS	Cr	321	1360	460	1245	1383	449	320
ICP-MS	Co	51.7	61.1	53.7	67.2	66.2	66.2	61.9
ICP-MS	Ni	337	525	346	469	530	413	402
ICP-MS	Rb	17.7	13	14.8	13	9	14.9	13.8
ICP-MS	Sr	21.1	223	39.6	203	326	73.2	16.5
ICP-MS	Cs	0.51	0.511	0.37	0.334	0.232	0.54	0.36
ICP-MS	Ba	130	160	150	170	190	170	120
ICP-MS	Sc	3.3	44	3.4	40	30	4.2	4.3
ICP-MS	V	69	204	63	191	138	75	57
ICP-MS	Ta	0.01	0.31		0.26			
ICP-MS	Nb	0.45	5	0.54	4	2	0.61	0.61
ICP-MS	Zr	5	80	4.9	70	39	4.6	4.2
ICP-MS	Hf	0.16	2.2	0.11	2.2	1.2	0.12	0.12
ICP-MS	Th	0.9	1.04	0.6	1.02	0.57	0.7	0.8
ICP-MS	U	0.1	0.208	0.08	0.228	0.124	0.08	0.1
ICP-MS	Y	2.66	15	0.98	13	9	1.54	1.77
ICP-MS	La	11.2	13.85	4.7	12.08	6.09	7	8.1
ICP-MS	Ce	21.9	31.06	8.48	26.84	14.72	13.05	15.8
ICP-MS	Pr		4.01		3.68	2.074		
ICP-MS	Nd		17.84		16.71	9.6		
ICP-MS	Sm		4.05		3.98	2.37		
ICP-MS	Eu		1.234		1.275	0.832		
ICP-MS	Gd		3.76		3.826	2.303		
ICP-MS	Tb		0.53		0.55	0.333		
ICP-MS	Dy		3.02		3.154	1.942		
ICP-MS	Ho		0.544		0.578	0.356		
ICP-MS	Er		1.418		1.473	0.92		
ICP-MS	Tm		0.183		0.193	0.121		
ICP-MS	Yb		1.11		1.17	0.76		
ICP-MS	Lu		0.157		0.163	0.104		
ICP-MS	Cu	87	153.5	70.3	163.5	126.5	64.2	68.7
ICP-MS	Zn	59	66	49	68	62	75	61
ICP-MS	Mo	0.33	0.3	0.29	0.45	0.23	0.35	0.3
ICP-MS	Ag	0.04	0.11	0.04	0.11	0.05	0.03	0.03
ICP-MS	Cd	0.05	0.07	0.04	0.07	0.04	0.19	0.04
ICP-MS	Te	0.01	0.03	0.02	0.03	0.01	0.01	0.01
ICP-MS	Tl	0.06	0.12	0.09	0.09		0.1	0.05
ICP-MS	Pb	2.7	6.8	3	4.6	1.4	21.6	2
ICP-MS	Sn	0.3	0.3	0.2	0.3	0.2	0.3	0.3
ICP-MS	Sb							
ICP-MS	Ga	3.38	3.22	3.02	4.23	2.79	4.03	2.77
ICP-MS	Ge	0.11	0.11	0.1	0.11	0.12	0.13	0.12
ICP-MS	As	0.4	0.3	0.4	0.5	0.2	0.3	0.3
ICP-MS	Se	0.3	0.3	0.3	0.3	0.2	0.2	0.3
ICP-MS	W	0.05	0.05		0.06		0.05	
ICP-MS	Li	4.1	3.3	4.4	3.6	2.4	3.8	3.2
ICP-MS	Be	0.14	0.08	0.07	0.13	0.07	0.12	0.1
ICP-MS	S	300	600	500	900	300	300	200
ICP-MS	Bi	0.01	0.03	0.02	0.04		0.02	
ICP-MS	Au	0.001	0.004	0.001	0.019	0.001		
ICP-MS	Pt				0.139			
ICP-MS	Pd	0.002	0.001	0.002	0.18	0.004	0.005	0.001

Method	Sample	JL-035 Pyroxene-porphyritic melano-gabbro	JL-036 Pyroxene-porphyritic melano-gabbro	JL-038 Pyroxene-porphyritic melano-gabbro	JL-039 Pyroxene-porphyritic melano-gabbro	JL-040 Pyroxene-porphyritic melano-gabbro	JL-040vein Pyroxene-porphyritic melano-gabbro	JL-104 Pyroxene-porphyritic melano-gabbro
XRF	SiO_2	47.74	47.01	45.64	45.73	45.73	60.25	
XRF	TiO_2	1.01	1.01	0.88	0.91	1.07	1.85	
XRF	Al_2O_3	7.54	6.19	5.59	7.72	5.95	13.36	
XRF	Fe_2O_3	14.33	13.96	15.78	15.39	15.75	10.21	
XRF	MnO	0.22	0.22	0.23	0.22	0.24	0.09	
XRF	MgO	17.09	18.74	20.86	18.04	19.53	2	
XRF	CaO	9.4	10.27	8.48	9.42	8.76	5.75	
XRF	Na_2O	1.31	1.21	1.08	0.97	1.16	3.3	
XRF	K_2O	0.51	0.43	0.37	0.53	0.52	1.33	
XRF	P_2O_5	0.1	0.1	0.11	0.07	0.11	0.56	
XRF	Cr_2O_3	0.19	0.22	0.23	0.17	0.2		
XRF	SrO	0.03	0.02	0.02	0.03	0.02	0.07	
XRF	BaO	0.02	0.02	0.01	0.02	0.01	0.07	
	LOI	0.28	0.27	0.14	0.52	0.3	0.78	
	Sum	99.77	99.67	99.43	99.74	99.34	99.63	
ICP-MS	Ti	1470	1450	1420	1480	1630	1790	0
ICP-MS	P	420	410	380	310	480	2340	
ICP-MS	Cr	350	1754	409	368	1594	5	1667
ICP-MS	Co	52.9	54.2	71.4	66.6	62.7	26.3	
ICP-MS	Ni	317	551	468	396	588	5.8	505
ICP-MS	Rb	12.1	13	14.9	15.8	13	12.9	8
ICP-MS	Sr	40.1	197	24.1	105.5	223	50.6	146
ICP-MS	Cs	0.41	0.483	0.36	0.41	0.418	0.4	0.409
ICP-MS	Ba	150	90	110	130	140	80	
ICP-MS	Sc	3.5	42	4.5	4.6	41	4.4	51
ICP-MS	V	61	223	54	64	204	70	201
ICP-MS	Ta		0.36			0.34	0.01	0.25
ICP-MS	Nb	0.48	6	0.45	0.31	6	0.82	4
ICP-MS	Zr	3.6	95	3.5	4	86	7.2	61
ICP-MS	Hf	0.1	2.9	0.08	0.1	2.4	0.18	1.7
ICP-MS	Th	0.5	1.42	0.6	0.4	1.15	5.1	0.76
ICP-MS	U	0.06	0.291	0.08	0.06	0.232	1.73	0.146
ICP-MS	Y	1.24	16	1.04	1.17	14	17.5	12
ICP-MS	La	5.2	14.7	4.6	4.1	13.08	60.8	9.01
ICP-MS	Ce	10.3	33.52	8.55	7.94	30.05	116.5	21.25
ICP-MS	Pr		4.46			4.01		2.919
ICP-MS	Nd		19.63			17.47		13.35
ICP-MS	Sm		4.39			4.04		3.23
ICP-MS	Eu		1.292			1.231		0.995
ICP-MS	Gd		4.099			3.761		3.152
ICP-MS	Tb		0.584			0.533		0.455
ICP-MS	Dy		3.24			3		2.548
ICP-MS	Ho		0.585			0.544		0.464
ICP-MS	Er		1.529			1.404		1.188
ICP-MS	Tm		0.196			0.184		0.156
ICP-MS	Yb		1.21			1.13		0.97
ICP-MS	Lu		0.168			0.158		0.132
ICP-MS	Cu	83.8	106.5	89.9	182	120.5	17.8	
ICP-MS	Zn	74	48	75	58	62	30	
ICP-MS	Mo	0.27	0.28	0.28	0.37	0.25	0.71	
ICP-MS	Ag	0.07	0.06	0.04	0.09	0.1	0.04	
ICP-MS	Cd	0.07	0.03	0.05	0.04	0.05	0.07	
ICP-MS	Te	0.01	0.02	0.02	0.03	0.02	0.01	
ICP-MS	Tl	0.04	0.06		0.05	0.1	0.03	
ICP-MS	Pb	4.6	4.7	1	2.3	4	5.9	3.5
ICP-MS	Sn	0.3	0.2	0.2	0.2	0.3	1.3	
ICP-MS	Sb						0.06	
ICP-MS	Ga	3.23	2.91	2.64	4.85	2.98	10.05	
ICP-MS	Ge	0.12	0.11	0.13	0.13	0.13	0.32	
ICP-MS	As	0.4	0.2	0.2	0.4	0.3	2.9	
ICP-MS	Se	0.3	0.3	0.3	0.3	0.4	0.7	
ICP-MS	W	0.06					0.08	
ICP-MS	Li	2.9	2.9	2.6	4.9	2.6	12	
ICP-MS	Be	0.07	0.07	0.06	0.11	0.08	0.73	
ICP-MS	S	300	400	300	500	400	200	0
ICP-MS	Bi	0.03	0.01	0.01	0.02	0.02	0.02	
ICP-MS	Au	0.001	0.002		0.001	0.001		
ICP-MS	Pt		0.025		0.018			
ICP-MS	Pd	0.003	0.02	0.001	0.008	0.007		

Method	Sample	JL-105 Pyroxene-porphyritic melano-gabbro	JL-107 Pyroxene-porphyritic melano-gabbro	JL-110 Pyroxene-porphyritic melano-gabbro	JL-114 Pyroxene-porphyritic melano-gabbro	JL-022 Grano-phyric gabbro	JL-043 Grano-phyric gabbro	JL-047 Grano-phyric gabbro
XRF	SiO_2					49.73	52.4	50.29
XRF	TiO_2					1.64	3.63	1.93
XRF	Al_2O_3					14.15	13.15	9.64
XRF	Fe_2O_3					15.37	13.78	12.44
XRF	MnO					0.24	0.23	0.21
XRF	MgO					5.67	3.67	9.07
XRF	CaO					8.42	6.41	11.45
XRF	Na_2O					2.11	2.56	1.75
XRF	K_2O					1.33	2.16	1.19
XRF	P_2O_5					0.13	0.34	0.24
XRF	Cr_2O_3							0.1
XRF	SrO					0.05	0.07	0.04
XRF	BaO					0.05	0.09	0.03
	LOI					0.7	1.12	1.23
	Sum					99.59	99.61	99.61
ICP-MS	Ti	0	0	0	0	1400	1680	1450
ICP-MS	P					620	1410	850
ICP-MS	Cr	2169	2089	2141	2004	361		200
ICP-MS	Co					26.2	21.7	24.2
ICP-MS	Ni	555	444	578	581	76	43	70.9
ICP-MS	Rb	9	16	8	11	43	46	19
ICP-MS	Sr	150	177	183	171	291	638	48.6
ICP-MS	Cs	0.299	0.681	0.356	0.311	3.671	0.7	0.49
ICP-MS	Ba					190	180	80
ICP-MS	Sc	50	53	50	45	51	33	4.4
ICP-MS	V	185	215	167	208	231	488	141
ICP-MS	Ta	0.2	0.42	0.2	0.25	0.4	0.98	
ICP-MS	Nb	4	7	5	5	7	14	0.06
ICP-MS	Zr	54	101	61	68	60	233	13.1
ICP-MS	Hf	1.6	2.7	1.5	1.9	1.7	6.2	0.37
ICP-MS	Th	0.68	1.56	0.68	0.89	1.05	3.19	1.2
ICP-MS	U	0.153	0.31	0.136	0.168	0.257	0.638	0.17
ICP-MS	Y	10	14	12	12	17	31	5.22
ICP-MS	La	8.4	17.34	9.27	10.46	10.78	33.16	10.5
ICP-MS	Ce	19.79	33.76	19.57	24.4	23.14	76.65	22.2
ICP-MS	Pr	2.676	4.138	2.628	3.311	2.919	10.121	
ICP-MS	Nd	12.05	17.76	11.75	14.96	12.57	43.72	
ICP-MS	Sm	2.96	4.01	2.8	3.54	2.96	9.64	
ICP-MS	Eu	0.97	1.294	0.94	1.065	0.973	2.969	
ICP-MS	Gd	2.898	3.707	2.731	3.348	3.132	8.706	
ICP-MS	Tb	0.41	0.531	0.389	0.483	0.506	1.196	
ICP-MS	Dy	2.341	2.986	2.2	2.709	3.152	6.536	
ICP-MS	Ho	0.432	0.539	0.397	0.5	0.639	1.181	
ICP-MS	Er	1.099	1.408	1.017	1.267	1.813	3.053	
ICP-MS	Tm	0.143	0.182	0.131	0.163	0.257	0.395	
ICP-MS	Yb	0.88	1.11	0.8	1.02	1.65	2.45	
ICP-MS	Lu	0.123	0.155	0.111	0.14	0.243	0.335	
ICP-MS	Cu					93.1	99.9	167
ICP-MS	Zn					75	96	149
ICP-MS	Mo					0.66	1.12	0.65
ICP-MS	Ag					0.07	0.06	0.04
ICP-MS	Cd					0.1	0.13	0.2
ICP-MS	Te					0.02	0.02	0.02
ICP-MS	Tl					0.03	0.08	0.09
ICP-MS	Pb	1.8	3.9	7.3	2.7	10.5	7	11.2
ICP-MS	Sn					0.7	1.1	0.5
ICP-MS	Sb					0.19		
ICP-MS	Ga					7.81	8.02	5.82
ICP-MS	Ge					0.16	0.24	0.14
ICP-MS	As					1.7	0.7	1.6
ICP-MS	Se					0.3	0.5	0.4
ICP-MS	W					0.1	0.05	0.07
ICP-MS	Li					11.2	8.3	8.9
ICP-MS	Be					0.24	0.35	0.14
ICP-MS	S	0	0	0	0	200		900
ICP-MS	Bi					0.06	0.07	0.05
ICP-MS	Au							0.002
ICP-MS	Pt					0.008		0.008
ICP-MS	Pd							0.013

Method	Sample	JL-065 Diabase	JL-066 Diabase	JL-069 Diabase	JL-072 Diabase	JL-074 Diabase	JL-075 Diabase	JL-076 Diabase
XRF	SiO_2	45.26	47.36	49.04	47.72	48.52	47.27	46.3
XRF	TiO_2	2.27	1.21	1.45	1.43	1.4	1.29	1.16
XRF	Al_2O_3	9.92	15.25	14.32	14.12	14.54	14.78	14.95
XRF	Fe_2O_3	16.63	14.68	14.28	13.2	14.5	14.72	13.99
XRF	MnO	0.21	0.21	0.2	0.21	0.2	0.2	0.19
XRF	MgO	13.76	7.42	6.43	7.11	7.16	7.66	8.64
XRF	CaO	8.17	10.13	9.99	11.33	9.79	10.08	9.86
XRF	Na_2O	2.14	2.14	2.35	2.33	2.23	2.25	2.33
XRF	K_2O	0.6	0.51	0.65	0.71	0.61	0.56	0.59
XRF	P_2O_5	0.22	0.12	0.15	0.15	0.13	0.12	0.12
XRF	Cr_2O_3	0.12	0.02	0.01	0.01	0.01	0.01	0.01
XRF	SrO	0.03	0.02	0.02	0.03	0.02	0.02	0.02
XRF	BaO	0.02	0.02	0.02	0.03	0.01	0.02	0.01
	LOI	0.31	0.42	0.74	1.18	0.47	0.85	1.35
	Sum	99.67	99.51	99.65	99.56	99.59	99.84	99.52
ICP-MS	Ti	2590	2010	1790	2120	1970	1820	1530
ICP-MS	P	930	480	590	400	540	520	420
ICP-MS	Cr	290	7	20	36	6	11	10
ICP-MS	Co	60.7	27.9	23.4	20	24.9	24.1	33
ICP-MS	Ni	535	84.2	59	64.1	72.8	76.9	128.5
ICP-MS	Rb	14.5	10.6	14.5	15.5	10.3	12.7	8.7
ICP-MS	Sr	16.3	50.3	46.7	74.4	47	53.2	54.7
ICP-MS	Cs	1.06	0.42	0.58	0.83	0.38	0.44	0.88
ICP-MS	Ba	50	50	100	80	50	70	30
ICP-MS	Sc	4.3	2.1	3.3	3.7	2.2	2.8	3
ICP-MS	V	165	162	174	116	185	165	157
ICP-MS	Ta	0.01						
ICP-MS	Nb	0.43	0.16	0.07	0.12	0.15	0.1	0.07
ICP-MS	Zr	8.5	8.9	10.2	14.1	12.3	7.5	7.5
ICP-MS	Hf	0.26	0.26	0.27	0.32	0.31	0.22	0.21
ICP-MS	Th	1.3	1.2	1.5	1.1	1.3	1.1	1.4
ICP-MS	U	0.15	0.28	0.33	0.33	0.33	0.23	0.28
ICP-MS	Y	9.94	6.85	8.4	6.5	9.06	6.39	6.2
ICP-MS	La	13.9	6.5	8.3	6.1	7.9	6.1	6.3
ICP-MS	Ce	30.2	14.25	18	12.6	17.35	13.45	13.35
ICP-MS	Pr							
ICP-MS	Nd							
ICP-MS	Sm							
ICP-MS	Eu							
ICP-MS	Gd							
ICP-MS	Tb							
ICP-MS	Dy							
ICP-MS	Ho							
ICP-MS	Er							
ICP-MS	Tm							
ICP-MS	Yb							
ICP-MS	Lu							
ICP-MS	Cu	113	185	173	116	194	127	141
ICP-MS	Zn	90	53	64	44	54	49	60
ICP-MS	Mo	0.66	0.37	0.48	0.5	0.37	0.29	0.33
ICP-MS	Ag	0.04	0.05	0.04	0.04	0.06	0.03	0.1
ICP-MS	Cd	0.06	0.06	0.06	0.06	0.05	0.04	0.05
ICP-MS	Te	0.01		0.01	0.01	0.01	0.01	0.01
ICP-MS	Tl	0.04	0.05	0.09	0.15	0.02	0.02	0.03
ICP-MS	Pb	2.4	2.1	3	3.2	1.7	2.2	3.8
ICP-MS	Sn	0.6	0.5	0.5	0.5	0.5	0.4	0.5
ICP-MS	Sb							0.15
ICP-MS	Ga	5.48	7.54	7.89	6.45	7.54	7.52	7.83
ICP-MS	Ge	0.16	0.09	0.1	0.1	0.11	0.1	0.11
ICP-MS	As	0.5	0.8	1	0.7	0.7	0.7	0.6
ICP-MS	Se	0.6	0.4	0.5	0.4	0.5	0.5	0.5
ICP-MS	W	0.09	0.06	0.07	0.07	0.08	0.05	
ICP-MS	Li	8.9	5.8	7.7	21.4	7.3	6.9	13.7
ICP-MS	Be	0.32	0.12	0.11	0.16	0.1	0.11	0.15
ICP-MS	S		200	200				
ICP-MS	Bi	0.02	0.02	0.03	0.02	0.03	0.02	0.02
ICP-MS	Au	0.002	0.003	0.003	0.002	0.002	0.003	0.003
ICP-MS	Pt							
ICP-MS	Pd	0.001	0.016	0.017	0.015	0.014	0.014	0.015

Method	Sample	JL-055a Diabase	JL-055b Diabase	JL-057 Diabase	JL-060 Diabase	JL-061 Diabase	JL-008 Iron formation	JL-046 Iron formation
XRF	SiO_2	48.25	46.72	48.16	48.05	48.21		
XRF	TiO_2	1.45	0.89	1.41	1.2	1.26		
XRF	Al_2O_3	14.59	16.22	14.31	15	15.25		
XRF	Fe_2O_3	15.03	13.49	14.76	14.35	14.21		
XRF	MnO	0.22	0.18	0.2	0.2	0.2		
XRF	MgO	6.3	8.93	6.55	8.1	7.25		
XRF	CaO	10.04	10.31	10.1	9.74	10.18		
XRF	Na_2O	2.19	2.13	2.29	2.18	2.23		
XRF	K_2O	0.64	0.4	0.55	0.51	0.54		
XRF	P_2O_5	0.15	0.09	0.15	0.13	0.13		
XRF	Cr_2O_3	0.01	0.02	0.01	0.01	0.01		
XRF	SrO	0.02	0.02	0.02	0.02	0.02		
XRF	BaO	0.02	0.03	0.03	0.02	0.02		
	LOI	0.79	-0.04	1.02	0.3	0.23		
	Sum	99.71	99.39	99.56	99.8	99.75		
ICP-MS	Ti	1850	1450	1960	1890	2160	0	0
ICP-MS	P	630	390	580	490	530		
ICP-MS	Cr	10	165	15	7	8	24	149
ICP-MS	Co	27.3	42.8	22	30.7	27		
ICP-MS	Ni	58.3	234	48.6	115.5	79.9	16	61
ICP-MS	Rb	24.7	9	18.9	10.7	10.9	8	80
ICP-MS	Sr	47.4	166	51.9	46.6	58.1	15	370
ICP-MS	Cs	0.72	0.327	0.6	0.41	0.44	1.102	0.264
ICP-MS	Ba	140	50	140	50	50		
ICP-MS	Sc	3.3	35	3.3	2.5	2.2	16	36
ICP-MS	V	190	170	181	156	162	5	313
ICP-MS	Ta		0.19		0.01	0.01		0.38
ICP-MS	Nb	0.14	3	0.09	0.26	0.23		6
ICP-MS	Zr	12.6	55	15.6	7.6	10.2	7	69
ICP-MS	Hf	0.29	1.6	0.42	0.24	0.31	0.2	1.8
ICP-MS	Th	1.5	1.02	1.7	1.1	1.2	0.08	0.78
ICP-MS	U	0.32	0.295	0.4	0.22	0.29	0.037	1.312
ICP-MS	Y	11	15	12.45	7.54	8.46	8	24
ICP-MS	La	7.7	5.88	8.8	6	6.9	1.04	20.41
ICP-MS	Ce	17.7	13.23	20.4	13.75	16.15	1.97	38.64
ICP-MS	Pr		1.762				0.281	3.808
ICP-MS	Nd		7.94				1.43	14.33
ICP-MS	Sm		2.17				0.45	3.43
ICP-MS	Eu		0.818				0.046	1.31
ICP-MS	Gd		2.632				0.706	4.197
ICP-MS	Tb		0.442				0.125	0.682
ICP-MS	Dy		2.813				0.931	4.358
ICP-MS	Ho		0.582				0.224	0.916
ICP-MS	Er		1.716				0.757	2.662
ICP-MS	Tm		0.241				0.122	0.373
ICP-MS	Yb		1.56				0.89	2.38
ICP-MS	Lu		0.234				0.159	0.338
ICP-MS	Cu	186.5	130.5	166	163.5	182.5		
ICP-MS	Zn	85	49	52	59	52		
ICP-MS	Mo	0.37	0.3	0.46	0.35	0.46		
ICP-MS	Ag	0.03	0.04	0.04	0.05	0.05		
ICP-MS	Cd	0.11	0.05	0.07	0.06	0.06		
ICP-MS	Te	0.01			0.01			
ICP-MS	Tl	0.08	0.04	0.17	0.04	0.06		
ICP-MS	Pb	2.9	1.7	2.6	1.9	2.1	0.6	6.2
ICP-MS	Sn	0.5	0.4	0.3	0.4	0.5		
ICP-MS	Sb	0.05						
ICP-MS	Ga	7.88	6.98	7.83	6.5	7.49		
ICP-MS	Ge	0.12	0.09	0.1	0.08	0.1		
ICP-MS	As	1	1	0.9	0.7	0.7		
ICP-MS	Se	0.3	0.2	0.4	0.4	0.4		
ICP-MS	W		0.07	0.05	0.06	0.06		
ICP-MS	Li	7.2	3.5	7.5	4.5	5.6		
ICP-MS	Be	0.11	0.08	0.08	0.07	0.08		
ICP-MS	S		200		200	200	0	0
ICP-MS	Bi	0.04	0.01	0.02	0.01	0.02		
ICP-MS	Au	0.003	0.002	0.002	0.003	0.003		
ICP-MS	Pt		0.006					
ICP-MS	Pd	0.012	0.012	0.015	0.013	0.016		

Method	Sample	JL-007 Mafic meta-volcanic	Method	Sample KD:	9451	9452	9453	9454
XRF	SiO_2		XRF	SiO_2	48.1	45	43.1	43.8
XRF	TiO_2		XRF	TiO_2	1.12	1	0.82	0.75
XRF	Al_2O_3		XRF	Al_2O_3	5.46	5.2	4.57	3.87
XRF	Fe_2O_3		XRF	Fe_2O_3	15.65	17.3	15.95	16.75
XRF	MnO			FeO				
XRF	MgO		XRF	Fe_2O3_t	0.00	0.00	0.00	0.00
XRF	CaO		XRF	MnO	0.21	0.2	0.24	0.22
XRF	Na_2O		XRF	MgO	22.3	23.2	25.2	26.2
XRF	K_2O		XRF	CaO	8.01	7.31	8.53	8.54
XRF	P_2O_5			LOI				
XRF	Cr_2O_3			Sum	100.85	99.21	98.41	100.13
XRF	SrO							
XRF	BaO		ICP-MS	Ti	0	0	0	0
	LOI		ICP-MS	P				
	Sum		ICP-MS	Cr %	0.27	0.31	0.2	0.29
			ICP-MS	Cr ppm	2700	3100	2000	2900
ICP-MS	Ti	0	ICP-MS	Co %	0.012	0.014	0.014	0.017
ICP-MS	P		ICP-MS	Co ppm	120	140	140	170
ICP-MS	Cr	155	ICP-MS	Ni %	0.09	0.097	0.078	0.108
ICP-MS	Co		ICP-MS	Ni ppm	900	970	780	1080
ICP-MS	Ni	54	ICP-MS	Cu %	0.008	0.013	0.013	0.03
ICP-MS	Rb	2	ICP-MS	Cu ppm	80	130	130	300
ICP-MS	Sr	20	ICP-MS	Zn %	0.01	0.01	0.02	0.02
ICP-MS	Cs	0.138	ICP-MS	Zn ppm	100	100	200	200
ICP-MS	Ba		ICP-MS	Pb %				
ICP-MS	Sc	54	ICP-MS	S %	0.09	0.12	0.16	0.19
ICP-MS	V	329	ICP-MS	S ppm	900	1200	1600	1900
ICP-MS	Ta	0.17	ICP-MS	As %			0.01	
ICP-MS	Nb	3	ICP-MS	Au			0.001	0.004
ICP-MS	Zr	71	ICP-MS	Pt	0.015	0.017	0.018	0.026
ICP-MS	Hf	2.1	ICP-MS	Pd	0.008	0.008	0.011	0.038
ICP-MS	Th	0.27						
ICP-MS	U	0.065						
ICP-MS	Y	23	Method	Sample KD:	9459	9460	9461	9462
ICP-MS	La	3.23	XRF	SiO_2	43.6	40	40.8	40.8
ICP-MS	Ce	9.52	XRF	TiO_2	0.84	0.73	0.71	0.74
ICP-MS	Pr	1.543	XRF	Al_2O_3	3.96	3.61	3.67	3.71
ICP-MS	Nd	8.17	XRF	Fe_2O_3	14.75	13.5	14.7	16.15
ICP-MS	Sm	2.73		FeO				
ICP-MS	Eu	0.572	XRF	Fe_2O3_t	0.00	0.00	0.00	0.00
ICP-MS	Gd	3.615	XRF	MnO	0.15	0.13	0.15	0.2
ICP-MS	Tb	0.639	XRF	MgO	27.8	27.6	28.6	29.4
ICP-MS	Dy	4.309	XRF	CaO	5.84	4.38	4.09	2.82
ICP-MS	Ho	0.901		LOI				
ICP-MS	Er	2.676		Sum	96.94	89.95	92.72	93.82
ICP-MS	Tm	0.392						
ICP-MS	Yb	2.62	ICP-MS	Ti	0	0	0	0
ICP-MS	Lu	0.39	ICP-MS	P				
ICP-MS	Cu		ICP-MS	Cr %	0.4	0.48	0.44	0.51
ICP-MS	Zn		ICP-MS	Cr ppm	4000	4800	4400	5100
ICP-MS	Mo		ICP-MS	Co %	0.014	0.013	0.016	0.017
ICP-MS	Ag		ICP-MS	Co ppm	140	130	160	170
ICP-MS	Cd		ICP-MS	Ni %	0.14	0.131	0.164	0.179
ICP-MS	Te		ICP-MS	Ni ppm	1400	1310	1640	1790
ICP-MS	Tl		ICP-MS	Cu %	0.005	0.001	0.001	0.02
ICP-MS	Pb	0.4	ICP-MS	Cu ppm	50	10	10	200
ICP-MS	Sn		ICP-MS	Zn %	0.01	0.01	0.01	0.01
ICP-MS	Sb		ICP-MS	Zn ppm	100	100	100	100
ICP-MS	Ga		ICP-MS	Pb %				
ICP-MS	Ge		ICP-MS	S %	0.15	0.11	0.11	0.16
ICP-MS	As		ICP-MS	S ppm	1500	1100	1100	1600
ICP-MS	Se		ICP-MS	As %		0.01		0.01
ICP-MS	W		ICP-MS	Au				0.004
ICP-MS	Li		ICP-MS	Pt	0.065	0.075	0.114	0.135
ICP-MS	Be		ICP-MS	Pd	0.096	0.106	0.164	0.21
ICP-MS	S	0						
ICP-MS	Bi							
ICP-MS	Au							
ICP-MS	Pt							
ICP-MS	Pd							

Method	Sample KD:	9455	9456	9457	9458	9467	9468	9469
XRF	SiO_2	43.3	42.5	44.1	44.2	39.6	41	41.7
XRF	TiO_2	0.85	0.87	0.8	0.8	0.68	0.7	0.71
XRF	Al_2O_3	4.5	4.81	4.08	4.39	3.61	3.69	3.73
XRF	Fe_2O_3	16.75	17.5	16.5	17.35	14.45	15.5	15.6
	FeO							
XRF	Fe_2O3_t	0.00	0.00	0.00	0.00	0.00	0.00	0.00
XRF	MnO	0.23	0.24	0.2	0.21	0.18	0.2	0.21
XRF	MgO	27.8	28.3	28.4	28.2	29.1	29.8	30
XRF	CaO	7.14	6.59	6.16	4.66	3.3	3.02	3.06
	LOI							
	Sum	100.57	100.81	100.24	99.81	90.92	93.91	95.01
ICP-MS	Ti	0	0	0	0	0	0	0
ICP-MS	P							
ICP-MS	Cr %	0.43	0.43	0.42	0.46	0.38	0.43	0.4
ICP-MS	Cr ppm	4300	4300	4200	4600	3800	4300	4000
ICP-MS	Co %	0.016	0.016	0.017	0.018	0.016	0.016	0.017
ICP-MS	Co ppm	160	160	170	180	160	160	170
ICP-MS	Ni %	0.136	0.138	0.134	0.228	0.174	0.17	0.186
ICP-MS	Ni ppm	1360	1380	1340	2280	1740	1700	1860
ICP-MS	Cu %	0.023	0.027	0.008	0.139	0.033	0.053	0.052
ICP-MS	Cu ppm	230	270	80	1390	330	530	520
ICP-MS	Zn %	0.02	0.02	0.02	0.02	0.01	0.02	0.02
ICP-MS	Zn ppm	200	200	200	200	100	200	200
ICP-MS	Pb %							
ICP-MS	S %	0.15	0.18	0.14	0.52	0.24	0.22	0.23
ICP-MS	S ppm	1500	1800	1400	5200	2400	2200	2300
ICP-MS	As %		0.01					
ICP-MS	Au	0.001	0.004		0.025	0.004	0.011	0.006
ICP-MS	Pt	0.027	0.043	0.026	0.206	0.118	0.073	0.088
ICP-MS	Pd	0.038	0.061	0.041	0.357	0.158	0.122	0.138

Method	Sample KD:	9463	9464	9465	9466	9476	9477	9478
XRF	SiO_2	40.1	40.1	39.7	39.6	42.4	42.4	42.6
XRF	TiO_2	0.7	0.66	0.7	0.68	0.72	0.72	0.72
XRF	Al_2O_3	3.56	3.47	3.71	3.6	3.91	3.92	3.85
XRF	Fe_2O_3	15.9	15.05	13.9	14.05	15.3	15.95	16.15
	FeO							
XRF	Fe_2O3_t	0.00	0.00	0.00	0.00	0.00	0.00	0.00
XRF	MnO	0.21	0.17	0.15	0.16	0.2	0.2	0.21
XRF	MgO	29.2	29.5	28.6	28.9	29.8	29.4	29.4
XRF	CaO	2.78	3.02	4.03	3.54	3.6	3.85	3.48
	LOI							
	Sum	92.45	91.97	90.79	90.53	95.93	96.44	96.41
ICP-MS	Ti	0	0	0	0	0	0	0
ICP-MS	P							
ICP-MS	Cr %	0.46	0.42	0.38	0.37	0.41	0.39	0.27
ICP-MS	Cr ppm	4600	4200	3800	3700	4100	3900	2700
ICP-MS	Co %	0.016	0.015	0.015	0.015	0.016	0.015	0.016
ICP-MS	Co ppm	160	150	150	150	160	150	160
ICP-MS	Ni %	0.174	0.164	0.154	0.17	0.164	0.166	0.131
ICP-MS	Ni ppm	1740	1640	1540	1700	1640	1660	1310
ICP-MS	Cu %	0.055	0.01	0.001	0.033	0.027	0.047	0.032
ICP-MS	Cu ppm	550	100	10	330	270	470	320
ICP-MS	Zn %	0.01	0.01	0.01	0.01	0.01	0.02	0.01
ICP-MS	Zn ppm	100	100	100	100	100	200	100
ICP-MS	Pb %							
ICP-MS	S %	0.14	0.17	0.23	0.37	0.18	0.23	0.17
ICP-MS	S ppm	1400	1700	2300	3700	1800	2300	1700
ICP-MS	As %	0.01			0.01		0.01	
ICP-MS	Au	0.01	0.003	0.002	0.008	0.005	0.007	0.006
ICP-MS	Pt	0.075	0.093	0.071	0.094	0.038	0.069	0.037
ICP-MS	Pd	0.117	0.134	0.091	0.148	0.065	0.096	0.053

Method	Sample KD:	9471	9472	9473	9474	9475	9485	9486
XRF	SiO_2	41.4	40.5	41	41.6	42.3	48.7	47.8
XRF	TiO_2	0.69	0.63	0.69	0.68	0.69	1.21	1.31
XRF	Al_2O_3	3.68	3.34	3.71	3.7	3.79	6.91	6.93
XRF	Fe_2O_3	15.55	15.3	15	15.2	15.1	13.8	14.25
	FeO							
XRF	Fe_2O3_t	0.00	0.00	0.00	0.00	0.00	0.00	0.00
XRF	MnO	0.2	0.18	0.19	0.2	0.19	0.2	0.21
XRF	MgO	30	29.8	28.9	29.6	30	15.5	16.35
XRF	CaO	3.17	3.57	4.13	3.85	3.78	8.76	9.18
	LOI							
	Sum	94.69	93.32	93.62	94.83	95.85	95.08	96.03
ICP-MS	Ti	0	0	0	0	0	0	0
ICP-MS	P							
ICP-MS	Cr %	0.5	0.5	0.51	0.41	0.4	0.13	0.15
ICP-MS	Cr ppm	5000	5000	5100	4100	4000	1300	1500
ICP-MS	Co %	0.016	0.018	0.017	0.016	0.017	0.01	0.01
ICP-MS	Co ppm	160	180	170	160	170	100	100
ICP-MS	Ni %	0.191	0.204	0.177	0.192	0.184	0.085	0.088
ICP-MS	Ni ppm	1910	2040	1770	1920	1840	850	880
ICP-MS	Cu %	0.064	0.043	0.042	0.043	0.043	0.074	0.068
ICP-MS	Cu ppm	640	430	420	430	430	740	680
ICP-MS	Zn %	0.02	0.01	0.01	0.01	0.02	0.02	0.02
ICP-MS	Zn ppm	200	100	100	100	200	200	200
ICP-MS	Pb %							
ICP-MS	S %	0.28	0.38	0.28	0.27	0.27	0.58	0.4
ICP-MS	S ppm	2800	3800	2800	2700	2700	5800	4000
ICP-MS	As %					0.01		
ICP-MS	Au	0.013	0.008	0.008	0.006	0.007	0.016	0.012
ICP-MS	Pt	0.091	0.127	0.083	0.078	0.087	0.089	0.076
ICP-MS	Pd	0.16	0.196	0.134	0.138	0.142	0.144	0.124

Method	Sample KD:	9479	9481	9482	9483	9484
XRF	SiO_2	43	42.5	47.7	47.7	47.6
XRF	TiO_2	0.76	0.71	1.29	1.44	1.32
XRF	Al_2O_3	3.97	3.72	7.11	7.67	7.01
XRF	Fe_2O_3	15.1	15.85	14	14.3	14.35
	FeO					
XRF	Fe_2O3_t	0.00	0.00	0.00	0.00	0.00
XRF	MnO	0.2	0.21	0.21	0.2	0.2
XRF	MgO	26.1	26.9	16.05	14.75	16.2
XRF	CaO	5.45	4.68	9.01	8.49	8.93
	LOI					
	Sum	94.58	94.57	95.37	94.55	95.61
ICP-MS	Ti	0	0	0	0	0
ICP-MS	P					
ICP-MS	Cr %	0.24	0.21	0.13	0.12	0.13
ICP-MS	Cr ppm	2400	2100	1300	1200	1300
ICP-MS	Co %	0.014	0.015	0.009	0.01	0.011
ICP-MS	Co ppm	140	150	90	100	110
ICP-MS	Ni %	0.099	0.094	0.044	0.081	0.079
ICP-MS	Ni ppm	990	940	440	810	790
ICP-MS	Cu %	0.009	0.009	0.008	0.075	0.066
ICP-MS	Cu ppm	90	90	80	750	660
ICP-MS	Zn %	0.01	0.02	0.01	0.02	0.02
ICP-MS	Zn ppm	100	200	100	200	200
ICP-MS	Pb %					
ICP-MS	S %	0.12	0.12	0.18	0.53	0.5
ICP-MS	S ppm	1200	1200	1800	5300	5000
ICP-MS	As %					
ICP-MS	Au			0.003	0.018	0.015
ICP-MS	Pt	0.012	0.013	0.017	0.074	0.067
ICP-MS	Pd	0.011	0.009	0.006	0.128	0.106

Method	Sample KD:	9487	9488	9489	9490	9491	9492
XRF	SiO_2	48.1	47.9	47	47.7		
XRF	TiO_2	1.29	1.56	1.39	1.44		
XRF	Al_2O_3	7.01	8.22	7.33	7.66	12.2	11.6
XRF	Fe_2O_3	14.45	14.7	14.4	15.05		
	FeO						
XRF	Fe_2O3_t	0.00	0.00	0.00	0.00	0.00	0.00
XRF	MnO	0.21	0.24	0.2	0.21	0.24	0.25
XRF	MgO	16.9	14.6	16.95	15.95	4.84	4.29
XRF	CaO	8.72	8.14	7.59	7.98	6.96	6.72
	LOI						
	Sum	96.68	95.36	94.86	95.99	24.24	22.86
ICP-MS	Ti	0	0	0	0	0	0
ICP-MS	P						
ICP-MS	Cr %	0.14	0.09	0.1	0.1		
ICP-MS	Cr ppm	1400	900	1000	1000		
ICP-MS	Co %	0.011	0.01	0.011	0.009	0.006	0.005
ICP-MS	Co ppm	110	100	110	90	60	50
ICP-MS	Ni %	0.047	0.045	0.049	0.05		
ICP-MS	Ni ppm	470	450	490	500		
ICP-MS	Cu %	0.011	0.018	0.013	0.013	0.008	0.011
ICP-MS	Cu ppm	110	180	130	130	80	110
ICP-MS	Zn %	0.02	0.02	0.02	0.02		
ICP-MS	Zn ppm	200	200	200	200		
ICP-MS	Pb %						
ICP-MS	S %	0.06	0.28	0.57	0.22	1.3	1.88
ICP-MS	S ppm	600	2800	5700	2200	13000	18800
ICP-MS	As %	0.01	0.01				0.02
ICP-MS	Au		0.003	0.001	0.001	0.004	0.003
ICP-MS	Pt	0.011	0.015	0.014	0.013		
ICP-MS	Pd	0.007	0.007	0.007	0.008	0.001	

APPENDIX 4

Mineral Chemistry data

DDH EK-02 Sample: ED-15

		Olivine 1	Olivine 2	Olivine 3	Olivine 4	Orthopyx 1	Clinopyx 1
Atomic	**Si**	1.0	1.0	1.0	1.0	1.9	1.9
	Al	0.0	0.0	0.0	0.0	0.1	0.1
	Ti	0.0	0.0	0.0	0.0	0.0	0.0
	Fe	0.4	0.4	0.4	0.4	0.4	0.2
	Mg	1.6	1.6	1.6	1.6	1.5	0.9
	Ca	0.0	0.0	0.0	0.0	0.1	0.8
	Na	0.0	0.0	0.0	0.0	0.0	0.0
	K	0.0	0.0	0.0	0.0	0.0	0.0
	Total	3.0	3.0	3.0	3.0	4.0	4.0
	% Forsterite	78.8	79.2	78.7	79.8		
	% Enstatite					78.2	48.5
	% Ferrosilite					17.9	8.4
	% Wollastonite					3.9	43.1
Oxide wt%	**SiO_2**	39.9	39.7	40.3	39.6	55.8	54.7
	Al_2O_3	0.0	0.4	0.1	0.0	1.9	2.2
	TiO_2	0.1	0.0	0.0	0.0	0.8	0.7
	FeO	20.1	19.6	20.1	18.7	12.1	5.5
	MgO	42.0	41.8	41.7	41.6	29.7	17.7
	CaO	0.1	0.1	0.0	0.1	2.1	21.8
	Na_2O	0.2	0.3	0.4	0.2	0.0	0.5
	K_2O	0.0	0.1	0.1	0.0	0.1	0.0
	Total	102.5	102.0	102.7	100.3	102.4	103.0

DDH EK-02 Sample: ED-16

		Olivine 1	Olivine 2	Olivine 3	Olivine 4	Orthopyx 1	Clinopyx 1
Atomic	**Si**	1.0	1.0	1.0	1.0	2.0	1.9
	Al	0.0	0.0	0.0	0.0	0.0	0.1
	Ti	0.0	0.0	0.0	0.0	0.0	0.0
	Fe	0.4	0.4	0.4	0.4	0.4	0.2
	Mg	1.6	1.6	1.6	1.6	1.6	0.9
	Ca	0.0	0.0	0.0	0.0	0.1	0.8
	Na	0.0	0.0	0.0	0.0	0.0	0.0
	K	0.0	0.0	0.0	0.0	0.0	0.0
	Total	3.0	3.0	3.0	3.0	4.0	4.0
	% Forsterite	78.5	79.2	79.6	79.5		
	% Enstatite					78.5	47.9
	% Ferrosilite					19.0	9.6
	% Wollastonite					2.5	42.5
Oxide wt%	**SiO_2**	39.9	40.3	40.1	40.2	56.5	54.4
	Al_2O_3	0.0	0.2	0.1	0.2	1.2	2.3
	TiO_2	0.1	0.1	0.1	0.0	0.7	0.8
	FeO	20.5	19.7	19.1	19.4	13.0	6.3
	MgO	42.0	42.1	41.9	42.2	30.2	17.6
	CaO	0.1	0.0	0.1	0.1	1.4	21.7
	Na_2O	0.2	0.3	0.3	0.4	0.2	0.5
	K_2O	0.0	0.0	0.0	0.0	0.0	0.0
	Total	102.7	102.6	101.8	102.6	103.1	103.7

DDH EK-02 Sample: ED-17

		Olivine 1	Olivine 2	Olivine 3
Atomic	**Si**	1.0	1.0	1.0
	Al	0.0	0.0	0.0
	Ti	0.0	0.0	0.0
	Fe	0.4	0.4	0.4
	Mg	1.6	1.6	1.6
	Ca	0.0	0.0	0.0
	Na	0.0	0.0	0.0
	K	0.0	0.0	0.0
	Total	3.0	3.0	3.0
	% Forsterite	80.1	80.1	80.0
	% Enstatite			
	% Ferrosilite			
	% Wollastonite			
Oxide wt%	**SiO_2**	38.7	38.7	38.9
	Al_2O_3	0.3	0.2	0.1
	TiO_2	0.0	0.0	0.0
	FeO	18.6	18.3	18.7
	MgO	41.9	41.4	42.2
	CaO	0.2	0.2	0.1
	Na_2O	0.1	0.3	0.3
	K_2O	0.0	0.0	0.0
	Total	99.9	99.2	100.3

DDH EK-02 Sample: ED-18

		Olivine 1	Olivine 2	Olivine 3		Plagioclase 1
Atomic	**Si**	1.0	1.3	1.0	**Si**	9.9
	Al	0.0	0.0	0.0	**Al**	6.0
	Ti	0.0	0.0	0.0	**Ti**	0.0
	Fe	0.4	0.2	0.4	**Fe**	0.1
	Mg	1.6	1.1	1.6	**Mg**	0.0
	Ca	0.0	0.0	0.0	**Ca**	2.0
	Na	0.0	0.0	0.0	**Na**	2.1
	K	0.0	0.0	0.0	**K**	0.1
	Total	3.0	2.7	3.0	**Total**	20.1
	% Forsterite	81.1	81.4	78.9	**% Albite**	50.5
	% Enstatite				**% Anorthite**	48.0
	% Ferrosilite				**% Orthoclase**	1.6
	% Wollastonite					
Oxide wt%	**SiO_2**	39.0	56.1	38.5	**SiO_2**	54.9
	Al_2O_3	0.4	0.6	0.2	**Al_2O_3**	28.5
	TiO_2	0.1	0.1	0.0	**TiO_2**	0.3
	FeO	17.5	12.7	19.1	**FeO**	0.5
	MgO	42.1	31.2	40.2	**MgO**	0.0
	CaO	0.0	0.3	0.1	**CaO**	10.1
	Na_2O	0.3	0.4	0.3	**Na_2O**	5.9
	K_2O	0.1	0.0	0.0	**K_2O**	0.3
	Total	99.4	101.4	98.4	**Total**	100.6

DDH EK-02 Sample:		ED-04			
		Olivine 1	Olivine 2	Olivine 3	Clinopyx 1
Atomic	**Si**	1.0	1.0	1.0	1.9
	Al	0.0	0.0	0.0	0.1
	Ti	0.0	0.0	0.0	0.0
	Fe	0.5	0.4	0.4	0.2
	Mg	1.5	1.6	1.6	0.9
	Ca	0.0	0.0	0.0	0.8
	Na	0.0	0.0	0.0	0.0
	K	0.0	0.0	0.0	0.0
	Cr				0.0
	Total	3.0	3.0	3.0	4.0
	% Forsterite	76.5	78.9	80.5	
	% Enstatite				48.6
	% Ferrosilite				10.7
	% Wollastonite				40.7
Oxide wt%	**SiO_2**	38.3	38.3	38.5	50.8
	Al_2O_3	0.2	0.3	0.0	3.4
	TiO_2	0.0	0.0	0.0	0.8
	FeO	21.5	19.5	18.0	6.4
	MgO	39.1	40.9	41.8	16.4
	CaO	1.3	0.2	0.0	19.0
	Na_2O	0.1	0.1	0.1	0.5
	K_2O	0.0	0.1	0.0	0.0
	Cr_2O_3				0.9
	Total	100.4	99.4	98.5	98.2

DDH EK-02 Sample:		ED-02			
		Olivine 1	Olivine 2	Olivine 3	Orthopyx 1
Atomic	**Si**	1.0	1.0	1.0	1.9
	Al	0.0	0.0	0.0	0.1
	Ti	0.0	0.0	0.0	0.0
	Fe	0.4	0.4	0.4	0.4
	Mg	1.6	1.6	1.6	1.5
	Ca	0.0	0.0	0.0	0.1
	Na	0.0	0.0	0.0	0.0
	K	0.0	0.0	0.0	0.0
	Cr				0.0
	Total	3.0	3.0	3.0	4.0
	% Forsterite	80.1	81.8	81.7	
	% Enstatite				78.4
	% Ferrosilite				18.0
	% Wollastonite				3.5
Oxide wt%	**SiO_2**	38.7	39.4	38.6	54.5
	Al_2O_3	0.4	0.2	0.3	2.0
	TiO_2	0.1	0.1	0.0	0.8
	FeO	18.5	16.9	16.8	12.0
	MgO	41.7	42.6	42.1	29.2
	CaO	0.2	0.1	0.2	1.8
	Na_2O	0.0	0.1	0.2	0.5
	K_2O	0.0	0.0	0.1	0.1
	Cr_2O_3				0.2

	Total	99.6	99.5	98.2	101.2

DDH EK-02 Sample:		ED-01			
		Olivine 1	Olivine 2	Olivine 3	Olivine 4
Atomic	**Si**	1.0	1.0	1.0	1.0
	Al	0.0	0.0	0.0	0.0
	Ti	0.0	0.0	0.0	0.0
	Fe	0.4	0.3	0.3	0.4
	Mg	1.6	1.7	1.6	1.6
	Ca	0.0	0.0	0.0	0.0
	Na				
	Total	3.0	3.0	3.0	3.0
	% Forsterite	81.7	82.6	82.6	81.7
	% Enstatite				
	% Ferrosilite				
	% Wollastonite				
Oxide wt%	**SiO_2**	38.1	39.8	39.8	38.6
	Al_2O_3	0.1	0.0	0.1	0.3
	TiO_2	0.1	0.1	0.1	0.0
	FeO	17.0	16.7	16.0	16.8
	MgO	42.4	44.3	42.7	42.1
	CaO	0.2	0.1	0.1	0.2
	Na_2O				
	Total	98.0	100.9	98.8	98.0

DDH EK-02 Sample:		ED-03			
		Olivine 1	Olivine 2	Olivine 3	Olivine 4
Atomic	**Si**	1.0	1.0	1.3	1.3
	Al	0.0	0.0	0.0	0.0
	Ti	0.0	0.0	0.0	0.0
	Fe	0.3	0.3	0.2	0.2
	Mg	1.6	1.7	1.1	1.1
	Ca	0.0	0.0	0.0	0.0
	Na				0.0
	Total	3.0	3.0	2.7	2.7
	% Forsterite	82.9	83.8	84.7	82.4
	% Enstatite				
	% Ferrosilite				
	% Wollastonite				
Oxide wt%	**SiO_2**	39.9	40.0	57.2	55.0
	Al_2O_3	0.2	0.0	0.6	0.8
	TiO_2	0.0	0.2	0.4	0.1
	FeO	16.2	15.3	10.4	11.6
	MgO	43.9	44.4	32.2	30.3
	CaO	0.1	0.0	0.7	0.6
	Na_2O				0.1
	Total	100.3	99.9	101.4	98.5

DDH EK-02 Sample:		ED-05			
		Olivine 1	Olivine 2	Olivine 3	Clinopyx 1
Atomic	**Si**	1.0	1.0	1.0	2.0
	Al	0.0	0.0	0.0	0.1
	Ti	0.0	0.0	0.0	0.0
	Fe	0.3	0.4	0.3	0.2
	Mg	1.6	1.6	1.7	1.0
	Ca	0.0	0.0	0.0	0.7
	Total	3.0	3.0	3.0	4.0
	% Forsterite	83.3	81.7	83.6	
	% Enstatite				52.6
	% Ferrosilite				9.0
	% Wollastonite				38.4
Oxide wt%	**SiO_2**	40.4	40.2	39.2	54.3
	Al_2O_3	0.3	0.3	0.2	2.0
	TiO_2	0.2	0.0	0.1	0.6
	FeO	16.0	17.1	15.2	5.7
	MgO	44.6	42.8	43.3	18.6
	CaO	0.1	0.4	0.0	18.9
	Total	101.5	100.7	98.0	100.1

DDH EK-02 Sample:		ED-06				
		Olivine 1	Olivine 2	Olivine 3	Olivine 4	Clinopyx 1
Atomic	**Si**	1.0	1.0	1.0	1.0	2.0
	Al	0.0	0.0	0.0	0.0	0.1
	Ti	0.0	0.0	0.0	0.0	0.0
	Fe	0.4	0.4	0.4	0.4	0.2
	Mg	1.6	1.6	1.6	1.6	1.0
	Ca	0.0	0.0	0.0	0.0	0.7
	Total	3.0	3.0	3.0	3.0	4.0
	% Forsterite	81.7	79.8	81.3	81.7	
	% Enstatite					51.7
	% Ferrosilite					10.3
	% Wollastonite					38.0
Oxide wt%	**SiO_2**	40.0	40.0	40.4	39.8	54.7
	Al_2O_3	0.0	0.1	0.1	0.2	2.0
	TiO_2	0.0	0.0	0.0	0.2	0.7
	FeO	17.3	18.8	17.7	17.2	6.5
	MgO	43.3	41.7	43.3	43.0	18.3
	CaO	0.2	0.2	0.1	0.1	18.7
	Total	100.9	100.9	101.6	100.3	101.0

DDH EK-02 Sample:		ED-31				
		Olivine 1	Olivine 2	Olivine 3	Olivine 4	Clinopyx 1
Atomic	**Si**	1.0	1.0	1.0	1.0	2.0
	Al	0.0	0.0	0.0	0.0	0.1
	Ti	0.0	0.0	0.0	0.0	0.0
	Fe	0.4	0.4	0.4	0.4	0.2
	Mg	1.6	1.6	1.6	1.6	1.0
	Ca	0.0	0.0	0.0	0.0	0.8
	Na	0.0	0.0	0.0	0.0	0.0
	Total	3.0	3.0	3.0	3.0	4.0
	% Forsterite	78.6	79.4	81.1	81.2	
	% Enstatite					50.5
	% Ferrosilite					9.9
	% Wollastonite					39.5
Oxide wt%	**SiO_2**	40.0	39.8	40.5	40.0	54.0
	Al_2O_3	0.2	0.2	0.1	0.2	1.9
	TiO_2	0.0	0.0	0.1	0.1	0.5
	FeO	20.1	19.0	17.8	17.7	6.3
	MgO	41.6	41.1	42.7	42.8	17.8
	CaO	0.1	0.2	0.1	0.2	19.4
	Na_2O	0.1	0.2	0.2	0.2	0.4
	Total	102.2	100.5	101.4	101.1	100.2

DDH EK-02 Sample:		ED-07				
		Olivine 1	Olivine 2	Olivine 3	Olivine 4	Clinopyx 1
Atomic	**Si**	1.0	1.0	1.0	1.0	2.0
	Al	0.0	0.0	0.0	0.0	0.1
	Ti	0.0	0.0	0.0	0.0	0.0
	Fe	0.4	0.4	0.4	0.4	0.2
	Mg	1.6	1.6	1.6	1.6	1.0
	Ca	0.0	0.0	0.0	0.0	0.7
	Na	0.0	0.0	0.0	0.0	0.0
	Total	3.0	3.0	3.0	3.0	4.0
	% Forsterite	79.9	80.1	80.7	80.4	
	% Enstatite					54.6
	% Ferrosilite					10.3
	% Wollastonite					35.0
Oxide wt%	**SiO_2**	40.3	40.2	39.8	39.3	54.0
	Al_2O_3	0.2	0.2	0.1	0.3	1.9
	TiO_2	0.0	0.1	0.0	0.0	0.5
	FeO	19.1	18.9	18.3	18.1	6.3
	MgO	42.6	42.8	42.8	41.6	17.8
	CaO	0.2	0.3	0.1	0.2	19.4
	Na_2O	0.4	0.4	0.2	0.2	0.4
	Total	102.7	103.0	101.4	99.7	100.2

DDH EK-02 Sample: ED-32

		Olivine 1	Olivine 2	Olivine 3	Orthopyx 1	Clinopyx 1	Clinopyx 2	Clinopyx 2
Atomic	**Si**	1.0	1.0	1.0	1.5	1.9	1.9	1.9
	Al	0.0	0.0	0.0	0.0	0.1	0.1	0.1
	Ti	0.0	0.0	0.0	0.0	0.0	0.0	0.0
	Fe	0.5	0.4	0.4	0.6	0.2	0.2	0.2
	Mg	1.5	1.5	1.6	2.2	1.0	1.0	1.0
	Ca	0.0	0.0	0.0	0.1	0.7	0.7	0.8
	Na	0.0	0.0	0.0	0.0	0.0	0.0	0.0
	Total	3.0	3.0	3.0	4.5	4.0	4.0	4.0
	% Forsterite	76.0	78.0	78.8				
	% Enstatite				76.0	51.1	50.0	50.6
	% Ferrosilite				22.2	10.9	11.4	10.6
	% Wollastonite				1.8	38.0	38.6	38.8
Oxide wt%	**SiO_2**	39.4	39.8	39.8	40.2	54.0	54.5	54.4
	Al_2O_3	0.0	0.1	0.1	0.2	2.1	2.0	1.8
	TiO_2	0.2	0.0	0.1	0.0	0.9	0.9	0.7
	FeO	22.1	20.3	19.7	20.4	6.9	7.3	6.8
	MgO	39.2	40.4	41.0	39.1	18.3	18.0	18.3
	CaO	0.2	0.2	0.1	1.3	18.9	19.3	19.6
	Na_2O	0.3	0.2	0.2	0.1	0.2	0.4	0.4
	Total	101.2	101.0	101.0	101.2	101.3	102.5	102.0

DDH EK-02 Sample: ED-08

		Olivine 1	Olivine 2	Olivine 3	Clinopyx 1	Clinopyx 2	Clinopyx 3	Clinopyx 4
Atomic	**Si**	1.0	1.0	1.0	2.0	1.9	2.0	2.0
	Al	0.0	0.0	0.0	0.1	0.1	0.1	0.1
	Ti	0.0	0.0	0.0	0.0	0.0	0.0	0.0
	Fe	0.4	0.4	0.4	0.2	0.2	0.2	0.2
	Mg	1.5	1.6	1.5	1.0	1.0	1.0	1.0
	Ca	0.0	0.0	0.0	0.7	0.7	0.7	0.7
	Na	0.0	0.0	0.0	0.0	0.0	0.0	0.0
	Cr		0.0	0.0		0.0	0.0	0.0
	Total	3.0	3.0	3.0	4.0	4.0	4.0	4.0
	% Forsterite	78.0	78.5	77.9				
	% Enstatite				50.7	50.8	52.0	50.4
	% Ferrosilite				10.9	10.8	10.3	10.8
	% Wollastonite				38.5	38.3	37.7	38.7
Oxide wt%	**SiO_2**	39.6	39.5	40.3	54.0	54.1	54.7	55.1
	Al_2O_3	0.0	0.0	0.0	2.2	2.2	1.6	2.0
	TiO_2	0.0	0.2	0.0	0.5	0.8	0.6	0.7
	FeO	20.6	20.0	20.8	6.9	6.9	6.6	7.0
	MgO	40.8	41.1	41.2	18.1	18.2	18.7	18.2
	CaO	0.3	0.1	0.2	19.1	19.1	18.8	19.5
	Na_2O	0.0	0.2	0.3	0.3	0.4	0.4	0.4
	Cr_2O_3		0.1	0.1		0.8	0.7	0.5
	Total	101.3	101.1	102.9	101.0	102.5	102.0	103.4

DDH EK-02 Sample:		ED-09						
		Olivine 1	Olivine 2	Olivine 3	Orthopyx 1	Clinopyx 1	Clinopyx 2	Clinopyx 3
Atomic	**Si**	1.0	1.0	1.0	1.5	1.9	2.0	1.9
	Al	0.0	0.0	0.0	0.0	0.1	0.1	0.1
	Ti	0.0	0.0	0.0	0.0	0.0	0.0	0.0
	Fe	0.5	0.5	0.5	0.9	0.2	0.2	0.3
	Mg	1.4	1.4	1.4	2.1	1.0	0.9	0.9
	Ca	0.0	0.0	0.0	0.0	0.7	0.7	0.7
	Na	0.0	0.0	0.0	0.0	0.0	0.0	0.0
	Cr	0.0	0.0	0.0	0.0	0.0	0.0	0.0
	Total	3.0	3.0	3.0	4.5	4.0	4.0	4.0
	% Forsterite	72.8	73.2	73.9				
	% Enstatite				69.5	50.6	49.7	47.2
	% Ferrosilite				28.8	11.8	13.0	14.2
	% Wollastonite				1.7	37.6	37.2	38.6
Oxide wt%	**SiO_2**	39.1	38.4	38.8	38.9	53.8	51.9	51.5
	Al_2O_3	0.3	0.3	0.2	0.2	1.8	2.2	2.6
	TiO_2	0.1	0.1	0.0	0.0	0.6	0.8	1.3
	FeO	25.3	23.5	23.5	26.4	7.5	7.8	8.7
	MgO	38.0	36.0	37.4	35.7	18.1	16.6	16.2
	CaO	0.2	0.1	0.1	1.2	18.7	17.3	18.4
	Na_2O	0.3	0.2	0.4	0.1	0.4	0.6	0.6
	Cr_2O_3	0.2	0.0	0.1	0.0	0.7	0.2	0.2
	Total	103.3	98.6	100.5	102.5	101.7	97.4	99.5

DDH EK-02 Sample:		ED-33						
		Clinopyx 1	Clinopyx 2	Clinopyx 3	Clinopyx 4		Plagioclase 1	Plagioclase 2
Atomic	**Si**	2.0	1.9	2.0	1.9	**Si**		9.7
	Al	0.1	0.1	0.1	0.1	**Al**		6.1
	Ti	0.0	0.0	0.0	0.0	**Ti**		0.0
	Fe	0.2	0.3	0.3	0.3	**Fe**		0.1
	Mg	0.9	0.9	0.9	0.9	**Mg**		0.1
	Ca	0.7	0.7	0.7	0.7	**Ca**		2.3
	Na	0.0	0.0	0.0	0.0	**Na**		1.8
	Cr	0.0	0.0	0.0	0.0	**K**		0.1
	Total	4.0	4.0	4.0	4.0	**Cr**		0.0
	% Forsterite					**% Albite**		43.3
	% Enstatite	48.4	47.9	47.8	46.1	**% Anorthite**		55.2
	% Ferrosilite	12.9	13.1	15.4	18.7	**% Orthoclase**		1.5
	% Wollastonite	38.6	38.9	36.7	35.2			
Oxide wt%	**SiO_2**	53.9	52.9	52.9	51.8	**SiO_2**	51.8	53.1
	Al_2O_3	2.2	1.9	2.1	2.4	**Al_2O_3**	29.2	28.3
	TiO_2	0.7	0.9	0.9	1.0	**TiO_2**	0.2	0.0
	FeO	8.1	8.2	9.5	11.1	**FeO**	0.7	0.7
	MgO	17.0	16.8	16.4	15.4	**MgO**	0.2	0.2
	CaO	18.8	18.9	17.6	16.3	**CaO**	12.0	11.5
	Na_2O	0.5	0.6	0.3	0.7	**Na_2O**	4.6	5.0
	K_2O					**K_2O**		0.3

	Cr_2O_3	0.1	0.2	0.0	0.2	**Cr_2O_3**	0.0	0.0	
	Total	101.2	100.3	99.5	98.9	**Total**	98.5	99.1	

DDH EK-02 Sample: ED-10

		Olivine 1	Olivine 2	Orthopyx 1	Clinopyx 1	Clinopyx 2	Clinopyx 3	Clinopyx 4	Plagioclase 1
Atomic	**Si**	1.0	1.0	2.0	2.0	2.0	2.0	1.9	10.2
	Al	0.0	0.0	0.1	0.1	0.1	0.1	0.1	5.7
	Ti	0.0	0.0	0.0	0.0	0.0	0.0	0.0	0.0
	Fe	0.4	0.6	0.5	0.3	0.3	0.2	0.3	0.1
	Mg	1.5	1.4	1.4	0.8	0.9	1.0	0.9	0.0
	Ca	0.0	0.0	0.1	0.8	0.8	0.7	0.7	1.6
	Na	0.0	0.0	0.0	0.0	0.1	0.0	0.0	2.3
	K	0.0	0.0	0.0	0.0	0.0	0.0	0.0	0.1
	Cr	0.0	0.0	0.0	0.0	0.0	0.0	0.0	0.0
	Total	3.0	3.0	4.0	4.0	4.0	4.0	4.0	20.1
% Forsterite, % Albite		77.6	70.9						57.1
% Enstatite, % Anorthite				70.1	44.3	46.2	52.4	48.2	40.1
% Ferrosilite, % Orthoclase				25.7	14.3	13.5	9.3	16.0	2.9
% Wollastonite				4.2	41.4	40.3	38.2	35.8	
Oxide wt%	**SiO_2**	38.9	38.2	54.4	54.2	54.0	52.5	52.0	57.3
	Al_2O_3	0.1	0.1	1.5	1.3	1.4	2.2	2.6	27.1
	TiO_2	0.0	0.0	0.7	0.6	0.6	0.6	1.1	0.1
	FeO	19.9	26.2	16.6	8.9	8.3	5.7	9.6	0.7
	MgO	38.7	35.8	25.3	15.4	15.9	17.8	16.2	0.1
	CaO	0.3	0.1	2.1	20.1	19.3	18.1	16.8	8.5
	Na_2O	0.6	0.0	0.0	0.7	0.7	0.2	0.5	6.7
	K_2O	0.0	0.0	0.0	0.0	0.1	0.1	0.0	0.5
	Cr_2O_3	0.1	0.0	0.3	0.2	0.2	0.7	0.0	0.0
	Total	98.7	100.4	100.9	101.4	100.5	97.9	98.8	101.0

Surface Sample: JL-28

		Olivine 1	Olivine 2	Olivine 3	Olivine 4	Clinopyx 1	Clinopyx 2
Atomic	**Si**	1.0	1.0	1.0	1.0	1.9	2.0
	Al	0.0	0.0	0.0	0.0	0.1	0.1
	Ti	0.0	0.0	0.0	0.0	0.0	0.0
	Fe	0.4	0.4	0.4	0.4	0.2	0.2
	Mg	1.6	1.6	1.5	1.6	0.9	0.9
	Ca	0.0	0.0	0.0	0.0	0.8	0.8
	Na	0.0	0.0	0.0	0.0	0.0	0.1
	K	0.0	0.0	0.0	0.0	0.0	0.0
	Cr	0.0	0.0	0.0	0.0	0.0	0.0
	Total	3.0	3.0	3.0	3.0	4.0	4.0
	% Forsterite	77.9	78.7	78.4	78.4		
	% Enstatite					48.7	47.9
	% Ferrosilite					10.7	8.9
	% Wollastonite					40.6	43.2
Oxide wt%	**SiO_2**	39.2	39.4	40.0	39.5	52.8	54.8
	Al_2O_3	0.1	0.1	0.4	0.1	2.7	1.5
	TiO_2	0.0	0.1	0.2	0.0	1.1	0.6
	FeO	21.1	20.2	20.4	20.6	6.8	5.7
	MgO	41.8	41.9	41.4	42.0	17.3	17.2

	CaO	0.0	0.0	0.1	0.0	20.0	21.6	
	Na_2O	0.3	0.3	0.3	0.2	0.5	0.8	
	K_2O	0.0	0.0	0.0	0.1	0.0	0.0	
	Cr_2O_3	0.0	0.2	0.0	0.0	0.8	0.5	
	Total	102.5	101.9	102.8	102.5	102.0	102.6	

Surface Sample: JL-31

		Olivine 1	Olivine 2	Olivine 3	Orthopyx 1	Clinopyx 1	Clinopyx 2	Clinopyx 3
Atomic	**Si**	1.0	1.0	1.0	1.9	2.0	1.9	2.0
	Al	0.0	0.0	0.0	0.1	0.0	0.1	0.1
	Ti	0.0	0.0	0.0	0.0	0.0	0.0	0.0
	Fe	0.5	0.5	0.5	0.4	0.2	0.2	0.2
	Mg	1.4	1.5	1.5	1.5	0.9	0.9	0.9
	Ca	0.0	0.0	0.0	0.1	0.8	0.7	0.8
	Na	0.0	0.0	0.0	0.0	0.1	0.0	0.1
	K	0.0	0.0	0.0	0.0	0.0	0.0	0.0
	Cr	0.0	0.0	0.0	0.0	0.0	0.0	0.0
	Total	3.0	3.0	3.0	4.0	4.0	4.0	4.0
	% Forsterite	73.0	74.2	74.6				
	% Enstatite				76.2	46.3	48.8	46.1
	% Ferrosilite				21.0	9.8	12.0	11.3
	% Wollastonite				2.8	43.9	39.2	42.6
Oxide wt%	**SiO_2**	38.6	39.4	38.6	54.9	54.6	53.6	55.1
	Al_2O_3	0.4	0.3	0.0	1.4	1.1	2.1	1.3
	TiO_2	0.0	0.0	0.1	0.6	0.4	0.6	0.6
	FeO	24.8	23.8	23.0	13.9	6.2	7.5	7.2
	MgO	37.6	38.4	38.0	28.4	16.5	17.1	16.4
	CaO	0.1	0.1	0.2	1.5	21.8	19.1	21.1
	Na_2O	0.2	0.5	0.2	0.3	0.7	0.5	0.8
	K_2O	0.0	0.0	0.0	0.0	0.1	0.0	0.0
	Cr_2O_3	0.0	0.0	0.0	0.2	0.0	0.8	0.4
	Total	101.7	102.5	100.1	101.1	101.3	101.3	102.8

Surface Sample: JL-36

		Olivine 1	Olivine 2	Olivine 3	Olivine 4	Clinopyx 1	Clinopyx 2		Plagioclase
Atomic	**Si**	1.0	1.0	1.0	1.0	1.9	1.9	**Si**	9.5
	Al	0.0	0.0	0.0	0.0	0.1	0.1	**Al**	6.3
	Ti	0.0	0.0	0.0	0.0	0.0	0.0	**Ti**	0.0
	Fe	0.5	0.5	0.6	0.6	0.2	0.2	**Fe**	0.1
	Mg	1.4	1.5	1.4	1.4	0.9	0.9	**Mg**	0.1
	Ca	0.0	0.0	0.0	0.0	0.8	0.8	**Ca**	2.2
	Na	0.0	0.0	0.0	0.0	0.0	0.0	**Na**	1.9
	K	0.0	0.0	0.0	0.0	0.0	0.0	**K**	0.1
	Cr	0.0	0.0	0.0	0.0	0.0	0.0	**Cr**	0.0
	Total	3.0	3.0	3.0	3.0	4.0	4.0	**Total**	20.3
	% Forsterite	72.1	73.7	69.2	71.9			**% Albite**	45.8
	% Enstatite					45.1	45.8	**% Anorthite**	52.7
	% Ferrosilite					10.5	11.6	**%Orthoclase**	1.5
	% Wollastonite					44.3	42.6		
Oxide wt%	**SiO_2**	37.5	37.3	36.9	36.7	51.5	51.5	**SiO_2**	52.6
	Al_2O_3	0.3	0.3	0.2	0.3	1.7	1.9	**Al_2O_3**	29.6
	TiO_2	0.1	0.0	0.0	0.1	0.6	0.6	**TiO_2**	0.2
	FeO	24.4	23.3	26.6	24.8	6.4	7.2	**FeO**	0.7
	MgO	35.4	36.6	33.6	35.6	15.3	15.8	**MgO**	0.3

	CaO	0.1	0.2	0.0	0.1	21.0	20.4	**CaO**	11.4
	Na_2O	0.5	0.4	0.6	0.3	0.3	0.6	**Na_2O**	5.5
	K_2O	0.1	0.0	0.1	0.1	0.0	0.1	**K_2O**	0.3
	Cr_2O_3	0.0	0.0	0.0	0.1	1.0	0.3	**Cr_2O_3**	0.0
	Total	98.4	98.0	98.0	98.0	97.8	98.5	**Total**	100.5

Surface Sample: JL-40

		Olivine 1	Olivine 2	Olivine 3	Olivine 4	Clinopyx 1	Clinopyx 2
Atomic	**Si**	1.0	1.0	1.0	1.0	1.9	1.9
	Al	0.0	0.0	0.0	0.0	0.1	0.1
	Ti	0.0	0.0	0.0	0.0	0.0	0.0
	Fe	0.5	0.5	0.5	0.6	0.2	0.2
	Mg	1.4	1.5	1.5	1.4	0.9	0.9
	Ca	0.0	0.0	0.0	0.0	0.8	0.8
	Na	0.0	0.0	0.0	0.0	0.0	0.0
	K	0.0	0.0	0.0	0.0	0.0	0.0
	Cr	0.0	0.0	0.0	0.0	0.0	0.0
	Total	3.0	3.0	3.0	3.0	4.0	4.0
	% Forsterite	73.0	74.1	73.9	71.9		
	% Enstatite					47.1	46.8
	% Ferrosilite					12.8	12.0
	% Wollastonite					40.2	41.2
Oxide wt%	**SiO_2**	37.9	37.9	37.1	37.3	51.3	51.1
	Al_2O_3	0.0	0.2	0.0	0.4	2.6	2.4
	TiO_2	0.0	0.0	0.0	0.2	0.8	1.1
	FeO	23.7	23.2	23.6	24.7	7.7	7.2
	MgO	36.0	37.4	37.4	35.4	16.0	15.7
	CaO	0.1	0.2	0.3	0.2	19.0	19.2
	Na_2O	0.1	0.3	0.4	0.3	0.6	0.7
	K_2O	0.0	0.0	0.0	0.1	0.1	0.0
	Cr_2O_3	0.0	0.0	0.0	0.0	0.7	0.3
	Total	97.7	99.2	98.8	98.6	98.7	97.7

Surface Sample: JL-11

		Olivine 1	Olivine 2	Olivine 3	Olivine 4	Clinopyx 1	Clinopyx 2
Atomic	**Si**	1.0	1.0	1.0	1.0	2.0	2.0
	Al	0.0	0.0	0.0	0.0	0.1	0.1
	Ti	0.0	0.0	0.0	0.0	0.0	0.0
	Fe	0.4	0.4	0.4	0.4	0.2	0.2
	Mg	1.6	1.6	1.6	1.6	0.9	0.9
	Ca	0.0	0.0	0.0	0.0	0.8	0.8
	Na	0.0	0.0	0.0	0.0	0.0	0.1
	K	0.0	0.0	0.0	0.0	0.0	0.0
	Cr	0.0	0.0	0.0	0.0	0.0	0.0
	Total	3.0	3.0	3.0	3.0	4.0	4.0
	% Forsterite	79.4	79.8	78.9	79.0		
	% Enstatite					48.5	47.7
	% Ferrosilite					9.7	8.7
	% Wollastonite					41.8	43.6
Oxide wt%	**SiO_2**	37.5	39.2	38.8	39.1	52.8	54.5
	Al_2O_3	0.2	0.2	0.3	0.2	1.7	1.3
	TiO_2	0.0	0.0	0.0	0.1	0.6	0.4
	FeO	18.7	18.9	19.4	19.2	6.0	5.5
	MgO	40.4	42.0	40.7	40.5	16.8	16.9

	CaO	0.2	0.2	0.1	0.0	20.1	21.5		
	Na_2O	0.4	0.5	0.3	0.3	0.2	0.8		
	K_2O	0.1	0.0	0.1	0.1	0.0	0.0		
	Cr_2O_3	0.0	0.0	0.2	0.0	0.7	0.3		
	Total	97.4	101.0	99.8	99.4	98.9	101.1		

Surface	Sample:	JL-14							
		Olivine 1	Olivine 2	Olivine 3	Clinopyx 1	Clinopyx 2	Clinopyx 3		Plagioclase
Atomic	**Si**	1.0	1.0	1.0	2.0	2.0	2.0	**Si**	9.7
	Al	0.0	0.0	0.0	0.1	0.1	0.1	**Al**	6.2
	Ti	0.0	0.0	0.0	0.0	0.0	0.0	**Ti**	0.0
	Fe	0.5	0.5	0.5	0.2	0.2	0.2	**Fe**	0.1
	Mg	1.5	1.5	1.5	0.9	0.9	1.0	**Mg**	0.0
	Ca	0.0	0.0	0.0	0.8	0.8	0.7	**Ca**	2.1
	Na	0.0	0.0	0.0	0.0	0.0	0.0	**Na**	2.0
	K	0.0	0.0	0.0	0.0	0.0	0.0	**K**	0.1
	Cr	0.0	0.0	0.0	0.0	0.0	0.0	**Cr**	0.0
	Total	3.0	3.0	3.0	4.0	4.0	4.0	**Total**	20.2
	% Forsterite	75.4	74.6	75.4				**% Albite**	48.4
	% Enstatite				46.5	48.7	52.9	**% Anorthite**	50.1
	% Ferrosilite				9.9	10.3	12.9	**%Orthoclase**	1.4
	% Wollastonite				43.6	41.0	34.2		
Oxide wt%	**SiO_2**	38.8	38.3	38.7	53.6	52.9	53.5	**SiO_2**	54.4
	Al_2O_3	0.1	0.3	0.2	1.5	1.7	1.5	**Al_2O_3**	29.3
	TiO_2	0.2	0.0	0.0	0.6	0.6	0.6	**TiO_2**	0.1
	FeO	22.1	22.8	22.4	6.1	6.4	8.0	**FeO**	0.4
	MgO	37.9	37.6	38.5	16.2	16.9	18.5	**MgO**	0.1
	CaO	0.0	0.1	0.1	21.1	19.8	16.7	**CaO**	10.8
	Na_2O	0.4	0.4	0.4	0.5	0.4	0.5	**Na_2O**	5.8
	K_2O	0.1	0.1	0.1	0.0	0.0	0.1	**K_2O**	0.3
	Cr_2O_3	0.0	0.0	0.1	0.4	0.6	0.6	**Cr_2O_3**	0.0
	Total	99.5	99.6	100.4	100.0	99.5	100.0	**Total**	101.2

Surface	Sample:	JL-26						
		Olivine 1	Olivine 2	Olivine 3	Orthopyx 1	Clinopyx 1	Clinopyx 2	Clinopyx 3
Atomic	**Si**	1.3	1.3	1.0	2.0	2.0	2.0	2.0
	Al	0.0	0.0	0.0	0.0	0.1	0.0	0.1
	Ti	0.0	0.0	0.0	0.0	0.0	0.0	0.0
	Fe	0.3	0.4	0.6	0.5	0.2	0.1	0.2
	Mg	1.0	0.9	1.4	1.5	0.9	0.9	0.9
	Ca	0.0	0.0	0.0	0.1	0.8	0.9	0.8
	Na	0.0	0.0	0.0	0.0	0.0	0.0	0.0
	K	0.0	0.0	0.0	0.0	0.0	0.0	0.0
	Cr	0.0	0.0	0.0	0.0	0.0	0.0	0.0
	Total	2.7	2.7	3.0	4.0	4.0	4.0	4.0
	% Forsterite	74.6	71.4	71.1				
	% Enstatite				74.2	45.5	46.8	46.3
	% Ferrosilite				23.2	11.5	7.6	12.5
	% Wollastonite				2.6	43.0	45.6	41.2
Oxide wt%	**SiO_2**	55.9	54.2	37.7	55.0	54.4	55.8	53.8
	Al_2O_3	0.5	0.8	0.3	1.1	1.4	0.7	1.7
	TiO_2	0.0	0.0	0.0	0.3	0.9	0.2	0.6
	FeO	16.9	18.3	26.8	15.2	7.2	4.9	7.8
	MgO	27.8	25.7	36.9	27.3	15.9	16.9	16.2

	CaO	0.5	0.4	0.1	1.4	20.9	22.9	20.0	
	Na_2O	0.1	0.3	0.5	0.4	0.5	0.3	0.5	
	K_2O	0.1	0.0	0.0	0.0	0.0	0.1	0.1	
	Cr_2O_3	0.0	0.0	0.0	0.1	0.4	0.0	0.2	
	Total	101.9	99.8	102.1	100.7	101.4	101.6	100.9	

Surface	Sample:	JL-15							
		Olivine 1	Olivine 2	Olivine 3	Orthopyx 1	Orthopyx 2	Orthopyx 3	Clinopyx 1	Clinopyx 2
Atomic	**Si**	1.0	1.0	1.0	2.0	2.0	2.0	1.9	2.0
	Al	0.0	0.0	0.0	0.0	0.0	0.0	0.1	0.0
	Ti	0.0	0.0	0.0	0.0	0.0	0.0	0.0	0.0
	Fe	0.6	0.6	0.6	0.4	0.5	0.5	0.3	0.2
	Mg	1.4	1.4	1.4	1.4	1.4	1.5	0.9	0.9
	Ca	0.0	0.0	0.0	0.1	0.1	0.0	0.8	0.8
	Na	0.0	0.0	0.0	0.0	0.0	0.0	0.0	0.1
	K	0.0	0.0	0.0	0.0	0.0	0.0	0.0	0.0
	Cr	0.0	0.0	0.0	0.0	0.0	0.0	0.0	0.0
	Total	3.0	3.0	3.0	4.0	4.0	4.0	4.0	4.0
	% Forsterite	69.2	69.4	68.9					
	% Enstatite				73.5	73.4	74.5	46.5	45.1
	% Ferrosilite				22.7	24.0	23.1	13.3	12.4
	% Wollastonite				3.8	2.5	2.3	40.2	42.5
Oxide wt%	**SiO_2**	37.9	36.9	37.1	54.5	55.2	54.1	53.3	54.8
	Al_2O_3	0.4	0.1	0.5	1.0	0.9	1.0	2.1	0.8
	TiO_2	0.1	0.0	0.1	0.6	0.4	0.3	1.0	0.5
	FeO	27.6	26.8	27.3	14.8	15.8	15.0	8.2	7.8
	MgO	34.8	34.1	33.9	26.9	27.1	27.1	16.2	15.9
	CaO	0.1	0.0	0.0	1.9	1.3	1.2	19.5	20.8
	Na_2O	0.3	0.4	0.5	0.4	0.2	0.2	0.4	1.0
	K_2O	0.1	0.0	0.0	0.0	0.0	0.1	0.0	0.0
	Cr_2O_3	0.0	0.1	0.0	0.1	0.2	0.2	0.2	0.2
	Total	101.2	98.4	99.5	100.2	101.2	99.2	100.9	101.7

Surface	Sample:	JL-23							
		Olivine 1	Olivine 2	Olivine 3	Clinopyx 1	Clinopyx 2	Clinopyx 3		Plagioclase
Atomic	**Si**	1.0	1.0	1.0	1.9	2.0	2.0	**Si**	10.1
	Al	0.0	0.0	0.0	0.1	0.1	0.1	**Al**	5.8
	Ti	0.0	0.0	0.0	0.0	0.0	0.0	**Ti**	0.0
	Fe	0.6	0.6	0.5	0.2	0.2	0.2	**Fe**	0.1
	Mg	1.4	1.4	1.4	0.9	0.9	1.0	**Mg**	0.0
	Ca	0.0	0.0	0.0	0.8	0.8	0.7	**Ca**	2.0
	Na	0.0	0.0	0.0	0.0	0.0	0.0	**Na**	1.9
	K	0.0	0.0	0.0	0.0	0.0	0.0	**K**	0.1
	Cr	0.0	0.0	0.0	0.0	0.0	0.0	**Cr**	0.0
	Total	3.0	3.0	3.0	4.0	4.0	4.0	**Total**	20.0
	% Forsterite	70.9	71.9	72.8				**% Albite**	48.4
	% Enstatite				47.3	46.4	51.9	**% Anorthite**	49.5
	% Ferrosilite				12.3	11.5	10.8	**%Orthoclase**	2.0
	% Wollastonite				40.4	42.1	37.3		
Oxide wt%	**SiO_2**	37.9	37.5	38.4	52.6	53.0	53.2	**SiO_2**	54.7
	Al_2O_3	0.0	0.0	0.2	2.1	1.4	1.8	**Al_2O_3**	26.8
	TiO_2	0.0	0.0	0.0	0.8	0.5	0.4	**TiO_2**	0.2
	FeO	26.2	24.8	24.7	7.5	7.0	6.5	**FeO**	0.6
	MgO	35.8	35.6	37.0	16.2	15.9	17.6	**MgO**	0.1

	CaO	0.1	0.1	0.2	19.2	20.1	17.6	**CaO**	10.1
	Na_2O	0.2	0.3	0.2	0.4	0.5	0.3	**Na_2O**	5.4
	K_2O	0.0	0.0	0.0	0.0	0.0	0.0	**K_2O**	0.4
	Cr_2O_3	0.3	0.0	0.0	0.5	0.2	0.8	**Cr_2O_3**	0.0
	Total	100.6	98.4	100.5	99.2	98.6	98.2	**Total**	98.4

Surface	Sample:	JL-20		
		Olivine 1	Olivine 2	Clinopyx 1
Atomic	**Si**	1.0	1.0	2.0
	Al	0.0	0.0	0.1
	Ti	0.0	0.0	0.0
	Fe	0.5	0.6	0.2
	Mg	1.4	1.4	0.9
	Ca	0.0	0.0	0.8
	Na	0.0	0.0	0.1
	K	0.0	0.0	0.0
	Cr	0.0	0.0	0.0
	Total	3.0	3.0	4.0
	% Forsterite	72.6	71.2	
	% Enstatite			45.3
	% Ferrosilite			11.5
	% Wollastonite			43.2
Oxide wt%	**SiO_2**	37.1	38.3	53.1
	Al_2O_3	0.4	0.1	1.3
	TiO_2	0.1	0.2	0.7
	FeO	24.4	25.9	7.2
	MgO	36.1	35.9	15.9
	CaO	0.0	0.1	21.1
	Na_2O	0.3	0.4	0.7
	K_2O	0.0	0.1	0.0
	Cr_2O_3	0.1	0.0	0.4
	Total	98.5	100.9	100.3